Approaches to Monitoring Dissolution, both on the Surface and in the Bulk

AYRES, CHARLOTTE,LOUISE

Approaches to Monitoring Dissolution, both on the Surface and in the Bulk

By Charlotte Louise Ayres

A thesis submitted in fulfilment of the requirements for the degree of

Doctor of Philosophy

Department of Chemistry, Durham University

2021

Abstract

Dissolution of tablets into their component parts is an important method by which orally-administered formulations are assessed by the pharmaceutical industry. Analysis of dissolution is routinely performed using UV-Vis spectroscopy, which enables compounds containing chromophores to be monitored in the bulk dissolution media. Two additional techniques for monitoring dissolution have been explored with a plan to improve analytical resolution and enhance mechanistic understanding.

The first technique explores surface dissolution imaging (SDI) through UV-Vis technology. Dual-wavelength imaging equipment was used to record changes occurring at the interface between a chromophore-containing solid and a liquid during dissolution. The SDI technique was successfully applied to single crystals, solvates and gels allowing physical and concentration changes to be monitored concurrently. Image analysis software was additionally applied to the UV-Vis absorbance data and the relative stability of a series of solvates was determined.

The second technique monitors dissolution using mass spectrometry (MS) of the bulk liquid. The detection and quantification of a range of APIs and excipients (with and without chromophores) was achieved. Analysis of multiple components by MS without chromatography was found to be subject to significant variability as a result of ion suppression and ion enhancement phenomena. These effects were explored in a step-wise manner to determine the impact of interference and the potential for developing a robust instrumentation configuration to monitor dissolution on-line and in real-time.

The work concludes that each technique has the potential to enhance our understanding of dissolution: SDI through visualising the changes occurring directly in-between the solid and liquid, and MS by enabling the monitoring of soluble excipients in addition to APIs. Although SDI and MS both have limitations preventing their use in conventional dissolution monitoring, each offers a unique opportunity to guide the research and development of new chemical entities and formulations, particularly those exhibiting challenging poorly soluble behaviour.

Supervisory Team

Durham University, Chemistry Department: Professor Jonathan W. Steed

Previously of Durham University, Division of Pharmacy: Dr David J. Berry

Industrial team at AstraZeneca: Dr James Mann, Dr Andy Ray and Dr Stephen Wren

Declaration

The work presented in this thesis was undertaken at Durham University Division of Pharmacy and Durham University Chemistry Department between October 2014 and August 2020. It is the original work of the author except where otherwise stated or acknowledged. No part of this thesis has been submitted for any other degree in this, or in any other university.

Statement of Copyright

Financial Support

Thank you to AstraZeneca and the Engineering and Physical Sciences Research Council (EPSRC) for their funding.

Additional Support

Thank you to Durham University Chemistry Department (Dr Jackie A. Mosely) and Division of Pharmacy (Dr David J. Berry) for providing me with the initial opportunity to undertake this research.

Thank you to Professor Jonathan W. Steed of Durham University Chemistry Department for accepting me into the Steed Research Group and for continuing to support this research.

Thank you to Professor Andy Husband for providing me with honorary membership of Newcastle University School of Pharmacy.

Thank you to Professor Jesper Ostergaard (University of Copenhagen), Dr Jim Lenke, Breeze Outhwaite and Hayley Watson for support with the SDi2 equipment and understanding. Thank you to Dr Daniel Markl at the University of Strathclyde and Dr Marion Weinzierl at Durham University Advance Research Computing for support with MATLAB analysis. Thank you to Dr Dmitry Yufit for support with the Single-Crystal XRD equipment and understanding. Thank you to Neil Holmes and Paul White of the Chemistry Engineering Workshop for producing dissolution frames, SDi2 lids and single crystal holders. Thank you to George Rodgers at Silicone Engineering, Blackburn for the samples and information.

Acknowledgements

Thank you to all those who believed in me along the way! As with many challenges in life, this has been a team effort in so many a sense. It has been quite the journey, with lessons and losses at every turn, but an incredible amount of joy too, and I could not have reached the end without the love, support and belief of so many special humans. Here are just a few of them:

To my husband, Phil, our rainbow boy, Rudy, and the rest of our family (Tolly, Alfie, Duggee, Rosie and the chickens) – thank you for being there to cry on, laugh with and remind me of what was truly important when I forgot. To my ridiculously patient and loving mother – thank you for never even for a moment doubting that I could do this. To my first "proper" chemistry teacher, Mr Ayres (also known as Dad) – thank you for inspiring and nurturing my love of science. To my siblings, Megan and David, and Westy and Caitlin, and my brand new beautiful niece, Elfine – I hope you're enjoying the sunshine at either end of this crazy world, we will be coming for holidays soon, no excuses now. To Laura, Tom and Leo – your love and support, as always, was there whenever I needed it no matter what else the world was throwing at you and for that I am so grateful. And also to Grandma, for leading me back to the North East.

Thank you for trusting in me, Jon, and helping me to believe in myself (eventually). Dave, Rach, Will and Tom – what a journey this was, I am so grateful for your support. To the AstraZeneca team: Stephen, Andy, James and Tony – I am hugely grateful for all your expertise, time, honesty and belief, although I realise I took far more than my fair share. Pete, Dave, Vian, Andy and Chris – we made it, and thank you for your endless patience with my many questions. To Jim Lenke – thank you for accepting my out of the blue message and generously offering your time and expertise to support me from the other side of the world, especially in the middle of a pandemic. To the Queen's Crew – thank you for letting me be an honorary member. And to the GEL squad (past and present) – I am so grateful for being welcomed so whole-heartedly into such a supportive research group. To the Durham Uni IT team, particularly Craig Condron, Chris Kiddle and Alan Harland – you are superheroes. As are the Durham Uni Counselling Service, especially Caroline, thank you so much for truly listening.

Dr Hannah, Dr MJ, Dr Milly, Dr Catey, Dr Jane, Dr Alecia, Dr Tal, Dr Brette, Dr Jess, Dr Amy, Dr James and Dr Tavleen – each of you amazing humans showed me that this could be done in spite of any barrier, and inspired me to keep going when things got tough, thank you from the bottom of my heart! To the MI and the YM book club – thank you for your friendship and listening to me whine about this for so long (I promise not to make you read it). Emma – your friendship, cakes and love were such a huge part of pulling me through, and Kathy – your love and care for both me and my bundle of trouble made it possible to actually do so much of this work, thank you both for believing in me. To the incredible Hartlepool Tri Club, in particular Darrel, Kirsty, Hannah, Sam and Sarah – thank you for the opportunities to escape from my mind. To all the wonderful humans that supported me with becoming a mother, breastfeeding and surviving with a toddler – I'm particularly looking at you Neda, Lorraine, Emilie and La Leche League – thank you! To Louise and Eli for the many dog walks and chats at the very start of this journey. To all the Pharmacy Ladies, particularly my Saturday buddies, Shak and Ellie, for keeping me smiling (and young, ish). To Hartlepool Petpals for your time and care, not just of Alfie, but the whole family. And finally, to Dr Polly – the very first person to believe that I could do this… how much do I wish that you were here to celebrate with a glass of wine (or a G&T) and some Grey's?! I miss you!

This thesis is dedicated to Rudy; never let anyone tell you what you can or can't achieve in life, but may you spend it following your dreams rather than chasing pieces of paper!

"Things falling apart is a kind of testing and also a kind of healing. We think that the point is to pass the test or to overcome the problem, but the truth is that things don't really get solved. They come together and they fall apart.

The healing comes from letting there be room for all of this to happen: room for grief, for relief, for misery, for joy."

Pema Chödrön

Table of contents

List of abbreviations

API	Active Pharmaceutical Ingredient
BP	British Pharmacopoeia
BCS	Biopharmaceutics Classification System
CEM	Chain Ejection Model
CI	Chemical Ionisation
CRM	Charged Residue Model
DC	Direct Current
EI	Electron Ionisation
ESI	Electrospray Ionisation
FaSSGF	Fasted State Simulated Gastric Fluid
FaSSIF	Fasted State Simulated Intestinal Fluid
FDA	Food and Drug Administration
FeSSGF	Fed State Simulated Gastric Fluid
FeSSIF	Fed State Simulated Intestinal Fluid
GC/MS	Gas Chromatography Mass Spectrometry
GI	Gastro-intestinal
GTP	Gamlen Tablet Press
HPLC	High Performance Liquid Chromatography
ICH	International Classification Harmonisation
ID	Inner Diameter
IEM	Ion Evaporation Model
IM	Intra-muscular
IR	Infra-red
IV	Intravenous
LC MS	Liquid Chromatography Mass Spectrometry
LED	Light-emitting Diode
LGC	Laboratory of the Government Chemist
LI MS	Loop Injection Mass Spectrometry
MALDI	Matrix-Assisted Laser Desorption / Ionisation
MRA	Mass Rate Attenuator
MS	Mass Spectrometry
MS/MS	Tandem Mass Spectrometry
NMR	Nuclear Magnetic Resonance
OTC	Over The Counter
PEEK	Polyetheretherketone (non-fluoropolymer tubing)
PhEur	European Pharmacopoeia
PVP	Povidone / Polyvidone / Polyvinylpyrrolidone
QA / QC	Quality Assurance / Quality Control
QDa	Acquity QDa Detector
RF	Radio Frequency
SC	Subcutaneous
SGF	Simulated Gastric Fluid
SIF	Simulated Intestinal Fluid
SIM	Selected Ion Monitoring

SMM	Small Molecule Mix
TIC	Total Ion Current
TICC	Total Ion Current Chromatogram
TOF	Time-of-Flight
UPLC	Ultra High Performance Liquid Chromatography
USP	United States Pharmacopoeia
UV-Vis	Ultra-Violet Visible Spectroscopy

List of conferences and posters

British Mass Spectrometry Society Conference, 2015, poster: “Monitoring tablet dissolution by mass spectrometry: developing an understanding”.

AstraZeneca, PhD day, 2018, poster: “Monitoring tablet dissolution by mass spectrometry: exploring API and excipient relationships".

Macrocyclic and Supramolecular Chemistry Conference, 2018, poster: “Dissolution as a means to rank stability”.

AstraZeneca, PhD day, 2019, flash presentation: “Dissolution: a means to rank stability”.

1. Introduction

1.1 General introduction to dissolution

Dissolution in a technical context is the action or process of solvation, and can be broadly defined as the mixing of two phases to produce a new homogeneous phase known as a solution.[1,2] In the context of this work, the new phase is a liquid containing one or more initially solid solutes and one or more liquid solvents, with solvation defined as the formation of stabilising interactions between solute(s) and solvent(s).[1] Dissolution is a kinetic process and is therefore distinct from solubility, which concerns the end result of a thermodynamic equilibrium*.[3,4] While the relevance of dissolution testing spans multiple settings from pure chemistry to engineering and geology, the majority of this work will consider solutes of pharmaceutical relevance.[5–7]

Dissolution testing is used routinely throughout pharmaceutical development to understand the rate at which a solid-state active pharmaceutical ingredient (API)† enters a solution. This may involve its release from a dosage form‡ but may also concern the API alone.[3,8,9] The purpose of the test has evolved from solely providing a quality control check in batch release, to additionally being used in the prediction of clinical performance.[10,11] In line with this expanding role, dissolution methodologies are continuously developed to improve analytical resolution and enhance mechanistic understanding.[12,13]

This work considers two approaches to monitoring dissolution: (i) surface dissolution imaging using UV-Vis and (ii) bulk dissolution monitoring using mass spectrometry. Surface dissolution imaging uses UV-Vis technology to record the changes occurring at the interface between a solid and liquid.[13] The recently developed equipment captures an image each second, with a novel detector chip providing spatially resolved

* Thermodynamic equilibrium refers to a fixed temperature (and pressure) with no chemical reactions or transfer of matter taking place and therefore no spontaneous change occurring.

† The API may also be referred to as the drug substance and is defined as the chemical which exerts the pharmacological effect on the patient. API and drug substance will be used interchangeably throughout this work.

‡ The dosage form is the drug or pharmaceutical product, medicine or formulation which includes excipients and enables the API to be administered to the patient. Dosage form, drug product and formulation will be used interchangeably throughout this work.

absorbance values. This enables concentration and physical changes to be monitored throughout dissolution, with the potential to apply this to a variety of solutes, including single crystals and gels. Mass spectrometry (MS) is an analytical technique historically associated with significant cost and expertise.[14] The development of user-friendly equipment has led to its application within dissolution monitoring whereby the solvent (or dissolution media) is analysed as a dosage form dissolves.[15] Unlike UV analysis, MS has the potential to monitor components without a chromophore and may allow an enhanced mechanistic understanding of dissolution, particularly in relation to the role of excipients in drug release.

Each technique offers a different perspective to monitoring dissolution, either through focussing solely on the interface, or through observing changes in the solvent bulk. These contrasting approaches also present distinct challenges. The introduction to this research begins with the theory underpinning dissolution, solubility and crystallisation, before discussing conventional methods for dissolution testing in the pharmaceutical industry, and then moves on to the fundamentals of UV technology and MS equipment. The aims and objectives are clearly divided into those relevant to surface dissolution imaging and those specific to MS. The overall purpose of the research is to explore both the benefits and the limitations of using each approach to further the current understanding of dissolution.

1.2 Mechanisms, models and theory

A brief exploration of the formation of solids can be considered fundamental to understanding their subsequent dissolution. This section will therefore begin by outlining the solid forms landscape before describing crystallisation and polymorphism, and their relevance to the pharmaceutical industry. A summary of the relationship between solid state and solubility will be discussed before delving into the subsequent impact that these properties have upon dissolution. The mechanisms of disintegration and deaggregation will also be explored before, finally, the many models describing the foundations of dissolution are examined.

1.2.1 Solid forms landscape

A macroscopic solid material, such as an API, is comprised of molecules that may be arranged in a variety of ways; the packing of these molecules and the interactions between them determine its properties and form the basis of crystal engineering.[16] This is a complex topic of the utmost importance to the pharmaceutical industry for formulation and drug delivery, as well as intellectual property considerations.[17] An outline of the solid forms landscape can be seen in Figure 1.1, and while the majority of these materials fall outside the scope of this work, they constitute a vast area of research and have wide-reaching implications independent of the pharmaceutical industry.

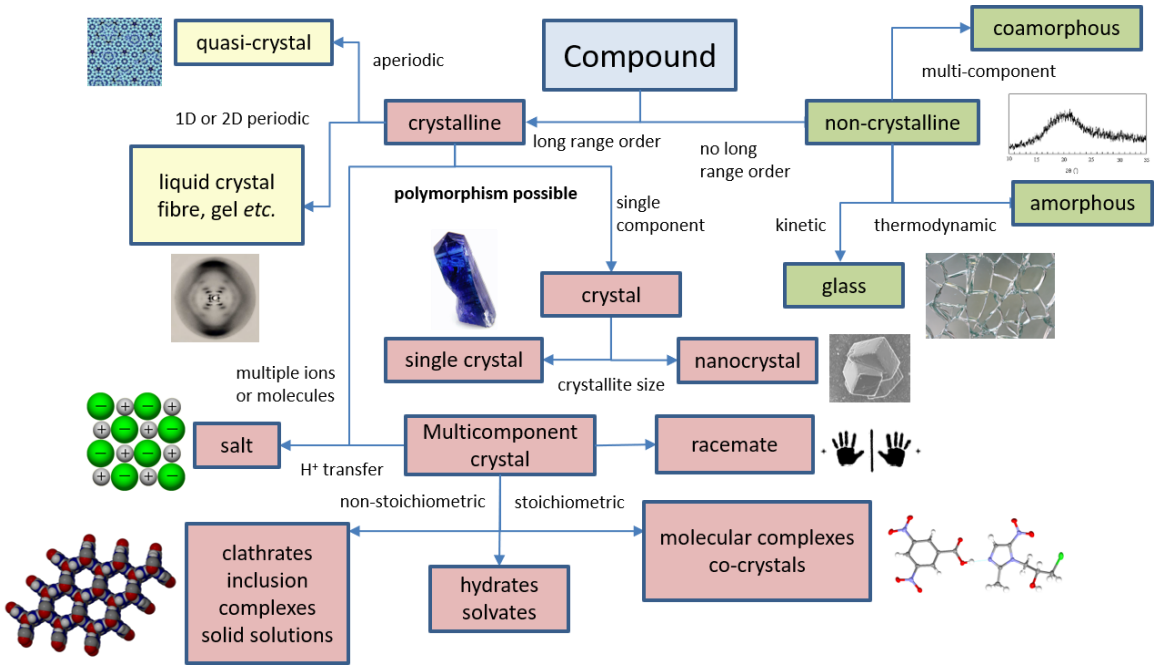

Figure 1.1 - Solid forms landscape for molecular materials, reproduced with permission.[16]

New candidates for pharmaceutical development are screened at an early stage to determine the variety of solid forms available and their subsequent chemical, physical and biopharmaceutical properties.[18] Typically this process includes consideration of stability, dissolution and manufacturability and involves both experimental and computational methods to ensure the most appropriate form is selected for development.[19–21] There are examples of solid-state transformations occurring both during development and also after reaching the market, which have had a serious impact upon efficacy and therefore patient safety.[8,22] Detailed solid-state

characterisation early in development is therefore desirable for scientific and intellectual property purposes, as well as being essential for safety and regulatory requirements.[23–25]

1.2.2 Crystallisation, polymorphism and amorphous material

Historically, crystalline material has been selected for development due to its long range order, which enables ease of characterisation, reproducibility and stability, relative to its amorphous counterparts.[26] The formation of crystalline materials most commonly occurs as a non-equilibrium phenomenon from a supersaturated solution and is best explained through two key steps: nucleation and growth.[27] Nucleation is often divided into two categories: primary, which can be homogeneous or heterogeneous, and secondary, see Figure 1.2. Currently it is a poorly understood process with both classical and non-classical theories available to describe the spontaneous formation of a solid phase. The common theme for nucleation theory is that within a supersaturated solution there is a dynamic assembly and dissociation of component molecules or ions encountering, recognising each other and aggregating into nuclei of varying size.[16,28]

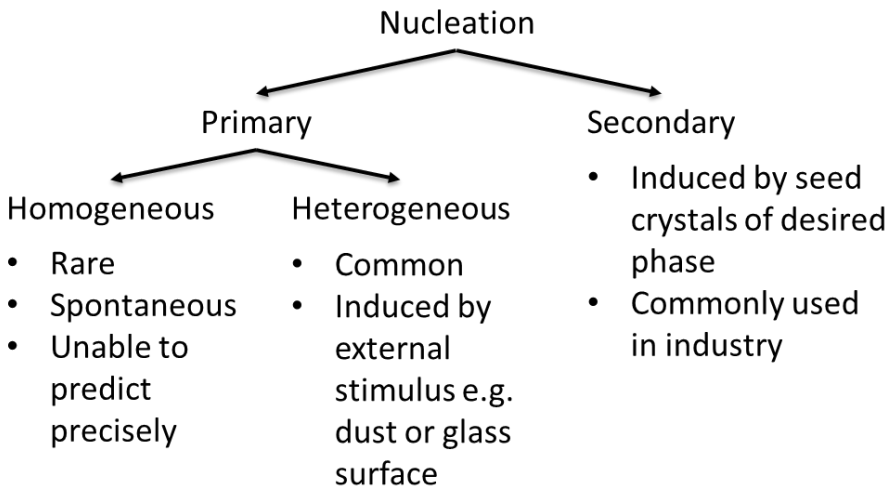

Figure 1.2 – Nucleation categories and their definitions.

Classical nucleation theory (CNT) states that one of these nuclei will eventually exhibit more than transient stability by forming at a critical size whereby the energy required to form a new and unstable solid-solution interface is recoverable from the free energy gain (stability) of creating a bulk crystalline material.[16] In CNT these initial nuclei are

considered to be spherical, and have the same density, structure and composition as the final crystal structure.[29] The most relevant non-classical theory suggests that nucleation may actually be a two-step process, with formation of an initial disordered precursor as a dense liquid phase, prior to the appearance of a crystalline nucleus.[30,31] An outline of these two models is summarised in Figure 1.3.

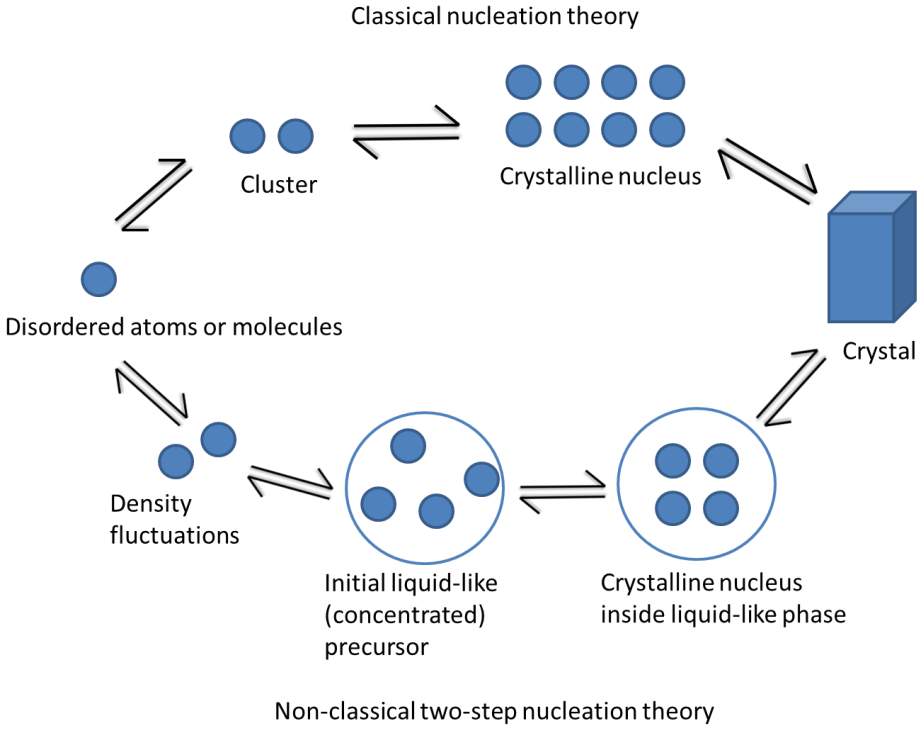

Figure 1.3 - Classical nucleation theory (top pathway) and the two-step (bottom pathway) non-classical nucleation model.

Following nucleation, further molecules accrete on the surface of a stable nucleus within a solution allowing it to evolve into a macroscopic crystalline solid.[16] Crystal growth is then considered in terms of two steps: i) mass transport of solute ions or molecules from the bulk environment through a boundary layer to the crystal surface, followed by ii) their incorporation into the crystal.[32,33] There are a number of theories to explain this growth, with the exact mechanism through which it occurs dependent upon two factors: supersaturation of the solution in which it is growing and surface roughness of the crystal.[16,34] An increasing level of supersaturation is thought to increase surface roughness, which in turn influences the ability of the growth unit to incorporate into the crystal, and enables multilayer growth mechanisms to occur simultaneously thereby influencing surface roughness.[16] Additionally, at higher levels

of supersaturation there is increased free energy available to form interfaces, thus the critical nucleus size for runaway growth to occur is smaller.

The resulting structures are ultimately influenced by both kinetic and thermodynamic contributions, and the processes of nucleation and growth may therefore result in the formation of varying structures, both crystalline and non-crystalline. Crystalline solids may appear as polymorphs, whereby long range order remains but the molecules are packed differently. Alternatively amorphous material may be produced, defined by a lack of periodicity, which results in materials that are typically less thermodynamically stable and exhibit faster dissolution than their crystalline counterparts.[16,35] Ostwald's Rule of Stages states that typically the least stable polymorphic form will form first (dominated by the first to nucleate), with increasingly stable modifications produced in stages.[36] The free energy associated with metastable forms means that they are expected to be more soluble than their corresponding stable polymorphic form at any given temperature; this includes amorphous material which would generally be expected to have the highest solubility.[35,37–39] Therefore, in understanding the formation of solids, we are conversely provided with insight into the dissolution and solubility of a substance, and vice versa. However, it is important to note that these processes are not simply opposites.[4]

1.2.3 Solubility

The USP dedicates a general chapter to the topic of solubility and defines equilibrium solubility as "the concentration limit, at thermodynamic equilibrium, to which a solute may be uniformly dissolved into a solvent when excess solid is present".[40] It measures the capacity of a solvent to hold solute and can be considered an end-point, with dissolution describing the process through which one arrives there.[3,4] If an equilibrium is unable to be achieved then any measure of solubility is termed 'apparent'; it may be transiently higher if conditions enable supersaturation but may also be reduced if insufficient time is allowed for the solute to dissolve to completion.[40] Equilibrium solubility is therefore dependent solely upon these previously described intermolecular interactions (solute to solute, solvent to solvent and solute to solvent), whereas apparent solubility can be affected by numerous properties including the conditions of measurement, see Figure 1.4.[4,40,41]

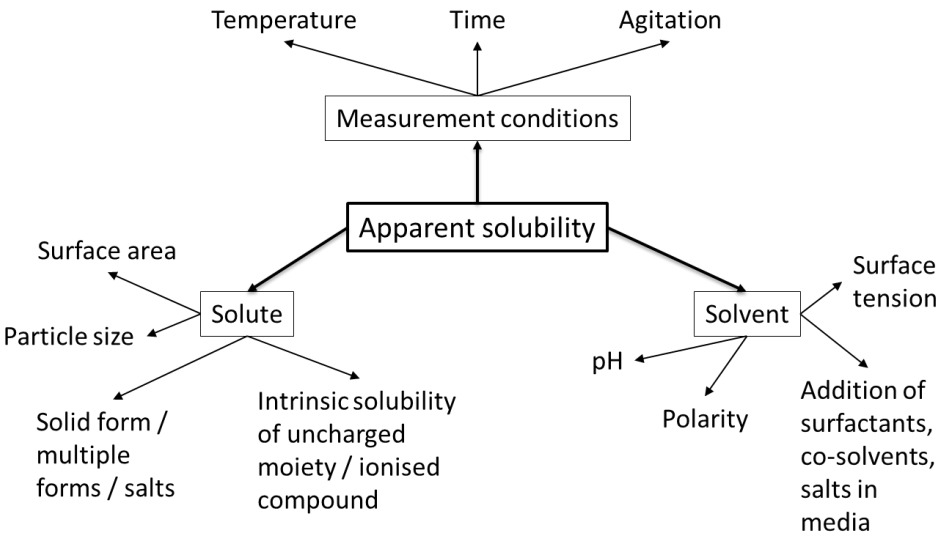

Figure 1.4 – Summary of factors affecting apparent solubility of a solute in solvent where equilibrium solubility has not been attained or verified.

The resulting solution may contain either the original solute chemical entity, which might be fully recoverable unaltered by dissolution, or it may contain a compound that is different from the original solute, as a result of ionisation, for example.[4] These considerations must be taken into account when obtaining solubility measurements, as well as when observing dissolution of a substance. In the case of ionisable acids and bases, measurements will be further influenced by the presence of salts or counter-ions within the solvent or dissolution media.[42–44]

The process of dissolution can also initiate solid state changes, hence an understanding of the polymorphic landscape is crucial when determining solubility.[18,45,46] Historically, transformations between forms during experimental studies have made it challenging to produce reliable estimates for solubility and dissolution enhancements of solid-state modifications, particularly when considering amorphous compounds.[35,38,47,48] The kinetics of these solution-mediated phase transformations were initially modelled by Cardew and Davey in 1985 and reported as a balance between dissolution of a metastable form and growth of a relatively stable form (or forms) at supersaturated concentrations.[45,49–52] This remains relevant to dissolution today as the use of high throughput methods in drug discovery has led to an increase in new molecular entities (NME) with less favourable characteristics, such as poor solubility.[53] One strategy has

therefore been to utilise a range of solid-state modifications including polymorphs[§], salts, cocrystals and more recently coamorphous systems in the search for compounds with appropriate characteristics for development.[45,54–56] This requires an understanding of the relationship between intermolecular interactions and physical form, as well as how this influences solubility, dissolution rate and bioavailability, in addition to stability and manufacturability.[18,25] The pharmaceutical industry has therefore been a key driver in developing the ability to predict and control solid state properties, so that the physicochemical properties of a compound may be modified without impacting upon its pharmacology.[54,57,58]

1.2.4 Dissolution

Dissolution has already been distinguished from solubility by describing it as the process through which a molecularly dispersed homogeneous solution is produced from a solute and solvent.[4] It would therefore follow that the initial solute must reduce in size, which may occur through the additional steps of disintegration and deaggregation.[3] Disintegration, as defined by Markl and Zeitler, is "the mechanical breakup of a compressed tablet into small granules" and includes a range of mechanisms through which interparticulate bonds are broken.[59] Deaggregation, however, is a less well understood process, defined as the "chain of events wherein particle aggregates from the tablet disintegration process are further subdivided into smaller aggregates".[60] Dissolution and disintegration may occur concurrently or in succession, and their relationship is outlined in Figure 1.5.

[§] The International Conference on Harmonisation (ICH) and the US Food and Drug Administration (FDA) classify polymorphs as including anhydrous, hydrate and solvate forms.[18]

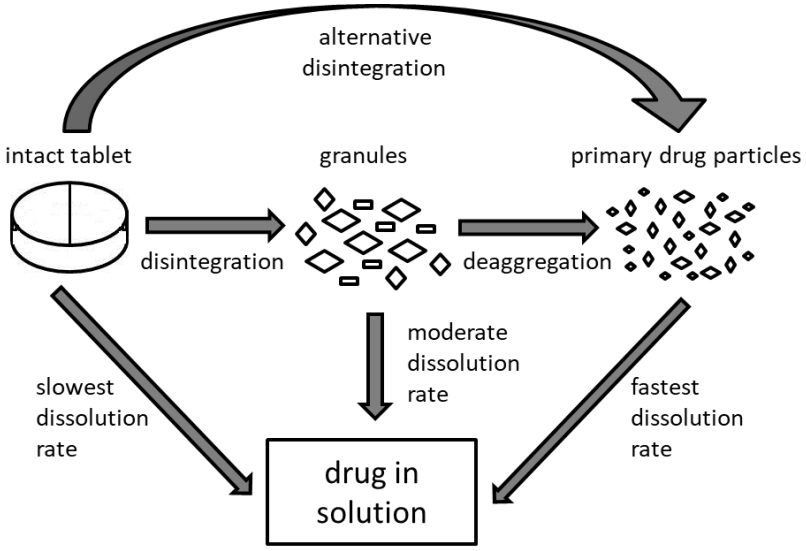

Figure 1.5 – The relationship between disintegration, deaggregation and dissolution when considering an immediate release orally administered solid formulation.

Historically, disintegration of the dosage form was considered the limiting step for a drug to exert a pharmacological effect, so official disintegration tests were published as early as the 1930's by the Swiss Pharmacopoeia (Helvetica) and adopted in 1950 by the US.[61,62] The disintegration test remains a valuable tool today and a variety of excipients are available to initiate disintegration via multiple mechanisms.[59,62–65] The relevance of disintegration and deaggregation to dissolution is clear: to increase the effective surface area of solute exposed to the solvent.[60] However, neither complete disintegration nor complete deaggregation implies that dissolution has occurred, hence an additional understanding of the solubility of the drug substance is of significant importance.[41]

The theory of dissolution mechanisms arguably began with the first law of diffusion defined by Fick in 1855.[66] This defines the rate of mass transfer through a unit area in relation to a concentration gradient and describes diffusion mechanisms within liquids, whereby a solute moves from a region of high concentration to that of low concentration.[66] Physical scientists, chemical engineers and eventually pharmaceutical scientists expanded upon the diffusion layer concept and defined equations, models and theories to incorporate interfacial transport and convection mechanisms.[67–72] However, it was not until the 1950's that dissolution was linked to the absorption of orally administered medication and bioavailability.[61,73,74] It took a further ten to

twenty years for the impact of formulation upon dissolution to be realised, with the first United States Pharmacopoeial (USP) guideline for setting dissolution standards published in the 1970s.[9,75,76] An extensive history of dissolution research, from 1897 to 2006, has been detailed by Dokoumetzidis and Macheras; consequently, only the theory and models pertinent to this work will be outlined.[61]

Assuming disintegration and deaggregation occur readily, dissolution can be considered a heterogeneous process in which a transformation takes place at the phase boundary between solid and liquid.[2,60] In Physiochemical Hydrodynamics, Levich breaks this down into three steps:

i) movement of reacting particles from the bulk solid to the reaction surface,
ii) chemical transformation of the reacting particle into a dissolved particle on the surface, and
iii) the transfer of products away from the reaction site.[77]

This simple explanation focusses on the chemistry of dissolution, however, it can also be considered in terms of the more complex processes taking place. In 2013, Siepmann and Siepmann further separated dissolution into five physical phenomena:

i) wetting of the drug particle,
ii) breaking of solid state bonds within the drug particle,
iii) solvation of the individual drug molecules,
iv) diffusion of the individual solvated drug molecules through the boundary layers, and
v) convection within the well-stirred bulk dissolution media.[2]

These processes occur in series, and dissolution rate is limited by the step which occurs the most slowly. From a pharmaceutical sciences perspective there are commonly considered to be three models to explore when discussing immediate release formulations; the models were outlined by Higuchi in 1967 and are still relevant today.[8,78] The first is the diffusion layer theory, the second is Danckwert's model and the third is the interfacial barrier model.

The most commonly applied is the diffusion layer theory, which is the culmination of work carried out at the start of the 20th century and discusses only two parts.[67,72,70,61,2]

The first part is formation of a stagnant or boundary layer between the surface of the solid and the bulk of the liquid due to adhesive forces.[2] There is suggested to be negligible mixing within this film relative to the bulk solution, and Higuchi states that an equilibrium exists between the solid and liquid.[78] The second part involves diffusion of solute from an area of high concentration at the surface into the lower concentration bulk solution following Fick's first law.[2] Assuming the bulk solution undergoes sufficient agitation and remains at a concentration below saturation, then diffusion of drug across this boundary layer is considered the rate-limiting step.[2,78]

Danckwert's model, which is also referred to as the penetration and surface renewal theory, states that continuously renewed macroscopic packets of solvent access the solid-liquid interface and absorb solute by diffusion.[78] The packet of solvent with dissolved drug is then carried away into the bulk solution and new surfaces are exposed for the process to begin again.[79] In this model the rate-limiting step is convection of the dissolved drug and there is a requirement for eddies or turbulence to move the packets through the bulk.[78] Finally, the interfacial barrier model which is also termed limited solvation theory, considers that the reaction at the surface of the solid is not instantaneous and steps i) to iii) described by Siepmann and Siepmann, may be the rate-limiting processes rather than the mass transport mechanisms.[2,78]

In summary, the three models claim varying levels of importance for each of the suggested steps and are best considered in combination. Siepmann and Siepmann recommend using mathematical equations to quantify the mass transport steps and highlight appropriate strategies for overcoming poorly soluble immediate release formulations.[2] For example, the rate at which dissolution occurs ($\frac{dW}{dt}$) can be defined using Equation 1.1, and represented, with terms explained, in Figure 1.6.[3,8,77]

$$\frac{dW}{dt} = \frac{AD(C_s - C_b)}{h}$$

Equation 1.1 – Diffusion Layer Theory

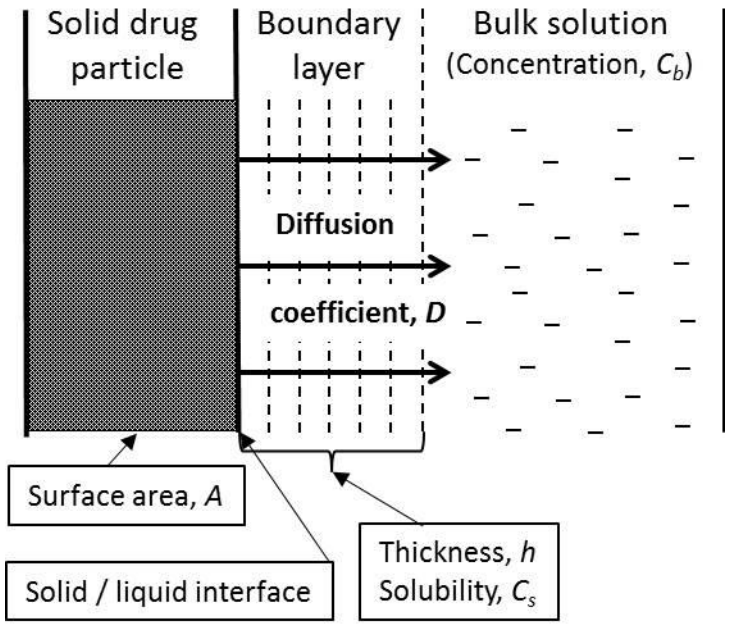

Figure 1.6 - Diffusion layer model for dissolution

Equation 1.1 is often expressed in multiple formats with varying terms and can be referred to as the Noyes-Whitney, Shchukarev or Nernst-Brunner equation.[67,77] It states that the amount of material dissolved per unit time is dependent upon the surface area available at the interface, the drug diffusion coefficient and the inverse of the boundary layer thickness in addition to a concentration gradient. The boundary layer is a well-defined parameter within the field of hydrodynamics and is based upon Nernst's Theory which states that immediately adjacent to the surface of a dissolving solid there will be an area of liquid which is at a saturated concentration.[72] Solute will move from this area of saturation (C_s) to the bulk solution (C_b) by molecular diffusion in a gradual process rather than a single step as Figure 1.6 might suggest.[2,80]

The boundary layer can be reduced in size or theoretically eradicated by amending the geometry of the test apparatus or the solvent flow (in the case of flow through cells) but predominantly the layer will be present.[80] In the case of conventional dissolution apparatus, the bulk solution is additionally agitated and undergoing macroscopic motion (flow) so it is thought to "entrain" solute particles from the boundary layer and transport them throughout the bulk solution by convection.[77] The combination of mass transport mechanisms are referred to as convective diffusion and the dissolution rate-limiting step(s) may vary depending upon intrinsic properties of the API and

numerous extrinsic conditions such as media viscosity. The impact of pH and common ion effects upon ionisable APIs can additionally result in an altered C_s at the interface, which may lead to reduced (or increased) dissolution rates, precipitation and phase transformations, hence the need for such extensive understanding of the API in development.[42,43,81]

Regardless of the model applied, dissolution is ultimately dependent upon many distinct but nevertheless connected processes occurring concurrently in order to produce a solution from a solid and liquid. Monitoring dissolution therefore involves reporting the extent of solid dissolving per period of time, and is dependent upon the initial interaction between solid and liquid, the stability of the dissolving solid (and the liquid dissolving it), physical and chemical properties of each component, and diffusivity, in addition to the experimental conditions. Observing different stages of the dissolution process will provide complementary information, hence, applying one technique to visualise the interface between solid and liquid, and another to analyse the bulk solution has the potential to deepen our understanding of the entire process.

1.3 Pharmaceutical research and development

Orally-administered immediate release tablets involve a solid dosage form entering the body via the gastrointestinal (GI) tract.[82] In simple terms the tablet is swallowed by the patient and progresses through the oesophagus into the stomach and intestines; the tablet must release API into solution along this route so that it is available for systemic absorption, usually via the small or large intestine, and thus able to exert a pharmacological effect on the patient[**].[2,83] It is important to note that absorption can only occur from a solution and is dependent upon the API crossing the gastrointestinal mucosa, which is termed permeability.[3,84] An API must therefore be soluble at the point of absorption, sufficiently stable in physiological fluids and present at a suitable concentration after any pre-systemic clearance (or first-pass metabolism).[3,83,85] The amount of API available for absorption and the rate or extent to which it is absorbed by the body is defined as bioavailability.[3] Dissolution, solubility, permeability and

[**] Absorption into the systemic circulation is key to exerting a clinical effect for the majority of orally-administered medication, however there are exceptions (e.g. loperamide to treat diarrhoea).

bioavailability are subject to a complex interplay between physicochemical and physiological properties, the details of which underpin the relevance and importance of dissolution testing to the pharmaceutical industry.[85–88]

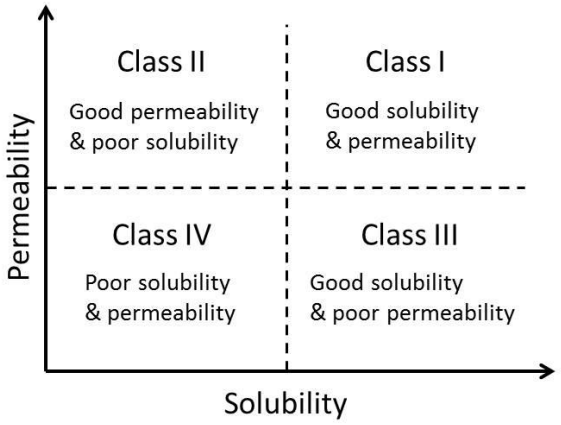

Figure 1.7 – The Biopharmaceutics Classification System (BCS). Good and poor and high and low are used interchangeably with respect to both solubility and permeability.

The pharmaceutical industry have historically used a framework named the biopharmaceutics classification system (BCS) to direct development by categorising APIs into four groups according to their dissolution, solubility and intestinal permeability[89], see Figure 1.7. Solubility is defined with regard to the highest dose to be administered and its ability to dissolve in aqueous media of 250 mL or less, over a pH range of 1.2 to 6.8 at 37 ± 1°C.[90,91] Permeability determination is comparatively complex and can be measured either directly *in vivo,* using human intestinal membrane or can be predicted with one of multiple systems dependent upon the stage of development.[90,92,93] Regardless of the method used, a highly permeable classification requires absorption to be 85% or more of the administered dose.[83,92] Additionally, rapid dissolution is achieved when "*85% or more of the labelled amount of drug substance dissolves within 30 minutes"* or very rapid when "*85% or more of the labelled amount of drug substance dissolves within 15 minutes*", with strict guidance on the dissolution set up including the media.[90,91] The BCS uses these definitions to provide insight into which key factor (dissolution, dose, permeability or solubility) is most likely to limit absorption and influence *in vivo* performance.[93]

The increasing pressure on pharmaceutical companies to bring medicines to market efficiently most often results in development of an API alongside both process and formulation.[94] A developability classification system (DCS) was proposed in 2010 and a refined developability classification system (rDCS) in 2018, to offer further suggestions regarding the use of BCS as a guide for API and oral formulation development.[93,95] However, the manufacture, purification or processing of an API (or formulation) may be adjusted during development to improve environmental impact, cost efficiency or as a consequence of scale up.[94,96] This may result in altered particle size distribution or morphology, hence a complete understanding of physicochemical properties may not be possible.[97–99] A quality by design (QbD) approach to development therefore encourages the rational development of medicines based on a mechanistic understanding of both product and process.[63,100] Specifications and controls on input materials (APIs, excipients etc) and process parameters are incorporated throughout development based on understanding and are used in conjunction with end product testing to ensure consistency of product.[101] Evaluating dissolution is therefore key to defining many of these critical quality attributes and takes place throughout development to aid mechanistic understanding, decision-making and *in-vitro-in-vivo* correlations, as well as at the end of routine manufactures to demonstrate quality and consistency of batches and ensure the safe and effective delivery of medicine to patients.[10,61,88,102]

1.3.1 Role of excipients

Formulating an API into an appropriate dosage form often includes the addition of other substances known as excipients, which by definition should have little or no pharmacological effect.[103,104] Orally-administered immediate release tablets are routinely manufactured with excipients for a variety of reasons, see Table 1.1.[3] The selection of excipient(s) requires scrutiny and rigorous testing to ensure compatibility with the API(s) and to understand the impact on bioavailability, formulation, manufacturing and stability.[99,103,105–108] Discussing the various roles of excipients in detail is outside the scope of this work, but it is relevant to note that one excipient may have multiple functionalities and may also in some cases be used as an API[104]; as

such excipient monographs contain functionality-related characteristics for guidance in addition to identity and purity regulations.[109]

Table 1.1 - Commonly used excipients in immediate release oral tablets[110]

Type of excipient	Common use in tablets	Examples
Lubricant	Manufacturability e.g. to aid flow during compression	Magnesium stearate – hydrophobic so may impact upon wetting and delay dissolution
Disintegrant	Improve bioavailability e.g. to aid tablet breaking up	Croscarmellose sodium – hydrophilic and highly absorbent, used to enhance disintegration
Diluent or filler	Manufacturability e.g. for better homogeneity and weight variability	Lactose, mannitol, microcrystalline cellulose – chosen to have limited effect on dissolution although they may help to improve wettability
Binder	Manufacturability e.g. to prevent tablet falling apart	Povidone – water-soluble, limited impact on dissolution
Coating	Patient acceptability e.g. for taste-masking or appearance	Hydroxypropylmethylcellulose (HPMC) – can be modified to delay dissolution

The presence of excipients within a formulation has the ability to inhibit or enhance dissolution, either by design or as a result of complex interactions (chemical, mechanical or physical) within the manufacturing process or with other components.[111–113] In very simple terms, as a tablet disintegrates the excipient(s) and

API will break free from the tablet structure and exist within the dissolution medium as either solid particles, as solute or as a combination of both. The ability to monitor release of excipients in addition to API could therefore be used to improve mechanistic understanding of the entire dissolution process and draw conclusions as to whether the rate-limiting step is disintegration of the dosage form or dissolution of the API.[19-21]

1.3.2 Dissolution testing methods

Conventional dissolution testing methods report the temporally-resolved percentage of drug dissolved for a dosage form.[114] Figure 1.8 shows a theoretical dissolution plot for an orally-administered immediate release tablet with a very rapid release rate. Profiles can provide information on API release kinetics in addition to the extent of dissolution, assuming samples are taken regularly.[115] Additionally they may highlight differences that can be attributed to formulation or manufacturing deviations, for example an altered drug substance particle size distribution or a variation in compression force during tabletting.[115]

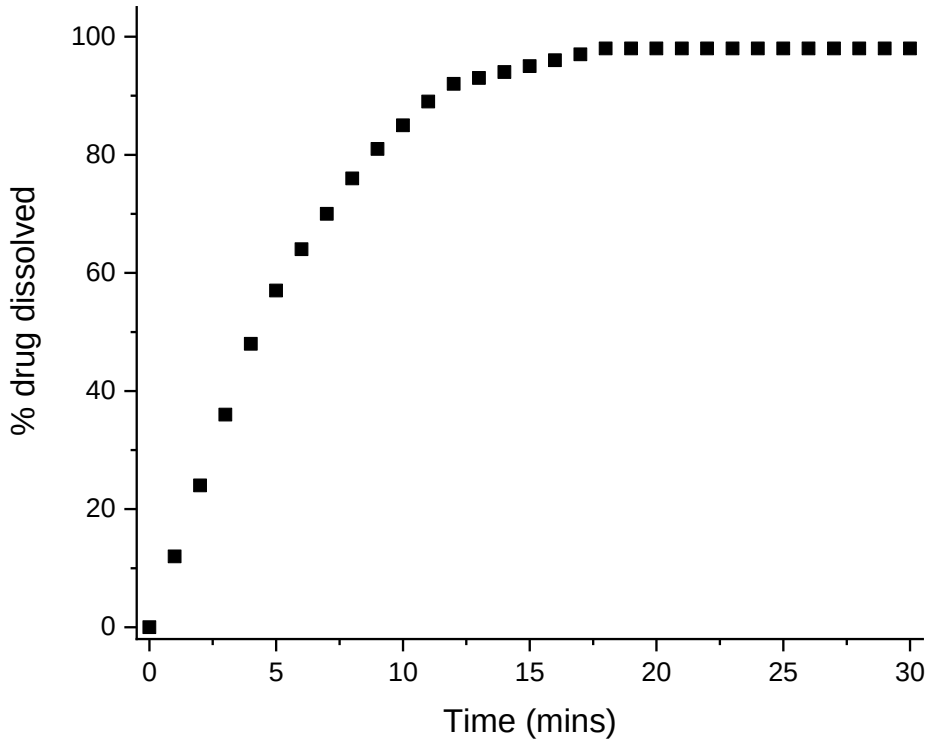

Figure 1.8 – Theoretical dissolution plot showing the percentage of drug dissolved versus time in minutes. Sampling has taken place every minute for a total of thirty minutes. Very rapid dissolution has been displayed by the dosage form, with more than 85% of the drug dissolved in less than fifteen minutes.

The United States, British and European Pharmacopoeia detail several methods for the dissolution testing of routine formulations, with an increasing emphasis on novel formulations.[114,116,117] For immediate release oral solid dosage forms the most commonly used techniques are the basket (apparatus I) or the paddle (apparatus II), and in special circumstances, the flow-through cell (apparatus IV).[40,114,118,119] A reciprocating cylinder (apparatus III) also exists although it is primarily used for modified release formulations.[40,120,121] The apparatus used depends on the characteristics of the dosage form under investigation and the reason for the testing.

The most appropriate compendial dissolution method for a drug is established during development and strictly defined in quality control (QC) methods to ensure patient safety and efficacy of the end product. Extensive information is therefore required regarding the methods used, see Table 1.2 in addition to the exact measurements of the equipment and any sampling points. This detail provides some assurance that dissolution measurements are comparable, and is listed in individual drug monographs to ensure clear guidance on the acceptance criteria for oral formulations.[40,121]

Table 1.2 – Details required for dissolution testing.

Method parameter	Details required
Apparatus used	Basket Paddle Flow-through cell (detail of design)
Dissolution medium	Composition, including pH Temperature (37 ± 0.5°C) Volume
Agitation / hydrodynamics	Rotation speed (basket or paddle) Position of basket / paddle / sampling Geometry of flow-through cell Flow rate of dissolution medium (flow cell)
Timings	Frequency of sampling, or Method for continuous monitoring
Analysis	Sample preparation(s) required Method(s) used Active ingredient(s) dissolved per time period

During development, however, a wider range of method parameters are used, particularly with a view to establishing a link with *in vivo* behaviour.[88,102] Alternative apparatus may be used to further mimic *in vivo* conditions, for example the TNO Gastro-Intestinal Model (TIM) multi-compartmental apparatus.[122] This is an *in vitro* computer-controlled system developed to be dynamic and simulate events within the gastrointestinal tract. Additionally, complex biorelevant dissolution media may be used to obtain more physiologically relevant information.[10,123] Biorelevant media is

the subject of significant research and while not the focus of this work, its impact upon sample analysis is important to consider.[123] The volume of dissolution media is often mentioned with regard to sink conditions and these are defined by the Pharmacopeia as "at least three times the saturation volume" for the API in question.[40] Non-sink conditions can lead to altered release rates and even supersaturation, and are particularly problematic for poorly-soluble APIs.[124,125] The use of flow-through cell technology is able to address this challenge with the option of an open-loop system in addition to recirculating dissolution media.[118,126]

The hydrodynamics of dissolution testing is a vast topic applicable to phenomena ranging from turbulence to boundary layers, and as such requires detailed consideration when developing new techniques or comparing results.[77] Hydrodynamics can be influenced by vessel design, sample placement and orientation, rotation of the sample, viscosity of the dissolution media and the media flow rates.[127–129] In low viscosity liquids such as aqueous media, the small changes in density that occur when a solid dissolves result in natural convection processes, which lead to mixing of the media and altered concentration gradients.[77] Minor changes in the set up or design of apparatus can also lead to changes in turbulence and mass transfer, which can lead to significant variation in reported dissolution rates.[130–134] Hydrodynamics are also affected by sampling from the dissolution vessel, which may be manual or automatic, depending upon the frequency of sampling as well as the complexity of sample preparation required prior to analysis.[135] Conventional dissolution methods specify a position for sampling apparatus so as to ensure a homogeneous sample for analysis. This provides information on the extent of drug dissolved in the bulk of the media, but bypasses the many processes occurring prior to this.

1.3.3 Intrinsic dissolution rate testing

An additional technique is intrinsic dissolution rate (IDR) testing. This is defined as the amount of drug dissolved per unit time per unit area (currently μg/min/cm^2) and is a rate phenomenon rather than a measure at equilibrium. Theoretically, IDR should be calculated using sink conditions so that boundary layer thickness is not a variable, and

with a non-disintegrating compacted sample, hence the equation for calculating IDR is derived from Noyes-Whitney:

$$j = \frac{Vdc}{dt} \times \frac{1}{A}$$

Equation 1.2 – Intrinsic Dissolution Rate

where j is referred to as dissolution flow or IDR (µg/min/cm^2), V is the dissolution media volume (mL), dc is the change in concentration of dissolved drug in the medium (mg/mL), dt is the time period over which this change takes place (min) and A is surface area of the compacted sample (cm^2).[136,137] The traditional method to calculate IDR involves plotting the cumulative amount of dissolved drug against time, and performing a linear regression.[40] The result may be curved if sink conditions are not maintained, but only the initial linear section is used to produce a dissolution rate in units of mass per second, which can then be divided by the surface area of compacted API to produce an IDR value.[3]

IDR measurements are used primarily to assess and compare inherent dissolution properties of an API, usually early in development or after changes to a manufacturing or purification process.[138,139] They have also been explored as a substitute for solubility in classifying drugs for development, for example when using the BCS.[136,137,140] However, a 2004 paper by Missel states that these dissolution rates are the result of both intrinsic and extrinsic factors. The USP chapter <1087> makes the same point and refers to general dissolution rates as dissolution flux, whereby intrinsic relates to the API, for example its solid state and physicochemical properties, and extrinsic relates to experimental test conditions such as temperature, pH or hydrodynamics.[40,80]

The conventional apparatus used to calculate IDR values is described in each Pharmacopoeia and traditionally includes a rotating disc of compacted sample, known as Wood's Apparatus, although a stationary disc set up is also outlined.[40,141] Additional techniques include a miniaturised rotating disc, rapid powder tests such as the microDISS and a flow-through UV imaging technique.[142–145] While each method maintains experimental conditions such as pH, temperature and ionic strength,

investigations have confirmed that differences in hydrodynamic conditions may result in variability between the IDR values obtained using different instrumentation.[12,146] Recent work has also confirmed that there can be both inter-laboratory and intra-laboratory variability between IDR values obtained using surface dissolution equipment, i.e. amongst different sites and instruments, and amongst different operators of the equipment.[147]

The variability of experimentally-obtained IDR values is of particular relevance when considering a substitution of IDR for solubility in classification systems such as the BCS or DCS (including refined).[93,95,136,148] For example, both 0.1 mg/min/cm^2 and 1 to 2 mg/min/cm^2 have been suggested as the boundary between low and high solubility, for modified Wood's apparatus and traditional Wood's apparatus, respectively.[137,140] While the alternative techniques to calculate IDR may enable mechanistic details and biorelevant information to be gleaned earlier in development from smaller amounts of API, further work is required to understand how the equipment, particularly surface dissolution imaging, may impact upon the calculations.[138,139,147,149] 'Intrinsic' dissolution rates, should therefore encompass more than just a number, particularly if multiple techniques are involved or ideally be used only for comparative purposes where equipment (and operating procedures) are kept consistent.

Extensive research into the use of UV imaging for IDR determination has been carried out both by Dr Asare-Addo's research group in Huddersfield University, and by Professor Østergaard's research group at Copenhagen University. The work from Huddersfield highlights the importance of considering compact surfaces when determining IDR and arguably provides evidence to support consideration of IDR as both a subjective and objective measurement.[150–152] Additionally the review of UV imaging by Professor Østergaard discusses those same challenges resulting from initial surface roughness and the potential for the SDi2 to encourage scientists to consider dissolution testing as both a quantitative and qualitative exercise.[13]

1.3.4 UV-Vis Spectroscopy

The concentration of API in a sample is routinely determined by ultra-violet visible spectroscopy (UV-Vis) either with or without prior liquid chromatography (LC) to

separate additional components of a formulation.[114] The use of this analytical technique relies upon the API containing a chromophore, which is the section of molecule capable of absorbing light, usually due to the presence of π bonds.[3] Light of a specific wavelength, or energy, results in the excitation of electrons and promotes their movement from the highest occupied molecular orbital (HOMO) to the lowest unoccupied molecular orbital (LUMO).[153,154] This absorbed energy is recorded by the spectrophotometer as a loss of transmission of light and corresponds to a specific wavelength, thus enabling a spectrum of absorbance versus wavelength to be produced.[155]

Exposure to discrete wavelengths of light known to induce electronic excitation in the sample molecule, can be used to measure concentration (c).[154] The extent of absorption (A) is in proportion to the number of chromophore-containing molecules present in the sample (i.e. the concentration), for a specified range of dilute concentrations.[153,154] It assumes no molecule is in the shadow of another and that all molecules contribute equally to the absorbance of light within the spectrophotometer.[154] Absorbance and concentration can be related by considering the molar absorption coefficient of the compound (ε) and the path length of the cell across which the light is transmitted (l) using the Beer-Lambert Law.[153,154] The molar absorption coefficient considers the ease by which the electronic transition can occur and is constant for a compound under the same conditions, see Equation 1.3.[154,156]

$$A = \varepsilon l c$$

Equation 1.3 - Beer-Lambert Law

The prior use of calibration standards (or reference spectra) analysed at the same wavelength (and preferably by the same equipment) enables the molar absorption coefficient of the compound (ε) to be calculated and the range of concentrations over which the law is applicable to be determined.[13,154] It requires that conditions are consistent and no other component within the sample absorbs light at this wavelength (or they must be separated by LC).[154] Formulations encompassing multiple chromophore-containing APIs, thus provide a challenge for standard UV-Vis

techniques, hence more selective measurement techniques provide a useful opportunity.

A blank containing all other components present in the sample (except the molecule being measured) is used to ensure that background signal or noise is taken into consideration[13] and it is additionally important to note that solvent-solute interactions and pH can influence the spectrum.[157] The working range of concentration capable of measurement with UV-vis spectroscopy depends upon the molar absorption coefficient of the molecule being studied; if this value is too high, then absorbance will be too great and dilution will be necessary to calculate concentration.[154] Possession of a chromophore is a limiting factor for monitoring components with UV-Vis spectroscopy and typically excludes excipients from being measured by traditional techniques.[15]

1.3.5 Current challenges and limitations

Dissolution profiles, rates and extent are influenced by a number of complex interlinking factors that can be attributed directly to the ingredients of a formulation (for example, polymorphic forms of the API or differing excipient grades) or the manufacturing conditions used (for example, dry powder mixing time for homogeneity), or they may occur as a result of the environment in which a tablet is stored (for example, high relative humidity conditions resulting in water uptake and tablet swelling).[111,138,158,159] Understanding the dissolution process and impact of each factor is an important part of development and allows control of conditions to ensure future manufactures result in a product of consistent quality, which is key to the safety and efficacy of the dosage form.[100] The purpose of this work is not to comment upon the biorelevance of dissolution testing techniques; however, compatibility with biorelevant and simulated pH media is an important consideration for dissolution testing methodology.

Conventional tablet dissolution techniques provide temporally-resolved information on the rate and extent of API release into the bulk media, however, they are limited in their ability to monitor excipient release or to demonstrate a thorough understanding of how the API is released into solution.[13,15] Extracting information on the role of

excipients during dissolution as well as visualising the processes involved at a surface level have the potential to influence formulation choice and guide manufacturing conditions to ensure appropriate release of the API.[106] This could ultimately improve efficiency of the development process and contribute to quality by design (QbD) ensuring that product quality is built in to manufacturing and based on a thorough understanding of what makes the medicine safe and effective.[10]

This work explores the relevance and importance of two novel dissolution techniques to the pharmaceutical industry and will include consideration of drug substance as well as drug product. The two techniques used to explore dissolution are 1) surface dissolution imaging using UV-Vis technology and 2) the monitoring of dissolution by mass spectrometry.

1.4 Novel technique one - surface dissolution imaging

1.4.1 Background

Surface dissolution imaging focuses on the interface between a solid and liquid.[13] Specialist dissolution equipment entered the commercial market in 2010 with the ActiPix™ SDI 300 developed by Paraytec Ltd. (York, U.K.), although earlier versions, such as the D100, were used as detectors within the separation sciences, see Table 1.3.[13,160–162]

The instrumentation is able to obtain spatially and temporally resolved UV absorbance data, with early versions requiring a band pass filter for single wavelength selection.[161,163] The last ten years have seen this imaging technology applied to a variety of dissolution challenges from understanding intrinsic dissolution rates (IDR) to solvent-mediated phase transformations to micro environmental pH monitoring, amongst many others.[145,164–167]

Table 1.3 – Surface dissolution imaging equipment development timeline

Timeline	Model name	Brief description of characteristics
2009	ActiPix™ D100	First quantitative UV area imaging detector system
2010 (commercial)	ActiPix™ SDI 300	Sample flow cell, syringe pump, single UV capability and 7 mm x 9 mm detector for surface dissolution imaging
2013	Sirius SDI	Same capabilities as SDI 300 but licensed to Sirius, with ActiPix™ Technology
2016	SDi2	Upgraded SDI with dual wavelength capability, whole dose cell, and 28 mm x 28 mm detector. Licensed to Sirius initially and then to Pion in 2017 but uses ActiPix™ Technology

Introduction of the SDi2 in 2016 has enabled this impressive range of applications to be explored further by including dual wavelength imaging across a much larger area with two distinct flow cells.[13,152,168] The ability to record light intensity data for two wavelengths allows either two APIs to be monitored concurrently, or physical changes such as swelling or erosion to be visualised alongside UV absorbance measurements.[13,169] Additionally, employing the use of a whole dose cell with larger imaging area enables formulations to be analysed.[151] This technique shows great potential to explore the minutia of dissolution and expand upon our current mechanistic understanding of the processes involved in drug release.[13,170]

1.4.2 UV imaging fundamentals

The surface dissolution imaging equipment, SDi2, includes a light source, integrated fluidics, a choice of two flow cells and an imaging system connected to a computer for data analysis, see Figure 1.9. Each part will be described in further detail with regard to its functionality and the impact the design has upon the information that can be obtained from it.

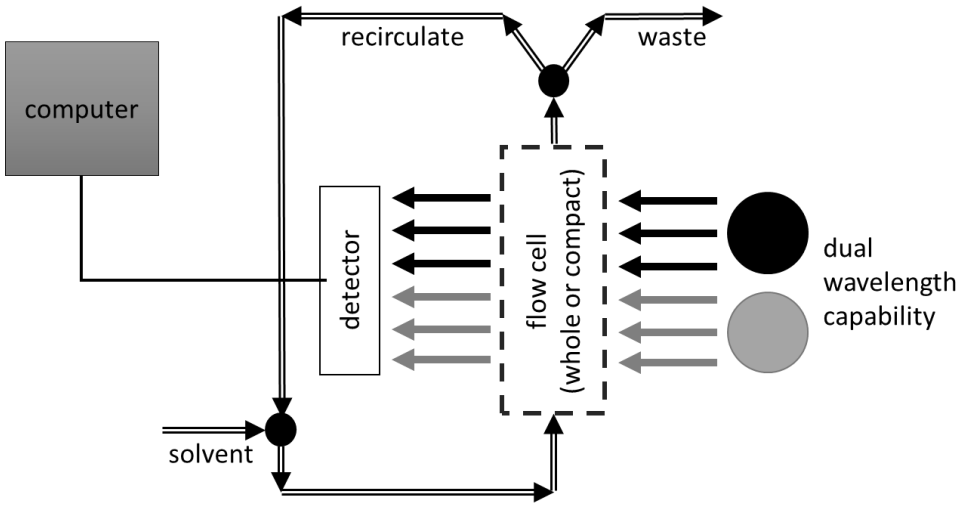

Figure 1.9 - SDi2 instrument outline.

Light source:

The light source includes four ultraviolet wavelength LEDs and one visible. The narrow bandwidth light-emitting diodes (LEDs) sit on one of two motorised tracks to enable dual capability for any combination of the five wavelengths (255, 280, 300, 320 and 520 nm).[168] The tracks sit side-by-side (horizontally) and move up and down depending on which of the LEDs are selected, see Figure 1.10. Track one sits on the left side of the SDi2 relative to the image through the compact flow cell (CFC), which is on the right side when looking directly at the LEDs, and contains the first four LEDs listed in the method section of the SDi2 software: i) 520, ii) 320, iii) 300 and iv) 255 nm. Track two sits to the right hand side relative to the image through the CFC (on the left hand side when looking directly at the LEDs) and contains the final four LEDs: v) 520, vi) 320, vii) 300 and viii) 280 nm.

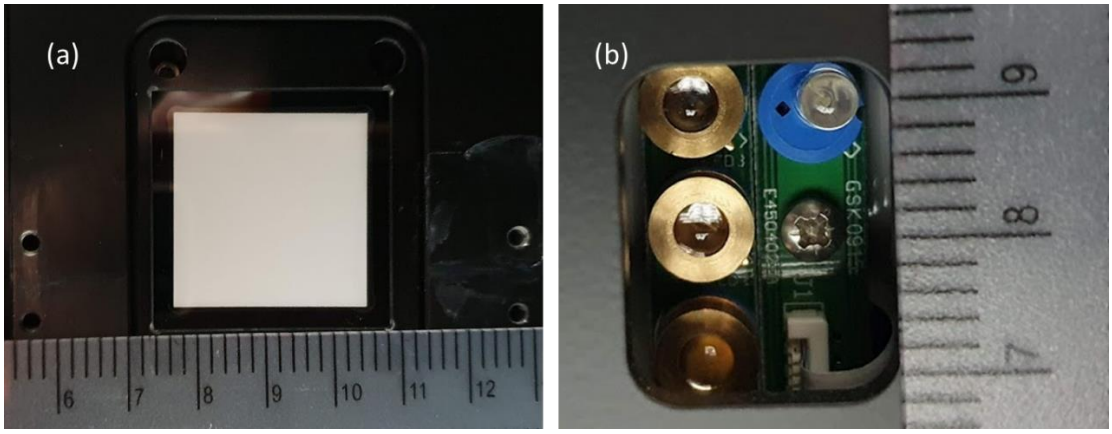

Figure 1.10 – Pictures taken inside the SDi2: (a) the white square shows the detector with a ruler for scale, and (b) a close up of the LEDs showing track two (with LEDs v – viii) on the left and track one (with LEDs i – iv) on the right. The LEDs at the very top were selected for use at the time of the photo being taken.

The ultraviolet wavelengths available are therefore 255, 280, 300 and 320 nm (± 5 nm) with a 520 nm (± 5 nm) visible wavelength. There is much discussion by users regarding the number of wavelengths available, however it appears to be a compromise for the current design limited in part by the working range of the detector (200 – 640 nm) and with a view to enable additional wavelengths in future through purchasing alternative LEDs.[171] The dual wavelength capability provides a significant advantage in interpreting images over its predecessors by enabling differentiation between light absorbance as a result of an API in solution versus light scattering due to an object physically obscuring the path.[13] Additionally, the novelty of simply visualising the dissolution process provides further improvement upon conventional techniques.[172]

Fluidics:

The fully integrated fluidics consists of tubing, displacement pumps and valves with a heater positioned to maintain the temperature of the flowing solvent, see Figure 1.11. All the tubing has an inner diameter of 1.4 mm and outer diameter of 3.2 mm, with multiple connectors and replaceable seals to reduce leakages.

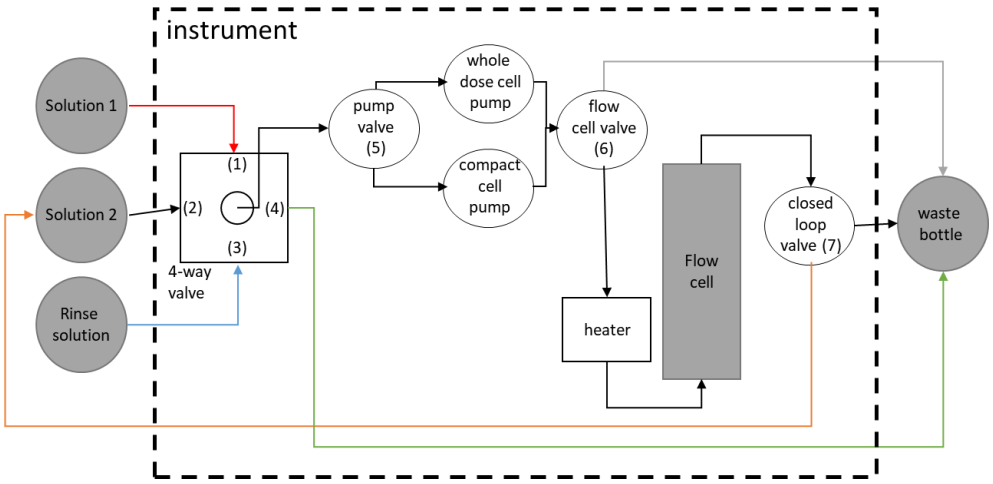

Figure 1.11 - SDi2 fluidics diagram, adapted from the Pion manual. The initial four way valve (1 – 4) is followed by three distinct valves that are either on or off (5 – 7) directing solvent around the instrument accordingly.

The initial four way valve enables the introduction of different solvents or dissolution media, and the three distinct valves, which can either be on or off, direct solvent around the instrument and through a flow cell. The set up can exist as a closed loop, whereby the solvent is recirculated back through the flow cell, or open loop with the "used" solvent pumped directly to waste. The flow rate throughout the fluidics system is defined within the method with the range available dependent upon which flow cell is in place. The whole dose cell (WDC) flow rates range from 6.2 – 24.6 mL/min and the compact flow cell (CFC) rates range from 0.8 – 2.2 mL/min.

Flow cells:

The compact cell was originally based upon the flow-through cell that was first described by Nelson and Shah in 1975.[173] Their work used a convective diffusion model to predict dissolution rates using compound properties (solubility and diffusion coefficient), shear rate and device dimensions (cell width and length).[174,175] The cell was designed to encourage laminar solvent flow throughout and enable fluid velocity to be solved for any point within the cell, thus providing the basis for the SDi2 detection zone measurements and IDR calculations.[80,175]

The whole dose cell is based upon the USP IV design with flow rate guidance to provide equivalent linear velocities and sufficient space to study dosage forms up to a maximum of 20 mm in length.[168] The cell was designed to monitor size changes in

dosage forms such as swelling or erosion, in particular when using matrices for extending drug release.[151] Both cells are shown in Figure 1.12 to provide an idea of size and orientation differences, with blue arrows included to highlight the flow of solvent.

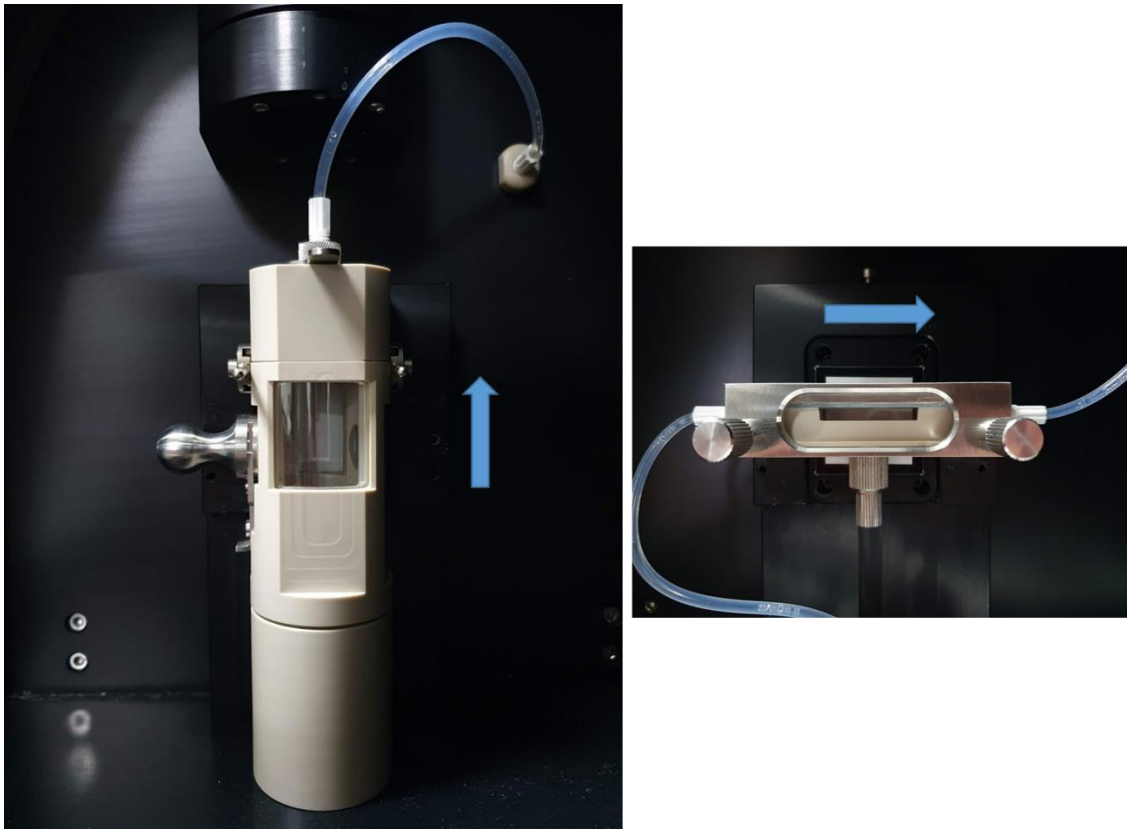

Figure 1.12 – Size and orientation comparison of the SDi2 whole dose cell (WDC) on the left and compact flow cell (CFC) on the right, with blue arrows showing the direction of solvent flow through each cell.

The CFC has a maximum fill volume of 1.54 mL and uses a specially designed sample holder and assembly for weighing out and manually compressing the sample *in situ*. Compaction of the sample is carried out with a load cell to enable this step to be repeatedly carried out to determine IDR measurements. This step has potential to impact upon dissolution and consideration should be given to the compaction properties of the sample being studied in addition to the surface of the compacted sample.[150,152,176,177] The cell is positioned in directly in front of the detector and the other side of the dark SDi2 compartment from the LEDs, see Figure 1.13.

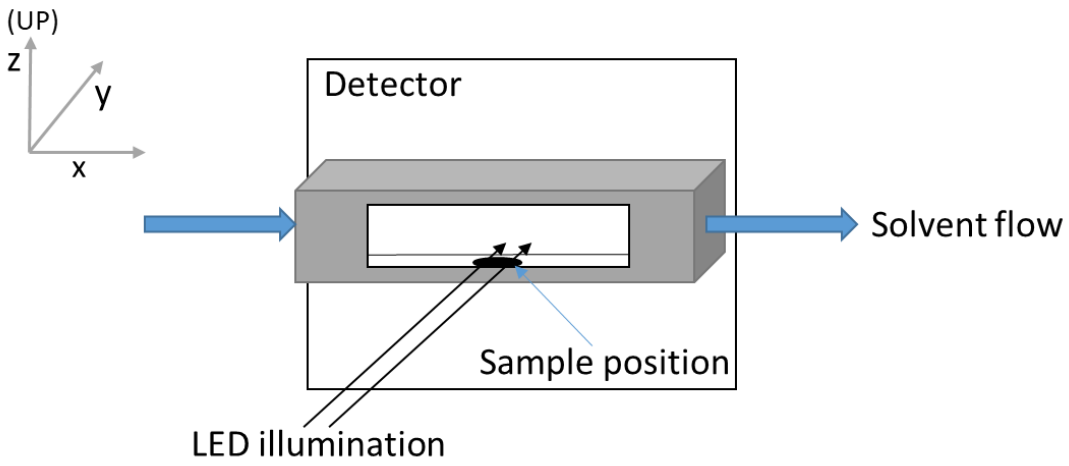

Figure 1.13 – Representation of the compact flow cell complete with detector, LEDs, solvent flow and sample holder position.

In comparison, the WDC has a larger fill volume of 60.3 mL, suitable for tablets and capsules.[168] The dosage form is held in the sample plug by handmade stainless steel wire clasps appropriate to the formulations being studied. The solvent flow runs from bottom to top, with a stopper and 2 mm glass beads in place to smooth flow, and a wire mesh sits before the outlet flow to reduce blockages. The design is based upon the USP IV flow-through cell often used for controlled-release dosage forms and poorly soluble formulations.[118] The cell is placed directly in front of the detector, and across the dark SDi2 compartment from the LEDs, see Figure 1.14.

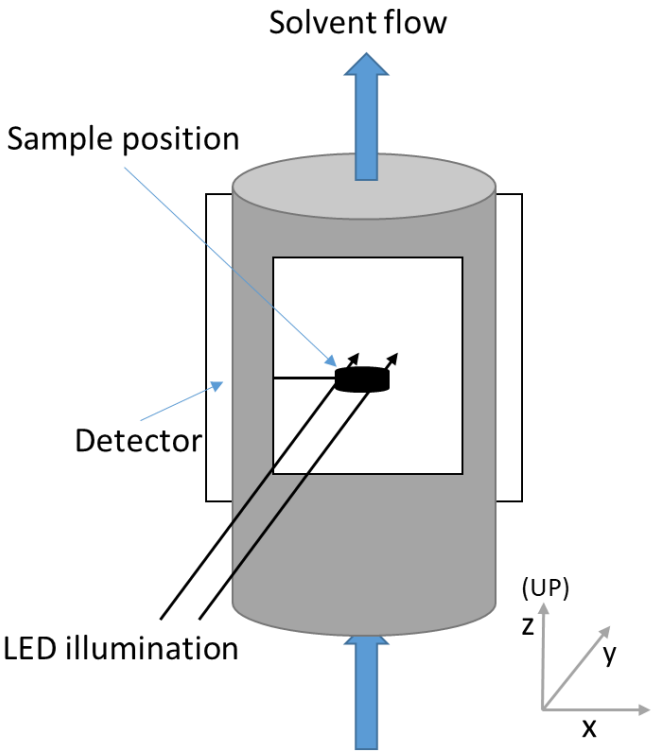

Figure 1.14 – Representation of the whole dose cell complete with detector, LEDs, solvent flow and sample position. Note that the drawing is not to scale and the LED illumination is perpendicular to the detector, through the whole dose cell viewing window.

Aside from fill volume, a key difference between cells is the direction of solvent flow; bottom to top for the WDC, and left to right for the CFC. The hydrodynamics within each cell are therefore different as a result of volume, shape, sample position and gravity.[178] The impact of hydrodynamics upon dissolution is extensively studied but is particularly relevant to surface dissolution imaging, hence this topic requires further consideration for each flow cell depending upon the sample being analysed and will be discussed in detail in Chapter 4. Single crystal surface dissolution imaging.[179–182]

Imaging:

Each method for a dissolution run is designed using the SDi2 software. This allows entry of data such as molar absorption coefficients, and controls detection wavelengths and solvent flow. The image size is also amended here - the imaging area is 28 x 28 mm with 2048 x 2048 pixels, which gives an effective resolution of 13.75 μm^2. This area is expressed in pixels using the bottom left corner of the camera chip as the origin. The WDC uses almost the entire area available (24 mm width x 28 mm height) but the compact cell uses 28 mm width and only 4 mm height, which can be

defined in pixel numbers using the top left 0, 1400 and bottom left 0, 900 as seen in Figure 1.15.

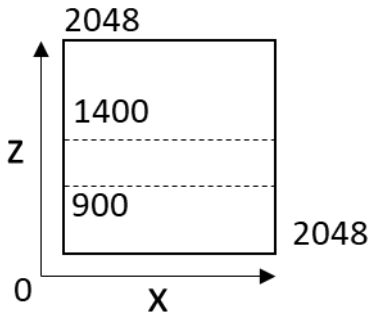

Figure 1.15 - Total imaging area in pixels with the smaller compact cell area marked out using dashed lines.

The ActiPix™ Technology detector is a complementary metal oxide semiconductor (CMOS) chip composed of photosensitive pixels that measure light intensity.[13,183] The chip includes a phosphor coated fibre optic taper, which ensures that all light striking the sensor array is converted to the visible range to allow the measurement of UV light and provides x2.5 magnification.[13,168,171,183] The technology was developed for on-line monitoring at single UV wavelengths, and uses an area imaging array rather than a linear photodiode array; this enables spatially resolved absorbance measurements to be obtained.[160] The method can be likened to a single beam spectrophotometer whereby a reference image is initially obtained so that a light intensity difference (absorbance) can be calculated.[171] The spatially resolved absorbance measurements are represented using a selection of colour maps. The default settings capture one frame per second per wavelength and methods are available to reduce the data size burden whilst maintaining either temporal resolution or spatial resolution.[168]

The data size burden can be reduced using subsampling and binning. Subsampling reduces temporal resolution by not saving every consecutive image; for example, subsampling of 10 saves every 10th frame, retaining the resolution but reducing how often data is obtained. Alternatively a practice known as binning can be used to reduce spatial resolution by changing the pixel area over which intensity data is collected. For example, 1 x 1 binning reports data for every pixel, whereas 2 x 2 binning saves an average across the four pixels thus reducing the effective resolution.

Analysis:

Finally, the data collection and analysis uses Sirius software on a Windows platform and produces a series of images for each wavelength, which can be exported as windows media videos. Each image contains absorbance per pixel through a defined colour map, a summary of which can be extracted to Microsoft Excel through use of highlighted measuring zones. Figure 1.16 and Figure 1.17 show images from the compact flow cell and whole dose cell, respectively. The measuring zones are highlighted in each image and are used to monitor absorbance throughout dissolution for each of the two selected wavelengths.

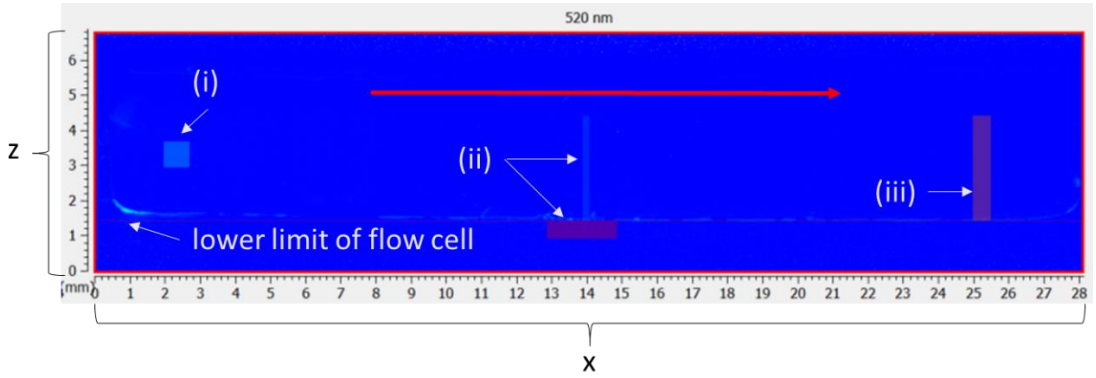

Figure 1.16 – Image of empty compact flow cell using the jet colour map and SDi2 Analysis software. Axes are referred to as 'x' and 'z', the wavelength is written above the image (520 nm), the red arrow shows the direction of solvent flow and the adjustable lower boundary of the flow cell is labelled at a height of 1.4 mm. The default measuring zones are (i) reference, (ii) surface and (iii) intrinsic dissolution rate (IDR), with the ability to adjust size and position, as well as include up to seven additional zones.

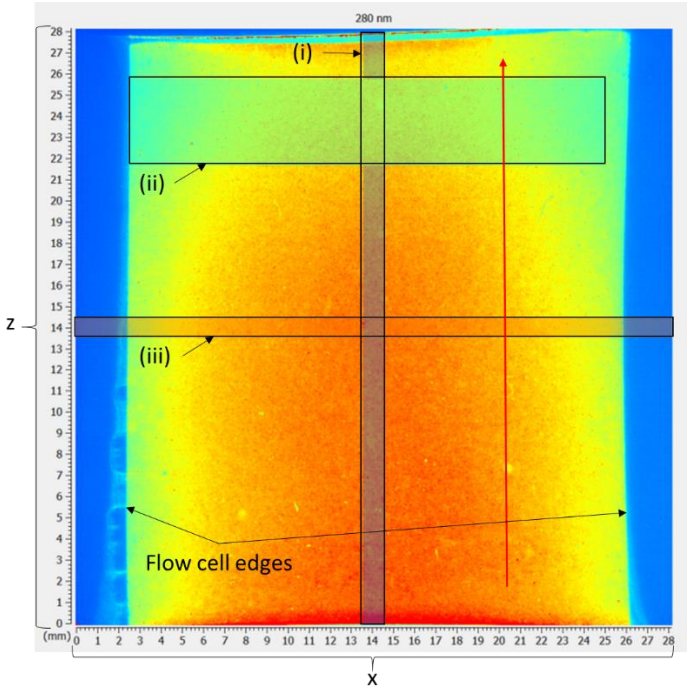

Figure 1.17 – Image of empty whole dose flow cell using the jet colour map and SDi2 Analysis software. Axes are referred to as 'x' and 'z', the wavelength is written above the image (280 nm), the red arrow shows the direction of solvent flow and the fixed flow cell edges are labelled. The default measuring zones are (i) height, (ii) average and (iii) width, with the ability to adjust size and positon, as well as include up to seven additional zones.

The raw data expressing absorbance per pixel is not easily extracted using the software provided so this forms part of the research objectives; image analysis software will be applied, with an assessment of the SDi2's true resolution capabilities to determine whether obtaining absorbance values per pixel is both feasible and accurate. The UV wavelength, with calibration, can be used to calculate sample concentrations, and the visible wavelength can be used to infer details about the sample's physical presence within the flow cell.[13,168,184]

1.4.3 The solid-liquid interface

The interface between solid and liquid is where transformation to a solution begins.[2,146] Imaging this phase boundary at both UV and visible wavelengths to monitor concentration as well as swelling, erosion or precipitation, has the potential to provide novel insights into the wetting, diffusion and convection steps occurring during dissolution.[2,13,185] Note that an understanding of bond breaking and solvation may potentially be inferred or determined using additional technology, but these two steps are considered to be outside the scope of this research.[2,13] Some of the early imaging

studies focussed on measuring concentration gradients at the surface of dissolving solids and observing the thickness of boundary layers.[161,163] These offer information on the ease by which dissolving solid leaves the surface of the solid and moves into the bulk, thus enabling calculation of dynamic solubility, diffusion rate and dissolution rate.[163,175,186] The impact of varying solvent flow rate upon these conditions also provided an insight into the role of convective-diffusion theory, however, early work was limited in its ability to distinguish between solid surface and API in solution at high concentrations.[13,161] The dual wavelength capability of the SDi2 will enable this to be addressed in yet more detail.

The solid phase under investigation may consist solely of an API or may be a formulation, depending upon the stage of research.[3] In the case of pure APIs, UV imaging has been discussed as an alternative to traditional intrinsic dissolution tests to enable characterisation with even smaller amounts of material and dissolution media.[145,163,167] Visualising early dissolution events such as the wetting process, has enabled the importance of compact surface properties upon initial kinetics to be revealed, leading to a recommendation to report IDR only after either the three or five minute mark.[145,150,152,187,188] The equivalence of IDR values obtained through this technique have also been the subject of extensive research.[145,150,152,164,165,187–192] The IDR calculations are based upon two equations, which will be discussed in detail in 3. Surface dissolution imaging intrinsic dissolution rate calculations. However, the software algorithms have yet to be published, preventing manual confirmation of any values obtained and leading to a recommendation to use IDR for ranking purposes rather than for quantitative comparison with other techniques.[13,147,175] Furthering our understanding of the software and attempting to replicate IDR calculations will form a part of assessing the suitability and exploring the limitations of surface dissolution measurements.

Extensive reviews of UV imaging within pharmaceutical development were published in 2017 and 2018.[13,167] These discussed details of the formulations explored to date, which covered oral, parenteral, transdermal and ophthalmic delivery systems.[13,167] Examples included gel matrices to model soft tissue for drug diffusion, the matching of indicator dyes to compound pKa values to visualise surface pH changes, exploration of

in situ solid form transformations during dissolution and drug release from implants, patches and gels.[165,166,193–199] While the majority of these systems fall outside the scope of this work, they highlight the versatility of the technique for a range of formulations and APIs, and the value of using spatially and temporally resolved UV imaging to provide real-time information about drug release, dissolution and transport.[13,167]

Surface dissolution imaging can be employed to monitor the phase boundary for swelling, erosion or precipitation, and to quantify the drug dissolved with respect to both time and location, thus providing detailed insights into the mechanics of dissolution. There are multiple examples of UV imaging being used to explore the role of excipients, particle size reduction and solid state modifications with scope to expand on each of these areas further.[58,152,185,188,200–202] The recent use of UV and visible imaging to compare forms has allowed unexpected physical processes to be reported which can explain differences between expected and experimentally-obtained IDR values.[150,152,170] The option to incorporate a Raman probe within the SDi2 enables the direct monitoring of form changes during dissolution, however, in the absence of such technology, surface monitoring can provide insights by allowing local concentrations to be calculated, the wetting process to be visualised and the balance between dissolution and precipitation to be measured.[165,170] These insights into solubility differences between forms may enable the fundamental understanding of surface kinetics at the interface between solid and liquid to be enhanced.[138,146]

Single crystals have been extensively explored to further understanding of this solid-liquid interface and have the potential to provide novel insights into both the fundamentals of dissolution and crystal growth, as well as the anisotropic nature of crystals.[97,138,203] Anisotropy refers to the concept that different faces of a crystal will possess different properties as a result of the molecular arrangement or orientation of functional groups at each surface.[97] This property of crystals has resulted in numerous studies over the years attempting to measure face specific energies, dissolution and surface defects.[204–209] A variety of techniques have been applied to explore single crystals such as surface characterisation, optical microscopy, computational modelling, including early UV imaging equipment.[210–215]

The dissolution of a single lidocaine crystal was observed using the SDI300 in 2011; the apparatus limited monitoring to a single UV wavelength and stagnant solvent conditions, but natural convection due to local density gradients was visualised with dissolved lidocaine pooling at the bottom of the cell.[216] In 2016 this work was expanded upon using both the D100 and SDI; this time the single lidocaine crystals were observed in a hydrogel matrix to suppress the density gradients, which allowed diffusion to be observed without convection.[169] Each of the studies developed our understanding of single crystal dissolution, however, both were limited by the equipment and its ability to monitor only a single wavelength, thereby forcing the researchers to choose between visualising physical changes or concentration changes. The newly developed SDi2, with its dual wavelength imaging, therefore provides an opportunity to explore single crystal dissolution in further detail.

1.4.4 Image resolution

The extent of detail able to be obtained from the SDi2 images will depend upon the resolution capabilities of the instrumentation. A thorough discussion of the LEDs, flow cells and detector is therefore required with special consideration given to their relative positions and any disturbances resulting from objects within the light path.

The LED motor positions are calibrated to ensure they align with each flow cell and imager upon starting an experiment. A check of LED power also takes place during this set up procedure and a dark image is taken to set exposure times, prior to obtaining I_0 (background) readings. A reference image is automatically obtained at the start of every run using a cell full of blank solvent. This background reference (I_0) is spatially resolved and applied to each pixel to enable light intensity differences to be calculated, which are translated to absorbance values (and potentially concentration).[171] Additionally, a background reference box can be placed within the cell to account for changes in the solvent over time, and unlike the initial reference data this can be switched on or off.

A visual representation of each set up for both the compact flow cell and the whole dose cell can be found in Figure 1.18 and Figure 1.19, respectively. These figures highlight the set up relative to each axis (x, y and z) but the scale is not representative.

The LED tracks are situated approximately 34 cm from the detector and the two tracks are 1 cm width apart, with each track having four LEDs.

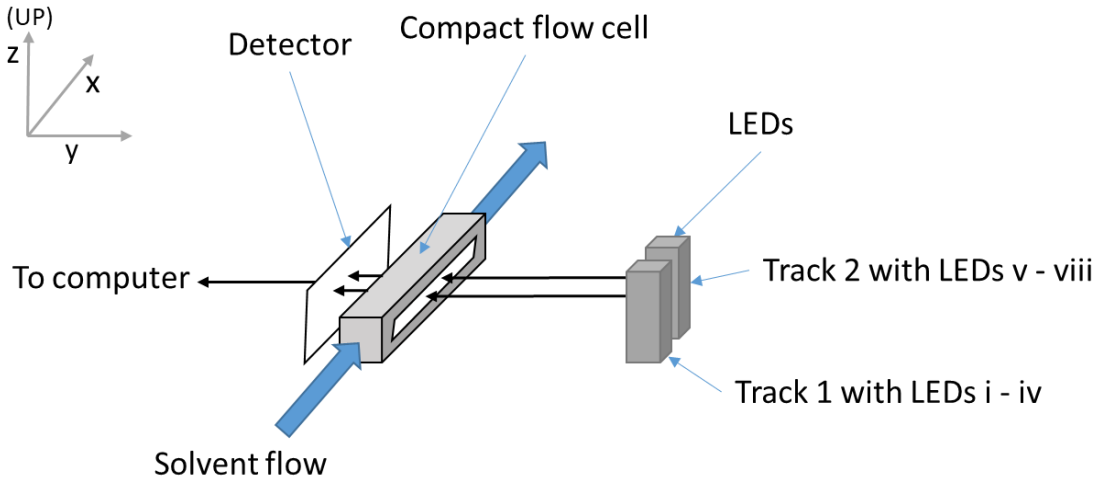

Figure 1.18 – Outline of the compact flow cell set up with direction of solvent flow and LED illumination in relation to position of cell and detector. Not drawn to scale.

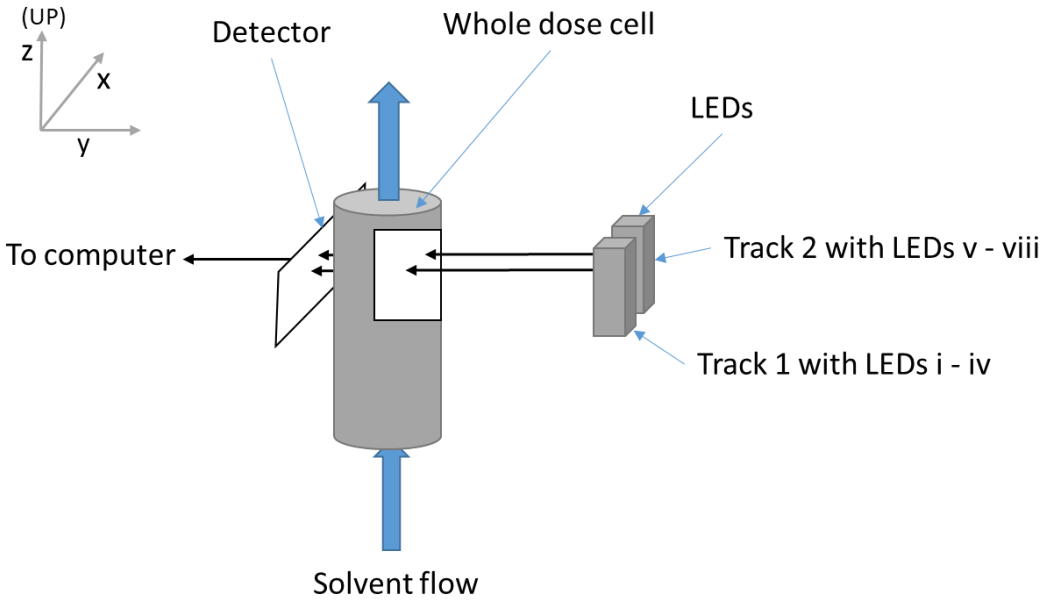

Figure 1.19 – Outline of the whole dose cell set up with direction of solvent flow and LED illumination in relation to position of cell and detector. Not drawn to scale.

The depth of the CFC, which can be defined as path length, is 0.9 cm and is consistent across the width of the cell. The WDC path length, however, is defined in the manual as ≤ 2.8 cm and takes into account the cylindrical nature of the cell. The changing path length is accounted for within the SDi2 software during data analysis of WDC dissolution.

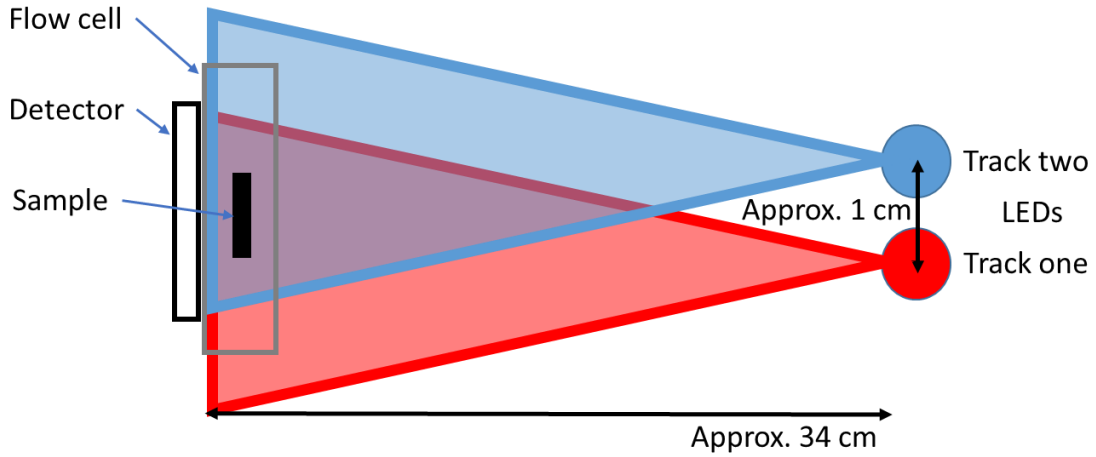

Figure 1.20 – Representation of LED illumination through the compact flow cell.

The sample position relative to the cell and detector will differ for each LED, see Figure 1.20. This is known as the parallax effect and occurs as a result of viewing an object through two different lines of sight. In addition to the position of the image relative to the LEDs, the resolution capabilities of the instrumentation require consideration. Pion UK Ltd state the effective pixel size (or resolution) of the SDi2 as 13.75 μm^2 within the instrument technical specifications.[168] Stainless steel balls of approximately 5 mm diameter and greater are used to confirm image resolution during set up of the equipment.[††] If single crystal dissolution is to be explored using the SDi2, the extent to which size changes can be confidently monitored and surface concentrations measured, will depend upon the relative position of the object as well as the resolution of the equipment.

1.4.5 Aims and objectives:

The SDi2 is the most recently developed equipment designed to monitor surface dissolution and as such would benefit from studies exploring its limitations, assessing its suitability to further our understanding of the dissolution process and determining its feasibility for additional applications.

[††] "The resolution of 13.75 μm^2 comes from the theoretical pixel size. The imaging area is 28 mm x 28 mm with 2048 x 2048 pixels i.e. 28 mm / 2048 pixels = 13.7 µm. This is not something which is confirmed or tested by Pion, it is calculated from the specs of the instrument. As part of our QC procedure the instrument is used to measure the diameter of a series of known diameter ball bearings (as small as 5 mm) to confirm the measurement functionality." From Analytical Services Scientist at Pion (email conversation).

The aims and objectives are:

- to explore the enhanced understanding obtained through visually monitoring dissolution with both UV and visible absorbance data,
- to further understanding of the use of both the novel whole dose cell and the compact flow cell with regard to hydrodynamics,
- to confirm the ability of the SDi2 to monitor and report absorbance per pixel,
- to explore the fundamentals of the IDR calculations using the SDi2 software,
- to develop a method for using the SDi2 to monitor single crystal dissolution,
- to utilise the dual wavelength capability of the SDi2 to monitor single crystal dissolution in terms of both concentration changes and physical changes, and
- to explore the application of image analysis software to the SDi2 absorbance data.

The overall aim is to assess the ability of the SDi2 to elucidate and dissect the dissolution process by both magnifying and visualising the process chemically and physically. Surface dissolution imaging will subsequently be applied to the field of supramolecular chemistry to explore its ability to rank the stability of polymorphs, using both UV and visible data to monitor concentration and size changes of a gel and single crystals. The most recent and extensive review of UV imaging by Professor θstergaard (Copenhagen University) focuses on its primary application within pharmaceutical analysis - this work aims to extend its reach yet further whilst also expanding our understanding of the fundamentals of the technique.[13]

1.5 Novel technique two - mass spectrometry

1.5.1 Background

The use of off-line mass spectrometry for dissolution testing is first mentioned by Wang *et al*. in a 2006 article discussing analytical techniques for dissolution testing.[217] It references work from 1999 applying tandem mass spectrometry to FOSAMAX® dissolution testing[218], yet no detailed information or publications pertaining to this work could be found in the literature and attempts to correspond with the original author were unsuccessful. A later publication by a member of the original team details the use of ion chromatography-ion spray mass spectrometry[219] to overcome the lack of

chromophore present in alendronate (FOSAMAX®). Additionally, in 2008, Hoti *et al.* optimised and validated an off-line liquid chromatography electrospray ionisation mass spectrometry (LC-ESI-MS) technique for the quality control dissolution testing of another molecule lacking a chromophore, rociverine.[220] Many other techniques have since been developed which include variations on MS, for example ion chromatography-inductively coupled plasma mass spectrometry.[221–223] However, the original discussion outlining mass spectrometry concluded that the major factors limiting its use for dissolution testing were the cost of equipment, incompatibility with official techniques and a lack of ruggedness and robustness in particular due to interferences from ion suppression.[217]

The cost and complexity of equipment are significant limitations which the MS community have worked hard to address, starting with the miniaturisation of mass analysers in the 1990s.[224] Further advances in technology have led to the production of equipment which is both compact, portable and user-friendly both at its interface and when introducing samples.[224–227] This *in situ* equipment enables the gathering of high quality data by non-experts[224] and more recently has encouraged the monitoring of reactions both on-line and in real time.[228–230] Validated methods have the potential to identify, quantify and selectively monitor single ions, in addition to obtaining accurate mass and elucidating structures.[224,231]

A more recent study demonstrated the use of on-line electrospray ionisation mass spectrometry (ESI-MS) to monitor the dissolution of pharmaceutical tablets.[15] The primary aim was to monitor components without a chromophore, which cannot be done using standard UV-Vis techniques.[15] The secondary aim was to monitor the process on-line with the potential to obtain information in real-time. Additionally, multiple components were monitored concurrently, unlike UV-Vis technology which would require the use of chemometric multicomponent analysis for unravelling the signals from the individual components.[232] This work confirmed the potential of ESI-MS for on-line monitoring but again highlighted the need to explore interference from APIs, excipients and dissolution media, defined as ion suppression and ion enhancement.[15] While matrix interference and method robustness continue to provide significant challenge, the development of less expensive and more user-

friendly equipment offers the opportunity to explore mass spectrometry as an analytical technique for monitoring dissolution in further detail.

1.5.2 Mass spectrometry fundamentals

MS instrumentation varies widely in terms of size, complexity and cost, however, they all encompass the following:

- a technique by which the sample is ionised
- separation according to *m*/*z* (mass-to-charge ratio), and finally,
- the detection of ions.

Prior to the analysis and detection of an ion within the high vacuum conditions of the mass spectrometer, the analyte or sample must be introduced to the ionisation source, see Figure 1.21.[233]

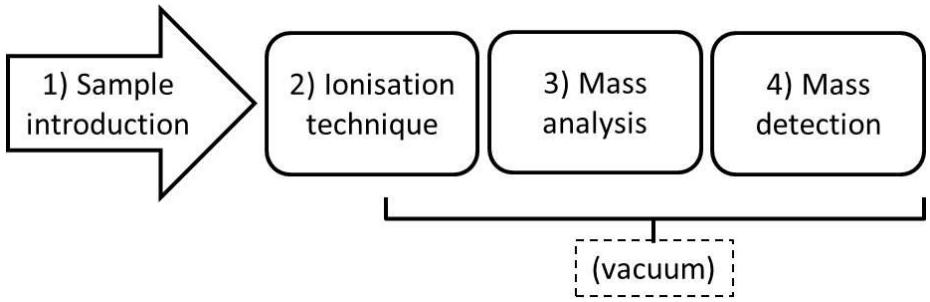

Figure 1.21 - Outline of sections of a mass spectrometer.

This outline will discuss the use of electrospray ionisation mass spectrometry specifically in relation to monitoring dissolution so will only consider samples introduced as liquids.

Sample introduction

The introduction of liquid samples is often coupled with chromatography; this upfront chemical separation can be used to improve sensitivity by introducing each component of the sample to the ionisation step separately.[231,234] It can also be used in place of diagnostic tests by comparing relative retention times of analytes which aids in identification.[231,233] Despite the benefits of chromatography, its use prevents real-time monitoring of dissolution, hence the ultimate aim is to sample from the dissolution bath and pass to the MS instrumentation with no separation. Throughout this development work, samples will be introduced to the mass spectrometer both with

and without prior chromatography to build understanding, and will vary from simple aqueous solutions to more complex biorelevant systems.

Electrospray ionisation

Ionisation is a prerequisite for MS analysis and can be defined as the formation of ions or charged particles.[233,235] Multiple techniques exist to produce these gaseous ions and the choice depends upon the sample properties and analysis required.[224,233] Electrospray ionisation was chosen for this work due to its ability to ionise a range of molecules with little fragmentation and to do this directly from aqueous solutions at atmospheric pressure.[14,236,237] It is a simple and versatile technique, capable of producing both singly and multiply charged ions with a high ionisation efficiency.[235,237] ESI was first attempted by Dole and his team in 1968,[238] before being developed by Yamashita and Fenn in 1984,[239] but its breadth of application and popularity has grown with the development of the interface between LC and MS.[240–242] The main benefit of ESI is its sensitivity, however, this can also be considered a disadvantage; all components of the solution may be ionised causing interference and leading to suppression or enhancement of the primary ion.[243]

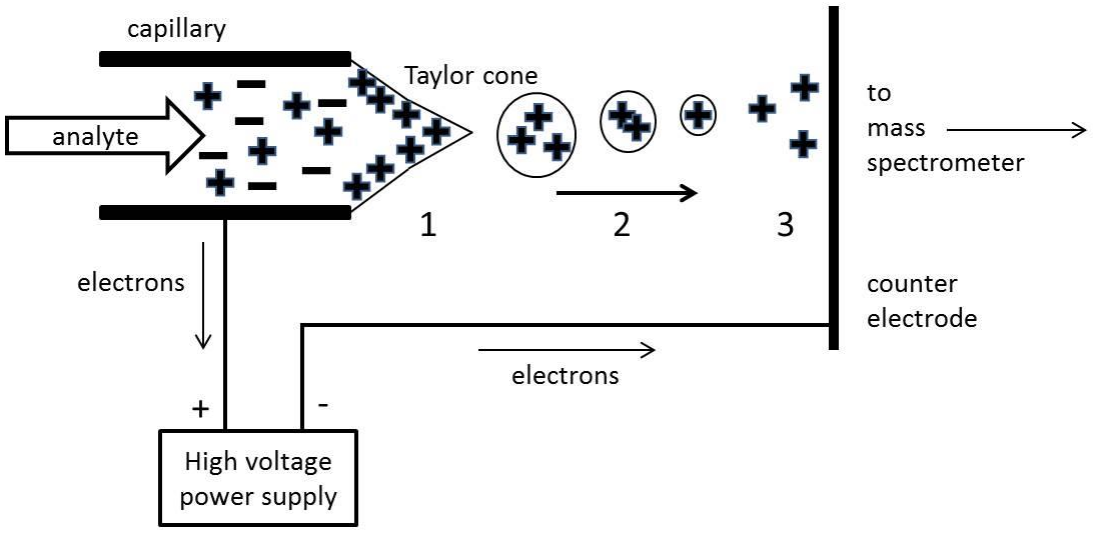

Figure 1.22 - Schematic of electrospray ionisation in positive mode outlining three steps 1) charged droplet production, 2) shrinking of droplets and 3) release of ions.

The process of electrospray ionisation is outlined in Figure 1.22, which is shown in the commonly used positive mode for the purposes of this explanation. Mode refers to the electric field applied to the capillary tip and can be "positive" (creation and release

of cations) or "negative" (creation and release of anions). Regardless of the mode, there are assumed to be three key steps which occur under atmospheric pressure:

1) charged droplet production from the Taylor cone formed at the capillary tip,
2) shrinking of the highly charged droplets and
3) release of gas-phase ions from the droplets.[236,242,244]

Mechanistic explanations of the first two steps are generally in agreement and are abundantly available in the literature.[235–237,241,242,245–247] To summarise, analyte in the form of a solution flows through a capillary tube to which a voltage is applied. The set up can be considered an electrochemical cell; the circuit is completed by the flow of charge through both droplets and ions, with oxidation and reduction reactions occurring at the capillary and counter electrode, respectively.[242,248] The presence of a negative counter electrode results in ion movement within the solution and encourages an accumulation of positive ions near the surface. This creates an electrostatic (Coulomb) force which pulls against the surface tension creating an elliptical shape at the tip of the capillary, which is referred to as a Taylor Cone. At sufficiently high voltages, the repulsion between the excess of positively charged ions in the tip results in the cone losing stability and emission of a fine spray is initiated.

The fine spray is thought to break into highly charged droplets that exist close to the Rayleigh stability limit whereby the surface tension counteracts the charge and electric field. As the droplets are heated and subjected to a de-clustering gas such as nitrogen, they undergo neutral solvent evaporation, which causes them to shrink whilst their charge remains constant. Desolvation continues until the repulsion created by the electric field overcomes the surface tension of the droplet creating another Taylor cone and jet fission, generating smaller charged droplets.[14,235]

Descriptions of the final ion release mechanism are considered incidental to the analyte(s) being studied and are more challenging to determine than the first two steps.[235,237,246] Three models are commonly described: 1) ion evaporation, 2) charged residue and 3) chain ejection.[235,237,242] The charged residue model (CRM) and the chain ejection model (CEM) are applied to the release of proteins, namely large globular species and disordered polymers, respectively.[235] Extensive work has been undertaken

to simulate protein charging but it is outside the scope of this research.[249–251] The ion evaporation model (IEM) is most relevant to the low molecular weight species used in this work. These exist in aqueous solution as ions, so the cycle of desolvation and fission simply continues until gaseous analyte ions are produced and released.[235,242] Counter and skimmer electrodes continuously draw the ions towards an inlet cone and into the mass analyser.[233]

Mass analysis

Mass analysis involves the separation of ions under a vacuum, according to their mass to charge ratio (*m/z*) and can be used to select either a single ion or a range of ions. The instrumentation used in this work includes time-of-flight (TOF) and quadrupoles. TOF mass analysis separates ions by virtue of velocity differences as they pass through the drift region of the flight tube (a section of the MS with no applied field).[233] Ions are accelerated from the source with a fixed kinetic energy (KE) defined mathematically in Equation 1.4, where resultant velocity (v) varies with the mass of the ion (m):

$$\boldsymbol{KE = \frac{1}{2}mv^2}$$

Equation 1.4 - Kinetic energy[233]

The length of drift region is constant, so ions with differing *m/z* reach the detector at different time points. The TOF analyser is capable of accurate mass measurements at a fast speed or duty cycle and advances in technology have resulted in designs which enable them to be incorporated into smaller MS equipment.[227] The single quadrupole in comparison is relatively cheap and easy to use as well as being physically small and robust, therefore making it a more suitable addition to a portable MS in an analytical lab.[15,227] Comparatively its data acquisition is slow but still sufficiently fast for monitoring dissolution in real-time (minutes rather than seconds) although it is generally considered a low resolution instrument.[228,233]

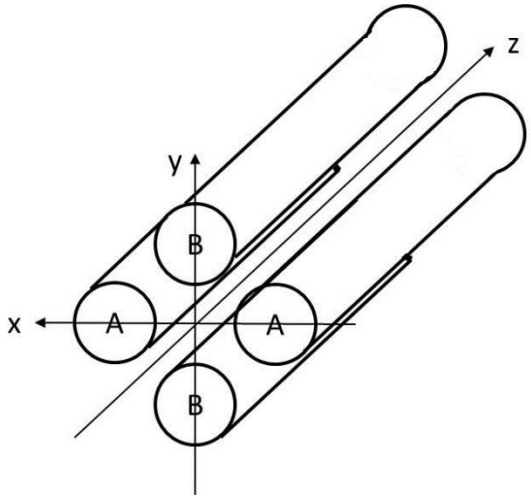

Figure 1.23 – Outline of a quadrupole mass analyser highlighting the electrodes arranged in pairs (A and B) and the three axes (x, y and z).

The quadrupole, shown in Figure 1.23, consists of cylindrical or hyperbolically shaped rod electrodes arranged in opposite pairs (A and B).[233] The movement of ions is influenced by a complex electrical field, which consists of an oscillating radio frequency (RF) between the rod pairs and a constant direct current (DC) throughout. The RF subjects the ions to accelerations in the x and y directions as they travel along the z axis; their trajectory through the quadrupole will vary according to the *m*/*z* ratio and potential applied, and if an ion reaches a rod it will discharge avoiding detection.[233] The quadrupole can be used in a scanning mode to separate ions according to their *m*/*z* ratio or in a selected ion monitoring mode (SIM) to enable only a specified *m*/*z* to maintain a stable trajectory.[227]

Mass detection

Multiple detectors exist whereby the flow of ions can be converted into a usable signal.[233] The majority of instruments and those used in this work rely upon the photomultiplier technique.[252] After passing through the mass analyser, ions hit a dynode which emits electrons; these accelerate to a phosphorous screen and stimulate the emission of photons. Photons are detected by a photomultiplier tube where a cascade occurs in a sealed vacuum multiplying the original ion by 10^6 or more.[252] In this way a single ion produces an amplified signal which remains proportional to the initial abundance of the ion and acts as a highly sensitive detector.[233,252]

The mass spectrum produced displays the relative abundance against *m*/*z* where *m* is the mass and *z* is the charge number.[233] Multiple terms can be used to describe the mass of molecules, however mass spectrometry uses nominal, monoisotopic and exact mass, rather than average or atomic mass.[234] The presence of naturally-occurring isotopes (variants of the same element with different numbers of neutrons) results in mass differences of several Da (Dalton); however the impact of this upon MS measurements depends upon the resolution of the detector, i.e. its ability to distinguish between peaks for ions of differing *m*/*z*.[233,253] Electrospray ionisation can produce singly and multiply charged ions, but the majority of this work focuses on the former.

1.5.3 Ionisation phenomena

Electrospray ionisation (ESI) in the context of this research involves filtered analyte from the dissolution bath which will consist of multiple components including API(s), excipient(s), solvent(s) and dissolution media. MS frequently uses chromatography to separate components so they are ionised one at a time, however, this challenges the ability to analyse on-line and prevents real-time data from being obtained. Using MS to monitor dissolution should provide the potential to qualitatively and quantitatively determine all components present in solution at each stage of the dissolution process as it progresses.[15] However, the presence of multiple components in the analyte solution during ESI is what leads to the phenomena of ion suppression and enhancement.[243]

Numerous studies on electrospray fundamentals have investigated the relationship between MS response and analyte characteristics, concluding that in addition to the design of the ESI source itself and the method used, each component of the solution has the potential to alter the ionisation process.[243,247,254–256] In this context the components include solvent(s), API(s), excipient(s) and dissolution media. Additives such as formic acid and acetic acid are frequently added to mobile MS solvents to enhance ionisation and improve signal to noise ratios, whilst unknown impurities and leachables from lab equipment may also be present.[257,258] Signal interference may therefore result from a number of factors.

The exact mechanism(s) by which ionisation phenomena occur is not fully understood, however, extensive research has been carried out to produce ionisation efficiency scales.[255,259] Ionisation efficiency can be defined as "*the extent to which analyte molecules in liquid phase are converted to gas-phase ions and detected*" and the research lists a range of influencing factors including pK_a, pH, hydrophobicity, surface activity and molecular volume amongst others.[259] To conclude and quote Liigand "*all these studies show that [the] electrospray mechanism is complex and affected by numerous factors"*.[255] Extending our understanding of ionisation phenomena is outside the scope of this research, however, its impact will be investigated for a controlled range of compounds, excipients and solvents (including dissolution media) to determine whether the effect is reproducible and quantifiable so that we may attempt to account for it during the on-line monitoring of dissolution.

1.5.4 Aims and objectives

Combining dissolution with mass spectrometry results in multiple challenges, from the practical limitations of the equipment, to the more complex phenomena that can occur when multiple components are ionised concurrently i.e. ion enhancement and suppression.[15,217] The continuous acquisition of data and reporting in real-time is a challenging proposition for analytical techniques, however visualising change in real time provides significant benefits and may enable further understanding of the mechanisms involved in dissolution.[15,228]

The aims and objectives are:

- to monitor components of the tablet both with and without a chromophore using MS
- to determine MS signal variability of single APIs and excipients in multiple solvents
- to enable multiple APIs and excipients to be monitored concurrently
- to determine the impact of dissolution media (both simple and more complex) on API and excipient MS signal
- to explore the impact of ion suppression and ion enhancement from and on each component (API, excipient and dissolution media)

- to detect and quantify components accurately using MS analysis without separation before ionisation, so as to monitor APIs and excipients on-line and in real-time, and
- to reproduce the proof of concept work using different systems and equipment.

The overall aim is to understand whether tablet compositions and dissolution media will impact upon ionisation phenomena, determine the extent to which any suppression and enhancement are occurring and ultimately adjust quantification accordingly to account for them. Work will include development and validation of the equipment set-up for dissolution and mass spectrometry, confirmation of the robustness of data, methods to enable on-line monitoring in real time and exploration of the most accurate method for analysing data to produce dissolution profiles. This work will be carried out using a range of model APIs, excipients and dissolution media.

2. Materials and Methods

2.1 Materials

2.1.1 Active Pharmaceutical Ingredients

A variety of active pharmaceutical ingredients (APIs) were selected based upon their differing physicochemical properties. Each of the APIs was purchased from Sigma-Aldrich, with the exception of chloramphenicol, which was obtained from Duchefa Biochemie. All were of a standard either meeting USP testing specifications or certifying them as reference material, see Table 2.4.

Table 2.4 - Active pharmaceutical ingredients additional information.

API	Supplier	CAS number	Chemical formula
Chloramphenicol	Duchefa Biochemie	56-75-7	$C_{11}H_{12}Cl_2N_2O_5$
Furosemide	Sigma-Aldrich	54-31-9	$C_{12}H_{11}ClN_2O_5S$
Guaifenesin	Sigma-Aldrich	93-14-1	$C_{10}H_{14}O_4$
Haloperidol	Sigma-Aldrich	52-86-8	$C_{21}H_{23}ClFNO_2$
Ibuprofen	Sigma-Aldrich	15687-27-1	$C_{13}H_{18}O_2$
Ibuprofen sodium	Sigma-Aldrich	31121-93-4	$C_{13}H_{17}NaO_2$
Ketoprofen	Sigma-Aldrich	22071-15-4	$C_{16}H_{14}O_3$
Paracetamol	Sigma-Aldrich	103-90-2	$C_8H_9NO_2$
Phenylephrine	Sigma-Aldrich	59-42-7	$C_9H_{13}NO_2$

A supply of Beechams® All-In-One over the counter cold and flu tablets was obtained from a local Pharmacy. These contained paracetamol, guaifenesin and phenylephrine with multiple excipients in a film-coated immediate release oral tablet, see Table 2.5.

Table 2.5 – Range of excipients within the Beechams® tablets.

Tablet		**Film coating**
Lactose	Purified talc	Hypromellose E464
Microcrystalline cellulose	Povidone	Titanium dioxide E171
Maize starch	Potassium sorbate	Polyethylene glycol 4000
Stearic acid	Pregelatinised starch	Lactose monohydrate
Colloidal anhydrous silica		

2.1.2 Excipients

A range of commonly used excipients for orally-dosed immediate release formulations were obtained as free samples from a variety of manufacturers:

- DFE Pharma supplied Pharmacel® microcrystalline cellulose, Primojel® sodium starch glycollate and Primellose® croscarmellose sodium.
- Roquette supplied Pearlitol® 160 C mannitol.
- Meggle Pharma supplied lactose as FlowLac® 100, GranuLac® 70, PrismaLac® 40 and SorboLac® 400.
- Peter Greven supplied Ligamed® magnesium stearate.
- BASF supplied povidone and crospovidone as Kollidon® 30 and CL, respectively.
- Colorcon supplied Pregelatinised Starch 1500.
- Forum SPI Pharma supplied Lubripharm® sodium stearyl fumarate.

All samples were used as received from the supplier with no further characterisation or analysis.

2.1.3 Solvents

A range of solvents were used for MS analysis which included acetonitrile (MeCN), methanol, isopropyl alcohol (IPA) and deionised water. These were HPLC grade and obtained from Fisher Scientific UK, with the exception of deionised water obtained from an Ondeo Purite Select Neptune Analytical water purifier within the chemistry

department (18.2 Ω). Formic acid, LCMS grade from Sigma-Aldrich, was used as a modifier for electrospray ionisation where required.

Solvents for surface dissolution imaging and crystallography included HPLC grade methanol obtained from Fisher Scientific UK and deionised water obtained from the Ondeo Purite Select Neptune Analytical water purifier within the chemistry department (18.2 Ω).

2.1.4 Dissolution media preparation

Surface dissolution imaging:

Dissolution media and solvents were prepared in advance and held in glass bottles at a raised temperature of 40 to 50 °C overnight (12 hours or more), with a rotating PTFE stirrer bar (25 x 6 mm) to enable degassing. Methanol was additionally submerged in a heated water bath and sonicated for a period of time (more than an hour) to remove excess gas. Note that Pion UK Ltd., supplied Nalgene HDPE bottles but these were found to degrade (regardless of the media being used) leaving white precipitate that could not be removed easily, it also blocked tubing and interfered with dissolution imaging.

Phosphate buffer of pH 6.8 (0.05 M) was prepared using monobasic potassium phosphate (KH_2PO_4) and sodium hydroxide (both supplied by Acros Organics). Pion instructions stated to dissolve 27.22 g of monobasic potassium phosphate in water and dilute with water to 1000 mL. Place 500 mL of the monobasic potassium phosphate solution in a 2000 mL volumetric flask, add 224 mL 0.2 M NaOH, then add water to volume and test pH.

Hydrochloric acid 0.1 M solution was prepared from concentrated hydrochloric acid (supplied by Fisher Chemicals). Deionised water was again obtained from an Ondeo Purite Select Neptune Analytical water purifier within the chemistry department (18.2 Ω).

Mass spectrometry:

Dissolution media was prepared in advance and held at a temperature of approximately 40°C overnight (12 hours or more) to enable degassing. Multiple

versions of each biorelevant dissolution media exist but for the purposes of the mass spectrometry work three blank media were produced: simulated gastric fluid (SGF), acetate buffer and fasted state simulated intestinal fluid (FaSSIF), see Table 2.6.

Table 2.6 - Dissolution media ingredients for blank simulated gastic fluid (SGF), acetate buffer and blank fasted state simulated intestinal fluid (FaSSIF).

SGF (blank), pH 1.2	Sodium chloride	0.2 mol
	Hydrochloric acid	0.2 mol
	Pure water	To 1 L
Acetate, pH 4.5	Sodium acetate trihydrate	0.02 mol
	Glacial acetic acid	0.03 mol
	Pure water	To 1 L
FaSSIF (blank), pH 6.8	Sodium dihydrogen phosphate	0.2 mol
	Sodium hydroxide	0.2 mol
	Pure water	To 1 L

The dissolution media are referred to as blank because they do not contain the complex additives such as proteins or enzymes but are produced to replicate the pH at that section of the gastrointestinal tract.

2.1.5 Single crystal studies

The clear nail varnish used for attaching and coating single crystals was stated as having the following ingredients: butyl acetate, ethyl acetate, acrylates copolymer, dipropylene glycol debenzoate, nitrocellulose, isopropyl alcohol, etocrylene, trimethylpentanediyl dibenzoate, CI 60725 (Violet 2).

Paracetamol single crystals were obtained by slow cooling a saturated solution of paracetamol dissolved in deionised water, before leaving the vial open on the bench to evaporate under ambient conditions.

A mono-iodinated 2,4,5-triphenyl imidazole derivative (molecular weight 422.265 g/mol) referred to as I-TPI was synthesized by Dr Jessica Andrews (Durham University) and used to produce a gel for the dissolution studies. The I-TPI gel forms from a methanol solution following a process of heating, sonication and crash cooling. The I-

TPI single crystal samples of Form SI and Form SII were obtained by leaving the vial of gel partially open on the bench under ambient conditions.

2.2 Methods and instrumentation for surface dissolution imaging

2.2.1 Image Analysis Software

Image analysis was carried out using MATLAB, 2018a 64-bit version using Windows 10, developed by MathWorks®. This "programming and numeric computing platform" allows algorithms or code, to be written for multiple functions, including image analysis. Training and support was provided by Dr Daniel Markl at the University of Strathclyde, in addition to his writing the original code to extract information from the SDi2 images. This code was further manipulated to refine it for each sample and to explore the information that could be obtained with it. Additional support in understanding and manipulating MATLAB code was provided by Dr Marion Weinzierl, a Research Software Engineer in the Advanced Research Computing Department at Durham University. The original code is presented in Appendix 1 – MATLAB original script with comments.

2.2.2 Powder X-ray Diffraction

Powder X-ray diffraction (PXRD) produces a specific pattern, commonly described as a fingerprint, for a material based upon its crystal lattice. It can be used to distinguish between polymorphs and produces a characteristic "halo" effect with amorphous material. The distinct patterns are shown on a plot of X-ray diffraction intensity against the diffraction angular parameter (2 theta or 2θ).

The equipment used was a Bruker D7 powder X-ray diffractometer, with samples mounted on a silicon single-crystal wafer. Analysis used CuKα radiation at a wavelength of 1.5418 Å and X-rays were produced at an operating voltage of 40 kV with an acceleration current of 40 mA. The range scanned was 4 to 40°, with a step size of 0.02° and a scan rate ranging between 0.5 and 1.5 s/step.

2.2.3 Single Crystal X-ray Diffraction

Single crystal X-ray diffraction (SCXRD) data was collected by Dr Dimitry S. Yufit (Durham University) using one of two instruments:

1. Bruker D8Venture diffractometer (Photon100 CMOS detector, IμS-microsource, focusing mirrors) equipped with a Cryostream 700+ (Oxford Cryosystems) open-flow nitrogen cryostat and using MoKα or CuKα radiation, with wavelengths of 0.71073 Å and 1.54178 Å, respectively.
2. XCalibur Agilent, Sapphire3 diffractometer equipped with a Cryostream 700 (Oxford Cryosystems) nitrogen cryostat and using MoKα radiation with a wavelength of 0.71073 Å.

Single crystals for only SC-XRD analysis were coated in perfluoro polyether 225 (crystallography) oil and mounted on a MiTeGen sample holder before being placed into the precooled cryostream and subjected to analysis. An additional method was also developed which attached the single crystals to a novel holder using varnish instead of crystallography oil to enable them to be used for dissolution after SC-XRD analysis. The data was processed by Dr Dimitry S. Yufit using Bruker APEXII software.

2.2.4 Surface Dissolution Imaging

Surface dissolution imaging was carried out using the SDi2, originally produced by Sirius Analytical Instruments Ltd, and later by Pion UK Ltd. The system details of the instrumentation and software are provided in Table 2.7.

Table 2.7 – SDi2 with Actipix Technology detailed system information.

Product Name	SiriusSDi2Collection
Application version Number	1.2.0.0
Camera Name	Cypress USB StreamerExample
Camera Driver Version	16908800
Camera Product	FX3
Camera Chip Type	CMV4000v3
Paraytec Led Mk2 Hub Device Name	Camera Hub
Paraytec Led Mk2 Hub Serial Number	A12OVJK5
Paraytec Led Mk2 Hub Driver Version	135704
Sirius Hub Firmware Version	E460302 – V1.03
Sirius Heater Serial Number	28/118167
Sirius SDi2 Analysis Version	3.0.22

Surface dissolution imaging utilises UV-vis technology to record and calculate changes in absorbance during dissolution. Detailed discussion of the instrumentation including its functionality, equipment set up(s), the method(s) used and data analysis techniques are included in detail in each of the three chapters discussing the use of surface dissolution imaging in monitoring dissolution.

Maintenance:

Pion recommend that the SDi2 is maintained through tubing flushes before and after every run, flow rate checks and a monthly assessment of the general running of the equipment. Flow rate checks involve manually running sample through different sections of the fluidics and measuring the volume of effluent obtained in a fixed period of time. This is done in triplicate and the error should be less than 10% as recommended by Pion. Monthly assessments include consideration of the heater, checking all seals and connections for leaks, cleaning cells thoroughly and checking for persistent bubbles.

QC test:

In addition, a QC test for the compact flow cell is defined within the SDi2 manual. Approximately 3 - 10 mg of ketoprofen sample is weighed into the 3 mm diameter holder and compacted using the load cell; 100 kg load over 60 seconds as recommended by Pion. The sample holder, complete with ketoprofen compact, is then inserted into the compact flow cell (CFC) and 0.1 M HCl dissolution media passed through the cell at a flow rate of 2.16 mL/min for twenty minutes. The manual provides guidance on the expected IDR values (5-8 µg/min/cm^2) and cumulative mass released (8-12 µg) at a wavelength of 254 nm. Values obtained outside this range require a discussion with Pion to determine the cause of variation.

Image Resolution:

The resolution capability of the SDi2 was assessed with grids obtained from Professor Østergaard (Copenhagen University) – the same grids were used in the previous work by Professor Østergaard's research group.[169] The grids were drawn using AutoCAD software and coated on a single side of 180 µm thick acetate to ensure identical line widths and distances between lines. The grid sizes range from 10 – 100 µm (in 10 µm

increments), with three additional grids of 200, 300 and 400 µm, whereby each line pair is defined as a printed line which absorbs the visible light, plus a transparent space between (no visible light absorbed) of equal width.

An SDi2 method using the CFC was selected to include no subsampling and 1x1 binning ensuring that each pixel intensity was saved at a rate of one frame per wavelength per second. Initially each grid was placed flat against the CMOS camera chip and a method run with no cell in place and no fluid passing between the LED and CMOS chip. Two wavelengths were selected (255 nm and 520 nm) for completeness and the SDi2 set to obtain intensity data for ten minutes as each grid was placed in front of the LEDs in turn.

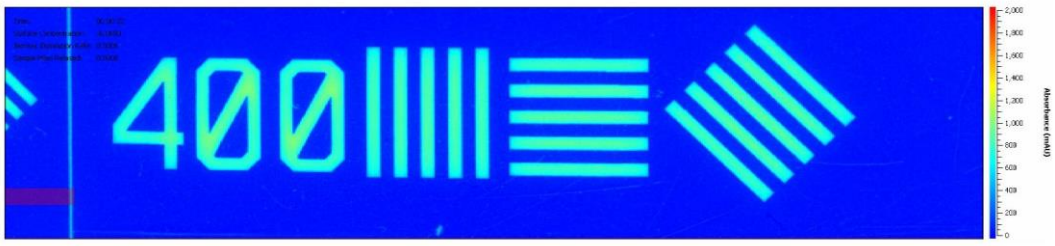

Figure 2.24 – Absorbance map using visible wavelength (520 nm) and the 400 grid. Shown in jet colour map and extracted from frame 24 of 591. Three distinct parts can be seen in the image: 1) 400 to show grid number, 2) vertical lines to test horizontal resolution, 3) horizontal lines to test vertical resolution, and 4) diagonal lines for completeness.

For data analysis, the zones for extracting data were removed or moved to one side wherever possible to enable the full images to be viewed. An image from the visible video, shown in Figure 2.24, shows the size of grid on the far left (400 µm), then three sets of five lines in three directions to test horizontal, vertical and diagonal resolution.

2.2.5 UV-Vis Spectroscopy

UV-vis analysis of samples was conducted using an Agilent Technologies Cary Series UV-vis Spectrophotometer. Standard UV-vis methodology was followed with a scan of the blank solvent being taken prior to sample analysis to remove background signal. The Agilent was used to scan for absorption across the UV-vis range, from 190 to 1100 nm, thus enabling the wavelength at which maximum absorption takes place to be found (λ_{max}) and guide the SDI method.

2.3 Methods and instrumentation for bulk dissolution monitoring

2.3.1 Compact production

A Gamlen GTP1 benchtop press was used for the production of compacts. Compacts were produced from simple formulations containing one API plus lactose and lubricant where necessary. Dry mixing was carried out using a Turbula mixer for five minutes and homogeneity confirmed by UV-vis absorbance of a dissolved sample relative to a series of standards.

The compaction method used a single fixed load at a speed of 60.0 mm min^{-1} with a die diameter of 6.0 mm and die height of 18.0 mm. A single compression with a load ranging from 50 to 500 kg was used, dependent upon the formulation being compressed, and the ejection function was switched on. Additionally a pre-compression function ranging from 0 to 300 kg was used for those formulations which required it.

Compacts were visually checked for defects and weighed prior to dissolution. Additional quality checks such as hardness, disintegration and friability were not carried out due to the limited number of compacts produced.

2.3.2 Dissolution

Sotax:

Early studies used the Sotax AT7 Smart USP II paddle dissolution apparatus at Queen's (former Stockton Campus, Durham University School of Pharmacy). Each glass vessel was filled with 900 mL of dissolution media and held in a water bath at 37°C. The paddle apparatus started stirring at 50 rpm once the tablet had been dropped into the vessel to ensure the tablet was not damaged. Samples of approximately 5 mL were taken manually using a syringe with PEEK tubing attachment at a series of time points the number of which was dependent upon the API or formulation being studied.

Durham:

The dissolution apparatus set up in the MS lab (within the Department of Chemistry at Durham) was also based upon the USP II paddle apparatus, and included a round-bottomed glass dissolution vessel capable of holding over 1000 mL of media held in place within a water bath using a metal frame. A paddle and rotor capable of stirring

at 50 rpm was fitted above the vessel and measured to sit at the specified position (according to the USP). Samples could be taken manually through holes in the vessel lid using PEEK tubing and a syringe, or a continuous flow of sample could be extracted from the vessel using a pump.

2.3.3 Mass rate attenuator

A Rheodyne mass rate attenuator (MRA), supplied by Kinesis Scientific Experts, was used to dilute flowing samples. A diagram showing the stages of MRA operation can be seen in Figure 2.25.

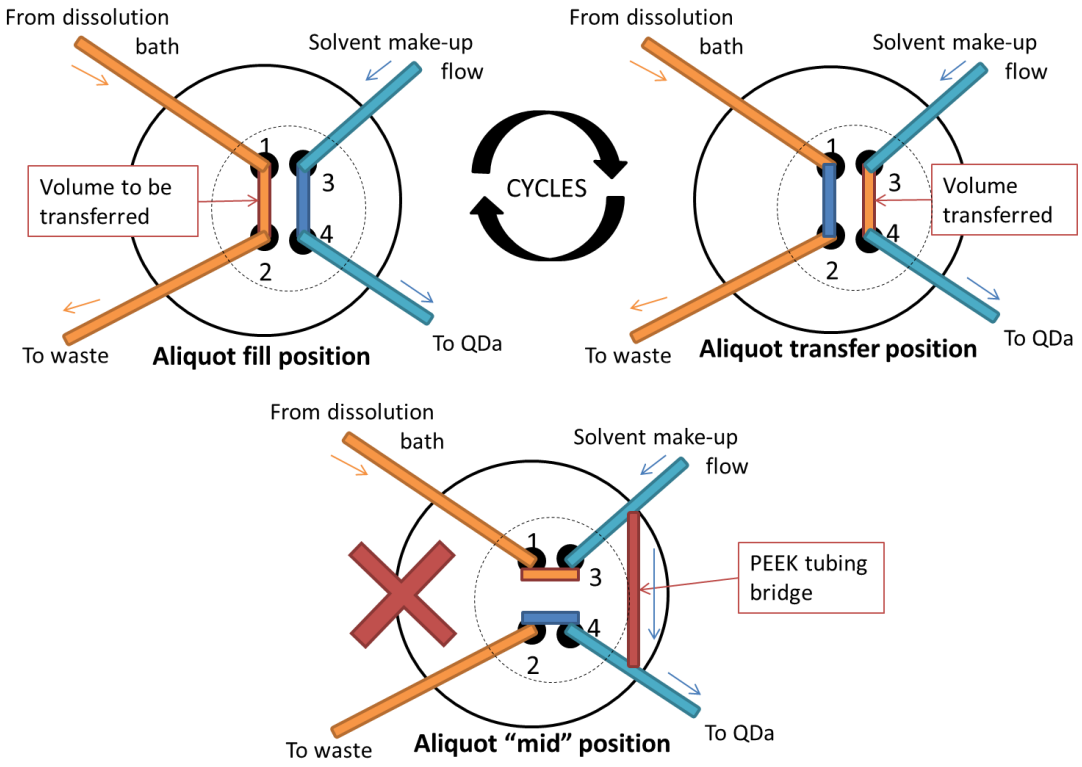

Figure 2.25 – Flow diagram for the mass rate attenuator (MRA) stages of operation. The central section (highlighted by the dotted lines) of the MRA cycles between the two positions with a "mid" step between each change (fill -> mid -> transfer -> mid -> fill -> mid -> transfer -> mid and so on).

The MRA injects aliquots, in the region of 0.022 to 0.300 µL, from a continuous flow of dissolution bath sample into a make-up flow of solvent. This dilution accommodates a high concentration of API or excipient, and a simulated pH dissolution media which may contain components that are not compatible with ESI-MS at undiluted concentrations thereby addressing one of the major challenges of combining dissolution and mass spectrometry.

The degree of dilution provided by the MRA can be amended during operation by varying the flow rates (of both the sample and the solvent) and the split factor setting which amends the aliquot volumes (of which there are three channels or "grooves" available) and frequency. Whilst the aliquot of sample is being transferred (i.e. the MRA is in the aliquot transfer position), the volume of solvent in the channel will move into the waste line, and the groove will be refilled with sample from the dissolution bath, which will then transfer into the solvent make-up flow and so on.

The MRA requires a PEEK tubing bridge to relieve pressure changes that occur as a result of the channels switching. Polyetheretherketone or PEEK tubing is used throughout HPLC and MS instruments for its inert non-fluoropolymer properties and comes in a range of inner diameter sizes ranging from 0.004 to 0.030 inches. The bridge is in place throughout the whole MRA cycle but is only shown on the "mid" stage diagram in Figure 2.25.

An Excel spreadsheet provided by the MRA manufacturer is used to navigate the dilution, split factor and flow rate calculations, see Appendix 2 – Mass rate attenuator (MRA) split factor and flow rates

An example of calculating split ratio from a specified flow rate is as follows:

- Flow of make-up solvent into MRA is 0.5 mL/min which is the same as the flow rate into the QDa
- Flow of dissolution bath sample into MRA is 1 mL/min which must be sufficient to refill the channel before it switches into the solvent make-up flow
- Therefore a split factor setting of 5 on the MRA would result in a dilution ratio of 125:1 using the 0.100 μL channel and running at 0.667 Hz.

The flow rate into the MRA and therefore QDa was kept at 0.5 mL/min wherever possible as this was recommended by Waters as optimal for ionisation. The dissolution bath sample flow rate was varied to accommodate the selected channel size and frequency.

2.3.4 Mass spectrometry (with and without chromatography)

Mass spectrometry was carried out primarily using the QDa, and where additional information or validation was necessary using the Synapt and the QToF. Each instrument is described below but further details of specific equipment set ups will be discussed in the relevant chapters. Instrument control and data processing for all three instruments was performed using MassLynx version 4.1, provided by Waters, UK and operated using Windows Versions 7 and 10.

Acquity QDa Detector:

Referred to as the "QDa", this is an electrospray ionisation single quadrupole mass detector prototype produced by Waters, UK. An outline of the QDa is shown in Figure 2.26.

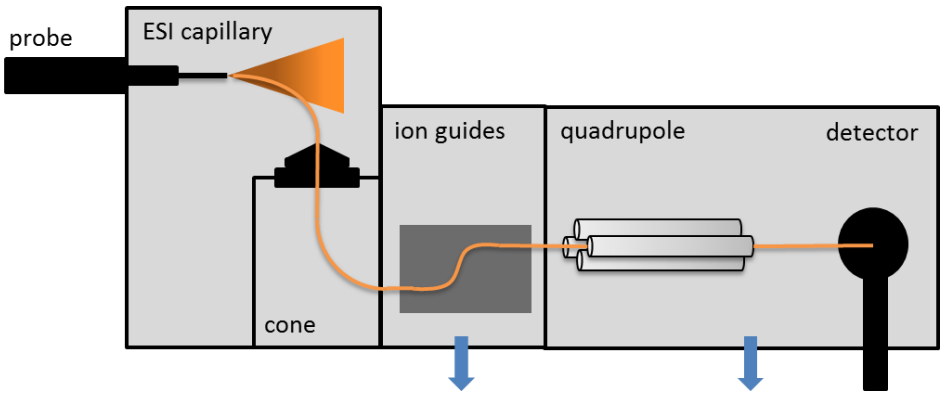

Figure 2.26 – A simplified schematic of the QDa Detector.

Designed to be versatile, efficient and relatively easy to use, with a small footprint, this work uses the pre-production beta version. The QDa was utilised in multiple configurations to accommodate both on-line and off-line sample analyses without chromatography. The ability of this detector to monitor dissolution in conjunction with discussions about its accuracy, precision, robustness and validation will form the basis of the three chapters discussing the use of mass spectrometry for monitoring dissolution.

Synapt G2-S High Definition Mass Spectrometer:

Referred to as the "Synapt", it is a hybrid high resolution quadrupole time-of-flight (QTOF) accurate mass system used with an electrospray ionisation source and produced by Waters, UK. The Synapt was coupled to a Waters Acquity LC with samples

able to be injected both with and without bypassing the HPLC C-18 column, see Table 2.8 for details of both the five and nine minute reverse phase gradient methods used. Solvent flow was set to 400 µL min^{-1} into the Synapt. The solvent mix was made up of water and acetonitrile (of varying composition) both with and without 0.1% v/v formic acid. Regular manual calibrations of the Synapt were carried out to confirm accurate mass using a small molecule mix in addition to the automatic internal lock-spray calibration during runs.

Table 2.8 – Solvent method for LCMS with the Synapt, where flow is consistently 0.400 mL/min and each solvent may or may not have 0.1% v/v formic acid dependent upon the sample being studied. A five (left time column) or nine (right time column) minute method can be used.

Time (mins)		**% Water**	**% Acetonitrile**
Initial	Initial	95	5
0.50	0.5	95	5
4.00	7.5	5	95
4.50	8.3	5	95
4.51	8.4	95	5
5.00	9.0	95	5

QToF Premier Mass Spectrometer:

Referred to as the "QToF", it is a high resolution quadrupole time-of-flight accurate mass with enhanced sensitivity and selectivity system, used with an electrospray ionisation source and produced by Waters, UK. The QToF was used coupled to a Waters Acquity LC with a solvent system of water and acetonitrile (of varying gradients) with 0.1% v/v formic acid.

2.3.5 Sample flow

Sample flow and injection was enabled by LC systems, which included an Agilent 1100 HPLC, Alliance 2795 LC and a Waters Acquity LC. Each provided either aliquots of sample or a continuous flow of sample in addition to an MS solvent for dilution. Additionally Restek LS class pumps provided a continuous flow of both sample and make-up solvents at controlled and specified flow rates.

2.3.6 UV-Vis Spectrophotometry

UV-vis analysis of standards and dissolution samples was conducted using an Agilent Technologies Cary Series UV-vis Spectrophotometer and a Jenway 6305 Spectrophotometer. Standard UV-vis methodology was followed with a scan of blank solvent being taken prior to sample analysis to remove background signal. The Agilent was used to scan for absorption across the UV-vis range, from 190 to 1100 nm, thus enabling the wavelength at which maximum absorption takes place to be found (λ_{max}). The Jenway was used at a single wavelength to monitor changes in absorption between samples and thus enable changes in concentration to be calculated in accordance with Beer's Law.

Appendix 1 – MATLAB original script with comments

The code was written by Dr Daniel Markl at the University of Strathclyde. It includes comments for training purposes and was written to enable the monitoring of size and concentration changes for samples in the compact flow cell of the SDi2. This is the original code from which further versions were produced to refine and adjust it according to requirements.

```
%%%
```

```
filename = '2019_03 CLA50 C ITPI S1 RUN 1';
% Read UV video
vidobj1=VideoReader(fullfile(folderFile,filenameUV));
% Read vis video file
vidobj2=VideoReader(fullfile(folderFile,filenameVis));
% Get number of frames of UV video
frames1=vidobj1.NUmberoffframes;
% Get number of frames of vis video
frames2=vidobj2.Numberoffframes;
% Inititalise videos for saving (if flag "saving" is active
if saving
   vFused = VideoWriter(fullfile(folderFile,[filename,'_Fused.avi']));
   vFused.FrameRate = vidobj1.FrameRate;
   open(vFused);
   vProcessed = VideoWriter(fullfile(folderFile,[filename,'_Processed.avi']));
   vProcessed.FrameRate = vidobj1.FrameRate;
   open(vProcessed);
end
% Allocate memory for properties of detected area for each frame
area_prop = zeros(min(frames1, frames2),4);
% Allocate memory for absorbance for each frame
AbsUV_edge_total = zeros(min(frames1, frames2),2);
f1 = 1627;
img_VisSampleHolder = read(vidobj2, frames2);
% Define region of interest (area with the crystal and wire)
img_ROI = [694.5 211.5 58 25];
% Get image of the wire only
img_VisSampleHolder_gray = img_VisSampleHolder(:,:,2);
img_VisSampleHolder_gray_crop = imcrop(img_VisSampleHolder_gray,img_ROI);
img_VisSampleHolder_crop = imcrop(img_VisSampleHolder,img_ROI);
% Initialise the blob analysis object for analysing the crystal area
```

```
tMatcher = vision.TemplateMatcher;
Hblob = vision.BlobAnalysis('AreaOutputPort',true,...
   'MajorAxisLengthOutputPort',true,...
   'MinorAxisLengthOutputPort',true,...
   'PerimeterOutputPort',true, ...
   'CentroidOutputPort', false, ...
   'BoundingBoxOutputPort',false);
% Process each frame
for f1 = 1:min(frames1, frames2)
   % Read frame "f1" from UV video file
   img_UV = read(vidobj1, f1);
   % Read frame "f1" from vis video file
   img_Vis = read(vidobj2, f1);
   % Generate false colour image from both UV and vis images
   C = imfuse(img_UV,img_Vis,'falsecolor','Scaling','joint','ColorChannels',[0 2 1]);
   % Use only the green channel
   C_gray = img_Vis(:,:,2);
   %% Not used
%    colormapImg = imcrop(img_Vis,[1540.5 7.5 7 353]);
% %    fig = figure(1312);
% %    fig.Position = [200 200 200 1200];
%    [Xtest,maptest] = rgb2ind(colormapImg,256);
% %    [Xtest,maptest] = ind2rgb(Xtest,maptest);
%    cmap = squeeze(mean(colormapImg(:,:,:),2));
   % Crop the single channel image, the UV and visible image to the ROI
   C_crop_gray = imcrop(C_gray,img_ROI);
   img_UV_crop = imcrop(img_UV,img_ROI);
   img_Vis_crop = imcrop(img_Vis,img_ROI);
   % Subtract the samples holder/wire from the single channel image to
   % separate the crystal
   C_crop_gray_cut = C_crop_gray - img_VisSampleHolder_gray_crop;
```

```
% Binarise the single channgel image / thresholding
% The threshold (70/255) was selected manually
bw = imbinarize(C_crop_gray_cut,70/255);
% Determine the edge of the crystal
bw_edge = edge(bw);
% Allocate memory
indxImg = zeros(size(img_UV_crop,1),size(img_UV_crop,2));
% Define the colour map
cmap = flipud(jet(256*6))*255;
% Get the absorbance for each of the pixel in the image
for i_px = 1:size(img_UV_crop,1)
   for j_px = 1:size(img_UV_crop,2)
      img_UV_crop_ij = double(squeeze(img_UV_crop(i_px,j_px,:)))';
      [~,indxImg(i_px,j_px)] = min(sum(abs(img_UV_crop_ij - double(cmap)).^2,2));
   end
end
% Calculate the absorbance for each pixel
UV_abs = (1-indxImg/size(cmap,1))*abs_scale;
% Align the UV image with the visible image
% Displacement of 10 pixels - not validated
bw_edge_UV = imtranslate(bw_edge,[10, 0],'FillValues',0);
% Identify the area of the
UV_abs_edge = UV_abs(bw_edge_UV==1);
% Create the data for the figure (make the edge red)
UV_abs_disp = UV_abs;
UV_abs_disp(bw_edge_UV) = 2;
C_crop_gray_r = C_crop_gray_cut;
C_crop_gray_g = C_crop_gray_cut;
C_crop_gray_b = C_crop_gray_cut;
C_crop_gray_r(bw_edge) = 255;
C_crop_gray_g(bw_edge) = 0;
```

```
C_crop_gray_b(bw_edge) = 0;
C_crop_gray_disp = cat(3,C_crop_gray_r,C_crop_gray_g,C_crop_gray_b);
% Calculate average and standard deviation of the UV absorbance
AbsUV_edge_total(f1,1) = mean(UV_abs_edge);
AbsUV_edge_total(f1,2) = std(UV_abs_edge);
% Create the plot with sub-figures
if plotting
    clf;
    fig = figure(1);
    fig.Position = [100 200 1400 600];
    str = ['Frame ',num2str(f1),'; Time ',datestr(seconds(f1/vidobj1.FrameRate),'MM:SS')];
    annotation('textbox', [0 0.9 1 0.1], ...
        'String', str, ...
        'EdgeColor', 'none', ...
        'HorizontalAlignment', 'center','FontSize',20)
    subplot(2,3,1), imshow(img_UV_crop,'InitialMagnification',900), title('UV image','FontSize',20)
    subplot(2,3,2), imshow(img_Vis_crop,'InitialMagnification',900), title('Visible image','FontSize',20)
    subplot(2,3,3), imshow(bw,'InitialMagnification',900), title('Processed binary image','FontSize',20)
    subplot(2,3,4), imshow(bw_edge,'InitialMagnification',900), title('Detected crystal edge','FontSize',20)
    subplot(2,3,5), imshow(C_crop_gray_disp,'InitialMagnification',900), title('Detected crystal edge on Vis image','FontSize',20)
    subplot(2,3,6), imagesc(UV_abs_disp), colormap(flipud(double(cmap))./256), axis equal, caxis([0 2]), colorbar
    str = {'Calculted UV absorbance';'with crystal shape';'(displacement of 10 pixels)'};
    title(str,'FontSize',20)
    set(gca,'FontSize',18,'FontWeight','bold','linewidth',2)
    axis tight;
    set(gcf,'color','w');
    if saving
        frame = getframe(gcf);
        writeVideo(vProcessed,frame);
    end
```

```
    end
    % Plot figure and create
    if plotting
        clf;
        fig = figure(112);
        fig.Position = [100 200 1400 300];
        imshow(C)
      if saving
          writeVideo(vFused,C);
        end
    end
    % Calculate various properties of the crystal area
    [area, major, minor, perim] = step(Hblob, bw);
    if ~isempty(area)
        area_prop(f1,1) = area(1);
        area_prop(f1,2) = major(1);
        area_prop(f1,3) = minor(1);
        area_prop(f1,4) = perim(1);
    end
end
% Save videos
if saving
    close(vFused);
    close(vProcessed);
end
%%
% Define the resolution of the camera
res = 13.75; %mu
% Define the starting frame of the dissolution study
startID = 90;
% Correct the data for outliers
```

```
area_crystal = area_prop(startID:end,1);
area_crystal = filloutliers(area_crystal,'spline','movmean',50);
time = linspace(0,length(area_crystal)/vidobj1.FrameRate,length(area_crystal));
% Plot the data
fig = figure(2);
fig.Position = [400 400 600 400];
plot(time/60,(area_crystal)*res^2*10^-6,'k','LineWidth',2)
xticks(0:1:floor(time(end)/60))
xlabel('Time (min)','FontSize',20)
ylabel('Crystal area (mm^2)','FontSize',20)
set(gca,'FontSize',20,'FontWeight','bold','linewidth',2)

axis tight;
set(gcf,'color','w');
if saving
   export_fig(fullfile(folderFile,[filename,'_area']), '-pdf', '-png');
end
major_crystal = area_prop(startID:end,2);
major_crystal = filloutliers(major_crystal,'spline','movmean',50);
minor_crystal = area_prop(startID:end,3);
minor_crystal = filloutliers(minor_crystal,'spline','movmean',50);
fig = figure(232);
fig.Position = [400 400 600 400];
h1 = plot(time/60,(major_crystal)*res,'k','LineWidth',2);
hold on;
h2 = plot(time/60,(minor_crystal)*res,'LineStyle','--','Color',[0.5 0.5 0.5],'LineWidth',2);
xticks(0:1:floor(time(end)/60))
xlabel('Time (min)','FontSize',20)
ylabel('Lengh of crystal (μm)','FontSize',20)
set(gca,'FontSize',20,'FontWeight','bold','linewidth',2)
leg = legend([h2,h1],'Minor axis','Major axis');
```

```
leg.Box = 'off';
axis tight;
set(gcf,'color','w');
if saving
   export_fig(fullfile(folderFile,[filename,'_lenght_axis']), '-pdf', '-png');
end
per_crystal = area_prop(startID:end,4);
per_crystal = filloutliers(per_crystal,'spline','movmean',50);
fig = figure(23122);
fig.Position = [400 400 600 400];
h1 = plot(time/60,(per_crystal)*res,'k','LineWidth',2);
xticks(0:1:floor(time(end)/60))
xlabel('Time (min)','FontSize',20)
ylabel('Crystal perimeter (µm)','FontSize',20)
set(gca,'FontSize',20,'FontWeight','bold','linewidth',2)
% leg = legend([h2,h1],'Minor axis','Major axis');
leg.Box = 'off';
axis tight;
set(gcf,'color','w');
if saving
   export_fig(fullfile(folderFile,[filename,'_perimeter']), '-pdf', '-png');
end
AbsUV_edge_total_crystal = AbsUV_edge_total(startID:end,:);
AbsUV_edge_total_crystal_ = filloutliers(AbsUV_edge_total_crystal(:,1),'spline','movmean',50);
AbsUV_edge_total_crystal_std = filloutliers(AbsUV_edge_total_crystal(:,2),'spline','movmean',50);
fig = figure(3);
fig.Position = [400 400 600 400];
h = shadedErrorBar(time/60,AbsUV_edge_total_crystal_,...
        AbsUV_edge_total_crystal_std,{'Color',[0.3 0.3 0.3]});
    h.edge(1).LineStyle = 'none';
    h.edge(2).LineStyle = 'none';
```

```
        h.patch.EdgeColor = 'none';
        h.patch.FaceAlpha = 0.8;
        h.mainLine.LineWidth = 2;
        handlesMain = h.mainLine;
        handlesShade = h.patch;
xticks(0:1:floor(time(end)/60))
xlabel('Time (min)','FontSize',20)
ylabel('UV absorbance at crystal edge (a.u.)','FontSize',20)
set(gca,'FontSize',20,'FontWeight','bold','linewidth',2)
leg = legend([handlesMain,handlesShade],{'Average UV absorbance','Standard deviation'});
leg.Box = 'off';
axis tight;
set(gcf,'color','w');
if saving
   export_fig(fullfile(folderFile,[filename,'_abs_edge']), '-pdf', '-png');
end
```

Appendix 2 – Mass rate attenuator (MRA) split factor and flow rates

Screenshot of the Excel worksheet – sections encircled with black contain the information for the example calculation.

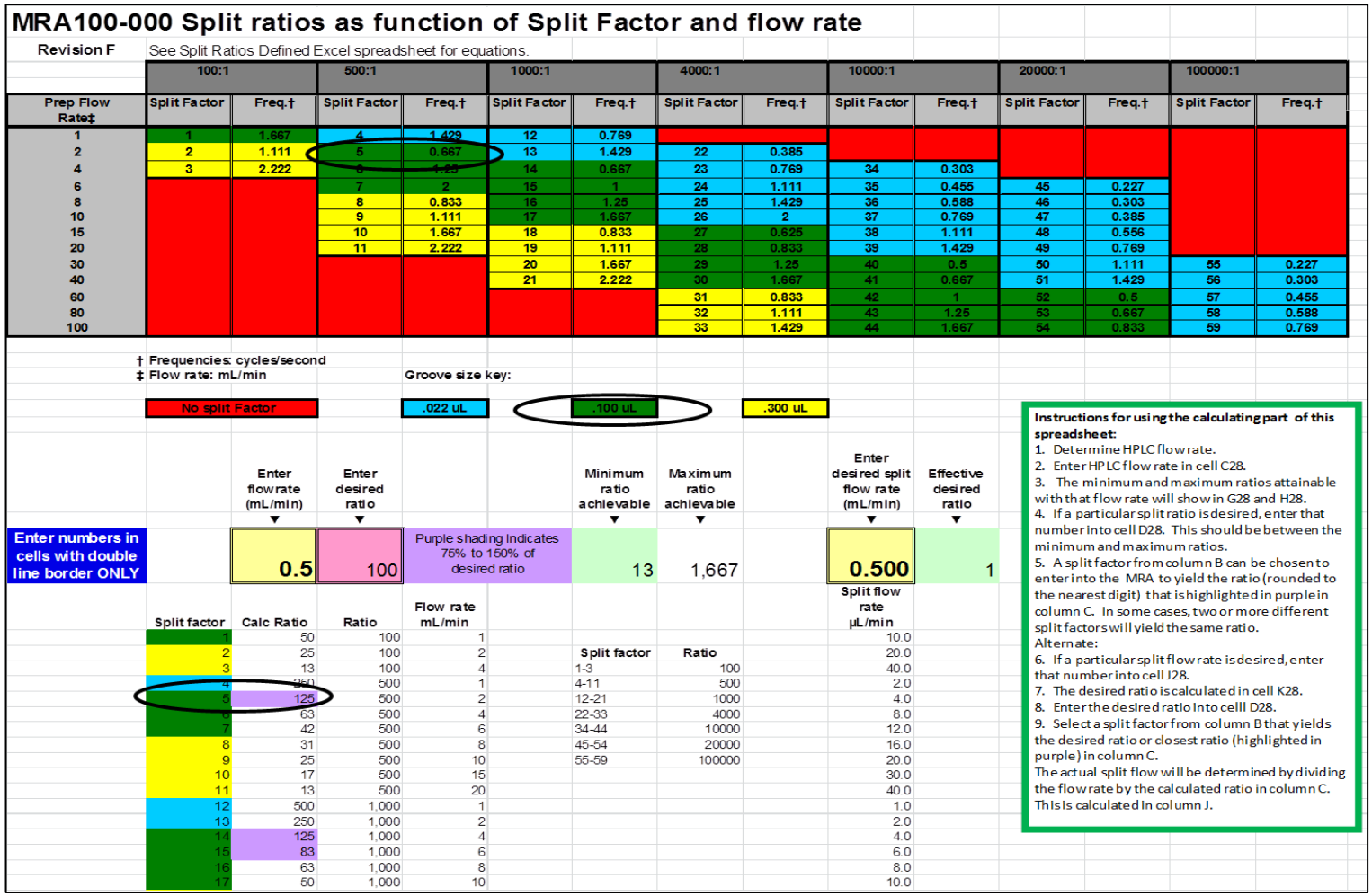

MRA100-000 Split ratios as function of Split Factor and flow rate

Revision F — See Split Ratios Defined Excel spreadsheet for equations.

Prep Flow Rate‡	100:1 Split Factor	100:1 Freq.†	500:1 Split Factor	500:1 Freq.†	1000:1 Split Factor	1000:1 Freq.†	4000:1 Split Factor	4000:1 Freq.†	10000:1 Split Factor	10000:1 Freq.†	20000:1 Split Factor	20000:1 Freq.†	100000:1 Split Factor	100000:1 Freq.†
1	1	1.667	4	1.429	12	0.769								
2	2	1.111	5	0.667	13	1.429	22	0.385						
4	3	2.222	6	1.25	14	0.667	23	0.769	34	0.303				
6			7	2	15	1	24	1.111	35	0.455	45	0.227		
8			8	0.833	16	1.25	25	1.429	36	0.588	46	0.303		
10			9	1.111	17	1.667	26	2	37	0.769	47	0.385		
15			10	1.667	18	0.833	27	0.625	38	1.111	48	0.556		
20			11	2.222	19	1.111	28	0.833	39	1.429	49	0.769		
30					20	1.667	29	1.25	40	0.5	50	1.111	55	0.227
40					21	2.222	30	1.667	41	0.667	51	1.429	56	0.303
60							31	0.833	42	1	52	0.5	57	0.455
80							32	1.111	43	1.25	53	0.667	58	0.588
100							33	1.429	44	1.667	54	0.833	59	0.769

† Frequencies: cycles/second
‡ Flow rate: mL/min

Groove size key: No split Factor | .022 uL | .100 uL | .300 uL

Enter numbers in cells with double line border ONLY	Enter flow rate (mL/min)	Enter desired ratio	Purple shading Indicates 75% to 150% of desired ratio	Minimum ratio achievable	Maximum ratio achievable	Enter desired split flow rate (mL/min)	Effective desired ratio
	0.5	100		13	1,667	0.500	1

Split factor	Calc Ratio	Ratio	Flow rate mL/min	Split factor	Ratio	Split flow rate µL/min
1	50	100	1			10.0
2	25	100	2	Split factor	Ratio	20.0
3	13	100	4	1-3	100	40.0
4	250	500	1	4-11	500	2.0
5	125	500	2	12-21	1000	4.0
6	63	500	4	22-33	4000	8.0
7	42	500	6	34-44	10000	12.0
8	31	500	8	45-54	20000	16.0
9	25	500	10	55-59	100000	20.0
10	17	500	15			30.0
11	13	500	20			40.0
12	500	1,000	1			1.0
13	250	1,000	2			2.0
14	125	1,000	4			4.0
15	83	1,000	6			6.0
16	63	1,000	8			8.0
17	50	1,000	10			10.0

Instructions for using the calculating part of this spreadsheet:
1. Determine HPLC flow rate.
2. Enter HPLC flow rate in cell C28.
3. The minimum and maximum ratios attainable with that flow rate will show in G28 and H28.
4. If a particular split ratio is desired, enter that number into cell D28. This should be between the minimum and maximum ratios.
5. A split factor from column B can be chosen to enter into the MRA to yield the ratio (rounded to the nearest digit) that is highlighted in purple in column C. In some cases, two or more different split factors will yield the same ratio.

Alternate:
6. If a particular split flow rate is desired, enter that number into cell J28.
7. The desired ratio is calculated in cell K28.
8. Enter the desired ratio into cell D28.
9. Select a split factor from column B that yields the desired ratio or closest ratio (highlighted in purple) in column C.

The actual split flow will be determined by dividing the flow rate by the calculated ratio in column C. This is calculated in column J.

3. Surface dissolution imaging intrinsic dissolution rate calculations

3.1 Introduction

The original surface dissolution imaging equipment, the D100, was designed to replicate the Nelson and Shah cell and provide laminar flow throughout, thus enabling Intrinsic dissolution rates (IDR) to be calculated using a smaller quantity of API.[145] The SDi2 has developed this idea and the instrument further by including the WDC to widen its application, however, the calculation of IDR is limited to the CFC only. The calculation of IDR for ketoprofen in acid is used as a model drug to confirm that the SDi2 is functioning correctly. The process of measuring IDR provides guidance for its use with single crystal dissolution, hence it will be discussed in detail.

The purpose of this discussion of IDR is to understand how varying the SDi2 settings can influence the value obtained and whether the instrument calculations can be replicated by using the described equations to manually obtain IDR values from absorbance. The unpublished algorithms for calculating IDR are first mentioned in Professor Østergaard's 2018 review and are still relevant today. The overall objective, however, is to obtain a deeper understanding of what can be gleaned from the instrument calculations when observing dissolution of single crystals rather than compacted samples.

3.1 Equations for calculations

The SDi2 analysis software calculates a series of IDR values using the defined zone (see Figure 1.16) along with a previously calculated molar absorption coefficient (obtained through calibration and also called the extinction coefficient). The SDi2 data analysis software reports IDR values as a plot against time and uses two equations to calculate it:

Equation 3.5:

$$j = \sum_{z=0}^{H/2} \frac{v_z M c_z W \Delta z}{S}$$

Equation 3.6:

$$v_z = \frac{3Q}{2HW}\left(1 - \left(\frac{(2z - H)^2}{H^2}\right)\right)$$

where j is the intrinsic dissolution rate (IDR, mg/min/cm^2), H is the height of flow cell channel (cm), z is the height above the z-origin or surface and is referred to as the pixel position, v_z is linear velocity at height z (cm/min), M is the molecular weight (g/mol), c_z is the concentration of sample at row z (mol/cm^3), W is the width of the flow cell channel which is the path length the light travels through (cm), Δz is the effective pixel height (cm), S is the surface area of the sample (cm^2) and Q is the volumetric flow rate (cm^3/min).

The equations are valid with the assumption that flow through the CFC is laminar and so a parabolic flow profile can be achieved, which enables the linear velocity to be calculated for any point within the cell. Parabolic flow only occurs once laminar flow has been established and is best defined with a diagram, see Figure 3.27.[77,173,175] The schematic highlights a maximum linear velocity found in the centre of the cell at H/2 and a linear velocity of zero at the cell walls. The lower surface is referred to as the z origin (z_0) and is defined by the user during data analysis.

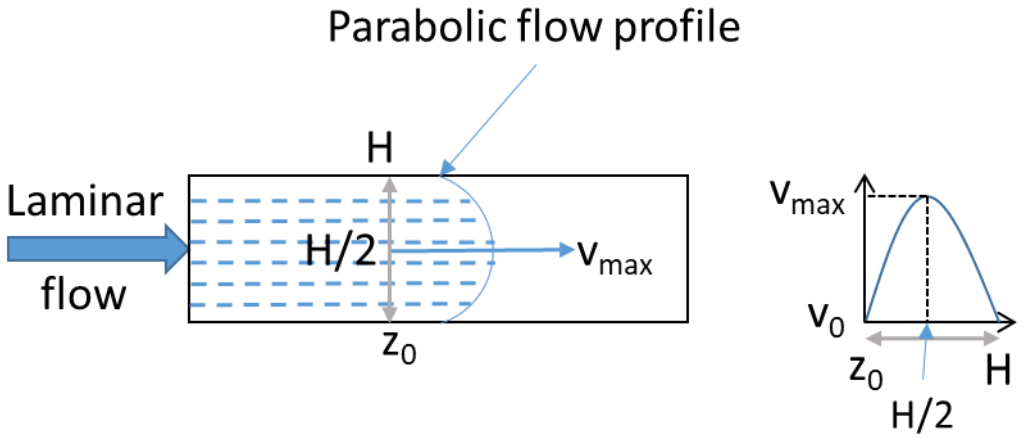

Figure 3.27 – Schematic side view of the compact flow cell showing laminar flow, the parabolic flow profile and a series of defined values for calculating intrinsic dissolution rate (IDR). H is the height of the flow cell, z_0 represents the lower surface of the cell, and v is the linear velocity. A cross-sectional slice through the flow cell at the grey arrow would produce the plot of linear velocity against z-axis position, shown to the right of the schematic.

The calculation of IDR is best understood by considering the passage of dissolved sample per unit time per unit area through a fixed point, see Figure 3.28. The CFC is considered in terms of pixel rows, with the amount of dissolved sample calculated for each row in the lower half of the cell before being added together to produce a value for j.

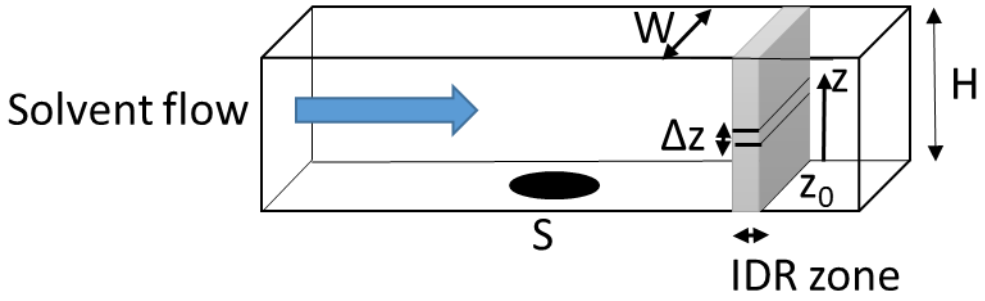

Figure 3.28 - Schematic of compact flow cell with details of intrinsic dissolution rate (IDR) measurements.

True laminar flow assumes there are horizontal straight lines of flow within the CFC with no mixing between upper and lower lines, only movement from left to right with the solvent flow (termed advection). In the case of a dissolving compact, which results in changing concentrations within this flowing solvent, there will be a drive towards an equilibrium of concentration that also results in diffusion of the dissolved sample upwards from these lower lines to upper lines, see Figure 3.29. The movement due to diffusion is accounted for through the volumetric flow rate (Q) and the calculation of linear velocity (v_z). Linear velocity through the CFC is at its maximum in the centre (H/2) as a result of the parabolic flow profile, hence any diffusion above this point will be minimal and IDR calculations only summate material passage in the lower half of the cell, from z_0 to H/2.

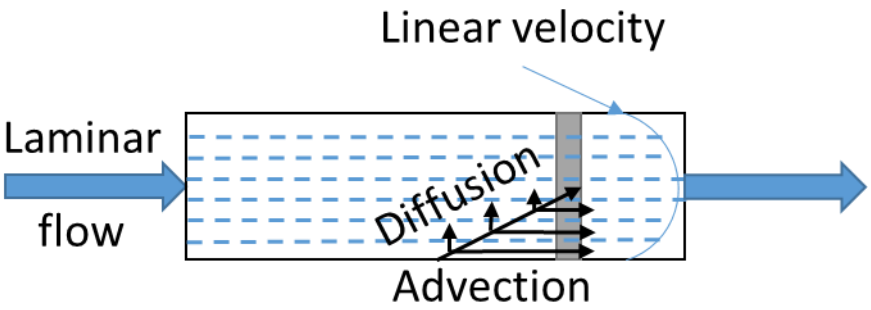

Figure 3.29 – Schematic of the compact flow cell showing the linear velocity parabolic profile and the direction of diffusion (upwards) and advection (left to right).

This is accounted for in Equation 3.6: wherein the linear velocity for each pixel height is calculated. Linear velocity is equal to the volumetric flow rate divided by the cross sectional area of the CFC. Halfway up the flow cell, 2z will be equal to H and will therefore result in the highest linear velocity value. The lower surface of the cell (z_0) conversely has a linear velocity value of zero, as shown in Figure 3.27. The IDR calculation methodology likens each pixel row to a spectrophotometer cuvette or cell, whereby the thickness of the flow cell is the path length. The Beer-Lambert Law is applied to each row and concentration calculated from the absorbance values. Each row is then summed up to a total per time period and divided by the surface area of the compact, which produces an IDR value.

3.2 Data analysis

The impact of data analysis upon the IDR value reported by the software will be explored in this section. In the context of this work, data analysis encompasses the entire method that is entered into the Sirius SDi2 Analysis software (Version 3.0.22) when extracting data from the series of images. This includes the start and end frames, the segment size, the height and width of each of the zones, their placement in both the x and z dimension, and any additional zones used. Each of these will be examined in turn using a single ketoprofen QC experiment for consistency. The expected IDR value for a ketoprofen QC check is 5-8 µg/min/cm^2 according to the Pion manual.[168]

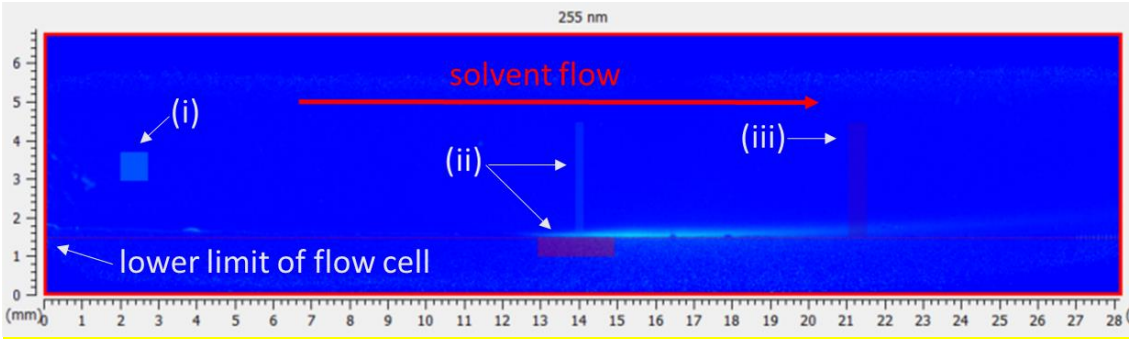

Figure 3.30 – Image of compact flow cell using the jet colour map and showing a compact of ketoprofen in place. The red arrow shows the direction of solvent flow and the adjustable lower boundary of the flow cell is labelled at a height of 1.54 mm. The measuring zones are in their default positions with default widths and heights, (i) reference, (ii) surface and (iii) intrinsic dissolution rate (IDR).

Figure 3.30 shows the placement of each of the three default zones in relation to a compact of ketoprofen, which is situated below the lower limit of the flow cell, where the horizontal zone (ii) is. Dissolving ketoprofen can be seen to move in the direction of solvent flow through the cell and passes initially through zone (ii) and then zone (iii) spreading slightly upwards and gradually through the cell as a result of diffusion and advection, respectively. Zone (i) is placed in the flow of incoming solvent so that it consistently provides a background reading of the blank solvent for reference if required.

3.2.1 Start frame, end frame and segment size:

The very start of the imaging process involves the cell filling with dissolution media. This influences the starting frame from which IDR values can be extracted. Although no guidance is provided on the shape of the IDR graph in the manual, recent experimental work has suggested that IDR values obtained in the first three to five minutes (180 to 300 secs) of dissolution should be discarded, as inaccurate measurements may result from the release of non-compacted surface powder during this time.[150,145,187] Additionally, this initial period often requires manual intervention to remove air bubbles that result from the empty cell being refilled after the initial blank media has been imaged. In the case of bubbles the cell is tipped to allow gravity to encourage the bubble through, which conversely results in more dense solution (that with a higher concentration of solute or loose particles) sinking through the cell.

The starting frame may therefore be input as zero, but the first section of data may need to be discarded when reporting IDR values to compare samples.

For the purpose of understanding the minutia of dissolution, these starting frames will likely offer a vast amount of information about early processes such as wetting of the compact.[2,13] This paves the way for discussions about the surface exposed to the solvent, the impact of compaction upon this and the impact upon the sample being investigated, for which significant research has been done recently by Ward *et al*.[150,152] This is an extensive area of research with numerous ramifications, however, it is not the purpose of this work and so it will not be addressed in this section.

The segment size states the time over which the absorbance values are averaged to calculate each IDR value per time period. The options include 10, 30, 60, 360 and 3600 seconds. Figure 3.31 demonstrates the difference in calculated IDR profiles for the same experiment analysed using the SDi2 software with segment times of 10, 30 and 60 seconds as the ketoprofen dissolution is routinely monitored for 20 minutes.

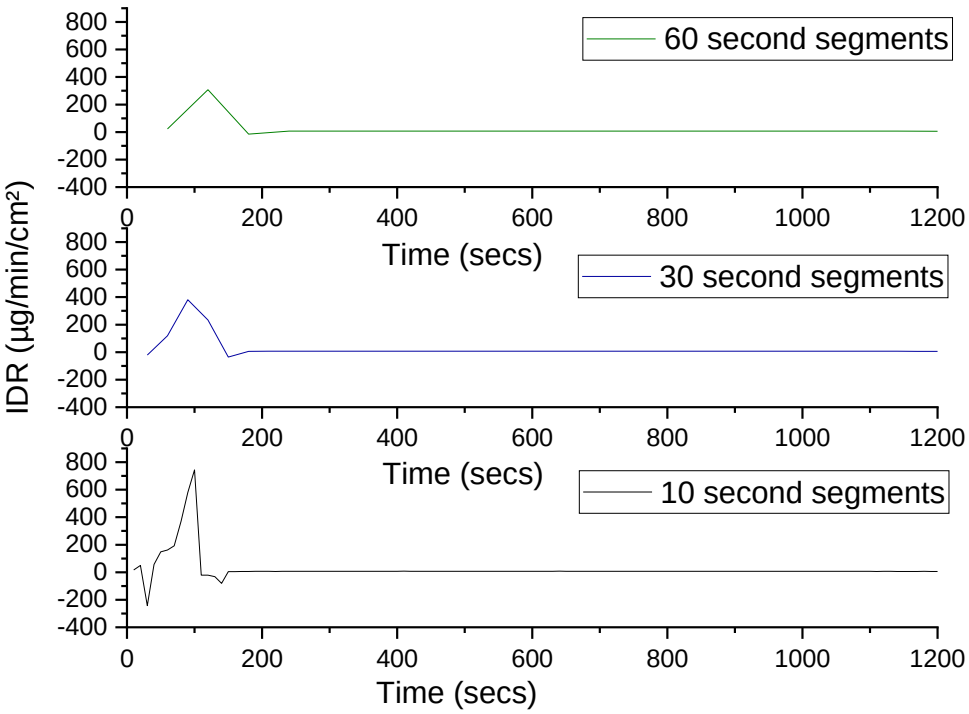

Figure 3.31 – SDi2 compact flow cell dissolution of ketoprofen in 0.1 M HCl at 2.16 mL/min. Intrinsic dissolution rate profile calculated using the default zone settings and varying segment sizes of 60 seconds (top), 30 seconds (middle) and 10 seconds (bottom).

Following the recent research findings and also the initial release of a bubble, Figure 3.32 shows the IDR profile after removing the initial five minutes of variable data, and highlights the smoothing effect of averaging over sixty instead of ten second segments. This may make for more consistent and repeatable IDR profiles for comparison with other samples and for further discussion of bulk dissolution. However, it neglects to take into consideration the initial processes occurring between surface and solvent, and arguably ignores some of the novelty of utilising surface imaging for exploring dissolution.

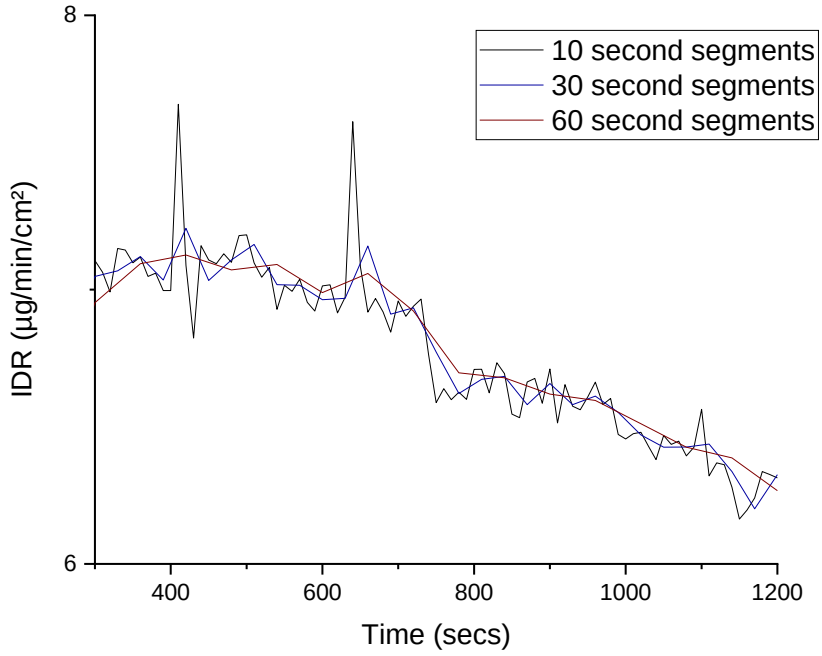

Figure 3.32 – SDi2 compact flow cell dissolution of ketoprofen in 0.1 M HCl at 2.16 mL/min from five to twenty minutes. Intrinsic dissolution rate profile calculated using default zone settings and varying segment sizes.

The analysis software provides the averaged IDR (for the defined segment size) and also calculates a standard deviation for each value; graphs showing the 10 and 60 second average IDR with standard deviation error bars are shown in Figure 3.33 for comparison. The smaller error bars for the data obtained using the larger time segment imply a more robust measurement.

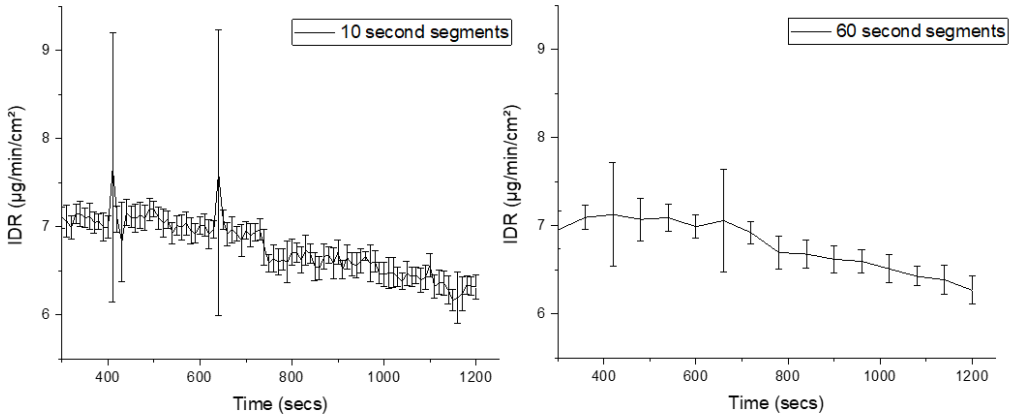

Figure 3.33 – Intrinsic dissolution rate profiles for the 10 and 60 second segment sizes, with error bars of standard deviation, calculated by SDi2 Analysis software.

The spikes or sudden variation in IDR around 410 and 640 seconds can be understood by viewing the video of dissolution. Each spike corresponds to a "glitch" in the images, and is unrelated to a change in release of ketoprofen from the compact. The series of images relating to the spike in standard deviation at approximately 410 seconds can be seen in Figure 3.34. A similar change in image is responsible for the spike at approximately 640 seconds. It is not clear why the glitches happen but they appear to be linked to the software and can be seen to impact upon the UV and visible images slightly differently. There is no simple method for excluding these frames from the data using the SDi2 Analysis software, however, this will be a possibility when using image analysis software. It highlights the importance of viewing the dissolution images alongside data interpretation rather than relying upon one in isolation.

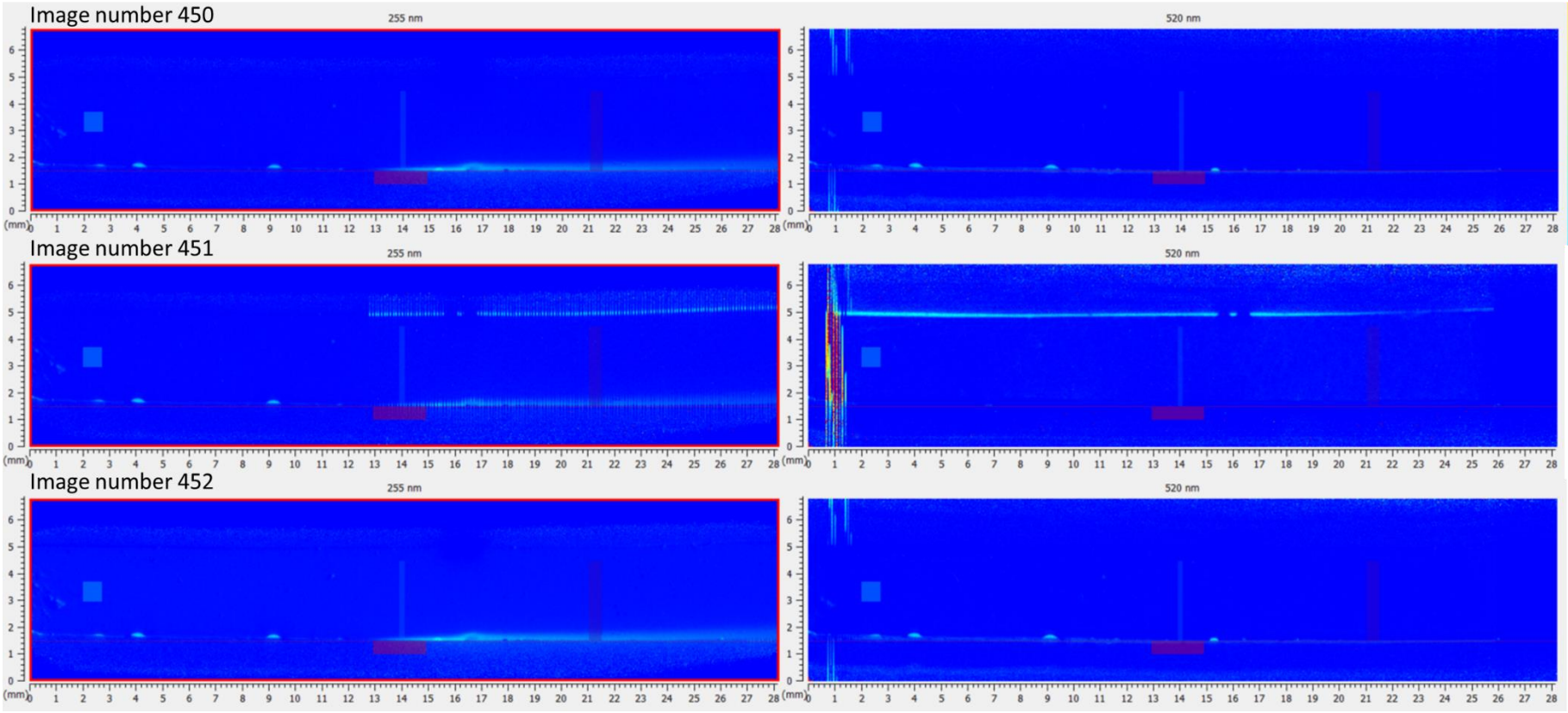

Figure 3.34 – SDi2 compact flow cell images showing a dissolving ketoprofen compact, with 255 nm image on left and 520 nm image on right. The three consecutive image numbers (450 at the top, 451 in the middle and 452 at the bottom) show the glitch that corresponds with the spike in standard deviation seen at approximately 410 seconds.

The IDR plot in Figure 3.32, appears to show two distinct stages to the dissolution: a stable trend between 300 and 720 seconds, and a linear decreasing trend between 720 and 1200 seconds. Further analysis of the data confirms again that excluding the initial 300 seconds significantly improves the overall standard deviation, and suggests that separating the data into three sections might help to explain the changes in IDR. Table 3.9 shows the IDR averages, standard deviation and relative standard deviation as a percentage (% RSD) per time segment used to obtain the data, and also for the differing sections over which the data is averaged.

Table 3.9 – Summary of averaged intrinsic dissolution rates and their standard deviation using different length time segments overall, and for each of the three sections of data.

	Average intrinsic dissolution rate (μg/min/cm^2) with standard deviation (σ)			
	0 – 1200 secs	0 - 300 secs	300 – 720 secs	720 – 1200 secs
10 sec segments	21.94 σ = 97.61 % RSD = 445	69.54 σ = 193.38 % RSD = 278	7.06 σ = 0.16 % RSD = 2.3	6.54 σ = 0.18 % RSD = 2.8
30 sec segments	22.80 σ = 71.00 % RSD = 311	77.99 σ = 141.96 % RSD = 182	7.05 σ = 0.09 % RSD = 1.3	6.52 σ = 0.16 % RSD = 2.5
60 sec segments	21.50 σ = 67.59	80.37 σ = 152.18	7.04 σ = 0.07	6.52 σ = 0.15

A regression analysis of the final two segments can be performed to determine the linearity of each, see Figure 3.35 and Figure 3.36. The IDR can be considered stable at 7.04 μg/min/cm^2 between five and twelve minutes, before decreasing linearly. The decrease after twelve minutes is likely due to depletion of ketoprofen from the compact and the subsequent loss of a constant surface area. Inspection of the dissolution video shows no significant visual change within the flow cell after twelve minutes, but the compact itself is unable to be visually assessed until after the run has completed. Guidance from the USP on reporting IDR states that it should be obtained from the initial linear section of the dissolution curve – this corresponds to a region of

stable IDR.[40] Curvature may suggest experimental problems such as cracking of the compact or saturation of the dissolution medium.[136]

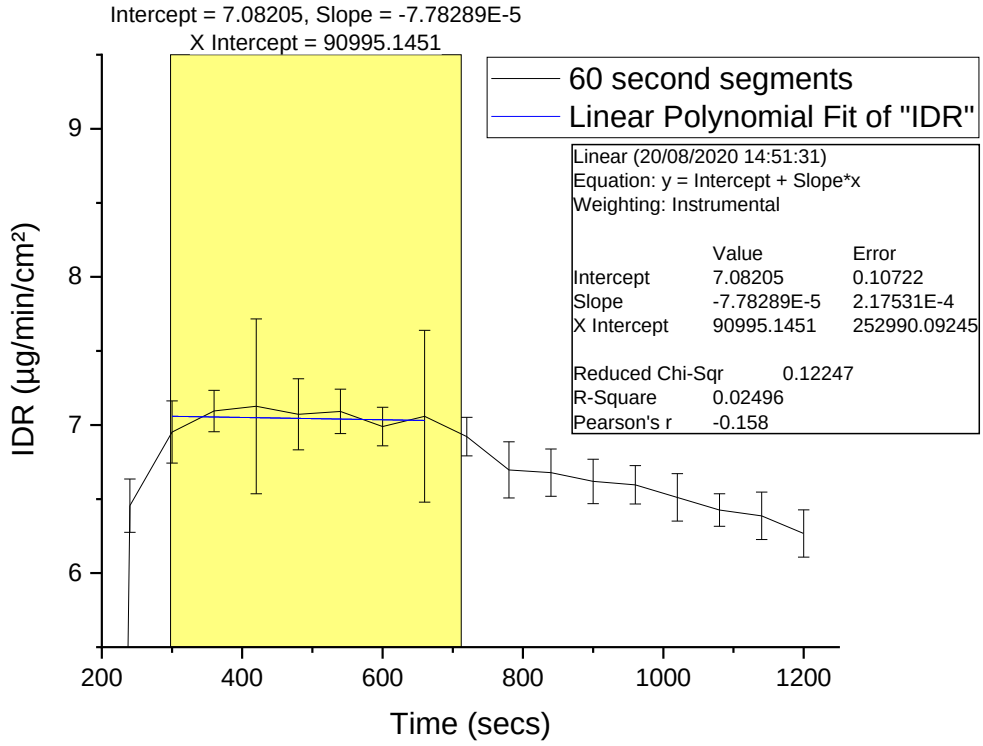

Figure 3.35 – Linear regression analysis for section of IDR between 300 and 720 seconds (highlighted region).

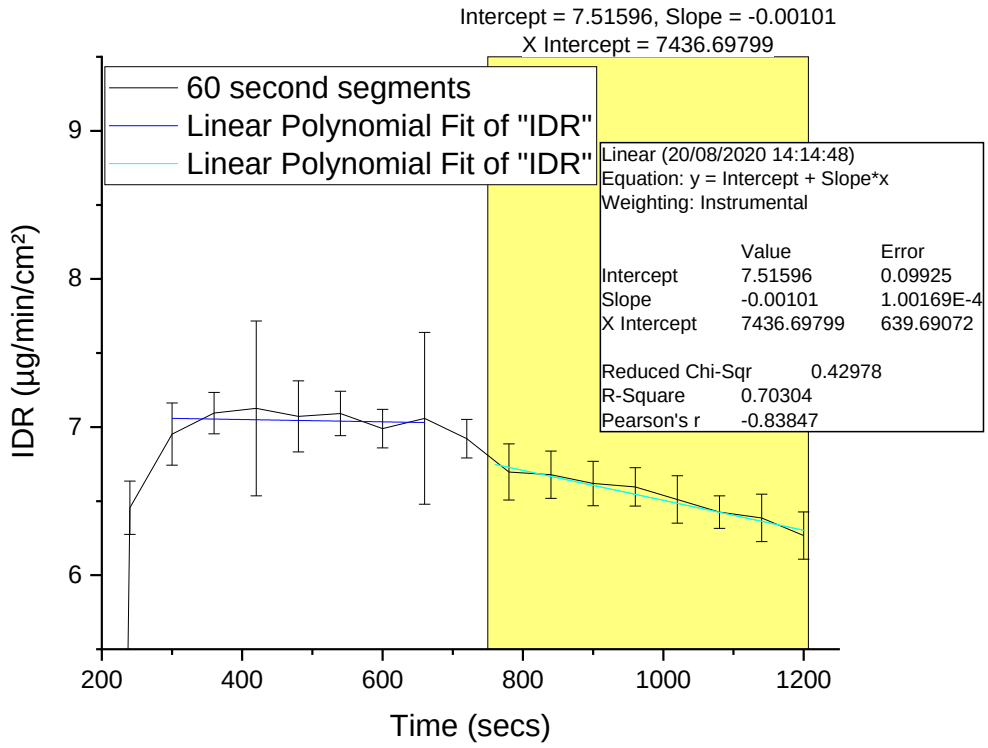

Figure 3.36 – Linear regression analysis for section of IDR between 720 and 1200 seconds (highlighted region).

The surface absorbance directly above the dissolving compact can be obtained using zone (ii) and visualised per time segment, see Figure 3.37. This provides an additional insight into the IDR value and in this instance excludes saturation of the dissolution media due to a reduction in surface absorbance over time. If saturation were occurring the absorbance at the surface would be expected to increase initially and then remain constant. Instead it is likely that the compact has been depleted and there is insufficient ketoprofen dissolving to maintain the maximum dissolution rate.

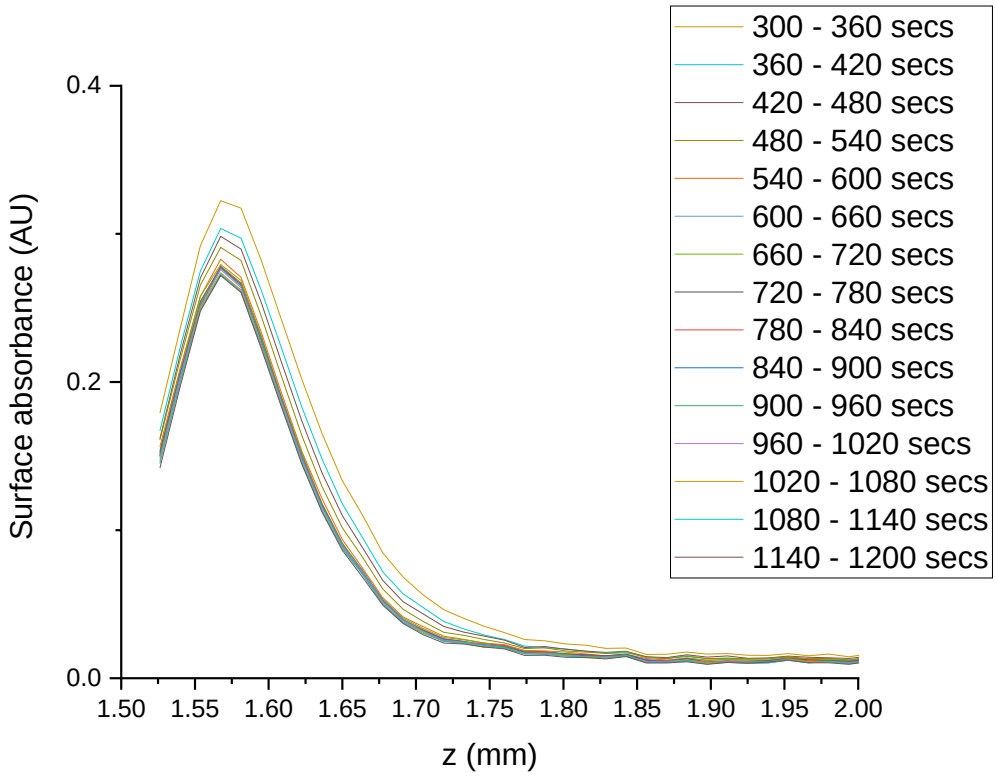

Figure 3.37 – Surface absorbance values up the height of the cell (z dimension), for a dissolving ketoprofen compact at 255 nm per sixty second segment (see key on right).

Figure 3.37 shows the difference in surface absorbance up and down the z dimension and shows an overall reduction throughout dissolution. Using the peak absorbance at a z position of 1.5675 mm, there is a more rapid change from 300 to 660 secs, than between 660 and 1200 secs, which is visualised more easily in a plot of surface absorbance versus time for that position, see Figure 3.38. This suggests that there is a depletion of ketoprofen available to dissolve from the surface after 660 secs and this causes the reduction in IDR value rather than saturation.

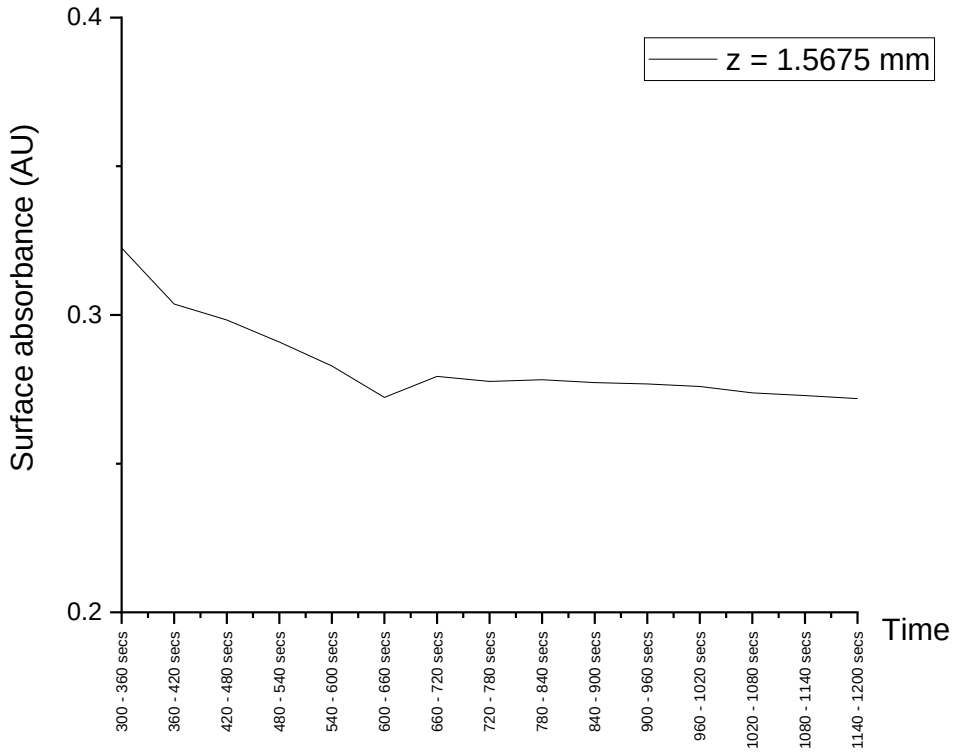

Figure 3.38 - Surface absorbance after 300 secs for a z position of 1.5675 mm.

In conclusion, the starting frame for exploring and understanding dissolution should ideally be zero, but when reporting IDR for comparative purposes, this should occur only after the cell has filled, bubbles have been removed and loose surface powder has stopped passing through; this usually requires the first five minutes to be excluded. The end frame must be reviewed according to the solubility of the sample being assessed, and may require multiple experimental runs to determine whether the plug of sample retains a smooth and constant surface area to allow for valid calculations. The USP guidance for IDR suggests it should be reported only using the initial linear section of the data, which in this instance makes it 7.04 μg/min/cm^2 and within the Pion expected range of 5-8 μg/min/cm^2 for ketoprofen in 0.1 M HCl flowing at 2.16 mL/min through the CFC.[168] Alternatively, if the purpose is to utilise UV-Vis surface imaging to unravel the minutia of dissolution, the early frames are likely to provide significant information about early processes over and above the data that can be obtained using traditional apparatus and bulk dissolution measurements.

3.2.2 IDR zone dimensions and placement:

To understand the relative importance of the dimensions and placement of the defined IDR zone (iii), each was altered and the subsequent influence upon reported IDR values explored for one experimental data set. The default settings in the software include height of zone as 3 mm, noting that Pion guidance suggests this should reach the maximum height at which dissolved sample can be seen, although the IDR calculations only include data up to half the height of the cell. The default width setting is 0.5 mm, and the z value should be set to the bottom of the cell. A 'find' button is present for calculating the internal surface automatically, however, this setting is crucial to obtaining accurate IDR values and regularly fails to find the lower surface so this should be done manually. Figure 3.39 highlights the IDR zone variables that will be explored to determine the impact they are able to have upon the calculated value.

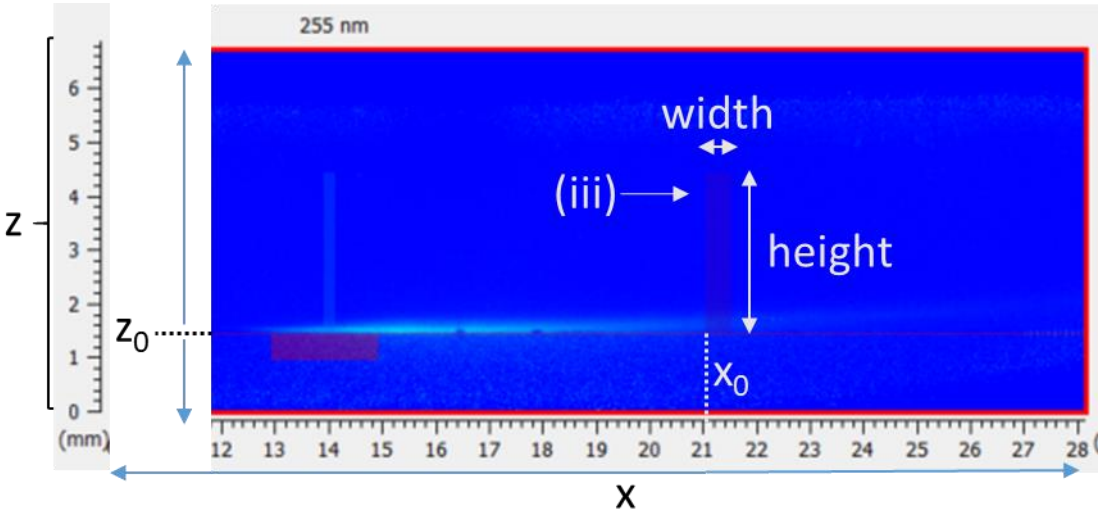

Figure 3.39 – Cropped image of compact flow cell using the jet colour map and showing a compact of ketoprofen in place. The IDR zone is labelled (iii) with default width (0.5 mm) and height (3.00 mm), position in x dimension (21.00) referred to as x_0 and position in z dimension (1.54 mm) referred to as z_0.

Height:

The guidance states that the minimum height of the zone must be greater than the height of the dissolving API. The dissolving API remained in the lower half of the cell as described previously; profile tracking within the SDi2 analysis software was used to view the changing concentrations throughout the cell, see Figure 3.40. Image (a)

shows that 1.0 mm above the surface there is no change is absorbance over 50 mAU, however, image (b) shows that there is some absorbance below 50 mAU even above the 3.0 mm height zone. This is unlikely to be result of diffusion and can be seen to the left of the dissolving compact suggesting that this is background noise.

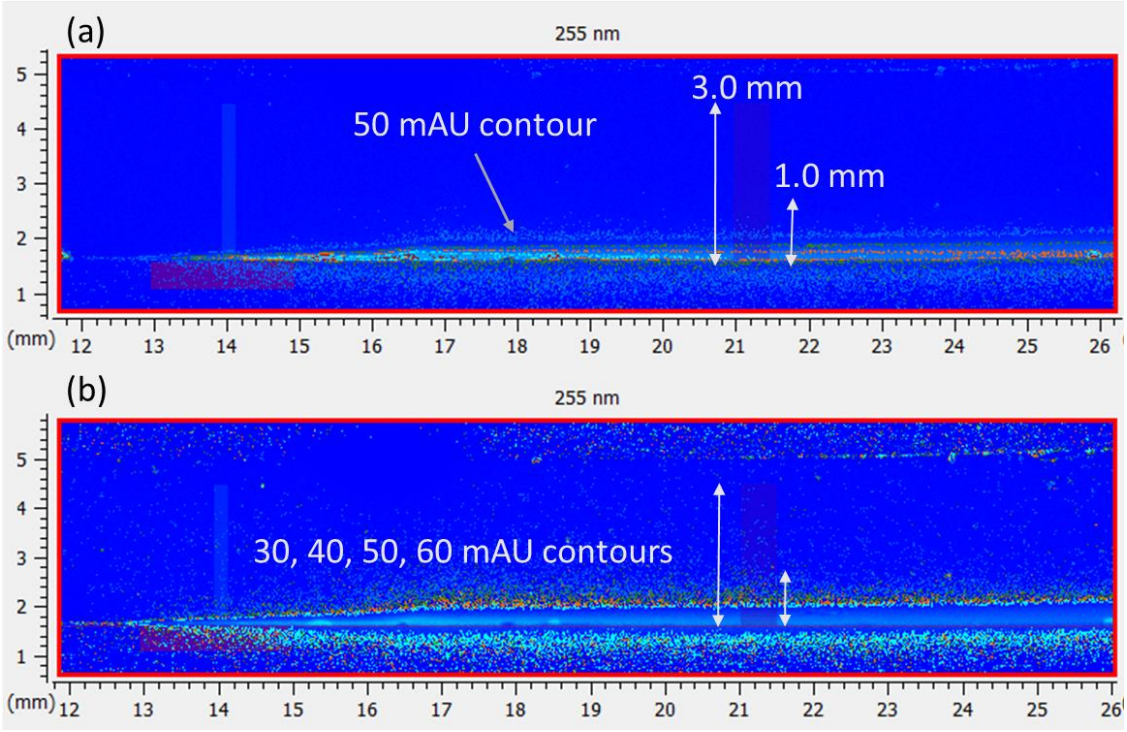

Figure 3.40 – Cropped and enlarged images of the compact flow cell using the jet colour map and showing a compact of dissolving ketoprofen. Image (a) shows a contour plot with absorbance of 50, 150, 250, 350, 450 mAU plotted. Image (b) shows a contour plot with absorbance of 30, 40, 50 and 60 mAU absorbance plotted. The default IDR zone height (3.0 mm) and the smallest zone height (1.0 mm) have both been highlighted in each image using double ended arrows.

The impact of zone height upon IDR values can be seen in Figure 3.41 and can be concluded to influence the reported values, which range from 5 to 12 µg/min/cm^2 for the same experiment analysed differently. The IDR is greatest for heights of 2.0 and 2.5, and lowest for heights of 1.0 and 1.5.

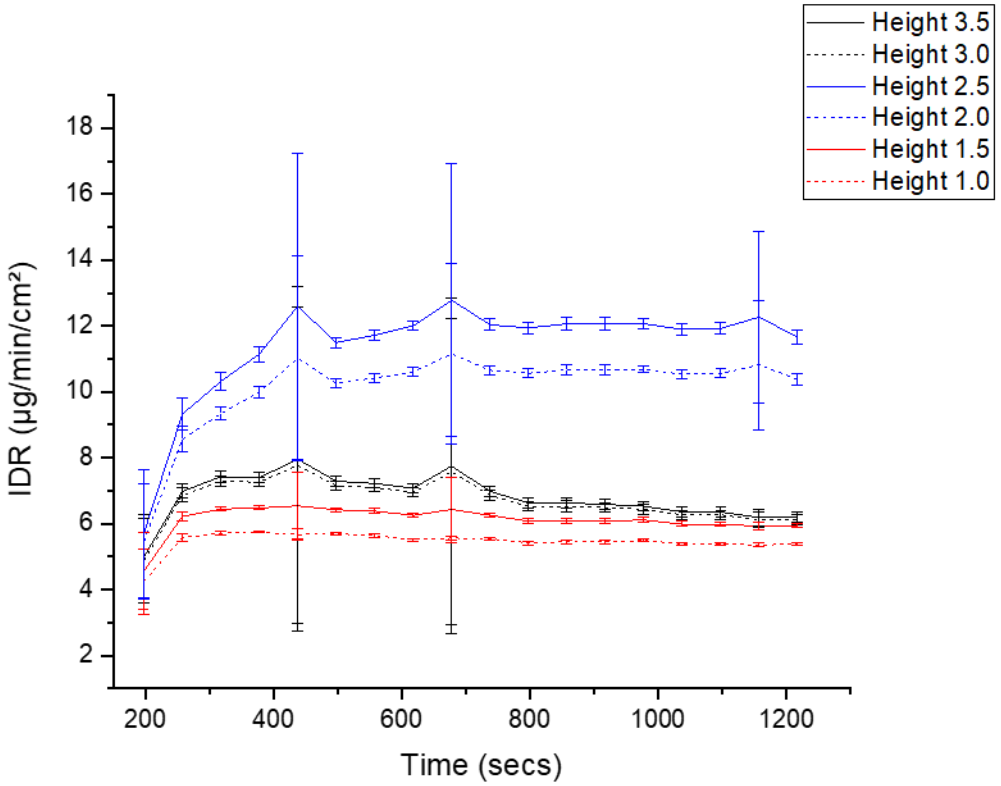

Figure 3.41 – SDi2 compact flow cell dissolution of ketoprofen in 0.1 M HCl at 2.16 mL/min from five to twenty minutes. Intrinsic dissolution rate profile calculated using a segment size of sixty seconds with default zone settings (width 0.5 mm, x at 25.00 mm and z_0 of 1.54 mm) but varying zone heights. The standard deviation is shown as error bars.

Utilising Equation 3.6, a reduction in zone height below half the height of the cell could theoretically reduce the amount of material passing through the IDR zone, which would result in a reduced IDR value. Increasing the height above the halfway point, however, should have little to no effect upon the calculation as pixel rows above H/2 will not be included in the summation of Equation 3.5. The height of the CFC channel is 4 mm, hence H/2 is 2 mm, and if z_0 is 1.54, then the halfway point would be a z position of 3.54 mm. The heights of 1.5 and 1.0 mm are shorter than the halfway position, so any material passing over this height would be missed and result in lower IDR values, which is consistent with the data observed. Heights above 2.0 mm would be expected to be consistent as any material observed above the halfway point would be excluded from the summation; additionally the change in absorbance observed above the halfway point in the cell should be excluded when the reference zone background absorbance is removed. The IDR values for heights of 2.0, 2.5, 3.0 and 3.5 are not consistent with this explanation and suggest that the equation may not be

applied as stated within the data analysis software. There is, however, more error observed with the heights of 2.0 and 2.5 mm, suggesting that 3.0 and 3.5 are most appropriate as default zone heights.

Width:

The influence of zone width upon IDR can also be assessed, although as expected, this has less of an impact relative to height, see Figure 3.42. The IDR values obtained for each variation of width settings is consistent with the default width of 0.5 mm, wherein the IDR is around 7 µg/min/cm^2. The exact placement of the zone in the x direction is not the same for all of the calculations in order to accommodate the change in width, and to avoid artefacts in the images. A comparison of the mean IDR for each width and placement, alongside the overall standard deviation confirms that (a) is the most robust option.

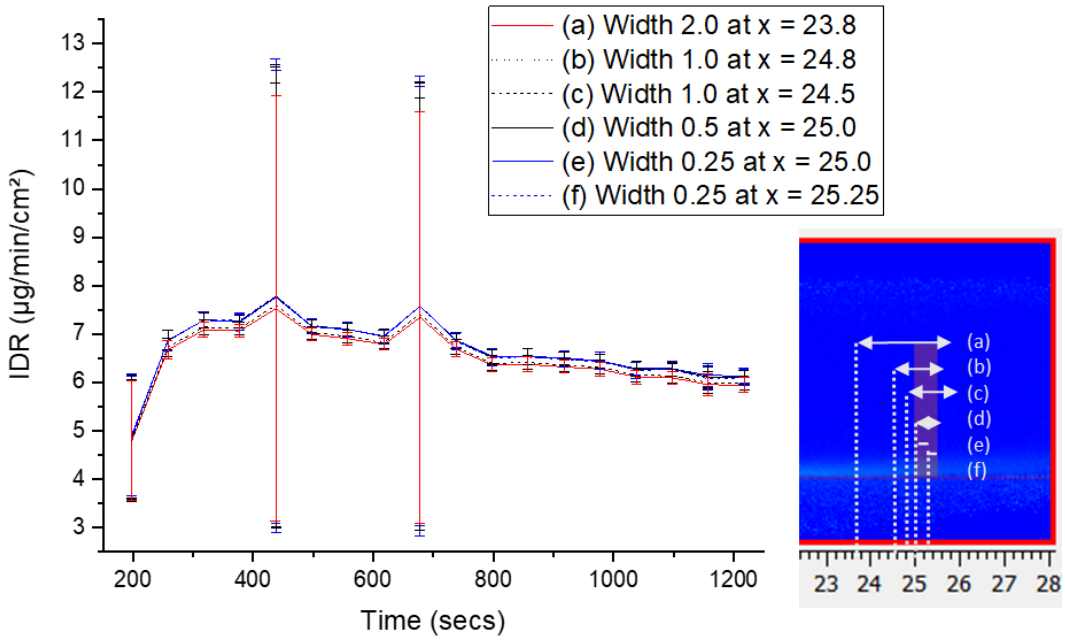

Figure 3.42 – SDi2 compact flow cell dissolution of ketoprofen in 0.1 M HCl at 2.16 mL/min from five to twenty minutes. Intrinsic dissolution rate profile calculated using a segment size of sixty seconds with default zone settings (height 3 mm and z_0 of 1.54 mm) but varying zone widths and slight differences in x placement to accommodate artefacts in the image. The standard deviation is plotted as error bars. The inset image shows the varying positions relative to the default, with x position shown using dotted vertical lines and width shown using the double ended arrows, except for (e) and (f) which use a dash to represent 0.25 mm.

Placement in x direction:

In addition to the dimensions of the zone, the placement of the zone can also be amended. The cell is three dimensional (x, y, z), but only two of these are visualised in the images (x, z) with the third being subjected to averaging across the path length (9 mm). Note also that the surface concentration data is normalised using a 3 mm effective path length (equal to the diameter of the compact surface). The influence of x placement does not appear to consistently increase or decrease the value of IDR obtained, see Figure 3.43, but there is variation from 3 to 8.5 µg/min/cm^2.

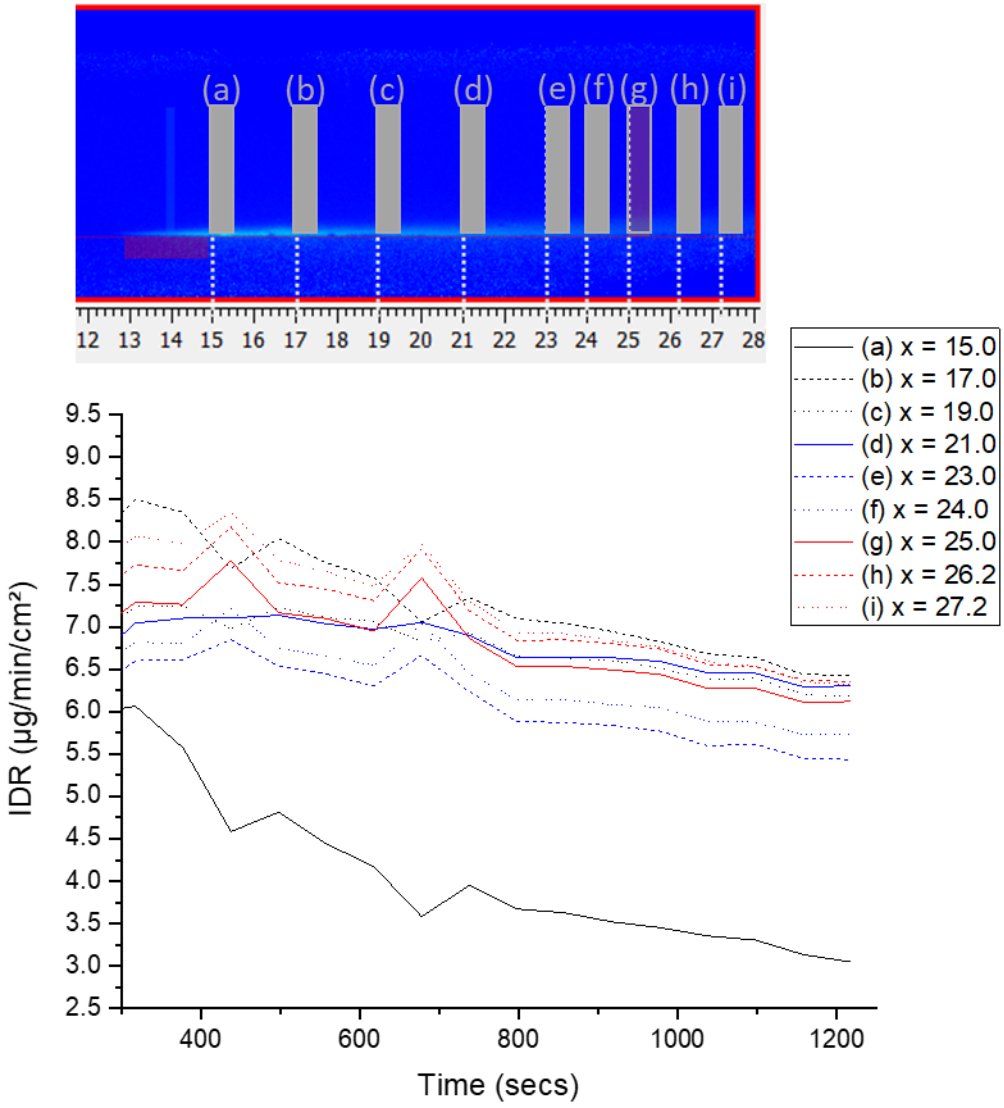

Figure 3.43 – SDi2 compact flow cell dissolution of ketoprofen in 0.1 M HCl at 2.16 mL/min from five to twenty minutes. Intrinsic dissolution rate profile calculated using a segment size of sixty seconds with default zone settings (height 3 mm, width 0.5 mm and z of 1.54 mm) but varying placement in the x direction. Inset is a cropped image showing the x placement of each IDR zone, with the default highlighted and labelled (g).

There is no clear or consistent pattern, but positions (b to d) stand out as they are not impacted by the image glitch (discussed in Figure 3.34) as significantly as the other positions (e to i) and therefore have lower RSDs making them a good choice for zone placement. Position (a) also produces data that is distinct from the other positions, with more than double the relative standard deviation (RSD) of the default (g), which suggests that it may be too close to the dissolving compact and a poor choice for zone position.

One could conclude from an understanding of the calculation that there may be a balance between height and position of zone, to accommodate diffusion. Positioning the zone closer to the dissolving compact would allow less time for diffusion to occur and theoretically enable a smaller zone height than if it were positioned further away from the compact, allowing more time for increased concentration gradients to reach higher up the cell. With this in mind, the optimum position in the x dimension will likely be dependent upon the substance dissolving; those which dissolve very quickly may benefit from the zone being positioned further away to allow for diffusion and advection in order that the concentration may not be so high as to saturate the detector. Alternatively, substances that are very poorly soluble may benefit from the zone being closer so as not to be detrimentally influenced by lower limits of detection.

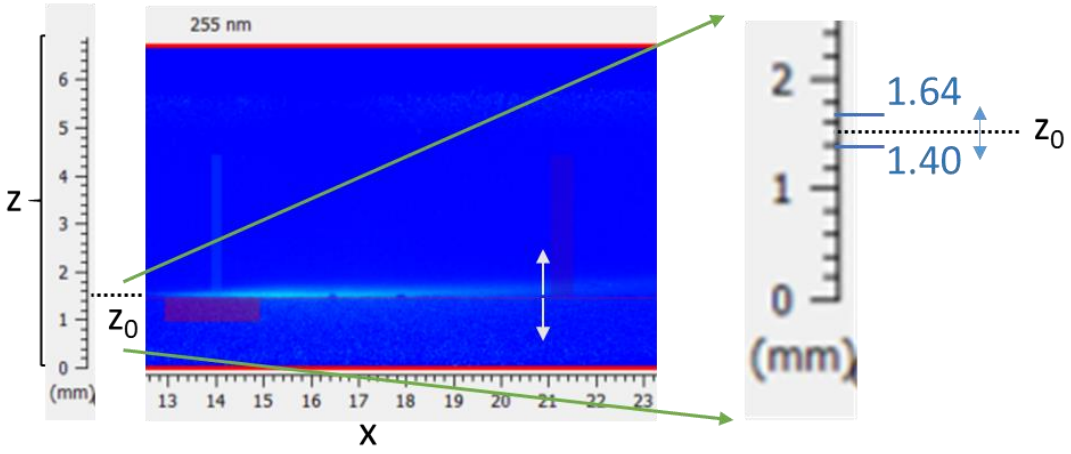

Figure 3.44 – Cropped image of the compact flow cell to highlight the defined bottom surface of the cell, with an enlarged z axis to show the full range of z values explored from 1.40 to 1.64 mm, with z_0 suggested as 1.54 mm.

Placement in z direction:

Finally, the determination of the bottom surface of the cell requires careful consideration as the z position has the potential to alter the value of IDR obtained, see Figure 3.44. There is a "Find" button present in the software, however, this defined the bottom of the cell for this data as 1.00, which is incorrect and forces the IDR value to be greater than 13 µg/min/cm^2. Moving the z position by as little as 0.1 mm can be seen to change the IDR by up to 2 µg/min/cm^2, see Figure 3.45, hence the need for consistency in setting up the zones. There does not seem to be an objective method for selecting the z position, but subjectively z = 1.53 / 1.54 looks to be the bottom of the inside of the cell.

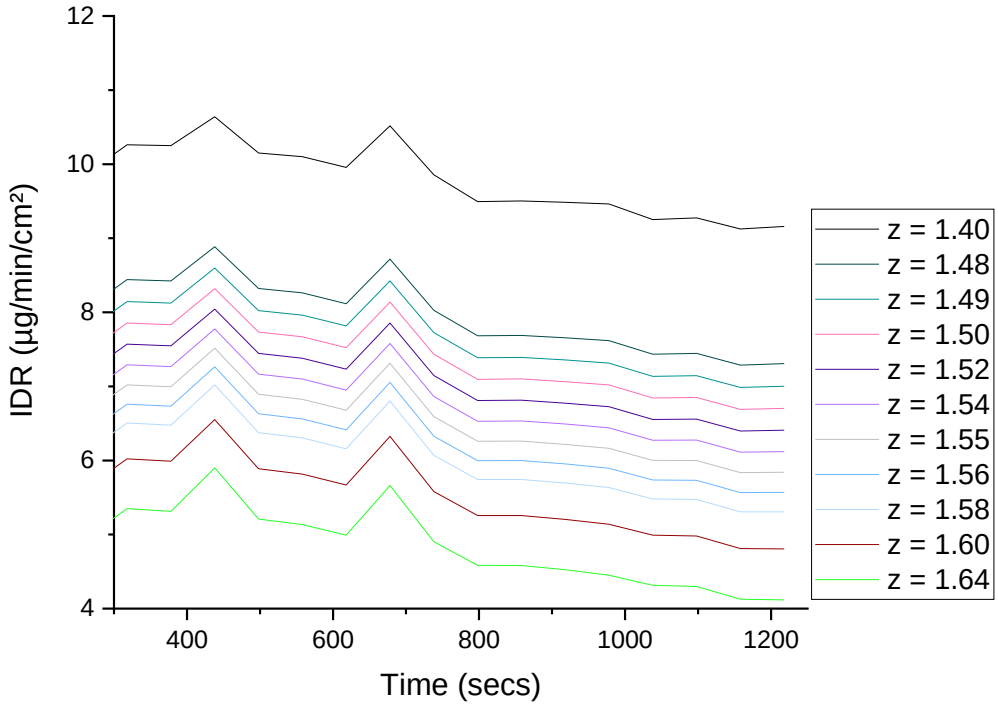

Figure 3.45 – SDi2 compact flow cell dissolution of ketoprofen in 0.1 M HCl at 2.16 mL/min from five to twenty minutes. Intrinsic dissolution rate profile calculated using a segment size of sixty seconds with default zone settings (height 3 mm, width 0.5 mm and x at 25.00 mm) but varying placement in the z direction. Note also that a position of z = 1.51 produced the same IDR profile as z = 1.50, a position of z = 1.53 produced the same IDR profile as z = 1.54, and z = 1.57 produced the same IDR profile as z = 1.58.

Figure 3.45 shows a clear trend that as the z position moves up the cell (from 1.54 to 1.64) more sample solution is missed and therefore the IDR value decreases. This also continues past the bottom of the cell, with IDR increasing down to 1.40 mm, which can be seen to be below the surface. This is potentially due to the presence of the edge of

the cell, which alters absorbance values. Consideration of the contour plots in Figure 3.40 provides confirmation that small absorbance changes can be seen under the bottom surface of the cell. Defining the bottom is therefore not as simple as determining when IDR stops increasing as it will falsely continue to increase past the true lower limit of the cell. It therefore requires subjective assessment by the user, which has the potential to introduce error, and has been discussed in detail in the recent interlaboratory studies.[147]

The physical placement of the CFC relative to the detector is determined by two screws, which hold the cell in one fixed position. The placement of the cell and detector relative to the LEDs, however, may be subject to change as the LEDs are positioned on two separate tracks. Each LED has a unique motor position that is accessed only through the Sirius Hub Settings (entered as motor steps from 0 to 2000) – note however that there are two LEDs each for wavelengths of 520, 320 and 300, so selecting consistent LED numbers rather than just wavelengths is important. This is particularly relevant for the analysis of images using advanced software to determine the edges of surfaces. This will be examined in more detail in Chapter 5. Software based analysis of dissolution imaging to determine the relative stability of an unusual series of solvate polymorphs, as there is scope to overlay images and accurately determine the difference between tracks in addition to observing the impact of the parallax effect.

3.2.3 Summary of data analysis:

The experimental determination of IDR may therefore be influenced significantly by the analysis of the data, which includes start and end frames, segment size, and zone dimensions and placement. Arguably, the reason for setting out to determine an IDR value may be the most relevant factor in the selection of an appropriate, fit for purpose method. IDR measurements are commonly used to compare APIs during pre-formulation studies, however, they are also used in predicting BCS and biorelevant dissolution properties.[136] A recent interlaboratory study was carried out to determine the extent of differences between IDR values calculated using an older version of the SDI; this work highlighted the importance of following a detailed method for both data

collection and data analysis, but confirmed that there is likely intrinsic variability between systems.[147]

The interlaboratory study defined the z-origin in such a way that is not possible with the new SDi2 software, collated data points only between 6 and 20 mins for most compounds (with the exception of 21 to 40 mins for tadalafil), undertook six replicates, and excluded any outliers from calculations. The exact method used with regard to zone position is not detailed or discussed, however, this new work suggests that it is crucial to be consistent with the placement and dimensions of the zone if comparisons are to be made between IDR values. An appropriately detailed method for determining IDR should ideally include:

- start frame,
- end frame,
- segment size,
- zone height,
- zone width,
- zone placement in x direction, and
- zone placement in z direction.

To summarise, if a robust and comparable IDR is required, the start frame and end frame should include only the linear section after the cell has filled and any bubbles have been removed, the segment size should be set to sixty seconds, the IDR zone height should be between 3.0 and 3.5 and the zone width should be 2.0. The zone placement in both the x and z directions should be defined and consistent, with the x position dependent upon solubility and the z position defined for individual instruments but reassessed at regular time intervals assuming limited movement of the cell in the z dimension. It may therefore prove prudent to state experimental details and settings when reporting or publishing SDI-determined IDR data as there is no firm conclusion regarding the relationship between IDR values obtained through different types of equipment or the degree of variability expected.[144,147,260]

3.2.4 Manual versus software calculation of IDR

The additional finding that IDR values obtained using the SDi2 software are inconsistent with IDR values manually calculated from the same raw data has been explored further in this section. Equation 3.5 and Equation 3.6 were used to calculate IDR manually. For the SDi2 CFC: H is 0.4 cm, W is 0.9 cm, S is 0.07 cm^2 and pixel height (Δz) is 0.001375 cm. The raw data extracted from the SDi2 is provided in absorbance units (AU) and supplied for each time segment (0-198, 198-258, 258-318 secs etc.) and pixel in the z direction (1.54, 1.55375, 1.5675 etc.). This data was input into Microsoft Excel and the IDR was manually calculated using the previously described equations. A plot comparing the manually calculated and the SDi2 calculated IDR values is shown in Figure 3.46.

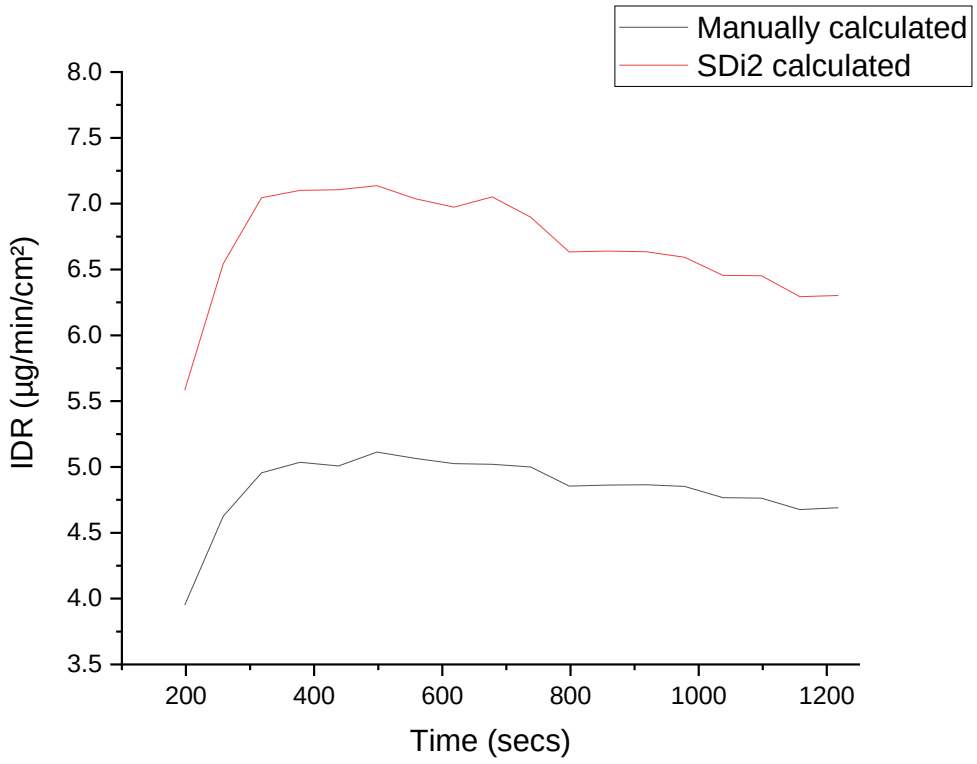

Figure 3.46 – Comparison between the manual IDR calculation using equations and raw data, and the SDi2 calculated IDR using the Analysis software for the same ketoprofen QC run with the same zone dimensions and location.

The difference between these two values at each time point was calculated and plotted, see Figure 3.47. While the total difference between the values varies, the ratio between the two is fairly consistent although it does increase gradually with time.

This suggests that there is likely to be a systematic difference between the two calculations.

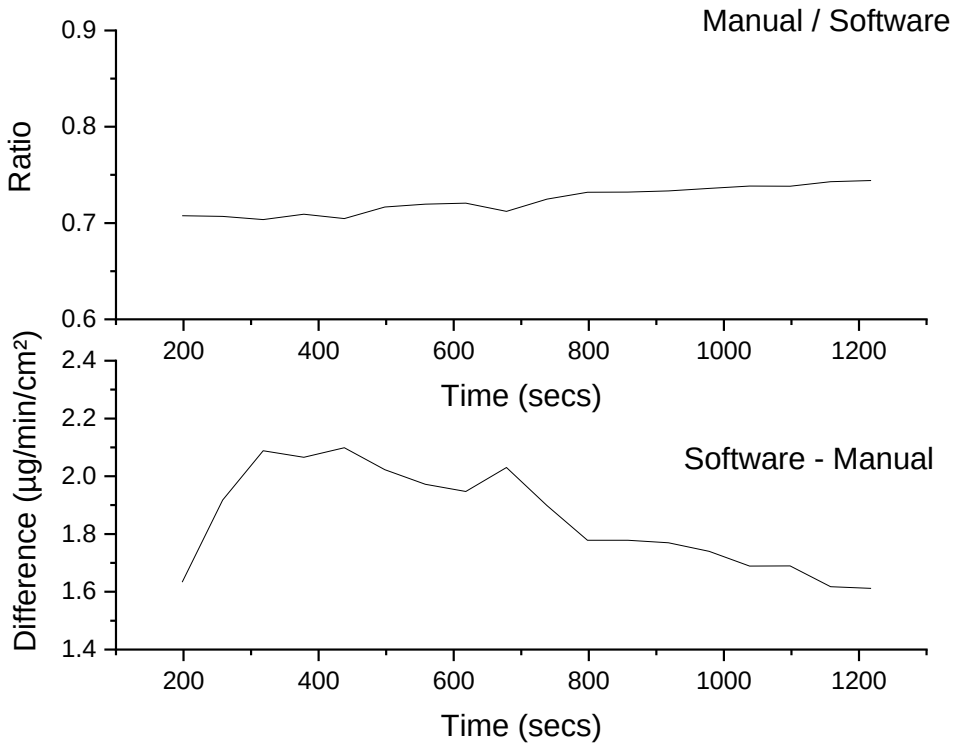

Figure 3.47 – Plot showing the calculated ratio of manual versus software calculated IDR values (top), and the total difference between SDi2 calculated and manually calculated IDR values (bottom).

The manual calculation can be broken down into a series of steps:

- Step 1: absorbance data for each pixel position for each time segment is converted to concentration using the previously obtained molar absorption coefficient for ketoprofen at a wavelength of 255 nm. Concentration is equal to the absorbance (in AU) divided by the molar absorption coefficient (15800 $M^{-1}cm^{-1}$ as stated in the SDi2 manual) and divided by the path length (0.9 cm). The concentration is therefore in M (moles per litre).
- Step 2: velocity at each pixel position (z) is calculated (v_z is velocity at z (cm/min or mL/min/cm^2) using equation 2 which uses the volumetric flow rate (Q = 2.16 mL/min), the height of the flow cell (H = 0.4 cm), the width of the flow cell (the same as the path length, W = 0.9 cm) and the pixel position or height above the

surface (z, cm). The velocity is lowest at the surface (both bottom and top of the cell) and greatest in the centre of the cell).

- Step 3: equation 1 has to be calculated in parts as it involves only the sum of data calculated from the surface or z-origin (z = 0) to H/2 (half-way up the height of the cell, which is 0.2 cm above the surface). The surface has been set to 1.54 mm, so half-way up is 3.5475 mm. The velocity at each pixel position calculated in step 2 is multiplied by the molecular weight (g/mol), the concentration at each position (mol/cm^3), the width of the flow cell (W = 0.9 cm) and the effective pixel height (0.01375 mm but use 0.001375 cm) and divided by the surface area of the sample (0.07 cm^2).
- Step 4: the sum of the previous step is calculated for each time segment to provide a value for j (IDR, mg/min/cm^2) for each time segment, although it is reported by the software as µg/min/cm^2.

It is not clear why IDR values calculated manually are different from those calculated using the software. Discussions with pharmaceutical industry experts have not uncovered any inconsistencies, other than extracting raw data as AU and not concentration, see Figure 3.48, which has been accounted for in the calculations.

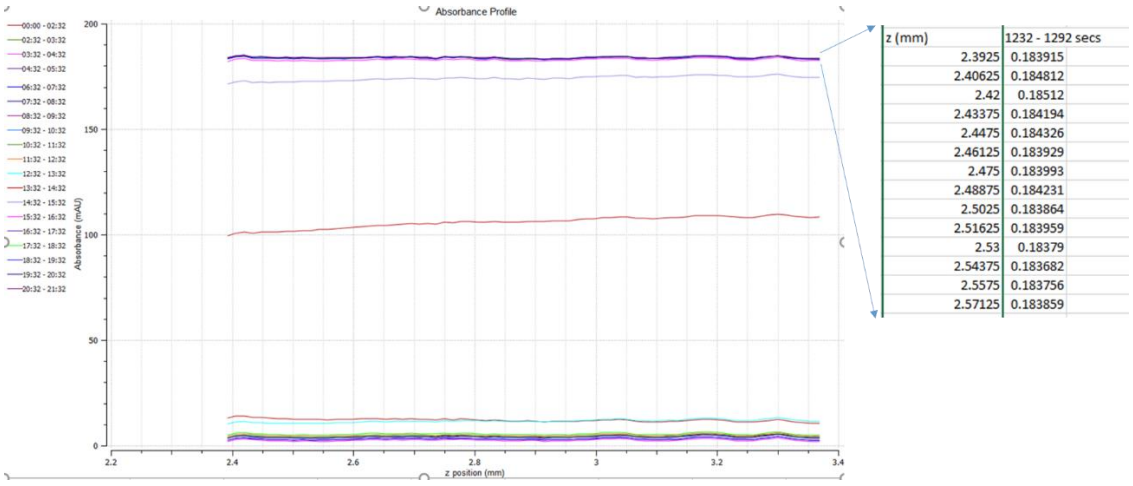

Figure 3.48 – SDi2 reported absorbance values both through Sirius software (graph) and extracted values (screenshot taken from Excel). Note that the graph reports in mAU but the raw extracted data shows AU, and altering the plot to concentration still results in reported values of AU.

Pion are working to determine the reason for this difference but a recommendation would be to exercise caution in interpreting individual IDR values and rather to suggest

that they should be used only for ranking purposes until further information can be obtained.

3.2.4 Sample mass released

In addition to calculating the IDR for samples analysed using the CFC, the SDi2 reports sample mass released. This is calculated by taking the IDR value (µg/min/cm^2), multiplying it by surface area (0.07 cm^2) to provide the mass released per time period (µg/min), which can then be multiplied by the time period over which it is extracted and units adjusted to provide the mass (in mg) released. This value can be plotted cumulatively against time. This was calculated manually to confirm the SDi2 calculation and a comparison of the two is shown in Figure 3.49.

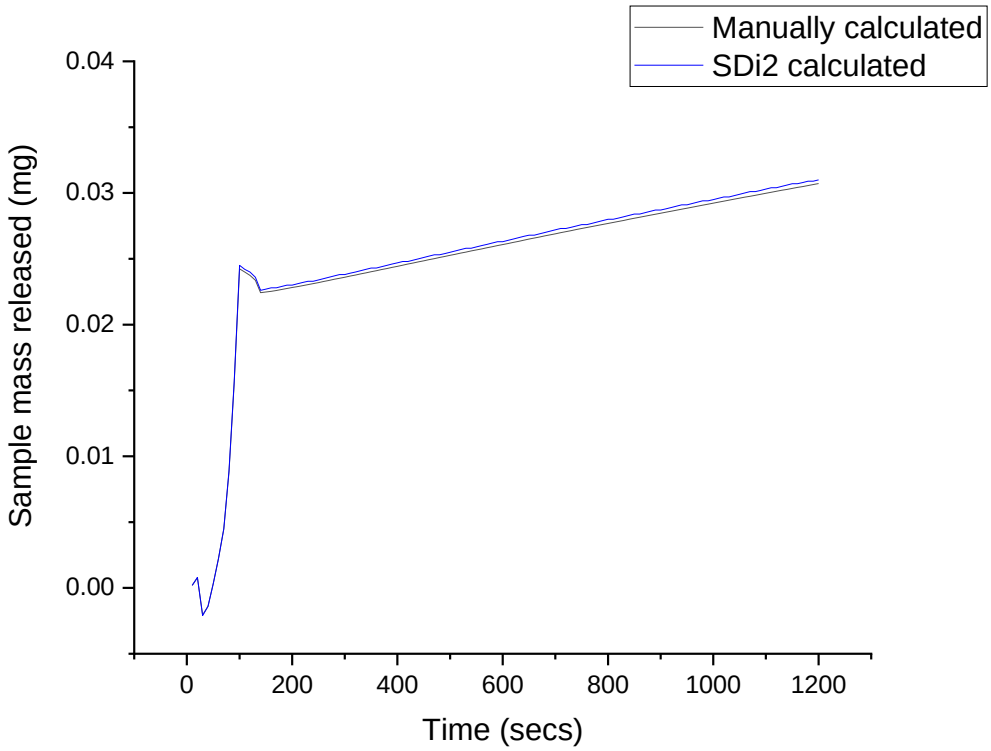

Figure 3.49 – Comparison of manually calculated sample mass released with that calculated by the SDi2 Analysis software.

The small difference between the two values is due to the number of decimal places that are reported. The manual calculation reports five decimal places compared with four for the SDi2 data, hence the difference between the two values increases slightly over time. The sample mass released is therefore independent of the surface area

from which it is being released, hence it can be used as a measure of dissolution from a changing surface size and shape. If the starting sample mass is known, it can also provide information on the percentage of sample released over time.

3.3 Conclusions

This chapter shows a single ketoprofen experiment analysed in multiple ways to produce different IDR values dependent upon the methods used. The relative importance of start and end images, segment sizes, smoothing, IDR zone dimensions and placement are each considered and a tentative conclusion drawn that the optimal position of the zone may be dependent upon the properties of the substance being monitored.

The SDi2 has been successfully developed to improve upon the previous designs of surface dissolution imaging equipment, primarily by the inclusion of dual wavelength capability. As with all developments there are challenges associated with the software and design that only become clear once the equipment is in frequent use. One challenge of note is that there is no cooling system in place with the left side compartment of the instrument housing the wiring and electronics resulting in the temperature inside the SDi2 often reaching 37°C and above.

In spite of these challenges, the SDi2 shows great potential for routinely enhancing our understanding of dissolution quite simply by recording the visual aspects of the process instead of solely relying upon numbers. While the visual observations may not at first glance provide objective data for defining dissolution mechanisms, they encourage analysts to consider the process as a whole rather than summarising it as simple plots of API released per time. Reporting this subjective data would further support the USP guidance of reporting only the linear sections of IDR plots, which could arguably be considered equally subjective and dismissive as to the importance of early wetting processes upon dissolution.

Finally, one possible limitation of the manual IDR calculations is the exclusion of a factor to accommodate the change in flow across the width or depth of the flow cell. In addition to the parabolic flow profile present in the z-dimension, there will be a profile with zero flow at the wall surfaces normal to the line of sight (ie across the

width of the cell or in the y-dimension). Absorbance is averaged across the width of the cell, but the overall movement of dissolved sample from left to right will be additionally influenced by this flow, hence this could be a source of some of the discrepancy between manually calculated and the SDi2 calculated IDR values. Further work would be required to test this as the flow profile for a rectangular channel (relative to a circular one) adds complexity to the calculations.[261] Enhancing understanding of the IDR calculations, particularly by confirmation through manually working with the raw data to replicate SDi2 values, would provide reassurance that these provide us with the correct information and would enable the pharmaceutical industry to take full advantage of this technology during pre-formulation, formulation development and technology transfers.

4. Single crystal surface dissolution imaging

4.1 Introduction

The morphology and surface chemistry of crystalline pharmaceuticals impacts upon wettability, (seeded) growth, manufacturability (particularly with regard to flow) and dissolution.[215] Establishing a link between these properties and the functional groups present at crystal surfaces is therefore an important undertaking. A number of specialist techniques have been applied to single crystals for this purpose, including microscopies (atomic-force, scanning ion-conductance and optical), Raman spectroscopy, and molecular modelling and simulations.[210,212,213,215,262,263]

Single crystal dissolution was first studied using real-time UV imaging in 2011.[216] The ActiPix SDI300 was used with scanning electron microscopy (SEM) to study a lidocaine single crystal dissolving in stagnant buffer. This proof of concept work confirmed that UV imaging had great potential to enhance dissolution understanding by spatially and temporally mapping concentration gradients around a single crystal. A further study from the same group, used the relatively newer SDI with a single crystal placed in a hydrogel and gained additional insights into diffusion boundaries.[169] This work concluded, however, that image interpretation was limited due to the single wavelength imaging available and the resolution capability of the instrumentation used.

The recent release of the SDi2, with its novel dual wavelength imaging, enhanced detector chip, fibre optic tapering for 2.5 times magnification and additional whole dose flow cell (WDC), provides further opportunity to explore single crystal dissolution.[13] Utilising both a UV and a visible wavelength allows for differentiation between physical obscuration versus a high solution concentration of a UV-absorbing species. For the first time, the technology is able not only to image the boundary between solid and liquid, but to distinguish between solid surface and dissolved substance. In addition, the WDC provides a larger imaging area for monitoring these changes and a greater volume for visualising concentration gradients than the compact flow cell (CFC). The SDi2 therefore possesses the potential to provide a relatively simple and robust method for comparing dissolution properties of single crystals and

may also provide an opportunity to explore face specific kinetics. This research will explore its potential and although it will not allow for understanding at a microscopic level, the extent of detail that can be confidently obtained will be determined.

4.2 Method development

Paracetamol was selected for these studies due to its well-established safety profile and low cost. The solid-form landscape of paracetamol is well-studied and relatively large crystals can be grown from supersaturated aqueous solutions by slow evaporation within a time-frame of a couple of days.[264–266] Paracetamol is currently known to exist in three polymorphic forms: Form I, II and III.[264] Form III is the most elusive and can be transiently obtained by cooling the melt, whereas Forms I and II possess the same molecular conformations with different packing, although Form II reverts back to I with time.[265] Crystals of paracetamol were taken from original solutions, dried using filter paper and used the same day. No further analysis of the crystals was deemed necessary for this stage of method development, although single crystal X-ray diffraction (SCXRD) confirmed that they were Form I, the commercially available polymorph.

The SDi2 was used for dissolution monitoring with deionised water at 37°C as the solvent. Previous studies utilised the SDI300 and SDI for single crystal dissolution, however, the design of the SDi2 is sufficiently different that method development was required to determine the most appropriate way in which to study the sample, to test the equipment limitations and also to understand the resolution capabilities of the detector. These differences and the methods used to modify the equipment appropriately will be discussed in detail throughout this chapter.

4.2.1 Flow cell hydrodynamics

The positioning of the crystal within each cell requires consideration in terms of its impact upon hydrodynamics. The SDi2 flow cells have been designed to encourage laminar flow throughout, using tapered sides to gradually increase or reduce volumes and with the introduction of glass beads into the bottom of the WDC to slow and smooth flow.[175,267] The placement of an object within either cell will therefore present a barrier to flow and result in turbulence.[268] This in turn will impact upon diffusion,

advection, boundary layers and concentration gradients, and ultimately the information we can obtain about a crystal's dissolution.

The WDC recommended method includes placing a tablet or capsule within a wire holder in the centre of the cell. The disruption of flow is therefore unavoidable with the current design but is likely to be less of a concern for a single crystal compared with an oral dosage form due to the vast size difference. The WDC is designed to mimic the USP IV apparatus in order to achieve laminar flow throughout, however, a comparison of techniques found the classification of "laminar" to be an over-simplification, with significant variation in hydrodynamics, not only between apparatus, but between locations within the apparatus too.[182] Detailed drawings of the WDC were unavailable, hence a rough outline is shown in Figure 4.50.

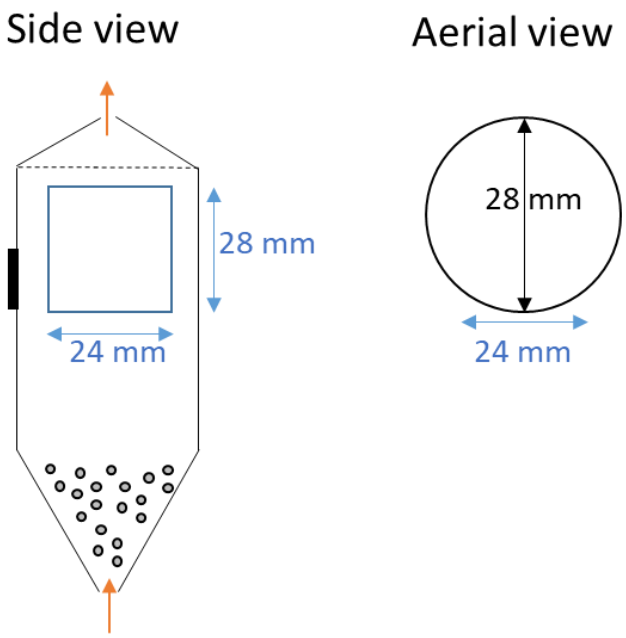

Figure 4.50 – Diagram showing inside the SDi2 whole dose cell from the front (side) and from above (aerial), with orange arrows showing the flow of solvent in and out of the cell. The imaging window is shown in blue. The side view shows the position of the numerous 2 mm glass beads in the bottom section, the wire mesh across the top and the holder for inserting the sample into the cell on the left. Not drawn to scale.

The volume within the CFC is just 1.54 mL compared with 60.3 mL in the WDC, suggesting that the same size crystal will have a larger impact upon flow within the CFC compared with the WDC. The SDi2 compact flow cell design differs from the original cell designs used for the ActiPix D100, SDi300 and Sirius SDI. Disruption of the laminar

flow through the CFC may theoretically be prevented by placing the crystal entirely within the sample holder, with the side of interest facing up into the cell, see Figure 4.51. This would also ensure exposure of only one face initially, however, it would prevent visual changes to the crystal from being monitored and therefore negate the benefits of using dual wavelength imaging.

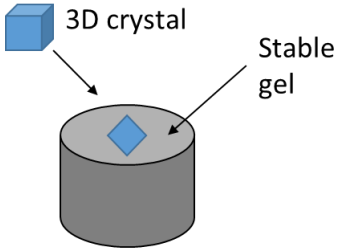

Sample holder showing
only one face of crystal

Figure 4.51 - Example of method for fixing crystal in sample holder. This would expose only one face and would limit the disruption to laminar flow within the CFC.

The placement of the crystal should therefore enable it to be viewed through the imaging area, which is limited to an area of 4 x 28 mm (height by width) within the CFC (compared with 28 x 24 mm in the whole dose cell). The placement is further reduced as a result of sample holder positioning, which is central to the width and accessible only via the bottom of the CFC. Detailed drawings of the CFC were unavailable, hence a rough outline is shown in Figure 4.52.

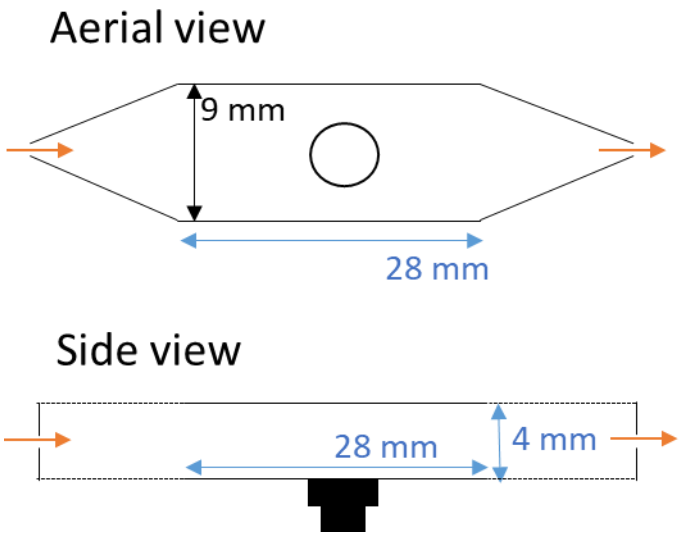

Figure 4.52 – Diagram showing the inside of the new SDi2 compact flow cell from above (aerial) and from the front (side), with orange arrows showing the flow of solvent in and out of the cell. The dimensions of the imaging window are shown in blue. Both views show the position of the 3 mm diameter sample holder. Not drawn to scale.

The tubing (of 1.4 mm inner diameter) connects directly to each side of the CFC, with tapering to the right and left (shown in the aerial view) but not above or below (as seen by the side view). It should be noted that the SDi2 differs from the original flow cell design used in previous imaging equipment (D100, SDI 300 and SDI), see Figure 4.53, wherein the tapering was above and below the inlet and outlet, but not to the left and right. Extensive work was carried out with the older design to visualise flow and confirm its laminar nature, including flow rate tests with microparticles.[175]

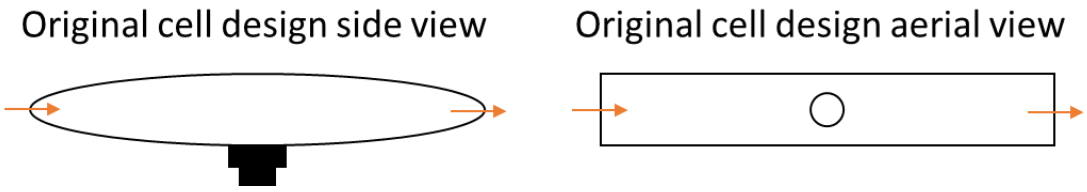

Figure 4.53 – Representation of the original SDI imaging equipment flow cell from the side (left) and from above (right). The orange arrows represent the flow of solvent through the cell and the sample holder can be seen in both views.

There is therefore a change in design from tapering above and below, to tapering at the sides, which may impact upon hydrodynamics, particularly with regard to the flow of dissolving sample through the cell. As an aside, the newer design results in pockets of air forming both above and below the solvent exit point as the cell fills with solvent, which require removal by both tipping and tapping the cell. However, once the cell is

full and free of air, the flow through is still assumed to be laminar, see Figure 4.54.[269] This occurs with steady flow through long straight vessels and results in a parabolic profile whereby flow tends from zero at the vessel walls to a maximum velocity in the centre.[77]

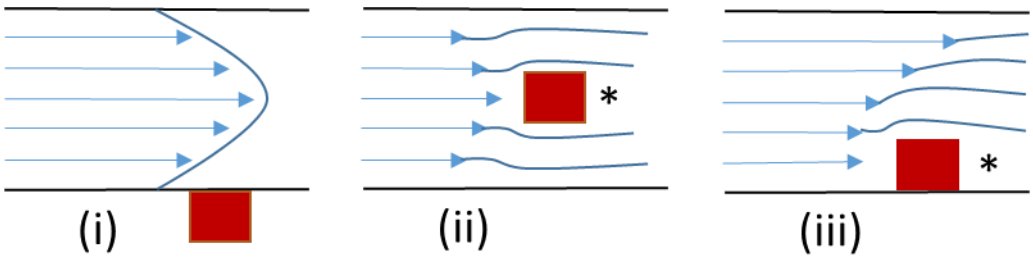

Figure 4.54 – Diagram showing the side view through the CFC with a crystal (represented by a red box) placed in three different positions showing its impact upon flow: (i) crystal surface at bottom of cell enabling laminar flow to continue with a maximum velocity in the centre and a tendency to zero at the top and bottom surfaces, (ii) crystal in the centre interrupting laminar flow resulting in a wake region (*), and (iii) crystal on the lower surface of the cell interrupting laminar flow and resulting in a wake region (*).

The dissolution and transport of sample through the cell can be considered in terms of molecular diffusion, due to differences in concentration, and advection, due to forced fluid flow.[173] If laminar flow is maintained, advection will occur from left to right, and diffusion will occur from bottom to top (normal to flow). However, if laminar flow is disrupted (as is the case in (ii) and (iii) of Figure 4.54) then there may be forced flow in additional directions. Flow through the cell may be further complicated by the impact of density changes as the sample dissolves; solvent with a higher concentration of sample dissolved will have a higher density than that with a lower concentration dissolved, and sink to the bottom of the cell, where the velocity is already reduced. Figure 4.55 provides a highly simplified representation of the different directions for fluid and sample flow, noting also that the channel is three-dimensional.

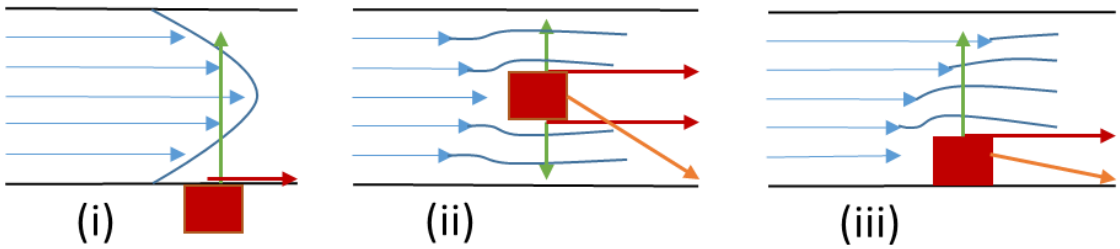

Figure 4.55 – Diagram showing the side view through the CFC with a crystal (represented by a red box) placed in three different positions. The blue arrows show the direction of fluid entering the channel, the red arrows show the expected direction for advection, the green arrows show the expected direction for diffusion, and the orange arrows show the likely impact of density changes upon flow.

One method by which this could be simplified would be to operate under stopped flow conditions once the cell is filled, which would prevent advection influences. In ideal circumstances the flow cell (and imager) could also be mounted vertically so that the effect of density would result in dissolved sample moving to the bottom and out through the cell. Although the current equipment design does not support this, a current line of research for the SDi2 is the design of novel cells (primarily through 3D printing), which fit into the equipment and allow for alternative orientations and dissolution methods.

An additional consideration is the orientation of the crystal with respect to flow. The crystal has been represented by a box in previous diagrams, however, it is unlikely to be symmetrical in shape, with multiple faces, of differing size and shape. The direction of flow relative to each of these faces will further impact upon hydrodynamics. If considering dissolution of just one face, then one train of thought is that this should be placed horizontally in the channel to enable solvent to pass over it in a similar way to monitoring the IDR of a compact. Additional CFC designs could again enable further exploration of flow at either end of the cell to determine how it differs and therefore whether it impacts upon concentration gradients and boundary layers; this would further influence the determination of face-specific dissolution kinetics but is outside the scope of this work.

In conclusion, flow cell hydrodynamics have the potential to influence many aspects of single crystal dissolution and its interpretation. They should be considered carefully with respect to each cell, to support the positioning of crystals, the method(s) used

and the extent of information we can extrapolate from each experiment. In turn, the SDi2 has the potential to provide a significant means to enhance our understanding of hydrodynamics by visualising the surfaces and concentration gradients throughout the dissolution process.

4.2.2 Attaching single crystals

Initial studies with the early imaging equipment used either a stagnant dissolution media, a putty-like removable adhesive (Bantex® Tack-all) or a hydrogel to hold the crystal in place throughout dissolution. The SDi2 has two distinct flow cells, each with the potential to be used for single crystal dissolution, however, neither was designed for this purpose. Consequently, the most appropriate method to secure a single crystal in place required investigation, noting that it should hold the crystal firm whilst enabling solvent (dissolution media) to flow through each cell.

A putty-like removable adhesive (Blu-tack®) was initially used to attach the crystal to the sample holder of the compact flow cell (CFC). This secured the crystal in place to an appropriate degree, however, the adhesive took up a lot of space within the CFC, see Figure 4.56.

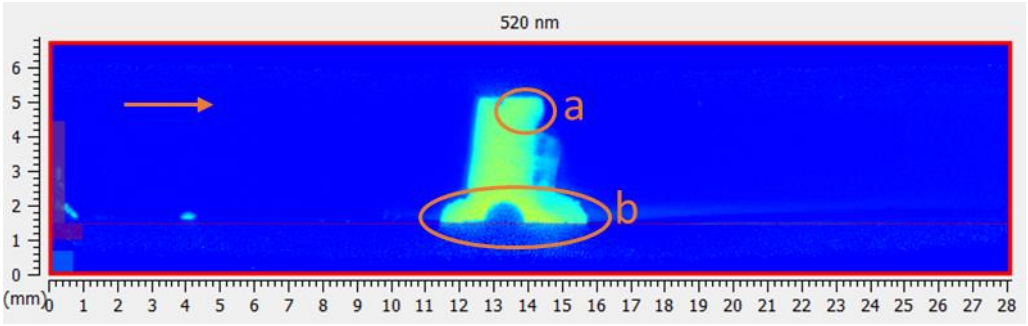

Figure 4.56 - SDi2 compact flow cell 520 nm image of a single paracetamol crystal held in place using a putty-like removable adhesive. The orange arrow in the top left shows the direction of solvent flow. The orange ovals highlight a) an air bubble and b) the putty holding the crystal in place. The crystal can be seen to span the full height of the flow cell.

The putty proved to be cumbersome and was not sufficiently secure to use within the whole dose cell (WDC), so a stainless steel wire clasp was bent into an appropriate shape, see Figure 4.57. This is the method recommended by Pion to hold tablets and capsules in place for routine dissolution studies with the SDi2. The clasp was successful at holding the crystal in place within the WDC, however, it obscured a lot of

the image thereby making absorbance measurements close to the crystal surface challenging to obtain.

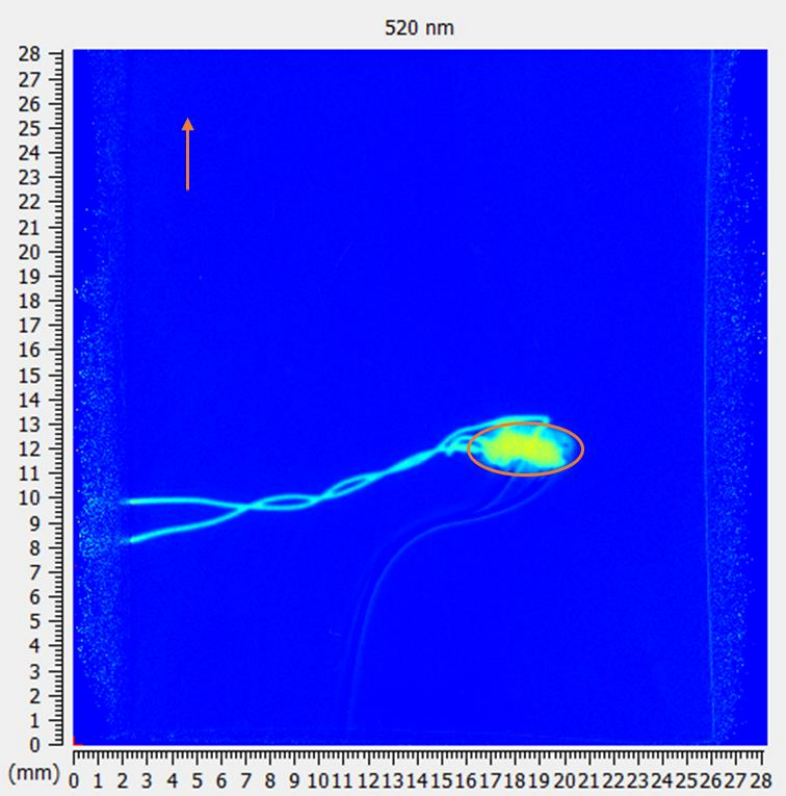

Figure 4.57 - SDi2 whole dose flow cell 520 nm image of a single paracetamol crystal held in place using a stainless steel wire clasp. The orange arrow in the top left shows the direction of solvent flow. The orange oval highlights the crystal within the clasp.

A perfluoro polyether 225 oil (used frequently in crystallography to mount crystals) was considered as an alternative adhesive, however the oil spread around the crystal and delayed dissolution. An additional method of attaching the crystal explored the use of clear nail varnish to 'glue' it to the stainless steel wire. This could be positioned more easily than the oil due to its increased viscosity and dried quickly fixing the crystal in position. Crystals were successfully and securely held in place using this method, in both the compact and whole dose flow cells, and even at the maximum flow rates for each cell, the images are shown in Figure 4.58.

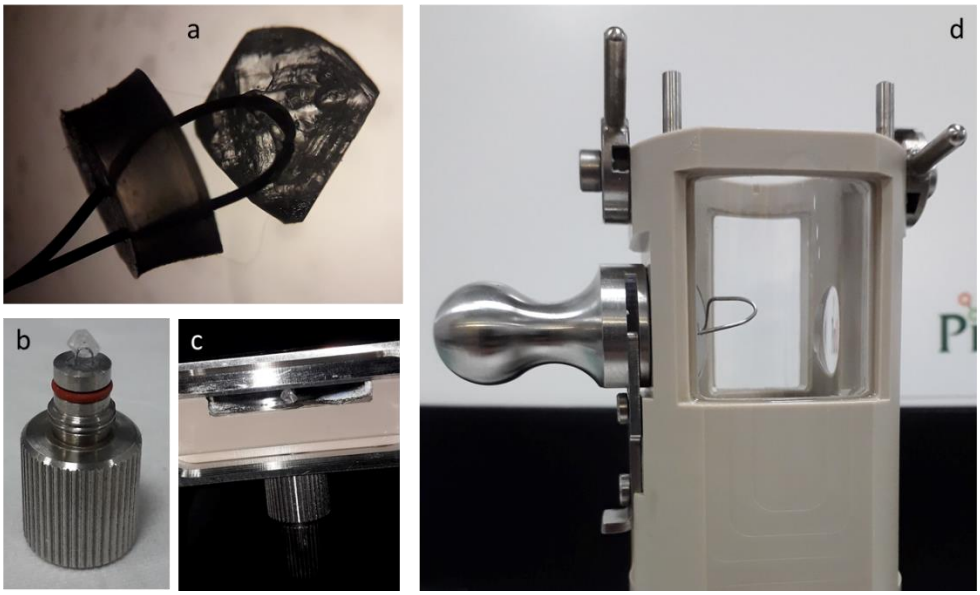

Figure 4.58 – Examples of crystal attachment to stainless steel wire using nail varnish: a) crystal is attached to wire which is threaded through rubber bung, b) this bung sits within the sample holder to provide a seal preventing loss of solvent, c) sample holder then fits into the compact flow cell, and d) whole dose cell is shown with wire threaded in ready for crystal to be attached.

The WDC sample holder has two holes in which to position either end of the wire, hence the crystal and wire could be positioned easily. The CFC sample holder, however, is designed to hold a compacted disc of sample, although during the initial stages of a run a rubber bung is positioned to prevent solvent leakage and provide a flat bottom to the cell. The wire was able to be carefully pushed through this bung in order to secure the crystal in place within the CFC and prevent leakage of solvent, see Figure 4.58 (a).

The coating of an entire crystal in nail varnish for four weeks confirmed that there was no visual change in the size or shape of the crystal over time, suggesting the varnish did not appreciably dissolve or degrade the crystal. This was deemed sufficient for the stage of research; compatibility with each compound being studied should be explored further when necessary. The additional advantages of using nail varnish to secure the crystal are its relatively easy removal using acetone, and its potential to be used to coat specific faces of the crystal thus inhibiting dissolution whilst remaining transparent.

To explore this theory further, a crystal of paracetamol was coated on all faces using the varnish, inserted into the WDC and monitored using the 255 nm and 520 nm wavelengths. Figure 4.59 shows the intact paracetamol crystal before and after thirty minutes of solvent flow (deionised water at 18 mL/min) confirming that dissolution was prevented from occurring on all faces of the crystal. The difference between images is the presence of the solvent front moving through the cell, to highlight that these are taken at the very start of the run and no change in absorbance can be observed around the crystal confirming that no dissolution is taking place. Some small bubbles have appeared on the wire holder itself by the end of the run, but there is no visual change to the crystal viewed either at 255 nm or 520 nm confirming that the varnish has been successful.

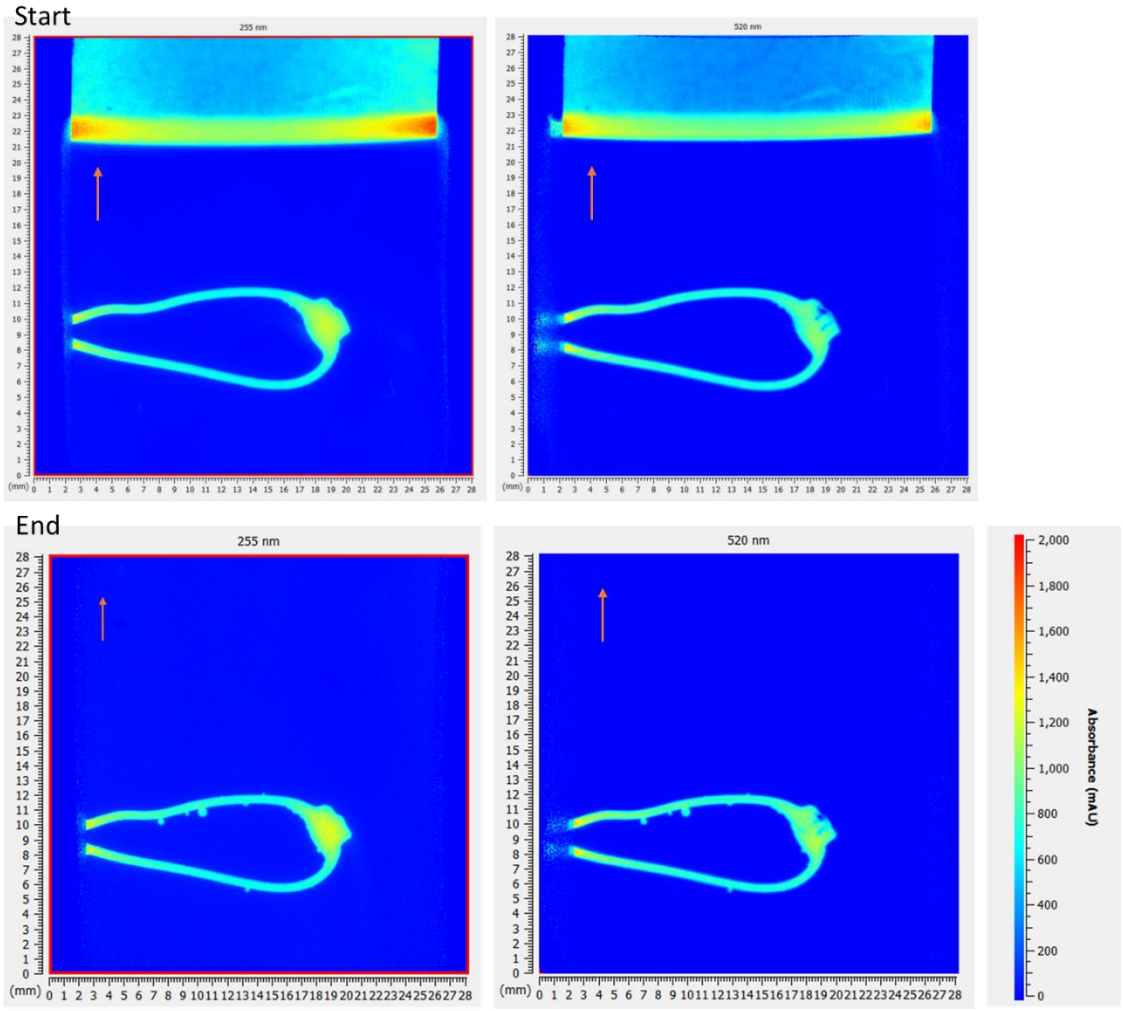

Figure 4.59 – SDi2 whole dose flow cell images for 255 nm (left) and 520 nm (right) with the absorbance key (far right). The orange arrow shows the direction of solvent flow. The images show a single paracetamol crystal coated on all sides in clear nail varnish to inhibit dissolution. The top images were obtained at the start of a run with the solvent front approximately 21 mm through the cell, and the bottom images were obtained at the end of 30 minutes of flowing deionised water through the cell.

In comparison, a crystal without varnish coating can be seen to dissolve rapidly in the flowing water, as shown in Figure 4.60. The 255 nm image shows a range of false colours from dark blue to red (see key for absorbance values), showing UV absorption across the cell is variable. This change is occurring as a result of paracetamol dissolving to produce areas within the cell showing a variety of concentrations throughout the flowing solvent. The solvent flows only in one direction (bottom to top) but dissolved paracetamol can be seen both above and below the crystal, suggesting that flow through the cell is not laminar as the USP IV calculated hydrodynamics may suggest but in this instance, they are instead turbulent. This turbulence is likely a result of

gravity and the changing density of the solution as an increasing amount of paracetamol dissolves. This level of detail, however, would not be possible from a routine bulk measurement of API release using conventional UV dissolution techniques. This experiment highlights the complexity of dissolution and the interplay of hydrodynamics, confirming the benefits from utilising an imaging technique to monitor dissolution.

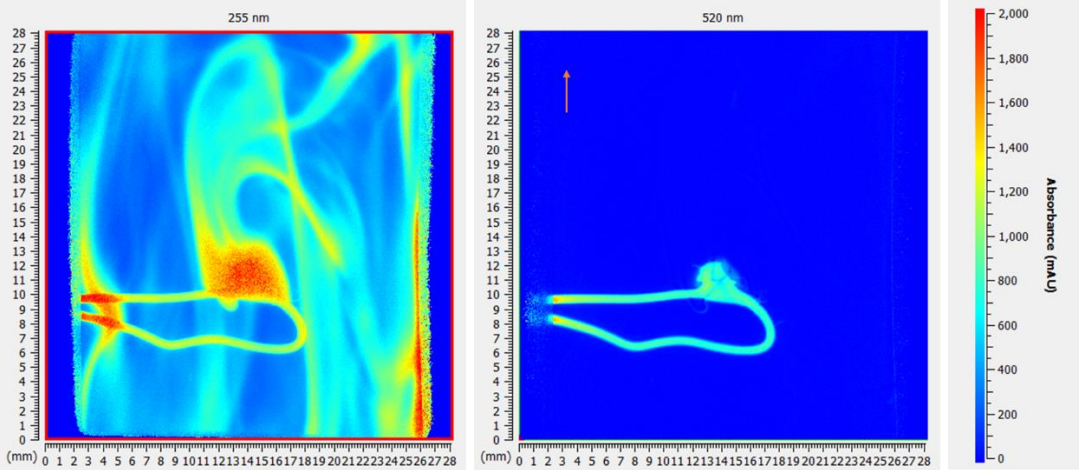

Figure 4.60 – SDi2 whole dose flow cell images for 255 nm (left) and 520 nm (right) with the absorbance key (far right). The orange arrow shows the direction of solvent flow. The images show a single paracetamol crystal attached to wire using nail varnish. The 255 nm image shows variations in absorbance throughout the cell as a result of the dissolving paracetamol.

The 520 nm image is relatively simple, showing only the wire holder with the attached single crystal. The bottom of the crystal is inhibited from dissolving due to the presence of the varnish, hence it cannot be easily differentiated from the bottom of the wire. The edge of the crystal fades gradually as it dissolves, allowing the physical change to be monitored (through the 520 nm images) in addition to the concentration change (through the 255 nm images).

The placement of the crystal relative to the wire and therefore the solvent will influence hydrodynamics and therefore dissolution. The method was therefore adjusted, attaching the crystal on the bottom of the wire and increasing the flow to the maximum recommended for the WDC, however, the flow of dissolving paracetamol continued to show similar extents of turbulence making it challenging to monitor dissolution at the surface due to the movement of dissolving sample in multiple

directions at the same time. In comparison, flow within the CFC appears to continue only in one direction (from left to right), see Figure 4.61.

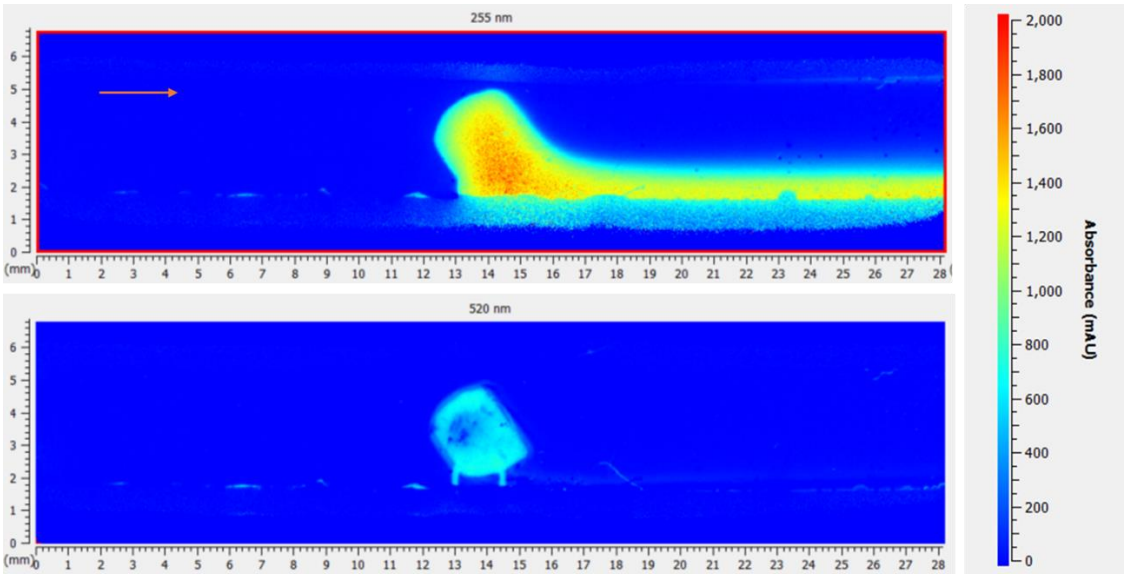

Figure 4.61 - SDi2 compact flow cell images for 255 nm (top) and 520 nm (bottom) with the absorbance key (far right). The orange arrow shows the direction of solvent flow. The images show a single paracetamol crystal attached to a stainless steel wire loop with varnish. These images were obtained 80 secs after starting solvent flow through the cell.

The dissolving paracetamol flows with the solvent direction, and as an increased amount of paracetamol dissolves, the density of the solution increases resulting in a concentration gradient. This is indicated by a higher absorbance at the bottom of the cell relative to further up, which can be monitored and measured simply in comparison with the complex gradients observed in the WDC, see Figure 4.60. The presence of the crystal can again be visualised using the 520 nm image, and the difference between physical presence of the crystal versus a high concentration of paracetamol observed by comparing the 255 nm and 520 nm images.

Absorbance values using a UV wavelength of 255 nm for both cells reached two absorbance units (AU) within eighty seconds of dissolution starting. The maximum absorbance the SDi2 is able to record is two AU with a loss of linearity occurring immediately prior to this.[168] This prevents concentration from being accurately calculated for those regions where the detector has been overloaded, however, one can conclude that the absorbance is a result of a high concentration of dissolved paracetamol and not a physical obscuration by pieces of crystal, as a result of having

both the UV and visible images available for analysis. This would not have been feasible with the earlier instruments and highlights a significant advantage of the SDi2.

A method to avoid saturation can also be considered, which involves using alternative or additional UV wavelengths to the λ_{max} to enable higher paracetamol concentrations to be measured without saturation. Note that 255 nm was chosen following the Pion guidance to select the wavelength closest to the USP monograph recommendation, which for chromatographic assays of paracetamol is 230 nm.[40]

4.2.3 Calibration of UV absorbance

The SDi2 is able to monitor two wavelengths per run (also referred to as a method) from a discrete range of five: 255, 280, 300, 320 and 520 nm. The Beer-Lambert Law is used to calculate the concentration of a solution, but first the molar absorption coefficient (ε) must be obtained through calibration. Routine UV-Vis spectroscopy includes a scan of absorption across multiple wavelengths to determine λ_{max}; in this instance, there may be scope to use multiple wavelengths to gather information on the lower concentration areas without falling outside the limit of detection, and also the higher concentration areas without saturating the detector. In addition, Pion recommends using the SDi2 instead of alternative UV instrumentation for all calibration experiments.

Solutions of paracetamol, in deionised water, were made at a series of defined concentrations, see Table 4.11 for details. The solutions were analysed at each UV wavelength using the CFC to determine linearity. The calibration method used is shown in Table 4.10, and this was run for two wavelengths at a time (255 and 280 nm, 300 and 320 nm).

Table 4.10 - SDi2 compact flow cell calibration method.

Time (min:sec)	Flow rate	Details	Cumulative time (secs)
10:00	3 mL/min	Blank deionised water	0 to 600
00:10 or 00:30	0 mL/min	Manually transfer line to sample solution	610 or 630
00:30	4 mL/min	Fill cell quickly	640 or 660
10:00	3 mL/min	Sample	1240 or 1260

The absorbance data was extracted using two manually set up zones, see Figure 4.62; one which provides an average across the x dimension and one which provides it across the z dimension. An average absorbance for each zone is then calculated per time segment, and in theory there should be very little to no difference between the two data sets, which is apparent in Figure 4.63.

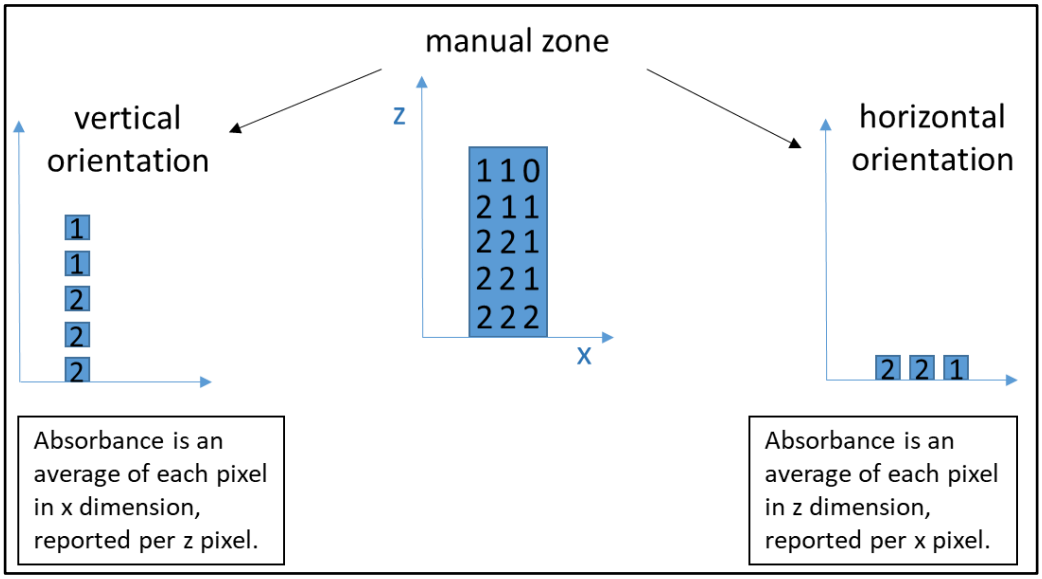

Figure 4.62 – Explanation of the two orientation options for obtaining absorbance values for a manual zone using the SDi2 Analysis software. To provide an example of how the zones work, an absorbance value of 0, 1 or 2 has been assigned to each pixel. These have then been averaged in the horizontal (x) dimension to provide an absorbance value per vertical orientation or z pixel. Additionally they have been averaged in the vertical (z) dimension to provide an absorbance value per horizontal orientation or x pixel.

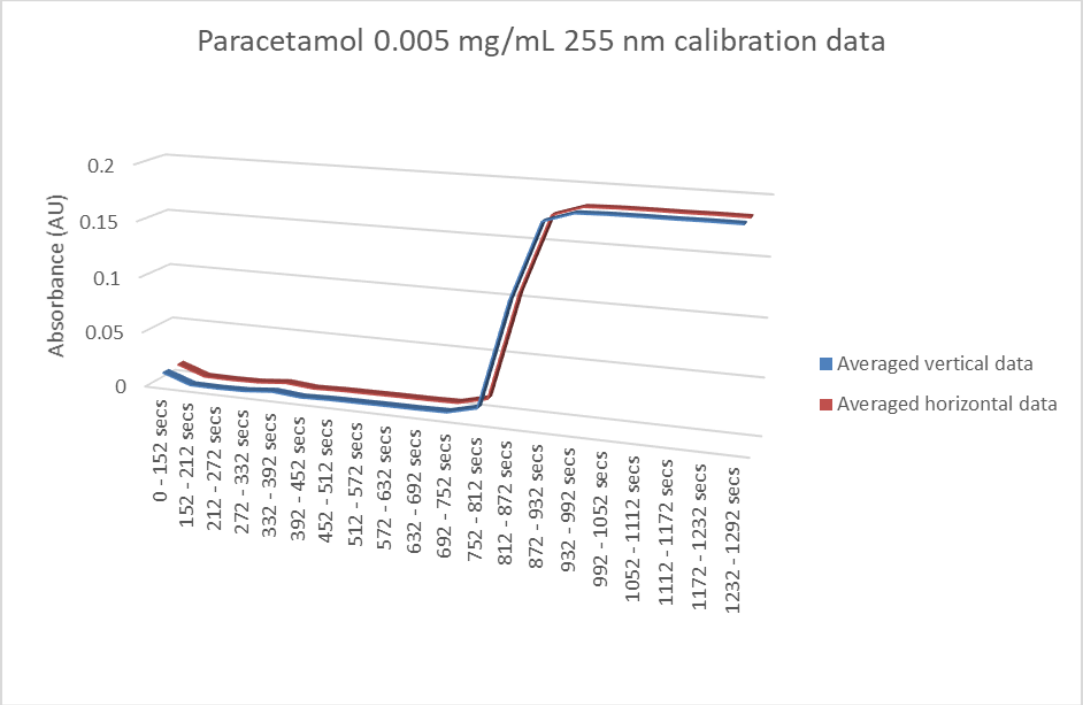

Figure 4.63 – SDi2 compact flow cell calibration for paracetamol in deionised water. Comparison of absorbance values obtained through averaging data in the vertical direction versus the horizontal direction for the same zone. From a time of 0 to 752 seconds, the sample is blank (deionised water) and from 752 seconds, the sample is paracetamol 0.005 mg / mL in deionised water.

Figure 4.63 shows a delay between transferring the line to the sample solution and observing an increase in absorbance. This is due in part to the length of tubing between sample and cell, in addition to the gradual displacement of blank sample from the flow cell, which results in a period of increasing absorbance from 692 secs and subsequent stabilisation from 932 secs. The maximum absorbance observed for each concentration at each wavelength was obtained using the SDi2 Analysis software, see Table 4.11.

Table 4.11 – Determining the maximum absorbance for each concentration of paracetamol at each UV wavelength available on the SDi2 during the calibrations.

	Max absorbance (AU) obtained at each concentration			
λ	**0.100 mg/mL**	**0.050 mg/mL**	**0.010 mg/mL**	**0.005 mg/mL**
255 nm	> 1.500	1.250	0.300	0.180
280 nm	1.000	0.525	0.105	0.050
300 nm	0.110	0.058	0.011 (variable)	Not tested
320 nm	0.010	0.011	Below 0	Not tested

The maximum absorbance the SDi2 can report is 2 AU, although the suggested maximum absorbance at which detector saturation occurs and linearity is considered lost has been recommended by Pion to be 1.5 AU. Absorbance values are an average per defined time segment, and are obtained only from the linear sections of the data observed. For example, in Figure 4.63, the absorbance of deionised water is calculated using the average of values obtained between 152 and 752 secs, and sample absorbance is calculated using the average of values obtained between 932 and 1292 secs. This is assessed and calculated for each calibration run and wavelength. The linearity of the relationship between concentration and absorbance guides the choice of UV wavelength(s) that will allow the full range of concentration gradients around a single crystal to be calculated. As an example, Figure 4.64 compares calibration data obtained for 255 nm and 280 nm.

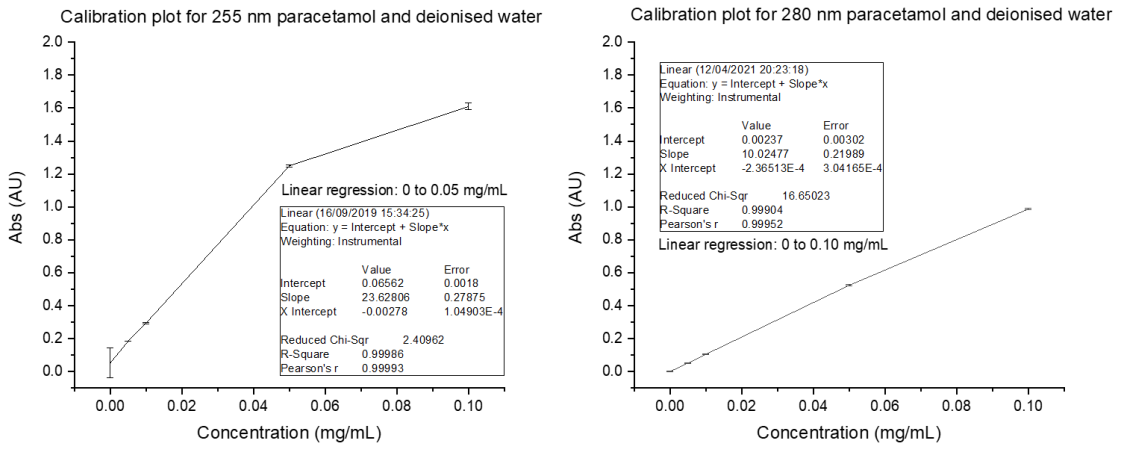

Figure 4.64 – SDi2 compact flow cell calibration for paracetamol in deionised water. Comparison of calibration plots for UV wavelengths of 255 nm (left) and 280 nm (right). Regression analysis has been applied to the linear section of each plot and the details included.

Figure 4.64 shows the calibration plot for 255 nm is linear up to a concentration of 0.05 mg/mL, and the plot for 280 nm is still linear at a concentration of 0.10 mg/mL. The details of linear regression are inset into each plot. This data highlights the need to use the most appropriate wavelength depending upon the information being sought for that experimental run and the range of absorbance values obtained. It also suggests that detector saturation occurs between 1.2 and 1.6 AU, as shown by the loss

of linearity on the plot for 255 nm, which corroborates the Pion recommended maximum of 1.5 AU.

Table 4.12 - SDi2 compact flow cell calibration for paracetamol in deionised water. Summary of calibration data for each wavelength, with calculated molar absorption coefficients, and recommended lower concentration limits and upper limits for linearity based upon current experimental data only.

λ	Calculated (ε) molar absorption coefficient ($M^{-1}cm^{-1}$) (to 2 d.p.)	Guide for lower concentration limit (mg/mL)	Guide for upper concentration limit (mg/mL)
255 nm	3989.24	0.005	0.050
280 nm	1763.23	0.005	> 0.100
300 nm	210.08	0.010	> 0.100
320 nm	12.71	0.050	> 0.100

A summary of the calibration data for each wavelength can be found in Table 4.12. The guide for lower and upper concentration limits are recommendations based upon current experimental data and may be expanded upon with additional work. However, the lower concentration limits (limits of detection) for 300 and 320 nm are 0.010 and 0.050 mg/mL respectively, below these concentrations the absorbance is indistinguishable from that of a blank sample of deionised water. For 255 nm the concentration above which linearity is lost is between 0.050 and 0.1 mg/mL, extrapolating from the linear section one could predict that a concentration of 0.060 mg/mL would give an absorbance of 1.5 AU – this should be confirmed with experimental data, so the maximum concentration that can be calculated with confidence using this data is 0.050 mg/mL. Comparatively, the maximum concentration of paracetamol in deionised water that can be calculated with confidence using a wavelength of 280 nm is 0.100 mg/mL. In summary, this means that the full range of concentrations can be calculated from absorbance if the most appropriate wavelengths are selected.

4.3 Results and discussion

The earlier studies by Østergaard *et al.* applying surface dissolution imaging to single crystals, were able to observe diffusion by using stagnant buffer and hydrogels, both to

hold the crystal in place and to simplify the complex hydrodynamics.[216] The lidocaine crystals used in these studies were chosen for their poor solubility, hence the highly soluble paracetamol in this work might be expected to dissolve rapidly. An almost saturated solution of paracetamol in deionised water was considered for use as the dissolving solvent to slow dissolution, however, it was not found to be necessary, with some of the paracetamol crystals used taking longer than twenty minutes to fully dissolve in flowing deionised water at 37°C. Utilising this novel method for holding single crystals and visualising their dissolution, paracetamol crystals were explored further with the SDi2 software with regard to monitoring both concentration and size changes.

4.3.1 Monitoring concentration using UV absorbance

The calculated molar absorption coefficients for each appropriate wavelength were used to determine the concentration surrounding a paracetamol crystal dissolving in deionised water flowing at 2.16 mL/min. A wavelength of 280 nm was selected to encompass the larger concentration range of 0.005 to at least 0.100 mg/mL, up to an absorbance of 1.5. Absorbance is converted to concentration using the Beer-Lambert Law, where in this instance the molar absorption coefficient (ε) for 280 nm is 1763 $M^{-1}cm^{-1}$ and the path length (l) is 0.9 cm. The concentration can also be converted from M (moles per litre) to mg/mL by multiplying by the relative molecular mass (151.16 g/mol). This can be done manually or the SDi2 Analysis software can be used, although a glitch in the software means that when extracting raw data it reverts back to providing absorbance (in AU) instead of concentration regardless of the settings used to calculate it.

Three manual zones were set up to monitor concentration changes across and around the same crystal analysed in the previous section. These zones were positioned according to Figure 4.65, with the two vertical zones, (ii) and (iii), having a width of 0.1 mm and the horizontal zone (i) having a height of 0.1 mm to provide sufficient resolution and a maximum number of data points for each dimension. The absorbance values were extracted in sixty second segments to reduce the data burden.

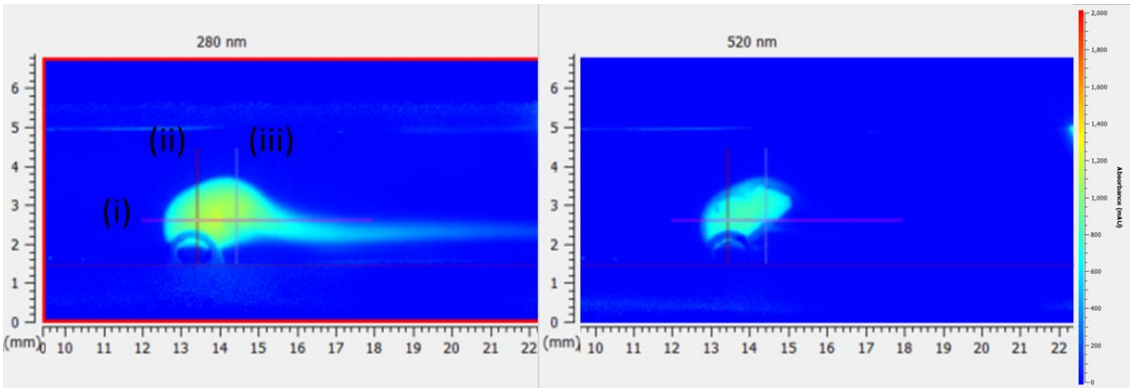

Figure 4.65 – SDi2 compact flow cell image at 280 nm (left) and 520 nm (right) showing a paracetamol crystal held on a steel wire loop and deionised water flowing from left to right through the cell. The absorbance key using the jet colour map is shown to the far right. Both images are from the start of dissolution (image number 53). The three additional zones to measure concentration can be seen horizontally (i) and vertically (ii) and (iii) across the crystal in both images. The images have been cropped in the x dimension to focus on the crystal and zones.

Figure 4.65 shows two images of the crystal, one at 280 nm and one at 520 nm. In both images the wire holding the crystal can be seen not as an increase in absorbance, but as a decrease due to the wire being present during the start-up section of the method, where the absorbance through the cell is blanked with solvent. The wire was placed in the cell for this to determine whether this would be advantageous to the method and is therefore seen as background absorbance, hence it appears as a hole through the bottom of the crystal in both the UV and the visible wavelength images.

The data can be extracted from each zone to produce a graph showing absorbance (or concentration) per time segment across either the x or z dimension. Looking first at the horizontal zone (i), the change in absorbance across the centre of the crystal can be monitored per time segment at different points. Figure 4.66 shows the variation in calculated concentration at specified positions in the x dimension at a z position of 2.6 mm, for each time segment. The maximum concentration of 0.12 mg/mL corresponds to an absorbance of 1.2 AU, confirming that no value may be at risk of saturation.

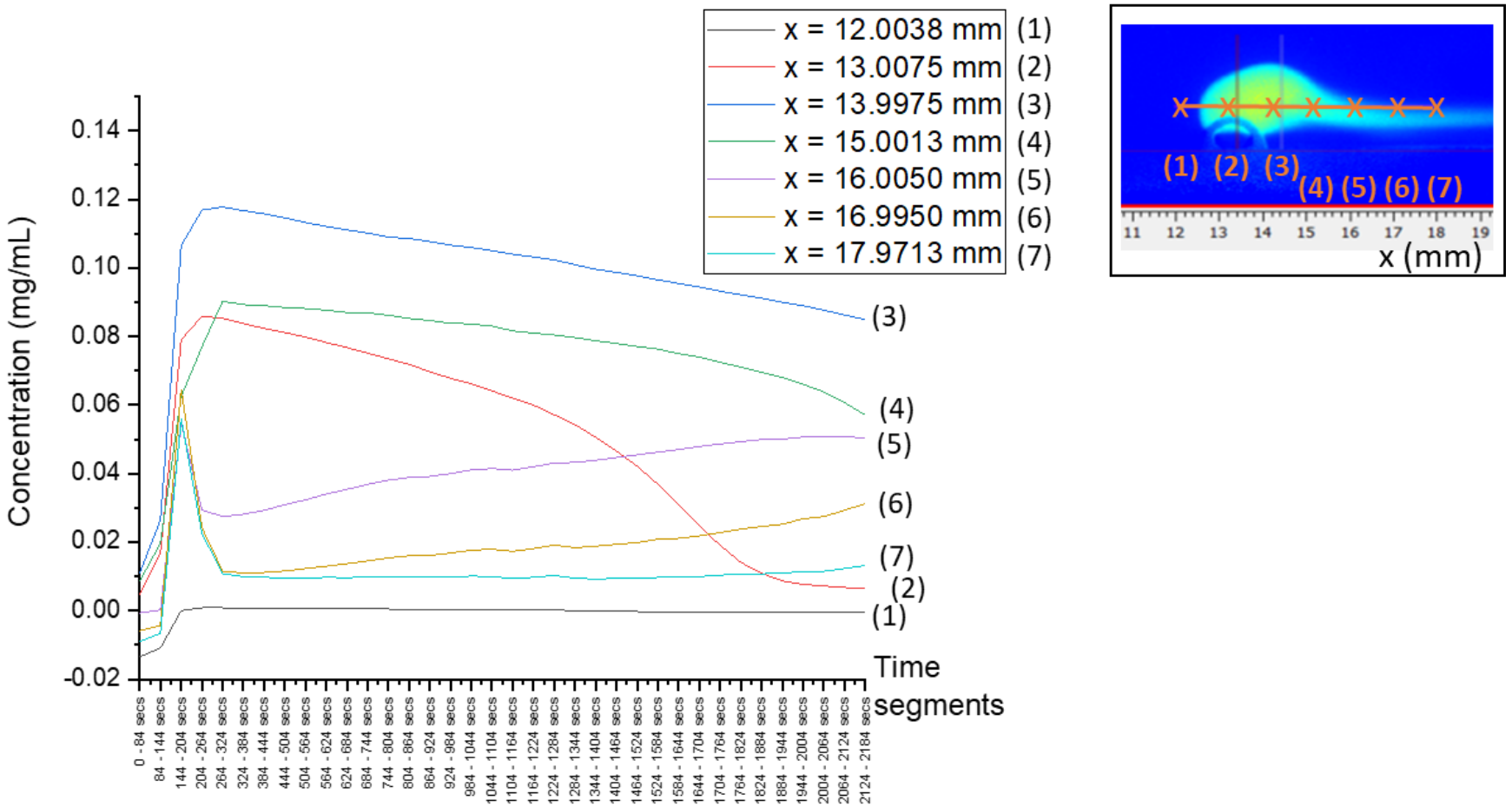

Figure 4.66 – Calculated concentration using absorbance at 280 nm for specified x positions along the horizontal zone (i) positioned in the z dimension at 2.6 mm. Inset picture shows a 280 nm image from the start with zone (i) highlighted in orange and each position plotted on the graph marked by an orange 'x' and number. The time segments are 0 to 84 secs, then every 60 secs after that until a total of 2184 secs.

The initial 264 seconds corresponds to the time taken for the cell to fill with solvent and bubbles to be removed, hence the concentration during this period increases from below zero (the absorbance has initially been blanked with solvent as is commonplace for UV spectroscopy). The position to the left of the crystal (1) maintains a concentration of zero from this point onwards, providing confidence in the methodology and confirming the observations from images, which clearly show an absence of dissolved drug to the left of the crystal. Position (2) shows a linear decline phase and then rapidly drops after twenty minutes (1200 secs) but does not reach zero. This position is in the path of the crystal but highlights that a change in absorbance can still be observed as the crystal dissolves and shrinks in size. Positions (3) and (4) both show a gradual consistent decline in concentration, with a steeper decline after 2000 secs for (4), which can again be linked to the crystal dissolving and shrinking in size. Conversely, positions (5) and (6) show a gradual increase in concentration throughout dissolution of the crystal, which is a result of dissolving paracetamol diffusing upwards in addition to it flowing from left to right. Position (7) shows a small increase towards the end of reporting, which is also likely a result of diffusion.

Concentration values are calculated from UV absorbance using the Beer-Lambert Law, which requires the molecule to be in solution for this to be applicable. An object such as the crystal, being physically present in the light path may therefore render the calculation of concentrations invalid. This would be applicable to positions (2) and (3) in this experiment as they are both in the path of the crystal throughout the monitoring period. They have nevertheless been included in this plot to highlight that their physical presence does not saturate the detector and is not distinguishable using UV absorbance or UV image alone. In this instance, the dual wavelength capability of the instrument is necessary to allow the crystal edge to be detected with the visible wavelength and observed in conjunction with the UV image so that concentration gradients may be determined for the interface between solid and liquid.

An alternative method for visualising the data is to plot concentration against x position for each time segment; a selection of time segments have been chosen to represent different points throughout dissolution, see Figure 4.67. Three arrows have

been placed on the plot to show the three distinct areas: (1) the section immediately to the left of the crystal, (2) the section in the vicinity of the crystal and (3) the section to the right of the crystal. Arrows (1) and (2) show a decrease in concentration with time, whereas arrow (3) shows an increase.

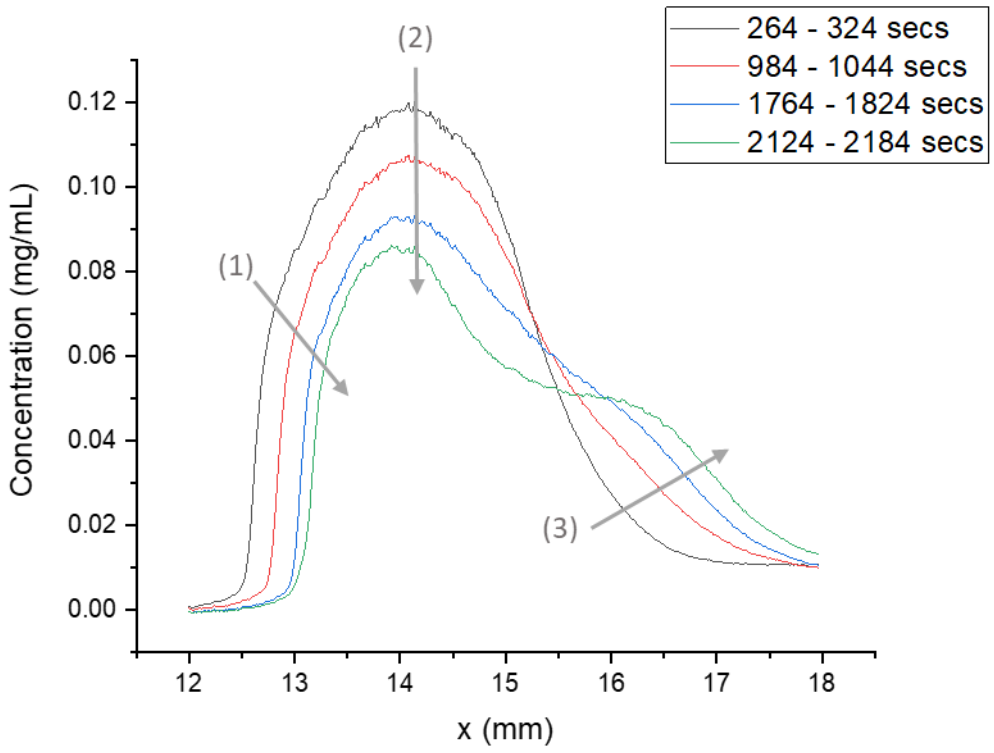

Figure 4.67 – Calculated concentration using absorbance at 280 nm for four time segments, across the horizontal zone (i) and positioned in the z dimension at 2.6 mm. Three grey arrows show the change in concentration (1) to the left of the crystal, (2) in the vicinity of the crystal and (3) to the right of the crystal, with time.

The decline is more rapid for the area highlighted by arrow (1) than (2). As the crystal reduces in size, the area of dissolving paracetamol around it shrinks in size too, which leads to the boundary layer around it shifting both downwards and inwards (the crystal is held in place at the bottom hence only the top and sides can dissolve). However, arrow (3) highlights an area where there is an increase in concentration with time and it becomes more diffuse. As the crystal dissolves and the concentration of paracetamol in the cell increases, in addition to advection following the flow of solvent from left to right, there will be an increased amount of diffusion occurring up through the cell due to the concentration differences between each layer of laminar flow.

Diffusion requires time to take place, hence the increase only occurs to the right of the crystal.

Similar plots of concentration versus position in the z dimension for selected time segments are shown in Figure 4.68 and Figure 4.70, and these correspond to the additional zones highlighted by (iii) and (ii), respectively, in Figure 4.65. Zone (iii) is positioned to the right of the crystal but monitors a vertical segment through the cell. The data in Figure 4.68, again shows distinct sections according to position, although in this instance they all show a decrease in concentration with time.

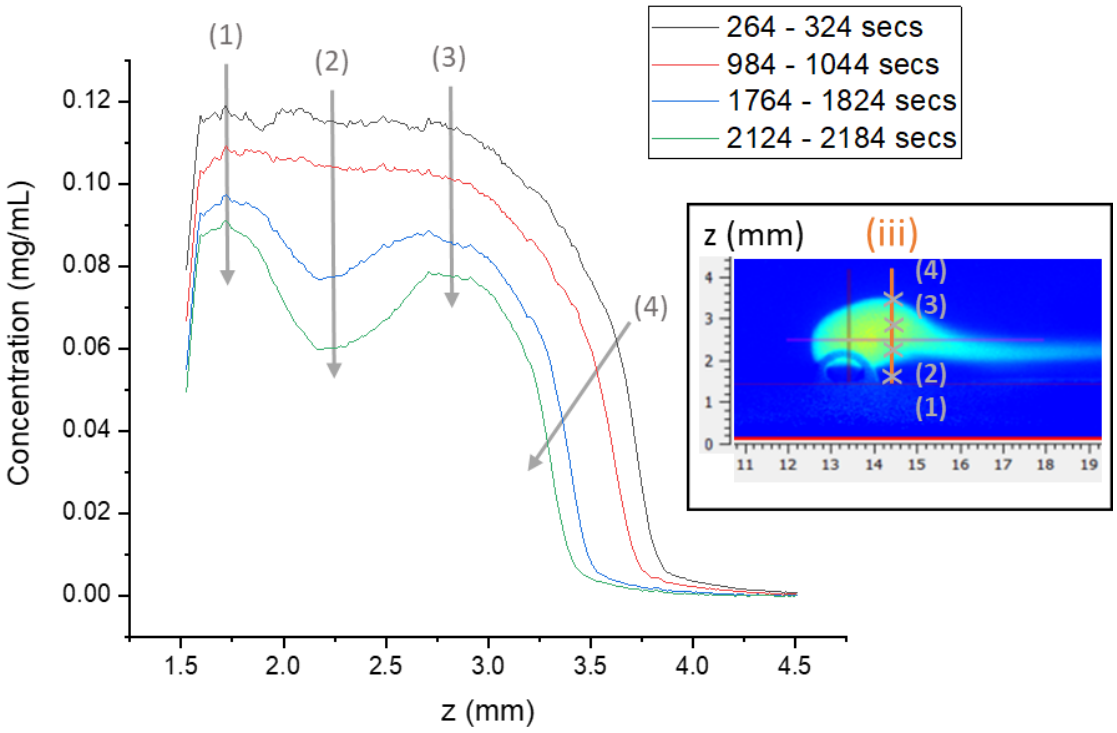

Figure 4.68 - Calculated concentration using absorbance at 280 nm for four time segments, across the vertical zone (iii) and positioned in the x dimension at 14.4 mm. Four grey arrows highlight the different segments relative to the crystal. Inset is the UV image showing the position of zone (iii) highlighted in orange, in addition to the position of the arrows highlighted by the grey crosses on the orange zone line, which correspond to (1), (2), (3) and (4).

Four grey arrows highlight different sections and relate to positions in the z dimension marked by grey crosses on the image in Figure 4.68. Position (1) is close to the z_0 position at the bottom of the cell and reduces in concentration over time, although it reports the peak concentration for each time segment, which suggests that dissolving

paracetamol sinks down the cell as might be expected due to its increased density relative to lower concentrations. However, the amount of dissolving paracetamol sinking to this position reduces over time. Position (2) shows a much greater decrease in concentration, which is again unexpected, but can be explained by viewing both the 280 nm and 520 nm images around this time point, see Figure 4.69. The crystal changes in shape resulting in position (2) falling just underneath the side of it, hence the reduction in absorbance and therefore calculated concentration.

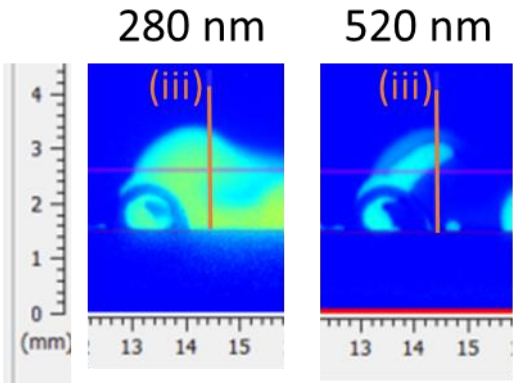

Figure 4.69 – Images from both 280 nm and 520 nm highlighting the change in crystal shape at 1764 secs that results in the concentration data observed across zone (iii).

Position (3) remains in the line of the crystal, hence it does not reduce as rapidly or to the same extent as position (2), but reduces more than position (1) suggesting a strong influence of density upon the movement of dissolving paracetamol. This can be visualised particularly well in Figure 4.69 with the increased absorbance in the 280 nm image at the bottom of the cell. Position (4) relates to a range of z positions, between z = 3.75 and 3.25 mm, but the trend overall shows a decrease in calculated concentration as the crystal reduces in size and the dissolving plume of paracetamol moves downwards whilst flowing from left to right, suggesting less diffusion occurs upwards through the cell.

The final zone (ii) highlighted in Figure 4.65, has been plotted as concentration per z position for a number of time segments, see Figure 4.70. An additional time segment of 2004 to 2064 secs has been added to this plot to aid in understanding the final time segment, which is significantly different from the previous ones. A vertical cursor has also been positioned at the bottom surface of the cell, z_0, to add clarity to this data -

the calculated concentration values plotted at z positions between 1 and 1.54 therefore relate to positions below the bottom of the CFC and can be ignored.

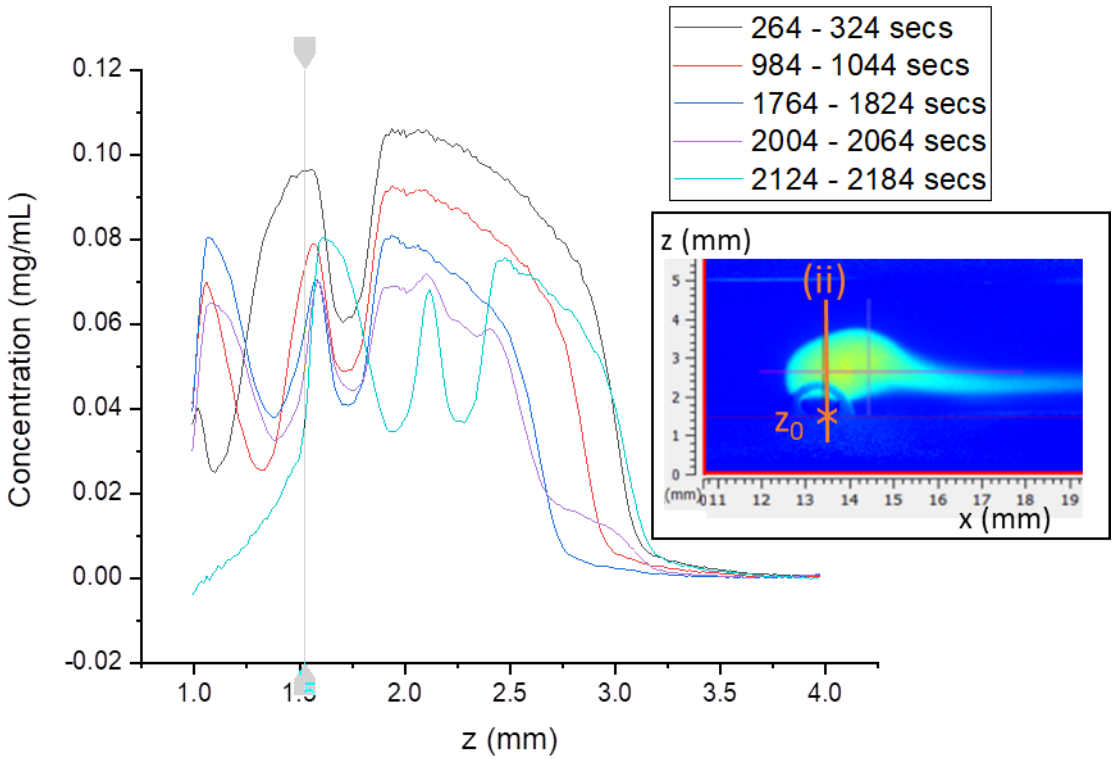

Figure 4.70 – Calculated concentration using absorbance at 280 nm for five time segments, across the vertical zone (ii) and positioned in the x dimension at 13.4 mm. The vertical cursor is positioned at the bottom surface of the cell (z_0 = 1.54 mm). Inset picture shows a 280 nm image from the start with zone (ii) highlighted in orange and the z_0 position marked by an orange 'x'.

The first three time segments (264 – 324, 984 – 1044 and 1764 – 1824 secs) in Figure 4.70 show a gradual reduction in calculated concentration for all positions across zone (ii). This zone is positioned upon the crystal, hence the absorbance value, which is used to calculate concentration, will reflect the physical presence of the crystal in addition to the paracetamol in solution. It may therefore be more appropriate to present these values as absorption rather than concentration. The observed changes over time will be the same whether presented as absorbance or concentration, hence they will be referred to as calculated concentration to make the point that they do not solely reflect paracetamol in solution.

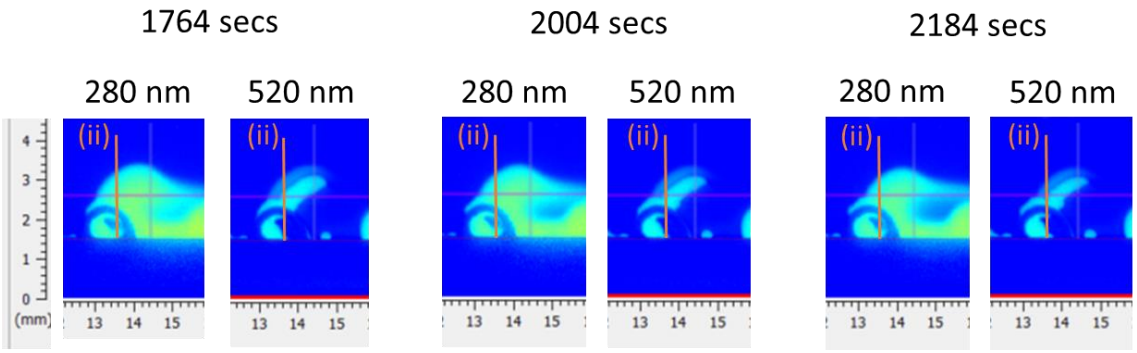

Figure 4.71 - Images from both 280 nm and 520 nm for three time points throughout the dissolution of a single paracetamol crystal. Zone (ii) is highlighted in orange for each image.

The calculated concentrations for the final two time segments (2004 – 2064 and 2124 - 2184 secs) do not appear to follow the previous profiles, and must again be interpreted using the images available for both wavelengths, see Figure 4.71. The visible images show the presence of an object below the left section of wire and the continued presence of an object above the left section of wire. These artefacts appear as increases in concentration on the plot, but when interpreted with the images, suggest that they are more likely a result of a bubble attached to the wire in addition to the remaining varnish attached to the top of the wire.

The wire holding the crystal, having been included in the start-up section of the run, remains as if it were invisible throughout dissolution, with the absorbance value at this position corrected for its presence. It is tempting therefore to correlate the initial dip in concentration at a z position of 1.75 mm for the first four time segments, with the wire. However, upon closer inspection the wire sits at a higher z position of approximately 2 mm. The SDi2 therefore appears to be picking up absorbance additional to the physical presence of the wire, with the position of 2 mm for the first four time segments showing calculated concentrations above 0.07 mg/mL. The final time segment shows two dips in concentration at z positions of 2 and 2.25 mm, with some absorbance between them. An interesting observation is that the steel wire utilised to hold the crystal has a diameter of 0.2 mm. One possible and very feasible explanation is that the position of the wire during the start-up and during the run (with crystal attached) has slightly changed, resulting in a shift between blanked positions. Additionally the presence of varnish to hold the crystal in place on the wire will affect light absorbance and although it will remain present after the crystal has dissolved, it

was not present during the start-up runs so will not be blanked out in the same way as the wire has been. One way to resolve this challenge may be to remove the wire during the start-up section of the run, although this will add a separate challenge in distinguishing the physical presence of the wire versus the crystal.

Overall, this section highlights the sensitivity of the SDi2 method in detecting changes in absorption (and therefore calculated concentration) at different positions throughout the cell over time. It also confirms once again the advantages of being able to visualise dissolution using both a UV and a visible wavelength. The ability to understand whether an absorbance relates to a concentration change or a physical obscuration is supported greatly by the dual wavelength capability. It should be noted that there is great disparity between the reported maximum solubility of paracetamol in water, which is approximately 14 mg/mL at 25°C, and the maximum concentration of 0.120 mg/mL observed with the SDi2 (at 37°C).[270] This confirms that the solution has not reached saturation and sink conditions have been maintained throughout this example by means of the flowing of solvent and highlights an additional advantage of the SDi2 technique over the more traditional dissolution methods.

4.3.2 Dissolution flux and mass released using UV absorbance

The SDi2 Analysis software produces a default report for the CFC when the molar absorption coefficient (ε) and molecular mass are inputted. The report includes surface absorbance (mAU), intrinsic dissolution rate (IDR) with standard deviation (μg/min/cm^2), and sample mass released (mg). All of these are per time segment and according to the defined start and end frames. These calculations are appropriate when analysing a compact of sample, but when using the CFC to monitor the dissolution of a single crystal require further consideration. Figure 4.72 highlights the default three zones for the CFC that are used to calculate this report.

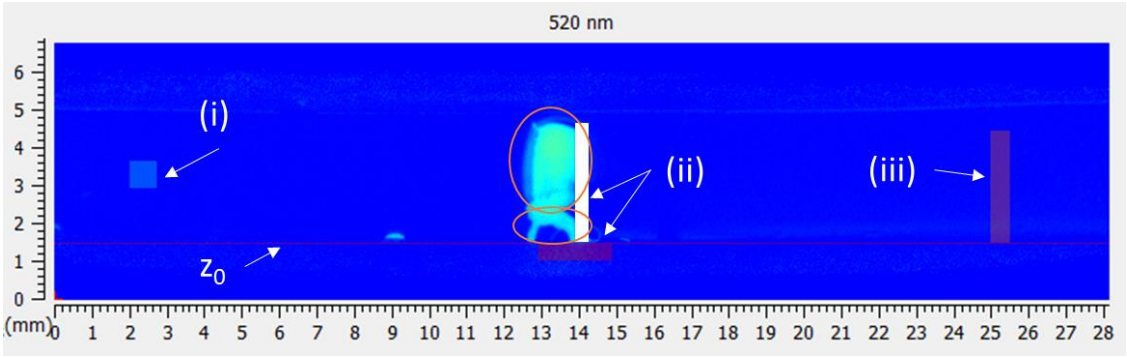

Figure 4.72 – Image of the compact flow cell with zones highlighted for calculating: (i) background reference, (ii) surface absorbance (additionally coloured in white) and (iii) intrinsic dissolution rate. The bottom surface of the flow cell is labelled z_0 and both the crystal and the wire holding it are circled in orange.

The background absorbance calculation continues to be useful, but the surface absorbance calculation is not appropriate due to the presence of the wire holding the crystal and the placement of the crystal in the centre of the cell. The IDR zone monitors absorbance changes and may still be used, but the IDR value it produces is no longer relevant because the surface area of the crystal is constantly changing. Instead the raw IDR data (µg/min/cm^2) can be manipulated to remove surface area (0.07 cm^2) and leave the dissolution flux (µg/min), which can be plotted per time period, see Figure 4.73. This data, when used in combination with both the UV and visible images throughout dissolution, see Figure 4.74, helps to further understand dissolution of a crystal.

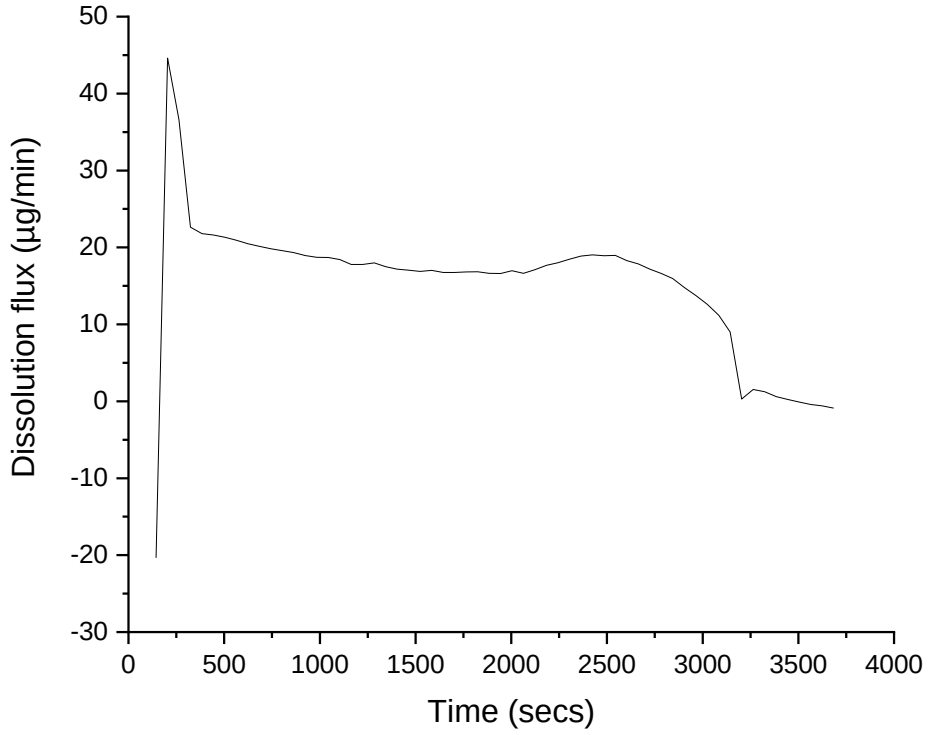

Figure 4.73 – SDi2 compact flow cell calculated dissolution flux using intrinsic dissolution rate data for a paracetamol crystal dissolving in deionised water flowing at 2.16 mL/min. The zone was set up at a position of 23.00 in x dimension, 1.54 in z dimension with a width of 0.50 mm and a height of 3.00 mm.

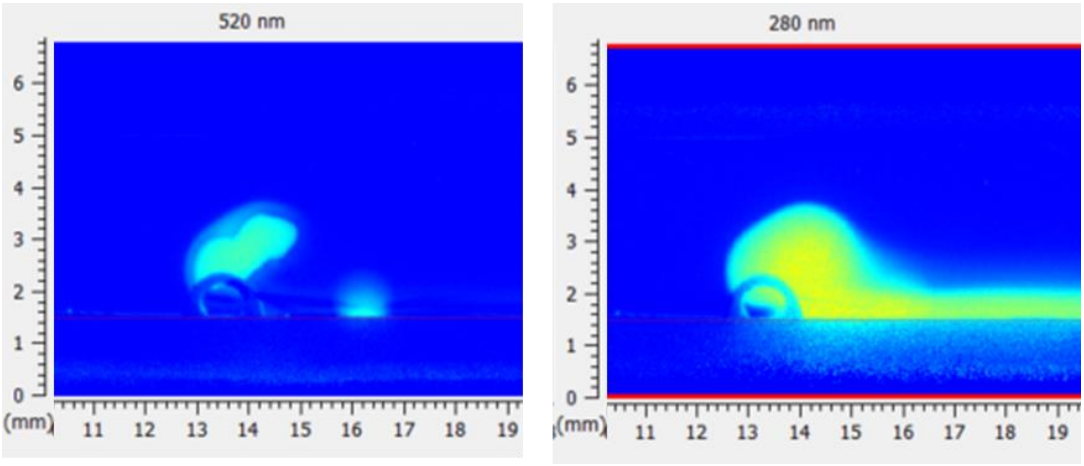

Figure 4.74 – SDi2 compact flow cell image at 520 nm (left) and 280 nm (right) showing a paracetamol crystal held on wire loop with deionised water flowing from left to right through the cell. In addition to the main crystal held in the centre of the cell on the loop, a smaller piece of crystal can be seen at the bottom of the cell to the right. In the 280 nm image the small piece of crystal is hidden by the plume of dissolving paracetamol coming from the main crystal and flowing right.

The initial negative flux seen in Figure 4.73, is likely caused by the solvent front moving through the cell and the removal of an air bubble by opening the hatch and tipping the

cell. The initial peak at approximately 250 secs can then be correlated with a small piece of crystal detaching from the main body and falling to the bottom of the cell whilst continuing to dissolve, see Figure 4.74. This would increase the surface area available for paracetamol to dissolve from and thus increase the dissolution flux, which quantifies the amount of paracetamol passing through the zone (labelled (iii) in Figure 4.72) per minute.

The sample mass released, which is automatically reported by the SDi2 can also be utilised, see Figure 4.75. This is calculated using the concentration of sample released through the IDR zone downstream of the dissolving crystal; the surface area is multiplied out to provide the dissolution flux which is then multiplied by the time segment with an adjustment for units to provide the mass (in mg) released, and this is plotted cumulatively against time.

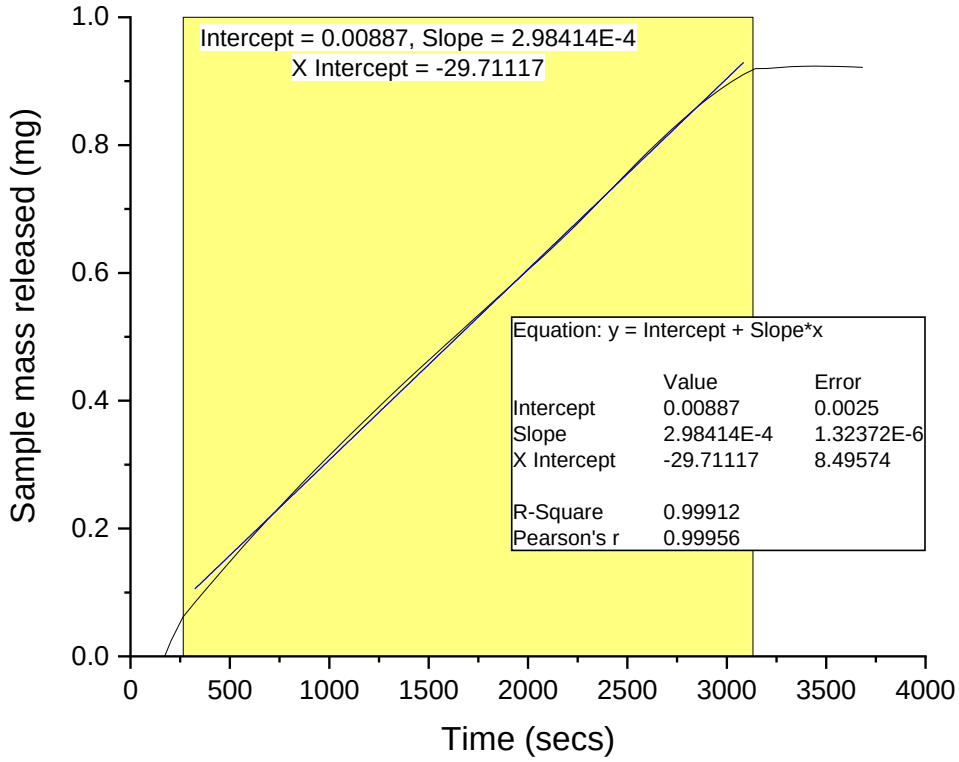

Figure 4.75 - SDi2 compact flow cell calculated sample mass released for a paracetamol crystal dissolving in deionised water flowing at 2.16 mL/min. The zone was set up at a position of 23.00 in x dimension, 1.54 in z dimension with a width of 0.50 mm and a height of 3.00 mm. Linear regression has been applied to the section highlighted in yellow, with details inset.

Figure 4.75 shows a rapid initial release of sample which correlates with the smaller piece of crystal detaching from the main body. A constant rate of mass release is then achieved between 600 and 2900 secs, before the mass released plateaus at 0.9 mg, confirming the crystal is fully dissolved after 3000 secs. The continuous (zero order) release rate makes it likely that dissolution is occurring through an erosion mechanism, which could be further confirmed by looking at how the crystal changes in size with time.[2,3]

4.3.3 Monitoring size change using visible absorbance

Monitoring dissolution with dual wavelength capabilities enables a UV wavelength to capture concentration changes and the visible (520 nm) wavelength to observe objects that are physically obscuring light transmission through the flow cell. The absorbance of visible light can theoretically be used therefore, to infer details about size changes during dissolution. There are two Pion-suggested methods for monitoring size changes using the visible wavelength: one for the CFC and one using the WDC. Both will be described and applied to single crystal dissolution, with their advantages and limitations discussed, along with a suggested new method for the CFC. The Pion compact flow cell method and then whole dose cell method are explained first as these outline the theory and practical aspects of monitoring size change with the visible wavelength.

Method 1 – Pion compact flow cell zones

Pion recommend a method for monitoring size which utilises the seven available additional zones; absorbance is reported every 0.01375 mm in the z axis and every 0.0137 / 0.0138 mm (alternating) in the x axis, however the minimum zone size permitted by the software is 0.02 mm. The zones can therefore be spread evenly over the area to be monitored or the process of extraction can be repeated multiple times adjusting the zones to obtain visible absorbance data per 0.02 mm, as shown in Figure 4.76.

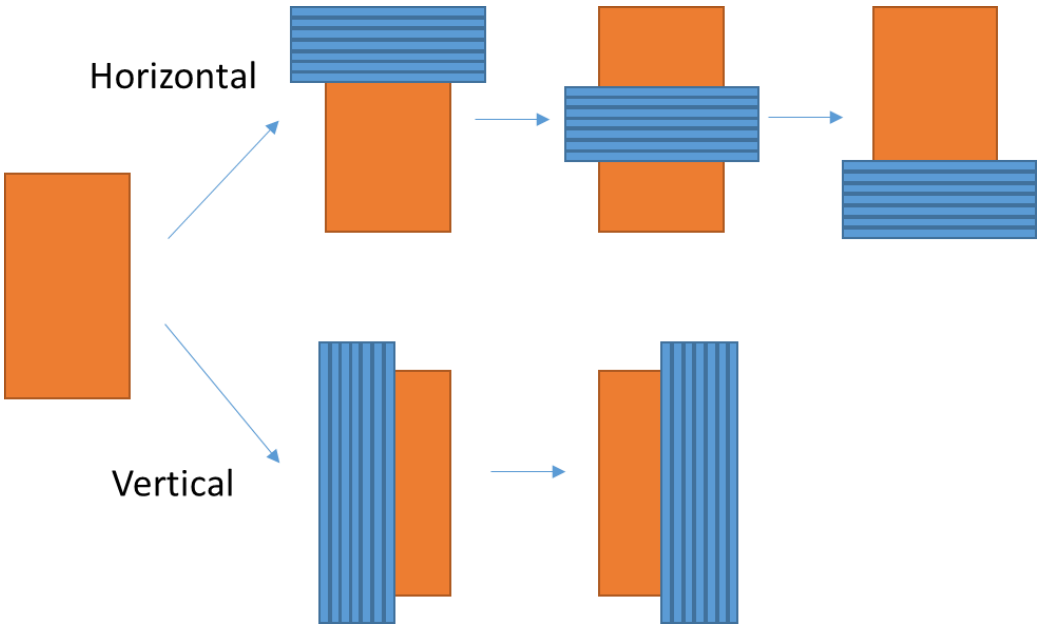

Figure 4.76 – Representation of Pion method for monitoring size changes using the visible wavelength. The orange rectangle represents a dosage form or crystal and the blue lines represent each of the seven additional zones. The zones can be positioned in multiple ways and used to monitor size across the horizontal axis or the vertical axis.

The method requires the orientation to be defined as either vertical or horizontal, with each providing data per (0.01375 mm) pixel for the oppositely named dimension. In this instance horizontal was selected, with x defined as 12.4 mm and the width as 2 mm (this encompasses a range of 12.4 to 14.4 mm in the x dimension). Each of the seven zones was arranged to begin at a different z value with each height defined as 0.02 mm, and this was completed twice thus covering between 3.40 and 3.66 mm in the z dimension. Figure 4.77 shows the starting images from which absorbance readings were obtained, with the seven additional zones positioned in the centre of the crystal.

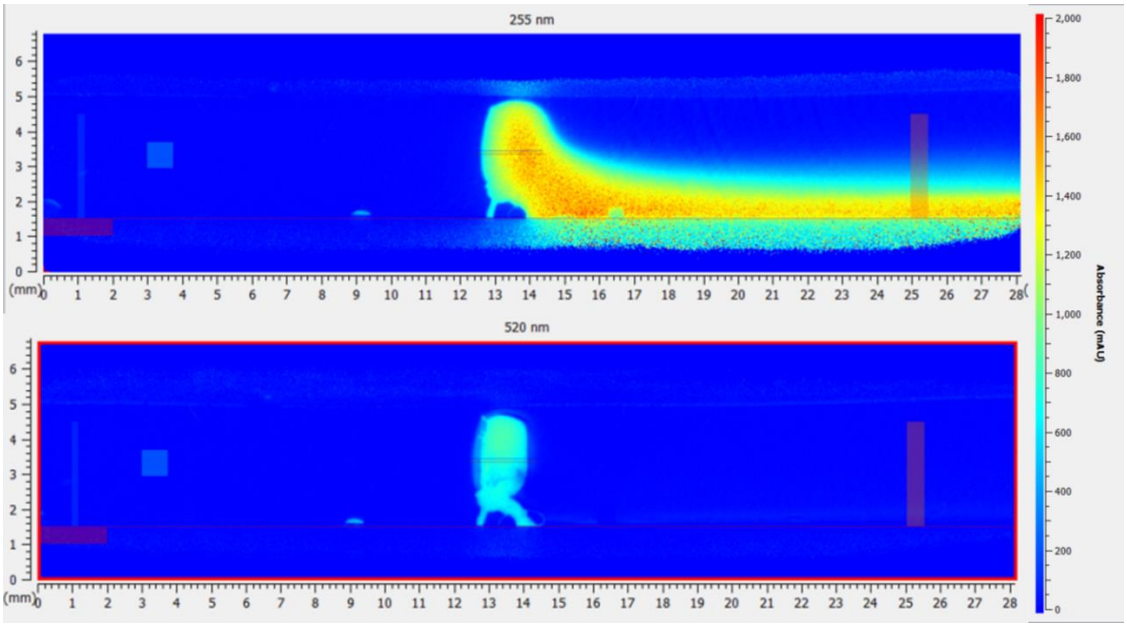

Figure 4.77 – SDi2 compact flow cell image at 255 nm (top) and 520 nm (bottom) showing a paracetamol crystal being held on steel wire loop and deionised water flowing from left to right through the cell. The absorbance key using the jet colour map is shown to the right. Both images are from the start of dissolution (image number 230). The additional zones set up to measure size change can be seen faintly across the centre of the crystal in both the 255 and 520 nm images. The z dimension is shown from 0 to 6 mm and the x dimension is shown from 0 to 28 mm.

The bottom 520 nm image of Figure 4.77 is the most relevant, as the method utilises absorbance of the visible wavelength and this image shows that these additional zones extend past either side of the crystal. The surface absorbance zone has been moved to the far left of the cell to aid in understanding the images, but the reference and IDR zones have been left in place. The raw data from these zones can be viewed in the SDi2 software as an absorbance profile and can also be extracted as a number of absorbance values, see Figure 4.78 and Table 4.13, respectively. Each of the data sets is for a single zone and must be extracted individually.

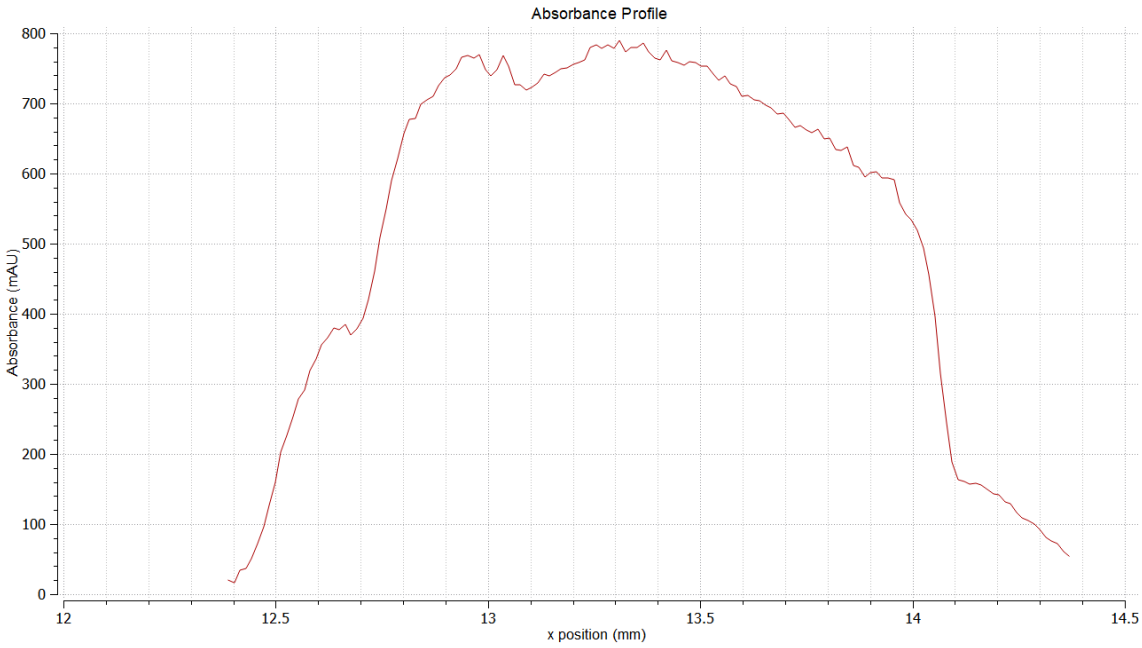

Figure 4.78 – 520 nm absorbance profile for a single zone for data obtained between 263 and 323 seconds of dissolution of a single paracetamol crystal in deionised water in the compact flow cell.

As an example, the profile shown in Figure 4.78 is one of fourteen for this time segment, and there were 26 time segments, making a total of 364 absorbance profiles to produce data for the section of crystal between 3.40 and 3.66 mm in the z dimension. Additionally, Table 4.13 provides the same data but in a different manner, reporting average absorbance values for each x position for each time segment (and repeats this for each zone). In its entirety there are 145 lines of data to capture each pixel, with twenty-six time segments, and all repeated for each of the fourteen zones.

Table 4.13 – Small section of raw 520 nm absorbance extracted from the SDi2 software for a single zone for two time segments to provide an example of the data produced. For the distance of 2 mm in the x dimension there are a total of 145 lines of data to capture each pixel with the distance alternating between 0.0137 and 0.0138 mm.

x (mm)	0 to 263 secs	263 to 323 secs
12.3887	0.02688 AU	0.02466 AU
12.4025	0.02757 AU	0.02447 AU
12.4162	0.03856 AU	0.03203 AU

The visible absorbance from each of the zones between 3.40 and 3.66 mm in the z dimension, was extracted from the SDi2 software into Origin and contour plots were produced. Each plot shows the visible absorbance per pixel (the x values reported

alternate between per 0.0137 and 0.0138 mm) in the horizontal dimension and per 0.02 mm in the z dimension (the smallest height available to select using the SDi2 software). This data was obtained for each sixty second segment throughout the thirty minutes of dissolution. This is challenging to represent visually, so data from one of the sixty second segments is shown in Figure 4.79.

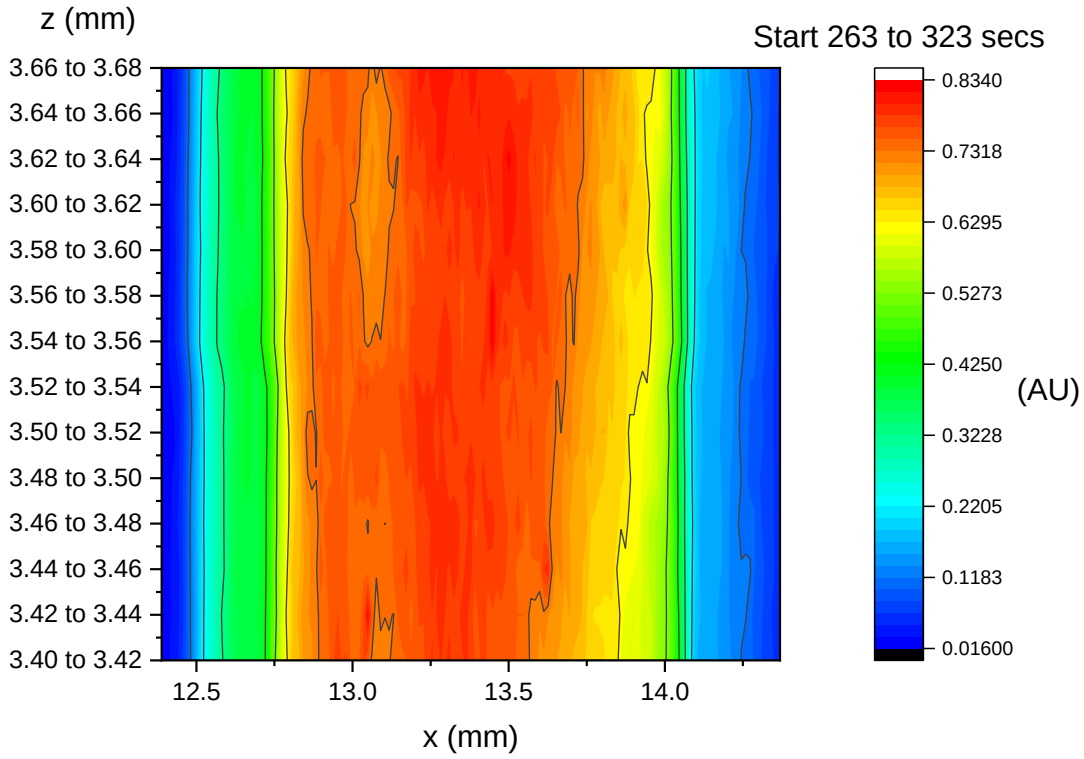

Figure 4.79 – Contour plot showing absorbance at 520 nm through a small section of a paracetamol crystal using a colour map with key provided on the right in absorbance units (AU). This is an average of absorbance data between 263 and 323 seconds, at the start of dissolution in deionised water.

The contour plot in Figure 4.79 shows a low absorbance as blue (< 0.3 AU) and a high absorbance as red (> 0.7 AU), noting that this uses 520 nm data and therefore provides information about the physical presence of crystal in the light path rather than differing concentrations of dissolved paracetamol. The absorbance in the centre of the plot is red and orange confirming the clear presence of an obstacle in the path of the visible light. The absorbance in this 0.28 x 2.00 mm section of image ranges from 0.0160 to 0.8340 AU, with absorbance gradually reducing from a maximum at the centre towards a minimum at the right and left edges, which correlates well with the image of the crystal relative to the zones and the cell. The point at which the solid

crystal surfaces become dissolving crystal or solution is not clearly defined, however, this is consistent with the presence of the boundary layer between a dissolving solid and liquid. The transition from solid to liquid is considered to be a gradual process rather than a distinct step,[2] and monitoring dissolution using a visible wavelength allows for further exploration of this, particularly with regard to the absorbance values which constitute a solid, liquid or in-between "dissolving" section.

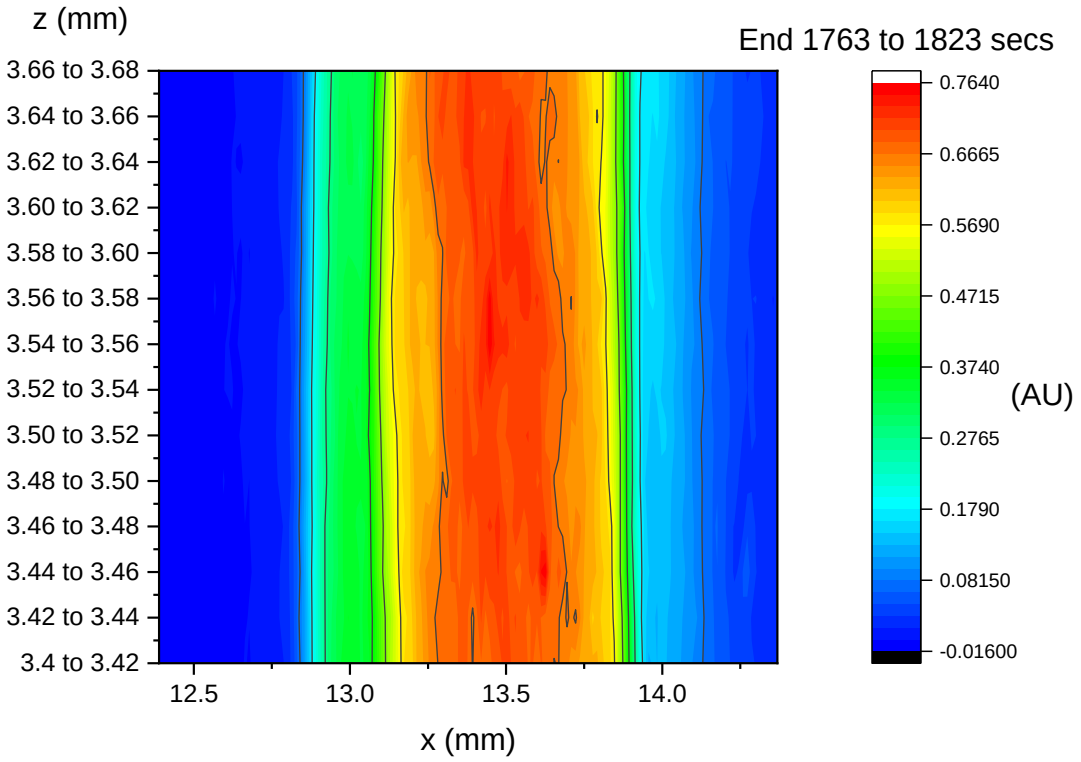

Figure 4.80 – Contour plot showing absorbance at 520 nm through a small section of a paracetamol crystal using a colour map with key provided on the right in absorbance units (AU). This is an average of absorbance data between 1763 and 1823 seconds of dissolution in deionised water.

Figure 4.79 shows the absorbance values at the start of dissolution, between 263 and 323 seconds, whereas Figure 4.80 shows the same area after 30 minutes of flowing deionised water (at 2.16 mL/min). Each colour map has a slightly different scale with a maximum absorbance in Figure 4.80 of 0.7640 AU, compared with a maximum absorbance of 0.8340 AU in Figure 4.79. This reduction in the maximum visible absorbance within the central section provides supporting evidence that the crystal is dissolving and therefore becoming less opaque with time. This inner section of higher absorbance (red / orange) reduces in width from Figure 4.79 to Figure 4.80 as the

crystal reduces in size due to dissolving and can be quantified by defining, for example, 0.5690 AU as the transition point between solid and liquid. In this case the width is calculated to reduce from approximately 1.5 mm to 0.75 mm, thus halving over this time period (and for this section of the crystal) and this can be repeated for the full length of the crystal with some additional work. Arguably, the definition of an absorbance value that represents a transition point between solid surface and liquid is an arbitrary one, and its consistency will enable comparison of size changes. Chapter 5. Software based analysis of dissolution imaging to determine the relative stability of an unusual series of solvate polymorphs, will explore how to support this process further through the use of image analysis and the correlation of the UV images with the visible data.

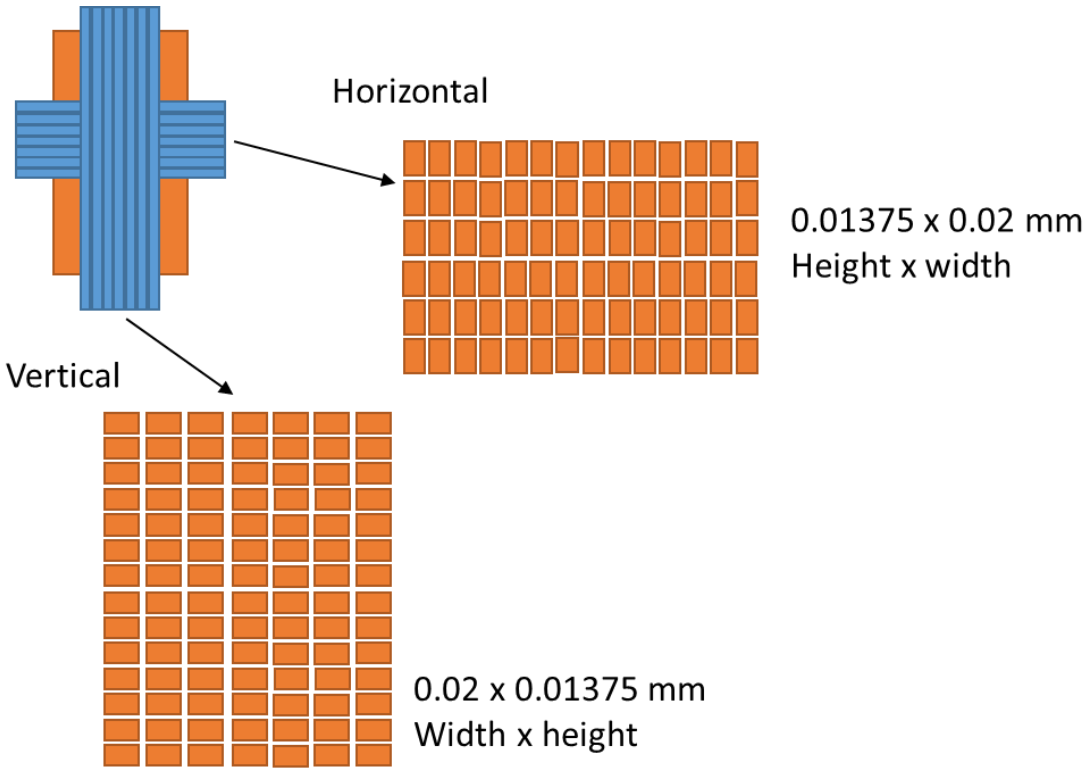

Figure 4.81 - Visual representation of each orientation through which to extract absorbance data. The large orange rectangle represents a solid dosage form or crystal. The blue rectangles represent the seven additional zones for monitoring absorbance. These may be in a horizontal orientation, producing absorbance data per 0.01375 mm x 0.02 mm area (h x w), or in a vertical orientation, producing absorbance data per 0.02 mm x 0.01375 mm area (h x w), which have been represented by the smaller orange rectangles.

In summary, the Pion method provides an extensive amount of data, which offers an opportunity to quantify the visible wavelength images through reporting of

absorbance values per 0.01375 x 0.02 mm sections. The method can also be repeated for the opposite dimension, in this case the crystal height by selecting vertical sections through the crystal, which would obtain the maximum amount of data from the experiment. The complexity of the data is easier to understand visually, hence Figure 4.81 has been produced in an attempt to summarise the process. Extracting data using both methods provides information on each dimension (x and z), in addition to providing information through time, however, this makes the data even more cumbersome, time-consuming and complicated to both extract and analyse.

Method 2 – Pion whole dose cell software

The WDC analysis software uses a tablet edge threshold to plot height and width changes for whole dose formulations. The WDC analysis software requires the solid particles and tablet edge thresholds to be set manually by the user. There is no Pion recommended setting for what constitutes a solid particle or a tablet edge, the user is encouraged to move the cursor over the areas where the edges appear to be on the 520 nm image and thereby determine an appropriate set of values. The profile tracking setting can be used to aid this by highlighting absorbance for a number of contours, see Figure 4.82.

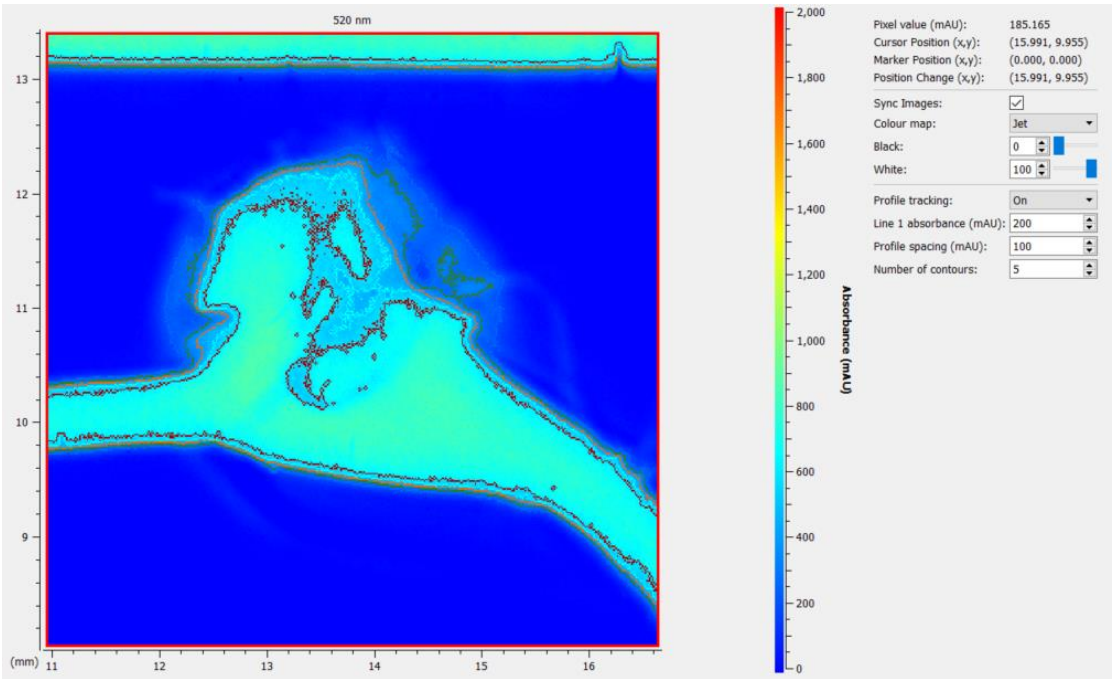

Figure 4.82 – SDi2 whole dose cell image at 520 nm showing a paracetamol crystal being held on a steel wire clasp and the solvent front of deionised water moving from bottom to top

through the cell (the current frame of 225 shows it at the very top). The jet colour map has been used to display the different absorbance values with the key on the right hand side, and profile tracking has been applied with five contours of 200 (grey, outer), 300 (green), 400 (orange), 500 (white) and 600 (red, inner) mAU.

The contours are applied to both wavelength images, however, only the 520 nm image has been shown for observing size changes. A significant challenge is that the paracetamol crystal and wire cannot easily be distinguished from each other, although some of this can be managed through altering the orientation of the crystal and the bending of the wire. As previously mentioned, the challenge of deciding upon an absorbance value that defines a solid crystal also remains. The gradual transition between solid, dissolving solid and solution can clearly be seen in the image, so the arbitrary definition of a minimum absorbance that constitutes a physical presence in the path of the light would simply allow this to be quantified consistently by the software.

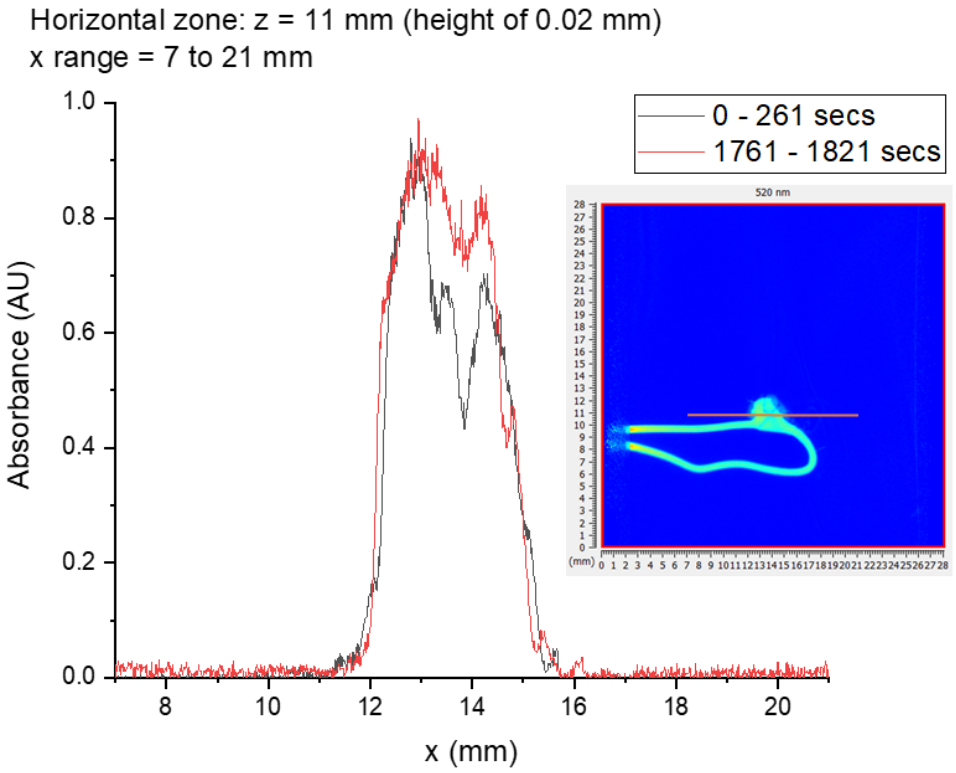

Figure 4.83 – Plot of visible absorbance versus x position for two time segments (start and finish) for a horizontal zone highlighted (and enlarged) in orange on the crystal image (inset).

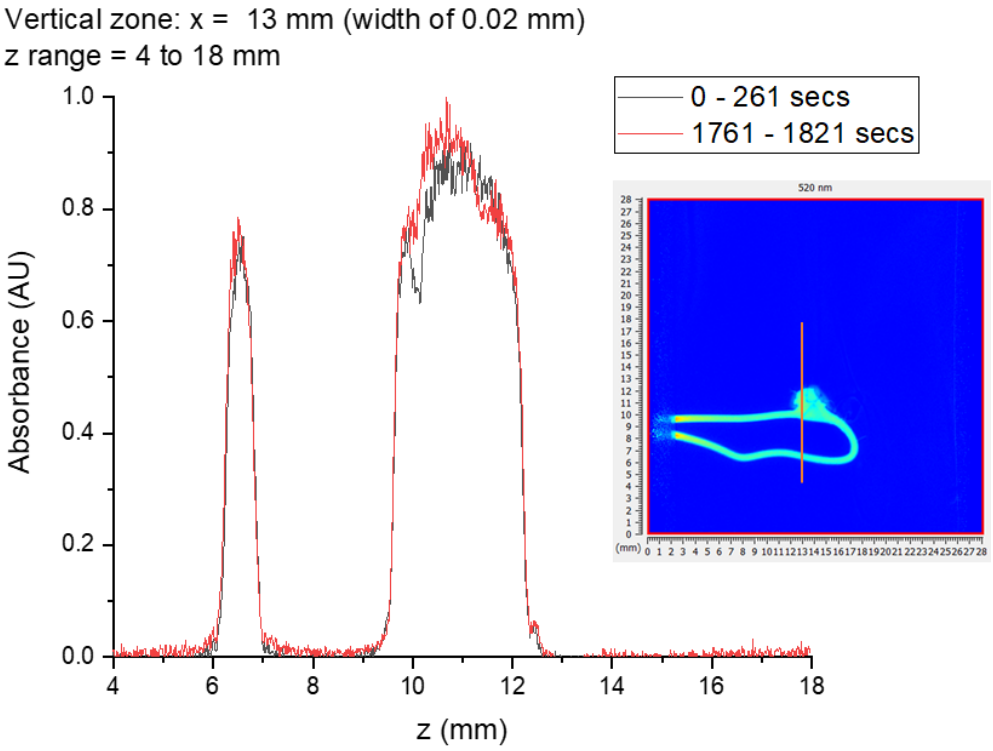

Figure 4.84 – Plot of visible absorbance versus z position for two time segments (start and finish) for a vertical zone highlighted (and enlarged) in orange on the crystal image (inset).

To explore this further for the WDC, two additional zones were set up to monitor absorbance both horizontally and vertically through the crystal shown in Figure 4.82. Plots showing the visible absorbance at the start and finish for the horizontal zone and the vertical zone are provided in Figure 4.83 and Figure 4.84, respectively. Both figures show distinct peaks in visible absorbance that correspond with the position of the crystal, which is between 11 and 16 in the x dimension, and between 9 and 13 in the z dimension. Figure 4.84 shows an additional peak, which corresponds to the lower section of wire; the zone was extended to include the lower wire in addition to the upper wire with crystal attached for comparison purposes. Both Figure 4.83 and Figure 4.84 show a sharp increase in visible absorbance in the presence of both crystal and wire, suggesting that the boundaries are distinct and not gradual as was the case with the CFC, which may be a result of the WDC turbulent flow disrupting the clear definition of any forming boundary layers.

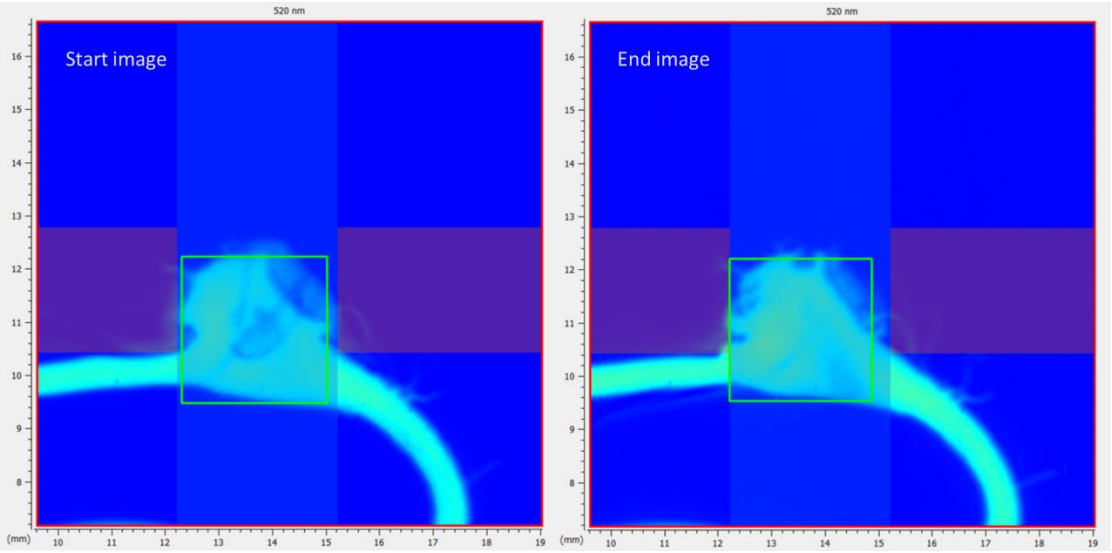

Figure 4.85 – SDi2 whole dose cell 520 nm image of paracetamol crystal attached to wire at start (left) and end (right) of thirty minutes of deionised water flowing at 4.08 mL/min. The box around the crystal is applied automatically by the software using the tablet edge threshold setting, which is 200 mAU in this example.

Utilising the WDC software and defining the tablet edge threshold as 200 mAU, the horizontal and vertical zones were set to encompass the whole crystal, which results in a box being drawn around it as shown in Figure 4.85. The data has been obtained per thirty second segments after the solvent front has moved past the crystal (3 minutes 20 seconds) and can be extracted as graphs of height and width changes (in addition to raw data and the video), see Figure 4.86 and Figure 4.87.

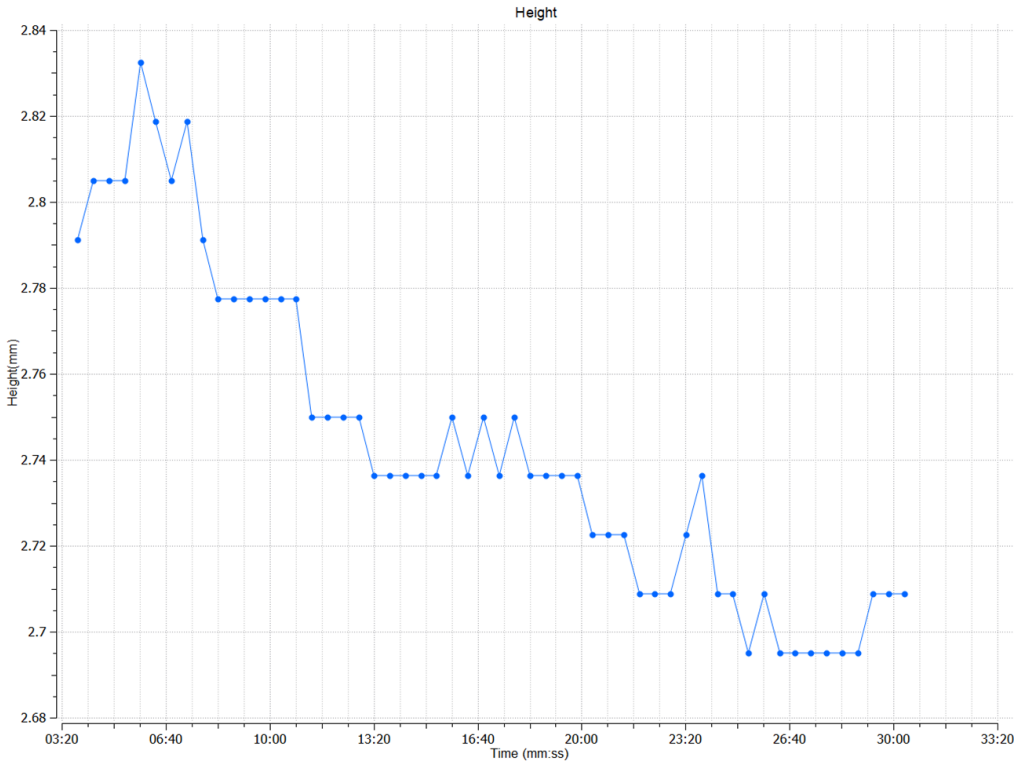

Figure 4.86 – SDi2 Analysis graph showing the change in height at the tallest point of the paracetamol crystal throughout the thirty minutes of flowing deionised water in the whole dose cell. Data obtained from the 520 nm image using an edge threshold of 200 mAU.

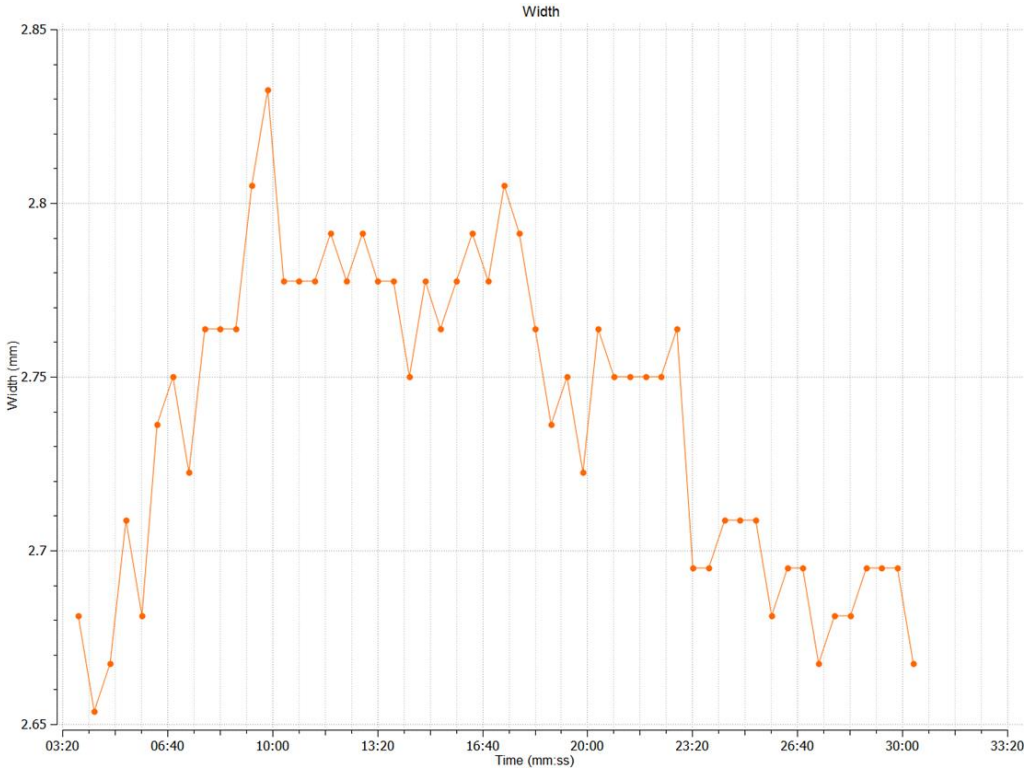

Figure 4.87 – SDi2 Analysis graph showing the change in width at the widest point of the paracetamol crystal throughout the thirty minutes of flowing deionised water in the whole dose cell. Data obtained from the 520 nm image using an edge threshold of 200 mAU.

The graphs provide measurements for the widest and tallest section but are unable to account for the finer details of the crystal. They also include sections of the wire holding the crystal, which will be of a consistent size but cannot be excluded or subtracted using the SDi2 software. Adjusting the tablet edge threshold changes the absolute size measured but does not change the extent of detail obtained or the inclusion of the wire holder. In summary, this WDC method lacks the finer detail required to be able to accurately measure the size change of a crystal throughout dissolution, in large part due to the turbulent flow through the cell. However, it provides supporting information about the definition of thresholds and their impact upon measurements, and also highlights that it may be possible to incorporate a similar threshold method into the CFC section of the SDi2 software for future instruments.

Method 3 – Novel compact flow cell zones

An alternative, novel method using fewer additional CFC zones was developed and explored to understand the information that could be obtained. Four additional zones were applied manually – two obtaining data in the vertical dimension (z) and two obtaining data in the horizontal dimension (x). Two large zones were placed over the whole crystal, a smaller zone was placed where the crystal was tallest and another smaller zone where the crystal was widest. The settings and methods used are detailed in Figure 4.88 and Table 4.14.

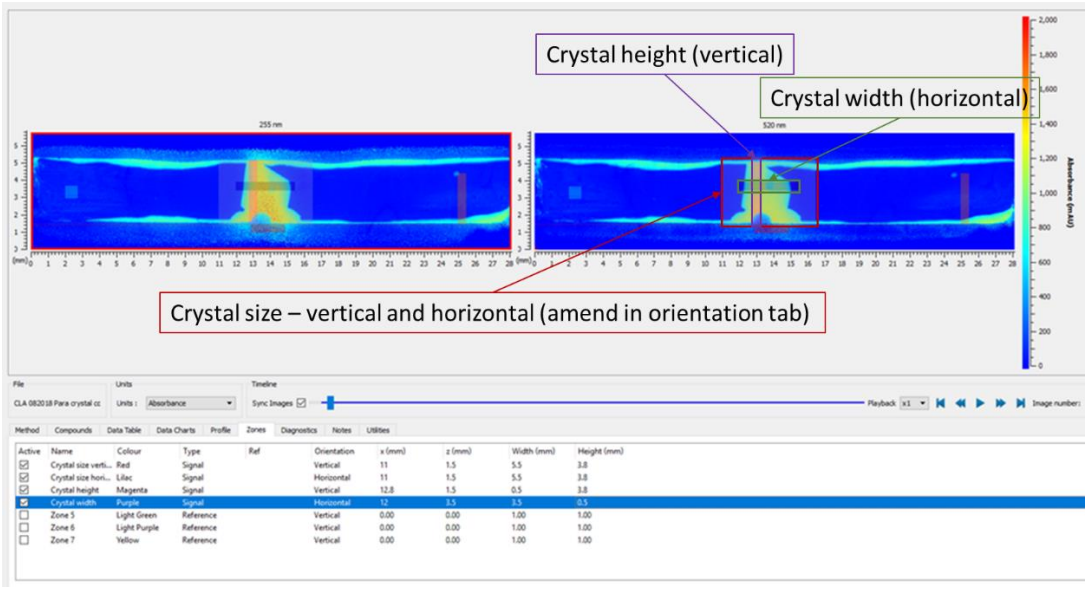

Figure 4.88 – Setting up the compact flow cell data analysis method for analysing a change in crystal size through the visible wavelength monitoring.

Table 4.14 – Comparison of details for a novel method of monitoring size change using the visible wavelength.

Zone name	Orientation	X (mm)	Z (mm)	Width (mm)	Height (mm)
Whole crystal (i)	Vertical	11	1.5	5.5	3.8
Whole crystal (ii)	Horizontal	11	1.5	5.5	3.8
Section height (iii)	Vertical	12.8	1.5	0.5	3.8
Section width (iv)	Horizontal	12	3.5	3.5	0.5

The method is described for a paracetamol crystal held with Blu-tac® and dissolved for 21 minutes in deionised water at 37°C. This run was selected not because it shows a particularly "good" example of single crystal dissolution, but because it highlights the varied and extensive information that can be extracted using this method, especially in combination with concentration monitoring and the viewing of images. Visible absorbance data was extracted for each zone, per segment of sixty seconds, and analysed using Origin software. A graph for each zone showing absorbance versus dimension for each time segment could then be plotted for each zone. Note that it took approximately sixty seconds for the CFC to be completely filled, so data obtained prior to this was excluded from each analysis. The whole crystal zones will be

discussed first, with only a small selection of time segments plotted for clarity, see Figure 4.89 and Figure 4.90.

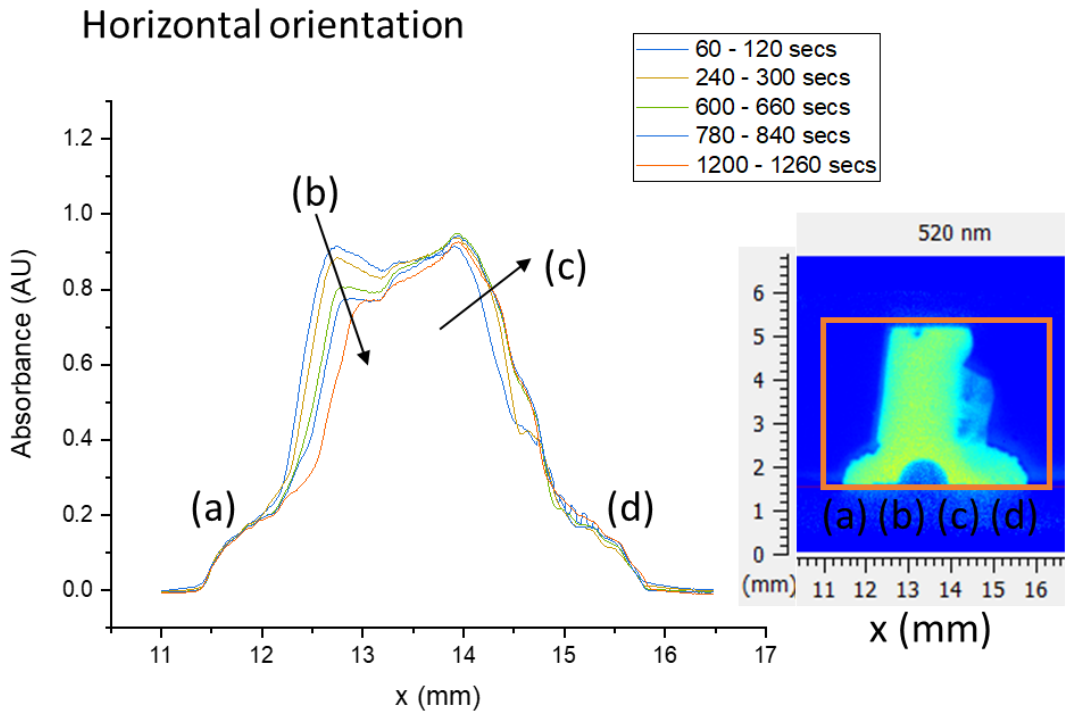

Figure 4.89 - Visible absorbance versus x position across the whole crystal in the horizontal orientation for a selected number of time segments. Labels from (a) – (d) show distinct sections of the plot and the arrows show the direction of change with time. Inset is a visible image of the crystal from the start of dissolution with the zone highlighted in orange and labels matched to the section of the crystal they correspond to.

Figure 4.89 shows the visible absorbance data per x position, hence it is averaged across the z dimension. The data is reported for the entirety of visible absorbance values within the highlighted rectangular zone, hence it incorporates the crystal in addition to the adhesive fixing it in place at the bottom. The areas labelled (a) and (d) correspond to the Blu-tac® and the absorbance values in these sections do not change throughout dissolution. The peak labelled (b) reduces throughout dissolution as the average absorbance reduces. This correlates well with a reduction in size of the crystal, which would be expected as it dissolves. The area labelled (c), however, increases in average absorbance over time, suggesting that while the left side of the crystal is decreasing in size (or opacity / density), the right side actually increases in size or becomes more opaque / more dense.

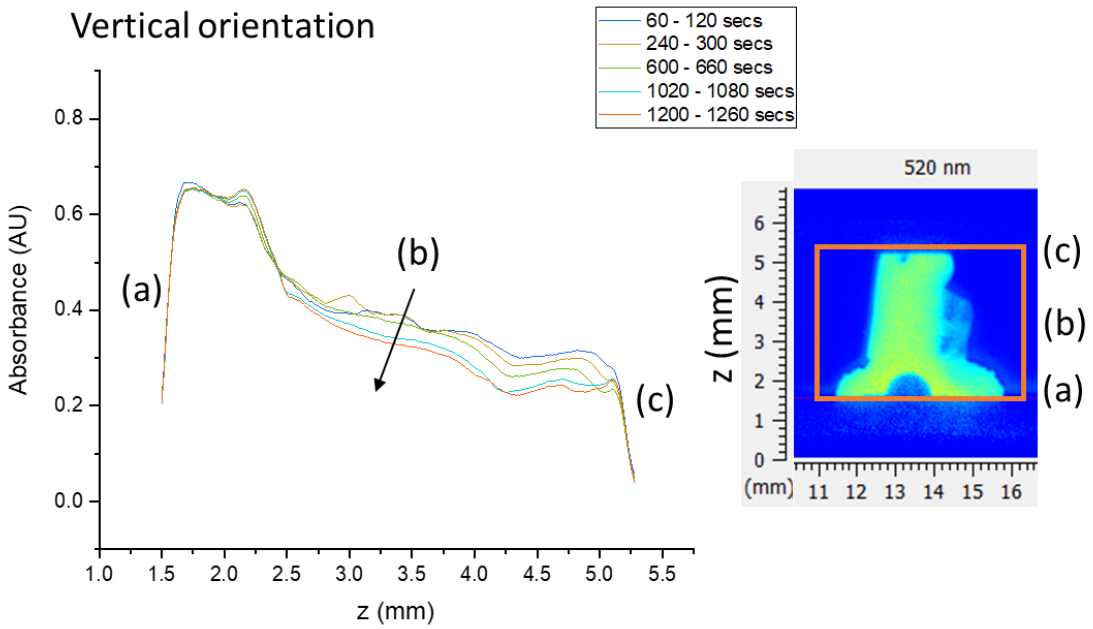

Figure 4.90 - Visible absorbance versus z position across the whole crystal in the vertical orientation for a selected number of time segments. Labels from (a) – (c) show distinct sections of the plot and the arrows show the direction of change with time. Inset is a visible image of the crystal from the start of dissolution with the zone highlighted in orange and labels matched to the section of the crystal they correspond to.

Figure 4.90 shows the reported visible absorbance per z position, hence this is averaged across the x dimension. The area labelled (a) corresponds with the bottom of the flow cell, where the crystal is held in the adhesive, and this remains constant throughout dissolution as expected. The area labelled (b) reduces in average visible absorbance across the length of the crystal throughout dissolution, which fits with the crystal reducing in size and density as it dissolves, thus becoming less opaque and absorbing less visible light. Label (c) refers to the top of the cell and crystal, and remains constant above the z position of 5 mm.

The area under the plot for each time segment can also be calculated and used to represent the size of the crystal and how it changes throughout dissolution, see Figure 4.92. A limitation of using one zone to cover the entire crystal is that for whichever orientation the data represents, it is an average in the other dimension (in addition to always being an average in the y dimension). Although this results in the measurement of absolute size being incorrect (this is compounded by the magnification within the SDi2 imaging software), the change in this number from start to finish and the rate at which it changes will be consistently calculated and looks to be

sufficient to draw comparisons between data. The start and end visible images with the highlighted zone are shown in Figure 4.91 to aid understanding of the additional plots in Figure 4.92.

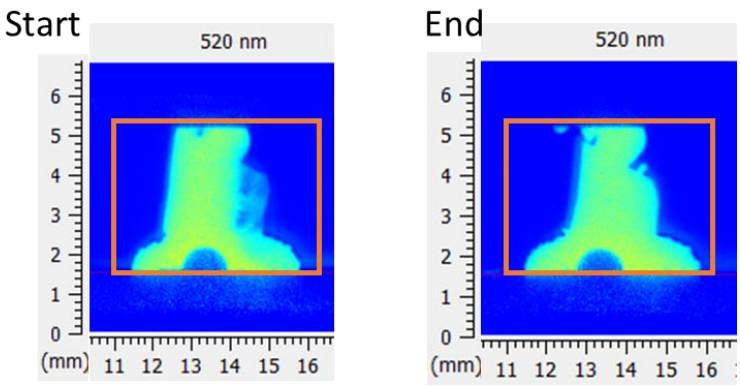

Figure 4.91 – Comparison of start and end images of crystal using visible wavelength, with zone highlighted in orange.

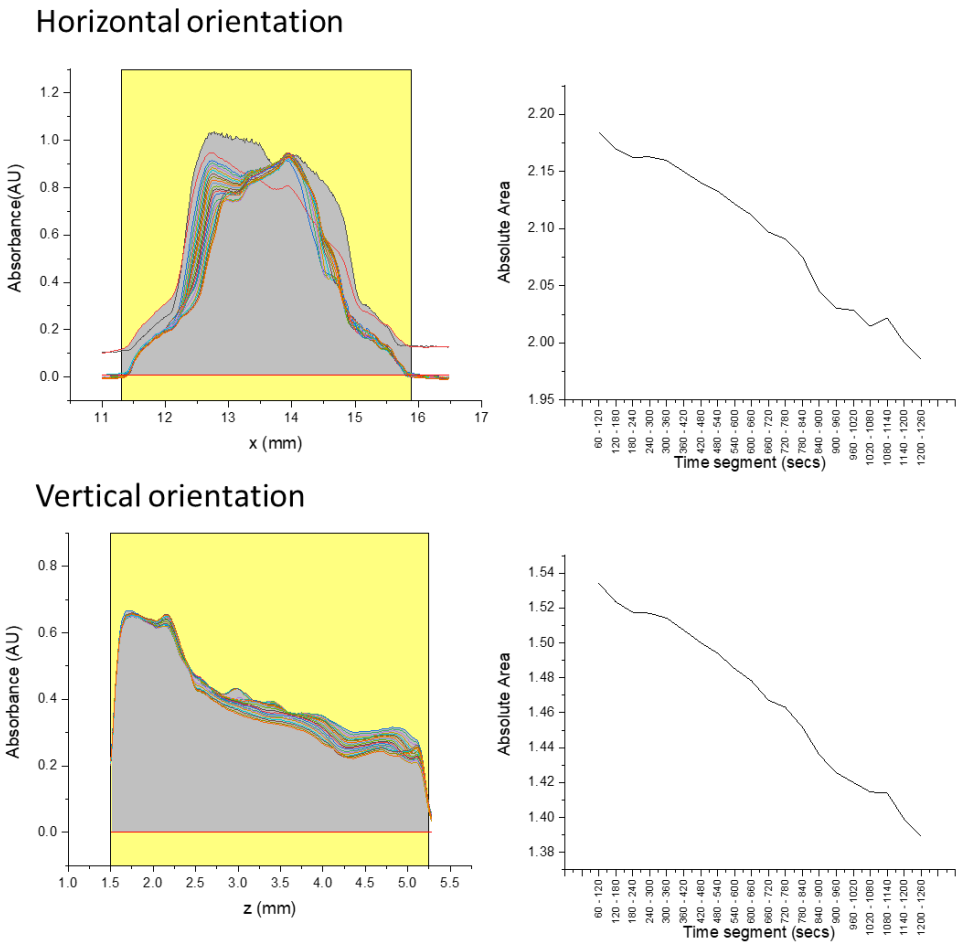

Figure 4.92 – Compact flow cell data for zones covering the entire crystal in both horizontal and vertical orientations. Left graphs show absorbance versus dimension (either x or z) for each time segment with the absolute area under each obtained using Origin software. Right graphs show absolute area plotted against time segment to represent the change in the size of crystal throughout dissolution.

Figure 4.92 shows on the left side the same plots as in Figure 4.89 and Figure 4.90, but with all the time segments included, and on the right side the absolute area is plotted against each time segment throughout dissolution. This provides a method of quantifying the reduction in average visible absorbance throughout dissolution, and concludes that both the horizontal and vertical dimensions reduce at a fairly constant rate. Linear changes in dissolution relate to zero order kinetics and suggest that dissolution is occurring through an erosion mechanism, as opposed to a diffusion mechanism.[3,8] This fits with the reporting of sink conditions within the CFC, which would enable high concentrations of dissolved paracetamol to move quickly through the cell, primarily by advection, thus dissolution is limited by the rate at which the crystal is able to erode rather than diffusion.

Erosion is likely to occur more rapidly on the left side of the crystal, as this will be experiencing the greatest impact pressure from the flow of solvent. This incoming solvent will also contain little-to-no dissolved paracetamol thereby renewing the concentration gradient across the boundary layer. The right side of the crystal will be experiencing a relatively lower solvent pressure, which results in the creation of turbulent wake regions or stagnation zones (see previous Figure 4.54 and Figure 4.93).[77,268] Assuming the flow of solvent in this region is sufficiently stagnant and the concentration of paracetamol dissolved in this stagnating solvent is increasing (dissolved paracetamol movement is limited to only diffusion), the conditions may be sufficient to result in growth on this side of the crystal, which could begin to explain the increase in average absorbance. This would require extensive further work to confirm, and it would be particularly interesting to identify the solid state properties of any areas of growth.

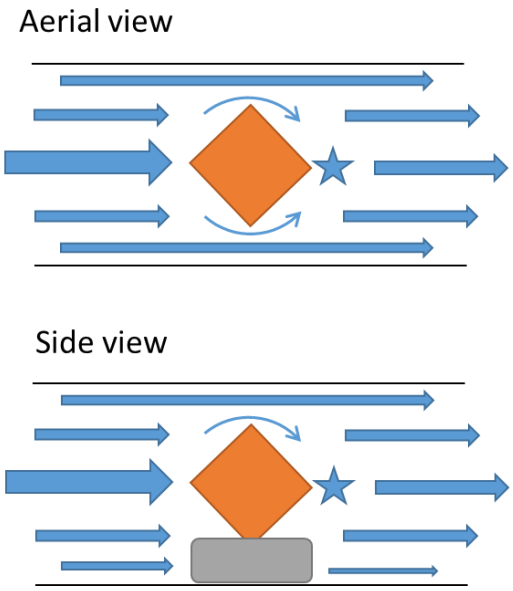

Figure 4.93 – Aerial and side view of the CFC, with a crystal represented by the orange diamond and solvent flow represented by the blue arrows. A blue star suggests a wake region whereby the presence of the crystal and adhesive (grey rectangle in the side view) interrupts the laminar flow.

This can be further explored by considering the additional sections of height and width, which will be discussed next. These have again been plotted with only a small selection of time segments plotted for clarity, see Figure 4.94 and Figure 4.95.

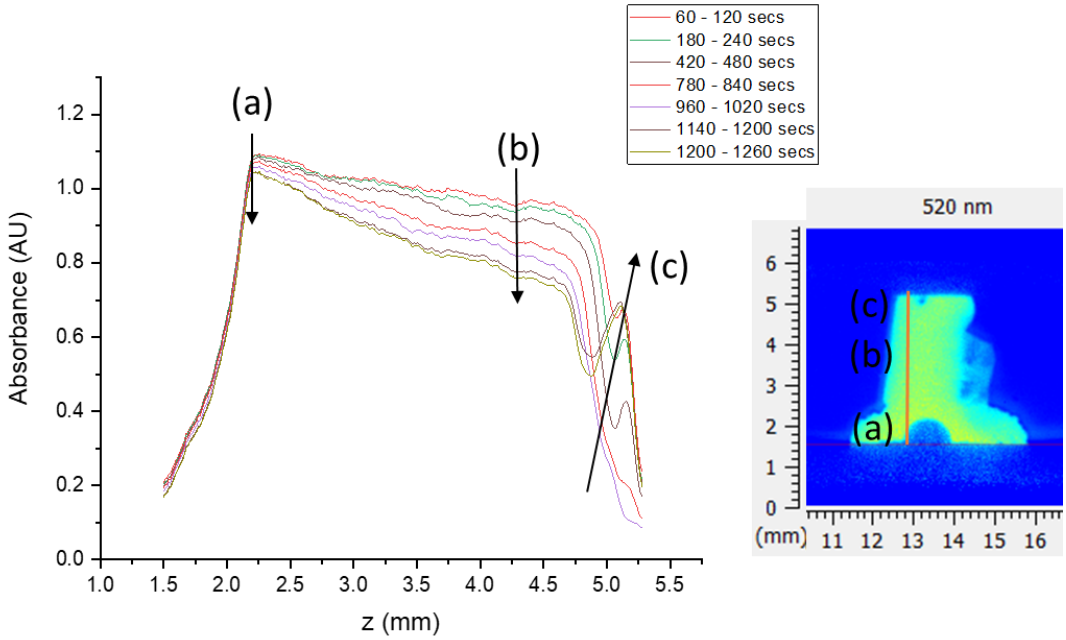

Figure 4.94 – Plot of visible absorbance versus z dimension for the tallest section of the crystal. The arrows labelled (a), (b) and (c) mark three distinct areas of change through time. The visible image of the crystal at the start is shown inset, with the zone highlighted in orange and the approximate positions of (a), (b) and (c) marked.

Figure 4.94 shows the change in absorbance with time for the zone positioned through the tallest section of the crystal and highlights three main areas of change. The first label (a) is positioned towards the bottom section of the CFC and corresponds to the area of the crystal being held in place by Blu-tack® in this instance. There is no change in absorbance here throughout dissolution confirming that although the adhesive was found to be bulky and insufficiently stable for the WDC, this data confirms it has worked sufficiently well for the CFC and does not swell or change in size or position to affect absorbance over time; this is consistent with the previous data for the whole cell visible absorbance values. Between (a) and (b) there is a reduction in visible absorbance, suggesting that the crystal becomes less opaque and is dissolving. Between (b) and (c) the initial reduction in absorbance can be correlated with the reduction in height of the crystal. By position (c) there is an increase in absorbance, which when interpreted with the visible images, highlights a bubble sticking between the top of the crystal and the top of the CFC. The cumbersome nature of the Blu-tack® may be partially to blame for this, significantly impacting upon solvent flow through the cell, in addition to the large crystal itself.

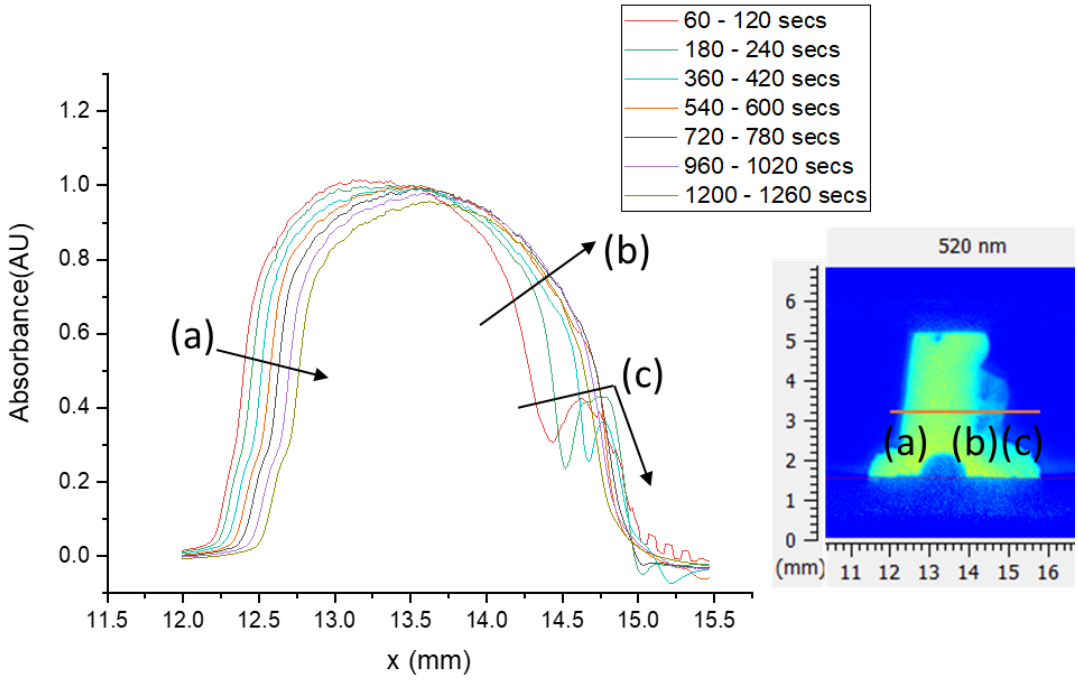

Figure 4.95 - Plot of visible absorbance versus x dimension for the widest section of the crystal. The arrows labelled (a), (b) and (c) mark three distinct areas of change through time. The visible image of the crystal at the start is shown inset, with the zone highlighted in orange and the approximate positions of (a), (b) and (c) marked.

Figure 4.95 shows the change in absorbance through time for the zone positioned across the widest section of the crystal and again highlights three main areas of change. Label (a) is positioned on the left side of the crystal and through the reduction of absorbance at these positions, confirms that the crystal face is undergoing erosion. There is little change in the visible absorbance between (a) and (b), in line with the central section of crystal remaining in place throughout this run. Between (b) and (c) the absorption data suggests that the crystal face expands in this direction, suggesting that as the crystal reduces in height, it increases in width. Upon viewing in conjunction with the UV images, the starting image shows a faint absorption to the right of the crystal, which is shown in Figure 4.95 for the 60 – 120 sec segment as the second red peak in absorbance at an x position of approximately 14.7 mm. This shoulder peak increases in size and merges into the main peak halfway through the run, appearing to suggest that the crystal increases in width.

To explore this data further the additional method for quantifying and visualising these absorbance changes was used. The area under each absorbance vs dimension graph in Figure 4.94 and Figure 4.95 was again calculated and plotted against time segment.

The data for each zone is presented in Figure 4.96 along with visible images of the crystal at the start and end of dissolution, relative to the monitoring zones, to aid understanding. The images in Figure 4.96 show a clear bubble appearing and moving sideways at the top of the crystal, and show a change in absorption to the right of the crystal.

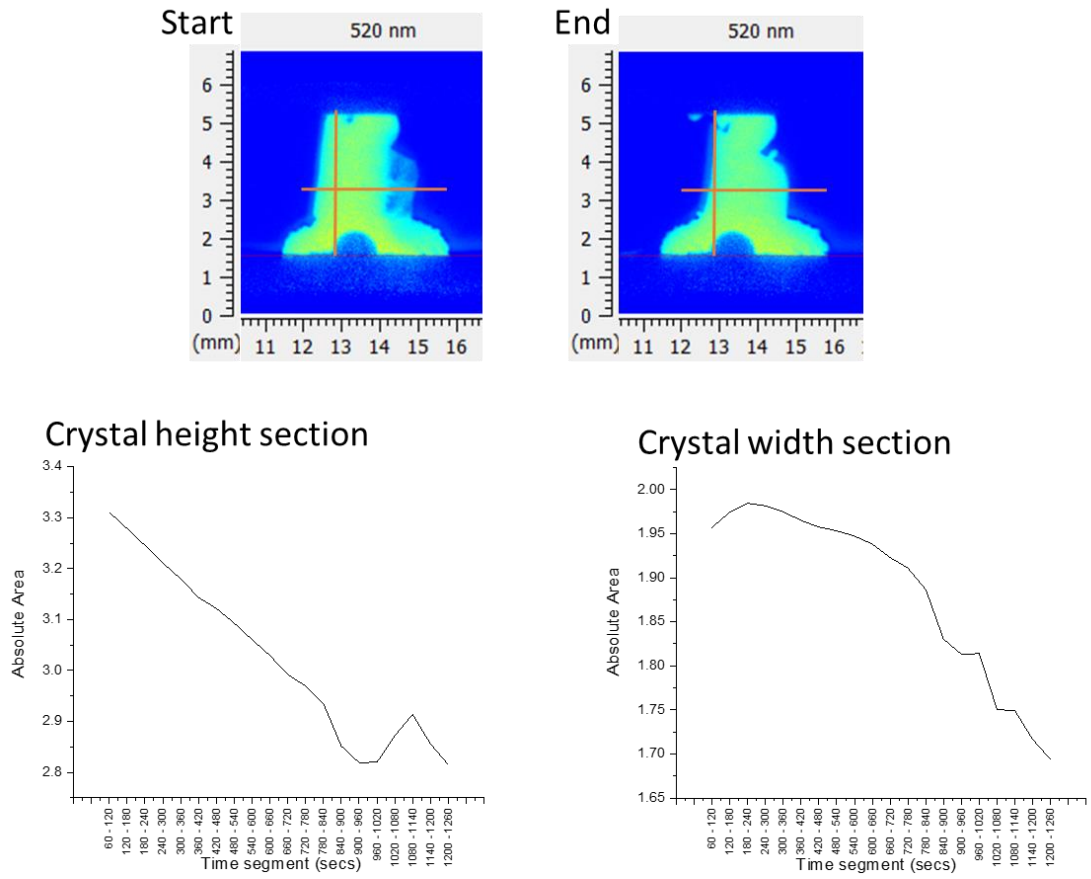

Figure 4.96 – Visible images of the crystal at the start and end of dissolution in addition to plots of absolute area versus time segment for the section through the crystal height and the section across the crystal width.

The plot of absolute area versus time segments for the crystal height section provides confirmatory data that the crystal reduces in height at a constant rate throughout dissolution, with the absolute area for the tallest section of the crystal decreasing between 60 and 960 seconds. The exception is the appearance of the bubble, which causes a brief increase in absolute absorbance between 960 and 1140 secs before it moves away. The reported data correlates well with the images and with the previously reported whole crystal data, which suggests an overall reduction in average absorbance with time, confirming that this is most likely due to the crystal reducing in

size as it dissolves. This height change was able to be monitored comparatively simply (relative to the previously-described Pion method) using only one zone across the tallest section of crystal.

The measurement of crystal width suggests that the absolute area for the widest section of the crystal increases initially for 240 seconds, then decreases, with a number of step changes occurring as it reduces. The visible images show a faint absorption area to the right of the crystal that increases in absorbance at the very start of the dissolution run. This supports the previous theory that the area to the right of the crystal is subject to less erosion and may instead result in conditions that support crystal growth due to the presence of stagnation zones. The overall width decreases however, suggesting that in total, erosion is occurring more rapidly than crystal growth, which is supported by viewing the UV images, which show the continuous diffusion of dissolving paracetamol through the cell. To support this, the UV absorption across the same section of crystal width was plotted per time segment and sample mass released was calculated, see Figure 4.97, Figure 4.98 and Figure 4.99.

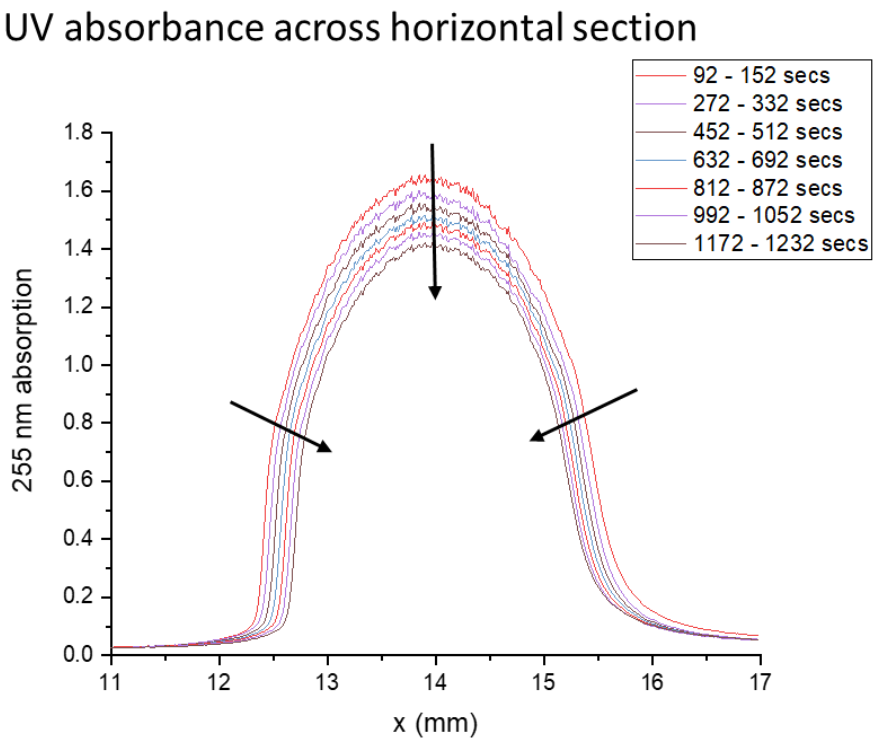

Figure 4.97 – UV absorbance through same horizontal section of crystal as the previously calculated visible absorbance.

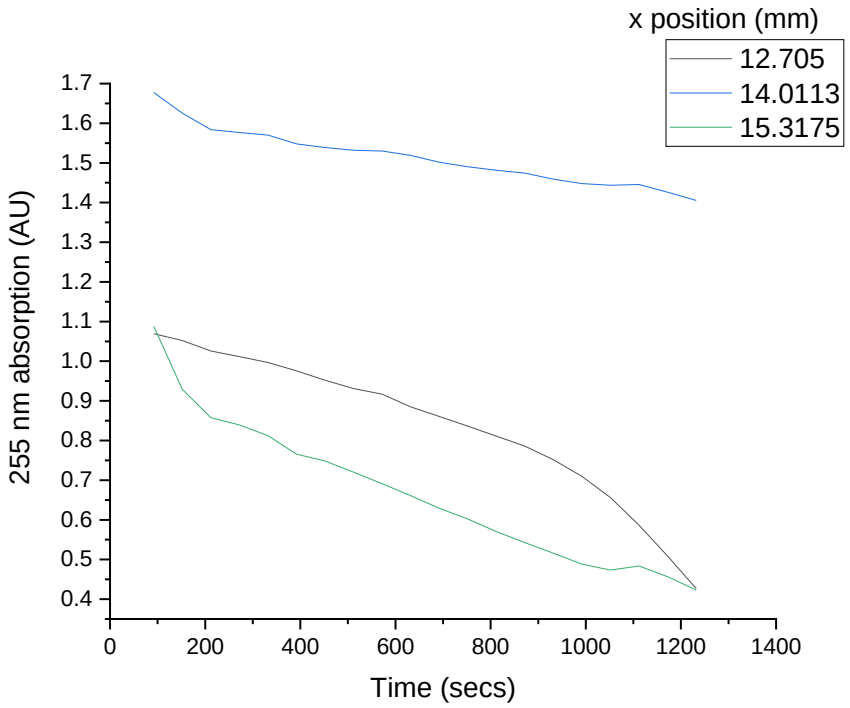

Figure 4.98 – UV absorbance with time for each of the x positions highlighted with arrows in the previous plot.

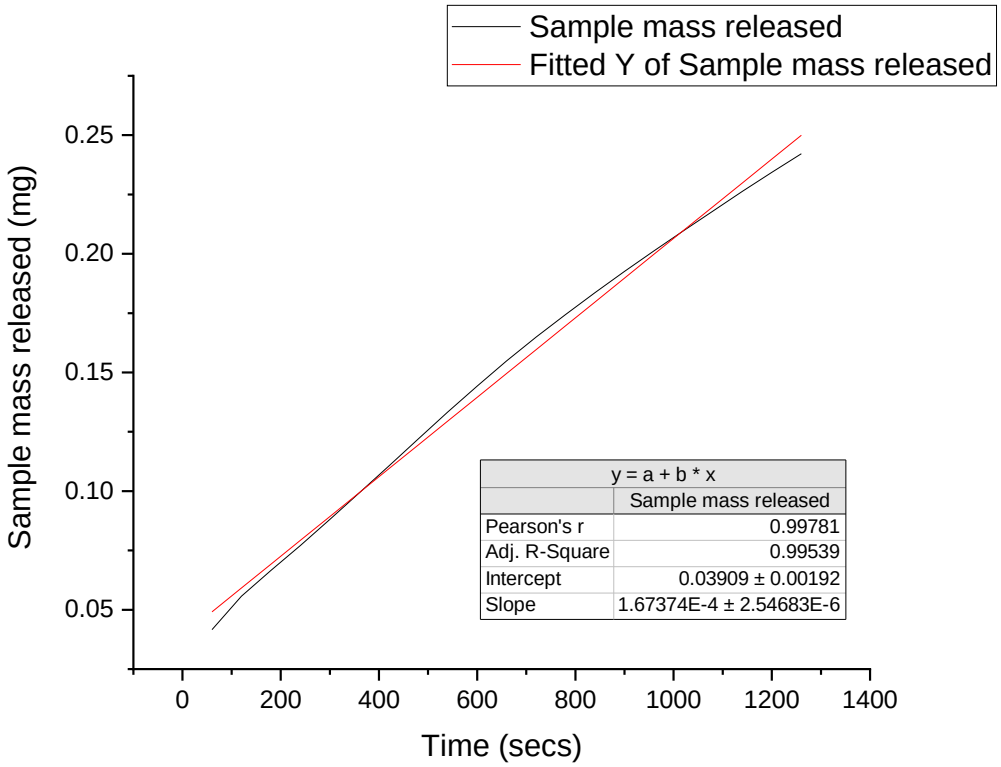

Figure 4.99 - Sample mass released calculated using the SDi2 software. Linear regression has been performed and is included (red line) with details reported inset.

Figure 4.97 shows the change in UV absorbance (255 nm) across the same horizontal section of the crystal. A selected number of time segments have been included and the arrows show the direction of change. UV absorbance can be seen to decrease across the full width of the crystal throughout dissolution to similar extents, but at different rates on either side of the crystal, as highlighted in Figure 4.98. Figure 4.99 reports the sample mass released throughout the time period monitored and provides further confirmation that overall, dissolution is occurring at a constant rate and therefore primarily through an erosion mechanism. The horizontal zone is positioned centrally, hence there will be very little diffusion above this point but there will be a large influence from density gradients, which results in higher concentration solution falling to the bottom of the cell, see Figure 4.100.

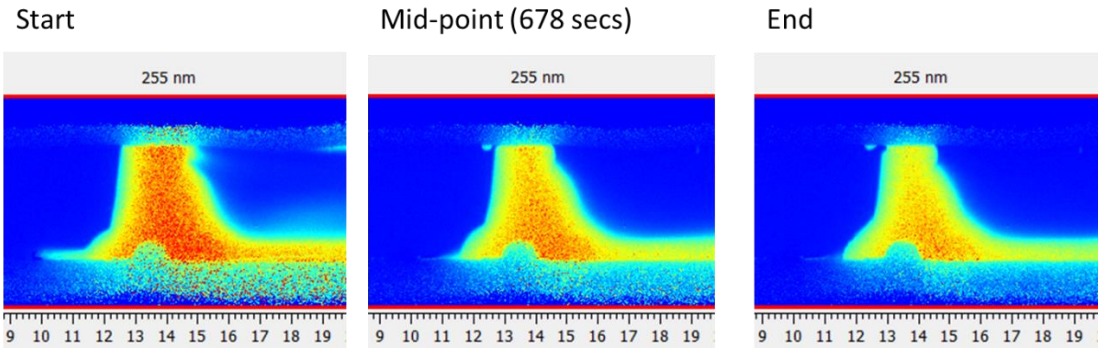

Figure 4.100 - CFC 255 nm images of the paracetamol crystal dissolving at the start, middle and end of the dissolution run.

Overall, this data confirms that visible absorbance information can provide a useful means to quantify size changes and dissolution mechanisms. Summary data can be extracted through simple methods and may allow dissolution mechanisms to be suggested. The key advantage of the SDi2, however, is the ability to monitor and quantify absorbance using two wavelengths, in addition to being able to view images of the process. It is the combination of data from each of these sources that helps to build the story of what may be occurring during the dissolution of a single crystal.

4.4 Conclusions and further work

This proof of concept work with paracetamol single crystals has enabled development of a method to attach single crystals in a flow of solvent in the whole dose cell and in the compact flow cell, and has enabled the monitoring of dissolution from a single

face. The novel dual wavelength imaging allows for concentration monitoring through UV measurements (with calibration to find the molar absorption coefficient), in addition to the monitoring of size and appearance changes through obtaining visible absorbance data. This expands upon the previous single wavelength monitoring work by enabling both physical and concentration changes to be observed concurrently as well as providing a method for fixing the crystal in place within the flow cell. An extensive range of concentrations can be observed through using additional UV wavelengths aside from the λ_{max} to avoid reaching absorbance values greater than 1.5 AU, after which linearity is lost. The concentration at any point within the flow cell throughout dissolution can be obtained for an area as small as 0.01375 mm x 0.0200 mm.

The influence that a physical obscuration has upon UV absorbance and therefore concentration calculations as yet requires further development. An exploration of the alignment between UV and Vis images may support a more precise determination of surface edges, although the literature agrees that a transition from solid to liquid through the boundary layer is actually the result of a gradual process rather than a step change.[2] As such the definition of a value to distinguish between solid and liquid may be considered unnecessary, and instead the use of a consistent but sensible value to enable comparisons to be drawn proves to be sufficient. In spite of this challenge, visualising dissolution in both UV and visible wavelengths provides a huge advantage over single wavelength imaging simply by confirming that a physical obscuration is present in the cell and may therefore influence the UV absorbance.

Additionally, although the resolution of SDi2 images by eye is comparable with the previous instrument (SDI), the dual wavelength capability of the newer equipment enables visible absorbance to be captured throughout dissolution. This data can then be used to extract information about size changes with a resolution of 0.0200 mm x 0.01375 mm, limited currently by the data extraction technique. Image analysis should support this process further and will allow exploration of this transition between a physical presence in the path of light and an absorbance due to a high concentration of dissolved sample, in addition to potentially improving resolution capabilities. This work also confirms that visible absorbance data can be extracted as an average

absorbance across a defined section, such as the tallest point of the crystal, to enable size changes to be calculated more simply.

Finally, the work flags a number of challenges for the dissolution monitoring of single crystals using a CFC, particularly with regard to the hydrodynamics. The orientation of the crystal relative to solvent flow influences dissolution through the creation of wake regions and affects the balance between diffusion, density gradients and laminar flow. The complexity of the hydrodynamics within the CFC would benefit greatly from further modelling to distinguish between that which is a result of the dissolution process and that which alters it. Placing the single crystal in the centre of the flow cell very clearly influences the hydrodynamics surrounding it, which will in turn influence the dissolution observed at each face. The use of stop flow may therefore prove to be useful in exploring single crystal dissolution further still, where stop flow refers to filling the CFC with solvent before stopping flow completely and monitoring the changes within the cell.

5. Software based analysis of dissolution imaging to determine the relative stability of an unusual series of solvate polymorphs

5.1 Introduction

The previous chapter described the development of a method to monitor single crystal dissolution using the SDi2 with its novel dual wavelength technology, enabling the imaging of both UV and visible absorbance through one of two flow cells. The work aimed to determine if the technology could establish a link between the functional groups present at crystal surfaces and their dissolution properties. The technique was used to visualise the surface of a dissolving solid in addition to the boundary layer (between solid and liquid) throughout dissolution. The SDi2 software was also examined to determine the level of detail it could provide.

The SDi2 is able to provide images showing the absorbance for both a UV and a visible wavelength, which allows for a more detailed interpretation of dissolution than single wavelength imaging. This monitoring of visible absorbance enables the reporting of size changes for single crystals throughout dissolution, although the absolute or exact crystal measurements are more challenging to define due to a combination of image magnification, 2-dimensional imaging of a 3-dimensional object, and the definition of threshold values to distinguish between solid surface and boundary layers. As stated previously, the resolution of absorbance data is limited by the SDi2 analysis software, which reports data for a minimum height or width of 0.02 mm, however, the absorbance data stored by the instrument allows for a resolution as small as 0.01375 mm^2.

The application of image analysis software was therefore explored to determine whether this could improve resolution and allow the extraction of absorbance values per pixel (0.01375 mm^2). It was anticipated that such analysis might aid in correlating the UV and visible images from the SDi2, in order to clarify a threshold between the solid surfaces and the dissolving solid. The single crystal methodology and image analysis technique was applied to a novel series of I-TPI polymorphs to determine whether the SDi2 in combination with imaging techniques may provide the means

through which to determine the relative stability of each polymorph, thereby reporting a stability series.

5.2 I-TPI background

The SDi2 method for monitoring dissolution of single crystals was applied to a supramolecular system involving a series of methanol solvates of a mono-iodinated 2,4,5-triphenyl imidazole derivative referred to simply as I-TPI. The compound was found to behave as an unusual example of Ostwald's rule of stages, which describes how crystallisation may occur in steps through a series of metastable forms before producing the most thermodynamically stable form.[36,271] This system was selected due to its unusual behaviour; I-TPI initially crystallises from methanol as a gel, which subsequently transforms to two solvate forms termed SI and SII, thus providing an opportunity to explore three distinct forms with differing relative stabilities.

Three forms of I-TPI were explored: a gel, Form SI and Form SII, see Figure 5.101. The transparent gel is formed by cooling a supersaturated solution of I-TPI in methanol and spontaneously crystallises as a kinetically-controlled cascade of polymorphic solvates. The metastable Form SII appears within the intact gel phase and with time transforms into the thermodynamically stable Form SI, concomitant with collapse of the gel. Form SI may also crystallise directly, but always with collapse of the gel. Work by Andrews *et al.* in determining the structure of the gel suggested that it can be considered "the first step in the crystallisation regime of I-TPI".[272]

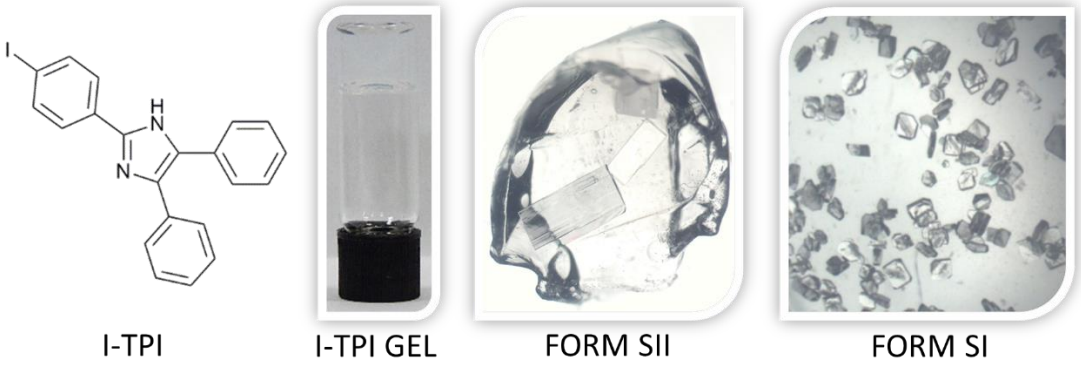

Figure 5.101 – The I-TPI system: I-TPI molecule, and photographs of the I-TPI gel, Form SII crystals within the gel and a number of Form SI crystals.

The differing thermodynamic stability between the three forms of I-TPI will therefore result in different dissolution rates for each; the most thermodynamically stable, Form SI, would be expected to dissolve the slowest and the least thermodynamically stable, I-TPI gel, would be expected to dissolve the quickest.[273] The ability to monitor single crystal dissolution with the SDi2 provides an opportunity to explore this I-TPI series further and determine: i) whether dissolution might be used to distinguish between each form and ii) whether it might offer sufficient information that the forms can be ranked according to their stability.

5.3 Methods

I-TPI was found to be insufficiently soluble in aqueous media, instead methanol was selected for dissolution as it is the solvent from which each of the solvates forms.[272] A range of experiments were undertaken to explore compatibility and confirm the settings to be used with the SDi2 methodology for single crystal dissolution:

a) a full UV absorption scan of I-TPI dissolved in methanol determined the most appropriate wavelength for calculating concentration,
b) a calibration plot of I-TPI dissolved in methanol for a range of concentrations was obtained, using the standard SDi2 procedure, to calculate the molar absorption coefficient (ε) for calculating concentration from absorbance,[168]
c) the IDR of I-TPI powder in methanol was calculated, for completeness and comparison. I-TPI powder contains a mixture of crystalline and amorphous material, hence powder X-ray diffractometry (PXRD) was also used to ensure that compaction of I-TPI into a disc for IDR measurements would not impact upon this.

The SDi2 was used to observe the dissolution of I-TPI powder from a compacted disc (IDR), a crystal of Form SI and a crystal of Form SII, in addition to the gel. The samples were measured using both the compact flow cell (CFC) and the whole dose cell (WDC). The temperature was set at the default of 37°C, which was not important in terms of biorelevance but necessary for consistency. The single crystal samples were secured in place with varnish and the gel samples were placed directly onto the wire without varnish. Gel samples were also grown *in situ* in the sample holder of the CFC to obtain

an IDR-type reading. A summary of analyses is provided in Table 5.15, with "single crystal method" referring to the use of wire to hold the sample (either a crystal or section of gel) in place.

Table 5.15 – Summary of I-TPI experiments using the SDi2.

	Compact flow cell	**Whole dose cell**
I-TPI powder	IDR	n/a
Gel (1.8% & 2.0% w/v)	*In situ* IDR	n/a
Gel (2.0% w/v)	Single crystal method	Single crystal method
Form SII	Single crystal method	Single crystal method
Form SI	Single crystal method	Single crystal method

I-TPI was synthesized by Dr. Jessica Andrews (Durham University) according to the published method and characterised using ^{1}H and ^{13}C NMR spectroscopy, mass spectrometry and elemental analysis to ensure purity.[272,274] The white powder was used for both gel and solvate preparation, in addition to IDR determination. For IDR determination approximately 5 mg of I-TPI powder was compacted to a disc with a 100 kg load for one minute.

The gel is produced using I-TPI powder dissolved in methanol at varying concentrations; the minimum gelation concentration (MGC) of I-TPI at ambient conditions is 1.9% w/v and when sonication and / or ice is used is 1.25% w/v. I-TPI gels for dissolution were formed using either 18 or 20 mg of I-TPI in 1 mL methanol. The powder was dispersed in methanol using sonication prior to dissolving it with gentle heat from a heat gun, and then rapidly cooling the sample with ice to produce the gel. Both concentrations of I-TPI were used for the *in situ* IDR measurements, but the higher concentration of I-TPI (20 mg) was used for the single crystal method measurements as this produced a more robust gel that could withstand handling and be placed upon the wire.

Gels used to grow crystals of Form SI and Form SII were produced using 18 mg of I-TPI in 1 mL methanol, these samples were subjected to three cycles of heating, sonication,

crash cooling with ice to produce a gel, and dissolution by heating, before they were left undisturbed at room temperature to crystallize. Crystals of Form SII were taken from the intact gel and used immediately for dissolution monitoring, whereas crystals of Form SI were taken after the gel had broken down.

Dissolution of each sample was undertaken using the SDi2 as described in Table 5.15, with either the whole dose cell or the compact flow cell in place. The 255 nm wavelength was applied to monitor concentration changes and the 520 nm wavelength was used to monitor size changes for each sample using both the SDi2 software and image analysis software. Image analysis was carried out using MATLAB and was used for three distinct purposes: a) image resolution clarification, b) correlating UV and visible absorbance, and c) size and concentration change monitoring for the I-TPI samples. Clarification of the image resolution utilised MATLAB to further resolve images of the grids originally used in Chapter 3. Surface dissolution imaging intrinsic dissolution rate calculations. The absorbance correlations utilised MATLAB to overlay images and determine the impact of the parallax effect described in this earlier chapter. Finally, the MATLAB code provided in Appendix 1 – MATLAB original script with comments, was modified to provide details of size and concentration changes throughout dissolution for a range of I-TPI samples.

5.4 Results and discussion

The results will be discussed in sections for clarity. The experimental pre-work determining SDi2 settings and compatibility will be discussed first, then the IDR results for I-TPI powder and the *in situ* gel, before the whole dose cell analyses and the compact flow cell analyses, both of which include a combination of UV and visible data in order to build a full picture of the dissolution process. The results of the image analysis work will then follow with reporting of the data obtained and a brief discussion of the script.

5.4.1 Experimental pre-work

a) UV absorption:

The UV-Vis spectrum of I-TPI in methanol was recorded to determine the most appropriate wavelengths to follow for dissolution monitoring with the SDi2, see Figure 5.102.

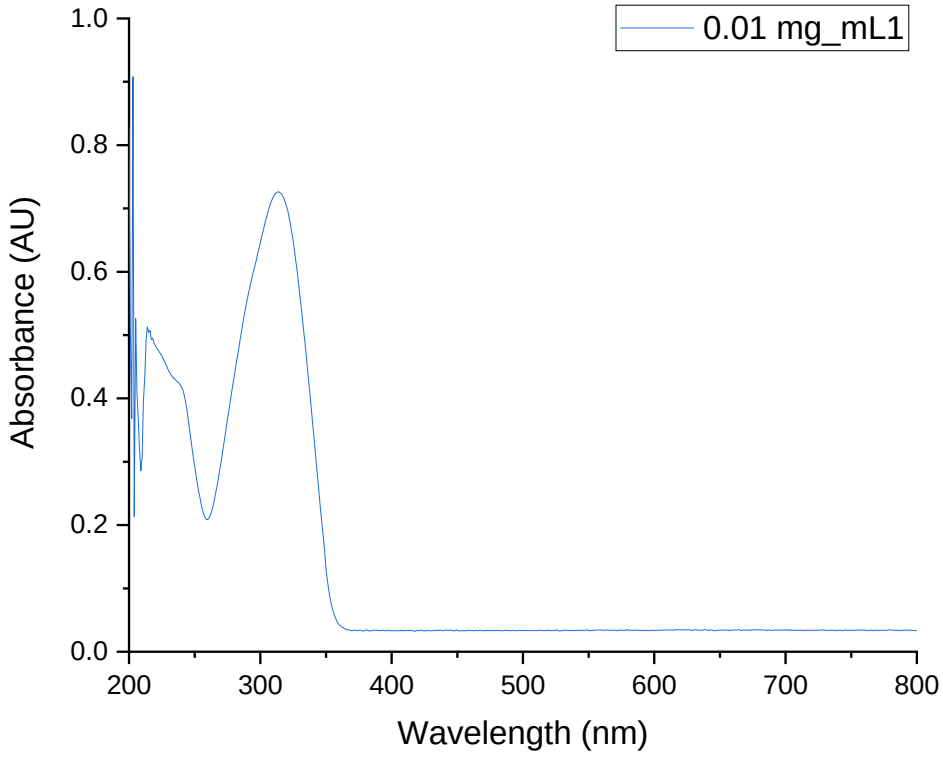

Figure 5.102 – UV-Vis spectroscopy full scan of I-TPI dissolved in methanol. Baseline corrected using blank methanol and repeated three times.

The UV options for monitoring with the SDi2 are 255, 280, 300 and 320 nm, therefore 255 nm was selected to allow higher concentrations to be monitored with a reduced risk of exceeding 1.5 AU on the SDi2.

b) UV calibration for the SDi2:

A series of samples of I-TPI dissolved in methanol across an appropriate range of concentrations (0.001 to 0.100 mg/mL) were analysed using the calibration method for the SDi2 with the 255 nm wavelength. A calibration plot was produced to calculate the molar absorption coefficient (ε) and enable I-TPI concentration to be calculated from absorption values throughout dissolution of the IDR compact, each single crystal (regardless of form) and the gel samples.

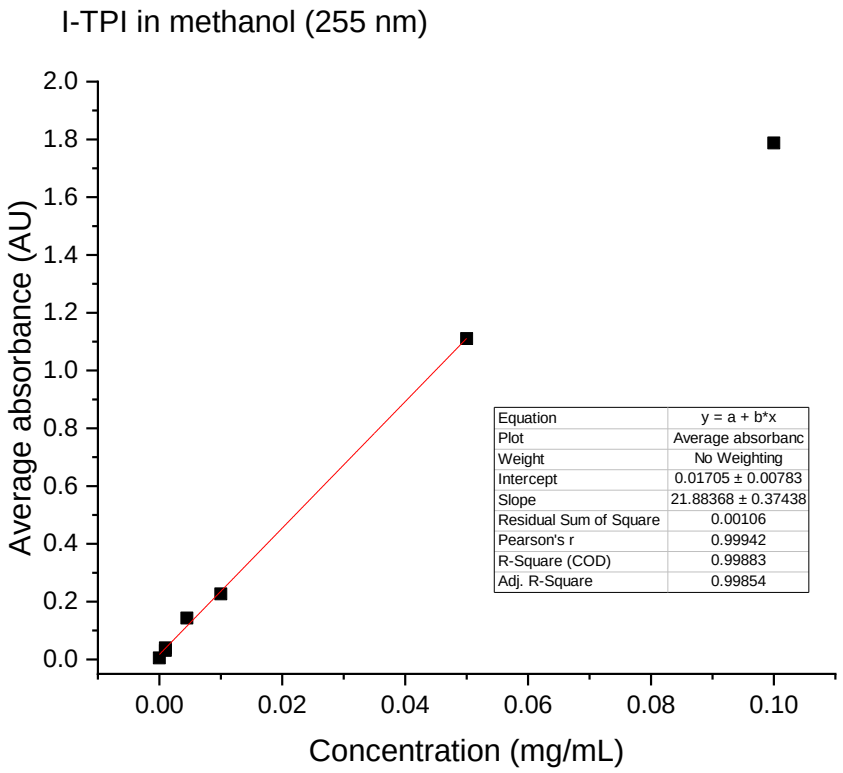

Figure 5.103 – Calibration plot for the SDi2 for I-TPI dissolved in methanol at a range of concentrations. Line of best fit applied to the first five data points with details inset.

The calibration plot in Figure 5.103 confirms a linear relationship between concentration and average absorbance between 0.001 and 0.045 mg/mL, with an R-squared value of 0.99883. Further calculation (adjusting mg/mL to mol / dm^3) produced a value of ε equal to 10270 $M^{-1}cm^{-1}$, which was used to calculate concentration from 255 nm absorbance using the SDi2. A guide for the lower and upper concentration limits is therefore 0.001 mg/mL and 0.045 mg/mL, respectively, although the upper concentration may be extrapolated beyond this point to a maximum absorbance of 1.5 AU.

c) Solid state characterisation:

The solid state behaviour of I-TPI is well characterised so the only additional work required was to ensure that compaction of the I-TPI powder for calculating IDR does not significantly alter its solid state properties.[271,272] Figure 5.104 shows the PXRD patterns for I-TPI powder versus I-TPI powder after compaction to produce IDR discs (the disc was subsequently ground gently back to a powder to enable analysis).

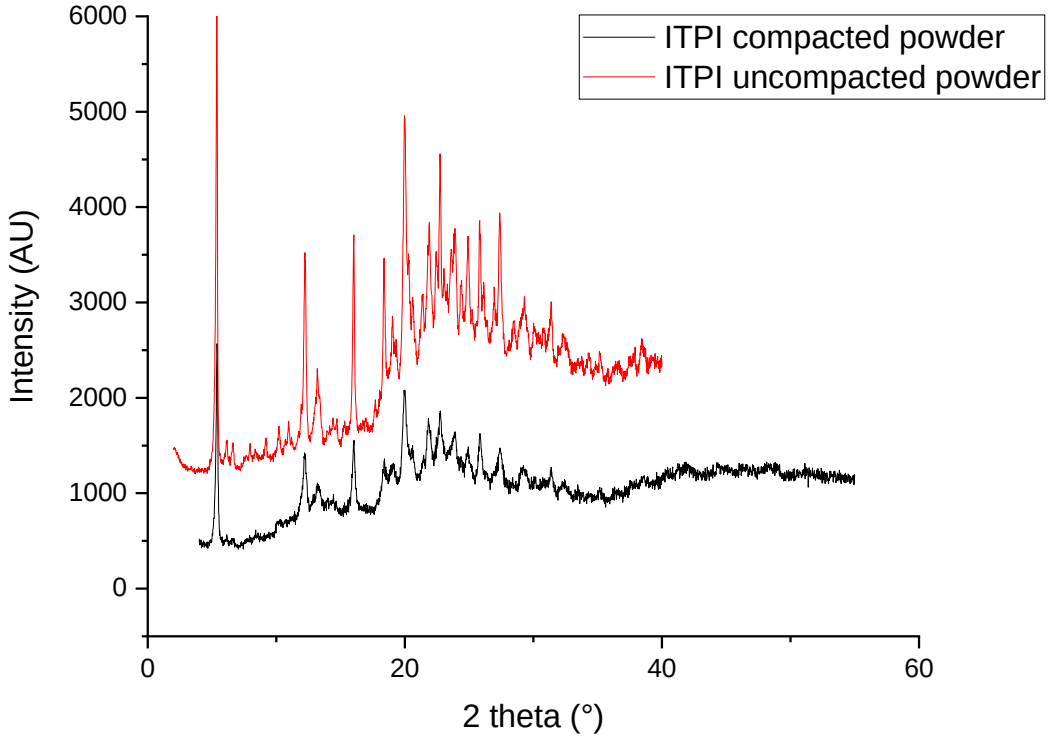

Figure 5.104 – Experimental PXRD patterns of I-TPI powder confirming no significant impact of compaction upon crystallinity or solid form.

The patterns shown in Figure 5.104 show that while there is some strain induced broadening, there is no clear difference to the overall pattern, with consistent peaks at 2θ angles of 12.3°, 18.4°, 20.0° and 22.7°. This confirms that compaction has had little effect on crystallinity or solid form for the material in this instance. The patterns confirm that both samples likely contain a mixture of both crystalline and amorphous material, which would fit with the way in which I-TPI powder is prepared (ending with precipitation from solution rather than crystallisation).

5.4.2 IDR determinations

a) I-TPI powder:

Four I-TPI compacted discs, each consisting of approximately 5 mg powder, were subjected to a standard IDR dissolution procedure using the CFC with methanol at 37°C flowing at 2.16 mL/min. Methanol was sonicated and heated prior to use to removed dissolved gases, however, it presented a significant challenge when used with the relatively small volume CFC and bubbles frequently appeared. This prevented clear

IDR values from being obtained, despite repeating the experiment multiple times; the results are reported in Figure 5.105.

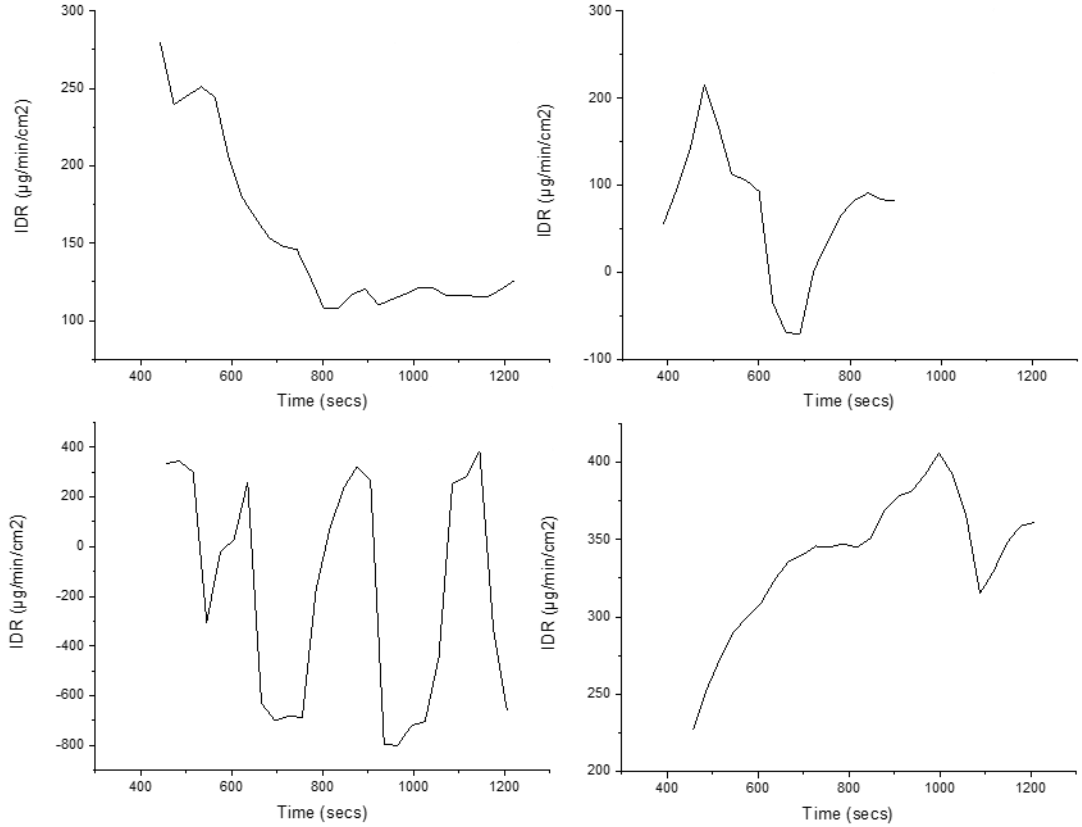

Figure 5.105 – IDR plots versus time for four compacted discs of I-TPI powder dissolving in methanol.

The values are highly variable and the data inconsistent, hence it is not possible to report an IDR for I-TPI from this work. The solubility of I-TPI powder in methanol is sufficiently high that an IDR value would provide little information in this instance, and this is as expected due to its part crystalline and part amorphous nature. Additionally, this work highlighted a number of challenges as a result of using methanol for dissolution; these include the presence of bubbles in addition to the degradation of seals between sections of the fluidics, which resulted in leakages and the replacement of the CFC lid.

b) Gel grown in situ:

A method for creating the gel within the CFC sample holder was developed, involving crash cooling a solution of I-TPI dissolved in methanol, and worked for both the 1.8 %

w/v and the 2% w/v solution. Pictures illustrating the technique are shown in Figure 5.106; note the importance of ensuring the top surface is flush by smoothing with a flat object immediately prior to inserting into the CFC for dissolution.

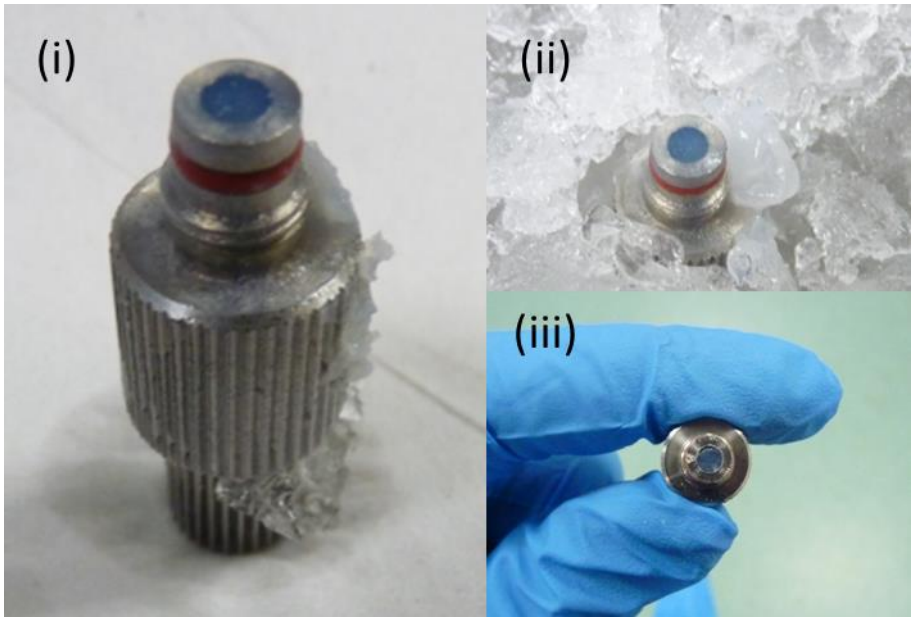

Figure 5.106 - I-TPI gel produced inside the compact flow cell sample holder using ice to crash cool a solution of I-TPI in methanol at both 1.8% w/v and 2.0% w/v. Picture (i) shows the cold sample holder with gel forming inside, (ii) shows the sample holder surrounded by ice and (iii) shows the top of the sample holder immediately before inserting into the compact flow cell having ensured the gel is flush with the top and any excess gel is removed.

The gel did not remain within the sample holder for long after being placed in the CFC, hence true IDR values could not be obtained, see Figure 5.107. The initial IDR value appears very high at 500 µg/min/cm^2 but this increases rapidly once the gel is no longer confined to the sample holder and dissolution can occur from all surfaces of the gel. The reported IDR value then drops rapidly to zero, confirming that the gel has fully dissolved. The movement of the gel can be clearly viewed in the visible images, see Figure 5.108, although the physical presence of the gel is fainter than the air bubble released from the holder. The 255 nm image shows dissolving I-TPI from the escaped gel sinking to the bottom of the cell, thereby confirming once again the influence of density gradients upon flow through the CFC.

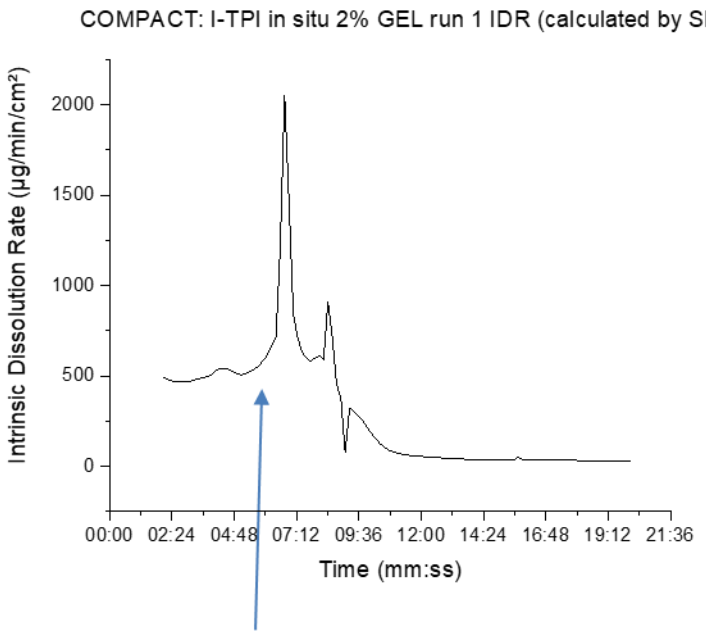

Figure 5.107 – IDR plot as calculated by the SDi2 for an I-TPI gel made *in situ* within the sample holder. The blue arrow shows the point at which the gel moved out of the sample holder and into the main section of the flow cell.

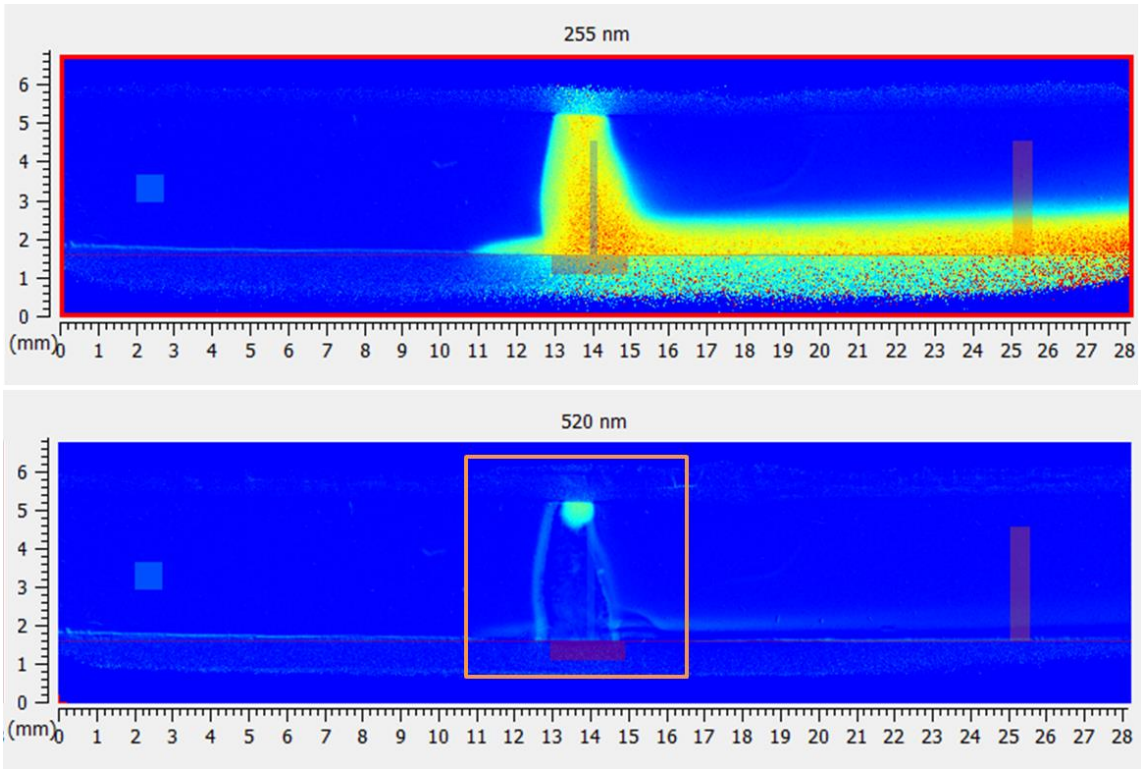

Figure 5.108 – Compact flow cell 255 nm (top) and 520 nm (bottom) images of I-TPI *in situ* gel having moved out of the sample holder and into the cell (highlighted with orange box), with additional air bubble.

The work was repeated multiple times, and the gel escaped the sample holder in all instances. The IDR plots are all presented in Figure 5.109 for information, including those attempted with a 1.8% w/v I-TPI gel, however these also escaped the sample holder preventing a true IDR value from being obtained for any gel sample using this method.

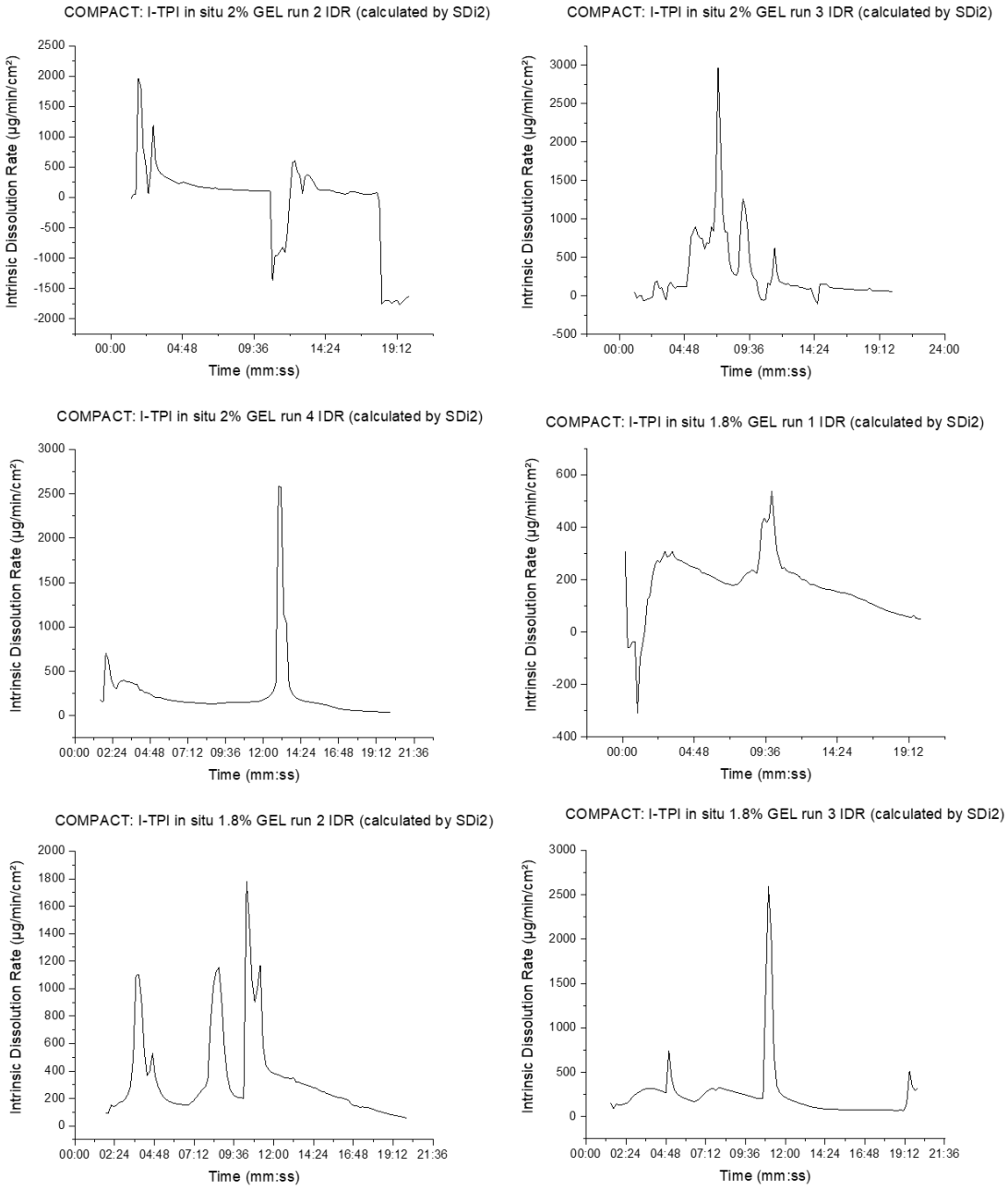

Figure 5.109 - IDR plots for the I-TPI gels made *in situ* within the compact flow cell sample holder.

The ability to produce a gel *in situ*, however, is a technique that could be utilised to hold a crystal in place, and it may be possible to modify successfully so that the gel is retained within the sample holder without influencing any surface activity using mesh. This requires further development to refine, but provides another opportunity for exploring supramolecular chemistry with the SDi2.

5.4.3 Using the SDi2 software to recreate a solvate stability series

The data obtained for each sample from each SDi2 flow cell is reported separately for the UV wavelength absorbance (255 nm) and for the visible wavelength absorbance (520 nm) for clarity.

a) Whole dose cell – UV absorbance:

The whole dose cell was used to monitor I-TPI concentration and sample size changes with the 255 nm and 520 nm wavelengths, respectively. The flow of dissolving I-TPI through the WDC appeared turbulent (as expected), so multiple manual zones were used to extract UV absorbance data throughout dissolution. The sample holder wire was bent appropriately to allow a horizontal and a vertical zone to be placed over the sample and monitor size changes using visible absorbance data as developed in Chapter 4. Single crystal surface dissolution imaging, see Figure 5.110. Figure 5.111 shows each of the samples mounted at the start of the dissolution process, note that the gel image had to be taken prior to the cell filling because it dissolved so rapidly, and Figure 5.112 shows the same samples mounted in the WDC after thirty minutes of dissolution.

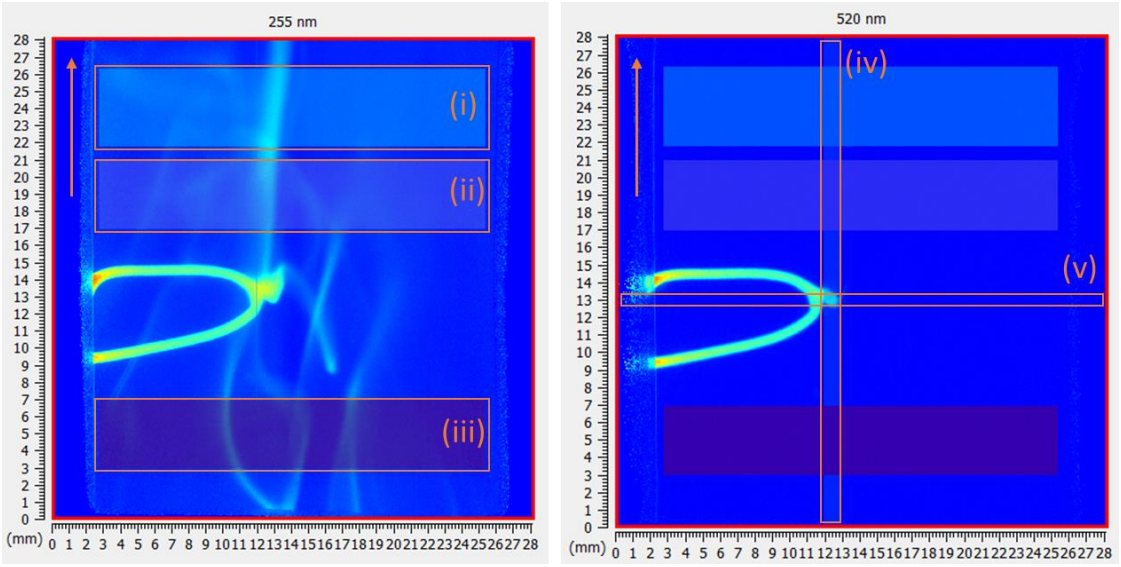

Figure 5.110 – Images of whole dose cell containing a single I-TPI Form SI crystal held on a wire, with manual zones highlighted in orange. The flow of 37°C methanol at 2.16 mL/min is marked with the orange arrow. The left 255 nm image monitors concentration changes through three zones: (i) top, (ii) middle and (iii) bottom. The right 520 nm image monitors size changes through two zones: (iv) vertical and (v) horizontal.

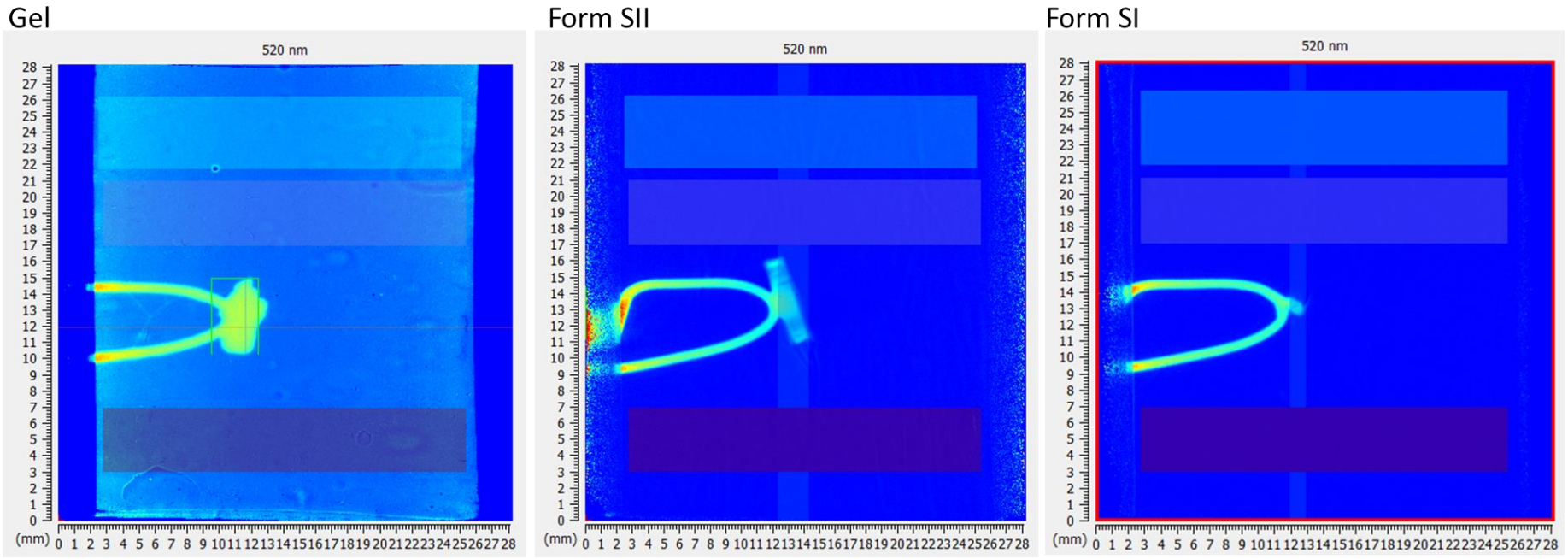

Figure 5.111 - Visible wavelength images of each I-TPI sample in the whole dose cell. The samples are attached to the wire with varnish. The image of the gel is from the start of the run, before dissolution can begin, with the empty cell. The images of Form SII and Form SI are from just after the cell has filled with methanol at the start of dissolution.

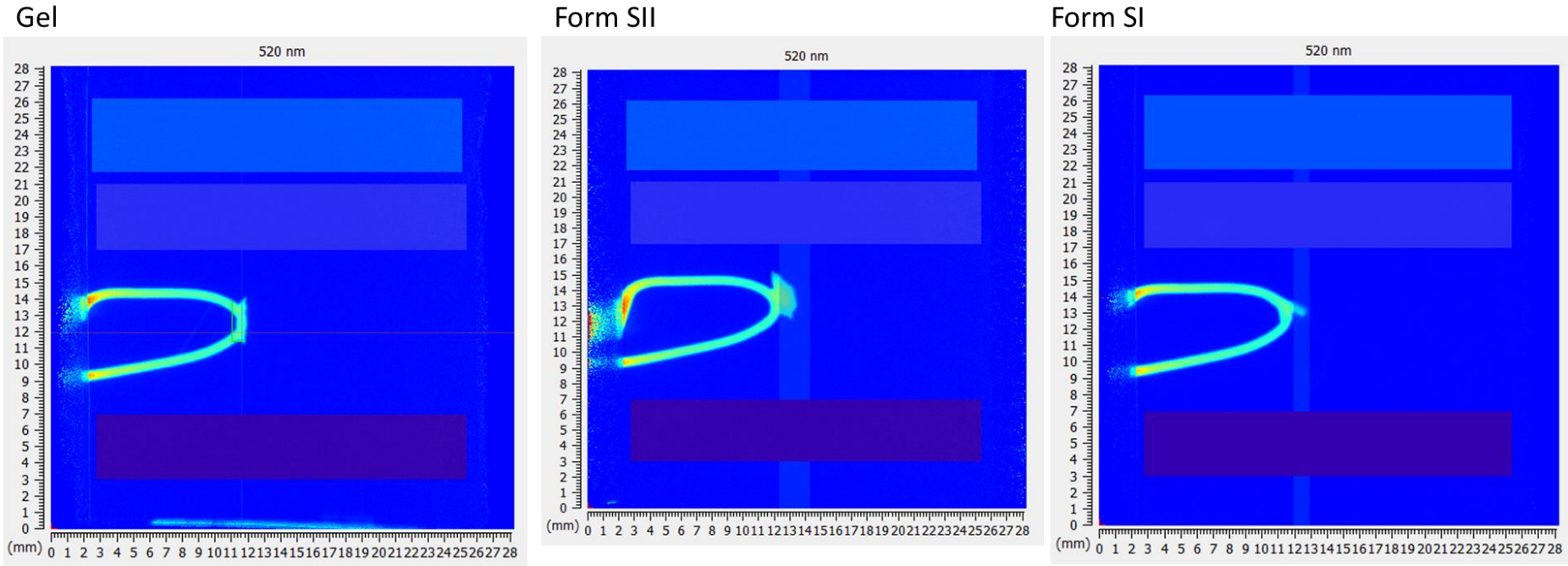

Figure 5.112 – Visible wavelength images of each I-TPI sample in the whole dose cell at the end of thirty minutes of dissolution. The samples are attached to the wire with varnish.

Each sample was observed to dissolve at different rates, as expected, with remains of Form SI and Form SII still present after 1800 secs of dissolution, whereas the gel dissolved rapidly and was no longer visible after only 660 secs had passed. The UV absorbance data was extracted per 10 second time segment for each zone and the average concentration was calculated throughout dissolution for the gel, Form SII and Form SI. The results are provided in Figure 5.113, Figure 5.114 and Figure 5.115, noting that the start of monitoring is reported just before 300 secs once the cell is filled with solvent, not at time zero. This results in a loss of initial data, which is particularly noticeable for the gel due to its rapid dissolution, but reduces the interference from the solvent moving through the cell.

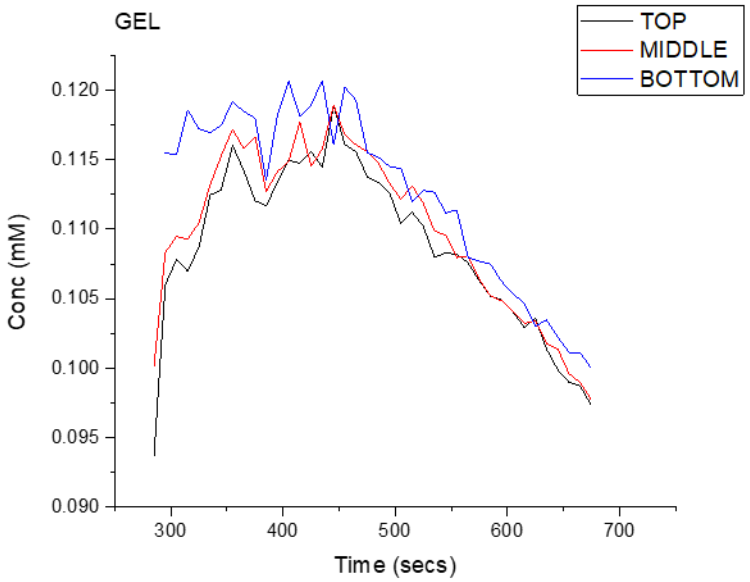

Figure 5.113 - Whole dose cell concentration monitoring for each UV zone throughout dissolution of I-TPI gel in methanol.

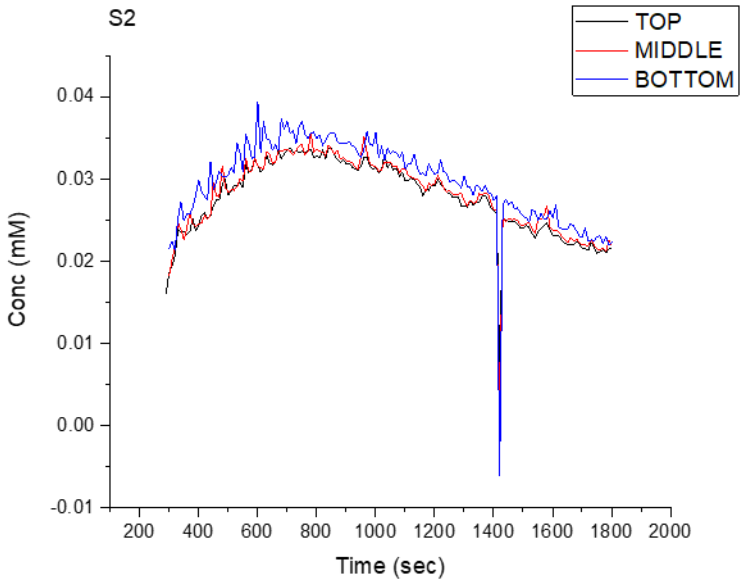

Figure 5.114 - Whole dose cell concentration monitoring for each UV zone throughout dissolution of a Form SII crystal in methanol.

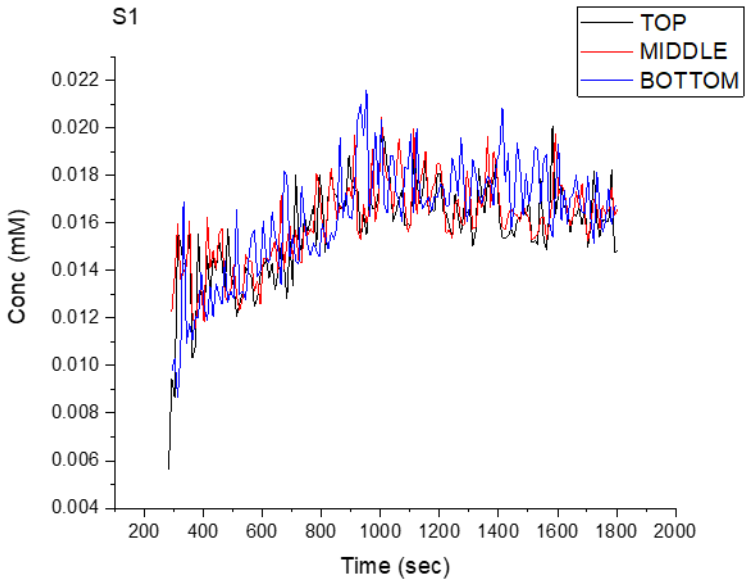

Figure 5.115 - Whole dose cell concentration monitoring for each UV zone throughout dissolution of a Form SI crystal in methanol.

Each sample (gel, Form SII or Form SI) results in a different concentration profile throughout dissolution. However, each figure shows little difference between the average concentrations reported for each zone (for each sample), with the bottom zone reporting the highest overall concentrations. This confirms that dissolving I-TPI is initially influenced by concentration gradients before being subjected to turbulence and does not solely flow in the direction of the solvent. This data suggests once again

that flow through the WDC is not laminar, which makes monitoring dissolution in this cell a significant challenge.

Figure 5.113 shows that the gel dissolves rapidly, with the concentration increasing rapidly to a peak within the first 450 secs. The decline is then linear, with each zone reducing at a similar rate between 450 and 670 secs. Form SII concentration can be seen in Figure 5.114 and initially increases very gradually to a peak concentration at 700 secs, before reducing linearly at a slower rate than the gel. There is an image glitch with in this data set observed just after 1400 secs, which impacts upon all three zones and is best observed visually in the SDi2 software. Finally, Form SI concentration is shown in Figure 5.115 and increases very gradually to a plateau around 1000 secs before remaining fairly consistent. The data shown for Form SI (Figure 5.115) appears more variable or "noisy" than the gel or Form SII, which may suggest that there is more variation around the cell, consistent with a slower release rate resulting in a more gradual increase in concentration and therefore density, in addition to slower diffusion.

The concentration values achieved are subject to additional scrutiny because there was no standardisation of size or shape with regard to the crystals or the gel sample used for dissolution. However, the maximum concentration observed for each sample can be seen on each plot (Figure 5.113, Figure 5.114 and Figure 5.115) and can be correlated with the dissolution and relative stability of each sample. The faster a sample dissolves, the higher the concentration expected, thus inferring a lower stability relative to a sample that dissolves more slowly and results in a lower concentration. The gel achieves the highest concentration and the largest variability, the metastable Form SII achieves a quarter of the gel concentration with a smaller amount of variability and the most stable Form SI reaches the lowest concentration (just over half that of Form SII).

b) Whole dose cell – visible absorbance:

The visible absorbance data was extracted from the horizontal and vertical zones outlined in Figure 5.110 and was reported as absorbance per x position, in addition to absorbance per z position, respectively, see Figure 5.116. Artefacts from the edges of

the cell and / or the wire can be seen at the extremities of each plot (x < 5 and x > 15, and z < 10 and z > 17). The absolute area was therefore extracted using Origin, as described previously, for only the central section, which corresponds with the position of the sample. The full data set of absorbance per position per time segment has been plotted for completeness, with arrows highlighting the change with time. However, the absolute area versus time segment provides a better indication of how size changes throughout dissolution.

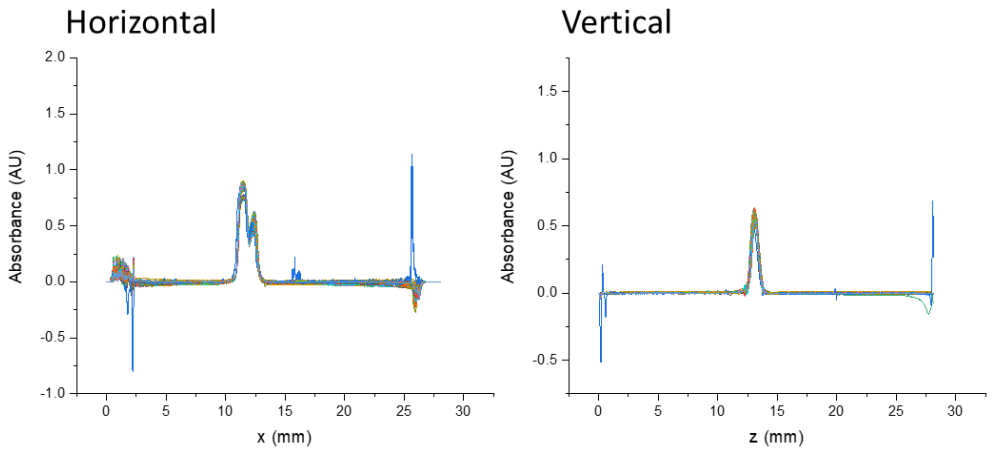

Figure 5.116 - Visible absorbance reported every ten seconds throughout dissolution in the x dimension (horizontal) and in the z dimension (vertical) for the full width and length of the whole dose cell, respectively.

Each sample will be looked at in turn starting with the gel, see Figure 5.117 and Figure 5.118, then Form SII, see Figure 5.119 and Figure 5.120, and finally Form SI, see Figure 5.121 and Figure 5.122. Some of the data has been reported from 200 secs as this is when the solvent front has moved past the sample, although the cell is not full of solvent until 300 secs, hence the importance of only extracting absolute area for the central section of the absorbance plot.

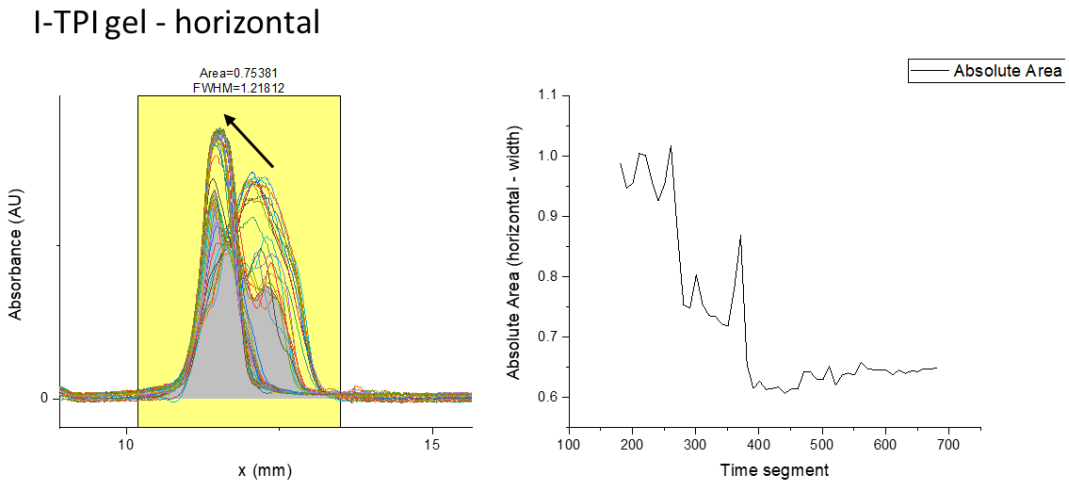

Figure 5.117 – Visible absorbance for I-TPI gel from across the horizontal zone. The left plot provides the absorbance per x position per 10 secs time segments with a black arrow showing how this changes with time. The yellow box highlights the section from which the absolute area is reported. The right plot shows the area of the crystal, as measured by visible absorbance, changing throughout dissolution.

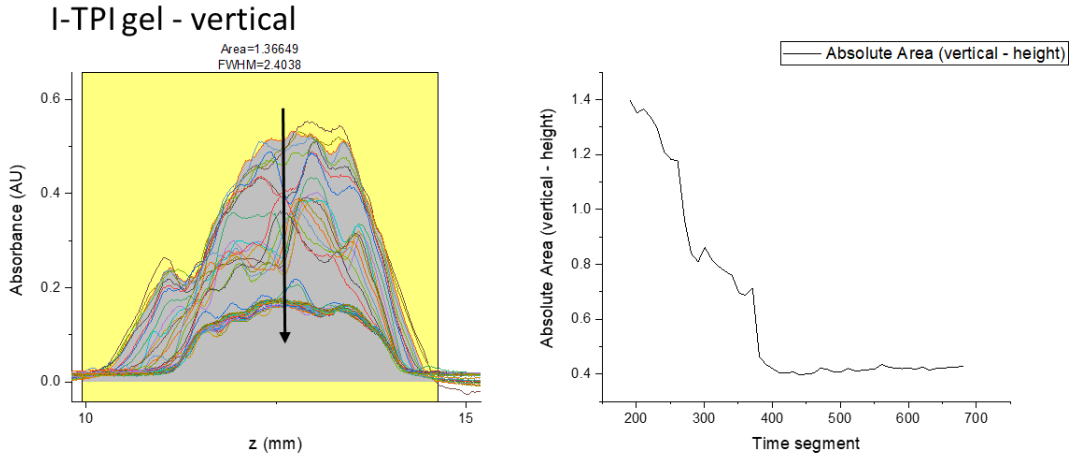

Figure 5.118 – Visible absorbance for I-TPI gel from through the vertical zone. The left plot provides the absorbance per z position per 10 secs time segments with a black arrow showing how this changes with time. The yellow box highlights the section from which the absolute area is reported. The right plot shows the area of the crystal, as measured by visible absorbance, changing throughout dissolution.

The gel height and width, as represented by absolute area, both decrease overall from the start to the end of the reported dissolution period, as shown in Figure 5.117 and Figure 5.118. The horizontal data (Figure 5.117) shows an initial reduction then a rapid increase, before the height then reduces again, whereas the vertical data (Figure 5.118) shows a more consistent reduction with time. When interpreted together, and viewed with the dissolution images, the gel can be seen to change in shape over this

time. The transparency of the gel may also influence the ability to monitor size changes from this data, as there continues to be I-TPI dissolving (as seen in the 255 nm images) long after the gel appears to be fully dissolved, which can be calculated at approximately 400 secs (through viewing the 520 nm image). Nevertheless, the gel shows a rapid reduction in size, which can be visualised using the 520 nm data.

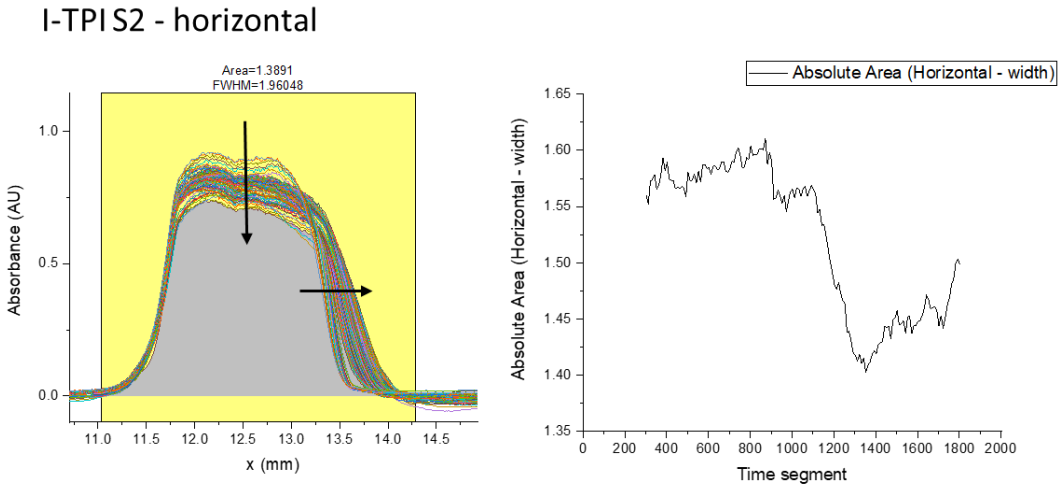

Figure 5.119 – Visible absorbance for I-TPI Form SII from across the horizontal zone. The left plot provides the absorbance per x position per 10 secs time segments with black arrows showing how this changes with time. The yellow box highlights the section from which the absolute area is reported. The right plot shows the area of the crystal, as measured by visible absorbance, changing throughout dissolution.

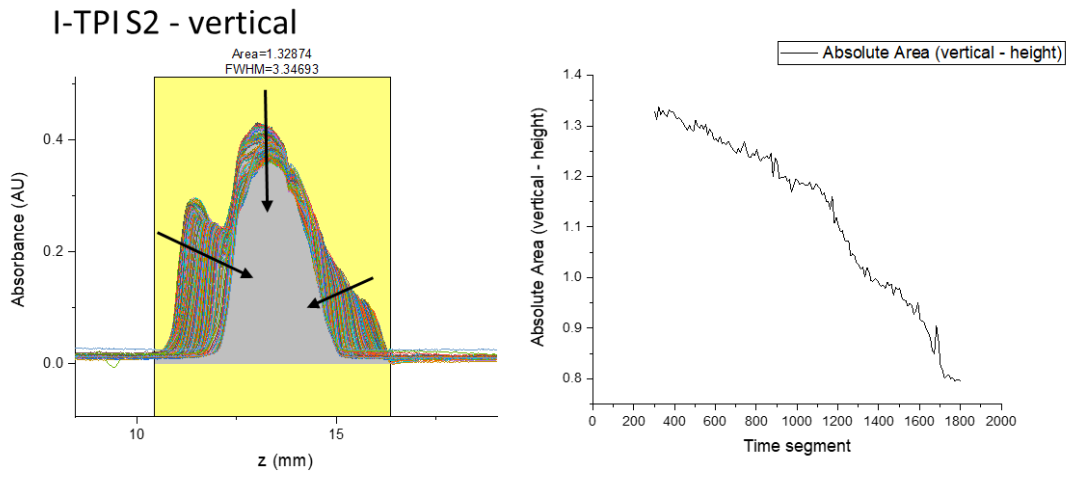

Figure 5.120 – Visible absorbance for I-TPI Form SII from through the vertical zone. The left plot provides the absorbance per z position per 10 secs time segments with black arrows showing how this changes with time. The yellow box highlights the section from which the absolute area is reported. The right plot shows the area of the crystal, as measured by visible absorbance, changing throughout dissolution.

The width and height change for I-TPI Form SII can be seen in Figure 5.119 and Figure 5.120, with height shown to decrease throughout dissolution. The width change is more variable, with some increases observed, which correlate with shape changes when the series of images are viewed. The change overall is a reduction in width, but this is not as clear as for the gel data, and shows a significant difference between the two forms of I-TPI, in spite of the gel sample being larger in volume than the Form SII sample.

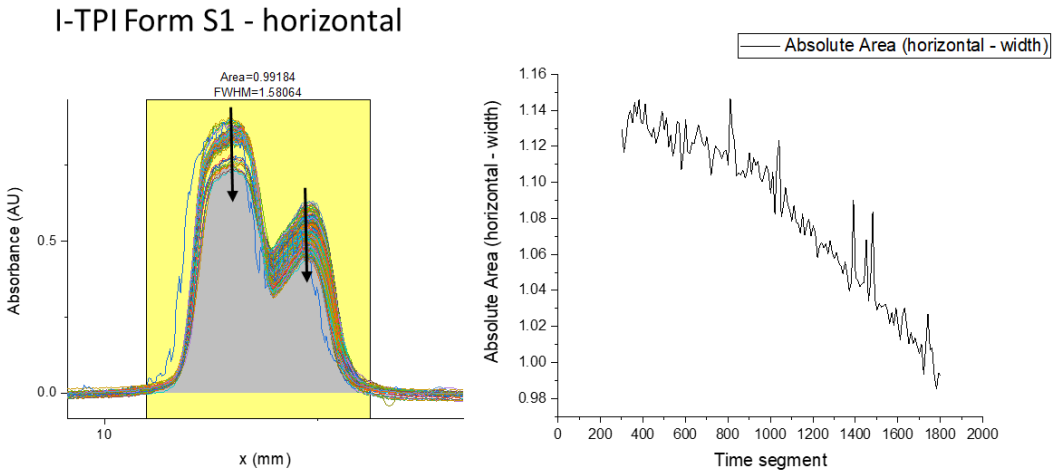

Figure 5.121 – Visible absorbance for I-TPI Form SI from across the horizontal zone. The left plot provides the absorbance per x position per 10 secs time segments with black arrows showing how this changes with time. The yellow box highlights the section from which the absolute area is reported. The right plot shows the area of the crystal, as measured by visible absorbance, changing throughout dissolution.

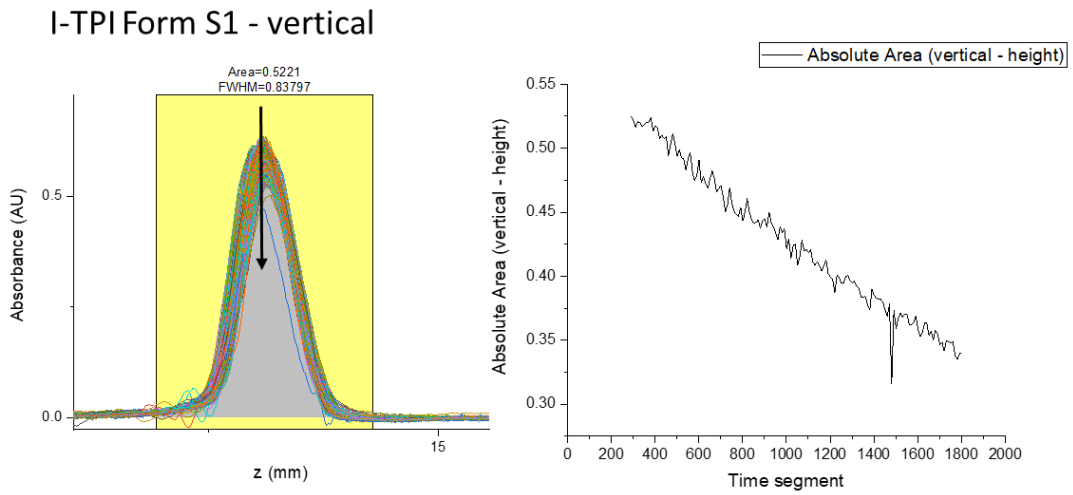

Figure 5.122 – Visible absorbance for I-TPI Form SI from through the vertical zone. The left plot provides the absorbance per z position per 10 secs time segments with a black arrow showing how this changes with time. The yellow box highlights the section from which the absolute area is reported. The right plot shows the area of the crystal, as measured by visible absorbance, changing throughout dissolution.

The width and height change for I-TPI Form SI can be seen in Figure 5.121 and Figure 5.122, with both dimensions reducing throughout dissolution. Both show variability as seen with the other reports of size change for Form SII and the gel, however, the reduction in size appears to proceed via a constant rate, allowing a line of best fit to be reported for the vertical plot, see Figure 5.123.

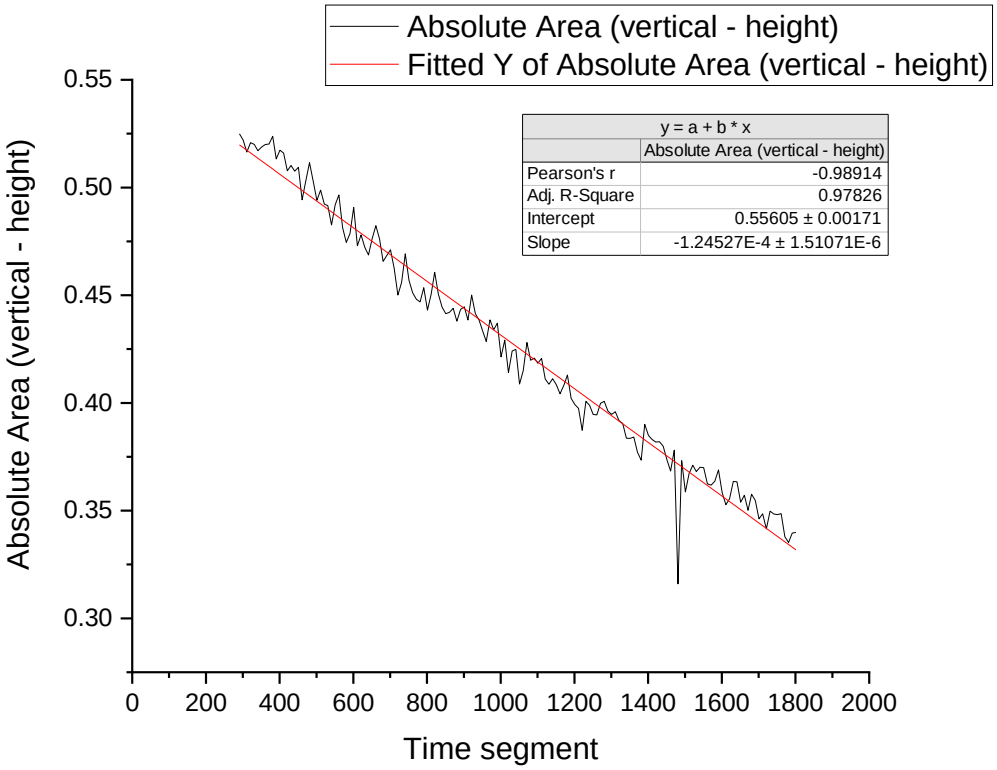

Figure 5.123 – I-TPI Form SI reduction in absolute area, as measured through visible absorbance (520 nm) through the vertical zone. The red line of best fit is included with details reported inset.

The change in size, as measured by absolute area under the absorbance versus x or z position, for each sample can be summarised for height and width, see Table 5.16.

Table 5.16 – Summary of size change data obtained using the whole dose cell and measured by the change in absolute area from absorbance versus dimension.

	Height decrease	**Width decrease**	**Approx. time (secs)**
Gel	1.00164	0.41077	200 (fully dissolved)
Form SII	0.46902	0.21089	1500 (solid remains)
Form SI	0.18974	0.16156	1500 (solid remains)

Direct comparisons of height and width, and even percentage size changes do not accurately exclude the influence of the wire holders, or account for the differences in starting size of each form. The size change data, however, can be used to rank the forms according to stability, with the gel showing the greatest absolute size changes in both dimensions, and Form SI showing the smallest absolute size changes, again, in both dimensions. In summary, the WDC successfully provided a means by which to

interpret absorbance data for both wavelengths and rank the forms according to their relative stability.

c) Compact flow cell – UV absorbance:

The CFC has previously shown less turbulence than the WDC and a method was defined in Chapter 4. Single crystal surface dissolution imaging, to allow single crystal dissolution to be monitored. The 255 nm UV wavelength was utilised again, with the software reporting IDRs that could be manipulated to calculate dissolution flux (µg/min), which shows the change in dissolution per time period. Additionally concentration changes could be monitored throughout dissolution for each sample being analysed.

Dissolution of I-TPI gel attached to a wire was carried out four times in total for the CFC, see Figure 5.124 for an example and outline of the zones used for measurements. In all instances the gel fell from the wire to the bottom of the cell within the first three minutes, and had completely dissolved by 5 minutes, as defined by a lack of visibility using the 520 nm absorbance. While the gel became transparent very rapidly in all examples, resulting in it being hard to visualise using the 520 nm images, concentration changes were still occurring for some time after this. The prolonged concentration changes appear to be a result of the flow through the cell, however, with the highest concentration sample and therefore most dense solution remaining at the bottom of the cell and moving through gradually. Interpreting the results with the images shows that this is the most likely explanation, rather than it being a result of remaining gel continuing to dissolve, see Figure 5.125.

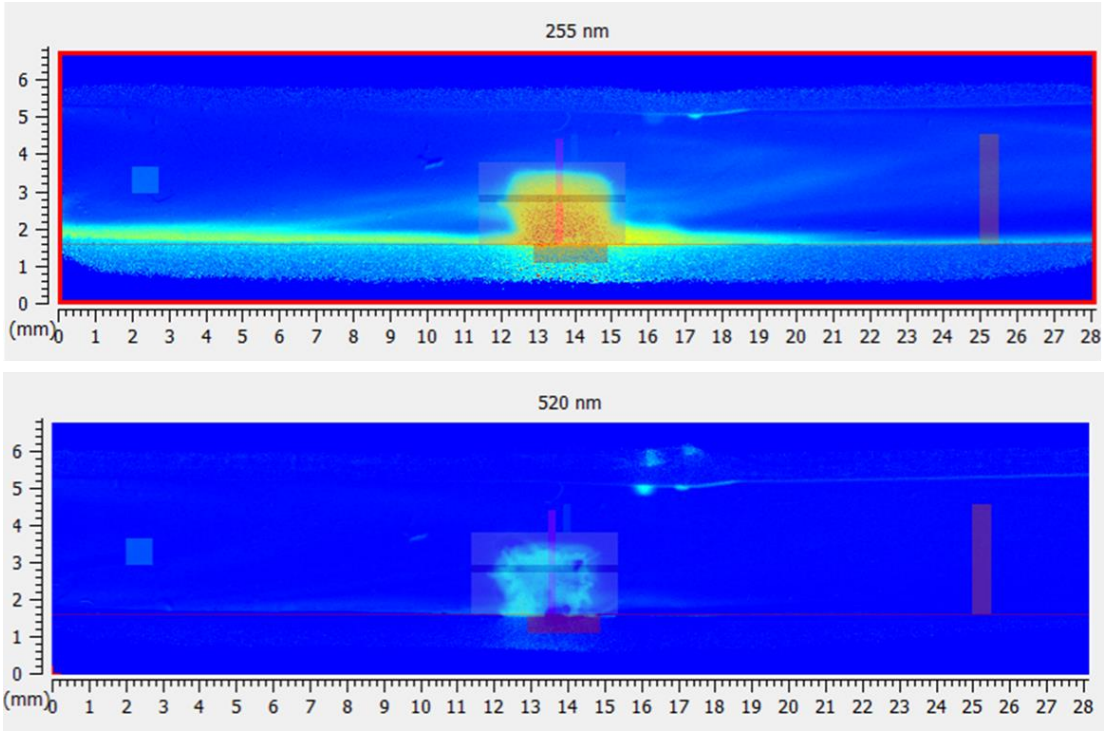

Figure 5.124 - Example of I-TPI gel attached to wire with default zones for background, surface and IDR measurements, in addition to multiple manual zones for measuring concentration changes and size changes throughout dissolution in methanol.

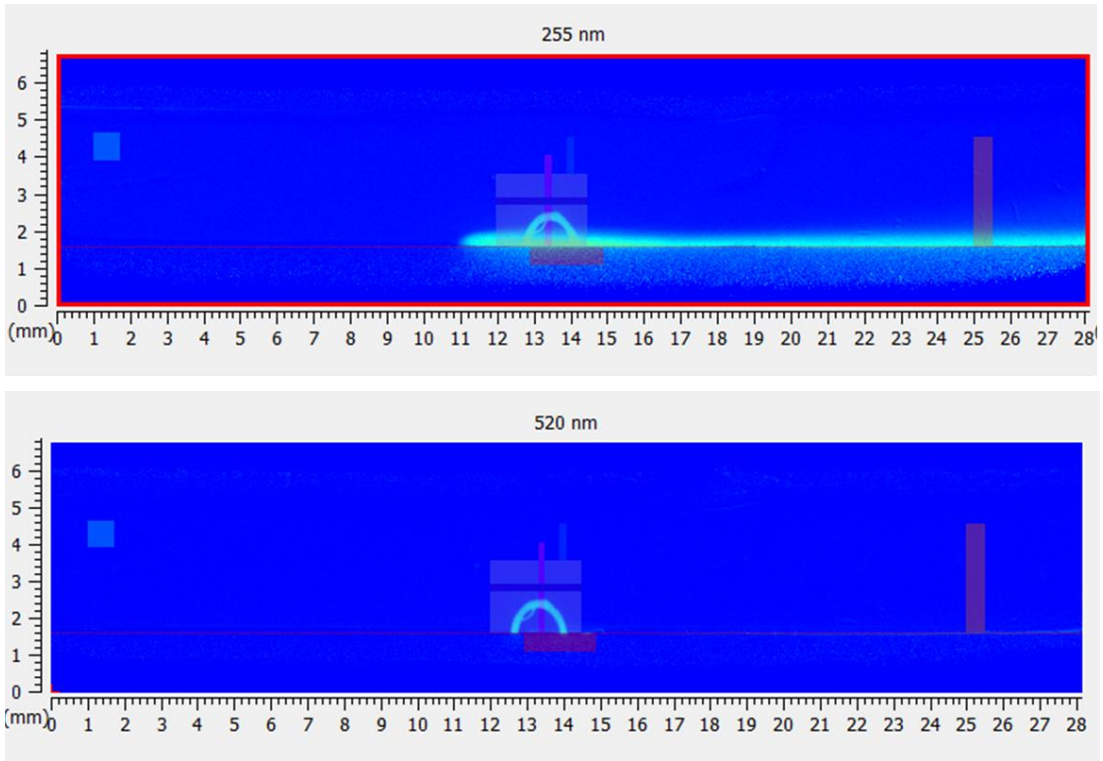

Figure 5.125 - Example of I-TPI gel dissolution showing only the wire left in the visible image (bottom). The UV absorbance image (top) shows dissolved I-TPI moving along the bottom of the cell.

Dissolution flux versus time can be plotted for all four gel runs in Figure 5.126 with runs 1 and 3 showing similar profiles. Runs 1, 2 and 3 show a rapid initial increase in dissolution flux, followed by a gradual decrease, which correlates with the increased density solution moving slowly through the cell (and therefore passing through the IDR zone). Run 4 shows a much more variable dissolution flux, which upon viewing the dissolution can be accounted for as the gel falls off the wire soon after dissolution begins followed by a large bubble moving into the flow cell, see Figure 5.127. The absolute dissolution flux values range from very negative values up to 80 µg/min, and are variable due to the different size gel samples.

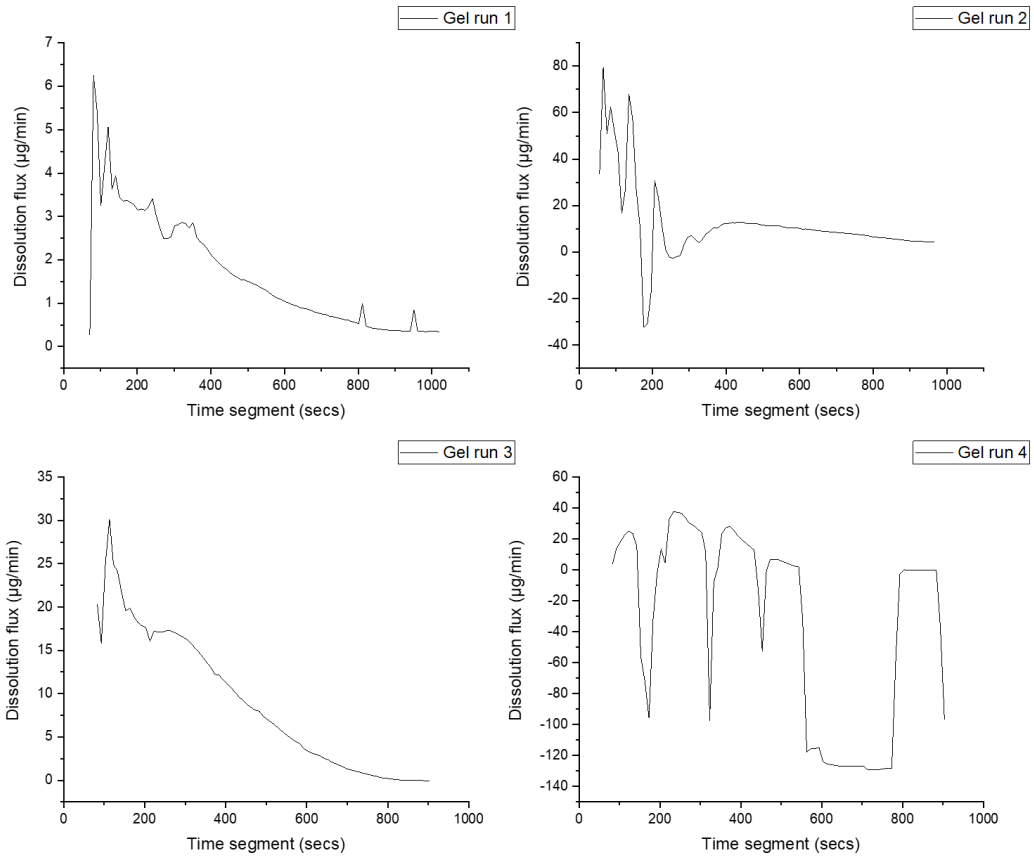

Figure 5.126 – Dissolution flux for I-TPI gel runs 1, 2, 3 and 4. Note the different scales on the y-axis for each plot.

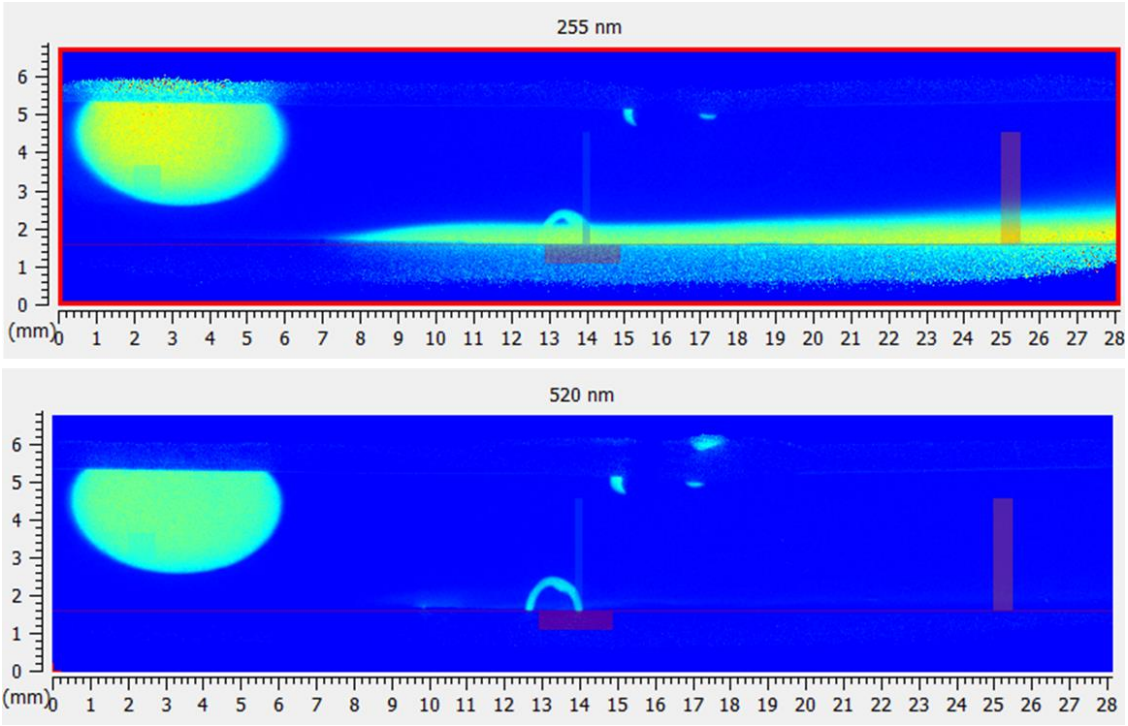

Figure 5.127 - I-TPI gel dissolution run 4 with a large bubble entering the compact flow cell and smaller bubbles appearing at the top of the cell.

Two sets of data for I-TPI Form SII were obtained despite its metastable nature, although one is limited in usefulness due to interference from bubbles; both dissolution flux plots are provided in Figure 5.128. Run 1 shows extensive interference from a bubble throughout, impacting upon the reported values, but is suggestive of a flux around 0 to 5 µg/min. Run 2 was interrupted at the start by a bubble, which was removed and dissolution allowed to continue, thus dissolution flux from 400 secs onwards shows a very gradual decline. Figure 5.130 shows that there is crystal remaining at the end of the dissolution, which is shown in the data by the flux tending towards but not actually reaching zero. The dissolved I-TPI again sinks to the bottom of the cell and moves slowly through the cell.

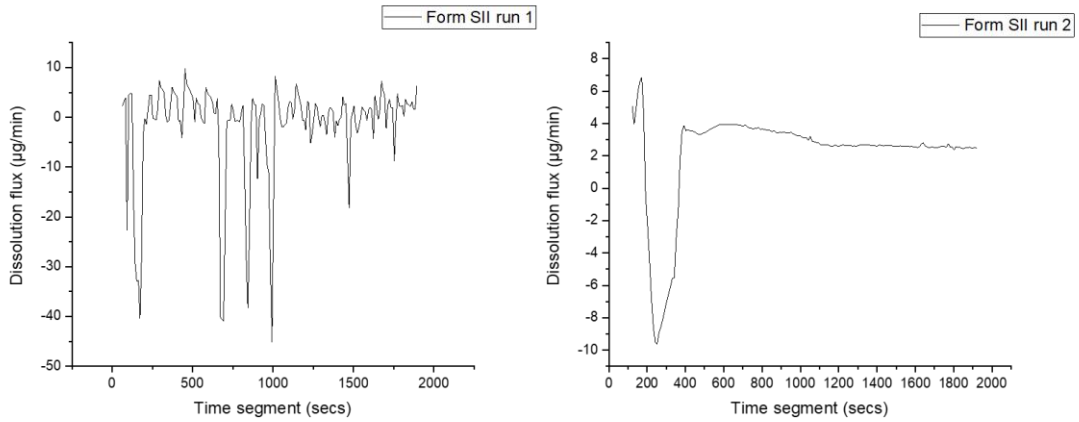

Figure 5.128 - Dissolution flux for I-TPI Form SII runs 1 and 2. Note the different scales on the y-axis for each plot.

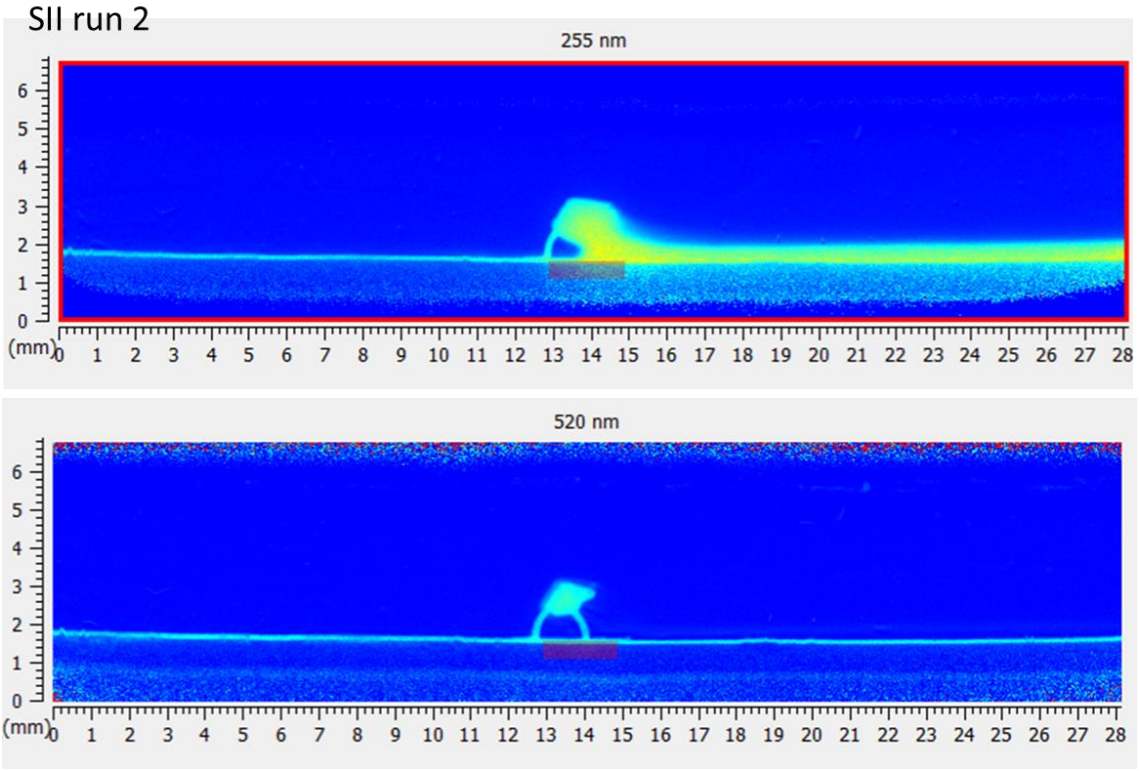

Figure 5.129 – I-TPI Form SII mounted on a wire and observed in the compact flow cell at 255 nm (top) and 520 nm (bottom). This image is from the start of dissolution.

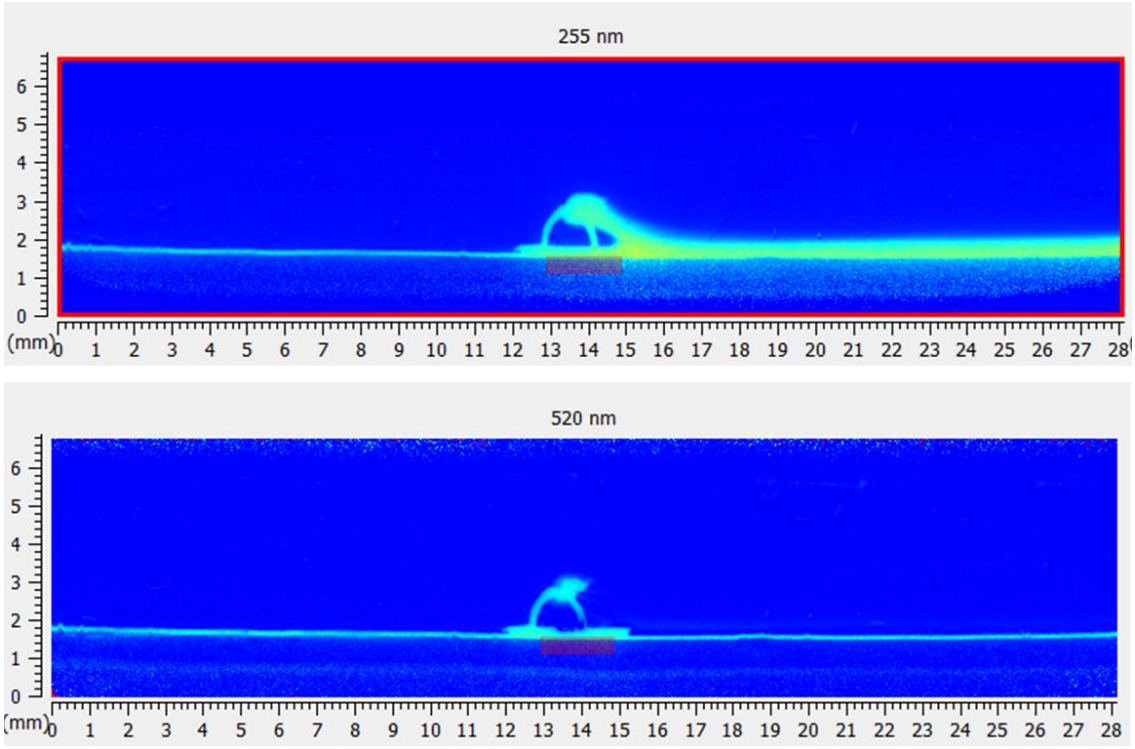

Figure 5.130 – I-TPI Form SII mounted on a wire and observed in the compact flow cell at 255 nm (top) and 520 nm (bottom). This image is from the end of the dissolution run (after thirty minutes).

The dissolution flux versus time data for I-TPI Form SI is shown in Figure 5.131 and shows an overall reduction in flux for all four runs, but significant variation between them, both in terms of profile and values for dissolution flux. Run 1 uses a relatively small crystal of Form SI, which fully dissolves by 28 minutes and shows a consistent decline in flux, see Figure 5.132. Run 3 uses a crystal approximately twice the size of run 1, which can be seen to dissolve rapidly initially and then more slowly until it is fully dissolved by 30 minutes. Run 4 uses a crystal similar in size to run 3, although it is positioned differently relative to the camera; it dissolves rapidly but is impacted upon by multiple bubbles (removed by tipping the cell) and the image shows crystal remaining after 31 minutes in addition to a leak at the top of the CFC. Run 5 shows a larger crystal again; it appears to dissolve more rapidly at first due to the removal of a bubble, resulting in dissolving I-TPI moving to the left (due to the tipping of the cell) thus increasing the flux at the start. The continual decline in flux from 900 secs is representative of the crystal dissolving gradually and allows a line of best fit to be plotted, Figure 5.133.

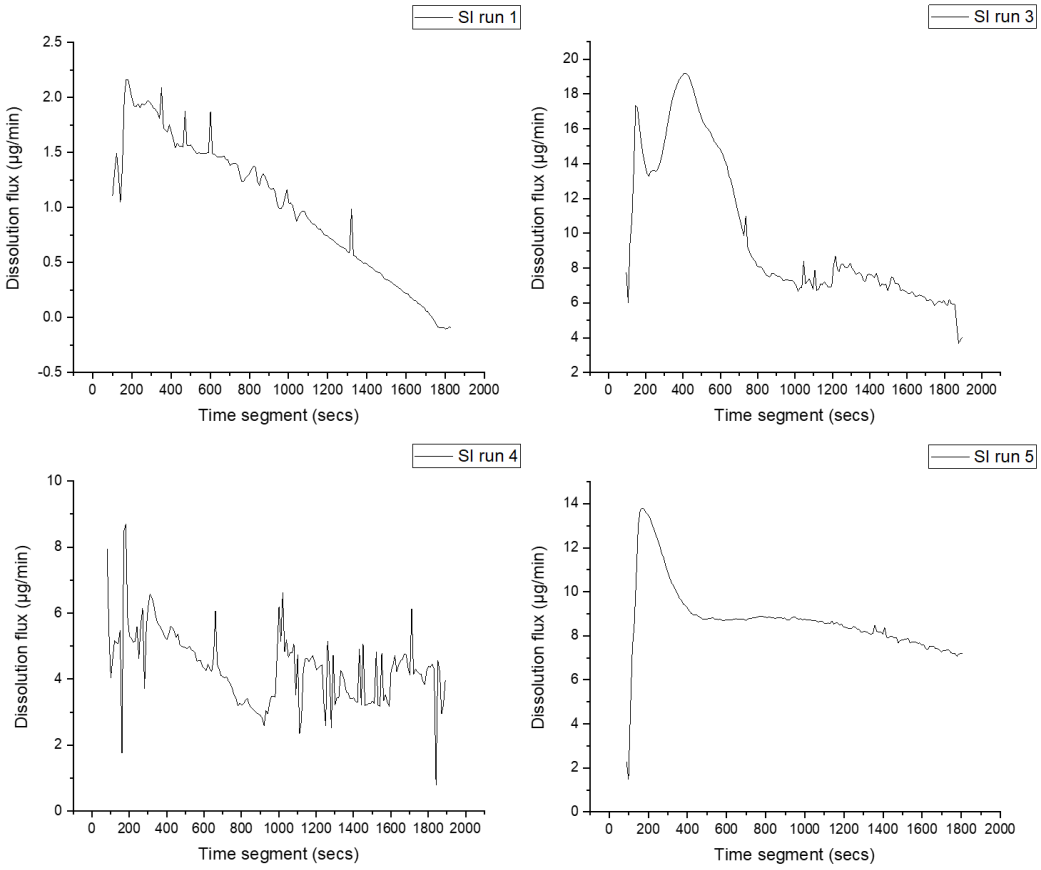

Figure 5.131 – Dissolution flux for I-TPI Form SI runs 1, 3, 4 and 5. Note the different scales on the y-axis for all four plots.

Figure 5.132 and Figure 5.133 show very different profiles, each with a linear section although the properties of the lines differ. The plots for each different form also differ, with variation between, but a general observation that the gels show very high initial flux, followed by a decrease and then a plateau, Form SII shows an almost linear flux throughout and Form SI showing periods suggestive of a linear decline in flux. One interpretation is that the gels release I-TPI (dissolve) rapidly, Form SII releases I-TPI at a fairly consistent rate and Form SI releases I-TPI more slowly as dissolution progresses. The data is highly variable, such is the nature of dissolving crystals of varying shapes and sizes which cannot be easily replicated, and so these observations should be considered in conjunction with additional data to further define the dissolution characteristics of the different forms of I-TPI.

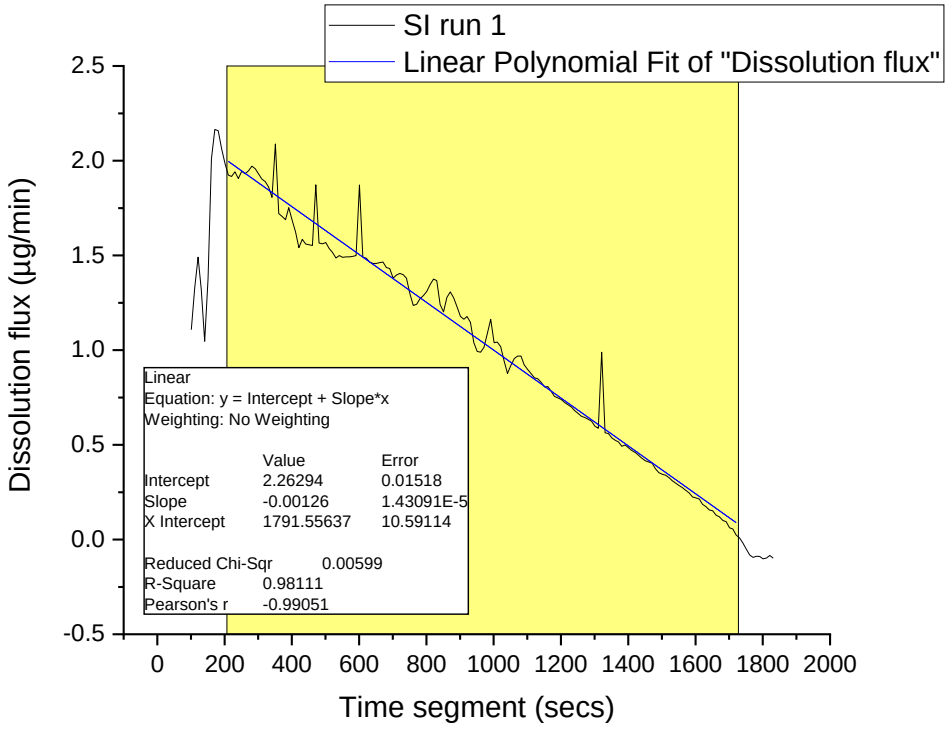

Figure 5.132 - Dissolution flux of I-TPI Form SI (run 1) with line of best fit along linear section, details inset.

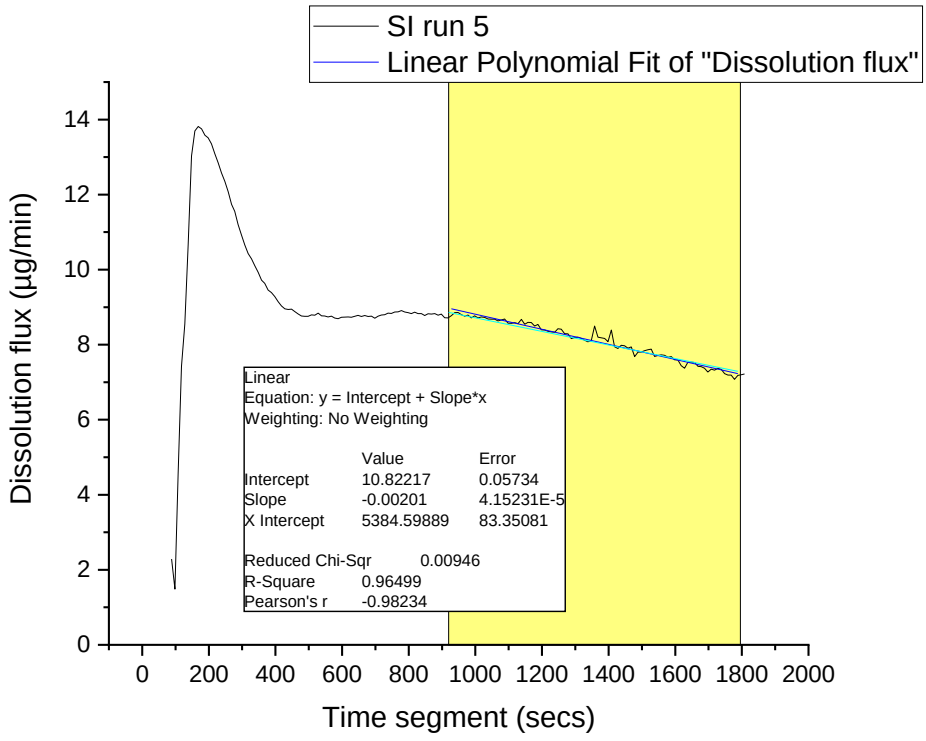

Figure 5.133 - Dissolution flux of I-TPI Form SI (run 5) with line of best fit along linear section, details inset.

Exploring the absorbance data extracted from the IDR zone expands this understanding, see Figure 5.134, Figure 5.135 and Figure 5.136. These plots show absorbance per z position for three time segments throughout dissolution, one from the start, one towards the middle and one at the end. Figure 5.134 plots absorbance for the I-TPI gel (run 1) and shows that the lowest point in the cell (z = 1.64 mm in this instance) reduces in absorbance throughout dissolution from 0.8 to 0.46. The height of the plume of dissolving I-TPI can be seen to reduce throughout dissolution too, from 3.50 mm to 2.75 mm, to 2.25 mm. This correlates with the gel dissolving rapidly but the dissolved and dense I-TPI solution moving more slowly through the cell.

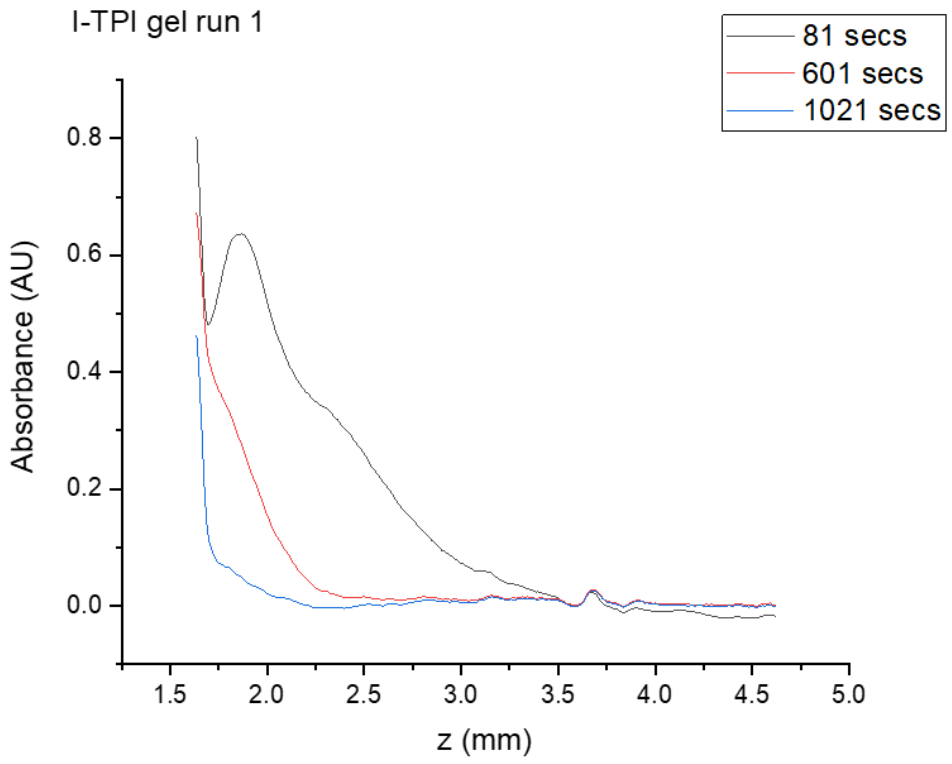

Figure 5.134 - Absorbance per z position through the IDR zone at the start (81 secs), middle (601 secs) and end (1021 secs) of dissolution for the I-TPI gel (run 1).

The I-TPI Form SII (run 2) is shown in Figure 5.135, with absorbance at the bottom of the cell showing a reduction throughout dissolution, but to a much smaller extent than for the gel run described previously. This indicates that there is only a small change in the amount of I-TPI dissolving throughout dissolution, even after 30 minutes. The plot suggests that the plume of dissolving I-TPI reduces in intensity from start to finish, and also slightly reduces in height from start to fifteen minutes in. From halfway through

dissolution to the end of dissolution, the plot shows the same profile, but shifts left, highlighting a small reduction in overall absorbance at this point in the cell, consistent with a fairly steady release of I-TPI with time.

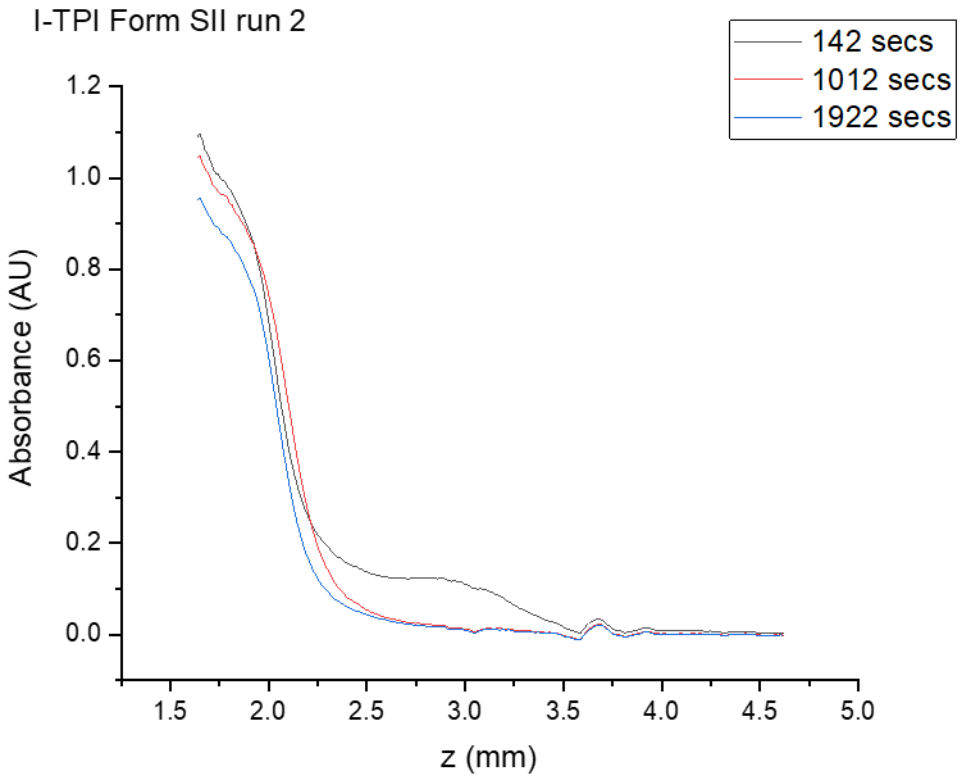

Figure 5.135 – Absorbance per z position through the IDR zone at the start (142 secs), middle (1012 secs) and end (1922 secs) of dissolution for the I-TPI Form SII (run 2).

The I-TPI Form SI (run 3) is shown in Figure 5.136, with absorbance at the bottom of the cell showing an increase throughout the first half of dissolution, before reducing by approximately half at the end of dissolution. This suggests that I-TPI release occurs more gradually, because the highest density and therefore highest I-TPI concentration sinks to the bottom of the cell. Although the crystal has fully dissolved by the end of the run, there is still a small plume of I-TPI passing through the IDR zone.

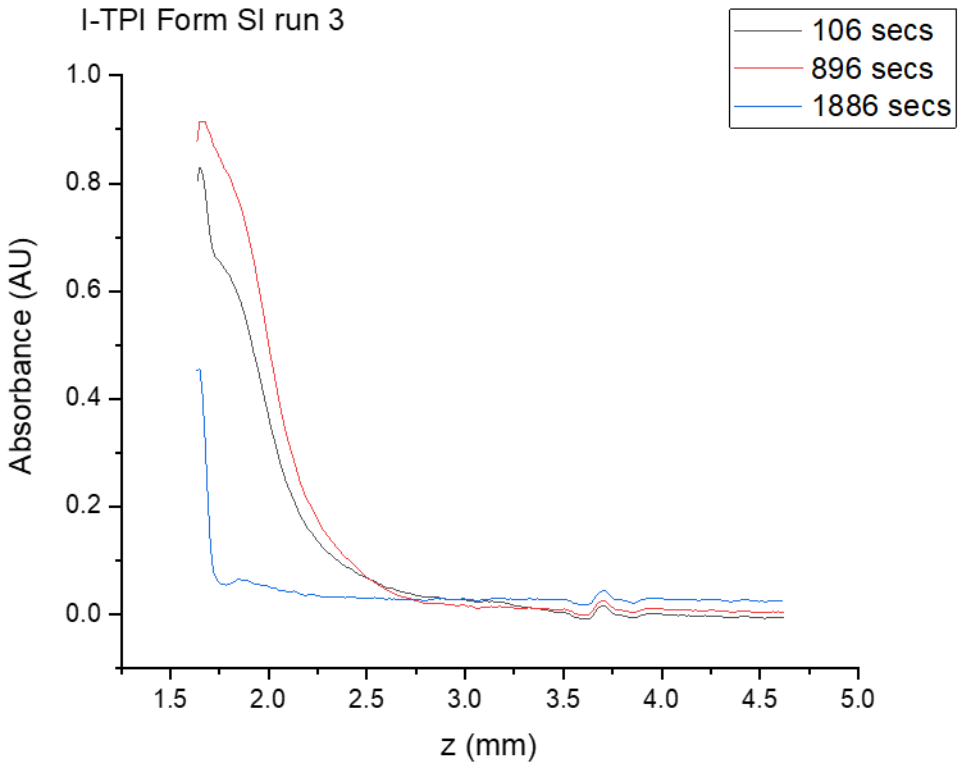

Figure 5.136 - Absorbance per z position through the IDR zone at the start (106 secs), middle (896 secs) and end (1886 secs) of dissolution for the I-TPI Form SI (run 3).

This additional absorbance information is best used in combination with the dissolution flux data, and provides more detail about the dissolution mechanisms occurring. The size of the sample being analysed impacts upon the absolute absorbance, but the rate at which absorbance changes and whether it increases or decreases throughout dissolution allows for an interpretations of whether diffusion might be limiting dissolution or whether erosion is.

d) Compact flow cell – visible absorbance:

Size changes were monitored in the CFC using the visible (520 nm) wavelength and a series of manual zones. The novel size monitoring zones described previously were used, two encompassing the whole size of the crystal or gel sample (vertical and horizontal), one spanning the width of it (section width), and one spanning its height (section height), see Figure 5.137. The position and size of these zones was tailored to each sample being analysed. The absolute area data was extracted for each zone and plotted against time to represent size changes throughout dissolution. The change in absolute area versus time segment will be presented for a sample of each I-TPI form.

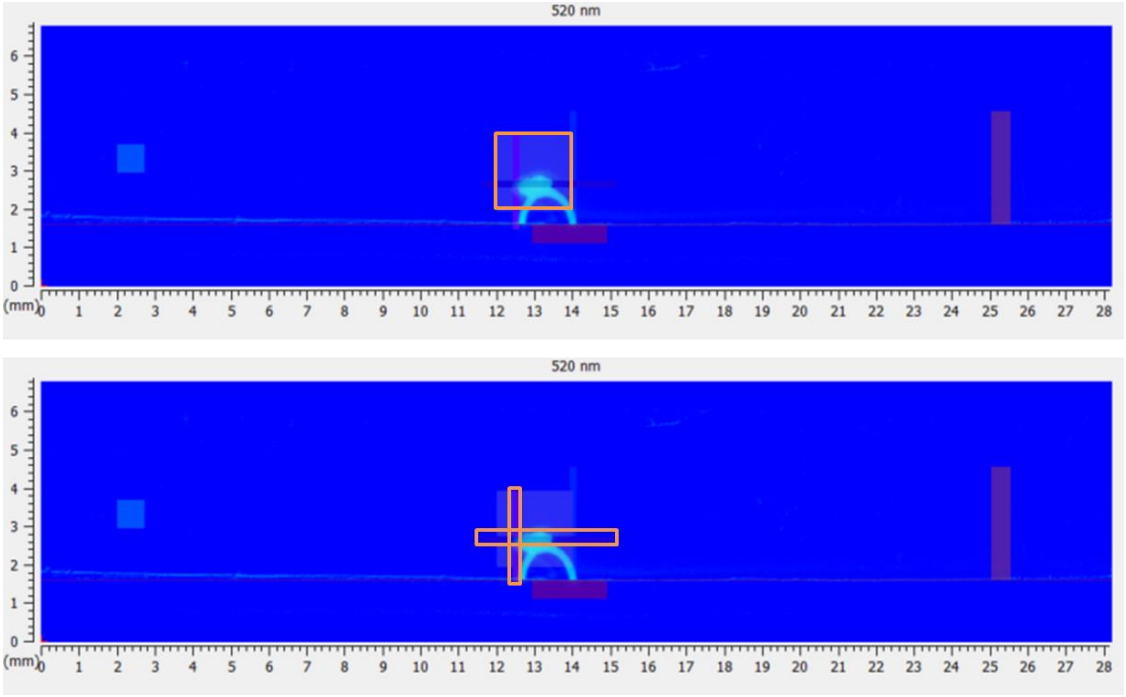

Figure 5.137 - Example of an I-TPI crystal in the compact flow cell, with the manual zones used to measure size change highlighted in orange. The top image shows the whole size zone for both vertical and horizontal measurements, and the bottom image shows the section zones for the height and the width of the sample.

The plots shown in Figure 5.138 are for an I-TPI gel, and include size change as measured using each of the four zones described. The top plots show height and width change, and the bottom plots show size change for the vertical dimension and for the horizontal dimension. The width of the gel appears to decrease instantly, but this can be explained by the gel falling from the wire straight away, preventing the gel from being measured by the section width zone. This zone was also placed above the wire, hence its minimum absorbance is zero. Each of the other measurements shows a reduction, however, there is significant interference from the presence of the wire, so they do not achieve zero absorbance even after the gel has fully dissolved.

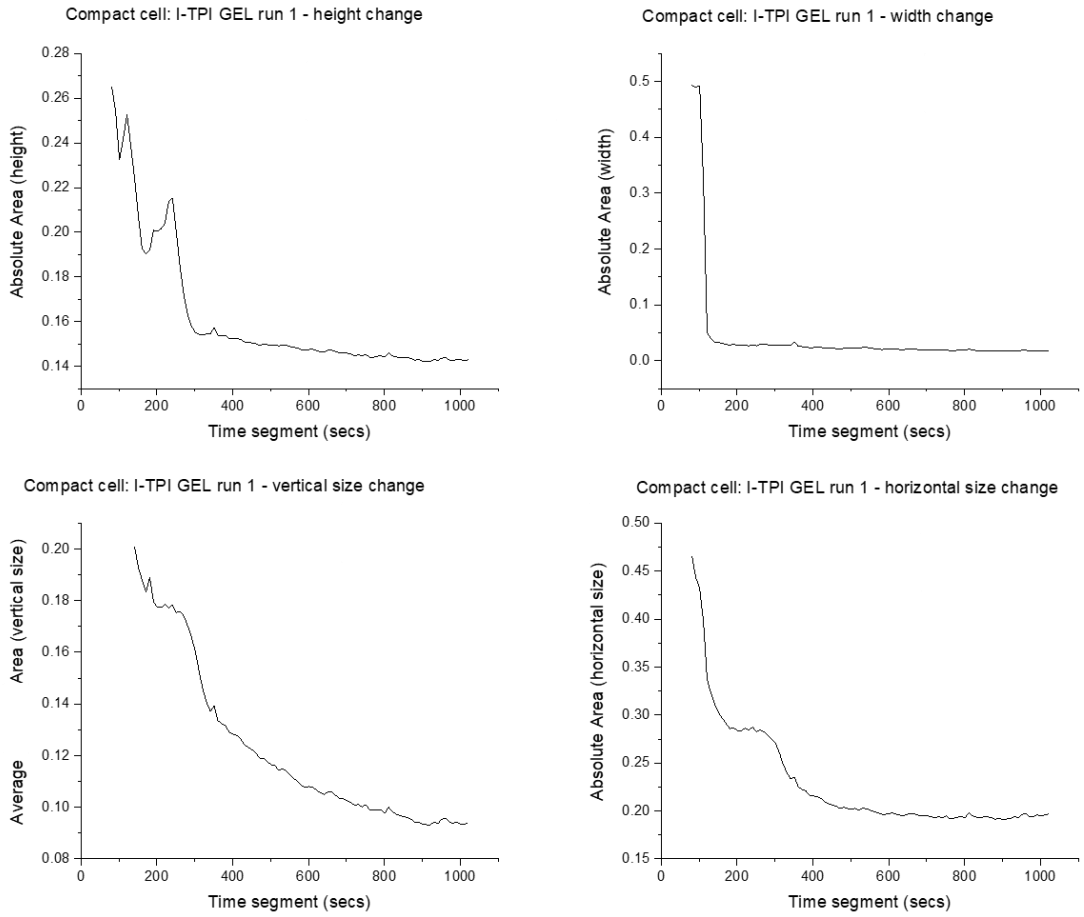

Figure 5.138 - I-TPI gel (run 1) size change measured through four zones in the compact flow cell.

I-TPI Form SII size change measurements for each zone are shown in Figure 5.139 and confirm an overall reduction for each. Two image glitches can be seen at approximately 300 and 800 secs, for all size measurements except the width; glitches are explained in Chapter 3. Surface dissolution imaging intrinsic dissolution rate calculations, and result in spurious data when extracting absorbance values and when viewing the images. It is not clear why these happen but they are reported as errors within the advanced monitoring section of the SDi2 software. The reduction in height and size (both vertical and horizontal) are all more gradual than for the gel, suggesting a less rapid dissolution and thereby confirming it as a relatively more stable form of I-TPI. The section width reading initially increases, which is caused by the rubber bung gradually moving up and slightly out of the sample holder between 400 and 800 secs. The movement physically shifts the wire and crystal upwards, resulting in the width

reading measuring a different section, although there is little impact upon the other measurements, see Figure 5.140.

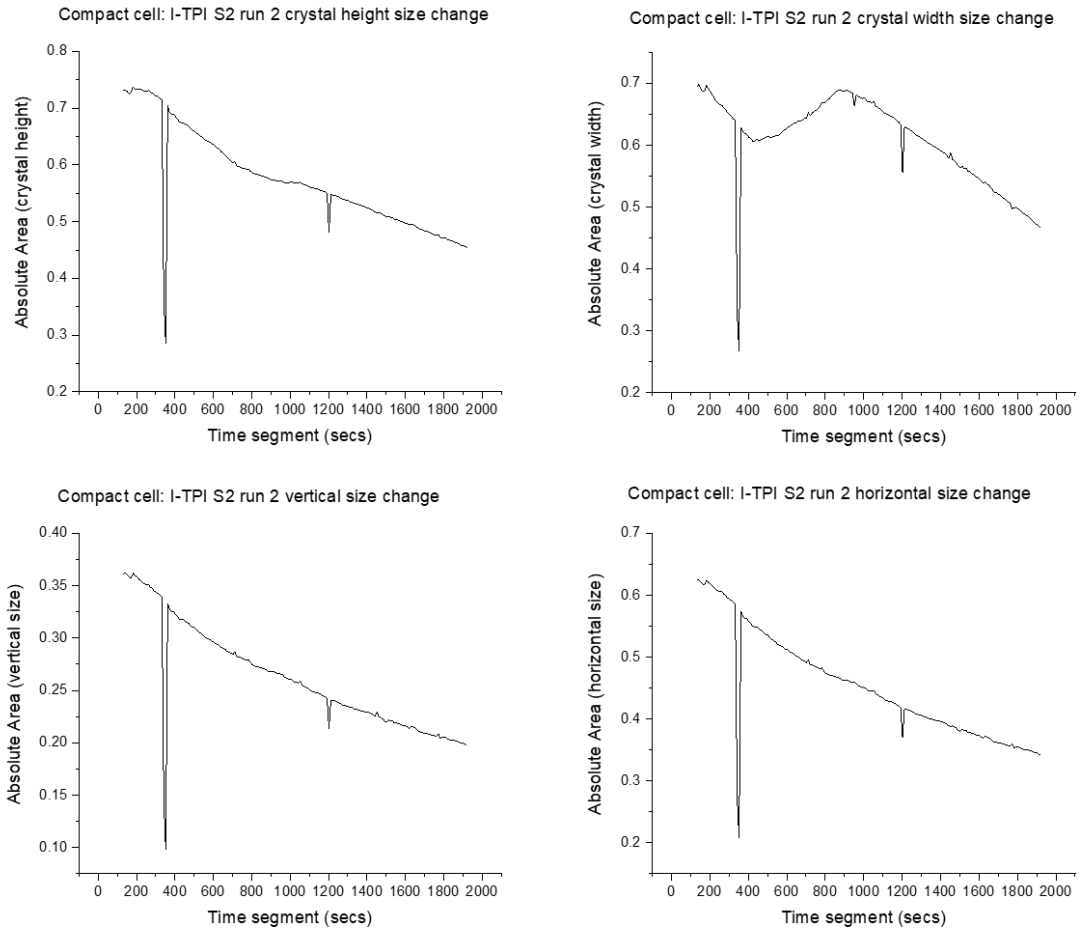

Figure 5.139 – I-TPI Form SII (run 2) size change measured through four zones in the compact flow cell.

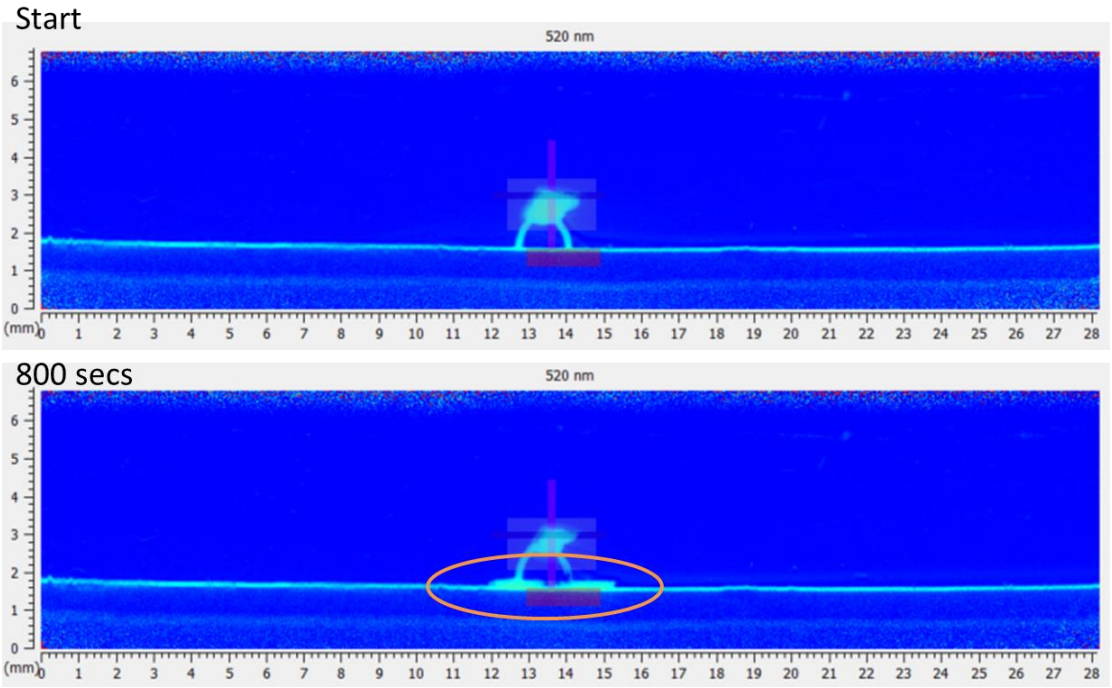

Figure 5.140 – I-TPI Form SII visible absorbance images with orange oval highlighting the appearance of the top of the rubber bung.

The measurements for I-TPI Form SI (run 3) confirm a gradual but linear reduction in absolute area (absorbance) for each zone. A line of best fit can be calculated for each plot, see Figure 5.141, Figure 5.142, Figure 5.143 and Figure 5.144. There is a linear reduction in size for all reported methods, with the width of the crystal appearing to reduce in size more rapidly than the height. The rapid decrease at the very end of the height and width plots (Figure 5.141 and Figure 5.142) correspond to the remnants of the crystal falling from the wire.

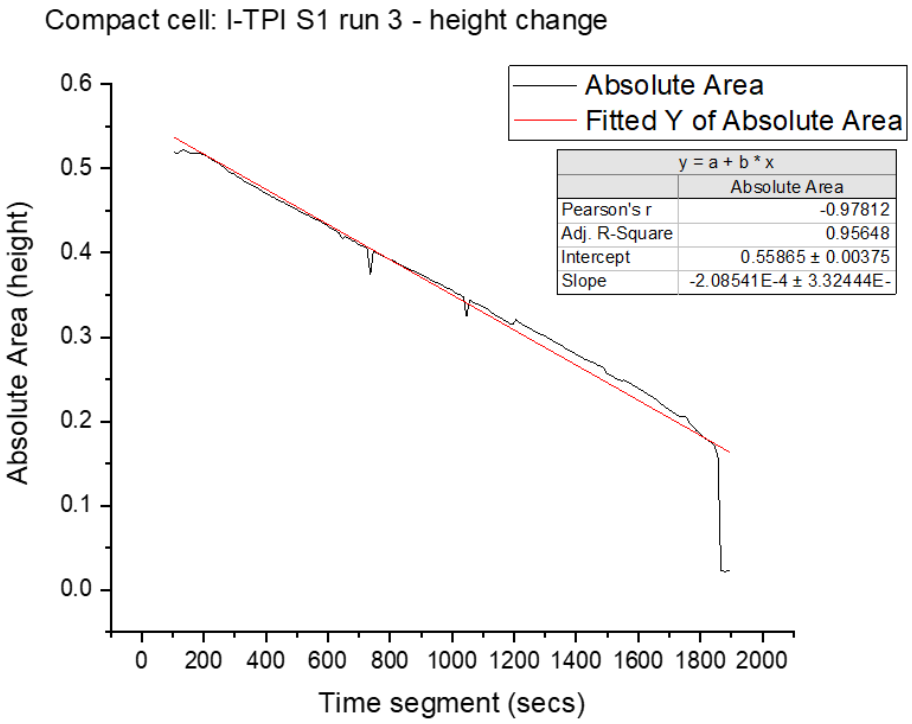

Figure 5.141 – I-TPI Form SI (run 3) height change as measured through visible absorbance, with line of best fit (details inset).

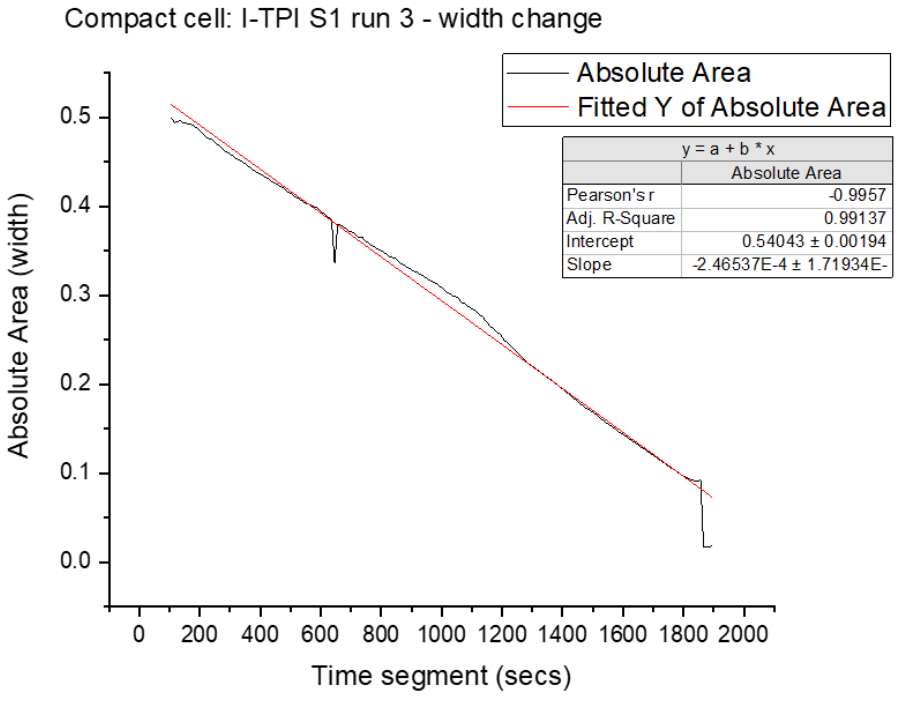

Figure 5.142 – I-TPI Form SI (run 3) width change as measured through visible absorbance, with line of best fit (details inset).

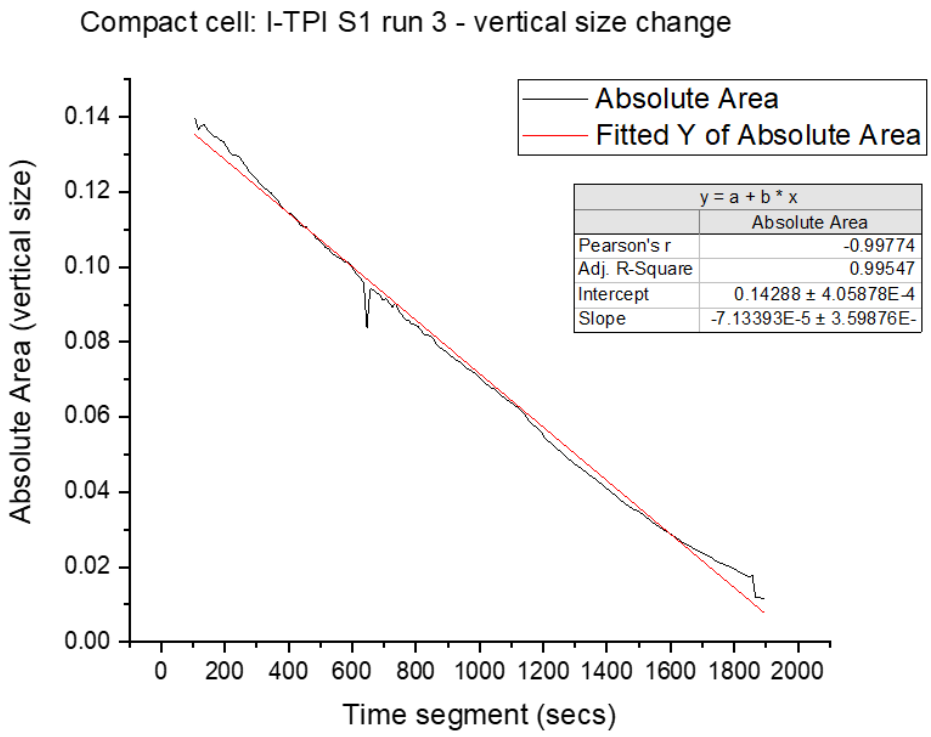

Figure 5.143 – I-TPI Form SI (run 3) vertical size change as measured through visible absorbance, with line of best fit (details inset).

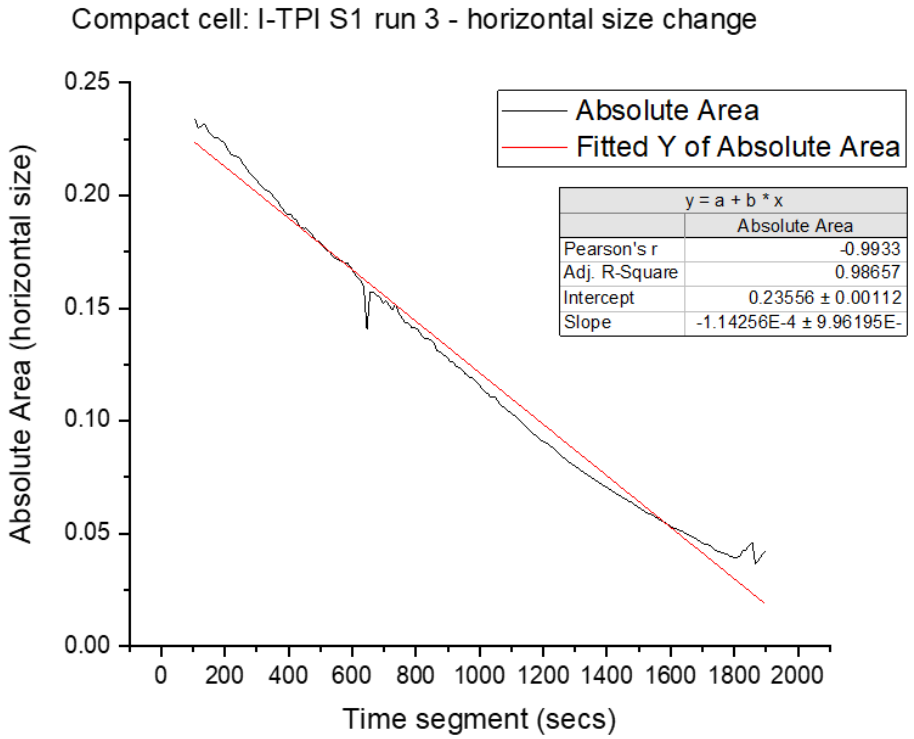

Figure 5.144 – I-TPI Form SI (run 3) horizontal size change as measured through visible absorbance, with line of best fit (details inset).

These four manual zones provide a relatively simple method for assessing and reporting size changes throughout dissolution for single crystals and some gel samples. The relative stability of each form of I-TPI can be explained using these size changes, with the gel reporting the fastest size change, Form SII reporting a more gradual size change and the Form SI profile suggesting an erosion mechanism, thereby highlighting a slower rate of dissolution due to a relatively lower solubility (greater stability). There are significant limitations, however, as the zones are influenced by the presence of the wire, and also any movement of the sample relative to the cell. To address the challenge of the wire, and also to enable the UV absorbance to be correlated with the visible absorbance, image analysis software was explored.

5.4.4 Utilising image analysis software

a) Image resolution:

Resolution in the previous work was defined as the maximum number of line pairs per mm (lp/mm) that could be resolved by eye. Visual observations of each grid confirmed that individual lines can be seen and differentiated down to the 30 grid in the horizontal direction, see Figure 5.145. The 40 grid enables horizontal, vertical and diagonal lines to be differentiated easily, whereas the 20 grid shows a lack of differentiation between lines in all three boxes and suggests that resolution at this level of detail is not possible to carry out by eye.

Figure 5.145 – Absorbance maps using visible wavelength (520 nm) and shown in jet colour map for (a) grid 20, (b) grid 30 and (c) grid 40.

This agrees with Professor Østergaard's findings for the previous version of this technology (the SDI), which confirmed resolution was between 12.5 (horizontal) and 16.7 (vertical) lp/mm and relates to grids of 40 and 30 µm respectively.[169] There is scope, however, to applying image analysis software and further improve resolution capabilities by relying upon the pixel resolution. Furthermore, the novel ability of the SDi2 to monitor two wavelengths simultaneously offers the advantage that the UV and visible images can be combined to infer a more detailed understanding of each.

The SDi2 manual reports a resolution of 13.75 μm^2 for the SDi2, based upon the theoretical effective pixel size of 2048 x 2048 (for the full imaging area of 28 cm x 28 cm). Image analysis software has been utilised to determine whether absorbance values can be obtained per 13.75 μm^2 area, or if resolution remains limited by the SDi2 Analysis software (13.75 µm x 20 µm) due to its data extraction methods. This will provide confidence in the reporting of size changes using image analysis techniques.

The CFC was used and each grid placed flat against the CMOS camera chip. The monitoring zones were excluded and the data for each wavelength was extracted to a

movie in the ".wmv" format using the jet colour map and at x 1 speed resulting in two videos (one for each wavelength monitored), each at 0.5 frames per second and with a total of 591 frames. The two videos were able to be analysed with MATLAB and a series of images extracted: one image for each grid for each wavelength, see Table 5.17.

Table 5.17 - Relation of video frame number (both UV and Vis) to grid size.

Grid size	Frame number
400	24
300	56
200	92
100	120
90	148
80	180
70	232
60	284
50	332
40	360
30	416
20	464
10	504

The SDi2 software allows the videos and therefore images to be extracted using a range of colour maps – the jet colour map was the default recommended by Pion at the time of training, and also appears the most frequently in discussions of SDI research, hence it was also used in this work. The CFC images theoretically map absorbance units per 13.75 μm^2 pixel within the cell, and include a default summary in the top left corner in addition to an absorbance key on the right hand side of the image, but do not include the x or z axes to provide relative dimensions.

Each image is in the format of 372 (height) x 1636 (width) x 3 uint8 (data type). The height and width refer to the number of pixels in each dimension, which is not comparable with the CFC width of 28 mm relating to 2048 pixels as described in the

manual.[168] The data type "3 uint8" means an unsigned (u) integer (int) with 8-bits of information (8). This refers to the three channels (R, G and B), where the value of each is a positive integer between 0 and 255, as represented by an 8-bit array. It can also be described as a "true colour" image referring to the fact that each pixel intensity is represented as a triplet of RGB values, or it can be considered an m-by-n-by-3 numeric array. The jet colour map encompasses 256 different "colours" using the three channels (RGB) to represent an absorbance range from 0 to 2,000 mAU.

Analysis of the visible absorbance maps will be discussed, with the aim of finding a method to analyse the original jet colour map image so that the grids can be routinely detected by the imaging software thus enabling resolution to be defined. The absorbance map for the visible wavelength and 400 grid is shown again in Figure 5.146 to provide context for the next steps.

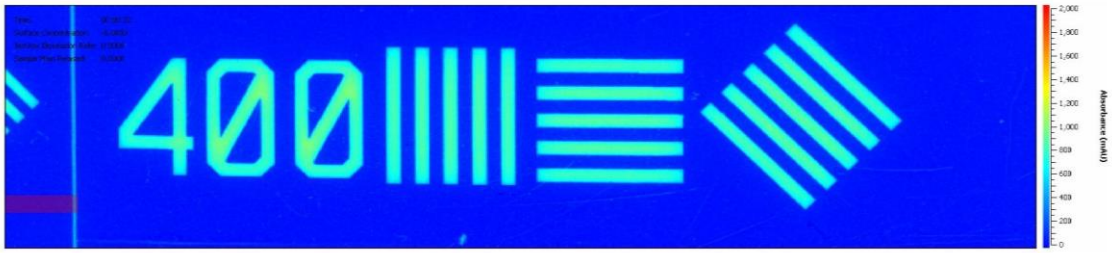

Figure 5.146 – Absorbance map using visible wavelength (520 nm) and the 400 grid. Shown in jet colour map and extracted from frame 24 of 591. Three distinct parts can be seen in the image: 1) 400 to show grid number, 2) vertical lines to test horizontal resolution, 3) horizontal lines to test vertical resolution and 4) diagonal lines for completeness.

MATLAB enables the colour image to be converted either to a grey scale image using the functionality [rgb2gray], see Figure 5.147, or to a black and white image using either its red, green or blue component. The grey scale function produces an m-by-n numeric array with the elements specifying intensity values ranging from 0 to 255, and the black and white or binary function produces an m-by-n logical array, with values of either 0 or 1. The green component was found to produce an image with clearer definition than the blue or red channels, see Figure 5.148.

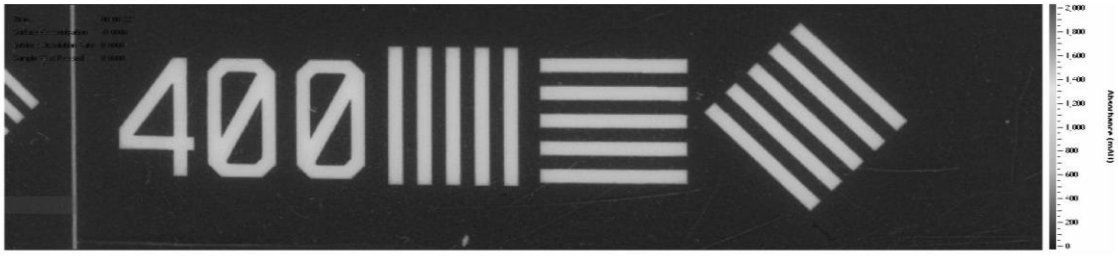

Figure 5.147 – Absorbance map using visible wavelength (520 nm) and the 400 grid. Converted from jet to grey colour map and extracted from frame 24 of 591.

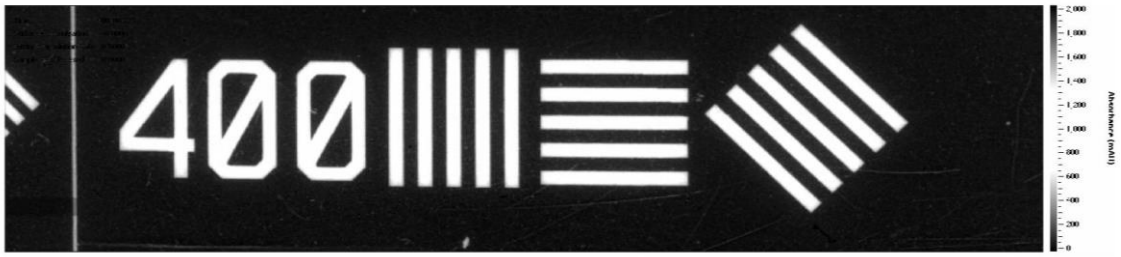

Figure 5.148 – Absorbance map using visible wavelength (520 nm) and 400 grid. Converted from Jet colour map to grey scale using the green component of the colour image only. Extracted from frame 24 of 591.

The grey scale image in Figure 5.148 can subsequently be converted to a black and white image using the threshold function, which provides a greater degree of control than converting directly via a single channel, however it can only be applied to a grey scale image and not to a full colour image. A threshold of 10/255 gives a poorly defined representation of the image, see Figure 5.149, and a threshold of 245/255 provides a clearer image but removes some of the detail at the edges, see Figure 5.150.

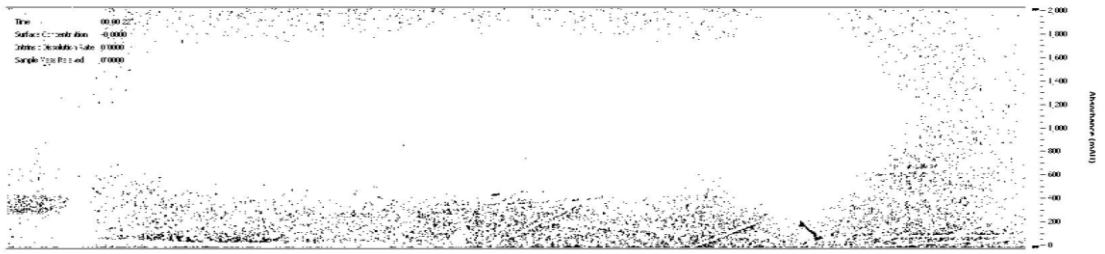

Figure 5.149 - Absorbance map using visible wavelength (520 nm) and 400 grid. Converted from Jet colour map to grey scale and then to black and white with a threshold of 10/255. Extracted from frame 24 of 591.

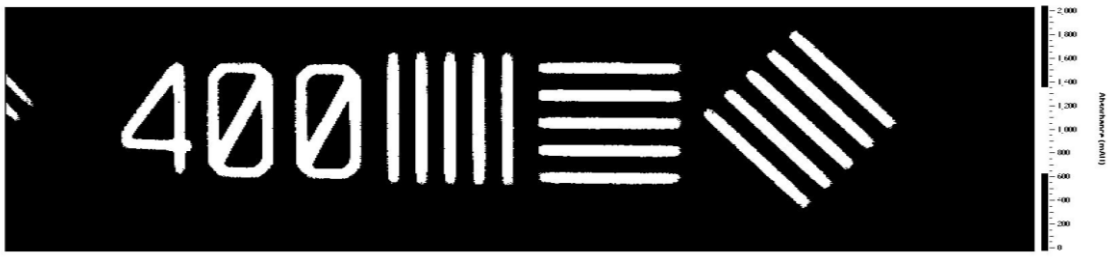

Figure 5.150 - Absorbance map using visible wavelength (520 nm) and 400 grid. Converted from Jet colour map to grey scale and then to black and white with a threshold of 245/255. Extracted from frame 24 of 591 using MATLAB.

Manual visual examination of the figure "4" on the grid, using both the original colour image and the grey scale image, suggests that a threshold of 100/255 is most appropriate for converting from grey scale to black and white whilst retaining detail, see Figure 5.151.

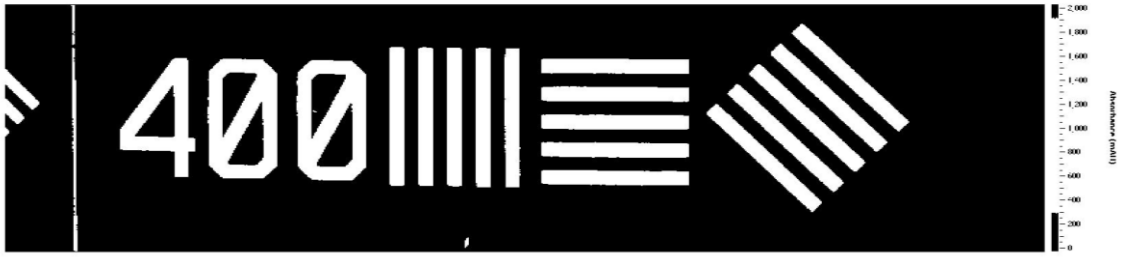

Figure 5.151 – Absorbance map using visible wavelength (520 nm) and 400 grid. Converted from Jet colour map to grey scale and then to black and white with a threshold of 100/255. Extracted from frame 24 of 591.

The same procedure was applied to the absorbance map or image of the 40 grid, see Figure 5.152. This image was then fused with the original image to confirm that this black and white version is representative of the original, see Figure 5.153. The images overlap well and there is little discrepancy between edges suggesting the 100/255 threshold is a good option for the next step, which is to apply a function to detect the edges of the image.

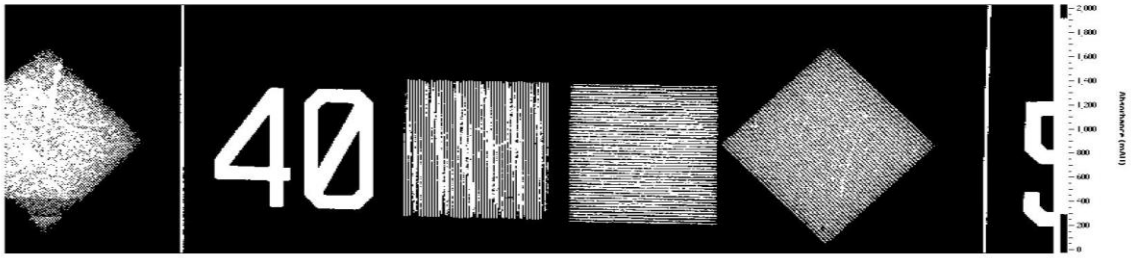

Figure 5.152 – Absorbance map using visible wavelength (520 nm) and 40 grid. Converted from Jet colour map to grey scale and then to black and white with a threshold of 100/255. Extracted from frame 360 of 591.

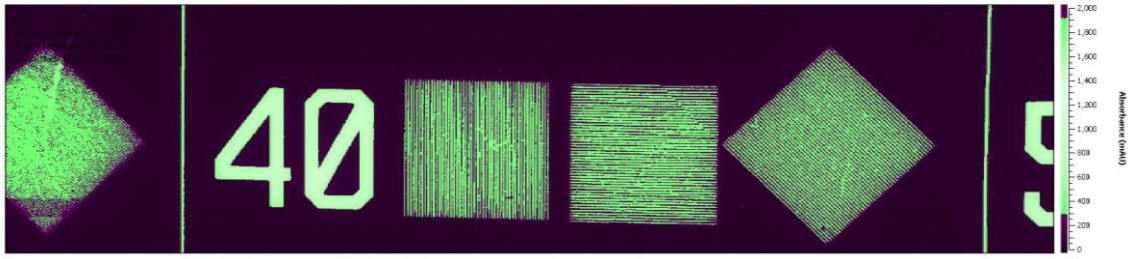

Figure 5.153 - Absorbance map using visible wavelength (520 nm) and 40 grid. Converted from Jet colour map to grey scale and then to black and white with a threshold of 100/255 fused with original Jet colour map image. Extracted from frame 360 of 591.

The edge functionality can only be applied to grey images, black and white images or images using a single component of RGB. There are three main options currently on MATLAB for this: 1) edge, 2) canny, and 3) prewitt. The black and white images with a threshold of 100/255 produce the clearest edges for all three options, see Figure 5.154, Figure 5.155 and Figure 5.156, although the canny function maintains the best image overall for the 40 grid, see Figure 5.155.

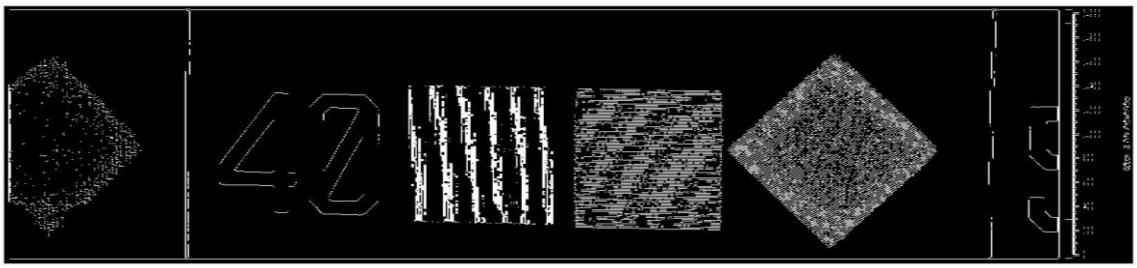

Figure 5.154 – Absorbance map using visible wavelength (520 nm) and 40 grid. Converted from Jet colour map to grey scale to black and white with a threshold of 100/255 and the edge function applied. Extracted from frame 360 of 591.

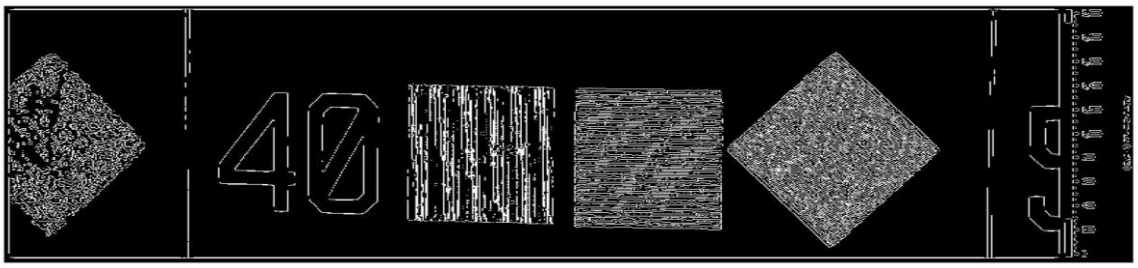

Figure 5.155 – Absorbance map using visible wavelength (520 nm) and 40 grid. Converted from Jet colour map to grey scale to black and white with a threshold of 100/255 and the canny edge function applied. Extracted from frame 360 of 591.

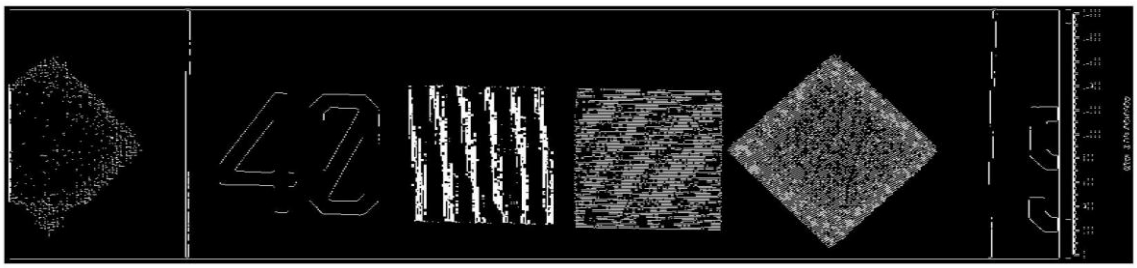

Figure 5.156 – Absorbance map using visible wavelength (520 nm) and 40 grid. Converted from Jet colour map to grey scale to black and white with a threshold of 100/255 and the prewitt edge function applied. Extracted from frame 360 of 591.

Alternatively, as mentioned previously, the video can be extracted directly from the SDi2 using a grey colour map instead of the jet colour map, see Figure 5.157. Unfortunately the reported images are still in the "372 x 1636 x 3 uint8" format, which means the data is represented by an m-by-n-by-3 numeric array. The image first has to be converted to an m-by-n array before the canny edge function can be applied.

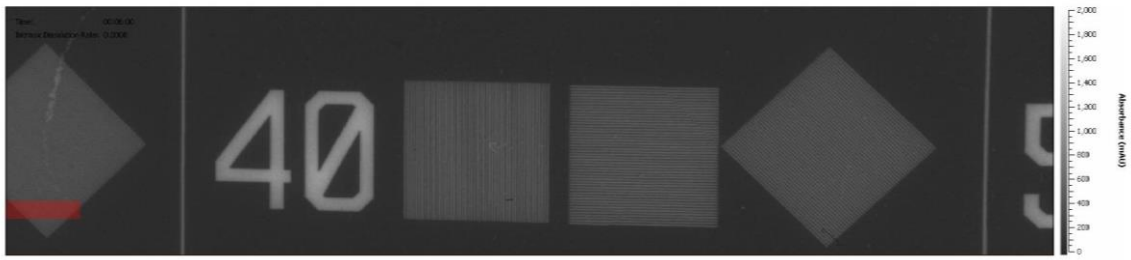

Figure 5.157 – Image extracted from SDi2 as a grey colour map video using visible wavelength and 40 grid. Extracted from frame 360 of 591.

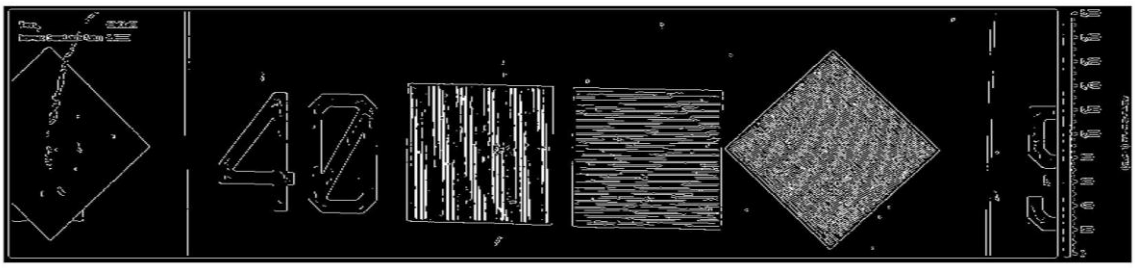

Figure 5.158 – Image extracted from SDi2 as a grey colour map video showing visible wavelength and 40 grid. The true colour image has been converted to grey scale image with the canny edge function applied using MATLAB. Extracted from frame 360 of 591.

Alternatively the original image can be converted to a black and white image using the threshold value. A manual examination of a range of threshold values results in 75/255 being selected, which then allows the canny edge function to be applied, see Figure 5.159.

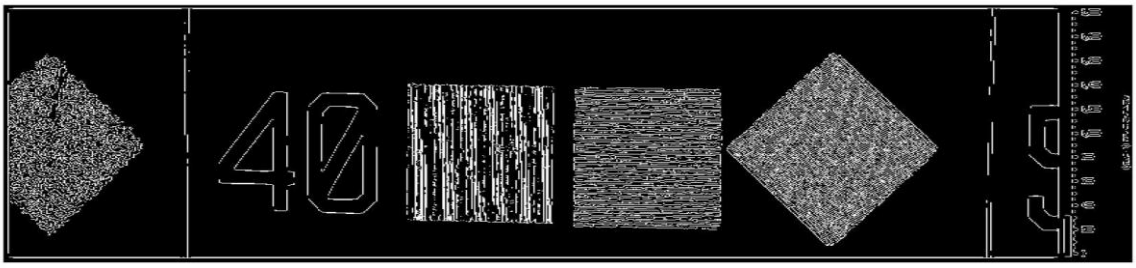

Figure 5.159 – Image extracted from SDi2 as a grey colour map video showing visible wavelength and 40 grid. The true colour image has been converted to a black and white image using a threshold of 75/255 before the canny edge function has been applied. Extracted from frame 360 of 591.

A comparison of Figure 5.155 and Figure 5.159 highlight a greater loss of detail with the latter image than the former, suggesting that resolution may be lost using this method, and confirming that extracting the SDi2 videos using the jet colour map is appropriate. Extracting using the grey colour map saves a small amount of memory, but does not enable a step to be skipped, and in both cases conversion to an m-by-n array is necessary (either through grey scale function or black and white threshold function in MATLAB) prior to being able to apply any of the edge functionalities. The recommendation would be to continue to use the jet colour map.

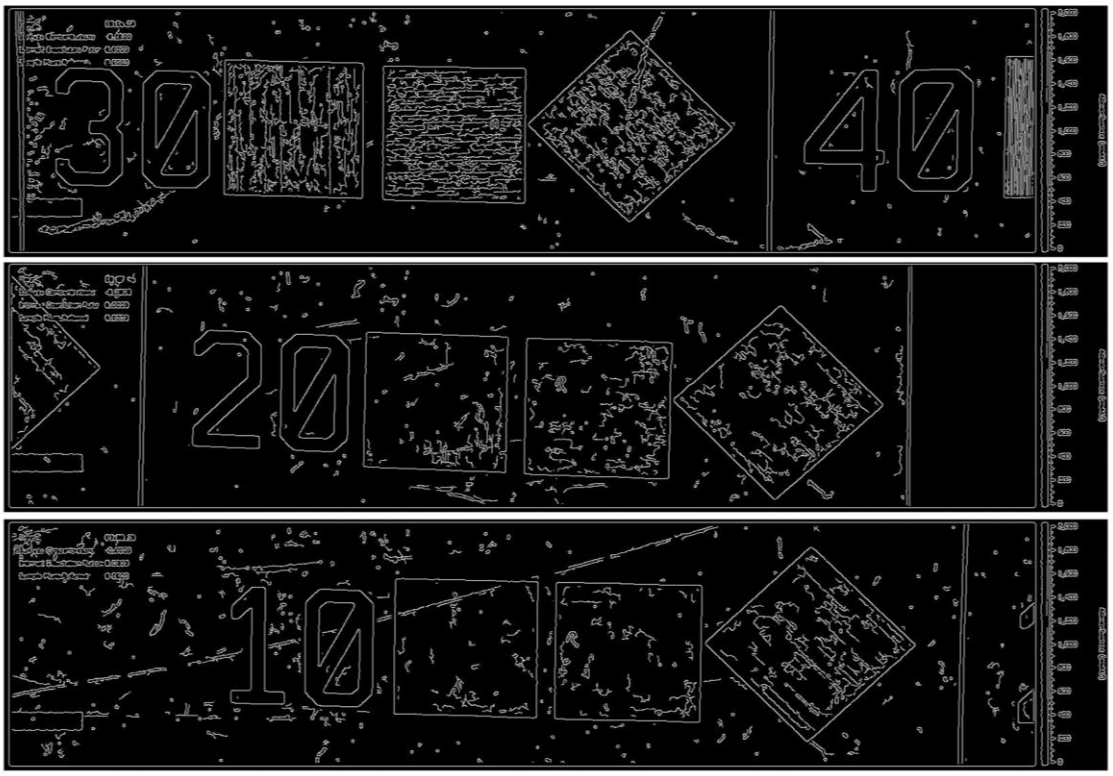

Figure 5.160 – Original images extracted from SDi2 as a jet colour map video showing visible wavelength and 10, 20 or 30 grids. The true colour images have been converted to a black and white image using a threshold of 75/255 before the canny edge function has been applied.

A suggested method for first extracting an image involves using the jet colour map, converting to grey scale, applying a threshold function (70/255 and 100/255 work for the grids) and then a canny edge function – this appears to be sufficiently robust to capture the majority of detail. However, there does not appear to be any improvement in resolution as a result and the previously reported resolution of 12.5 horizontal and 16.7 (vertical) lp/mm (relating to grids 40 and 30 µm respectively) remains most appropriate, see Figure 5.160. The aim to define a method of MATLAB image analysis for consistently identifying the grids has therefore been achieved, although it appears that a degree of subjectivity is required to define thresholds, and that these are likely to vary between images.

b) Correlating UV and visible absorbance data:

A significant limitation of historical work[216] was image interpretation due to the single wavelength imaging capability of the previous instruments (D100, SDI 300 and SDI) resulting in challenges when understanding whether a high absorbance (of UV

wavelength) was due to a high concentration of sample dissolved or something physically blocking the light path.[13] The SDi2 capability of visualising dissolution with both a UV and a visible wavelength should provide the opportunity to unravel this mystery. The image shown in Figure 5.161 shows a single crystal of paracetamol held on a steel wire loop with deionised water flowing from left to right through the cell. The image on the left shows UV absorbance (280 nm) and image on the right shows visible absorbance (520 nm), with manual zones positioned in exactly the same defined x and z positions for both.

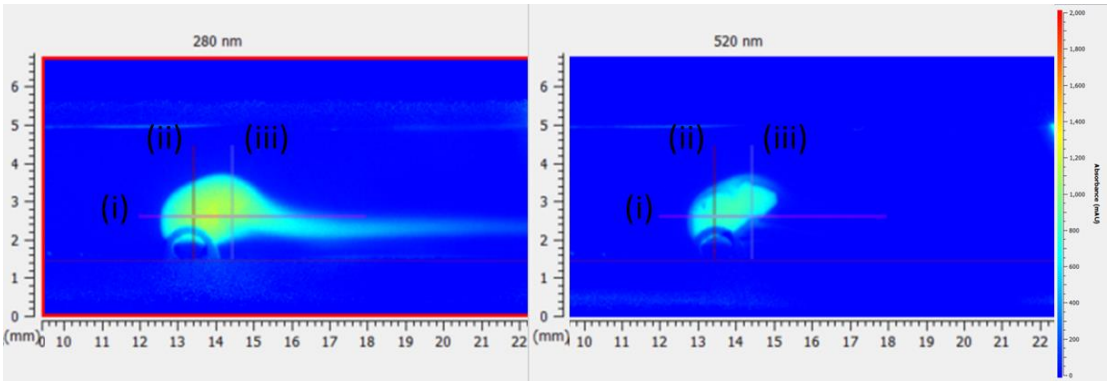

Figure 5.161 – SDi2 compact flow cell image at 280 nm (left) and 520 nm (right) showing a paracetamol crystal held on a steel wire loop and deionised water flowing from left to right through the cell. The absorbance key using the jet colour map is shown to the far right. Both images are from the start of dissolution (image number 53). The three additional zones to measure concentration can be seen horizontally (i) and vertically (ii) and (iii) across the crystal for both wavelengths. The images have been cropped in the x dimension to focus on the crystal and zones.

The 280 nm image clearly shows a trail of increased absorbance to the right of the crystal which is missing from the 520 nm image, confirming that it is indeed dissolved paracetamol rather than anything physically present in the light path. The crystal can be seen clearly in the 520 nm image due to the increased absorbance, although there are sections along the top where the edges are less well defined and may represent the transition between solid and solution, which is referred to as the boundary layer. Determining the edge of the crystal and the boundary layer for the 280 nm image would enable surface concentrations and gradients to be calculated, which could provide insight into the differences between crystal faces. The ability to correlate the UV image with the Vis image would make this possible.

The wire crystal holder can be seen in both images and was left in place for the initial run to obtain background absorbance so the baseline absorbance for that section of the image already accounts for it - it is therefore subtracted from further absorbance values. Looking closely at the images and using PowerPoint gridlines to compare positions, the position of the wire relative to the zones is not the same for the 280 and 520 images, see Figure 5.162.

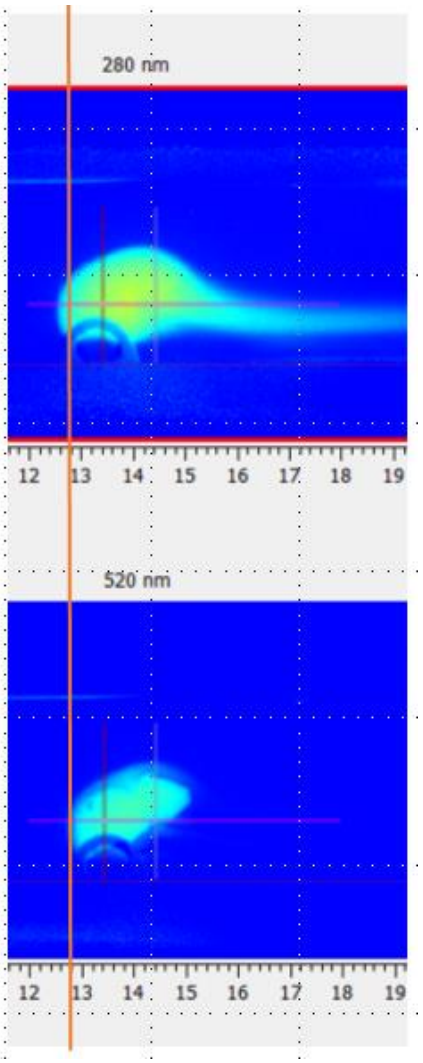

Figure 5.162 – SDi2 compact flow cell image at 280 nm (top) and 520 nm (bottom) showing a paracetamol crystal held on a steel wire loop and deionised water flowing from left to right through the cell. Both images have been cropped and are from the start of dissolution (image number 53). Three additional zones to measure concentration can be seen across the crystal for both wavelengths and an additional orange reference point has been placed in the same position across both images using gridlines to highlight the misalignment.

This is a crude way of visualising the misalignment, which could be more accurately observed with image analysis software. The misalignment is likely a parallax effect due

to the position of the LEDs side-by-side highlights that correlating UV and Vis absorbance remains a challenge, even with the dual wavelength capability of the new instrumentation. It is most easily observed using image analysis software, MATLAB, see Figure 5.163. In this figure a UV image and a visible image (taken from the same time point during dissolution) are presented; the two images have also been fused together using MATLAB with false colouring applied to highlight in green and purple the areas where the two images differ. The plume of dissolving crystal is highlighted in green, as expected because it is not present on the visible image. However, the position of the wire in the horizontal can also be seen to differ between the two images, suggesting the images cannot simply be overlaid to distinguish between solid and dissolving material.

It was found that applying a horizontal displacement of [7, 0] to one of the images enabled the UV and visible images to then be fused together successfully, see Figure 5.164. This suggests that a parallax effect (as discussed previously) is likely to be taking place and should be accounted for when comparing absorbance values, per x dimension, for different wavelengths. As an interesting aside, during the grid analysis work, a UV image was obtained and fused with a visible image, see Figure 5.165, and in this instance there was no misalignment. The difference between images is the absence of the full CFC and the start-up procedure. The start-up procedure for the SDi2 usually involves placing the CFC in front of the detector (in its usual position) and filling it with blank solvent to provide a background absorbance reading per pixel. This initial background reference cannot be removed, but it can be manipulated to take place without the cell in position, so that the background does not include the CFC or blank solvent, as was the case for the grid experiments.

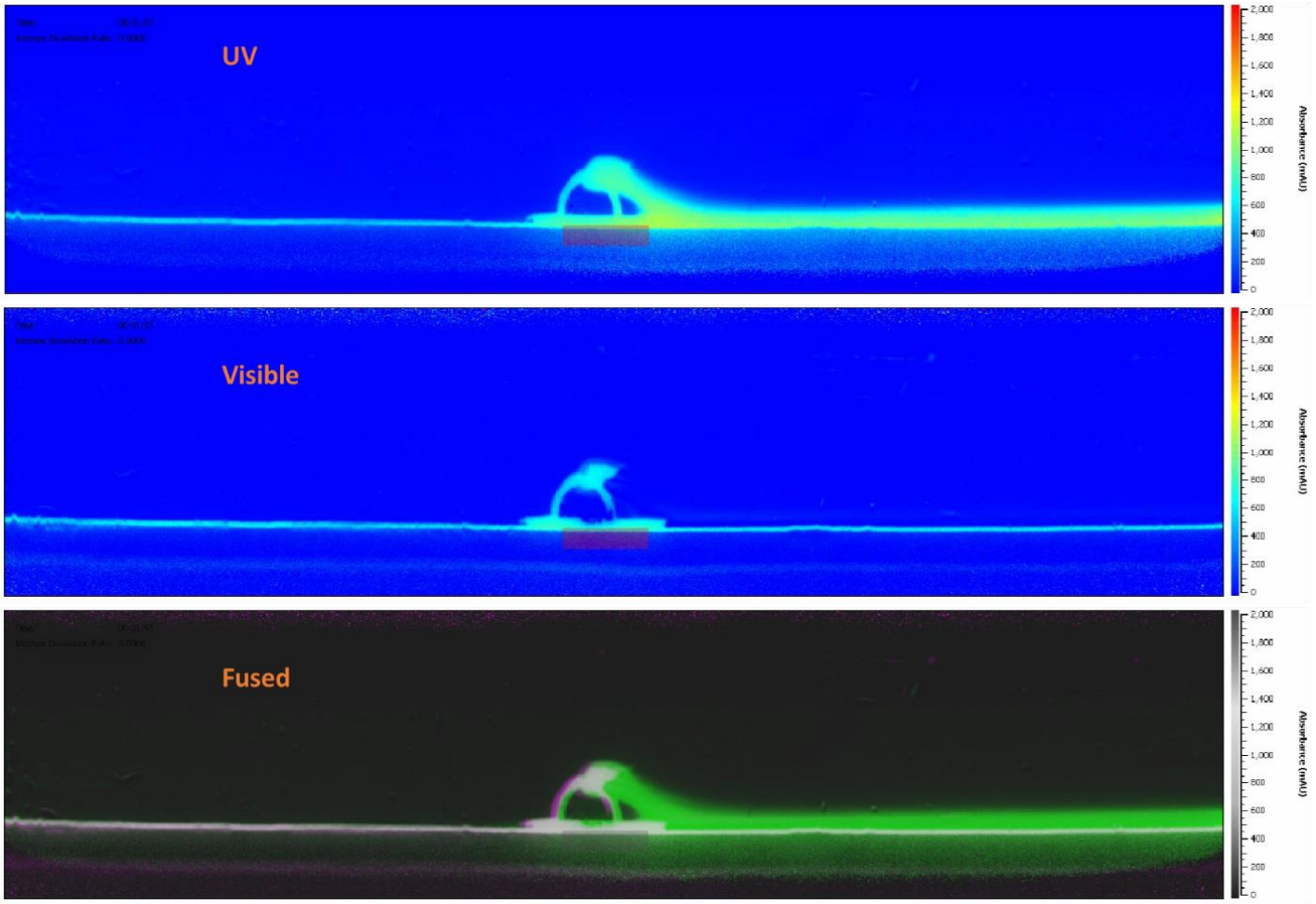

Figure 5.163 - Image of single crystal on wire in compact flow cell filled with solvent. The top image shows the UV absorbance, the middle image shows the visible absorbance and the bottom image utilises MATLAB to fuse them together.

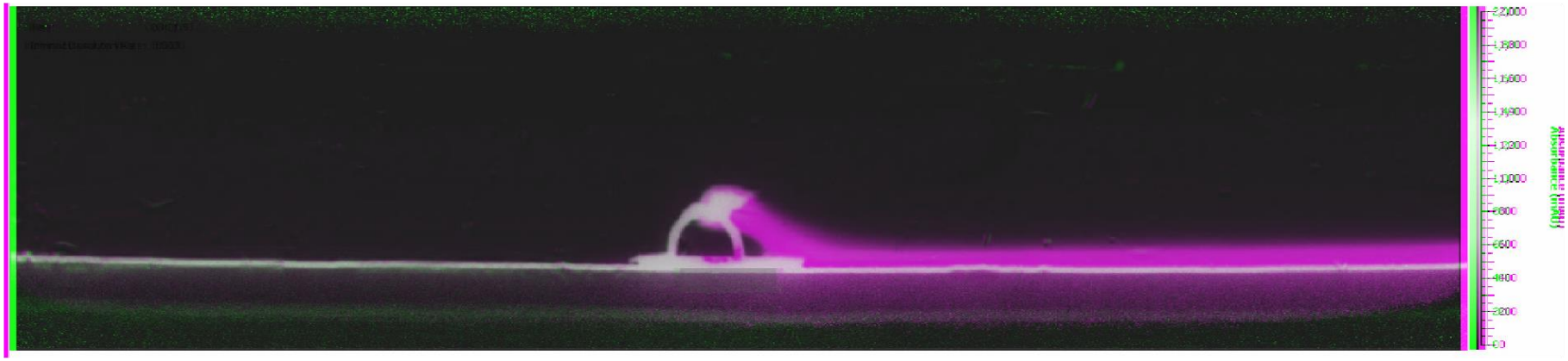

Figure 5.164 – Fused (UV and visible) and horizontally translated (displacement of [7, 0]) image of a single crystal on wire in the compact flow cell filled with solvent.

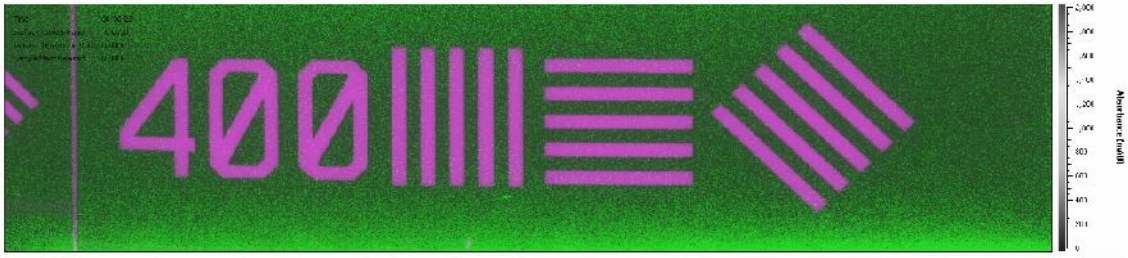

Figure 5.165 - Fused UV and visible images from resolution work using the grids.

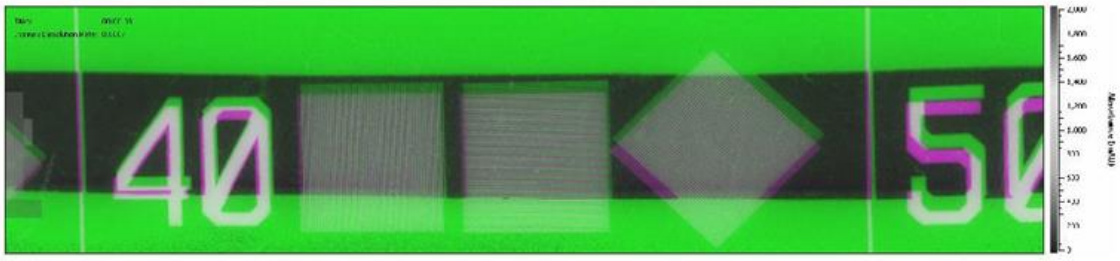

Figure 5.166 – Two visible images fused: one with cell full of deionised water and positioned in front of grid, and the other with the cell removed. Both images involved a start-up procedure with the cell in place and full of deionised water.

Figure 5.166 shows two visible images fused, both of which included a start-up procedure with a cell full of deionised water, one image includes the cell in position (in front of the grid) and the other did not. The fused image uses false colour again to highlight differences between the original images, and confirms both a horizontal and vertical shift, despite both being images using the visible wavelength, confirming that the presence of the full flow cell has a significant effect. This work highlights the importance of continuity during analysis, for example, ensuring the blank solvent and flow cell is in place during the start-up procedure if they are to be used during the analysis, and vice versa.

c) Monitoring size and concentration changes:

The work exploring MATLAB as a means to measure size changes during dissolution was carried out in collaboration with Dr Daniel Markl at the University of Strathclyde. Dr Markl has extensive experience with MATLAB and was able to write a series of algorithms to guide the software to report size changes and also concentration changes from the SDi2 visible absorbance and UV absorbance videos, respectively. The original code is provided in Appendix 1 – MATLAB original script with comments, with additional comments to explain each section's purpose. The code required manual

adjustments and modifications for each data set to accommodate the type of sample being analysed. Support in adjusting the algorithms came initially from Dr Markl and later also from Dr Weinzierl. The results are presented here with some detail of the challenges that were involved and a brief explanation of the method.

The MATLAB script uses both the UV and visible SDi2 videos, which are essentially a series of images taken throughout dissolution at a frame rate of one per second per wavelength. For example, a dissolution run of sixty seconds would result in thirty UV absorbance images, or frames, and thirty visible wavelength images. The reporting of data for each wavelength using this MATLAB script has not accounted for this, so the time scale is half the length it should be. It is easily adjusted, but running a MATLAB script requires hours and an extensive memory, hence the runs were not repeated but this should be considered for future work.

The MATLAB script was designed to report four outputs for each sample analysed: crystal perimeter, length of crystal, crystal area and UV absorbance at crystal edge. The I-TPI Form SI data is presented here first, as this is the simplest to explain and will subsequently aid understanding of the Form SII and the gel data. Each plot is produced in MATLAB, but the data has been extracted from only the SDi2 images (videos) and four manually-determined parameters. The first is the starting frame for dissolution to be calculated from (startID), and the second is the image region of interest (img_ROI), which incorporates the whole sample with as little wire as possible; this is the section that the image analysis software then uses. The threshold function described previously is also used to define the crystal edge (bw_threshold) and a displacement value is used to accommodate the shift between UV and visible images (x_displ) using the wire to line up the images. Resolution of the images is defined as 13.75 μm^2 in line with Pion's suggestion and the jet colour map is used with a maximum absorbance of 2 AU.

I-TPI Form SI:

The crystal perimeter plot in Figure 5.168 utilises a threshold value of 70/255 to find the edge of the crystal and was found by manually assessing the images using MATLAB, see Figure 5.167.

Figure 5.167 - Example of the impact of threshold function values upon a single crystal mounted on wire.

The script then applies this threshold throughout dissolution to measure the length around the crystal. The perimeter for Form SI run 1 decreases throughout dissolution, and reduces more rapidly as dissolution progresses. This plot implies that the crystal is fully dissolved by approximately 25 minutes (12.5 x 2, to accommodate the time adjustment), which fits with viewing the videos.

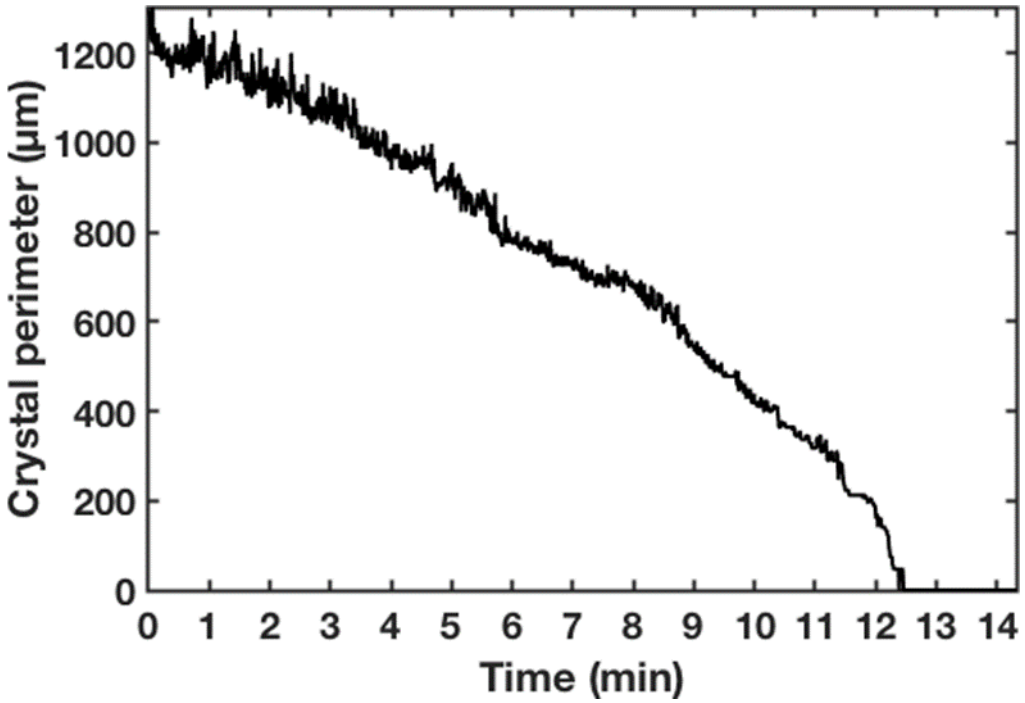

Figure 5.168 - I-TPI Form SI (run 1) crystal perimeter plot.

The crystal length plot in Figure 5.169 and the crystal area plot in Figure 5.170, utilise the same defined threshold value. The length of the crystal is reported in terms of its major axis and minor axis, dependent upon size, but both of which can be seen to reduce throughout dissolution although at different rates. The crystal area can also be seen to reduce, as would be expected, and declines linearly; this would lend itself to a

line of best fit, but the data is reported as a .pdf file, although raw data may be extracted using some extra coding within the script.

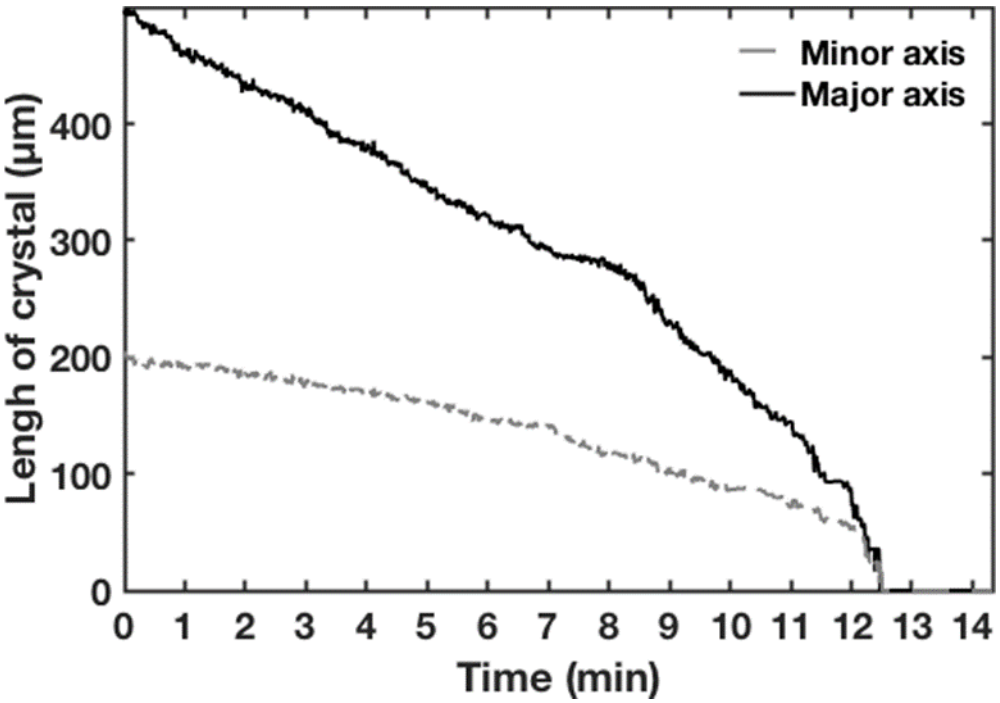

Figure 5.169 - I-TPI Form SI (run 1) length of crystal plot.

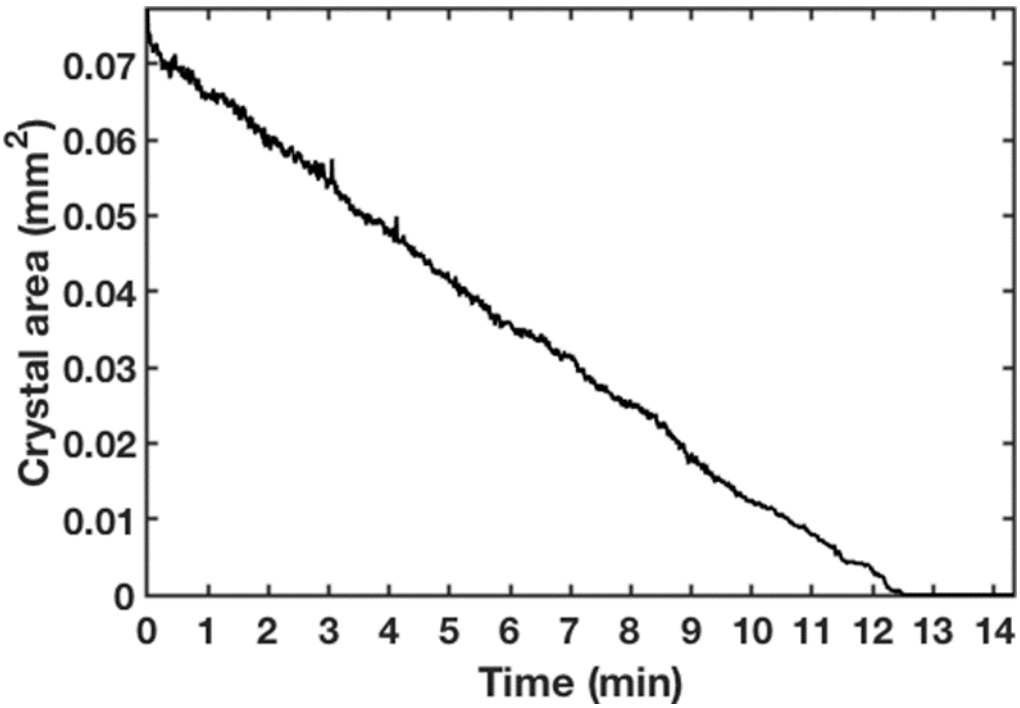

Figure 5.170 - I-TPI Form SI (run 1) crystal area plot.

Finally, the plot of UV absorbance at the crystal edge in Figure 5.171 also shows a reduction throughout dissolution. This plot is produced by selecting the region of

interest for both the UV and visible images, then manually ensuring that they can be lined up correctly using the image translate function – the position of the wire can be used to aid this. An absorbance is then assigned per pixel of the UV image using the defined colour map around the perimeter of the crystal. There is error involved in the assignment of absorbance based upon the colour map, hence standard deviation is calculated and plotted to accommodate this.

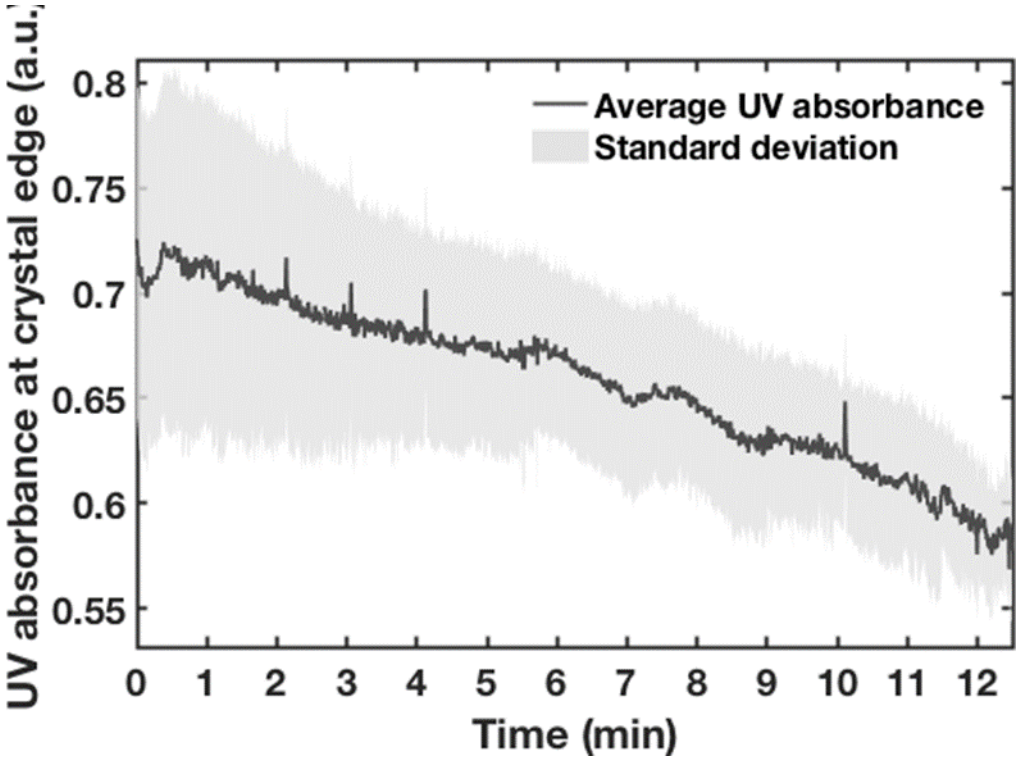

Figure 5.171 - I-TPI Form SI (run 1) UV absorbance (AU) at crystal edge plot.

The same procedure was followed for the I-TPI Form SI run 3 videos, with initial work carried out as described to define the manual parameters such as StartID and x_displ. All four plots show a reduction in either perimeter, length, area or UV absorbance throughout dissolution, see Figure 5.172, Figure 5.173, Figure 5.174 and Figure 5.175, respectively. This is the same data that was previously analysed using the SDi2 software, hence they can be compared directly. The crystal perimeter, length and area show linear plots in line with the previous data (see Figure 5.141, Figure 5.142, Figure 5.143 and Figure 5.144) and all sets of data confirm the crystal was fully dissolved by 30 minutes. The MATLAB data allows discussion about the size and dimensions of the crystal throughout dissolution, rather than how the size changes from start to finish,

which is all that the compact flow cell data allows to be reported confidently. Finally, the UV absorbance at the crystal edge shown in Figure 5.175 fits nicely with the maximum absorbance reported at the bottom of the IDR zone (see Figure 5.136), which ranged from 0.9 to 0.5 AU. The three different methods for analysis complement each other thus offering assurances that the data is representative of the dissolution process in addition to enhancing understanding.

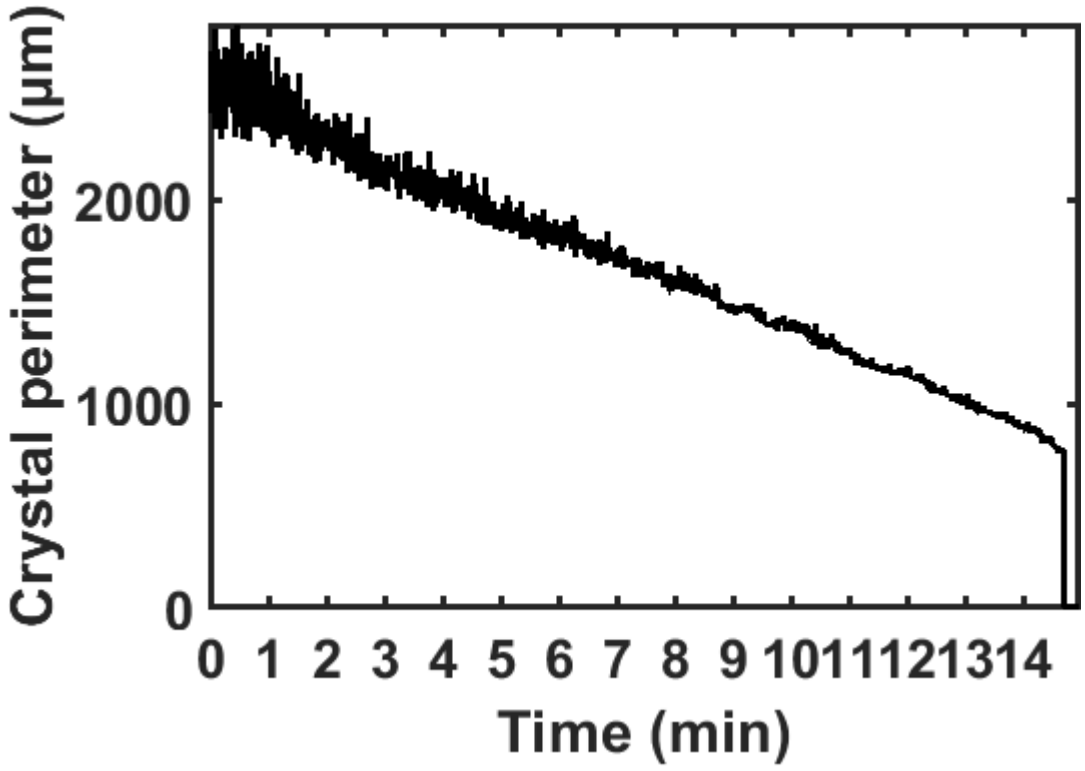

Figure 5.172 - I-TPI Form SI (run 3) crystal perimeter plot.

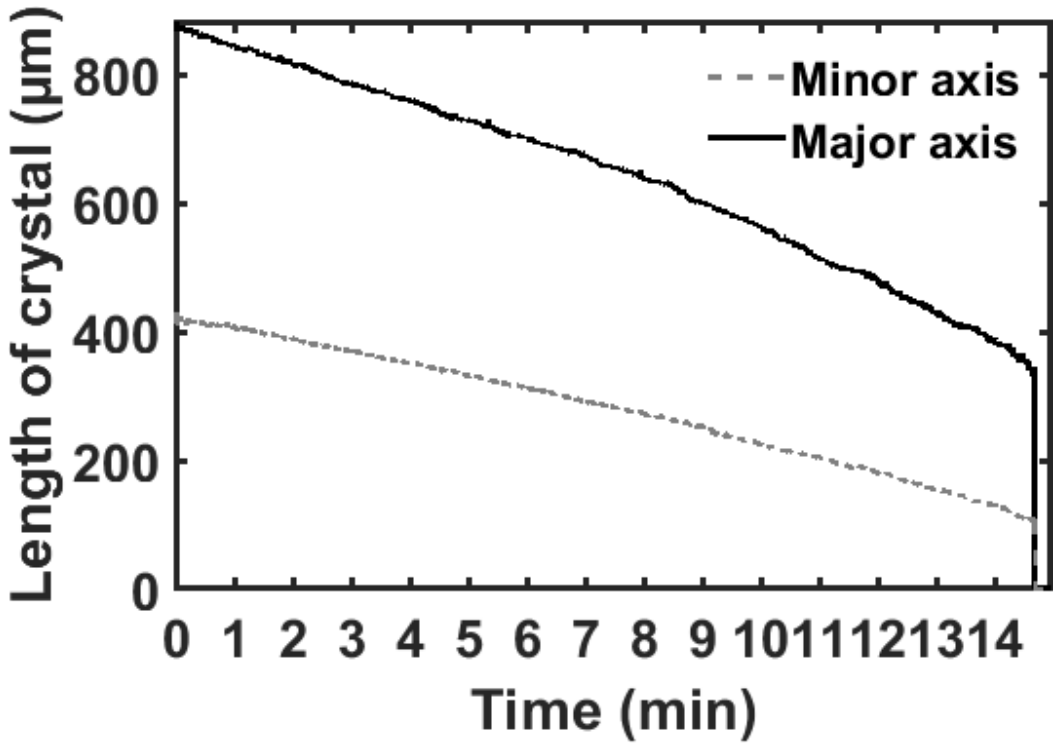

Figure 5.173 - I-TPI Form SI (run 3) length of crystal plot.

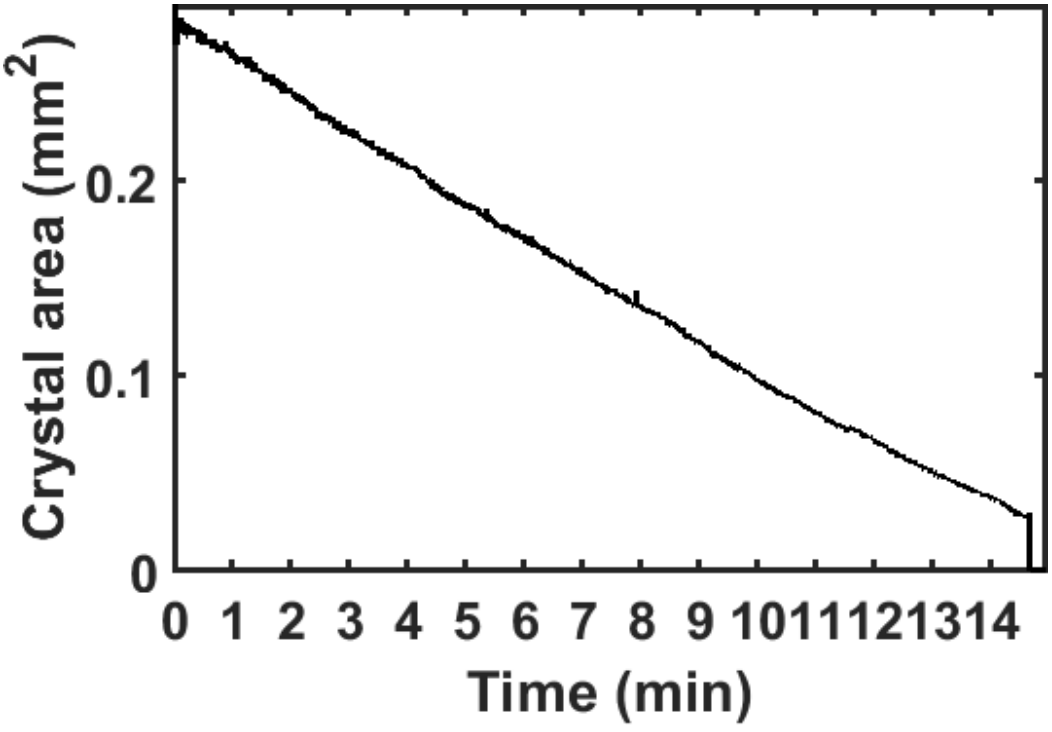

Figure 5.174 - I-TPI Form SI (run 3) crystal area plot.

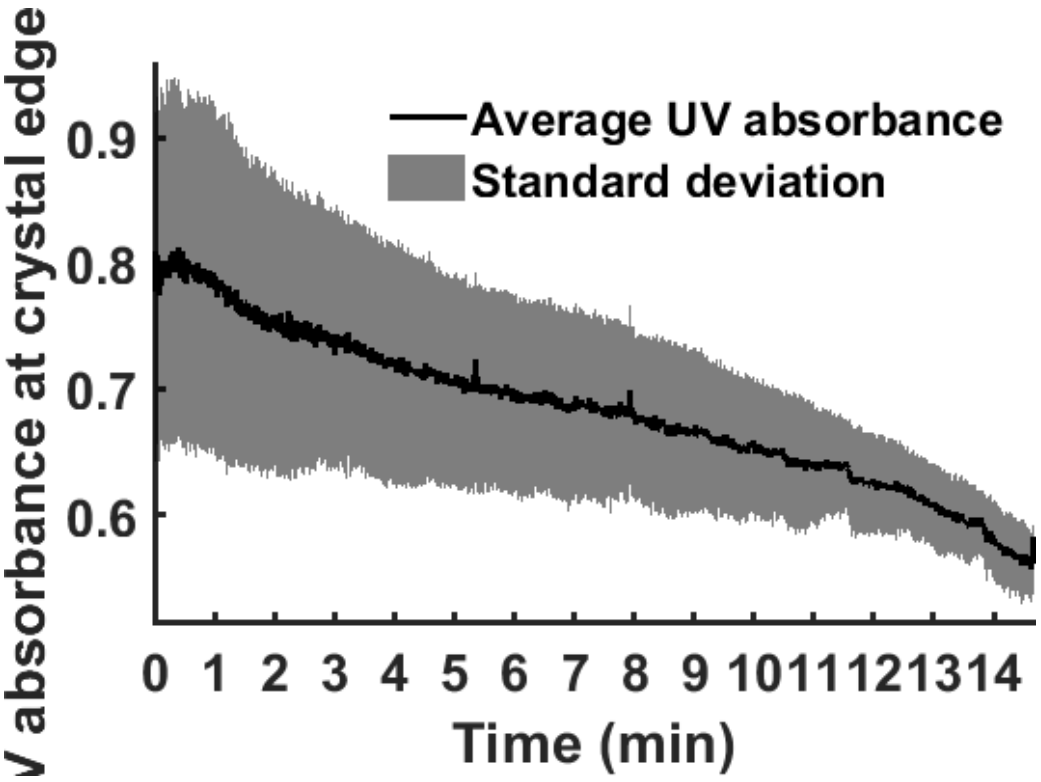

Figure 5.175 - I-TPI Form SI (run 3) UV absorbance (AU) at crystal edge plot.

I-TPI Form SII:

The process was repeated for I-TPI Form SII run 2, see Figure 5.176, Figure 5.177, Figure 5.178 and Figure 5.179 for crystal perimeter, length, area and UV absorbance at the edge, respectively. Each shows an overall reduction from start to finish of dissolution, however, the data is not as clear as with the previous plots. Analysis of this data using the SDi2 software, see Figure 5.139, suggested that there was an initial increase in crystal width in the first 6 minutes, prior to a decrease. This correlates with both the crystal perimeter and crystal length plots, see Figure 5.176 and Figure 5.177, whereby there is an initial increase, followed by a decrease with huge variation that results in the plot after six minutes appearing shaded. However, the extent of the size decrease from 6 to 30 minutes in each of the MATLAB reports does not fit with the knowledge that there is crystal remaining at the end of 30 minutes of dissolution. This can be attributed to the sample moving upwards through the cell as a result of the rubber bung shifting out of the sample holder, see Figure 5.140.

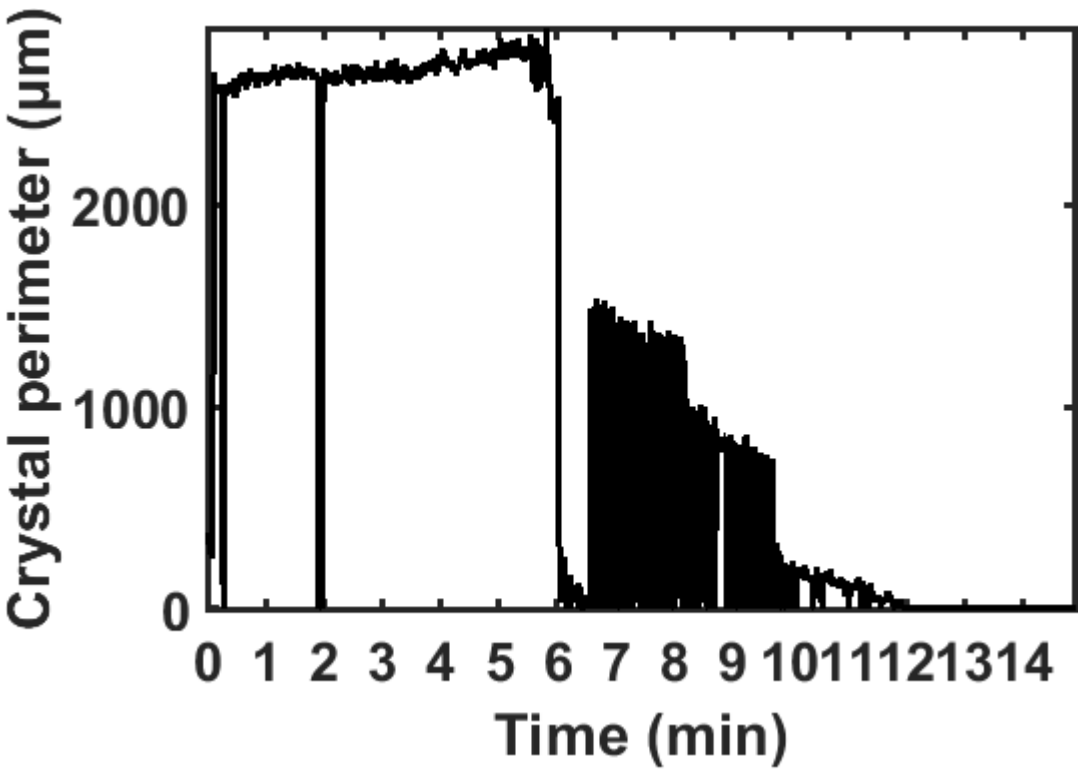

Figure 5.176 - I-TPI Form SII (run 2) crystal perimeter plot.

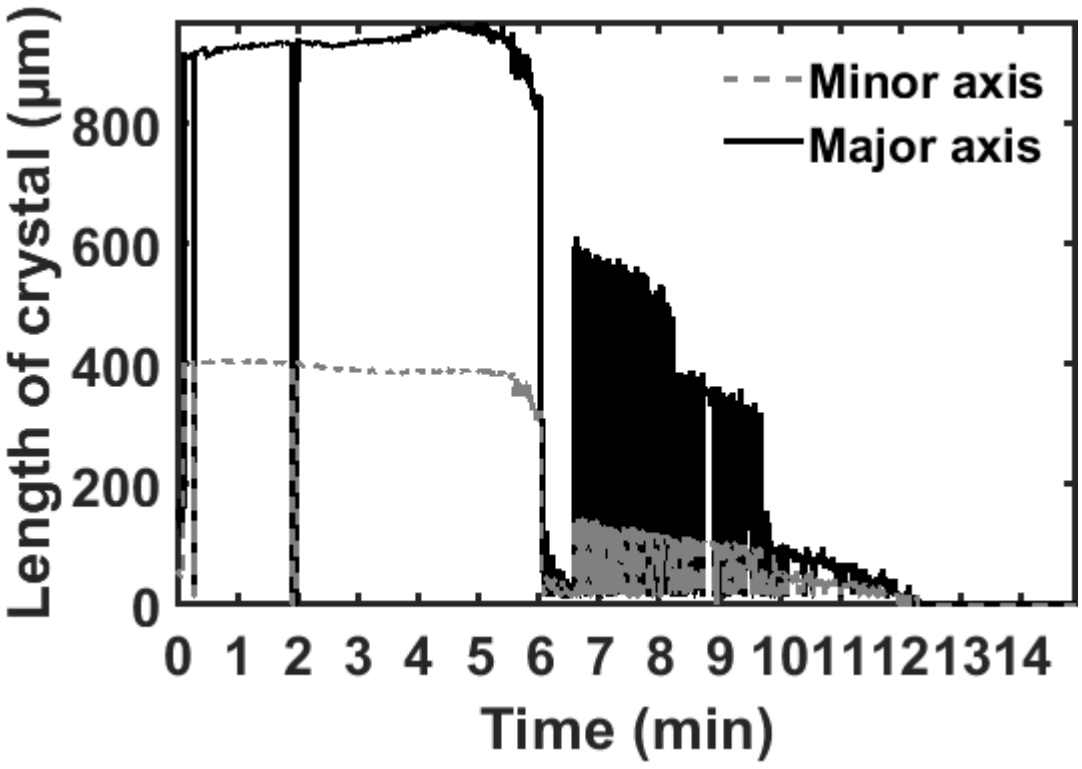

Figure 5.177 - I-TPI Form SII (run 2) length of crystal plot.

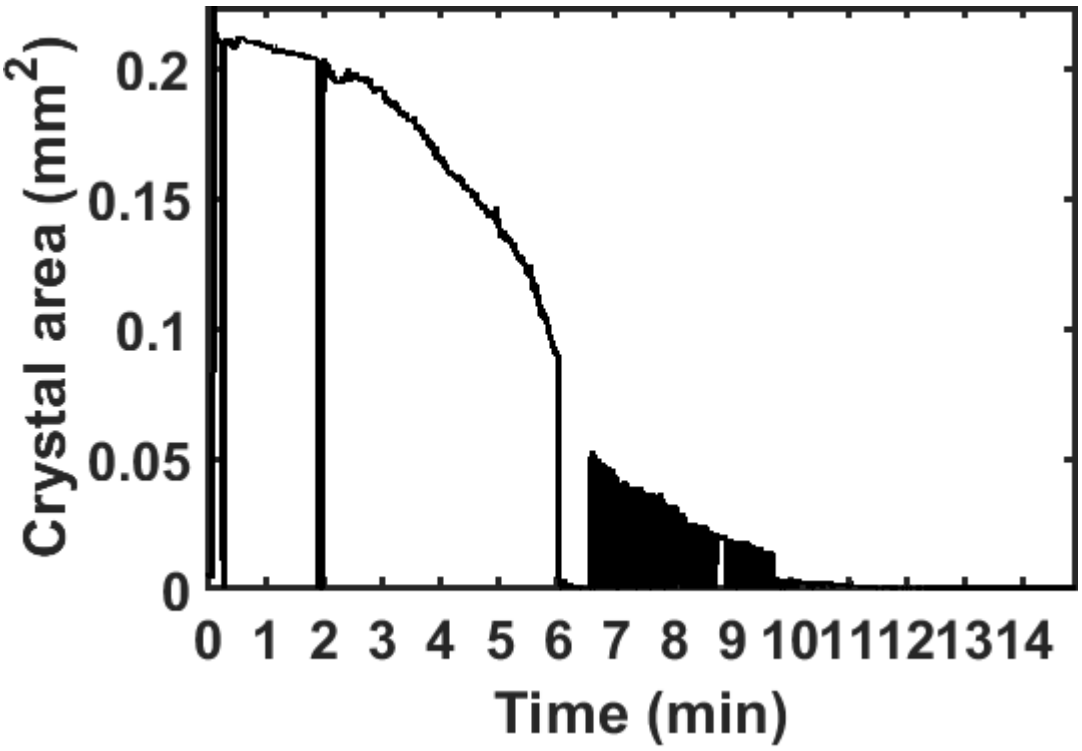

Figure 5.178 - I-TPI Form SII (run 2) crystal area plot.

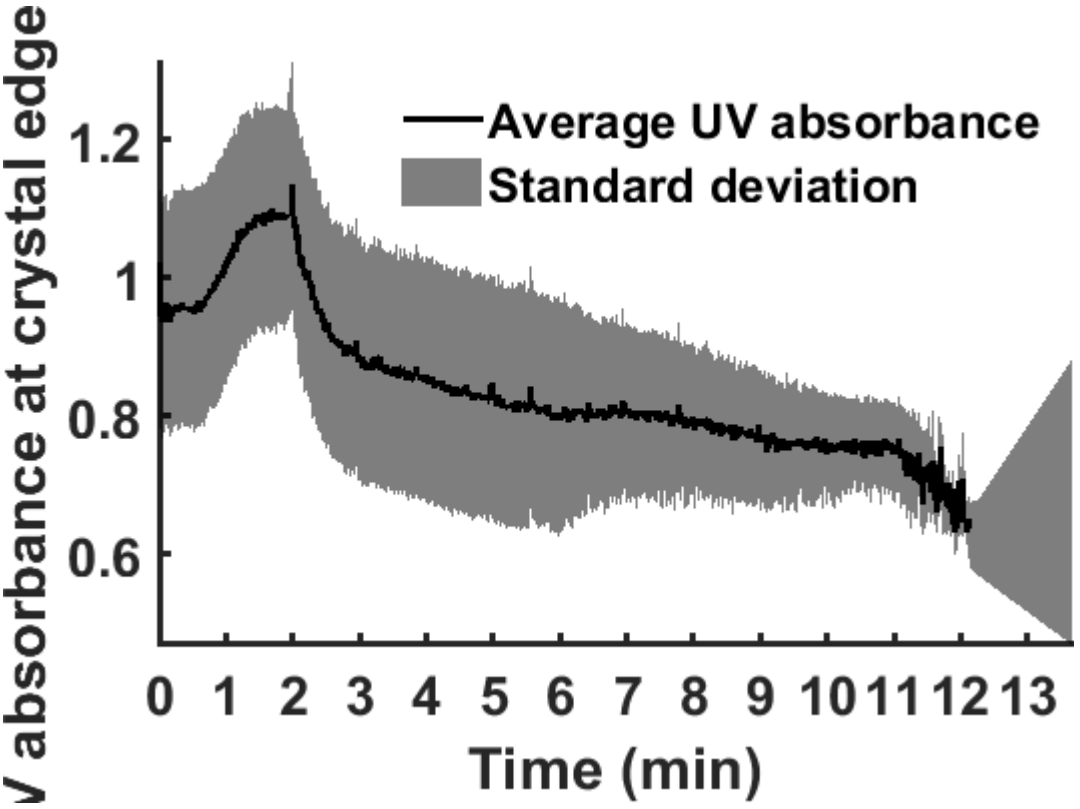

Figure 5.179 - I-TPI Form SII (run 2) UV absorbance (AU) at crystal edge plot.

Finally, the plot of UV absorbance at the crystal edge, see Figure 5.179, suggests an increase in absorbance at the start, followed by a gradual decrease. This only partly

fits with the previously reported absorbance through the bottom of the IDR zone (Figure 5.135), which reduced slightly from 1.1 to 0.95 throughout dissolution. However, the image analysis plot encounters an error at 12 mins (corresponding with 24 minutes of actual dissolution). The exact reason for this is unclear, but the absorbance values reported after 6 minutes will be altered by the movement of the bung, which will alter the position of the crystal relative to the start of dissolution, thus impacting upon the region of interest and subsequent alignment between the UV and visible images.

The I-TPI Form SII run 1 data was interrupted significantly by bubbles hence it is presented after run 2, but it provides some assurance that the first six minutes of the run 2 data is representative in its consistency, see Figure 5.180, Figure 5.181, Figure 5.182 and Figure 5.183. Crystal perimeter, length and area decline very gradually (if the noise of the bubbles is ignored) and UV absorbance also remains high between 0.8 and 1.0 AU.

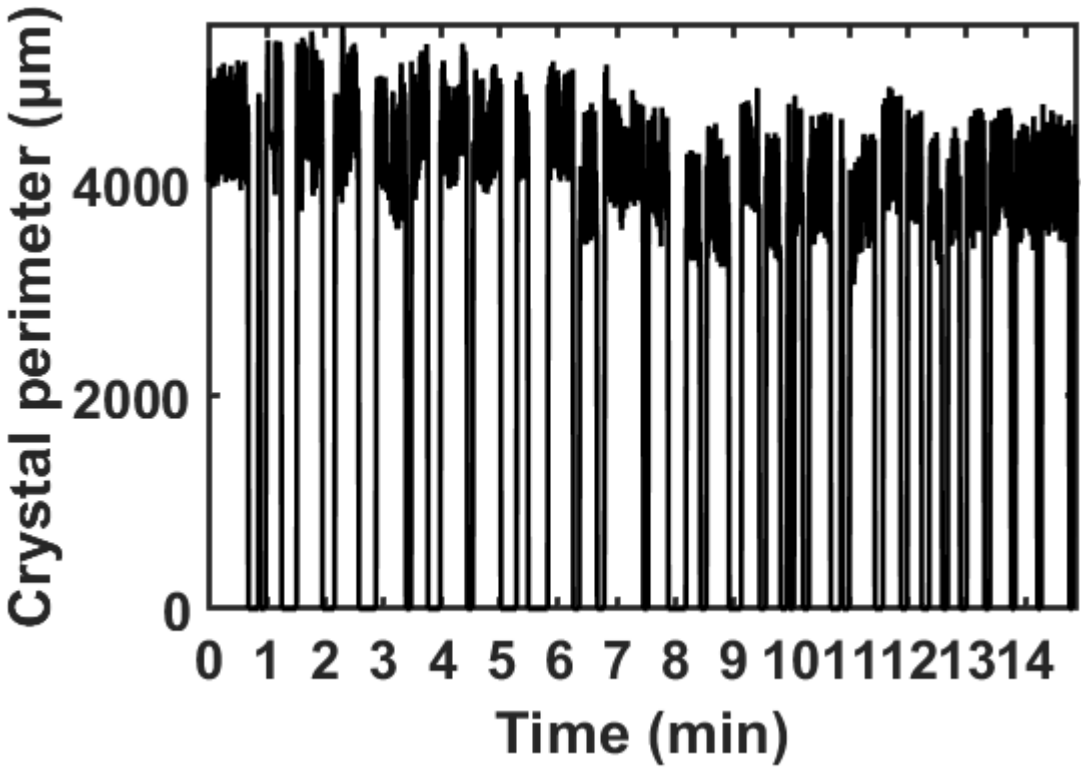

Figure 5.180 - I-TPI Form SII (run 1) crystal perimeter plot.

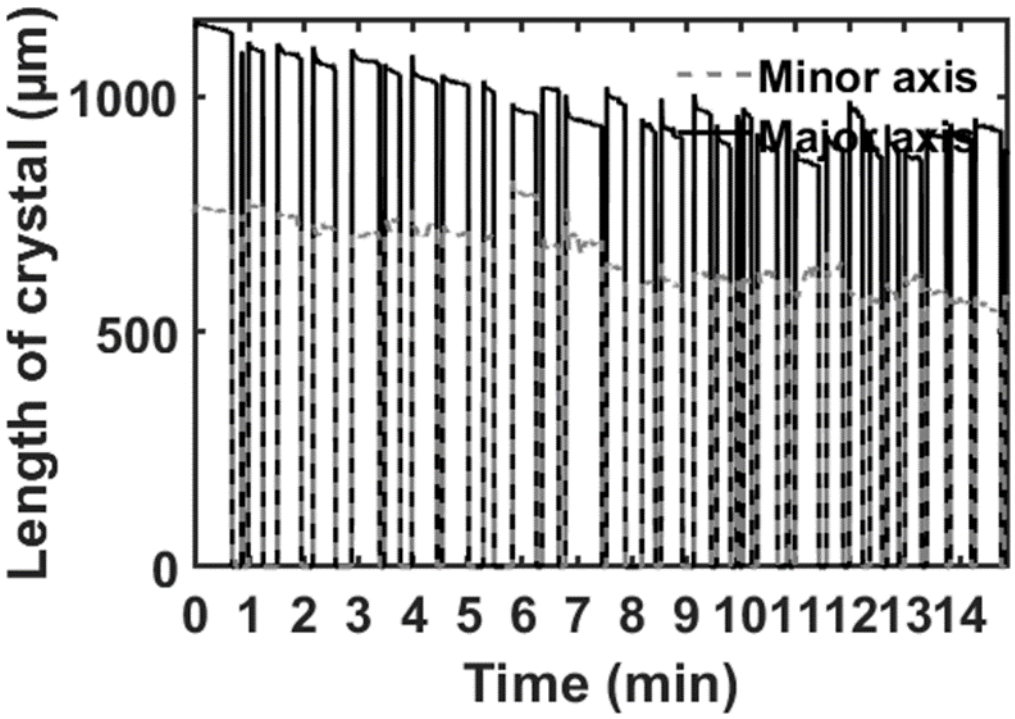

Figure 5.181 - I-TPI Form SII (run 1) length of crystal plot.

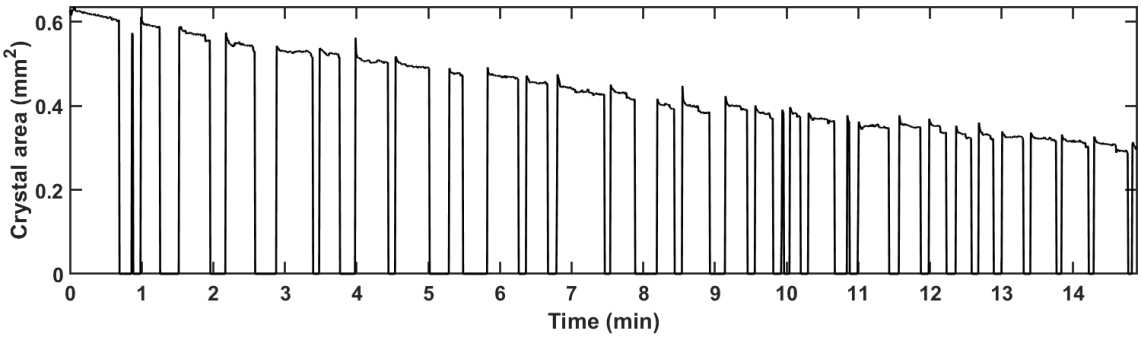

Figure 5.182 - I-TPI Form SII (run 1) crystal area plot.

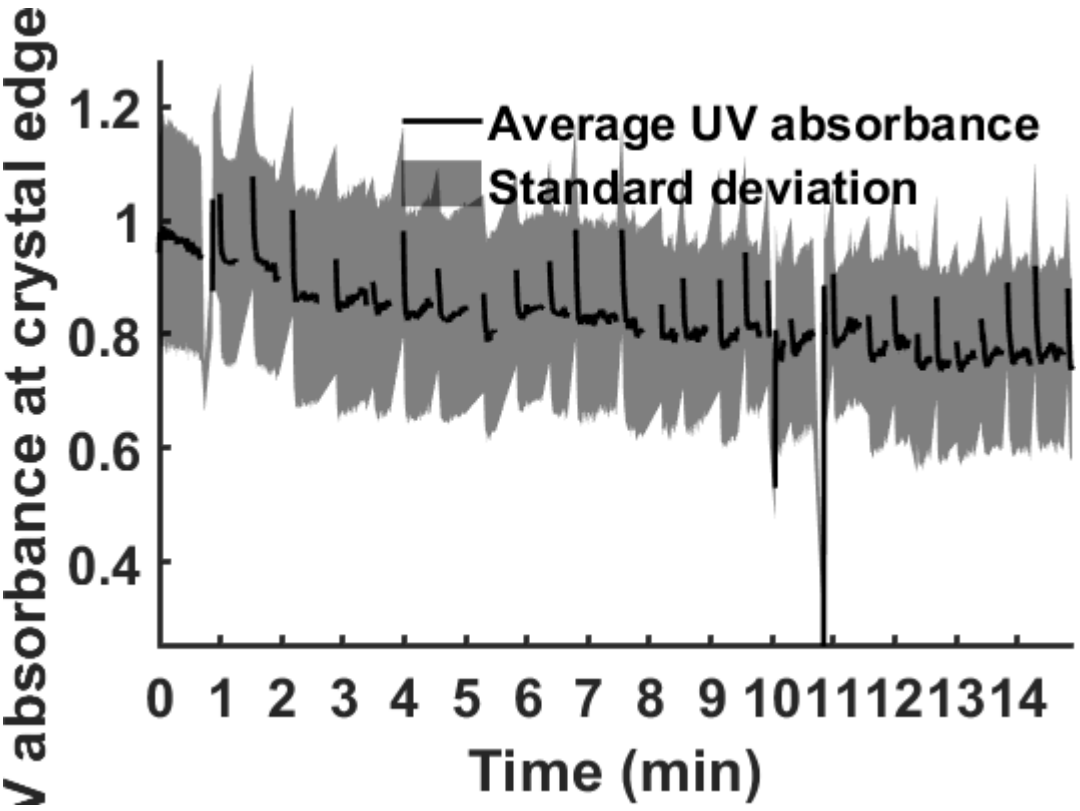

Figure 5.183 - I-TPI Form SII (run 1) UV absorbance (AU) at crystal edge plot.

I-TPI gel:

The MATLAB analysis of the I-TPI gel (run 1) can be found in Figure 5.184, Figure 5.185, Figure 5.186 and Figure 5.187. The sample is referred to as a crystal in the plot titles, but this is the result of a typographical error in the code, thus perimeter, length, area and edge actually refer to the gel. Defining the threshold for the gel was more challenging than for the previous crystals, particularly due to it falling from the wire and therefore moving out of the region of interest in the first three minutes. The region of interest could be expanded to include its new position, but this resulted in the wire being included in the size change calculations. The 50/255 threshold was the most effective at defining the gel edge, however, the plots show a rapid reduction in size in addition to some variation. This is likely due to a combination of factors including the transparency of the gel, its inability to remain in the same position on top of the wire, and its more malleable shape relative to the crystals. The uncertainty with the gel size ultimately impacts upon the reported UV absorbance, due to the edge being defined by the threshold and the algorithm, hence it is hard to draw any comparisons between this and the IDR zone absorbance reported previously in Figure

5.134. The reported UV absorbance does decrease slightly overall, but remains high between 0.8 and 1.0. It can also be correlated with reported changes in length – the increase in UV absorbance between 2 and 3 minutes (4 and 6 minutes using real dissolution time) corresponds to a decrease in length in both the major axis and minor axis.

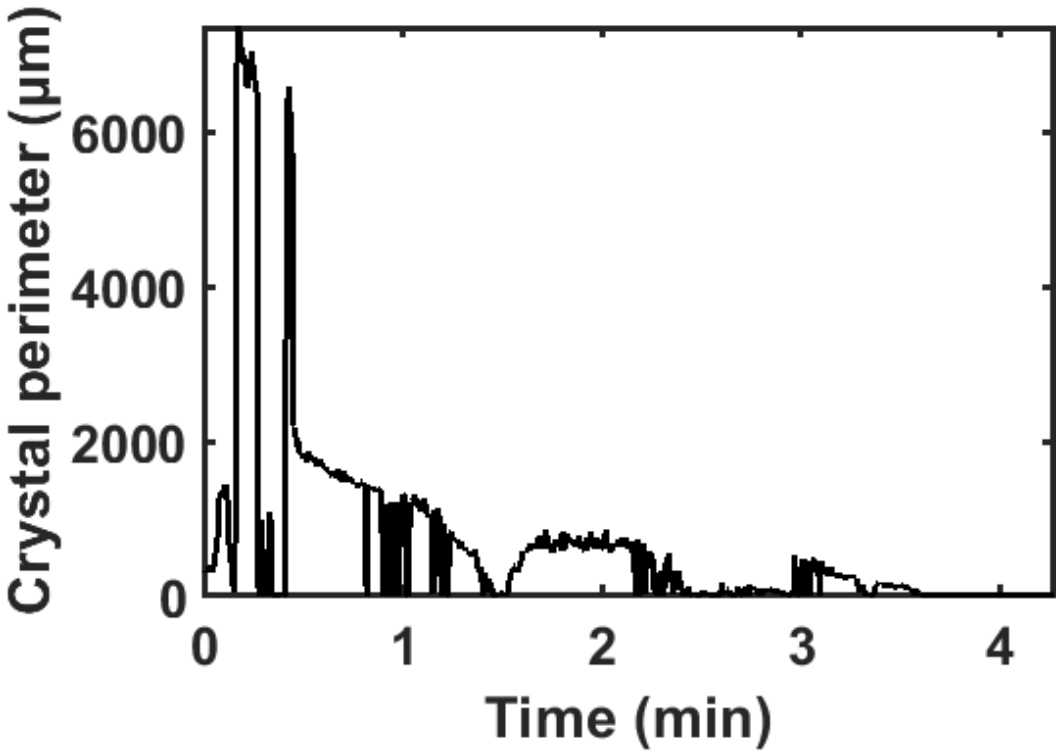

Figure 5.184 - I-TPI gel (run 1) gel ("crystal") perimeter plot.

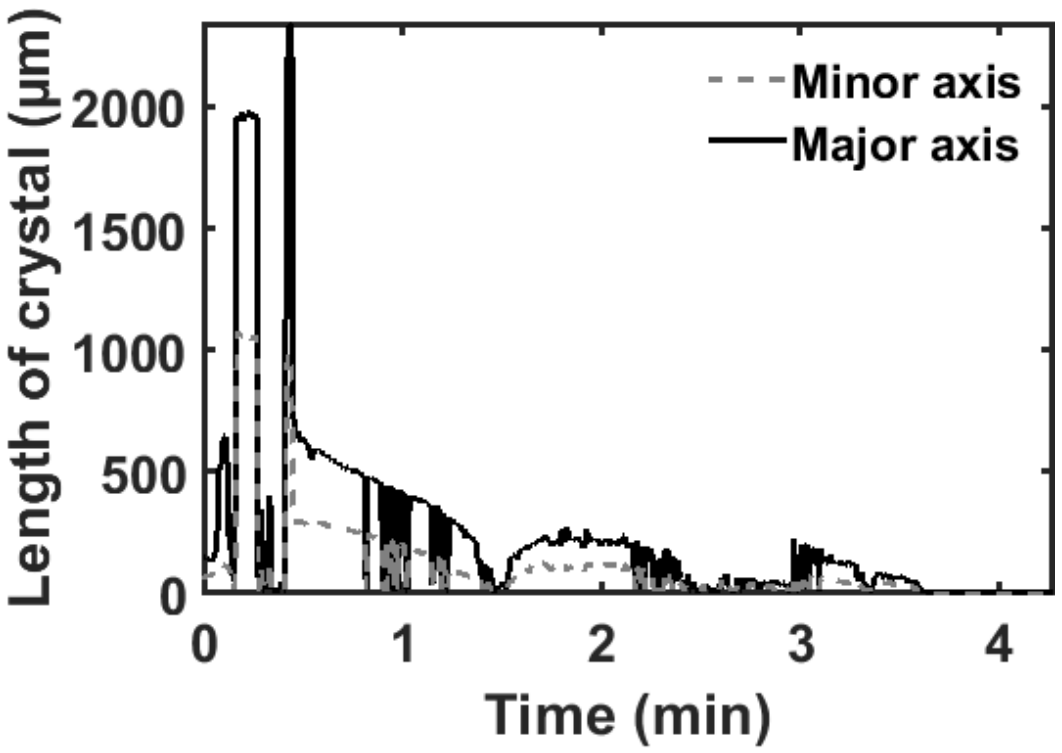

Figure 5.185 - I-TPI gel (run 1) length of gel ("crystal") plot.

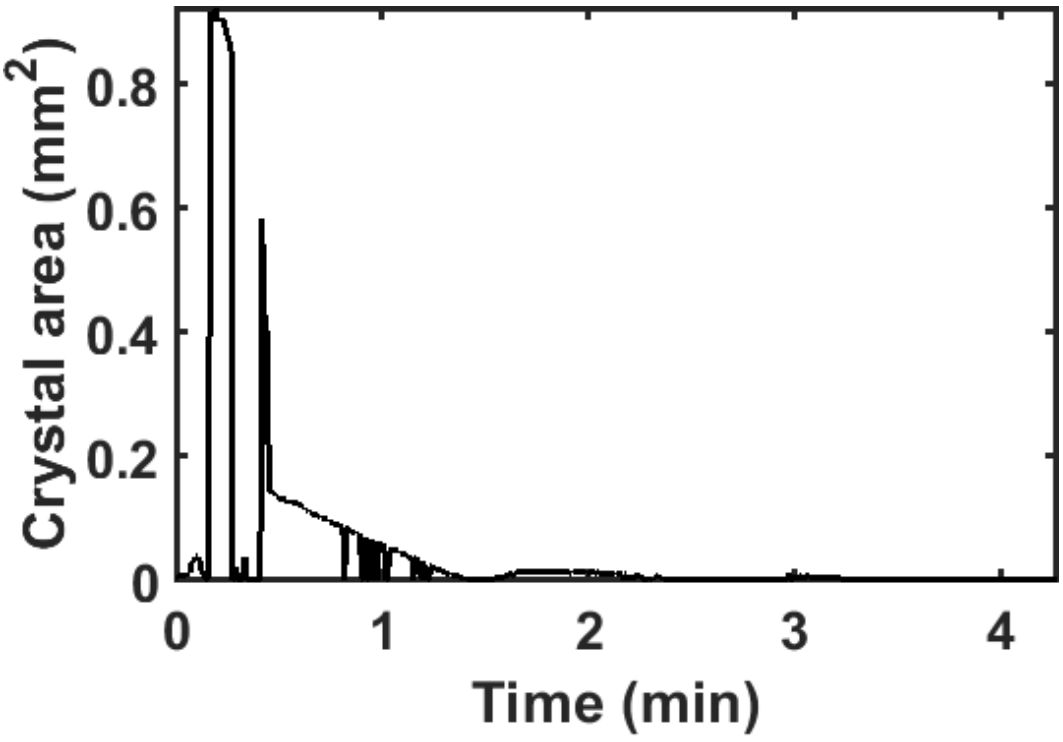

Figure 5.186 - I-TPI gel (run 1) gel ("crystal") area plot.

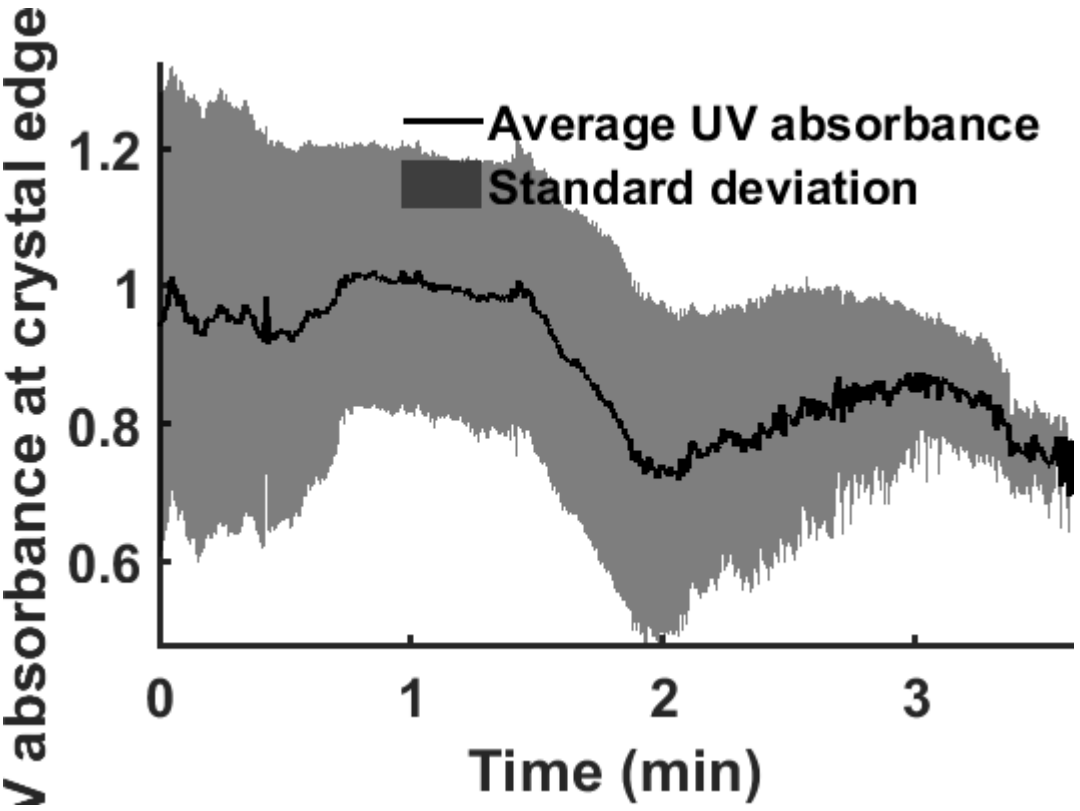

Figure 5.187 - I-TPI gel (run 1) UV absorbance (AU) at gel ("crystal") edge plot.

An additional I-TPI gel (run 4) was explored using the MATLAB script, to understand whether the challenges were specific to run 1 or if the algorithm required altering to accommodate gels. The four reports for perimeter, size, area and UV absorbance are presented in Figure 5.188, Figure 5.189, Figure 5.190 and Figure 5.191, respectively. There is variation again for all size changes, however, they correlate well with each other and with the knowledge that the gel dissolved fully within five minutes. The plot shown in Figure 5.191 is missing its time axis label, which should show that absorbance data was only calculated for 30 seconds in total (corresponding to one minute of actual dissolution time). The UV absorbance recorded suggests it remains high and fairly consistent between 0.9 and just over 1 AU throughout dissolution.

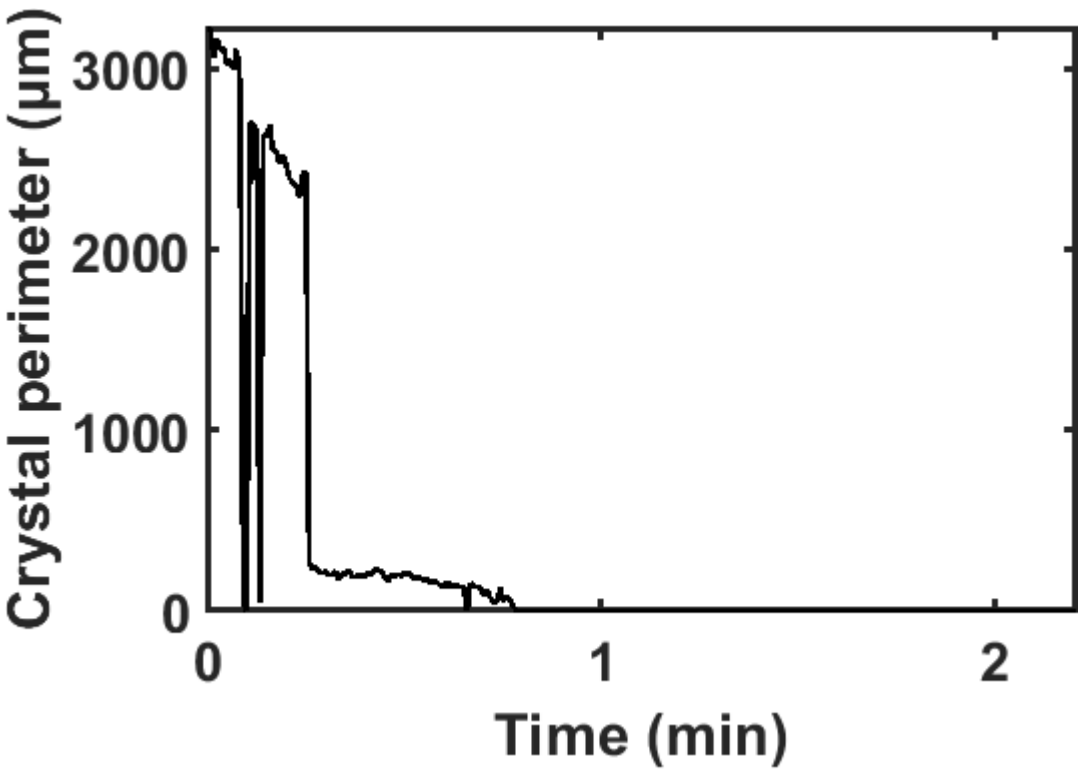

Figure 5.188 - I-TPI gel (run 4) crystal aka gel perimeter plot.

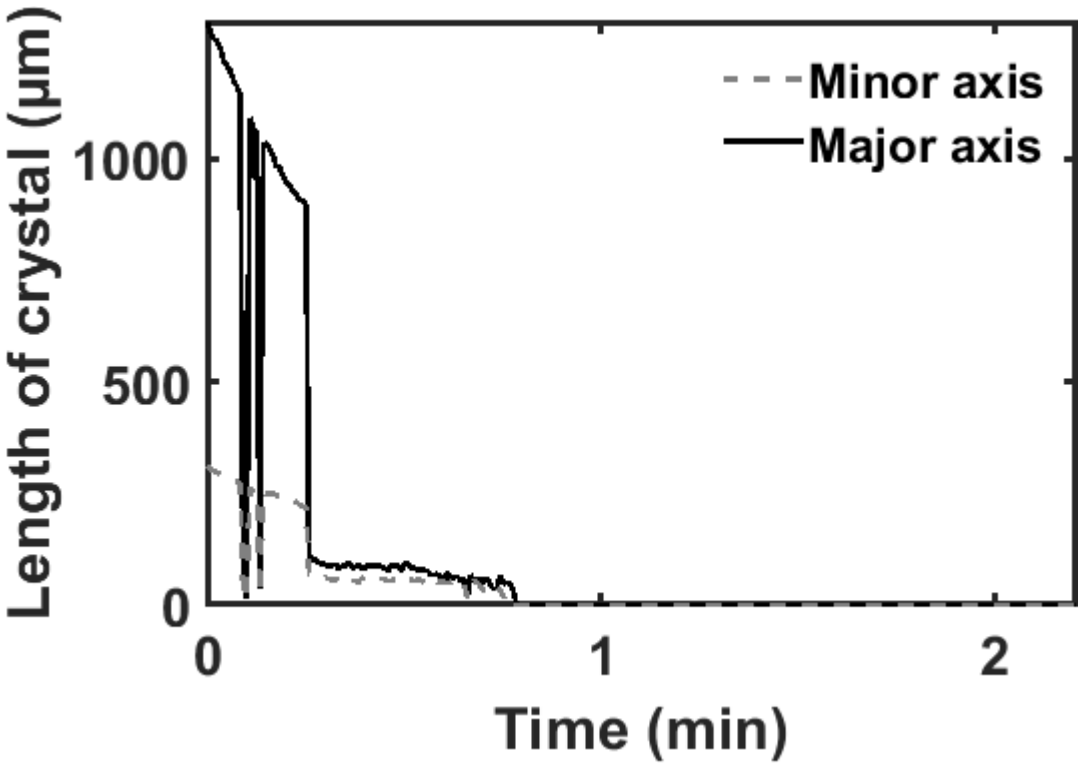

Figure 5.189 - I-TPI gel (run 4) length of crystal aka gel plot.

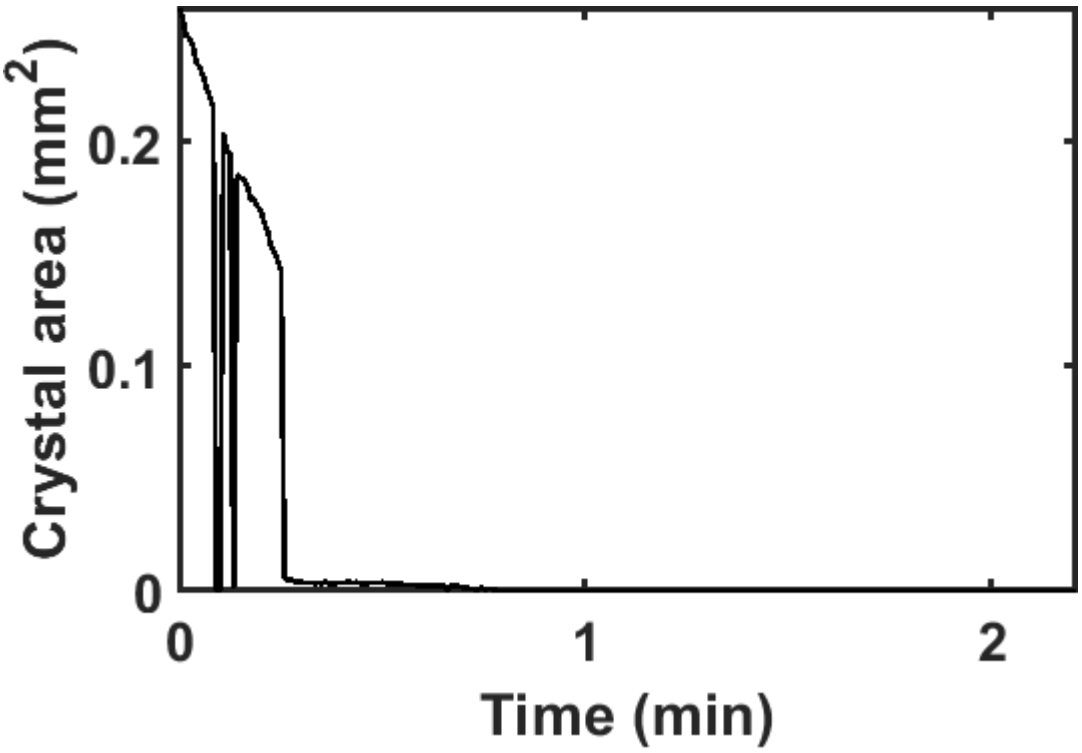

Figure 5.190 - I-TPI gel (run 4) crystal aka gel area plot.

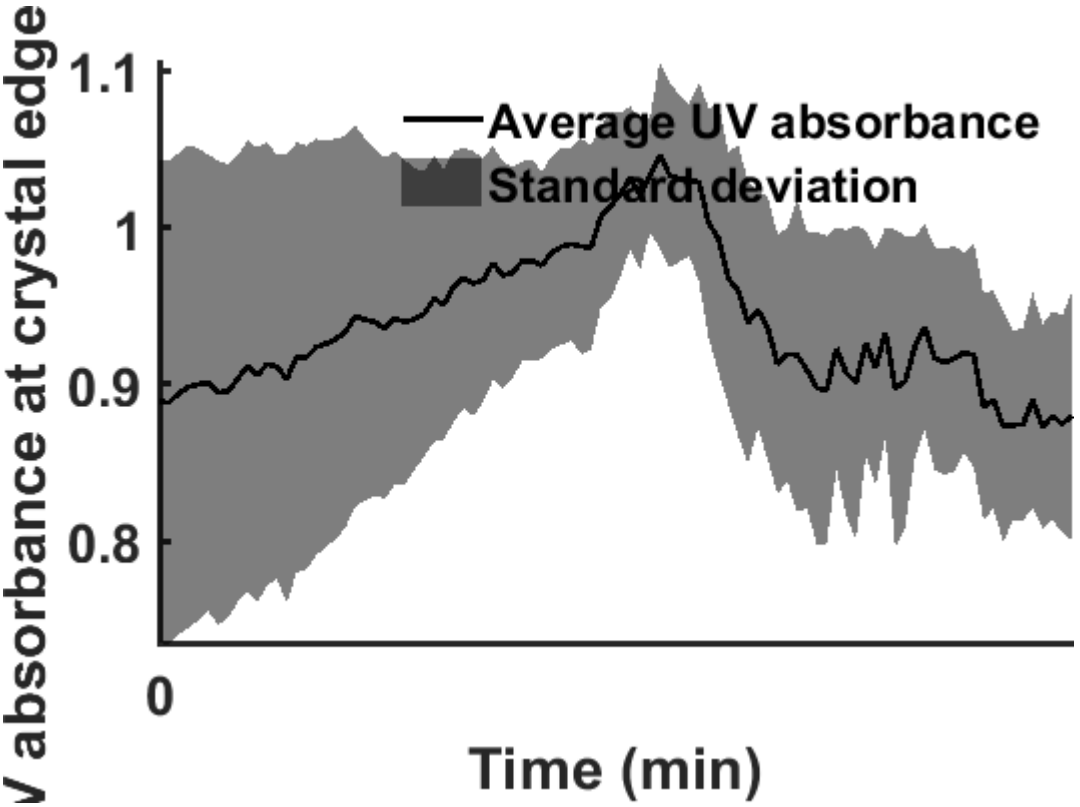

Figure 5.191 - I-TPI gel (run 4) UV absorbance (AU) at crystal aka gel edge plot. The time axis should show that UV absorbance has only been reported for the first thirty seconds (corresponding to the first minute of dissolution).

Summary:

Overall the data obtained through image analysis correlates with visual observations of the dissolution of each sample. In the examples where full dissolution occurred, for example SI run 1, gel run 1 and gel run 4, each of the three size measurements (perimeter, length and area) confirmed this observation and correlated well with the timings. The UV absorbance at the edge was only able to be reported for the period of time in which a sample was present, hence the plot for gel run 4 reports data for less than a minute, see Figure 5.191. Nevertheless, the absorbance values reported for Form SI are consistently lower than those reported for both Form SII and the gel, suggestive of SI dissolving more slowly and therefore being the most stable sample. The absorbance values reported for Form SII remain fairly consistent relative to the variation observed with the gel samples, although the gel data is very limited and therefore inconclusive. It would be beneficial to include measurements of UV absorbance at additional points throughout the cell to confirm changes in concentration during dissolution.

The application of image analysis to the dissolution of single crystals and gels has provided significant learning points to improve future analyses. The first point is that the crystal or gel or other sample must be positioned on top of the wire, enabling a region of interest to be defined which does not include anything other than sample. This makes defining the edges and calculating size much more simple. A second learning point is that the wire must be in the same position at the start and finish of dissolution, the example where the rubber bung shifted out of the sample holder resulted in significant uncertainties in the data due to the relative positions of the crystal being incorrect. Finally, it is ideal if the sample fully dissolves by the end of the dissolution process, as this enables the end image (of just the wire) to be subtracted from the initial image, thus removing interference from the absorbance of the wire.

This method clearly provides extensive information about the dissolution process and has the potential to be applied to all data sets, including those using the WDC. It enables the sample size to be measured in μm, and area to be reported in mm^2, which allows comparisons to be drawn between samples, although further scrutiny is required to determine the impact of the taper magnification upon this. It can also

convert a full image, or frame, from the jet colour map to a calculated intensity per pixel (13.75 μm^2), thus providing the opportunity to report absorbance (or calculate concentration) for any pixel in the cell; although the SDi2 software is thought to contain this information, it is currently limited in its ability to report this data to the user.

5.5 Conclusions and further work

In summary, the WDC provided sufficient information using the SDi2 software to reproduce the stability series for the solvates, and was not significantly limited in this instance by the turbulent hydrodynamics. There was, however, a loss of initial dissolution data due to the slow filling of the large cell, although this may be reduced slightly by increasing the initial flow rate. The CFC was subject to less turbulence than the WDC, but was still impacted by density gradients altering the flow of dissolving I-TPI through the cell. These likely aided the IDR / dissolution flux calculations however, by ensuring that dissolving I-TPI remained in the lower half of the cell but highlights once again that different hydrodynamic environments were present throughout even the smallest cell. Interpretation of the data from each cell required consideration of both the UV and visible absorbance values, as well as viewing of the videos, confirming the importance of utilising the many resources that the SDi2 has to offer.

The application of image analysis software enhanced these SDi2 offerings further still, providing the ability to report crystal size measurements. MATLAB analysis provides a method for correlating UV and visible absorbance within each cell, enabling an edge to be defined relatively easily, which results in being better able to explore the interface between solid, boundary layer and the bulk. It also has the potential to report absorbance values per pixel for both the UV and visible wavelength throughout dissolution. Finally, it does not currently offer an improved resolution when measuring with grids, but does provide an objective method through which to verify it.

Practical challenges presented themselves during the work in the form of samples falling from the wire holder, although this was less of an issue for the WDC, potentially due to the impact and orientation of the flowing solvent. The use of methanol as a solvent also presented multiple challenges, from the appearance of bubbles to the

degradation of seals within the SDi2 fluidics. The relatively new and expensive design of the SDi2 therefore required some modifications and quick-fixes to ensure continued usage, including a new silicone-sealed lid, machined using the department workshop and a free sample of platinum-cured silicone (Trans GP60, from Silicone Engineering, Blackburn).

In addition to the relative stability of the samples being analysed, their size also has an influence on reported dissolution characteristics. However, crystals of similar size and shape cannot easily be reproduced to enable replication of dissolution data. The data for each individual crystal is therefore specific to that sample, which is a significant challenge, not unique for this method, that is somewhat accounted for by reporting size changes instead of simply size. It is also aided by the use of MATLAB, although further work is required to understand the impact of the detector magnification upon these values.

In Chapter 4. Single crystal surface dissolution imaging, a method was developed for physically monitoring single crystals with SDi2 technology, and explored the ability to monitor changes in size and concentration using the SDi2 software. This chapter has extended that work further, reporting the ability to monitor dissolution of a gel, in addition to the application of image analysis software to better calculate size changes and monitor concentration around a defined solid edge. Finally, it has applied these additional techniques to I-TPI, distinguishing between forms, reproducing the solvate stability series and ultimately expanding understanding of each form's dissolution.

Many opportunities exist to further explore the application of image analysis with the SDi2, although the most pressing topic is arguably that of resolution. The SDi2 states a theoretical pixel size of 13.75 μm^2, however, this has yet to be confirmed experimentally and it is not clear how the x2.5 magnification impacts upon this. One can imagine a scheme of work comparing absorbance values extracted from the SDi2 software with those calculated using MATLAB in order to confidently conclude the resolution capabilities of the instrument and the software's ability to reproduce that data.

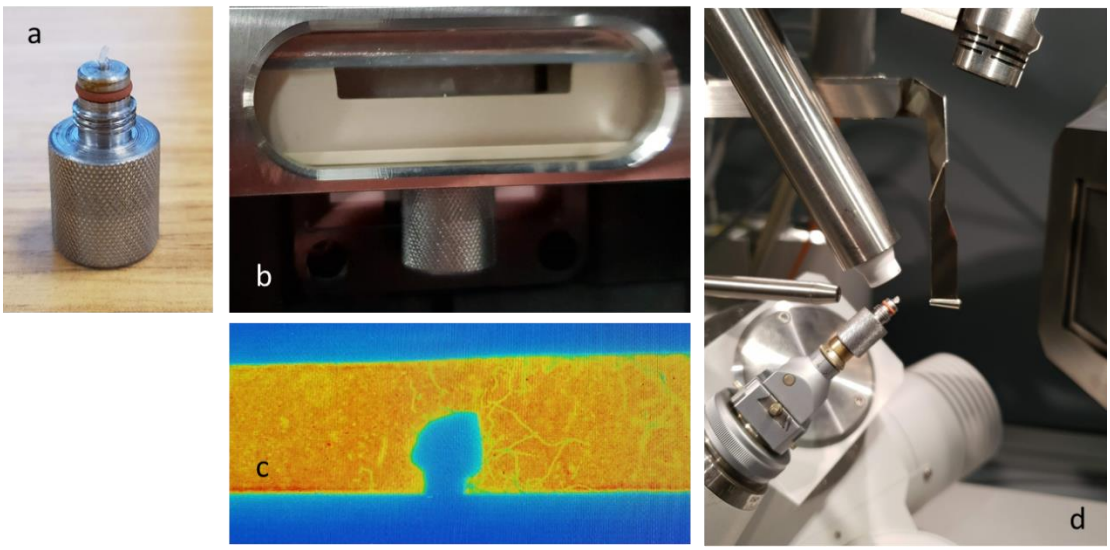

Figure 5.192 – Photographs of a) the novel single crystal sample holder with a single crystal attached highlighting its compatibility with b) the SDi2 compact flow cell, c) the SDi2 detector and d) the single crystal X-ray diffractometer equipment.

Finally, although this work has not succeeded in matching functional groups at the surface of crystals with dissolution properties, it has taken steps towards this by enabling four size measurements to be calculated for a sample: perimeter, major axis length, minor axis length and area, in addition to the measurement of UV absorbance at the sample edge. An exploration of face-specific dissolution would require successful transfer of samples between the SDi2 and the single crystal X-ray diffractometer (SCXRD), as such, work to produce a sample holder compatible with both instruments was started but significantly interrupted by the global pandemic (Covid-19). Figure 5.192 shows the first known version of a novel single crystal holder to enable SCXRD face-indexing of a crystal before its transfer to the SDi2 compact flow cell. This holder is hoped to provide an opportunity to develop single crystal dissolution with the SDi2 yet further still.

6. ESI-MS Equipment Set Up

6.1 Introduction

Electrospray ionisation mass spectrometry (ESI-MS) is routinely used with chromatographic techniques as the end "detector" for identification of the molecules present in a sample.[233,236] The development of an MS technique to monitor tablet dissolution and quantify multiple components on-line in real-time is a novel challenge which has been deemed possible, but not yet explored in sufficient detail to use routinely within pharmaceutical research and development.[15,220,228]

This chapter discusses the development of a combined tablet dissolution and electrospray ionisation mass spectrometry (ESI-MS) system to enable the monitoring of both active pharmaceutical ingredient(s) and excipient(s) release from oral dosage forms into biorelevant dissolution media.

The entire process can be broken down into stages:

i) dissolution
ii) filtration
iii) sample flow
iv) sample dilution
v) MS analysis,
vi) data processing and quantification.

The significant challenges from an equipment perspective are: a) the ability to continually sample from the dissolution bath without affecting sink conditions and dissolution rate, b) the filtration of large volume aqueous samples, including removal of undissolved particles to prevent delayed dissolution, tubing blockages and damage to MS equipment, and c) the ionisation of non-volatile dissolution media.

Minimal sample preparation will be undertaken to enable flow directly from dissolution bath to MS detector, primarily to obtain real-time information whilst also reducing cost of analysis. The release of each API and excipient should be visible in real-time, however method robustness and matrix interference constitute significant challenge when attempting to use mass spectrometry for quantification; additional

processing and data analysis may therefore be necessary to account for ion suppression or enhancement.[275]

Each step of the process will be described in detail including validation of the instrumentation setup and data analysis. This provides the basis for the subsequent two chapters exploring experimentally the impact of ion suppression and ion enhancement on dissolution monitoring by mass spectrometry.

6.2 Dissolution

The process of tablet or compact dissolution is highly complex[4] and can vary significantly between tablets made from a consistent formulation[135] and as a result of dissolution apparatus set up[130,131], hence much of the initial work to develop instrumentation utilised solutions of a known concentration instead of potentially variable samples from a dissolution bath. These are referred to as (known concentration) standards and are used routinely in many analytical techniques to produce calibration plots and enable quantification.[276] All standards were thoroughly dissolved using sonication and heat where required, with sufficient time and mixing allowed to ensure homogeneity prior to their analysis.

The dissolution apparatus was discussed in Chapter 2. Materials and Methods, and can be summarised as either Sotax or Durham dissolution kit. The intention was to replicate the USP II apparatus in terms of its practical aspects so as to challenge the equipment set up. The repeatability and significance of any dissolution profiles obtained using the Durham kit is limited but this will be highlighted when interpreting results. Samples were either taken manually at a series of time points or analyte was pumped continuously from the bath throughout dissolution of the compact.

6.3 Filtration

Samples taken from vessels containing a dissolving compact were subject to in-line filtration to remove any insoluble or undissolved particles prior to storage or analysis. Particles of soluble components not yet dissolved could continue dissolving during transportation thus inflating the concentration recorded for that time point. Additionally particles of any type could cause light scattering during UV analysis, as well as tubing blockages and damage to MS instrumentation.

To comply with regulatory dissolution testing requirements the size and composition of filter used should undergo extensive validation for each API in each dissolution media to ensure it is sufficiently inert and efficiently removes undissolved API for a defined period of time.[277,278] Filter validation is a critical, costly and time-consuming step in developing an analytical method, therefore it was deemed sufficient for this work to focus only on removing large particles to prevent further dissolution and blockages. Flow rates were regularly checked to exclude the likelihood of blockages and filters were replaced where necessary. The risk of contamination by extracting or leaching of chemicals from filters (or other equipment) was considered to be outside the scope of this research however it will be discussed when considering ion enhancement and suppression.[279–281]

A 10 μm stainless-steel solvent frit was selected to prevent large particles exiting the dissolution vessel and an additional in-line depth filter (of stainless steel housed inside PEEK) was placed prior to the MRA and QDa to further protect the equipment. The in-line filter excluded particles more than 0.5 μm in size with minimal dead volume (2 μL), which is comparable with routine dissolution testing and agrees with the *Encyclopaedia of Analytical Chemistry* definition of 0.45 μm as the boundary between undissolved particle and dissolved phase.[40,282] The particle size of insoluble excipients should also be considered throughout experimental studies to ensure that they will be excluded by the filters. The extent of delayed dissolution will be minimised by filtration but cannot be discounted entirely without extensive validation and so this will be taken into consideration when calculating error in dissolution profiles.

6.4 Sample flow

Sample flow into the MS can be divided into two experimental set-ups; aliquot MS and continuous flow MS. An aliquot can be defined as a known volume of sample and in the case of this work may range from 0.1 μL to 1 mL. Aliquot MS involves injection of a small volume of sample into a continuous flow of solvent which is directed for analysis. Continuous flow MS is more complex and involves the pumping of sample with or without dilution prior to analysis. The amount of sample extracted throughout dissolution requires consideration to ensure the volume of media remaining in the bath does not impact on concentration gradients (i.e. sink conditions are

maintained).[124,125,283] The equipment set up allows for excess sample to be returned to the dissolution bath if necessary, however the MRA switching mechanism results in aliquots of MS solvent entering the excess sample flow hence this was not carried out routinely to prevent contamination of the dissolution medium.

6.4.1 Aliquot MS

A known volume of sample is injected into a stream of solvent and directed into the MS either via an HPLC column (LCMS) or directly with no separation (loop injection, LI). Figure 6.193 provides a schematic of this process.

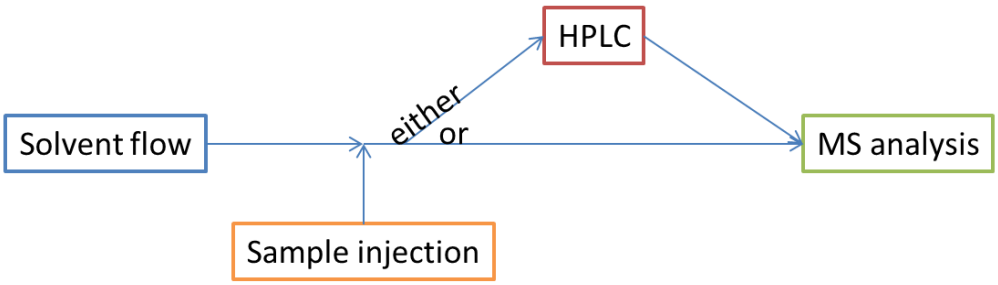

Figure 6.193 - Schematic of aliquot MS analysis.

This constitutes off-line analysis as the sample is not coming directly from the dissolution bath. It was utilised to determine limits of detection and working concentration ranges for the samples being studied. It was also used for some ion suppression and enhancement work due to instrumentation limitations. MS analysis could be carried out by the QDa, Synapt or QToF.

6.4.2 Continuous flow MS

Continuous infusion directed the sample straight into the MS or via a splitting device to provide dilution. Figure 6.194 shows a schematic of this arrangement.

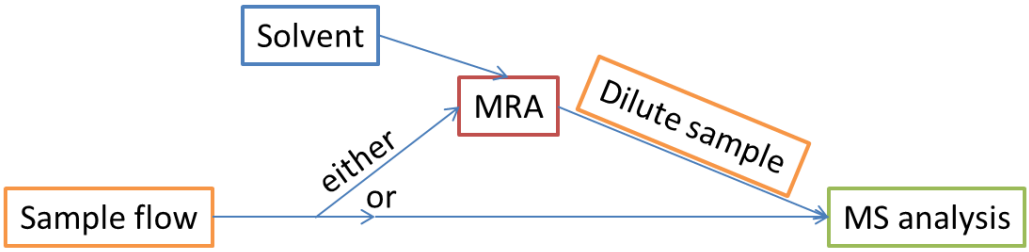

Figure 6.194 - Schematic of continuous flow MS analysis with MRA (mass rate attenuator) splitting device.

This constitutes on-line analysis as the sample is coming directly from the dissolution bath without sample preparation, although it may be subject to dilution. Known concentration standards were analysed with this set up to eliminate the inherent variability of dissolution and enable the role of the mass spectrometer to be explored. Note that only the QDa was used for MS analysis of continually flowing samples.

6.5 Sample Dilution

The mass rate attenuator (MRA) is described in Chapter 2. Materials and Methods, and was additionally used in the proof of concept work.[15] It is used to dilute flowing samples, and can accommodate a high concentration of API or excipient, as well as complex dissolution media which may contain components that are not compatible with ESI-MS. The degree of dilution provided by the MRA can be amended during operation by changing the split factor setting and frequency in addition to varying the flow rates of the sample and the solvent. The calculations used to determine these settings will be stated for each experiment where appropriate.

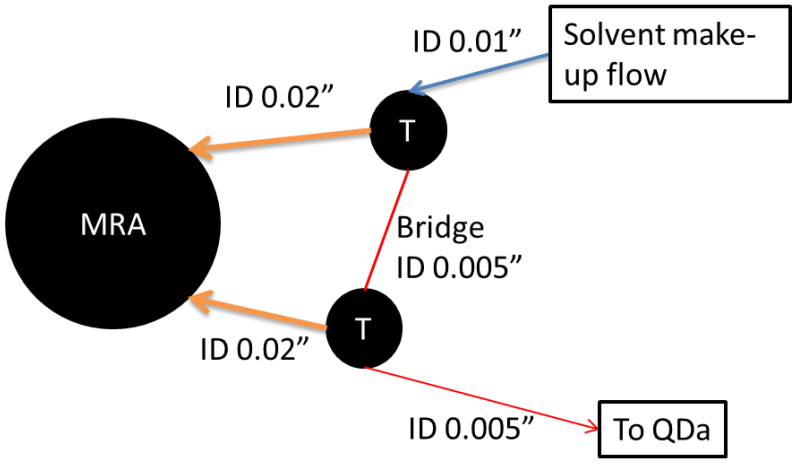

Figure 6.195 – Representation of the tubing used with bridge to equalize pressure from solvent make-up flow to QDa. Each T represents a zero volume T-piece used to connect the lines. ID is the abbreviation for inner diameter and is stated in inches consistent with manufacturer details.

The tubing either side of the MRA and across the PEEK bridge impacts upon pressure so the inner diameters for each section should be kept constant according to Figure 6.195. Experimental validation of pressure equalization could be confirmed by injection of a constant flow of water and acetonitrile 50:50 v/v both without and with the bridge in place; see Figure 6.196 and Figure 6.197, respectively. The figures show the total ion current (TIC) as a percentage of the maximum on the y-axis (representing

signal) with time measured in minutes on the x-axis. This work was carried out in collaboration with Dr Christopher Whitmore, also of Durham University.[284]

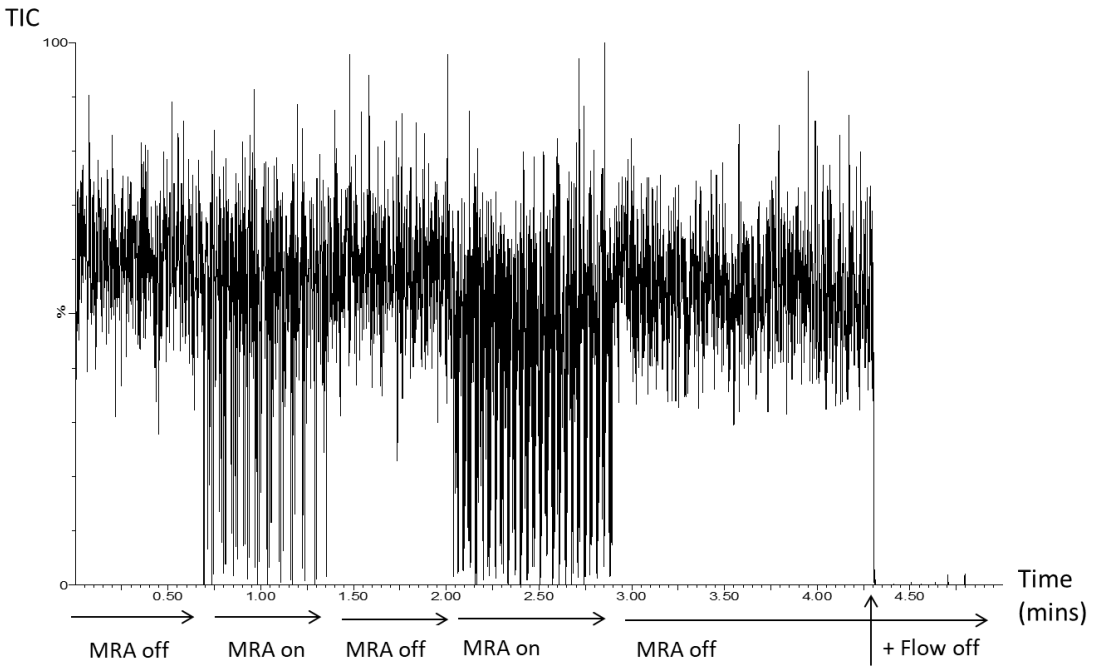

Figure 6.196 – QDa chromatogram for water and acetonitrile 50:50 v/v with MRA attached showing the difference in signal when MRA is switched on and cycling versus switched off when no bridge is in place.

Without the bridge in place, the switching on of the MRA causes signal instability, with the minimum ion intensity reducing to zero, see Figure 6.196. With the bridge in place, signal stability is maintained, irrespective of the MRA's status, see Figure 6.197.

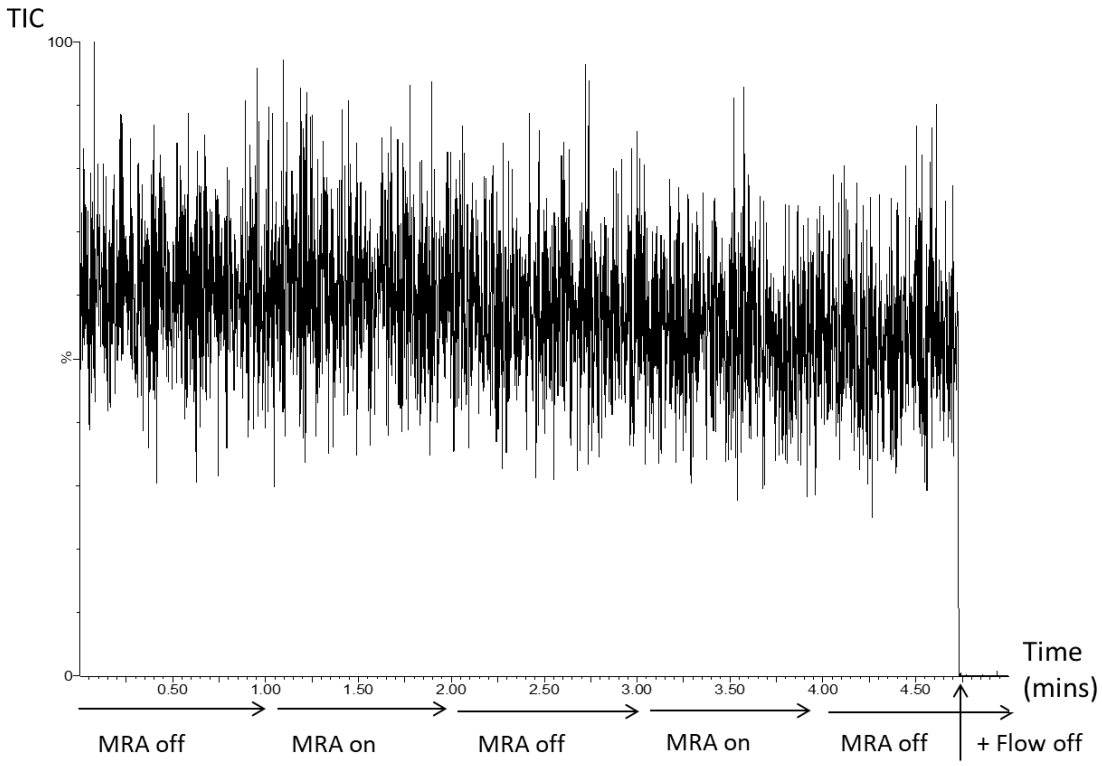

Figure 6.197 – QDa chromatogram for water and acetonitrile 50:50 v/v with MRA attached showing the difference in signal when the MRA is switched on and cycling versus switched off when a pressure stabilizing bridge is in place.

The validated bridge forms an integral part of the MRA set up; it can be assumed that whenever the MRA is mentioned and used, the bridge will be in place. It is important to note that some signal variation is inherent to the analysis of samples by MS and is not eradicated by the presence of the MRA or the bridge. This is shown clearly in Figure 6.198, which displays two chromatograms for paracetamol dissolved in a water and acetonitrile mixture flowing at 0.5 mL/min into the QDa both with (a) and without (b) the MRA.

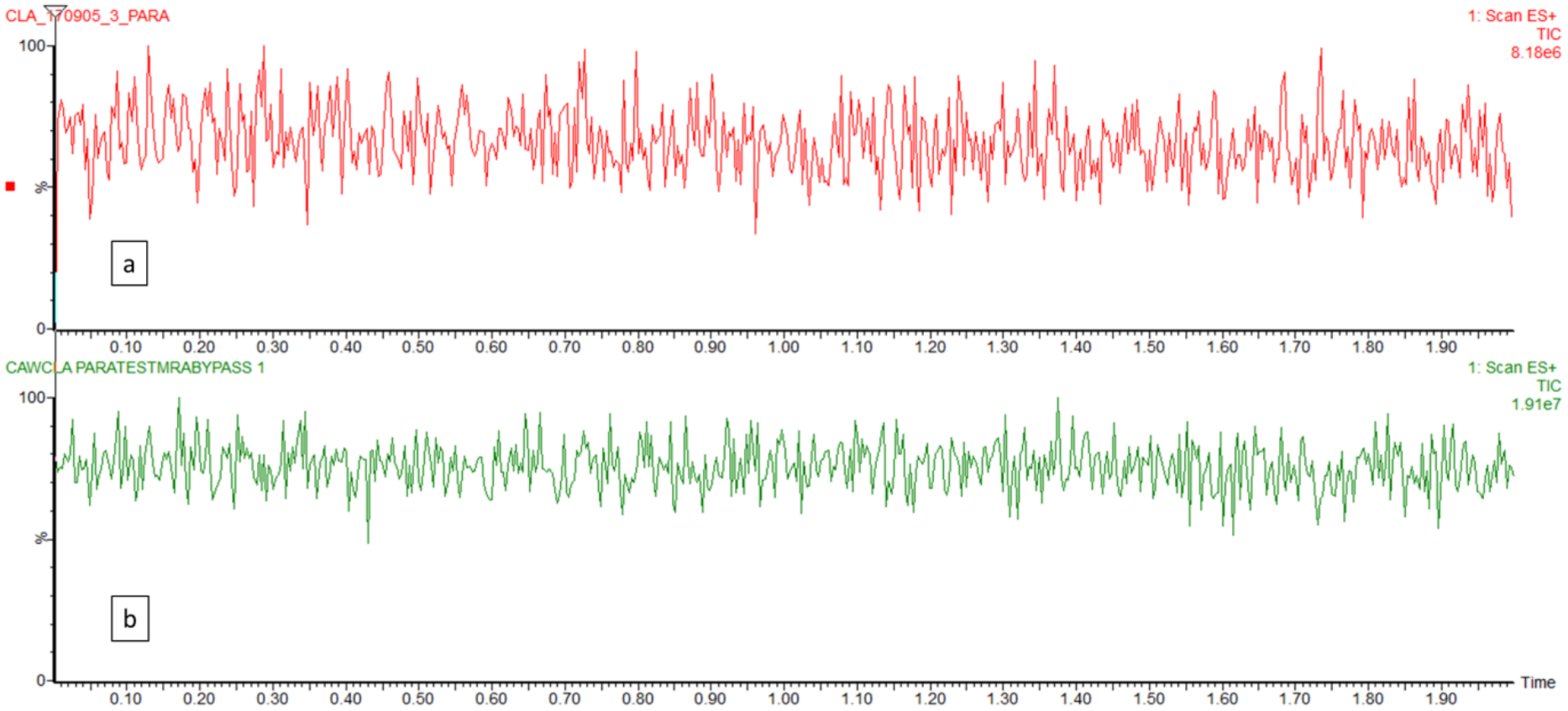

Figure 6.198 – QDa chromatograms comparing the total ion current signals (%) from continuous runs of paracetamol in water and acetonitrile 50:50 v/v per time (mins). Chromatogram (a) is 0.0293 mg/mL with the MRA connected and a dilution of 1:125 and (b) is 0.00266 mg/mL with the MRA bypassed.

Both chromatograms show the variation in total ion current (or signal) as a percentage of the maximum ion count over a period of two minutes. Each chromatogram is from the continuous analysis of a constant concentration sample, however, a reduced concentration of sample must be used when the MRA is bypassed to avoid saturation of the MS detector. As a result, the extent of signal variation cannot be compared quantitatively but a general observation can conclude that signal variation is seen both with the MRA in place and when it is bypassed.

The MRA switches an aliquot of sample into the solvent stream and passes it to the QDa. Despite the narrow volume inside the tubing from MRA to QDa there is likely to be some spreading and dilution of the aliquot within the solvent stream leading to differing concentrations reaching the QDa ready for ionisation as demonstrated in Figure 6.199.

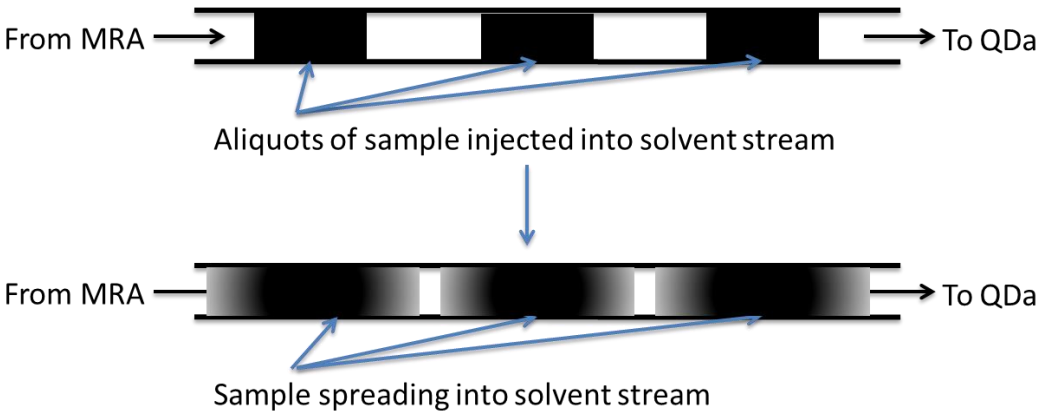

Figure 6.199 – Representation of the spreading of sample from defined volume aliquots into the solvent stream within the tubing between the MRA and QDa.

The tubing diameter and length were kept constant, and the flow, frequency and volume of solvent and MRA switching are defined, so the concentration variation will be dependent only upon the amount of sample present in the aliquot. The diffusion of sample from the aliquot into the solvent stream will vary with the starting concentration of sample and its diffusivity in the solvent. The impact of non-volatile dissolution media upon ionisation will also contribute to signal variation and instability. These will be discussed in further detail during the interpretation of results.

6.6 MS analysis

A total of three mass spectrometers were used for all sample analyses in this work. The Synapt and QToF are high resolution instruments capable of reporting *m/z* to four decimal places, whereas the QDa is a prototype designed for ease of use and as such is not capable of accurate mass. The Synapt and QToF were therefore used to confirm or explore findings from the QDa where further detail or confirmation of an ion's identity was required. They were used off-line to analyse aliquots of sample and as mentioned previously no attempt was made to use these for continuous monitoring of a flowing sample. The QDa however was explored for continuous flow monitoring of dissolution and the equipment set-up for this is shown in Figure 6.200.

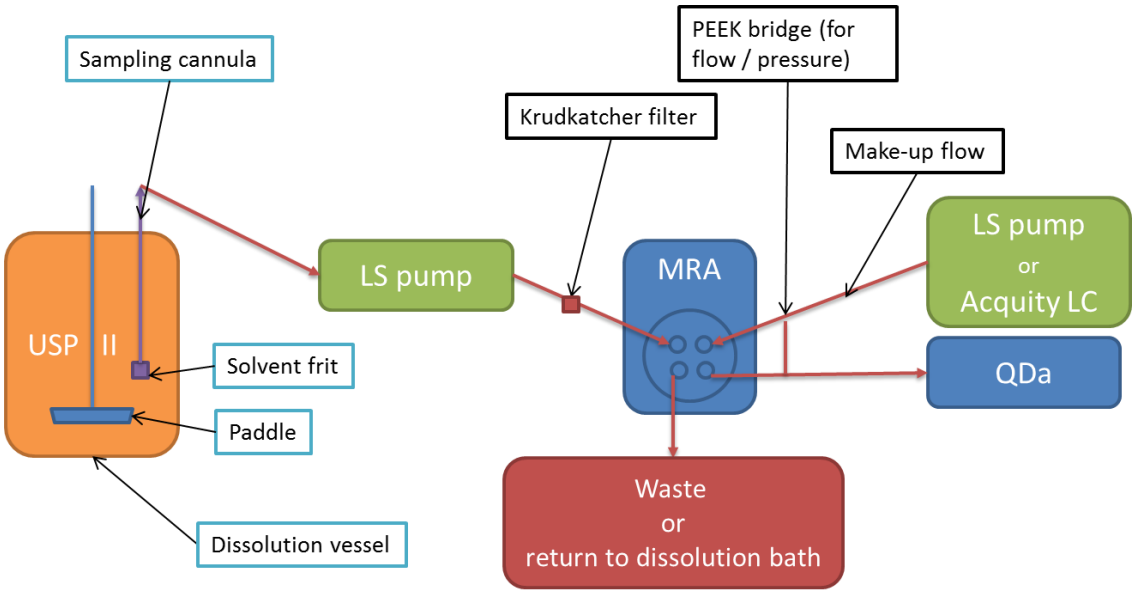

Figure 6.200 - Instrumentation set-up for continuous flow monitoring of dissolution by mass spectrometry.

As previously discussed, the QDa was chosen for its small footprint and relative ease of use. Its methods can be designed to monitor selected ions and / or full scans from 100 to 900 Da in either polarity (positive or negative electrospray). A password-controlled tuning page maintains its simplicity but enables the adjustment of additional settings where required. These experimental details are stored alongside the raw data for each run and can be accessed via the MassLynx software. Ionisation efficiency and ion stability can vary with capillary voltage, cone voltage, source temperature and probe temperature so the QDa default settings have been used to provide optimal analysis of

a variety of samples concomitantly. These defaults will be explored only where necessary to improve ion signal to noise ratios.

The QDa selected ion monitoring (SIM) function allows multiple ions to be followed in addition to or instead of a full scan. The combination of SIM with a full scan enables known ions to be visualised in real time alongside a full scan for supporting information. As an example, a method with five functions following phenylephrine, paracetamol, guaifenesin and lactose in addition to a full scan is shown in Table 6.18.

Table 6.18 - QDa method with multiple selected ions (functions 2 to 5) and a full scan of the entire mass range (function 1), method time of 10 minutes with sampling frequency of 5 Hz and a cone voltage of 20.

Function (channel)	Mass range / selected ion monitored (*m*/*z*)	Number of scans	Scan duration / dwell time (secs)
1	100 to 900	3032	0.117
2	150	3030	0.014
3	152	3030	0.014
4	221	3030	0.014
5	365	3030	0.014

The resultant chromatograms from the method in Table 6.18 are displayed in Figure 6.201. Chromatograms (a) to (d) show the selected single ions and (e) provides the total ion count from a scan of the full mass range possible. The number of scans within the analysis time is important for comparative quantification, hence the method used (the number of channels or ions followed), the time over which it is studied and the setting of the sampling frequency are important to note, and where quantification attempts are made, these should be consistent.

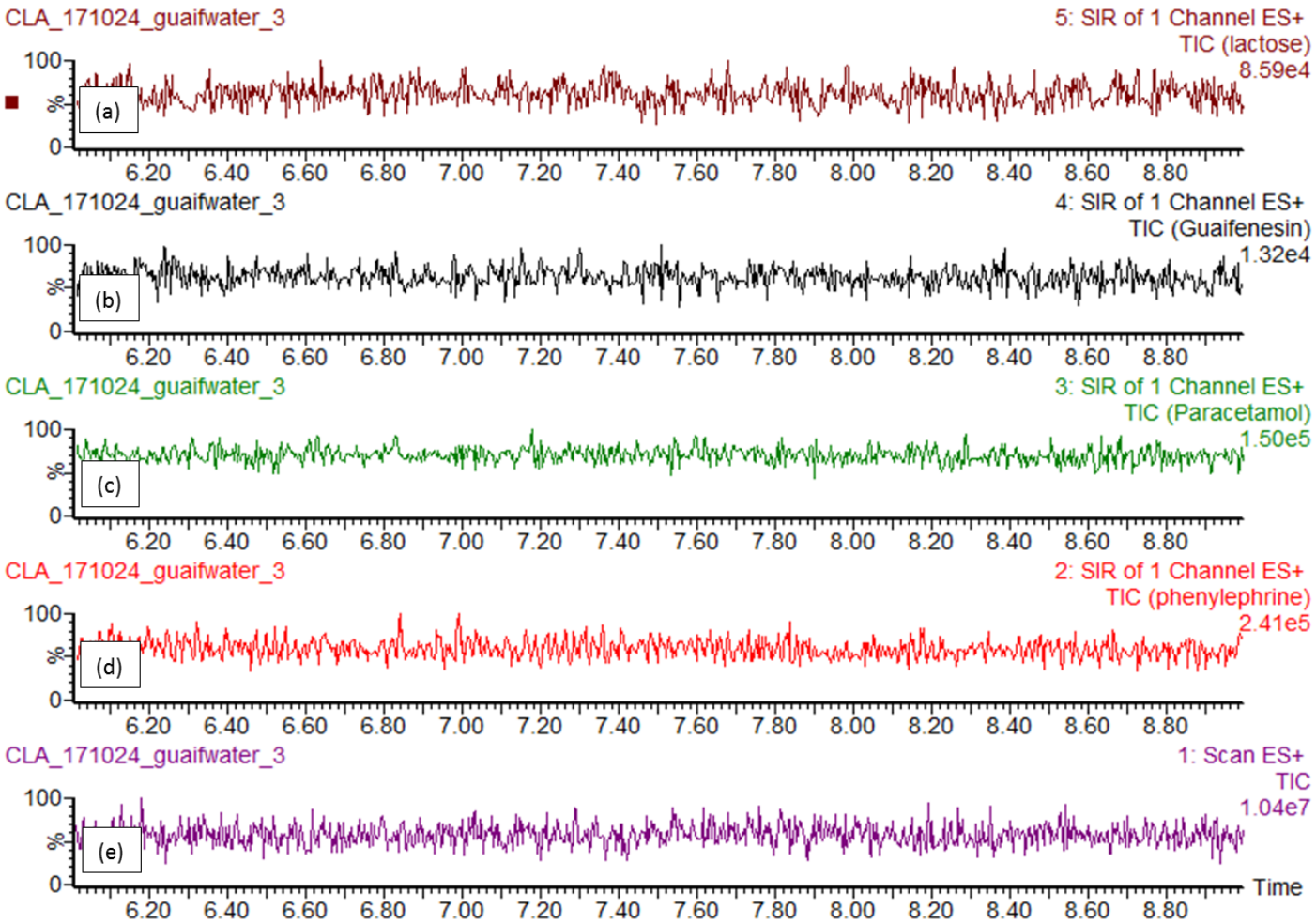

Figure 6.201 – QDa chromatogram using a method with five channels, (a) lactose at *m/z* 365, (b) guaifenesin at *m/z* 221, (c) paracetamol at *m/z* 152, (d) phenylephrine at *m/z* 150 and (e) total ion count of the full mass range (100 to 900 Da).

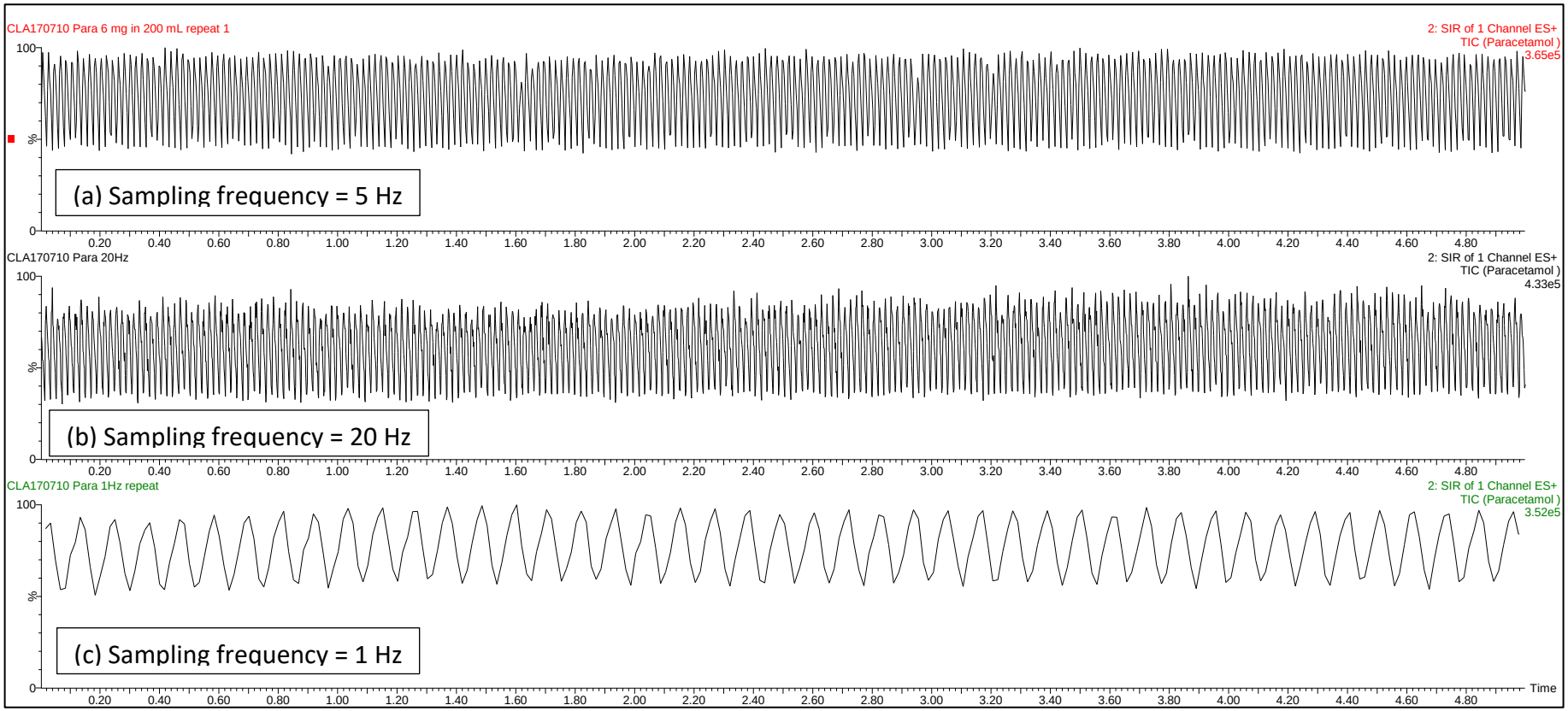

Figure 6.202 – QDa chromatograms for a consistent flow of sample with differing sampling frequencies (a) 5 Hz, (b) 20 Hz and (c) 1 Hz.

Figure 6.202 compares QDa chromatograms for analysis of the same sample using three different sampling frequencies. The sampling frequency on the QDa ranges from 1 to 20 Hz; a setting of 20 Hz provides twenty times more data points in the same time frame as a sampling frequency of 1 Hz. A rapid scanning process can influence ion statistics leaving shorter dwell times (see Table 6.19), which can result in anomalies. The dwell time or scan duration can be defined as the time available for a selection of ions or a single ion to be guided through the quadrupole and must enable sufficient ions to reach the detector; the sampling frequency must therefore allow an appropriate dwell time for each function within the method.

Table 6.19 - Summary of QDa five minute methods for comparison of sampling frequency

Scanning frequency:	**1 Hz**	**5 Hz**	**20 Hz**
Scan duration / dwell time (secs)	0.458	0.058	0.005
Number of scans in function 2 –> SIM of *m*/*z* 152 only	298	596	3156
Scan duration of function 1 (secs) –> full scan (100 to 900 Da)	0.533	0.133	0.080

The method specified in Table 6.19 includes a function 1 and function 2; function 1 is referred to as a full scan and requires the quadrupole to guide each ion between 100 and 900 Da, in turn, through the quadrupole, each with a stable trajectory so that they may reach the detector. Function 2 monitors only a single ion of *m*/*z* 152 rather than a range so only one stable trajectory must be maintained to guide the specified ion through the quadrupole. Function 1 therefore requires more time to complete than function 2, but both must take place within the time frame specified by the sampling frequency. A sampling frequency of 20 Hz, with two methods, therefore requires that less time is spent scanning each function to enable twenty samples to be run within a minute. As a result, fewer ions are guided through the quadrupole and this can lead to insufficient ions reaching the detector which manifests as a reduction in the total ion count. Alternatively, too long spent on each function can result in saturation of the detector as too many ions are guided through at once. There is also an inter scan delay between each function as the quadrupole settings change to alter the stable trajectory of the ions. The full duration of each scan therefore depends upon the

sampling frequency set in addition to the number of single ions being monitored and full scans.

In addition to the limitations of sampling frequency upon ion statistics, a very slow sampling frequency can result in so few data points within the same period that aliasing can be a risk. Aliasing can be defined as a phenomenon, which gives rise to an incomplete representation of data and can be explained by considering Figure 6.203.

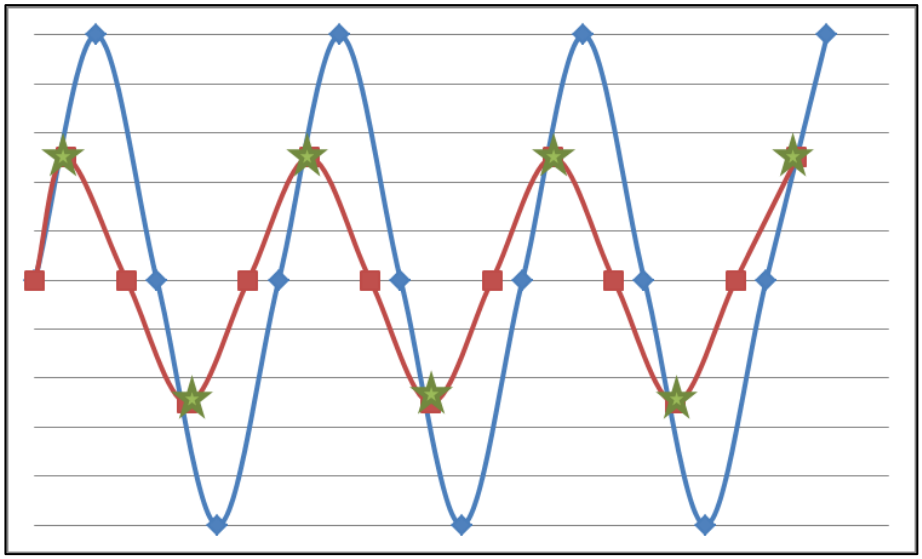

Figure 6.203 - Example of aliasing due to insufficient sampling frequency. The blue line is real data and the green stars are sampling time points, which give rise to incomplete representation of data by the red line.

Figure 6.203 shows the true data (blue line) and the slow sampling (green stars) which can give rise to an incomplete representation of that data (red line). The sampling frequencies of concern in this work are the MRA frequency by which a volume of sample is injected into the solvent stream, and the QDa sampling frequency setting previously described. The QDa frequency must be more than double the MRA frequency to ensure that aliasing does not occur. This is comparable with the NMR phenomenon leading to the '*Nyquist Criterion*' which states that you have to "sample [] at least twice per cycle to know the true frequency".[285]

A QDa sampling frequency of 5 Hz will avoid aliasing for all MRA settings (the highest MRA frequency possible is 2.222 Hz), additionally it provides more than sufficient data points for understanding the dissolution process (which takes minutes rather than

seconds to understand from a bulk solution perspective) and leaves time for ion statistics to be sufficiently large.

6.7 Data processing and quantification

The Synapt and QToF were used to confirm which ion to analyse for a specific API or excipient either by accurate mass elemental analysis or by MS/MS, both with HPLC separation prior to ionisation. The resultant chromatograms show peaks at elution times dependent on the molecule and solvent(s) used. Further analysis of the spectra that make up each peak provides the resultant ions is shown in Figure 6.204.

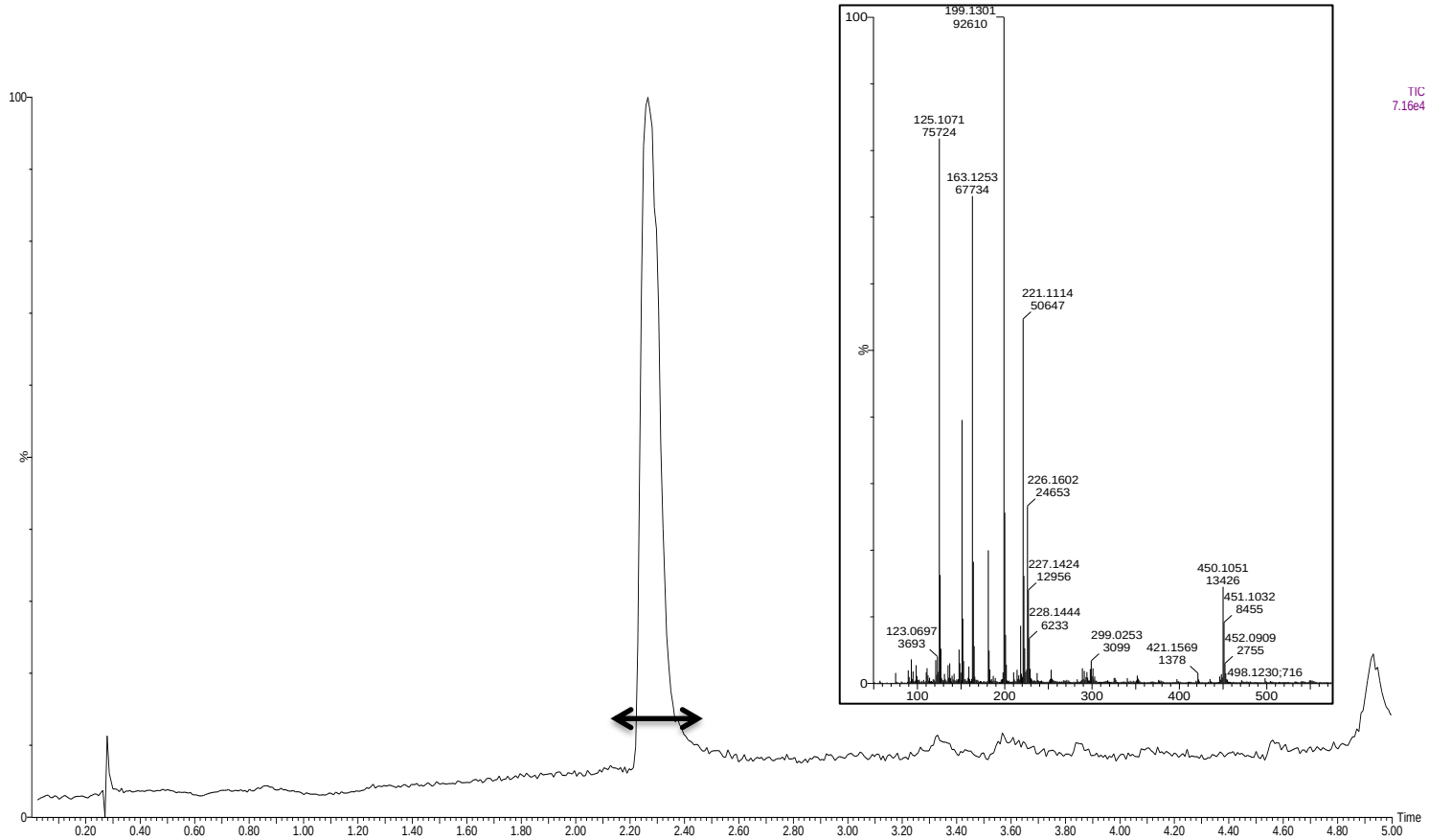

Figure 6.204 – QToF LCMS chromatogram with inset showing average spectrum of resultant ions. The inset spectrum is an average of the peak seen between retention times of 2.2 to 2.4 minutes (highlighted by the black double arrow).

Both the Synapt and the QToF were used to fragment ions by MS/MS to further confirm their identity. In this case, the method is set to gather and hold a specified ion, a voltage is applied to encourage fragmentation of this ion and any resultant ions are then analysed to confirm the likely identity of the original ion. The averaged spectrum from the relevant peak on the chromatogram can be extracted and the identity of any ion(s) confirmed by accurate mass elemental analysis.

The Synapt was additionally used to obtain a full mass spectrum (usually 50 to 2000 Da) for samples introduced by loop injection. Analysis of this data for quantification purposes involved extracting the mass of the ion of interest from the raw sample chromatogram and integrating the resultant peak; both peak height and peak area could be calculated. Figure 6.205 shows an example process for calculating peak height and area; the resultant data can be used to prepare calibration plots and calculate the concentration of unknown samples. In addition to peak height and area, a maximum recorded ion intensity is reported on the top right hand side of each chromatogram and can be extracted for sections of the data or for the entirety of it. There is signal variation throughout a run hence the maximum alone cannot be used for quantification but the range of variation in the TIC indicates ionisation consistency and efficiency, and may help to highlight suppression and enhancement phenomena.

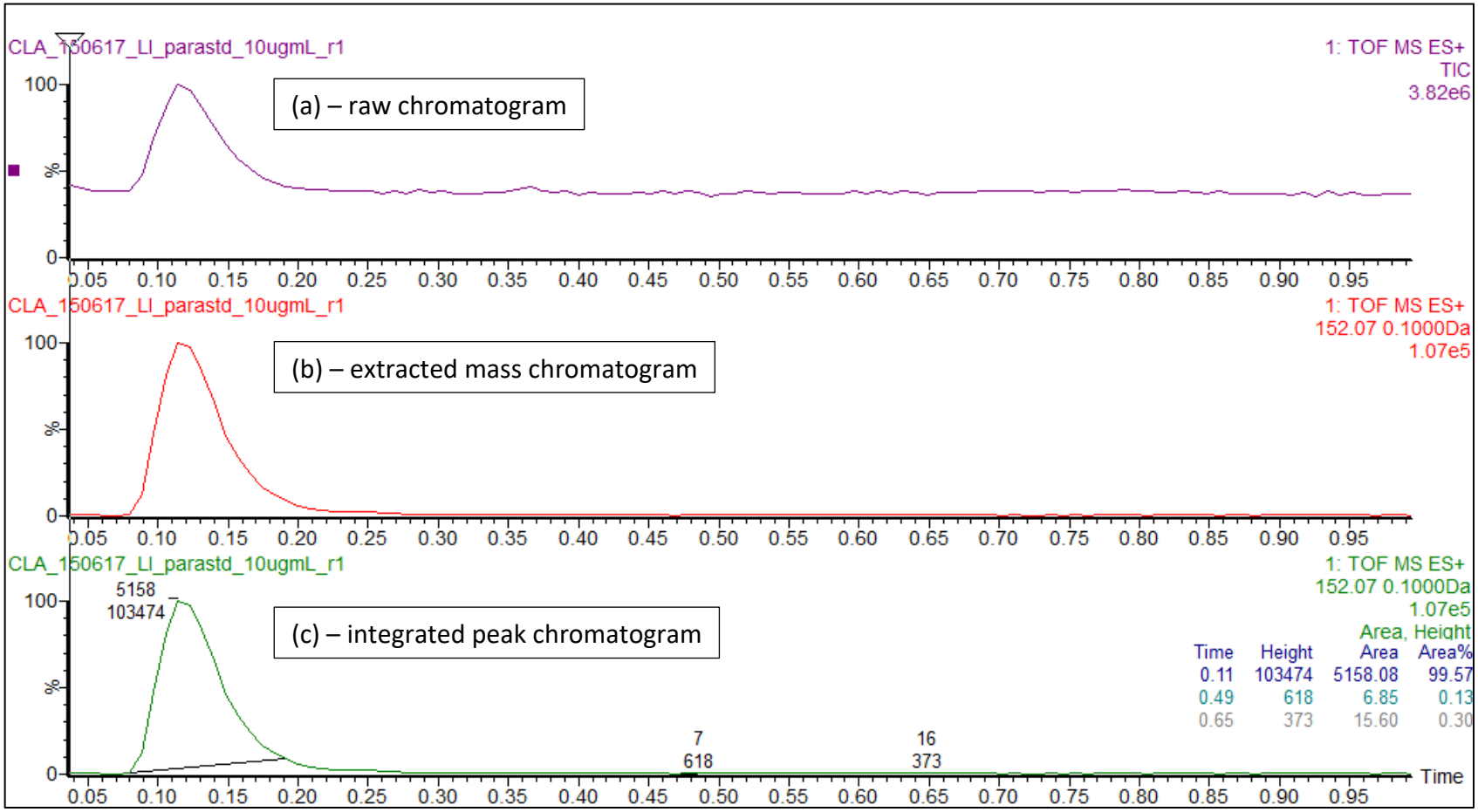

Figure 6.205 – Synapt quantification process showing (a) a raw chromatogram showing a TIC maximum intensity of 3.82e6 for paracetamol solution, (b) an extracted mass of 152.07 +/- 0.1 Da relating to paracetamol with a maximum intensity of 1.07e5 and (c) the integrated extracted mass peak with both height and area data (103474 and 5158, respectively).

Ion intensity is considered alongside peak shape to highlight the potential for detector overload. For example, a TIC of more than $9.00x10^8$ on the QDa would likely produce a flattened peak and a shift in reported mass, which would indicate detector saturation due to an overly strong signal. It is important to note that this will vary between methods and mass spectrometers, not just as a result of differing equipment but also as a result of detector age and usage.

The Synapt is capable of high resolution accurate mass analysis providing peak separation and identification accuracy even at low levels of sample. This enables the chemistry of sample solutions to be confirmed prior to QDa analyses, which cannot achieve accurate mass reporting. However, to prevent detector saturation, a lower concentration must be used for the Synapt when compared with the QDa due to their relative detector sensitivities. This can be explained by imagining packets of ions passing to the detector – in full scan mode a packet contains a number of ions of varying *m*/*z* values so the number of any one *m*/*z* will be lower than in SIM mode when a packet of ions will contain only those of a specified *m*/*z* value all "hitting" the detector at the same time. The high resolution of the Synapt means that the detector is more sensitive so fewer ions of each *m*/*z* value are required to cause an overload compared with the QDa. In summary, the range of concentrations able to be analysed and accurately quantified will vary between instrumentation and method used, so initial analyses include a close look at peak shape to rule out detector overload.

6.7.1 Calibration plots for quantification

The terms quantification and quantitation are considered interchangeable, however, quantification will be used for consistency.[286] The use of a calibration plot for quantification is commonplace in a variety of analytical techniques, including LCMS.[231,276,287] Analysing a series of known concentration samples using the same method employed for unknown samples allows the relationship between concentration and signal to be determined. It assumes that signal and concentration are proportional within lower and upper boundaries defined as the limits of quantification.[288] The upper boundary will be limited by detector saturation; as the detector becomes saturated with ions, the response will no longer be in proportion and it may not be possible to calculate concentration from signal.[289] The lower

boundary will be the limit of detection, which is defined as the lowest concentration of sample which can be distinguished consistently from a blank signal.[288]

The relationship between concentration and signal may also vary as a result of numerous instrument-related and sample-related factors.[290] This provides a valid rationale for using consistent equipment and methods to explore robustness and inherent variation. Additionally, the use of a range of samples to explore the concentration-signal relationship within a defined set of conditions can be considered a fundamental step towards assessing the use of mass spectrometry for monitoring dissolution.

It should be noted that LCMS quantification good practice states that standards should be analysed on the same instrument on the same day as unknown samples to determine calibration plots and allow quantification. Where possible and where applicable this was followed, however the limitations of mass spectrometry to monitor dissolution were important to explore in order to test robustness of the equipment set up and validate the technique.

6.7.2 Peak height versus peak area quantification

A comparison of the peak height and peak area methods for quantification was undertaken for both the Synapt and the QDa. A series of known concentrations of sample were analysed by loop injection (no dilution) on each instrument with all runs completed on the same day for each instrument. Each sample was run in triplicate and the peak height and peak area data was obtained using the quantification process described in Figure 6.205. Peak detection, smoothing and integration of the chromatograms using MassLynx was kept consistent. The calibration plots for the QDa and Synapt, for each method of calculation, are shown in Figure 6.206 and Figure 6.207, respectively.

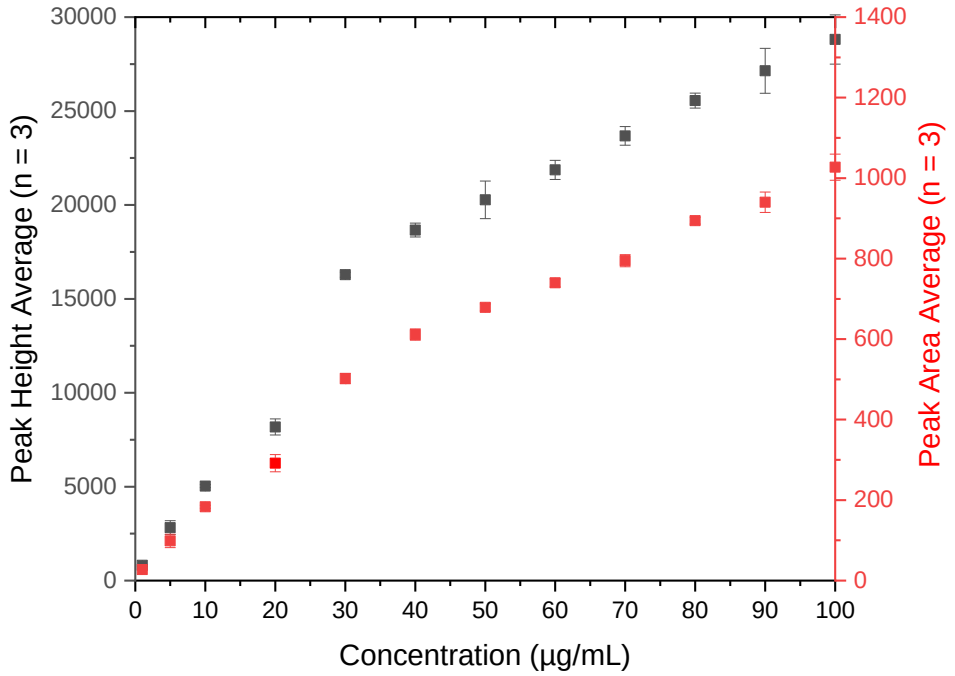

Figure 6.206 – Calibration plots showing a comparison between using area under peak (red) and peak height (black) for quantification of a series of standards using the QDa. Each point is the average of three runs with the standard deviation plotted as error bars.

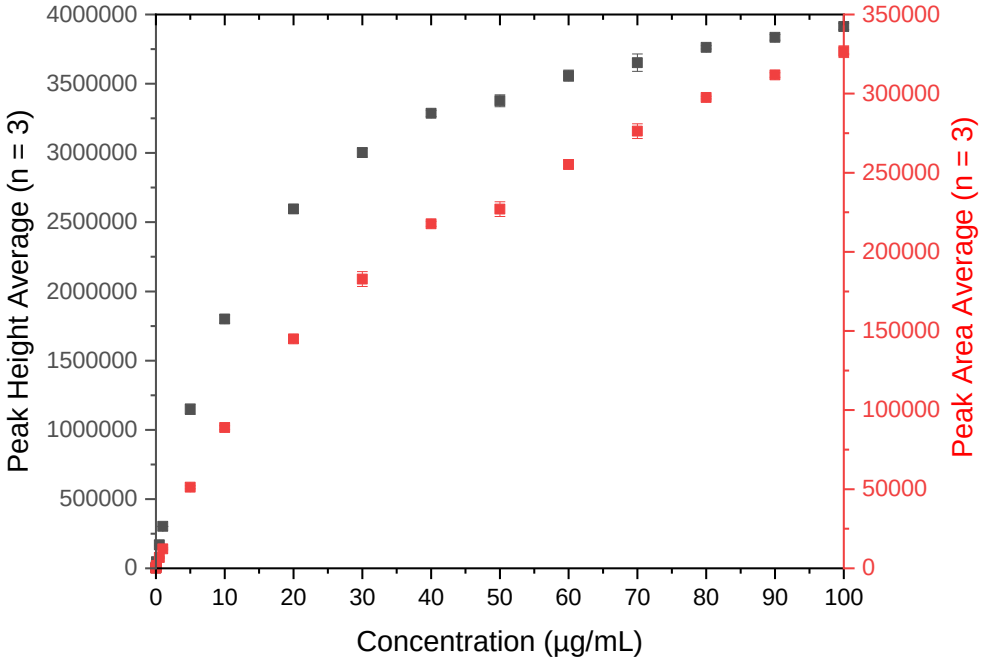

Figure 6.207 – Calibration plots showing a comparison between using area under peak (red) and peak height (black) for quantification of a series of standards using the Synapt. Each point is the average of three runs with the standard deviation plotted as error bars.

A quick comparison of the two methods for each instrument concludes that the relationship between signal and concentration is more linear at lower concentrations but may still be proportional using additional equations at higher concentrations. The plots show that both peak height and peak area produce similar shape calibration plots for each instrument. The data therefore suggests that either method will enable quantification within similar limits of detection and saturation, although the plots themselves are different with the QDa data almost appearing as two sets with a step between them. The analysis of each set of data should be carried out in a consistent manner with the same method used for both calibrations and concentration calculations. The calibration plots are not consistent between instruments as a result of their differing sensitivity; the Synapt curve has a much higher ion count and appears to start to plateau prior to the QDa curve which is consistent with the relative sensitivity and resolution of each instrument.

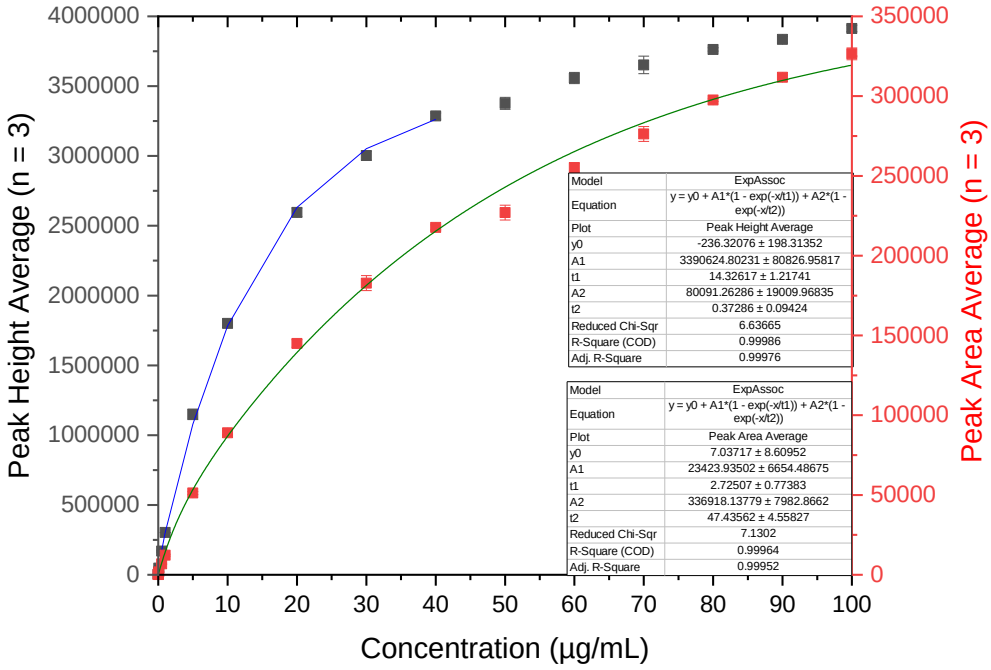

Figure 6.208 – Synapt calibration plots showing exponential curves fitted to the data, both in full for the peak area, and in part for the peak height.

Further analysis of each calibration plot allows equations to be fitted to the data, see Figure 6.208. Origin 2019 software has been used to model the data and fit an equation to each set. Details for each model fitted and the correlation are inset within

the figures; the details are not relevant to this chapter but will be discussed in detail as each calibration plot is studied.

6.7.3 Continuous flow quantification

In the case of continuous flow runs, the ion signal is subject to variation as the sample introduced for ionisation varies between dilute regions and concentrated ones. The series of peaks and troughs shown in Figure 6.209 suggest that there is insufficient length of tubing after the MRA to enable full mixing of sample throughout the solvent; Figure 6.199 provides a pictorial representation of the dilution or spreading. The length or inner diameter of tubing could be increased to encourage dilution but this would increase the delay between dissolution bath and MS analysis as well as impacting upon pressure. Additionally the pump manufacturers provide guidance for tubing lengths and inner diameters to ensure consistent solvent flow; the set up described reaches the maximum recommended length and ensures the correct pressure differentials for maintaining flow rates.

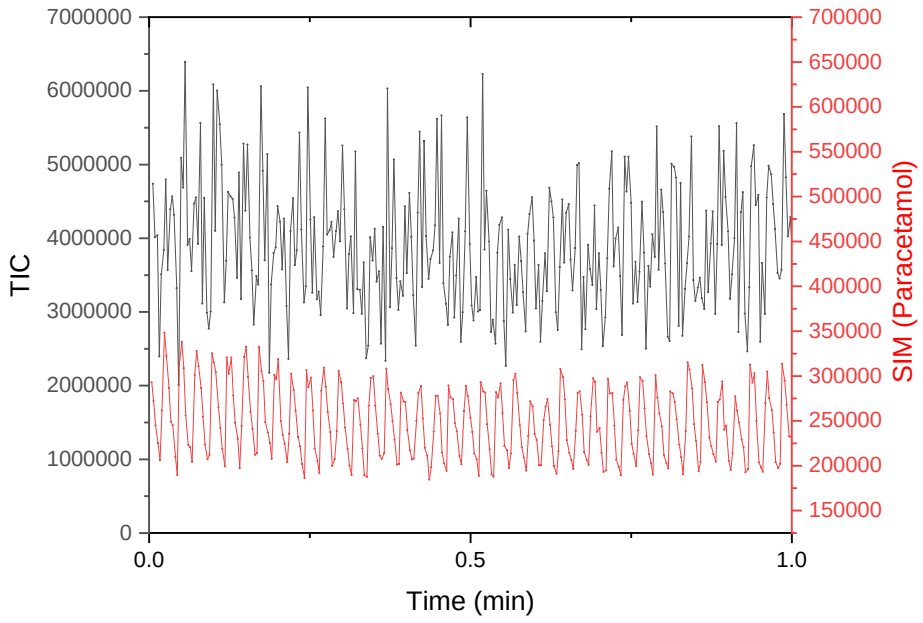

Figure 6.209 – Chromatogram showing consistent flow of a constant concentration sample. Total ion current shown in black and monitoring of a single ion shown in red, note the use of different scales for the Y-axis.

A chromatogram list can also be extracted using MassLynx; this list can be manipulated to provide mean, maximum and minimum recorded ion intensities in addition to calculating a moving average, see Figure 3.210. A plot of moving average against time

allows quantification of signal variation for the continuous monitoring of a single concentration samples.

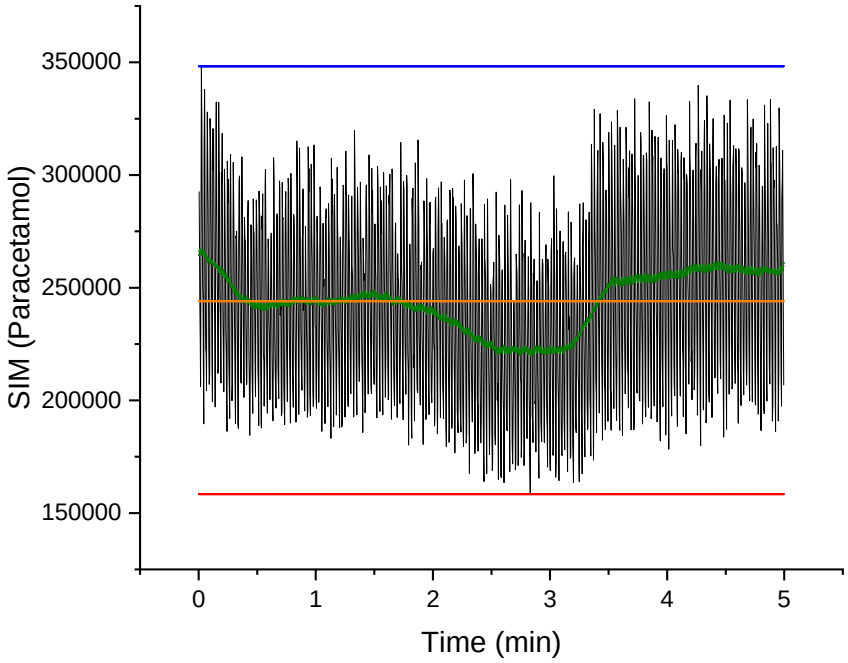

Figure 3.210 - Chromatogram for the monitoring of a single ion with the maximum intensity plotted in blue, minimum intensity plotted in red, mean intensity plotted in orange and a moving average plotted in green.

This signal variation can be used to generate an understanding of the uncertainty involved in simple quantification prior to more complex quantification calculations where multiple components are involved.

6.8 Summary

The development of mass spectrometry techniques to monitor dissolution will initially use solutions of known concentration (standards) rather than taking samples directly from the dissolution bath due to the potential for variation. A range of calibration standards bracketing the concentration of sample to be calculated will be analysed on the same instrument on the same day (where possible) to determine a calibration plot for quantification.

Aliquots of sample as well as continuous flows of sample will be explored to determine the limits of the technique. For sample aliquots, both peak area and height can be used for quantification but the method for calculating each must be consistent to

enable robustness and reproducibility to be understood. For the continuously flowing samples, a variation in both SIM and TIC signal is apparent. This is present even throughout analysis of a consistent flow of constant concentration sample; hence, a moving average should be calculated using the minimum and maximum ion intensities observed over time. A detailed investigation into the levels of uncertainty associated with quantification by each of the methods will be necessary and for each component of sample being analysed.

Off-line analysis with the QDa, Synapt and QToF will be utilised for much of the initial work to determine limits of detection, signal variation and working concentration ranges. It will then provide the basis from which to explore ion suppression and enhancement when multiple APIs and excipients are present in a solution, with on-line analysis and limited sample preparation the ultimate aim for monitoring dissolution by MS.

7. Exploring single components in simple solvent systems with ESI-MS

7.1 Introduction

The overall aim of this work is to explore the use of ESI-MS to monitor dissolution in the bulk of a solution. Routine dissolution techniques currently employ UV or HPLC/UV analysis, which most commonly monitor only the API component(s) of a formulation. The use of MS technology would allow non-UV-absorbing compounds to be observed, thereby including excipients such as sugars, in addition to following dissolution of multiple chemical species without requiring a separation step. In order to build upon the current understanding gained by Lewis *et al*., this chapter will explore the ease by which individual formulation components can be analysed and quantified using ESI-MS.[15] This will include monitoring components of the tablet both with and without chromophores, exploring MS signal variability of APIs and excipients, particularly with different solvents, and attempting to detect and accurately quantify components without the need for separation before ionisation. This work will provide the basis for understanding the ionisation relationships between components and determining the impact of ionisation phenomena (suppression and enhancement) upon the monitoring of dissolution.

The APIs, excipients and dissolution media were chosen to encompass a range of characteristics representative of those found within pharmaceutical development.[93] A key consideration for determining the extent of formulation development and dissolution testing required by regulatory authorities for an API is the biopharmaceutics classification system (BCS).[89,93] This information, with an emphasis on solubility, was therefore used to guide selection of the seven APIs listed in Table 7.20.[92] Each API is well established and thus well characterised compared with compounds still in development, which ensures better access to background information, lower cost and ease of supply, known impurity profiles and more complete safety information.

Table 7.20 - Active pharmaceutical ingredient (API) selection including biopharmaceutics classification system (BCS), solubility, molar mass and monoisotopic mass.

API	BCS[93,291,292]	BCS solubility[89]	Molar mass (g / mol)	Monoisotopic mass (Da)
Chloramphenicol	III	Good	323.132	322.012329
Furosemide	IV	Poor	330.745	330.007721
Guaifenesin	I	Good	198.216	198.089203
Haloperidol	II / IV	Poor	375.864	375.140137
Ibuprofen	II	Poor	206.281	206.130676
Paracetamol	I / III	Good	151.163	151.063324
Phenylephrine	II	Poor	167.205	167.094635

Table 7.20 lists the APIs, which include an antibiotic, diuretic, expectorant, antipsychotic, anti-inflammatory, analgesic and decongestant, respectively; their indications are not relevant to this work but all are available as orally-administered immediate release formulations.[293] The APIs include an example from each BCS (I to IV) and all are considered small molecules by MS standards (below 2000 Da).[294] The molar mass of each API is noted for concentration calculations and the monoisotopic mass for ESI-MS identification.

A range of excipients commonly used for immediate release formulations were additionally selected for MS analysis, see Table 7.21. The list includes a variety of molecular sizes and types, hence molar mass and monoisotopic mass have not been included and will be discussed on an individual basis. Excipients are manufactured to a variety of grades, which can influence the role they play within a formulation; these specifications include a variety of attributes ranging from particle size distribution to impurity profile.[110] In addition to the physicochemical properties of each excipient, the range and extent of impurities also have potential to impact upon ESI-MS through ionisation phenomena or adduct formation.[243,295] To simplify analyses, one supplier was chosen for each excipient in order to maintain continuity and where multiple grades or varieties have been included, the details are stated.

Table 7.21 – Excipient selection including abbreviations and usual roles in immediate release formulations.

Excipient	**Role in formulation**[110]
Croscarmellose sodium (CCS)	Disintegrant
Lactose	Diluent / Filler
Magnesium stearate	Lubricant
Mannitol	Diluent / Filler
Microcrystalline cellulose (MCC)	Binder / Diluent / Disintegrant / Filler
Povidone 30	Binder
Povidone CL (crospovidone)	Disintegrant / Dissolution enhancer
Sodium stearyl fumarate (SSF)	Lubricant
Sodium starch glycollate (SSG)	Disintegrant
Starch	Binder / Diluent / Disintegrant / Filler

The use of biorelevant dissolution media for dissolution testing is the subject of much discussion and debate; however, the purpose of this work is not to replicate *in vivo* conditions but to explore the feasibility of a new technique to monitor dissolution.[123] Dissolution media can range from simple pH buffers to complex physiologically relevant mixtures where pH, osmolality, buffer capacity and surface tension are tightly controlled.[296] Simple solvents will be used initially with a plan to add more complex additives gradually so that their impact on ESI-MS can be determined.

Water and acetonitrile are commonly used ESI-MS solvents, often used in combination at varying concentrations of each ranging from 0 to 100 percent volume per volume (% v/v). This mixture has been chosen for a number of reasons including cost and availability, their ability to dissolve a wide range of substances and the fact that they are both polar solvents. Additionally, acetonitrile is volatile which aids the electrospray process compared with a purely aqueous media requiring higher

temperatures and gas flow to obtain a stable spray.[297] The solvents can be used both with and without an ionisation modifier of 0.1% v/v formic acid.

The mechanism of electrospray ionisation is such that all components present in the solution reaching the ion source may become charged, including solvents and additives in addition to the analyte(s) of interest. These protonated or deprotonated molecules may then act as reagents, with the potential for gas-phase reactions to occur between the ions and molecules present.[297] In the positive mode of ESI, formic acid is therefore considered to encourage the production of $[M + H]^+$, the protonated ion, through influencing basicity, and it would follow that adding a base should encourage deprotonation to produce $[M – H]^-$ in the negative mode of ESI, however, research has shown that this is not the case, and weak acids again prove to be beneficial in both modes.[247,298,299] Researchers continue to explore the various drivers for these observations in ESI and currently conclude that they vary with differing instrument conditions, pH, polarity, relative gas-phase proton affinities, molecular volumes and volatility amongst many other factors.[300–302]

While the use of modifiers in MS, is frequently necessary and therefore routine, excluding all modifiers from this initial investigation would provide a clearer understanding of the true relationship between the concentration of components and the MS signal. Their exclusion may also prove to be beneficial if samples of dissolution media are returned to the dissolution bath in future on-line experiments, hence, wherever possible, modifiers have been excluded.

7.2 Method

A solution of each component (API or excipient) dissolved in water and acetonitrile 50:50 v/v was analysed using the Synapt, and in some cases the QToF, to determine the primary ion(s) of interest to follow, with elemental composition used for confirmation where necessary. In the case of very poorly soluble APIs, small volumes of additional solvents have been included to aid dissolution and are stated in the relevant sections. The solutions were then analysed using the QDa to confirm any ion(s) of interest were consistent with the Synapt analysis. The extent of ionisation

was explored in varying water and acetonitrile concentrations, with and without an ionisation modifier, and in both positive and negative modes of ESI-MS, where necessary.

The QDa and Synapt were used to analyse standards across a range of concentrations (0.005 and 100 μg/mL) to determine the limits of detection and produce a calibration plot for quantification of each component using each instrument. Each standard was run on each instrument three times and the instrument settings were kept consistent where possible with the ultimate aim of enabling concurrent analysis of multiple components with minor changes only. Regression analysis was then applied to each data set to determine the relationship between instrument signal and sample concentration, as described in the best practice guidance from LGC.[303,304]

A summary of analysis, which includes the model applied, an equation, the data used, constants to be applied and the error involved, can be found within each plot. The error includes either an R-squared value or an adjusted R-squared value. An R-squared value (R^2) measures how well the line fits the data using least-squares (with a value of one representing the best fit) and an adjusted R-squared value (R'^2) uses mean squares instead of sum of squares to take into account the number of residual degrees of freedom when a polynomial regression has been applied.[276] The R'^2 is relevant for plots where the relationship is not linear but rather polynomial, quadratic or cubic. Non-linear calibration curves require more measurements to solve and uncertainty estimation is more of a challenge but they are equally valid for understanding the relationship between concentration and instrument response.[304,305] Guidelines on analytical validation in relation to spectrometry data are provided by the International Conference on Harmonisation (ICH), and at the time of writing, Q2 (Validation of Analytical Procedures: Text and Methodology) and Q14 (Analytical Procedure Development) are being revised and combined.[306]

The equipment set ups are described in Chapter 6. ESI-MS Equipment Set Up, and in this initial work exploring the relationship between single components and signal, aliquots of sample have been injected into the MS instruments. In some cases LC has

also been used prior to ESI-MS, but these details will be provided for each section of work in order that appropriate conclusions may be drawn and the limitations of each individual set up understood.

7.3 Results and Discussions

All APIs listed in Table 7.20 were compatible with ESI-MS with the exception of ibuprofen, which will be discussed in detail. The chloramphenicol data, results and analyses are typical and provide a worked example of the steps involved in producing calibration plots and enabling quantification with ESI-MS. Detailed discussion of this data set has therefore been provided with additional examples of differing approaches to analysing the data included for completeness. The results and discussions for further APIs have been described more succinctly to avoid repetition.

The list of excipients in Table 7.21 are commonly used in oral formulations, but include molecules with poor aqueous solubility and / or high molecular weights, hence it was not possible to obtain good ESI-MS results for them all. Lactose, mannitol and povidone 30 were the only excipients sufficiently soluble in water and acetonitrile to enable ESI-MS analysis. The data obtained for each API is provided in alphabetical order, then each of the soluble excipients, before finally, the more challenging excipients are discussed.

The results for each component include a brief discussion about its medicinal uses, its chemical properties and structure, the primary ion(s) found using ESI-MS and then concentration response plots for both the Synapt and the QDa where appropriate. Note that in some examples the relationship is linear but in the majority of cases alternative regression analyses have been applied so as to describe the shape and enable concentration to be calculated from signal.

7.3.1 Chloramphenicol

Chloramphenicol is defined by the BCS as having good solubility and poor permeability.[292] In the British National Formulary (BNF) it is available in just one oral immediate release form: a 250 mg capsule formulated with the free base.[293] It is a

broad spectrum antibiotic reserved for use in life-threatening infections due to its association with serious haematological side effects.[293]

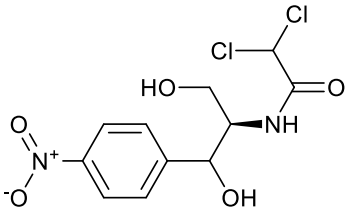

Figure 7.211 - Chloramphenicol chemical structure.

Chloramphenicol dissolved in a water and acetonitrile mix at 50:50 v/v was found to ionise effectively in negative mode ESI-MS with $[M-H]^-$ observed at *m*/*z* 321, which is in line with its monoisotopic mass, see Figure 7.211. Further confirmation that this signal was due to chloramphenicol came from the characteristic isotope pattern, which presents as a result of the two chlorine atoms within the molecule. An example is shown in Figure 7.212.

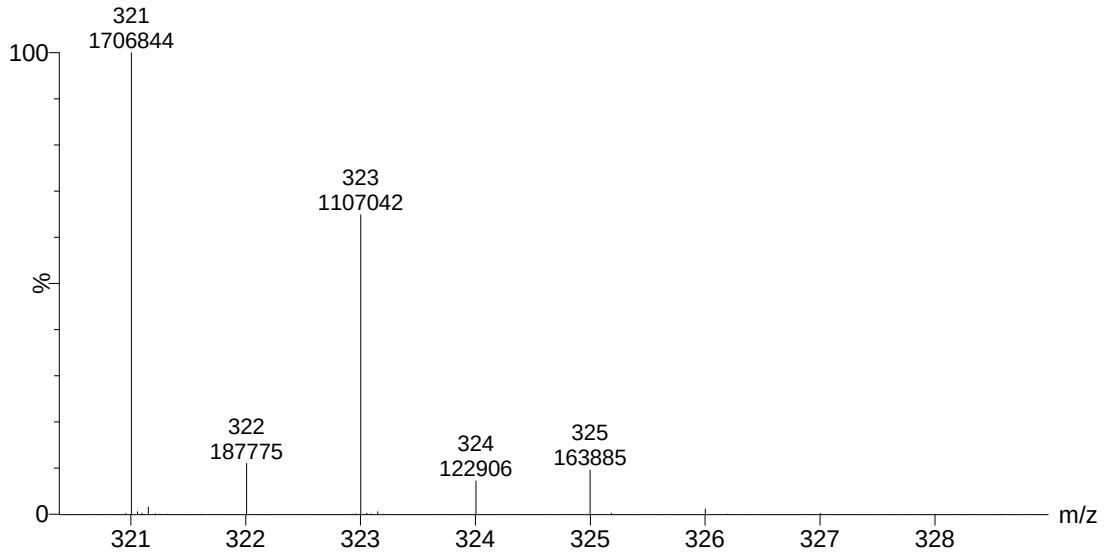

Figure 7.212 - Synapt negative ESI-MS spectrum highlighting the characteristic isotope pattern for chloramphenicol as a result of the two chlorine atoms. Peaks are annotated with *m*/*z* (top) and intensity of signal (bottom).

Chlorine exists as two isotopes ^{35}Cl and ^{37}Cl, with natural abundances of 75.28% and 24.22%, respectively.[307] In a molecule with two chlorine atoms present, there will be

three combinations of isotopes possible: 1) $^{35}Cl + ^{35}Cl$, 2) $^{35}Cl + ^{37}Cl$, and 3) $^{37}Cl + ^{37}Cl$. The remainder of the molecule (minus a hydrogen) adds up to 251, so the *m*/*z* values obtained through negative ESI-MS would be 1) 251 + 35 + 35 = 321, 2) 251 + 35 + 37 = 323 and 3) 251 + 37 + 37 = 325. The relative abundance of each would be in the ratio of 9:6:1, which should match the peak heights, although in this case we must also take into account carbon and nitrogen which have two isotopes each. Carbon exists as ^{12}C and ^{13}C at 98.99% and 1.11%, respectively, and nitrogen exists as ^{14}N and ^{15}N at 99.63% and 0.37%, respectively.[307] This accounts for the slight variation in relative intensities, and for the additional signals at 322 and 324, but provides additional confirmation that chloramphenicol could be monitored using a SIM method at *m*/*z* 321.

A series of chloramphenicol standards were produced using a water and acetonitrile mix at 50:50 v/v without the use of a modifier. The standards were analysed on both the Synapt and the QDa without HPLC. Quantification for each instrument was carried out using both peak area and peak height data for completeness, in addition to both with and without peak smoothing.

Synapt with peak smoothing:

The Synapt peak height and peak area data have been included on one plot for comparison, see Figure 7.213. The precision of individual data points is good, with each point representing the average of three runs and the standard deviation shown using error bars. The lower limit of quantification for the Synapt is 0.05 µg/mL and the relationship between signal and concentration appears to change around 50 µg/mL as both peak height and peak area begin to plateau. The relationship between response and concentration for each plot was explored using the Origin software, however, no fit could be found. Note that *m*/*z* 321 has been extracted from the full scan data (with an absorbance window of 0.1 Da) and the resulting peak integrated using the MassLynx software for the Synapt.

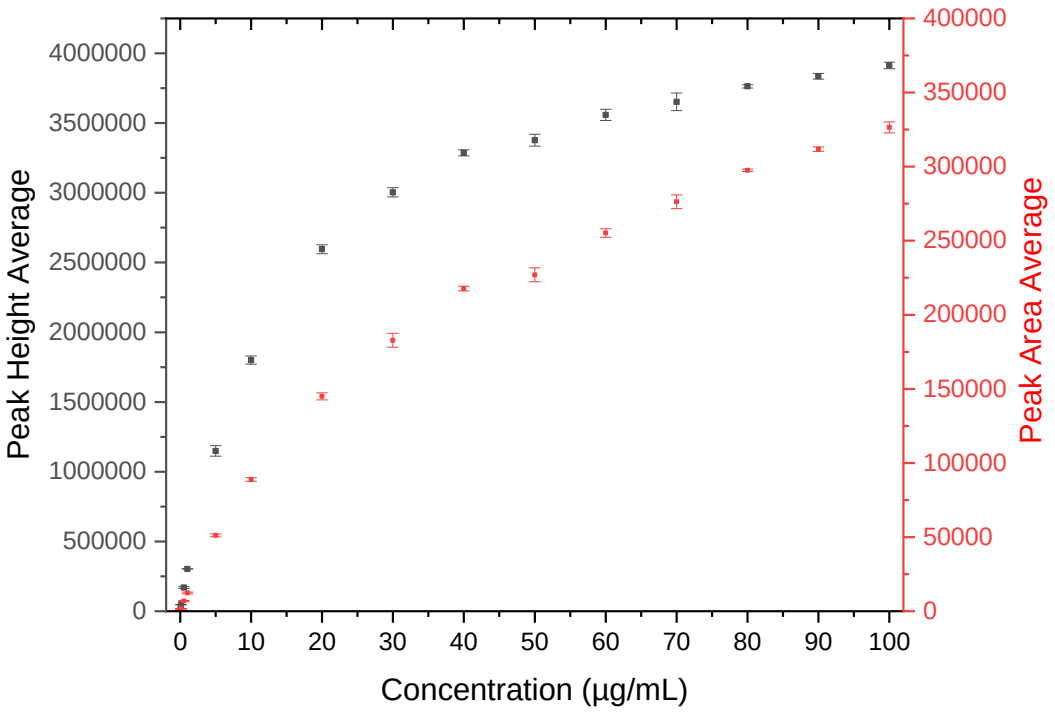

Figure 7.213 – Synapt calibration plots showing the relationship between signal and concentration for chloramphenicol. The average peak height data is shown by the black boxes and uses the y-axis to the left. The average peak area data is shown by the red boxes and uses the red y-axis on the right hand side. Each point is the average of three runs with the standard deviation shown by error bars.

QDa with peak smoothing:

The QDa calibration has utilised a full scan and a SIM method following *m/z* 321. The full scan provides confirmation that there are no other ions of interest being produced at different concentrations for this investigatory work, and the SIM enables simpler quantification. The calibration plots for the QDa are shown in Figure 7.214 with peak height and area included in one. The data points again show good precision with each point the average of three runs and the error bars showing the standard deviation. The chloramphenicol signal for standards below a concentration of 1 µg/mL was detectable but too small to be quantified using either peak height or peak area methods. The lower limit of quantification for the QDa can therefore be set at 1 µg/mL for this method of sample injection (1 µL) and analysis, which is double that found using the Synapt (0.05 µg/mL). Multiple regression analyses were again applied to determine the relationship between signal and concentration, and again, none fitted sufficiently well. The first three data points (1 µg/mL up to and including 10

µg/mL), appear to be distinct from the last eight data points (30 to 100 µg/mL) and there is a clear outlier at 20 µg/mL, for both the area plot and the height plot.

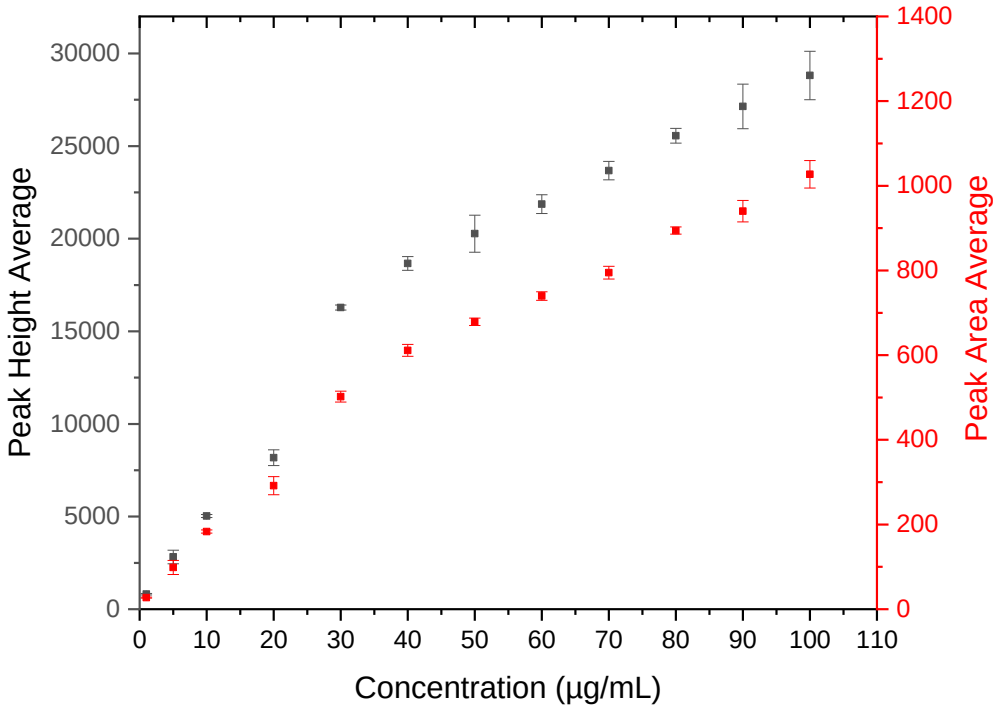

Figure 7.214 – QDa calibration plot showing the relationship between signal and chloramphenicol concentration. The average peak height data is represented by black squares and uses the y-axis to the left. The average peak area data is represented by red squares and uses the x-axis to the right. Each point is the average of three runs with the standard deviation shown using error bars.

The outlier at 20 µg/mL is most distinct for the QDa peak height data and is also present for the QDa peak area data, however it is not present in the Synapt analysis. The data points all show good precision and yet the same calibration standards were used in both which excludes the likelihood of there being an error in the sample itself. A quick glance at the QDa SIM signal for *m*/*z* 321 shows that as the sample concentration increases, the signal peak shape changes in addition to increasing in both height and width, see Figure 7.215.

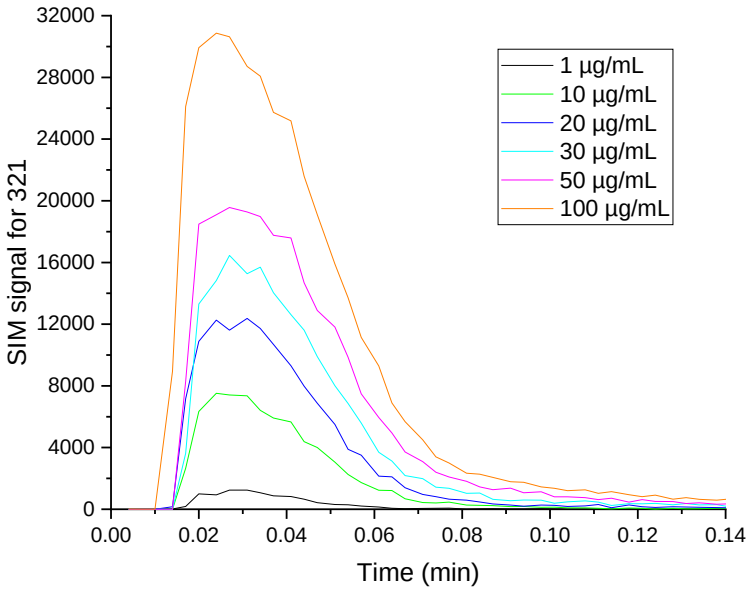

Figure 7.215 - QDa chloramphenicol selected ion monitoring (SIM) chromatogram for *m/z* 321 showing peak shape for a range of concentrations.

A closer look into the QDa SIM signal obtained for chloramphenicol standards between 10 and 30 µg/mL, Figure 7.216, again highlights that the data shows good overall precision. However, it also shows a change in peak shape that would impact upon the average peak height measurements for these concentrations and could also explain why the outlying point in the average peak area calibration plot is present but less distinct.

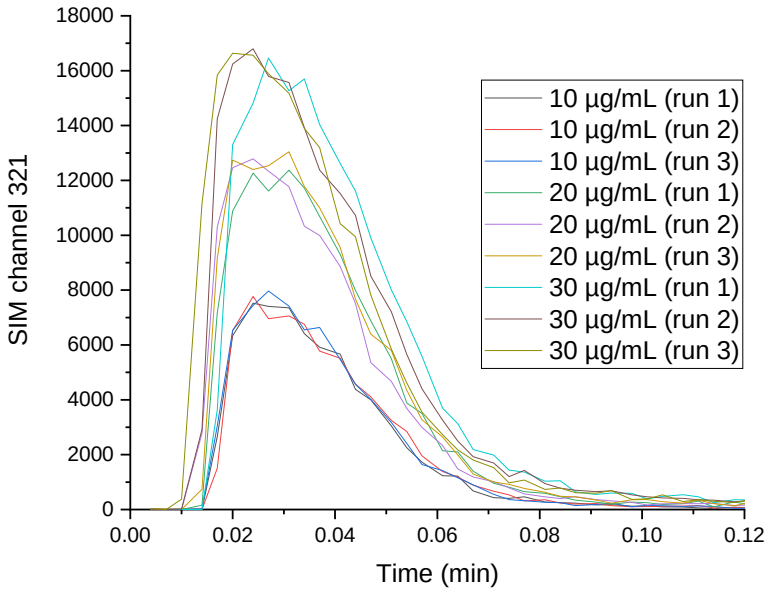

Figure 7.216 – QDa chloramphenicol selected ion monitoring (SIM) chromatograms for *m/z* 321 showing peak shape differences for each of the three runs at 10, 20 and 30 µg/mL.

The peak height looks to be flattened, which can signify saturation of the detector, however, the higher concentration peaks (50 and 100 µg/mL) do not show the same effect suggesting this is not the cause. This highlights the need to consider each individual peak shape when extracting peak area and height, and makes clear the limitation of using the automated peak detection and smoothing within the MassLynx software, see Figure 7.217.

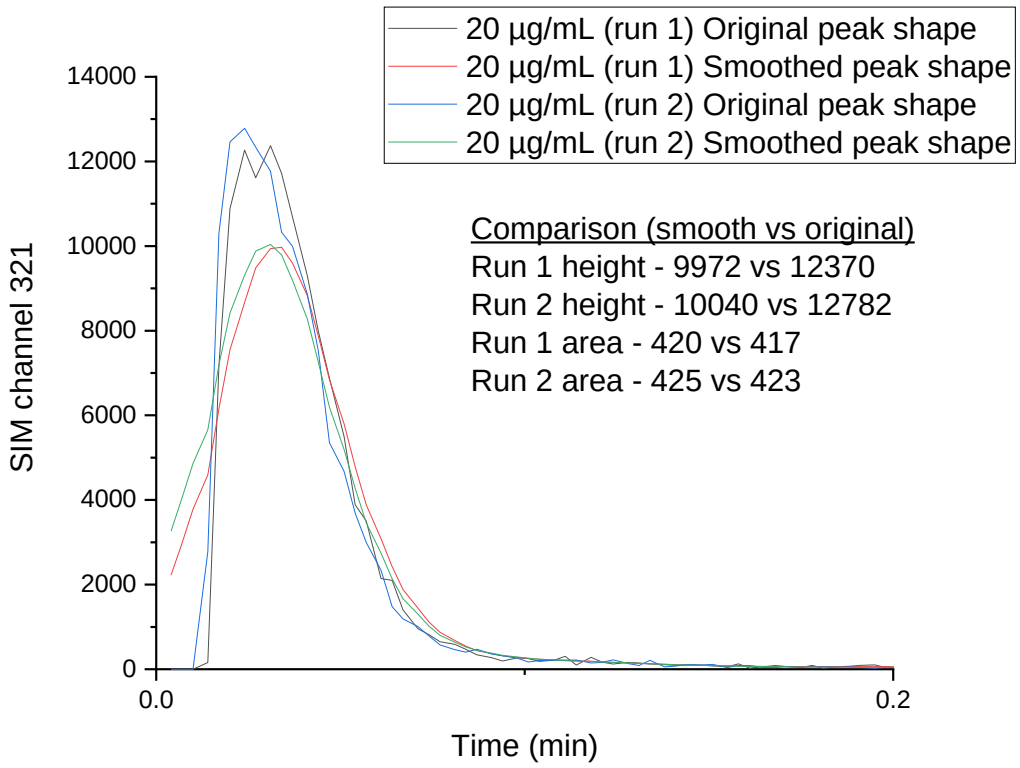

Figure 7.217 – QDa chloramphenicol calibration standard 20 µg/mL (run 1 and run 2) SIM channel 321 comparison showing the original flattened peak and the MassLynx smoothed peak. Inset is the difference in extracted height and area for the smoothed vs original peaks highlighting the importance of looking at individual peak shapes when collecting data.

QDa without peak smoothing:

A more detailed extraction of the peak height and area was repeated using the Origin software, focusing on absolute area with no smoothing, see Figure 7.218. This shows a more consistent relationship between concentration and response between the peak height and area, with reduced standard deviation error bars suggesting this is a more consistent method for extracting data.

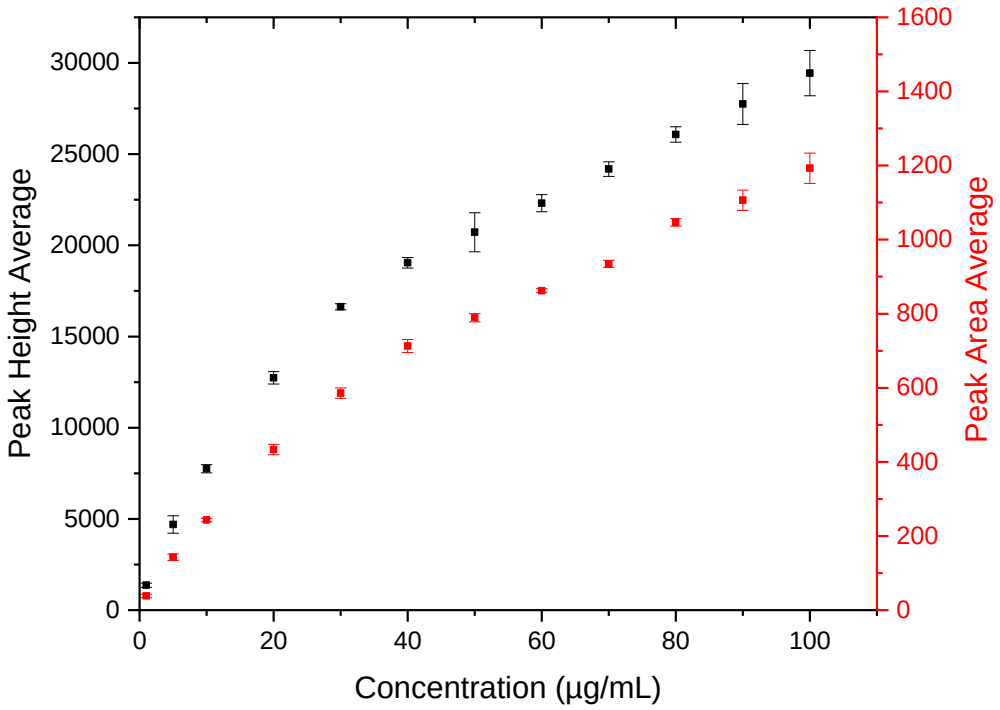

Figure 7.218 – QDa calibration plots using Origin to determine absolute area and peak height from the SIM channel data. The double y-axis plot shows the relationship between chloramphenicol concentration and average peak height (left y-axis with black markers) as well as average peak area (right y-axis with red markers). Each point is the average of three runs with the standard deviation shown using error bars.

Regression analysis was performed using the peak area average and the peak height average; the resulting data is shown in Figure 7.219 and Figure 7.220, respectively. The confidence bands increase after a concentration of 70 µg/mL for peak area, and after 80 µg/mL for peak height for the QDa. The adjusted R-squared value is improved for the equation fitted to the peak height data than the peak area data (0.99977 compared with 0.99943).

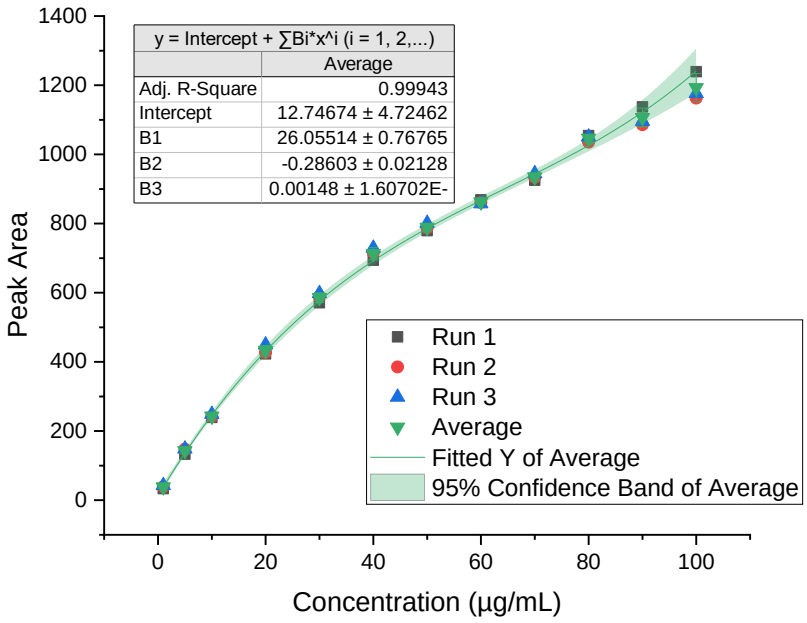

Figure 7.219 – QDa calibration data using Origin to determine absolute area from the SIM channel data with regression analysis applied to the average and additional data inset.

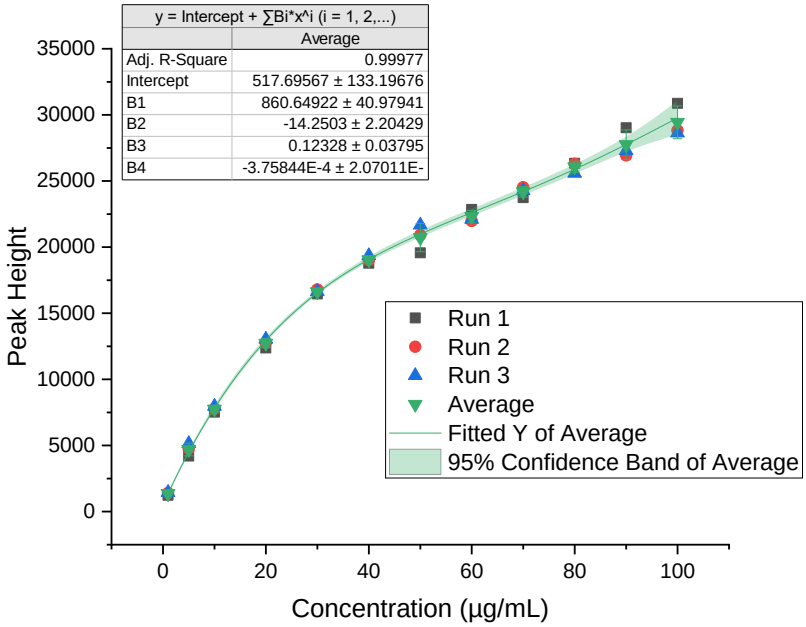

Figure 7.220 – QDa calibration data using Origin to determine peak height from the SIM channel data with regression analysis applied to the average and additional data inset.

Synapt without peak smoothing:

The peak shapes for the Synapt calibration data are shown in Figure 7.221 for comparison. These are more consistent and the signal is spread over a larger time period, hence the area and height would be expected to be less open to misinterpretation by the software. The tips of each peak, however, have been missed. Upon further investigation this is due to the Synapt scan time rather than saturation of the detector, as the characteristic isotope pattern remains consistent for each. This could be amended to scan more frequently and therefore include more data points, however, it would increase the data burden and the ion statistics (as previously discussed). The ability to capture the extent of the peak will also be dependent upon the time taken for maximum ionisation of the sample, which will vary with each concentration injected and therefore cannot easily be optimised for every run. It will be kept consistent for all runs and explored further only if necessary.

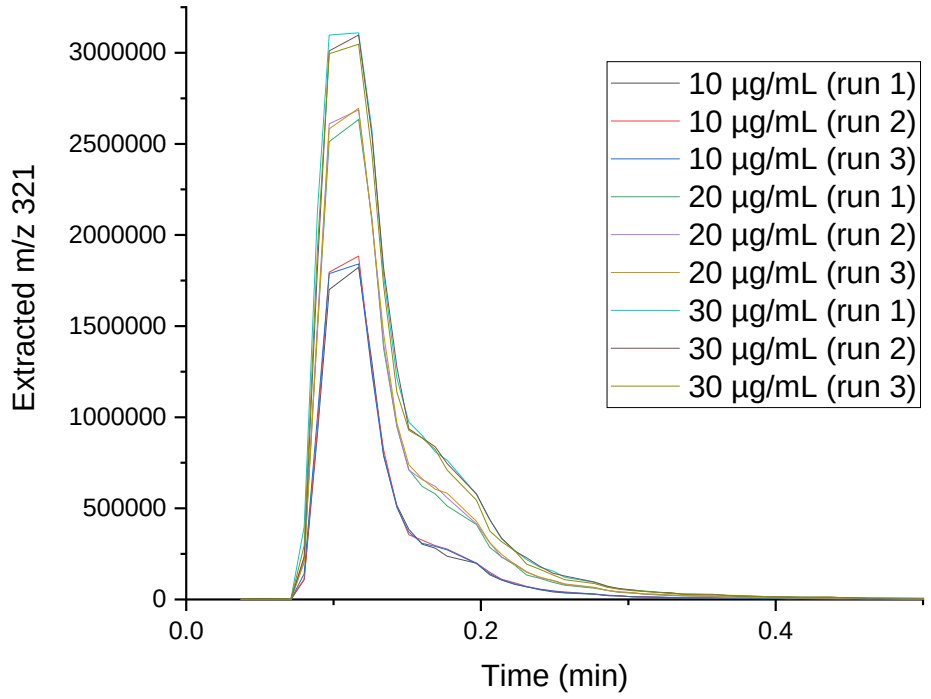

Figure 7.221 – Synapt chloramphenicol extracted chromatograms for *m/z* 321 showing peak shape differences for each of the three runs at 10, 20 and 30 µg/mL.

For completeness the Synapt data was re-extracted using Origin software (without peak smoothing) and the result can be found in Figure 7.222. The data differs between

methods of extraction, but the relationship between signal and concentration remains the same for both peak height and area for the Synapt, suggesting that it changes at a concentration of 50 µg/mL.

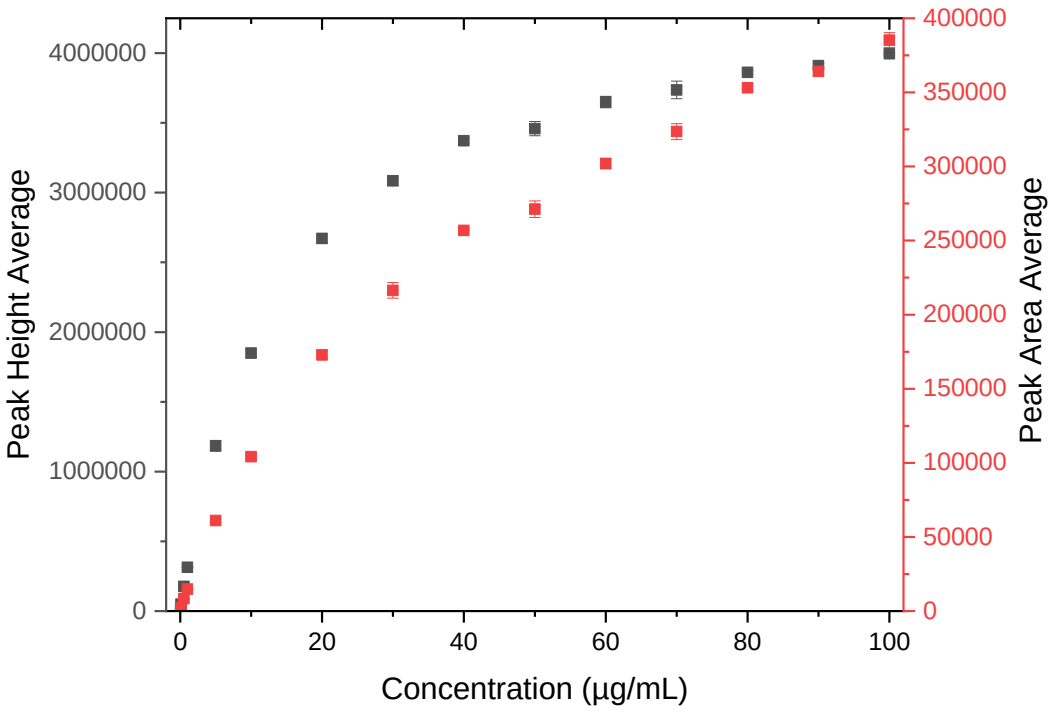

Figure 7.222 – Synapt calibration plots showing the relationship between signal and concentration for chloramphenicol using Origin to determine absolute area and peak height using extracted mass. The average peak height data is shown by the black boxes and uses the y-axis to the left. The average peak area data is shown by the red boxes and uses the red y-axis on the right hand side. Each point is the average of three runs with the standard deviation shown by error bars.

Regression analysis was performed using the peak area average and the peak height average; the resulting data is shown in Figure 7.223 and Figure 7.224, respectively. The confidence bands increase after a concentration of 10 µg/mL for peak area, and after 20 µg/mL for peak height for the Synapt. The adjusted R-squared value is slightly better for the equation fitted to the peak height data than the peak area data (0.99948 compared with 0.99878), which is consistent with the QDa findings.

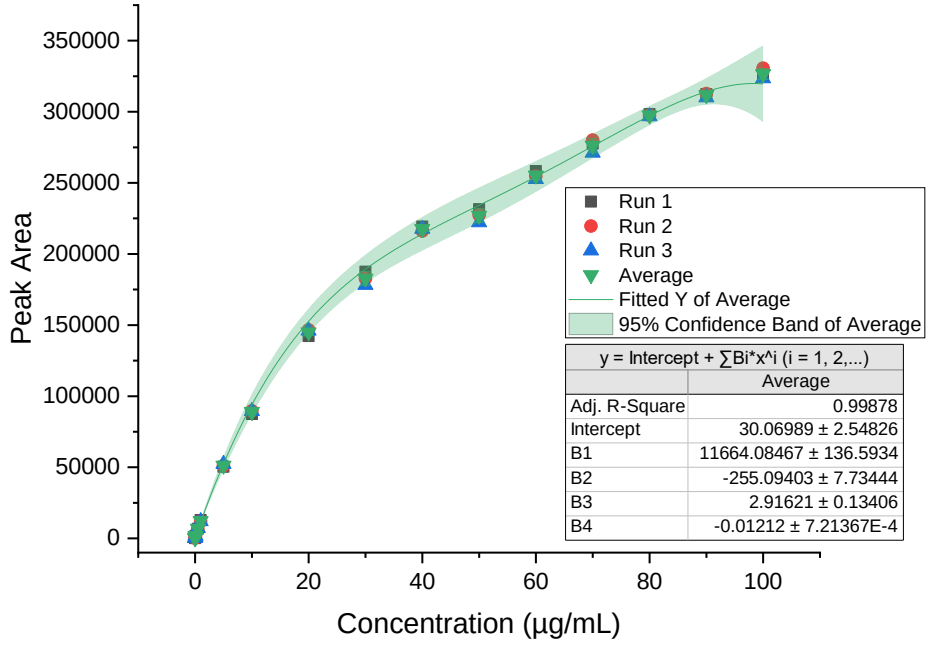

Figure 7.223 – Synapt calibration data using Origin to determine absolute area under the peak from extracted mass data with regression analysis applied to the average and additional data inset.

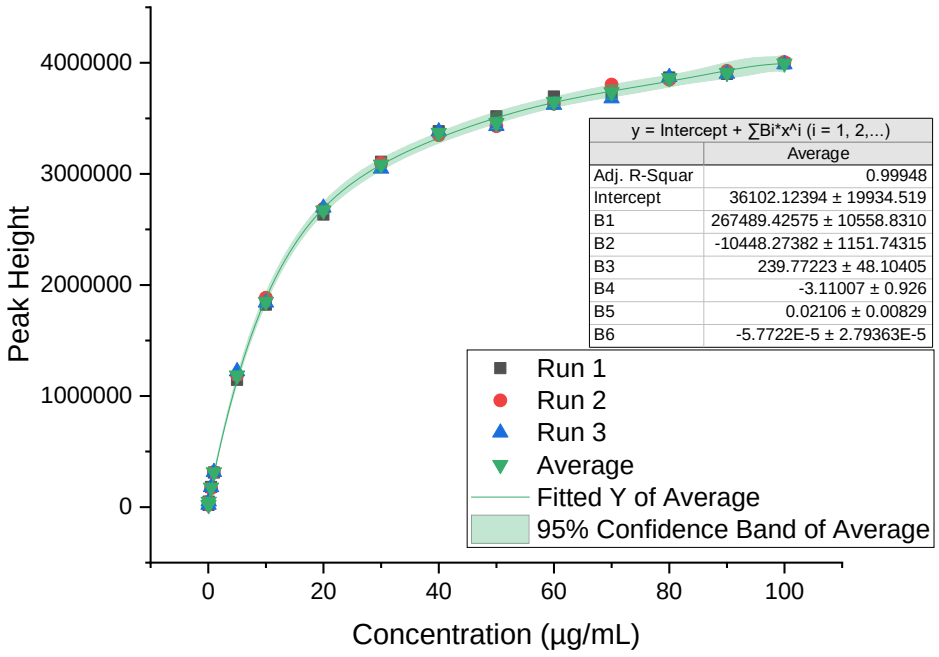

Figure 7.224 – Synapt calibration data using Origin to determine peak height from extracted mass data with regression analysis applied to the average and additional data inset.

Summary:

In summary, the QDa signal is more consistent across a larger concentration range for both peak height and peak area calculations, from 1 to 70 µg/mL, while the Synapt has a lower limit of detection, 0.05 µg/mL, but increased error at concentrations above 20 µg/mL when using peak height and above 10 µg/mL when using peak area. These findings are consistent with the different types of instrumentation used; the Synapt uses TOF mass analysis, which has a greater sensitivity and therefore lower limit of detection than the QDa's quadrupole, which in turn possesses a greater dynamic range and an extended limit for quantification.

Three additional concentrations of sample were analysed in triplicate on both the QDa and the Synapt, at the same time as the samples for each calibration to maintain consistency. The signal from these samples was analysed using the same methods used to extract each data set and produce the calibration plots. Both peak height and peak area data were used with the regression analyses for each calibration plot, and from these, concentrations were calculated, see Table 7.22.

Table 7.22 – Comparison of using initial calibration plots to determine concentration from signal for both peak height and peak area, for each instrument. The 95% lower and upper confidence limits are provided in brackets for each value.

Prepared concentration (µg/mL)	Peak height - experimentally determined concentration		Peak area – experimentally determined concentration	
	QDa	Synapt	QDa	Synapt
2.2	5.6 (4.7 - 6.5)	2.7 (2.5 - 3.0)	6.9 (6.5 - 7.2)	3.0 (2.9 – 3.3)
9.3	13.6 (12.3 - 15.1)	10.9 (8.7 - 13.7)	15.6 (14.9 - 16.4)	10.9 (10.5 – 11.4)
13.5	17.1 (15.6 - 18.8)	15.0 (12.1 - 18.5)	18.4 (17.6 - 19.3)	14.4 (13.9 – 15.0)

The prepared concentration values are within the 95% confidence limits for two of the three Synapt peak height determined concentrations. However, the majority of these experimentally-determined concentrations, including their 95% confidence limits, are consistently higher than the prepared concentrations, suggesting there is extensive and systematic error involved in calculating the line of best fit for both the peak area and the peak height data. The Synapt values are more closely aligned with the prepared concentrations than the QDa values, however, neither method resulted in the correct concentrations being calculated. Concentrations calculated from peak height values for the QDa are consistently closer to the prepared concentrations than those calculated using peak area, however, the difference between methods for the Synapt is less easily defined, with peak height values subject to larger confidence limits than peak area.

Consistency of QDa data:

A series of calibration standards covering the same concentration range was produced a year later and re-run on the QDa to give an indication of data repeatability and to

assess a necessary change in equipment set-up, as the LC injecting the sample had been replaced. The time-frame was sufficiently long that the instrument would be expected to produce different responses (good practice suggests running samples on the same instruments on the same day).[303] For further exploration of the relationship between signal and concentration and as a result of a change in instrumentation set-up, the volume of standard injected into the solvent flow increased from 1 µL for the initial run to 3 µL for the repeated run.

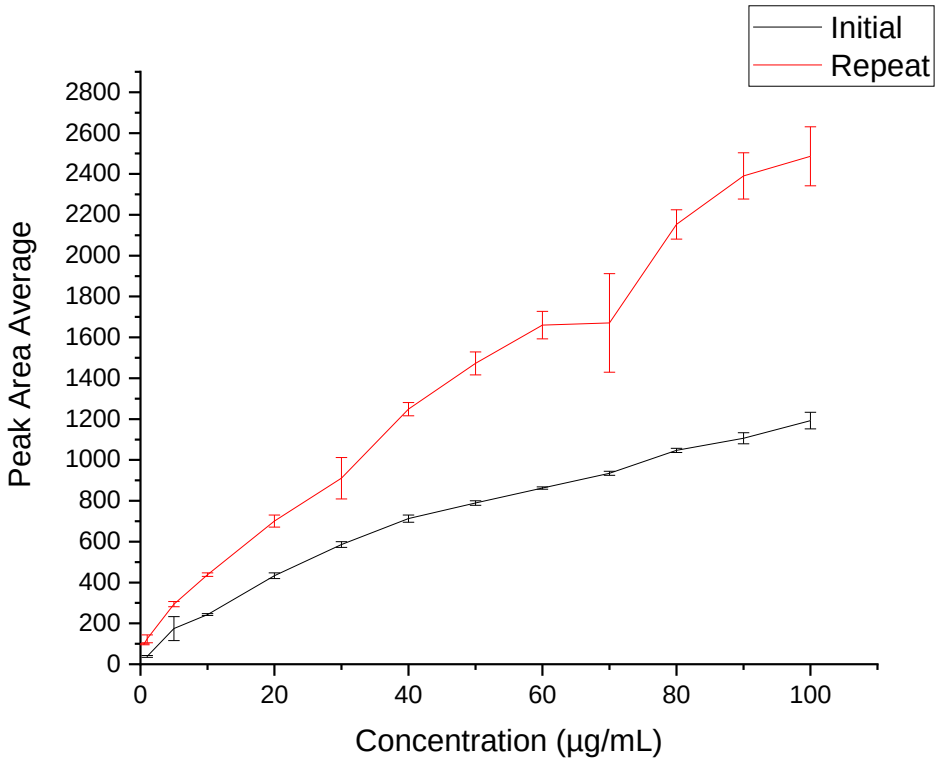

Figure 7.225 – QDa calibration plot showing the relationship between peak area of signal and chloramphenicol concentration for two separate calibrations run on the same instrument one year apart. The initial run (black points) injected 1 µL of sample and the repeated run (red points) injected 3 µL. Each point is the average of three runs with the standard deviation shown using error bars.

The relationship between concentration and signal as measured by peak area is shown in Figure 7.225 and confirms that the overall quantity of API reaching the instrument has an impact, although the signal increase from injection of 1 µL to 3 µL is not simply tripled. This increase in injected quantity appears to have little effect upon peak height, as shown in Figure 7.226, although both the repeated calibration plots show increased standard deviation error bars compared with the initial runs. Peak height is

limited in the extent to which it can change relative to peak area – the detector will saturate if too many ions present at once reaching a maximum peak height, but if they continue to present over a larger time period they will be measured as a larger peak area.

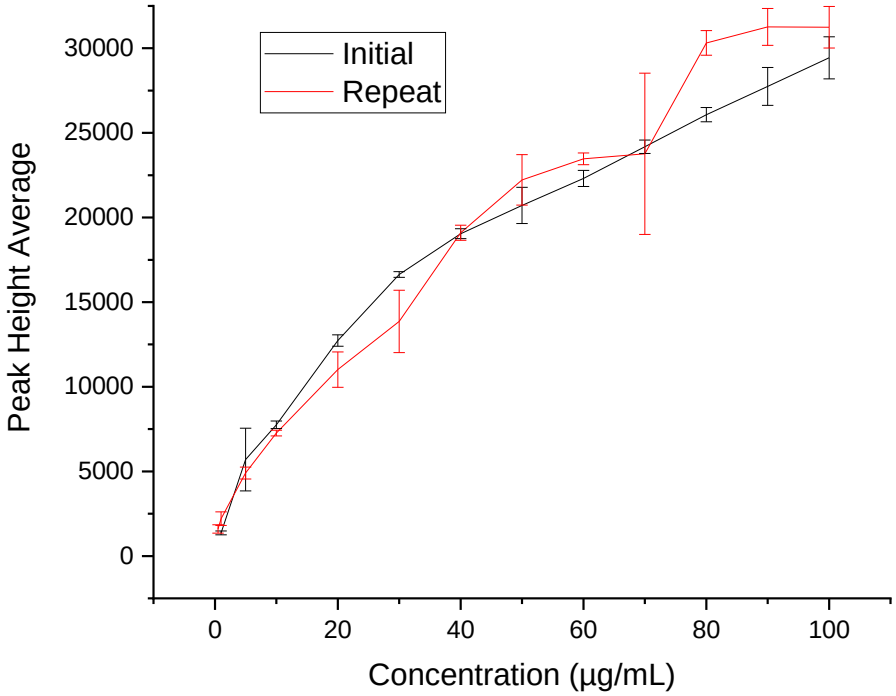

Figure 7.226 – QDa calibration plot showing the relationship between peak height of signal and chloramphenicol concentration for two calibrations run on the same instrument with the same method settings one year apart. The initial run injected 1 µL of sample and the repeated run injected 3 µL. Each point is the average of three runs with the standard deviation shown using error bars.

Caution should be exercised in comparing the results due to the time scale of experiments and the differing injection volumes. Upon first glance the repeated run appears to enable a concentration of 0.5 µg/mL to be distinguished from the blank, effectively extending the lower limit of quantification for the QDa from 1 to 0.5 µg/mL. However, this is arguably a result of the increase in total quantity of chloramphenicol injected into the MS not solely the concentration of standard.

One interpretation would be to discuss the lower limit of quantification as the concentration multiplied by the amount injected (total mass), which would be 0.0015 µg. In the previous run the lower limit of quantification, using the same method for

data analysis, was 1 µg/mL with 1 µL injected hence the limit would be stated as 0.001 µg. This suggests that the lower limit of quantification is consistent between both runs as the next concentration of standard to be analysed was 0.1 µg/mL, to make the amount injected 0.0003 µg, which cannot be distinguished from the blank. Additionally, it may be explained by considering dilution of the sample aliquot injected. This was introduced in Figure 6.199 and highlighted that an injected aliquot of sample will spread within a flowing stream of solvent, dependent upon diffusivity and tubing dimensions, so that the sample reaching the MS may vary in concentration from that injected. A change in size of aliquot from 1 to 3 µL may also impact upon the extent of diffusion that can occur, hence the larger plug may reach the MS less spread out and therefore less dilute than a smaller plug if all other conditions remained constant. This could explain the extended lower limit of quantification but does not enable a conclusion to be drawn as to whether the ESI-MS response is more sensitive to mass or concentration changes.

Table 7.23 – Comparison of using repeated calibration plots to determine concentration from signal for both peak height and peak area for the QDa.

Prepared concentration (µg/mL)	Peak height - experimentally determined concentration	Peak area – experimentally determined concentration
2.0	1.7 (1.0 to 2.4)	2.1 (2.0 to 2.3)
9.0	10.7 (9.9 to 11.7)	11.4 (10.9 to 12.0)
25.0	27.1 (25.0 to 29.6)	30.2 (28.5 to 32.3)

Three additional standards were run at the same time as the repeated calibration standards to again assess the ability to calculate concentration from signal and also provide a comparison with those previously calculated, see Table 7.23. The prepared concentrations covered a larger range than previously, 25.0 rather than 13.5 µg/mL, in line with the finding that the QDa dynamic range extends beyond 20 µg/mL. The

experimentally-determined concentrations were closer to the prepared concentrations for the peak height analysis than peak area, consistent with the previous findings.

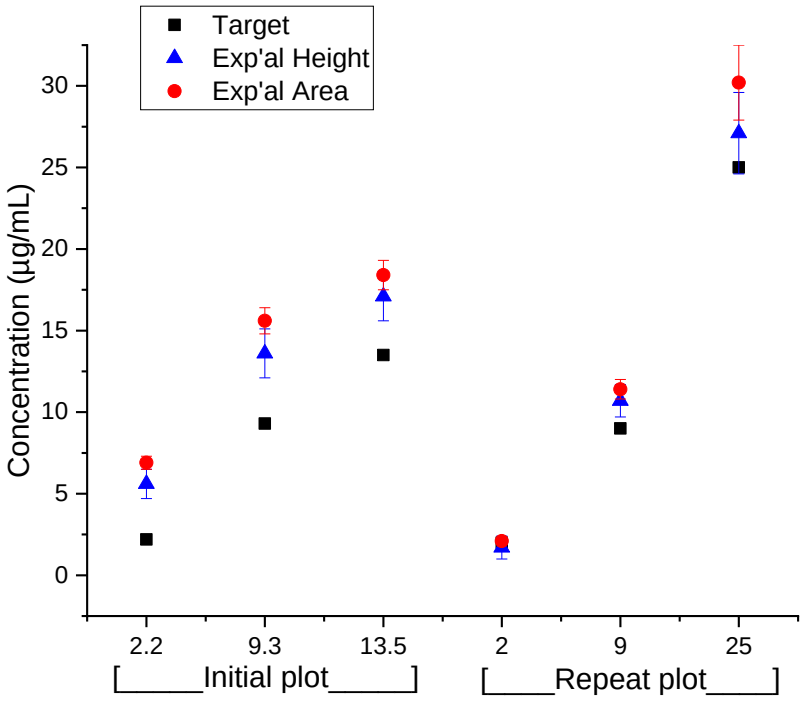

Figure 7.227 - Comparison of using initial and repeated calibration plots to calculate the concentration of known samples using both peak height and peak area. The known concentration of the samples is plotted as the target for each set of data.

A comparison of the initial calculated concentrations and the repeats can be viewed more easily when plotted together with error bars, see Figure 7.227. The repeated calibration plot shows improved accuracy and precision for the lowest determined concentration (2.0 µg/mL), and is slightly improved for the other two concentrations, however, both the initial and repeated sets of calibration plots consistently determine a higher concentration than that which was analysed. This over-estimation confirms that there is consistent and significant error in determining the concentration of chloramphenicol using the QDa calibration plots calculated using both peak height and peak area. Further work is required to determine the cause of this error.

7.3.2 Furosemide

Furosemide is classed as BCS IV, with poor solubility in water, reported as 0.01825 mg/mL at room temperature.[292,308,309] It is a commonly prescribed loop diuretic available as an oral immediate release tablets with strengths of 20 mg, 40 mg and 500 mg in the UK, in addition to various strengths of oral solution and also as a solution for injection.[293] It is an acidic carboxylic acid derivative, which is unstable in light and acidic media, but very stable in basic media and exhibits pH dependent solubility, which has resulted in frequent studies on its dissolution properties.[309–313] Furosemide was found to ionise effectively from solutions of water and acetonitrile at 50:50 v/v with formic acid present at 0.1% v/v using negative ESI-MS. This analysis produced ions of $[M\text{-}COOH]^-$ and $[M\text{-}H]^-$ which were observed at *m*/*z* 285 and 329 respectively, see Figure 7.228.

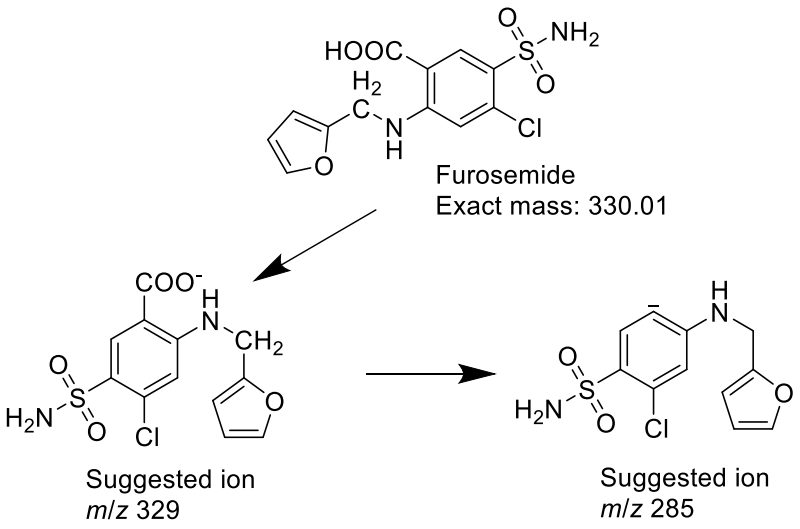

Figure 7.228 – Furosemide chemical structure and suggested formation of ions observed by ESI-MS.

The two ions of interest were present on both instruments (Synapt and QDa), with knowledge of the isotope abundance of sulphur and elemental composition by the Synapt providing confirmation of their identity. Both ions were observed across the range of concentrations analysed on the Synapt and the QDa (without HPLC), suggesting that they should both be assessed for quantification purposes.

QDa:

In the case of QDa quantification, the SIM function allowed both ions to be combined into one method, with the peak area used to produce the calibration plot found in Figure 7.229.

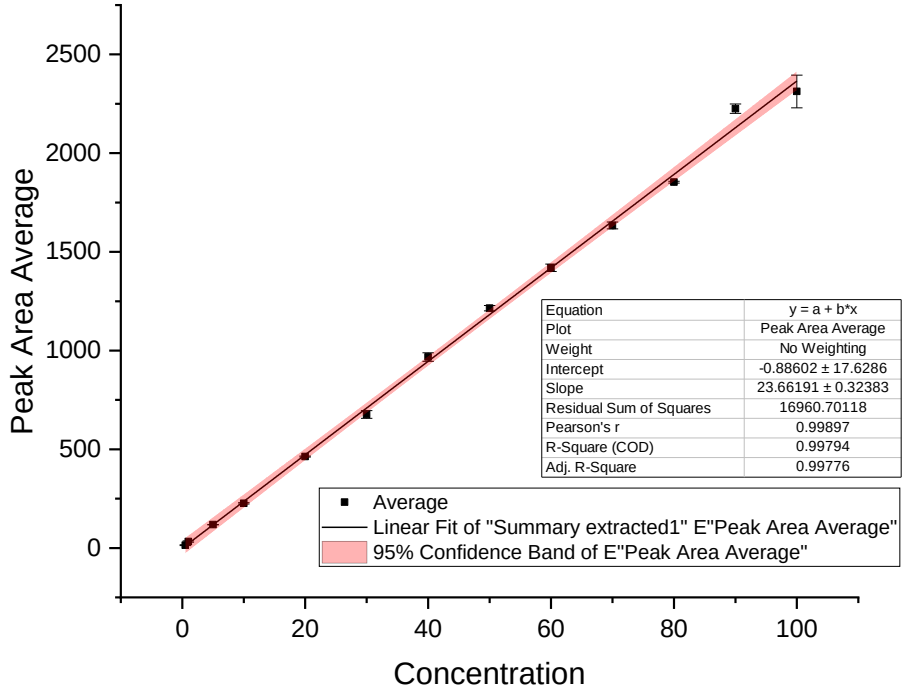

Figure 7.229 – QDa negative ESI-MS calibration plot showing the relationship between signal and furosemide concentration using average peak area data obtained through following both ions of interest concurrently (*m/z* 285 and 329). Furosemide standards are in water and acetonitrile (50:50 v/v) with formic acid (0.1% v/v). Each point is the average of three runs with the standard deviation shown using error bars. A red line of best fit has been plotted with regression data inset into the graph.

The relationship between furosemide signal and concentration, as measured using both ions of interest combined, is linear across this range for the QDa. The lower limit for quantification is 0.5 µg/mL and the R-squared value is greater than 0.99 signalling that the line of best fit has a low level of error; the outlier at 90 µg/mL suggests that the error may be greater at concentrations above 80 µg/mL. Three additional samples were analysed to determine whether each concentration could be calculated from signal using the line of best fit in Figure 7.229.

Table 7.24 - QDa experimentally determined concentrations for the three additional samples.

Prepared concentration (µg/mL)	Peak area - experimentally determined concentration	Lower and upper 95% confidence limits
2.2	2.5	-1.4 to 6.5
9.3	9.0	5.1 to 12.9
13.5	12.8	8.9 to 16.7

Table 7.24 shows the experimentally-determined values are close to the prepared concentration values, with the 95% confidence limits highlighting a comparable level of uncertainty for each sample. In summary, this linear relationship between concentration and signal builds confidence in utilising furosemide as a model compound to further understand the impact of the dissolution media and additional components upon QDa analysis.

Synapt:

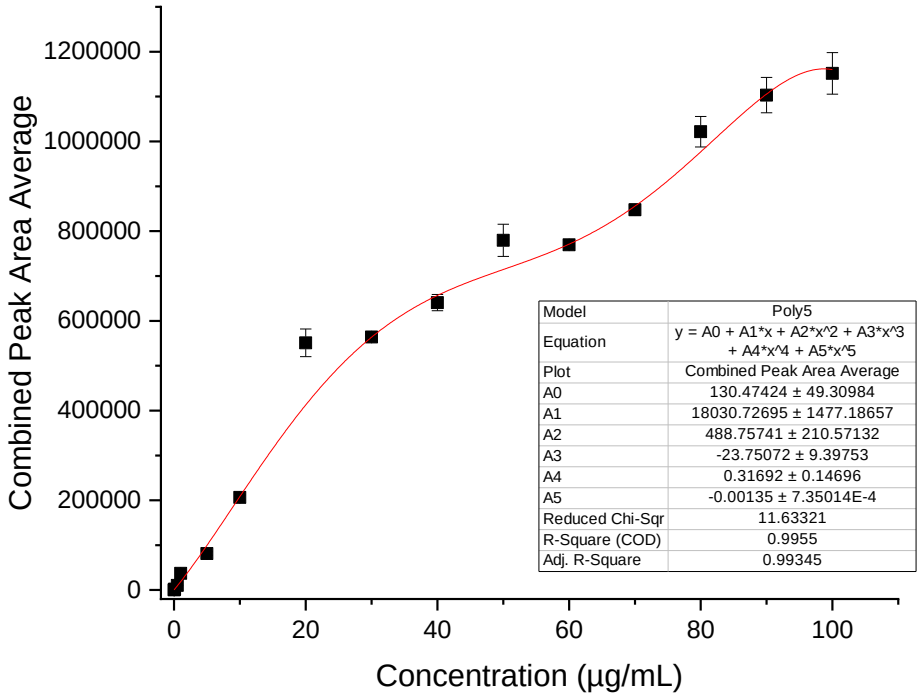

Figure 7.230 - Synapt negative ESI-MS calibration plot showing the relationship between signal and furosemide concentration using a combined peak area average obtained through extracting both ions of interest concurrently (*m/z* 285 and 329). Furosemide standards are in water and acetonitrile (50:50 v/v) with formic acid (0.1% v/v). Each point is the average of three runs with the standard deviation shown using error bars. The regression analysis is shown by the red line with the model data inset.

The range of samples were also run on the Synapt, and calibration data was extracted for the two ions combined, with regression analysis applied, see Figure 7.230. The Synapt calibration plot shows an adjusted R-squared value of 0.99 for the model applied but is significantly different from the linear QDa calibration plot. The relationship between signal and concentration was analysed further to determine whether the individual *m/z* values or the peak height data may be used more easily for quantification using the Synapt, see Figure 7.231 and Figure 7.232.

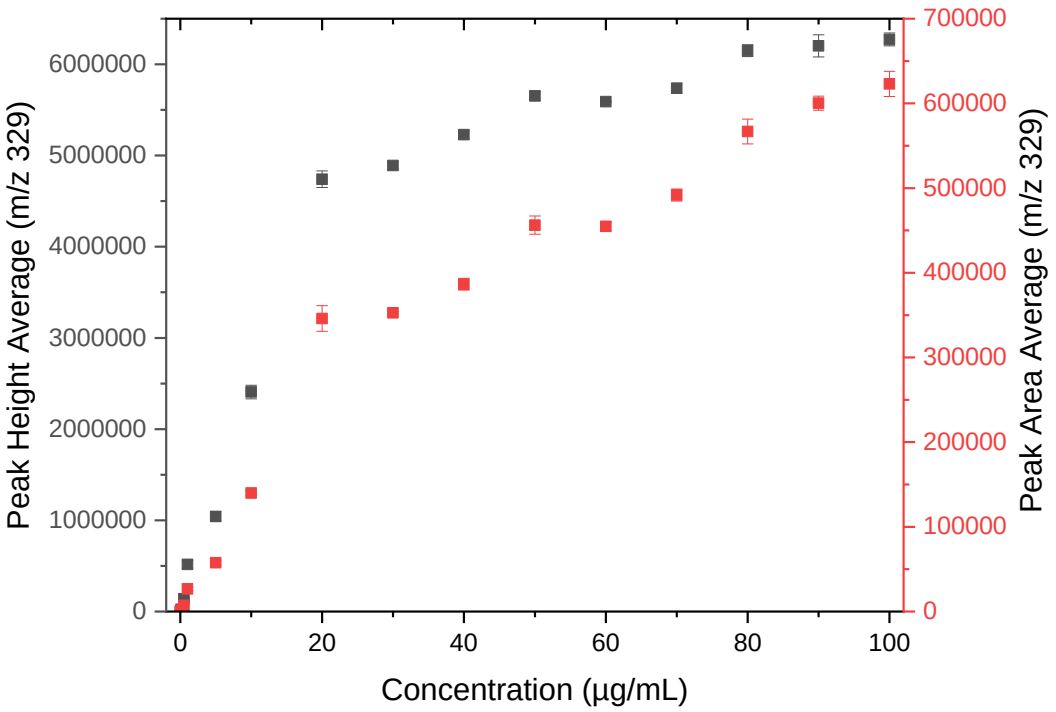

Figure 7.231 – Synapt calibration plot for m/z 329 for both peak height averages (black) and peak area averages (red). Each point is the average of three runs with the standard deviation shown using error bars.

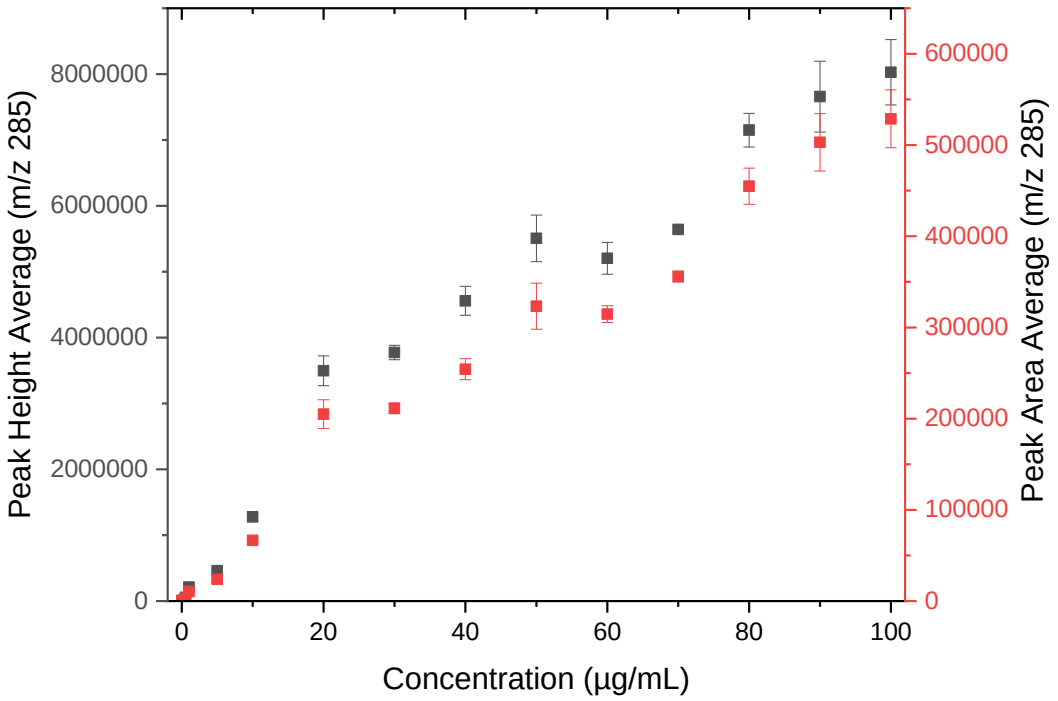

Figure 7.232 – Synapt calibration plot for m/z 285 for both peak height average (black) and peak area averages (red). Each point is the average of three runs with the standard deviation shown using error bars.

Neither the single *m/z* values nor the peak height data suggests a simple relationship between signal and concentration for the Synapt for furosemide and instead suggest that there may be step changes occurring between concentrations. In an attempt to further elucidate the relationship, the ratio of *m/z* 285 to *m/z* 329 across the concentration range has been represented using stacked columns, Figure 7.233. The ratio starts around 1:1 at the very low concentrations, then the predominant ion becomes *m/z* 329, with a ratio of 7:3 at a concentration of 1 µg/mL, before the ratio gradually returns to almost 1:1 at 90 µg/mL. A greater extent of furosemide fragmentation (on the Synapt) therefore occurs at these extremes of concentration, although the reasons for this are currently unclear.

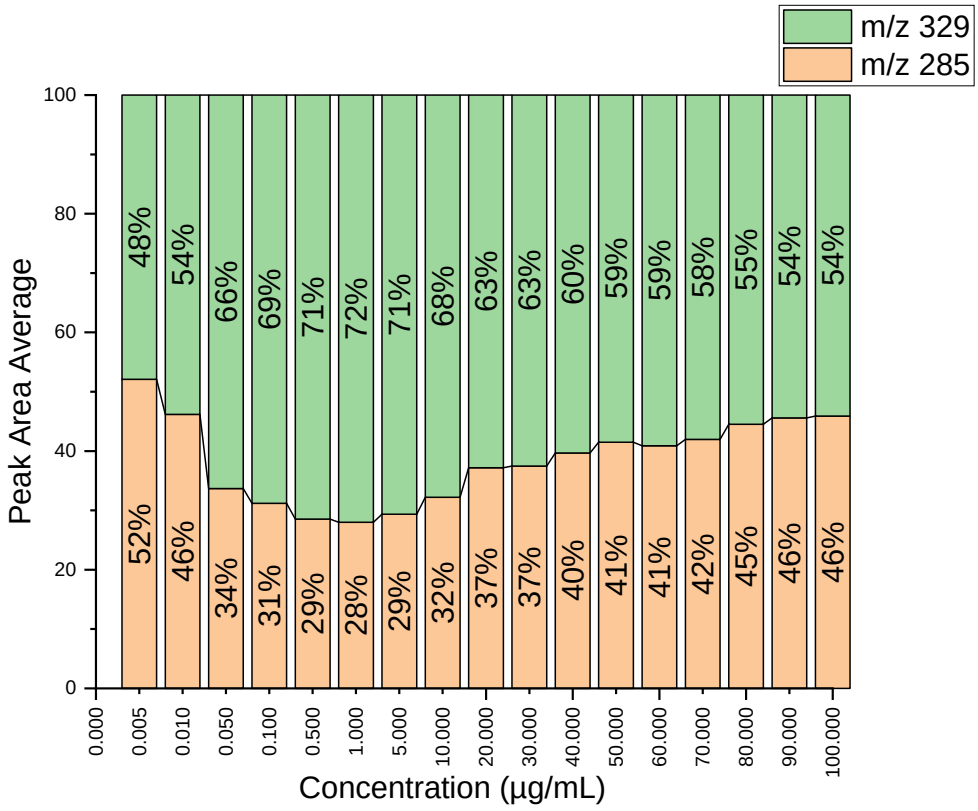

Figure 7.233 - Synapt calibration data for peak area averages highlighting the changing ratio of *m/z* 285 to *m/z* 329 across the concentration range.

Further analysis of the mass spectra revealed that an additional ion of *m*/z 681, which corresponds to $[2M + Na - 2H]^-$ appears at concentrations of 10 µg/mL and above on the Synapt. This may also account for some of the loss of linearity as dimers appear more frequently at higher concentrations due to the increased probably that two molecules of furosemide may find themselves together in one droplet towards the end of the electrospray process.[235] A detailed revisit of the QDa spectra found the dimer to be present only at concentrations of 30 and above on this instrument, highlighting the differences between the two instruments despite both ionisation mechanisms being classified as electrospray, see Figure 7.234.[256,314]

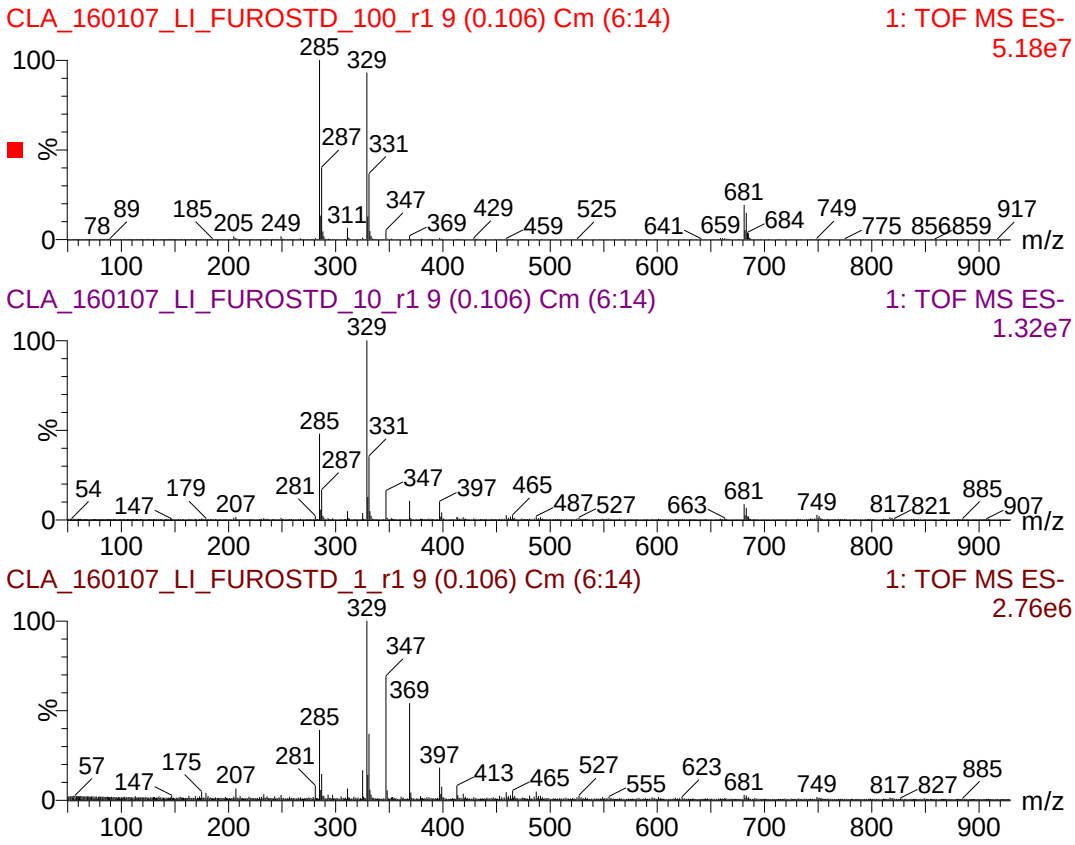

Figure 7.234 – Synapt mass spectra showing the presence and absence of the dimer (*m/z* 681) at three different concentrations: bottom plot is 1 µg/mL, middle plot is 10 µg/mL and top plot is 100 µg/mL.

Table 7.25 – Synapt experimentally determined concentrations using peak area for the three additional samples.

Prepared concentration (µg/mL)	Peak area - experimentally determined concentration	Lower and upper 95% confidence limits
2.2	2.3	2.1 to 2.6
9.3	8.8	8.1 to 9.7
13.5	11.8	10.8 to 13.0

For completion the three additional samples were run, analysed and concentration calculated using the initial average peak area calibration plot, Figure 7.230, which utilises the combination of ions used by the QDa (*m/z* 285 and 329). Table 7.25 shows

that the values are close to the prepared concentrations with confidence limits showing a reduction in error compared with the QDa determined values.

Summary:

This work highlights again the difference between the two instruments and confirms that the relationship between concentration and signal can vary greatly, even for two instruments utilising ESI, hence the importance of running the calibration standards on both and being consistent in the methods for data analysis. It also reveals that small changes in concentration may alter the electrospray process and change the predominant ions detected, thereby requiring multiple ions to be monitored concurrently to enable quantification.

7.3.3 Guaifenesin

Guaifenesin is an expectorant for treating coughs (often in combination with other APIs) through a variety of over-the-counter (OTC) preparations, which include cough syrups and oral immediate release capsules and tablets. It is in BCS I and has good solubility in water, reported as 50000 mg/L at 25°C.[315] It was found to ionise effectively in positive mode ESI-MS from solutions of water and acetonitrile at 50:50 v/v, both with and without formic acid at 0.1% v/v, producing $[M+Na]^+$ observed at *m*/*z* 221 and shown in Figure 7.235.

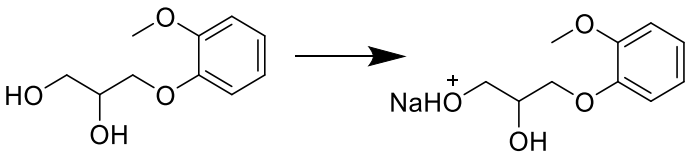

Figure 7.235 – Guaifenesin chemical structure and suggested formation of ion observed by positive ESI-MS.

A range of guaifenesin samples were run on both the Synapt and the QDa without HPLC to determine the relationship between signal and concentration using water and acetonitrile at 1:1 with 0.1% v/v formic acid.

Synapt:

Figure 7.236 suggests the Synapt calibration data follows a simple model with an R-squared value of greater than 0.99, which would enable experimental determinations

of concentration from peak area, with a greater precision at concentrations below 5 µg/mL.

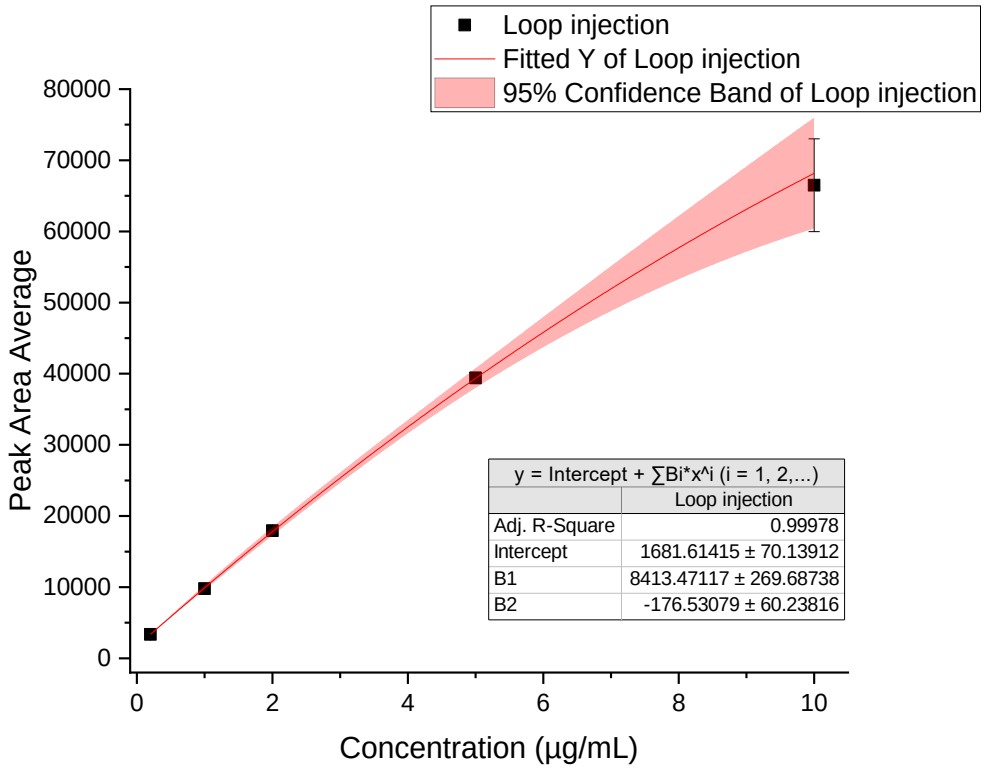

Figure 7.236 – Synapt calibration plot for guaifenesin in water and acetonitrile (50:50 v/v) with formic acid (0.1% v/v) by loop injection (no HPLC). Each point is the average of three samples, each run three times, with standard deviation shown using the error bars. Regression analysis has been applied to the average with the additional data inset.

QDa:

Figure 7.237 shows the relationship between signal and response for the QDa, again without HPLC. The concentration response curve follows a simple cubic model with an R-squared value of greater than 0.99, enabling the experimental determination of concentration from peak area for the QDa. Precision is greater for the lower concentrations, with error increasing after 5 µg/mL.

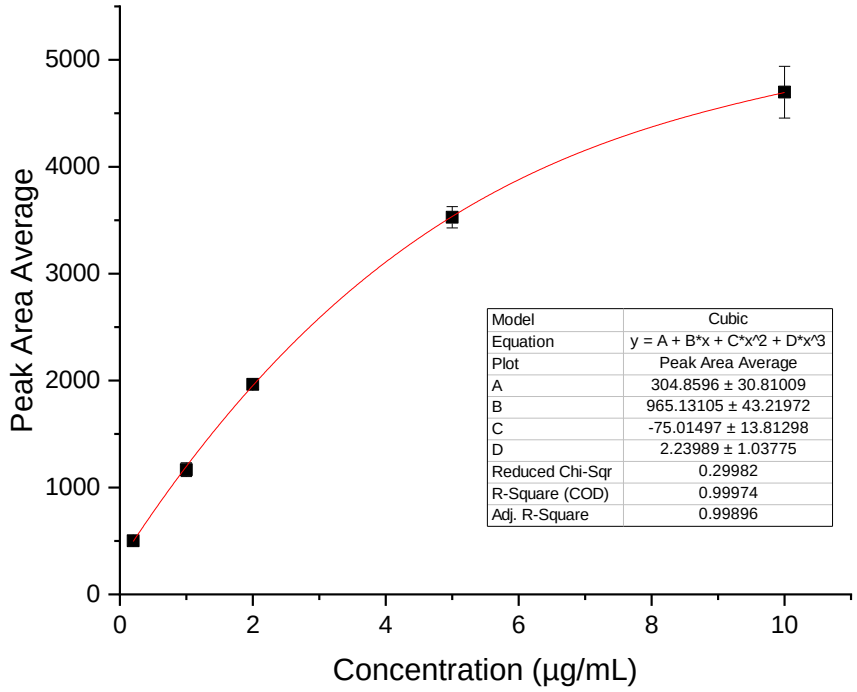

Figure 7.237 - QDa calibration plot for guaifenesin in water and acetonitrile (50:50 v/v) with formic acid (0.1% v/v). Each point is an average of three runs with the standard deviation shown using error bars. Regression analysis has been applied to produce the red line, with additional data inset.

Summary:

A smaller range of concentrations have been analysed for guaifenesin compared with other APIs, from 0.2 to 10 µg/mL, due to the earlier work by Lewis *et al* highlighting it as sensitive to ion suppression by other components, either in the formulation, dissolution media or both.[15] This is confirmed by an additional experiment using HPLC prior to Synapt MS analysis, see Figure 7.238.

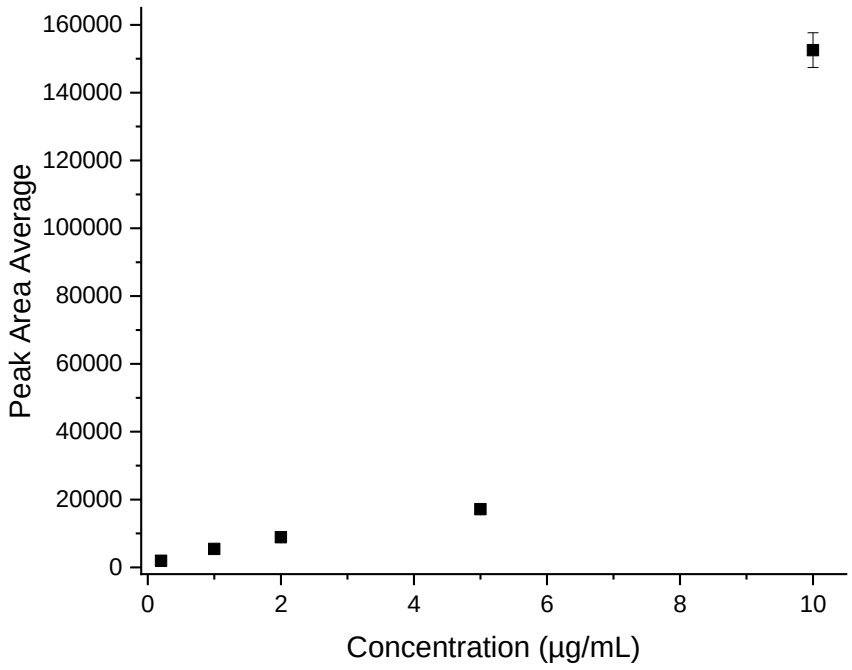

Figure 7.238 – Synapt calibration plot using HPLC prior to ionisation for guaifenesin in water and acetonitrile (50:50 v/v) with formic acid (0.1% v/v). Each point is the average of three samples, each run three times, with standard deviation shown using the error bars.

Figure 7.238 shows a linear relationship between signal and the lower concentrations, but between 5 and 10 µg/mL there is a larger increase in signal than expected. The concentration range is comparable with Figure 7.236 but the change in signal (as measured by peak area) from 5 to 10 µg/mL is significantly larger (an average peak area of 150,000 for HPLC analysis compared with 65,000 for loop injection analysis). This suggests that the guaifenesin signal in Figure 7.236 is subject to ion suppression; each sample contained only water, acetonitrile and formic acid, hence the suppression may be a result of any of these, a combination, or an impurity present within them. Further analysis of the full spectra for each run does not show any clear difference in ions present between them making it impossible to draw a conclusion as to the cause. This highlights the extent of suppression that can be seen as a result of solvent(s) and/or modifiers and makes guaifenesin an interesting choice for further work analysing multiple components concurrently.

7.3.4 Haloperidol

Haloperidol is classed as a poorly soluble API (BCS II / IV) with water solubility reported as 1.4 mg/L at 25°C.[315] It is available as immediate release oral tablets ranging from 500 µg to 10 mg, in addition to a range of oral solutions. It is weakly basic so can also be formulated as a salt and delivered as a depot injection to sustain absorption and improve the therapeutic profile.[316,317] It was found to ionise efficiently by ESI-MS in the positive mode from water and acetonitrile 50:50 v/v, both with and without formic acid at 0.1% v/v, to produce $[M+H]^+$ which was observed at *m*/*z* 376. The chemical structure of haloperidol, shown in Figure 7.239, contains one chlorine atom, which produces a characteristic isotope pattern that was used to aid identification.

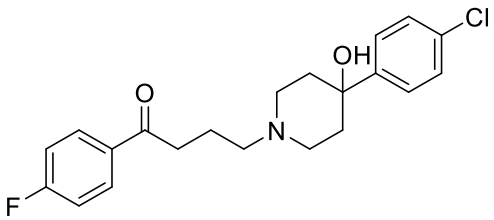

Figure 7.239 – Haloperidol chemical structure.

A series of concentrations of haloperidol dissolved in water and acetonitrile at 50:50 with 0.1% v/v formic acid, were analysed with the Synapt and QDa to explore the relationship between signal and concentration, see Figure 7.240 and Figure 7.241. The lower limit of quantification for the Synapt is 0.05 µg/mL, compared with 0.1 µg/mL for the QDa, and the signal on both instruments shows a plateau after 40 µg/mL. Regression analysis has been applied to the average peak area for each plot, with polynomial fits producing adjusted R-squared values of greater than 0.99 in both cases. The error also increases at concentrations greater than 10 µg/mL for both instruments, although the signal variation (as shown by the error bars) remains consistently small.

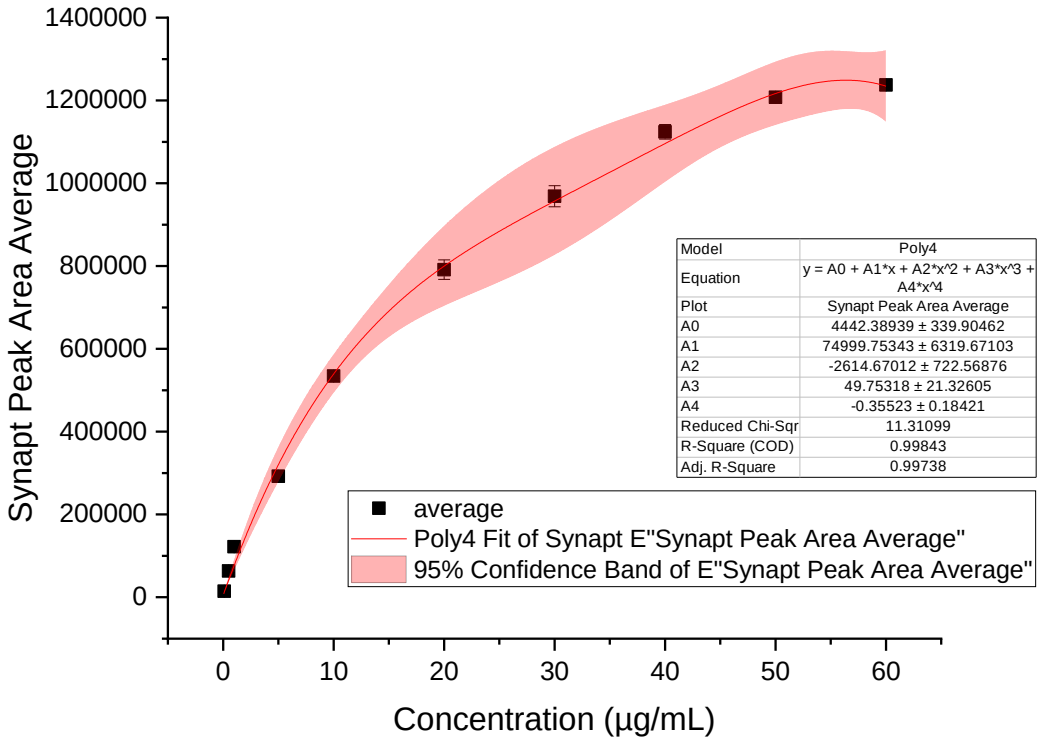

Figure 7.240 – Synapt positive ESI-MS calibration plot showing the relationship between signal and haloperidol concentration using peak area average. Haloperidol standards are in water and acetonitrile (50:50 v/v) with formic acid (0.1% v/v). Each point is the average of three runs with the standard deviation shown using error bars. Regression analysis has been applied with additional data inset.

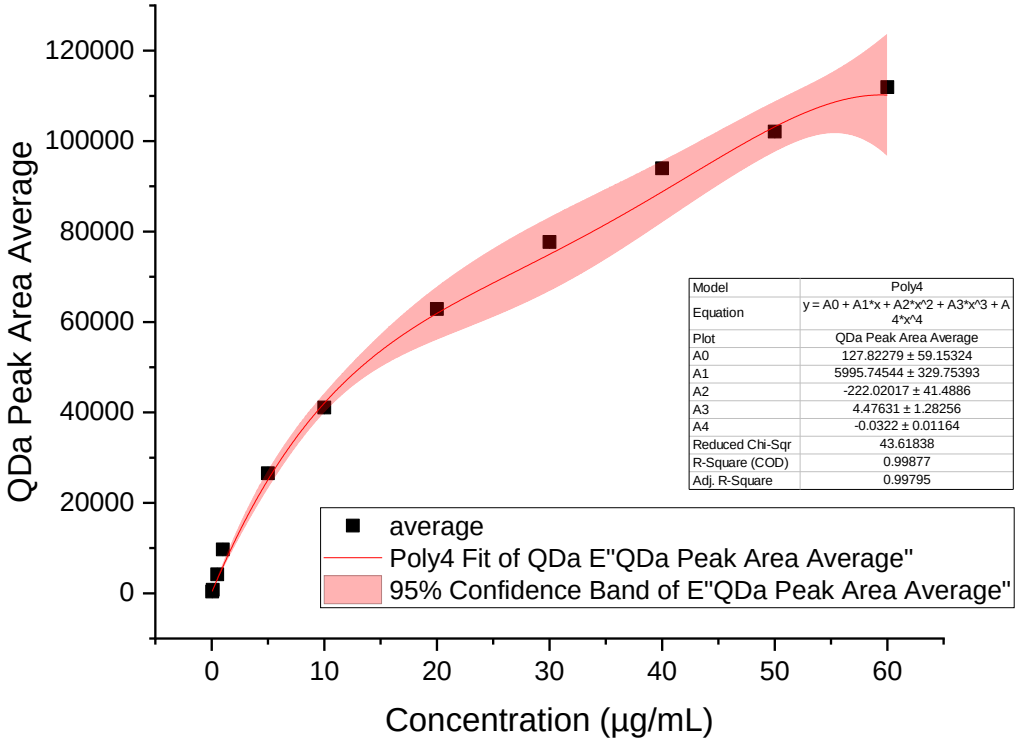

Figure 7.241 – QDa positive ESI-MS calibration plot showing the relationship between signal and haloperidol concentration using peak area average. Haloperidol standards are in water and acetonitrile (50:50 v/v) with formic acid (0.1% v/v). Each point is the average of three runs with the standard deviation shown using error bars. Regression analysis has been applied with additional data inset.

Three additional samples were run, analysed and their concentration calculated using the calibration plots for each instrument. Table 7.26 provides the calculated concentrations alongside the prepared concentration values; the QDa predictions are closest, with its confidence limits encompassing two of the three values.

Table 7.26 – Experimentally determined concentrations using peak area average for the Synapt and the QDa for three additional samples. These values are calculated using the full concentration range studied. The 95% lower and upper confidence limits are provided in brackets for each value.

Prepared concentration (µg/mL)	Synapt – peak area experimentally determined concentration	QDa – peak area experimentally determined concentration
2.2	3.0 (2.6 to 3.6)	3.4 (3.1 to 3.8)
9.3	7.6 (6.7 to 8.7)	9.3 (8.7 to 10.1)
13.5	12.3 (10.8 to 14.3)	13.7 (12.5 to 15.7)

The error for both calibration plots increases after a concentration of 10 µg/mL, which would suggest that calculating concentrations above this would be prone to more error, however, Table 7.26 states better predictions for the higher concentrations. Further exploration of the data shows that alternative polynomial fits can be applied to the data up to 10 µg/mL, see Figure 7.242. This would calculate 2.3 and 9.1 µg/mL for the Synapt, and 2.3 and 9.9 µg/mL for the QDa. The R-squared values are close to 1 in both cases, but a glance at the shape of the polynomial plot versus the number of data points highlights a significant amount of extrapolation and therefore a clear limitation in this analysis. Reducing the concentration range further results in more appropriately fitted regression analyses, see Figure 7.243.

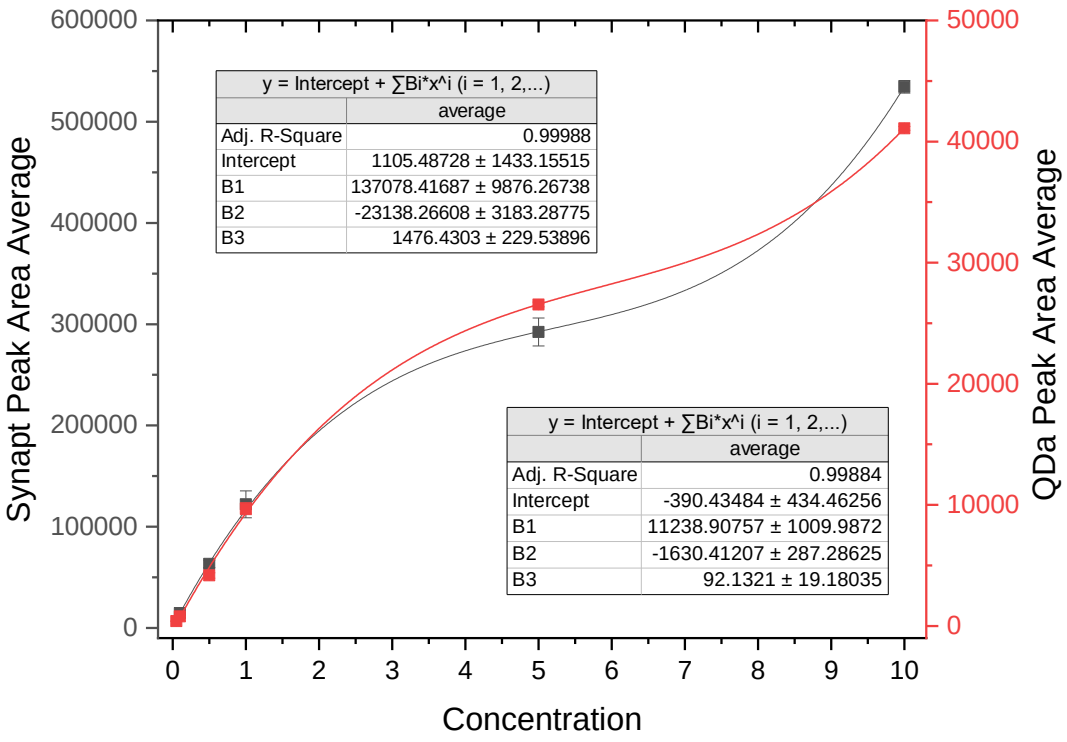

Figure 7.242 – Synapt and QDa calibration plots on left and right y-axes, respectively, showing only concentrations between 0.05 and 10 µg/mL. Each point is the average of three runs, with standard deviation shown using error bars.

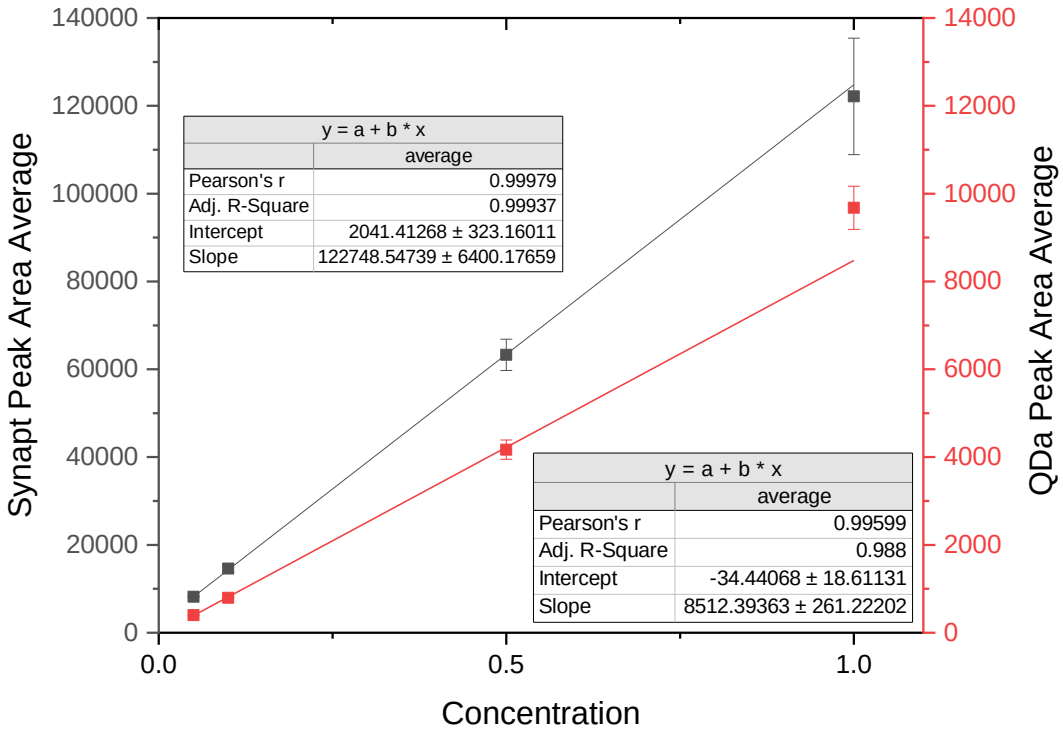

Figure 7.243 – Synapt and QDa calibration plots on left and right y-axes, respectively, showing only concentrations between 0.05 and 1 µg/mL. Each point is the average of three runs, with standard deviation shown using error bars. Linear regression has been applied to each, with the additional data inset (top – Synapt, bottom – QDa).

As expected from prior knowledge of each instrument, the QDa loses linearity prior to the Synapt but the linear regression analyses have R squared values above 0.99. The multiple regression analyses suggest that the relationship between signal and concentration might not be consistent across the range studied for haloperidol and it may be beneficial to understand in advance the section of plot that is most appropriate for calculating concentration.

7.3.5 Ibuprofen

Ibuprofen is a BCS II poorly soluble weak acid with reported solubility in water of 21 mg/L at 25°C.[318] It is a commonly used non-steroidal anti-inflammatory drug available in a number of formulations ranging from oral immediate release tablets to topical gels, and is utilised both as the free acid and a variety of salts to improve absorption.[319] The sodium salt was used in these initial investigations as it was readily soluble in the MS solvents. The chemical structure of each is displayed in Figure 7.244.

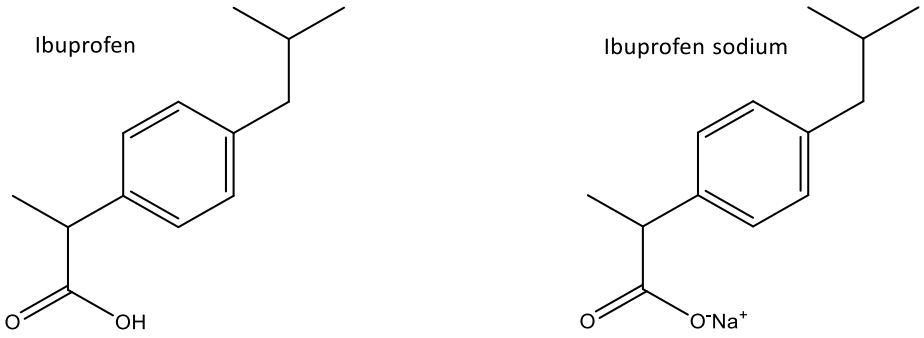

Figure 7.244 - Ibuprofen and ibuprofen sodium chemical structures.

Ibuprofen sodium was explored with positive and negative ESI-MS both with and without formic acid, and with the Synapt and QDa. An ion of interest was determined at *m/z* 251 in positive mode on the Synapt, which corresponds to $[M+Na]^+$ (where M refers to ibuprofen sodium). A series of concentrations of ibuprofen sodium were then analysed and a calibration plot produced for this instrument, see Figure 7.245. Regression analysis resulted in a line of best fit with an R-squared value of greater than 0.99 suggesting a good fit with minimal error at concentrations below 80 µg/mL down to a lower limit of detection of 0.05 µg/mL. The data point at 90 µg/mL does not fit within the confidence limits and appears to suggest a plateau between 80 and 100 µg/mL.

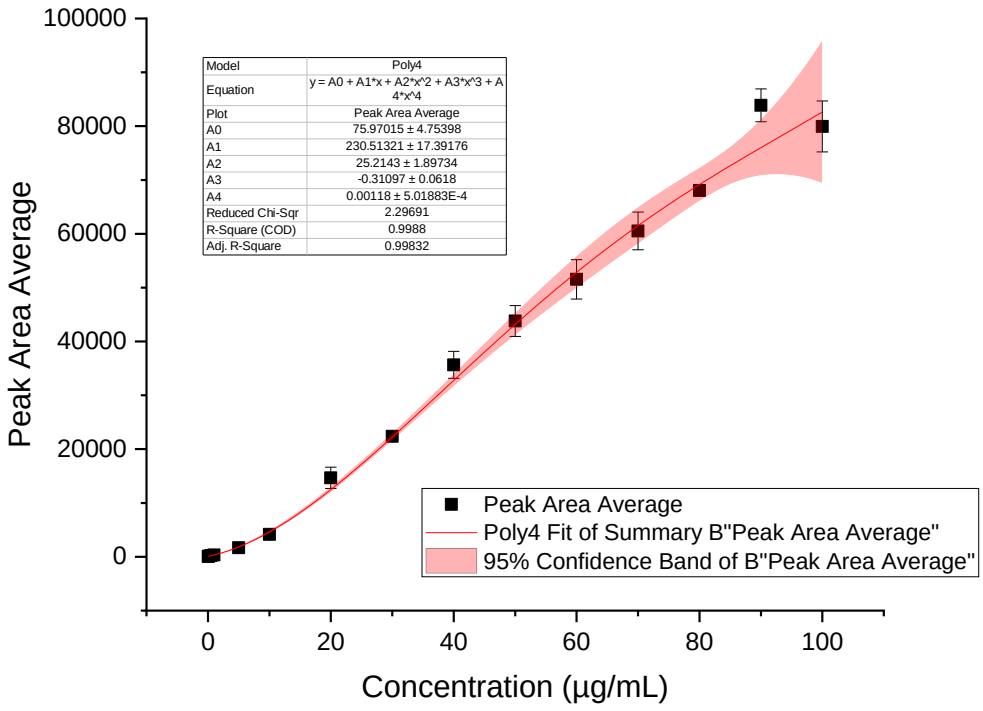

Figure 7.245 - Synapt ibuprofen sodium calibration plot for *m/z* 251 for peak area averages using positive ESI-MS. Ibuprofen sodium standards are in water and acetonitrile (50:50 v/v) with formic acid (0.1% v/v). Each point is the average of three runs with the standard deviation shown using error bars. Regression analysis has been applied with the additional data inset.

It was found that as the ibuprofen concentration being analysed was increased, an increasing number of clusters formed and could be observed within the spectra. Peaks with a regular mass difference of 228 Dalton, which corresponds to the addition of sodium salts of ibuprofen (*m/z* 251, 479, 707, 935 etc.) are present. The clusters are more prevalent at ibuprofen concentrations above 20 µg/mL. The capillary voltage and cone voltage were adjusted to understand if the clusters could be disrupted, and formic acid was excluded to understand if this too played a role in the negative mode. The changes proved unsuccessful but it was found that loop injected base peak intensity (BPI) chromatograms could be used to encompass both the single ion and the clusters, and produce an alternative calibration plot, see Figure 7.246 and Figure 7.247.

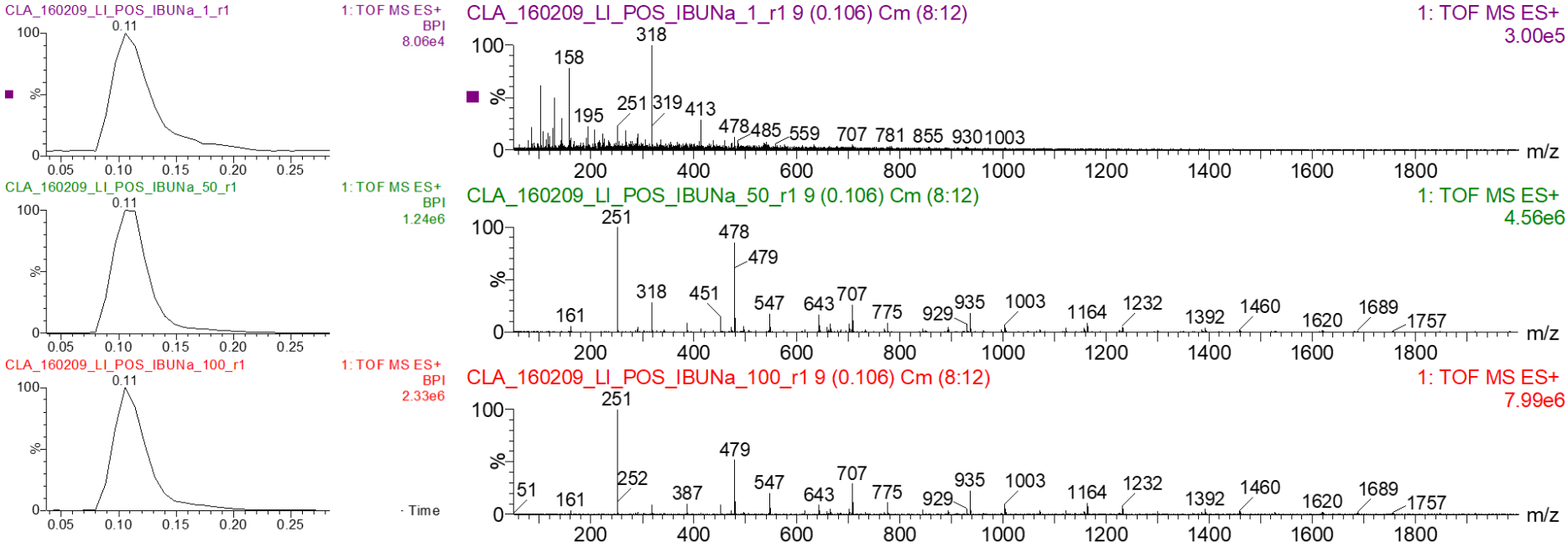

Figure 7.246 - Synapt positive ESI-MS loop injection base peak intensity chromatograms for three concentrations of ibuprofen sodium in MS solvent. Showing 1 µg/mL at the top, 50 µg/mL in the middle and 100 µg/mL at the bottom. The right side shows the ions present in each chromatogram between 8 and 12 seconds.

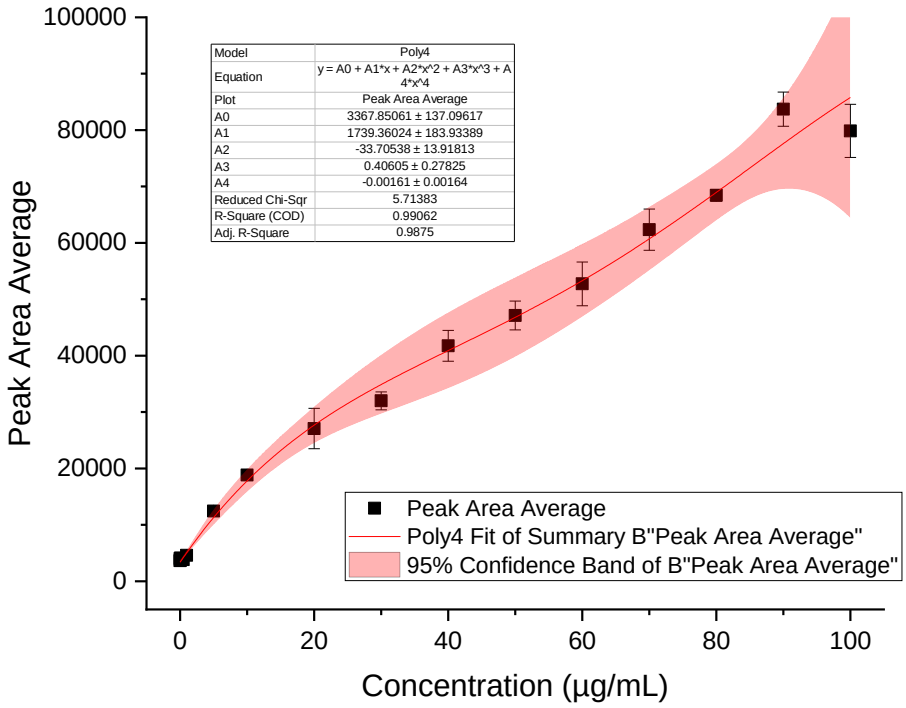

Figure 7.247 – Synapt positive ESI-MS calibration plot for ibuprofen sodium in water and acetonitrile (50:50 v/v) with formic acid (0.1% v/v). The data has been obtained using the BPI function in MassLynx with the full chromatogram peak integrated using Origin instead of extracting data for a single ion. Each point is the average of three runs with the standard deviation shown using error bars. Regression analysis has been applied to produce the red line, with additional data inset.

As an alternative to extracting signal only from an ion (or ions) of interest at each concentration, the BPI function in MassLynx was used to extract the base peak chromatogram, which could then be integrated in Origin and the peak area average calculated. The calibration plot in Figure 7.247 has been subjected to regression analysis and a polynomial equation fitted to calculate the red line. The adjusted R-squared is greater than 0.98, suggesting the fit is good and this alternative method has provided sufficient information to be able to predict concentration from signal. The lower limit of detection is 0.005 and there is a plateau after 80 µg/mL, although this has not been accounted for with the fitted line.

Table 7.27 – Synapt positive ESI-MS determined concentrations using peak area from extracted m/z 251 and using peak area of BPI chromatograms for three additional samples. The lower and upper 95% confidence limits are given in brackets.

Prepared concentration (µg/mL)	Peak area – *m/z* 251 experimentally determined concentration (µg/mL)	Peak area – BPI experimentally determined concentration (µg/mL)
2.2	2.4 (2.3 to 2.6)	2.5 (2.1 to 3.0)
9.3	8.9 (6.7 to 9.3)	8.4 (7.2 to 10.0)
13.5	13.2 (12.9 to 13.7)	11.8 (10.1 to 14.0)

The known standards (all below the plateau) were analysed to observe whether we might be able to predict concentration both with and without SIM. The results can be found in Table 7.27 and confirm that a relationship between signal and concentration has been identified in both cases. The predicted concentration lower and upper 95% confidence limits encompass all three prepared concentrations for both methods, concluding that both calibration plots can be used successfully, although as expected, the plot using data extracted only for *m/z* shows reduced error across all three concentrations.

The BPI method works well for a sample with only one molecule of interest, but would not provide suitable means for quantification if additional analytes were present, unless separation methods were employed prior to ESI-MS. Additionally, it could not be applied to the concentration series analysed by negative ESI-MS as there were no dominant ions produced, either with or without formic acid, and applying BPI resulted in a spread of intensity rather than a clear peak for integration. Analysis with the QDa in positive and negative ESI-MS, with and without formic acid, was unable to produce any ions of interest, although the reason for this is unclear. The literature findings for ibuprofen analysed by negative mode ESI-MS suggest that in the absence of formic acid, the $[M-H]^-$ should appear and a dimer adduct with sodium $[2M–2H+Na]^-$ may be found.[298,320] Neither of these was found in sufficient quantity throughout this work.

This may be explained by comparing the properties of ibuprofen sodium (used in this work) with ibuprofen (studied in the literature).

Ibuprofen is described as a molecule lacking a high degree of polarity; in a solution of water and acetonitrile, it will be sufficiently hydrophobic that it can move to the surface of the droplet and ionise efficiently relative to other more polar molecules according to Schug and McNair.[320] The conversion of ibuprofen to a salt with the addition of a sodium ion will clearly alter the polarity of the molecule (salts of drug molecules are designed to improve solubility for this reason), resulting in a more soluble but potentially less ionisable molecule by the negative method of ESI-MS. This may explain how the presence of formic acid in the positive ESI-MS enabled a calibration plot to be produced, but how, even without formic acid, ionisation was insufficient for quantification in the negative mode. It does not, however, explain the absence of ions on the QDa in the initial investigations in either mode. Time constraints prevented this from being explored further for this instrument.

7.3.6 Paracetamol

Paracetamol, also known as acetaminophen, is a commonly used analgesic on the World Health Organisation's Essential Medicine List.[291] It is commonly formulated as an immediate release 500 mg tablet for oral administration. Its BCS is defined as borderline I / III with an aqueous solubility of 23.7 mg/mL at 37 °C, and an historical classification of BCS IV.[291,321] It ionises readily in positive ESI-MS to produce $[M+H]^+$, which is observed at *m*/*z* 152. It is more readily ionised in the presence of formic acid, as expected, but can also be analysed from a water only solution. In addition to *m*/*z* 152, a decomposition product at *m*/*z* 110, can be observed, see Figure 7.248. This fragmentation is a result of the thermal decomposition of paracetamol during ESI and was studied by Gilpin and Zhou in 2004.[322] Decomposition increases with higher temperatures for source and probe, as well as with increased capillary and cone voltage, however, a balance must be struck between preventing decomposition and obtaining good signal to noise ratios for the ion of interest.

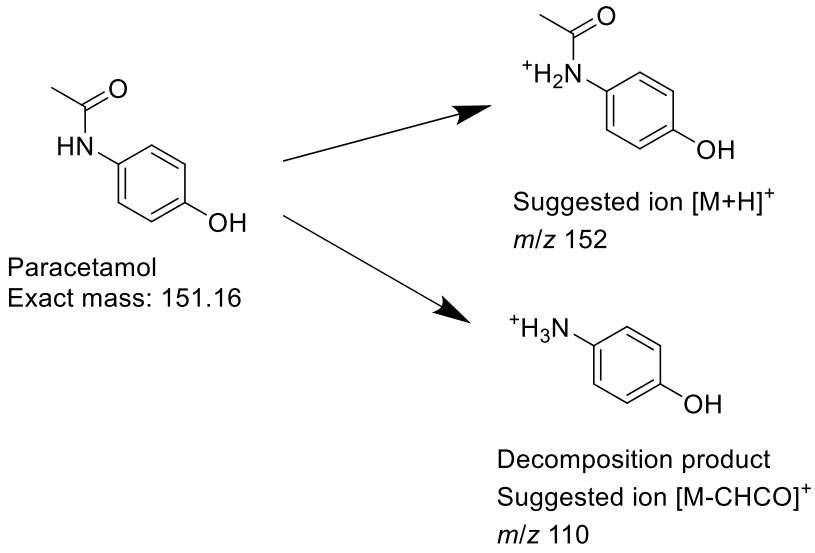

Figure 7.248 – Paracetamol chemical structure and suggested formation of ions observed by positive ESI-MS.

A solution paracetamol in water and acetonitrile 50:50 v/v was initially analysed to understand signal variation in response to the adjustment of QDa probe temperature, cone voltage and capillary voltage settings. Formic acid was excluded from the solution to provide the worst case scenario for signal to noise ratios. The default settings, which included a source temperature of 150 °C, probe temperature of 600 °C, cone voltage of 20 V and a capillary voltage between 1.0 and 1.5 kV were used successfully, and a sample of paracetamol dissolved in only water was also found to have a comparable signal.

A series of concentrations of paracetamol dissolved in water and acetonitrile 50:50 v/v with formic acid 0.1% v/v were analysed on the QDa and on the Synapt by loop injection to explore the relationship between concentration and signal for each instrument. Figure 7.249 shows the calibration plot for the Synapt with the paracetamol signal extracted using *m*/*z* 152.07 (+/- 0.1 Da). The lower limit of quantification for the Synapt is 0.05 µg/mL and there is a linear relationship up to 60 µg/mL with an R squared value of greater than 0.999. It is unclear whether the signal at 70 µg/mL is the start of the plateau or simply an outlier, but the linearity does not extend to 80 or 90 µg/mL, and by 100 µg/mL there is an increase in variability suggesting that the relationship is no longer suitable for quantification through these methods.

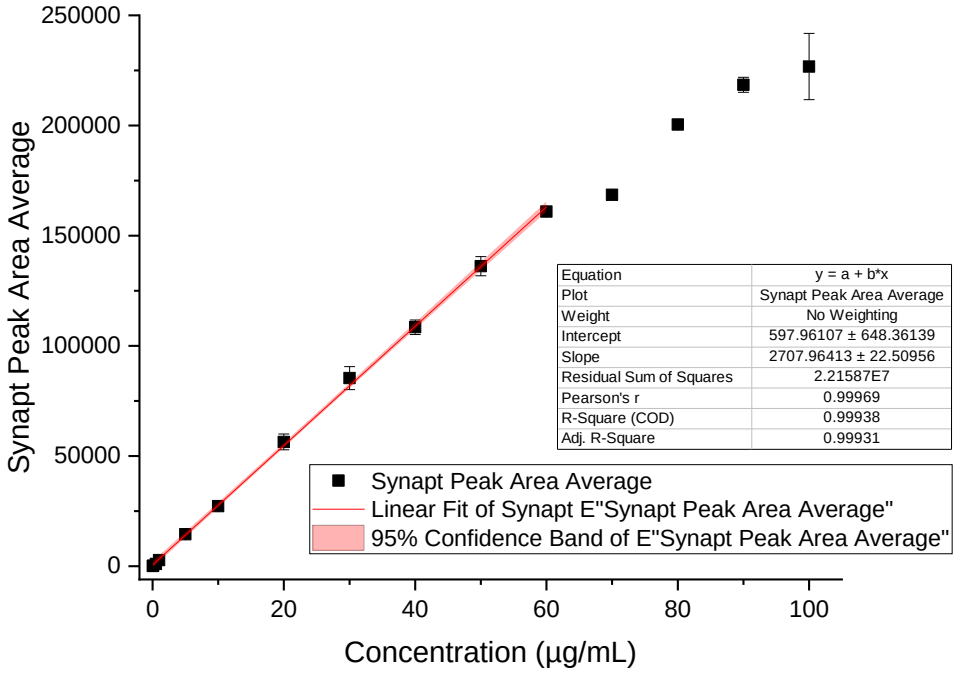

Figure 7.249 – Synapt positive ESI-MS calibration plot for paracetamol in water and acetonitrile (50:50 v/v) with formic acid (0.1% v/v). Each point is the average of three runs with the standard deviation shown using error bars. Linear regression has been applied to the data between 0.05 and 60 µg/mL with data inset.

The relationship between paracetamol concentration and signal using the QDa differs from the Synapt, see Figure 7.250. In this case paracetamol is extracted using a SIM channel of *m/z* 152. The lower limit for quantification is 0.1 µg/mL but regression analysis suggests a polynomial relationship with an adjusted R squared of greater than 0.9999. This enables quantification up to 100 µg/mL, although the confidence band widens at 90 µg/mL.

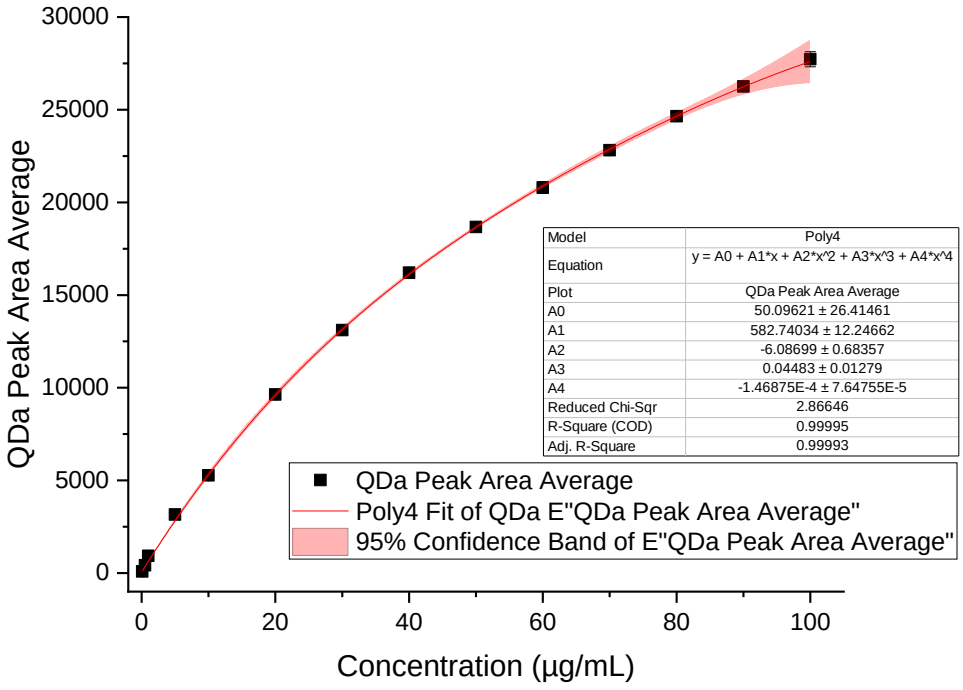

Figure 7.250 – QDa positive ESI-MS calibration plot for paracetamol in water and acetonitrile (50:50 v/v) with formic acid (0.1% v/v). Each point is the average of three runs with the standard deviation shown using error bars. Regression analysis has been applied with details inset.

Three additional concentrations of sample were run in triplicate on each instrument and the data analysed to calculate concentration from signal using each of the calibration plots. The results can be found in Table 7.28 and confirm that the Synapt calibration plot is appropriate for quantification purposes as the experimentally determined concentrations are accurate for two of the three samples, and within the confidence limits of the third. The QDa concentrations are all outside the confidence limits and higher than the prepared concentrations.

Table 7.28 – Experimentally determined concentrations using peak area average for the Synapt and the QDa for three additional samples. The 95% lower and upper confidence limits are provided in brackets for each value.

Prepared concentration (µg/mL)	Synapt – peak area experimentally determined concentration	QDa – peak area experimentally determined concentration
0.6	0.6 (-0.8 to 2.0)	1.6 (1.5 to 1.6)
3.8	3.5 (2.1 to 4.9)	5.4 (5.3 to 5.6)
9.3	9.3 (7.9 to 10.6)	11.2 (10.9 to 11.5)

A smaller section of the QDa calibration plot was extracted and regression analysis applied only to the section between 0.1 and 10 µg/mL to see if this improved accuracy by narrowing down the section being examined, see Figure 7.251. This alternative calibration plot was then used to calculate concentration from signal for the additional concentrations, however, the accuracy of the calculated concentrations remained poor with the prepared concentration still not within the confidence limits.

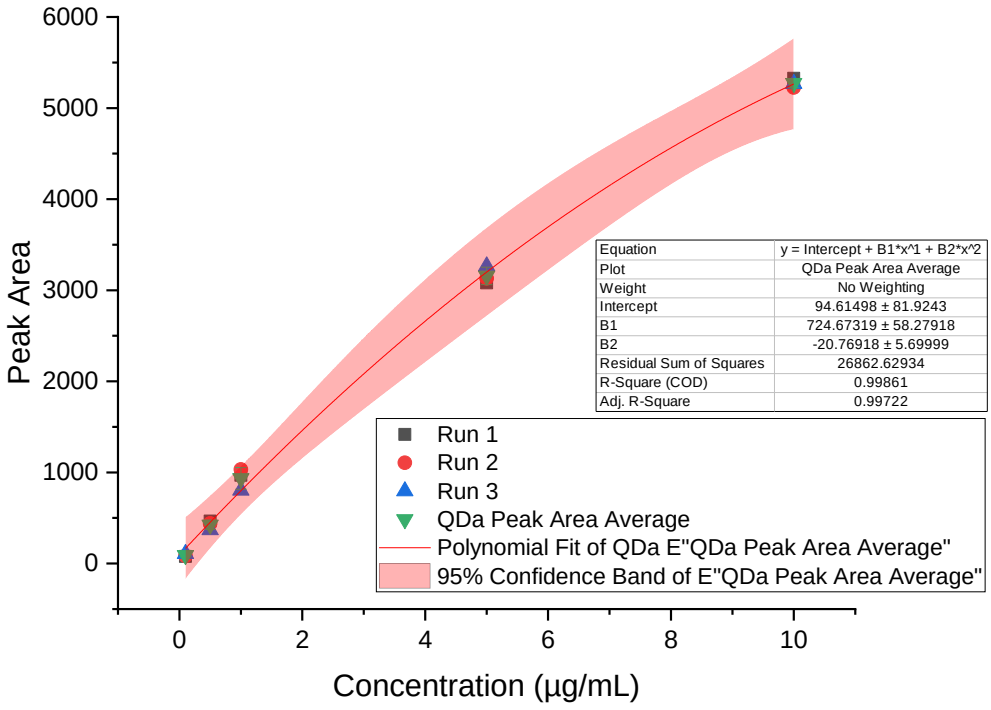

Figure 7.251 – QDa positive ESI-MS calibration plot for paracetamol in water and acetonitrile (50:50 v/v) with formic acid (0.1% v/v) for 0.1 to 10 µg/mL. Each point is the average of three runs with the standard deviation shown using error bars. New regression analysis has been applied with details inset.

The relationship between signal and concentration is significantly different between the two instruments, with the Synapt having a significantly higher response to the same concentration of paracetamol. It can be concluded to be more variable and therefore less accurate for quantification purposes with the QDa than with the Synapt. The variability of the signal on both instruments, however, appears to be good with narrow error bars below 90 µg/mL.

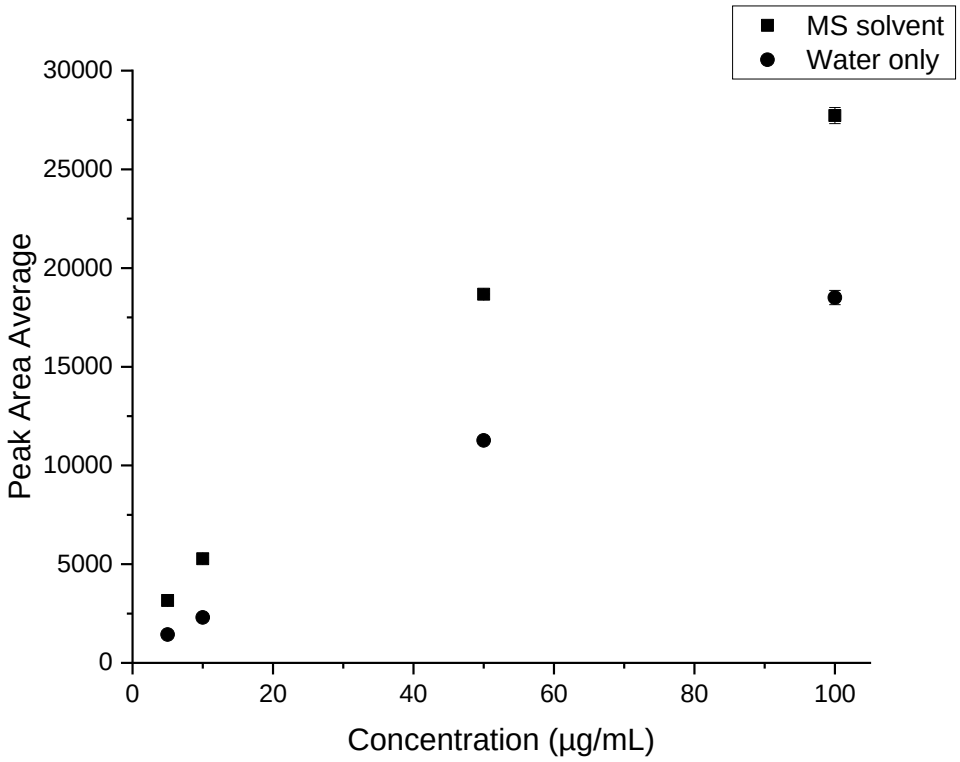

Figure 7.252 – QDa positive ESI-MS reduced calibration plot to compare two solvent mixes: i) paracetamol in water and acetonitrile (50:50 v/v) with formic acid (0.1% v/v) (labelled MS solvent) ii) paracetamol in water only. Each point is the average of three runs with the standard deviation shown using error bars.

Finally, a reduced number of paracetamol standards were made using water only, instead of water and acetonitrile 50:50 v/v with formic acid 0.1% v/v, and were analysed in positive ESI-MS on the QDa to compare ionisation efficiencies with the differing solvent mixes. Figure 7.252 shows the two calibration plots and confirms that the standards containing only water have a lower ionisation efficiency, which can be seen by comparing the peak area values. This is most likely due to a combination of reduced solvent volatility (due to the absence of acetonitrile) and the absence of the modifier formic acid. A result of this reduced ionisation efficiency is that lower concentrations may not be quantifiable, but higher concentrations can be analysed without saturating the detector, hence altering ionisation efficiency can prove to be an advantage in certain circumstances.

7.3.7 Phenylephrine

Phenylephrine is primarily a vasoconstrictor and available in multiple forms for a variety of uses ranging from treating hypotension to dilation of pupils.[293] It is often formulated as the hydrochloride salt, although a literature search also revealed historical use of a tannate salt to delay absorption and a bitartrate salt.[323] Phenylephrine was dissolved in water and acetonitrile 50:50 with formic acid 0.1% v/v. It was ionised in positive mode ESI-MS using the Synapt to confirm that the primary ion for quantification was $[M+H-H_20]^+$ and could be observed at m/z 150. This was consistent with early dissolution work by Lewis *et al* and the literature available, Figure 7.253 provides a brief outline.[15,324]

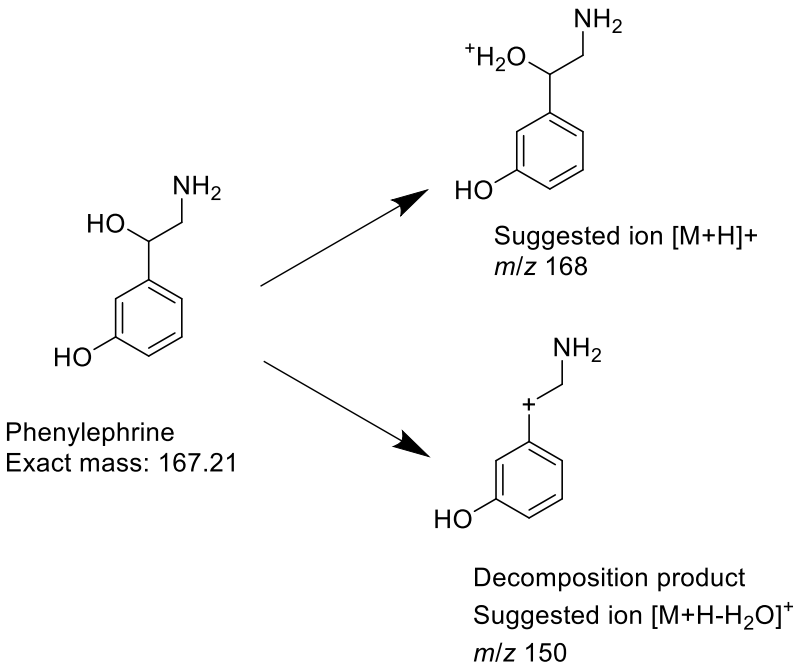

Figure 7.253 – Phenylephrine chemical structure and suggested formation of ions observed by positive ESI-MS.

Synapt:

LCMS analysis was used initially with a five minute reverse phase gradient method and phenylephrine was observed to elute between 0.8 and 1.2 minutes. Two peaks appeared to be present between these retention times, which upon closer inspection were joined together suggesting that it was either one continuous peak or two unresolved peaks. Analysis of the MS data pertaining to the sample eluting between

0.8 and 1.2 minutes confirmed that *m/z* 150 was dominant throughout. It is not clear why phenylephrine eluted over such a large time period resulting in such a broad band in this instance but a small range of concentrations were analysed to determine how best to quantify and produce a calibration plot with this information, see Figure 7.254. Calculation of the total area was made possible by splitting the data into two peaks, integrating each of them and adding them together. The range of concentrations tested was small and it appears to lose linearity after 1.2 µg/mL; regression analysis enables a polynomial equation to be fitted with a high degree of confidence prior to this loss of linearity. The lower concentration tested was 0.1438 µg/mL, which was easily distinguishable from blank solvent.

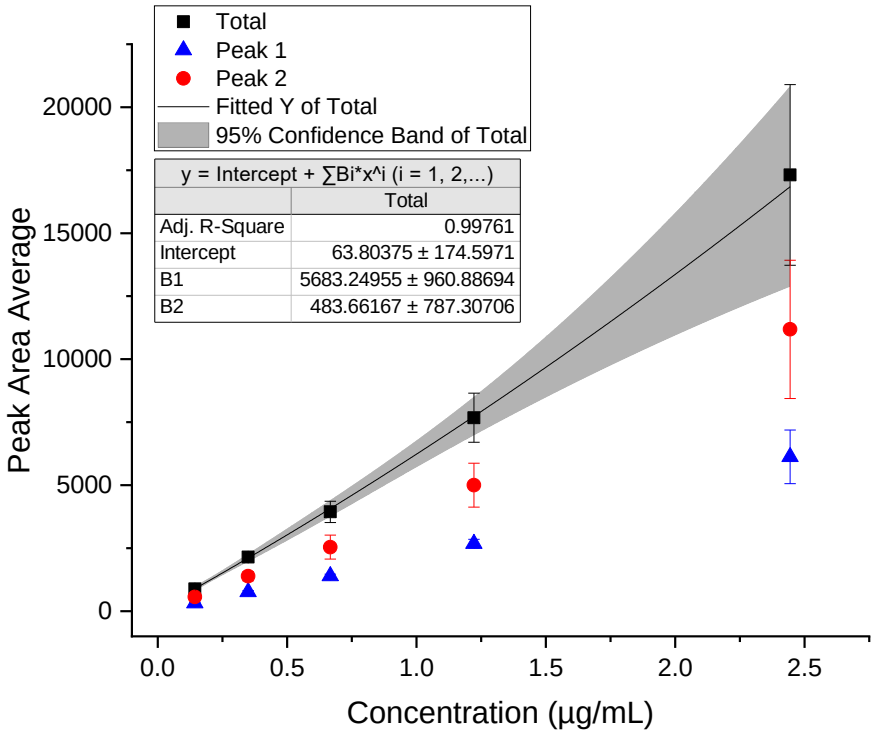

Figure 7.254 – Synapt positive mode LCMS calibration plot for phenylephrine using an extracted mass of *m/z* 150.14 (+/- 0.2 Da) from two retention times. The area between 0.8 and 1.2 minutes retention time was integrated assuming they were two peaks (peak 1 and peak 2) and these were added together to produce the total. Phenylephrine standards are in water and acetonitrile (50:50 v/v) with formic acid (0.1% v/v). Each plotted point is the average of three runs, with each concentration being run in triplicate, and the standard deviation is shown with error bars.

A slightly larger range of concentrations were analysed by loop injection (LI) on the Synapt, and the results plotted in Figure 7.255. The LI calibration plot is comparable

with the LC data in Figure 7.254, suggesting that the process used previously (i.e. adding together the area under each retention time peak) is appropriate. Figure 7.255 shows a linear relationship between signal and concentration, with an increase in error after 2 µg/mL. An additional concentration of 0.007 µg/mL was analysed and unable to be detected with these conditions, so the lower limit of detection lies between 0.007 and 0.098 µg/mL.

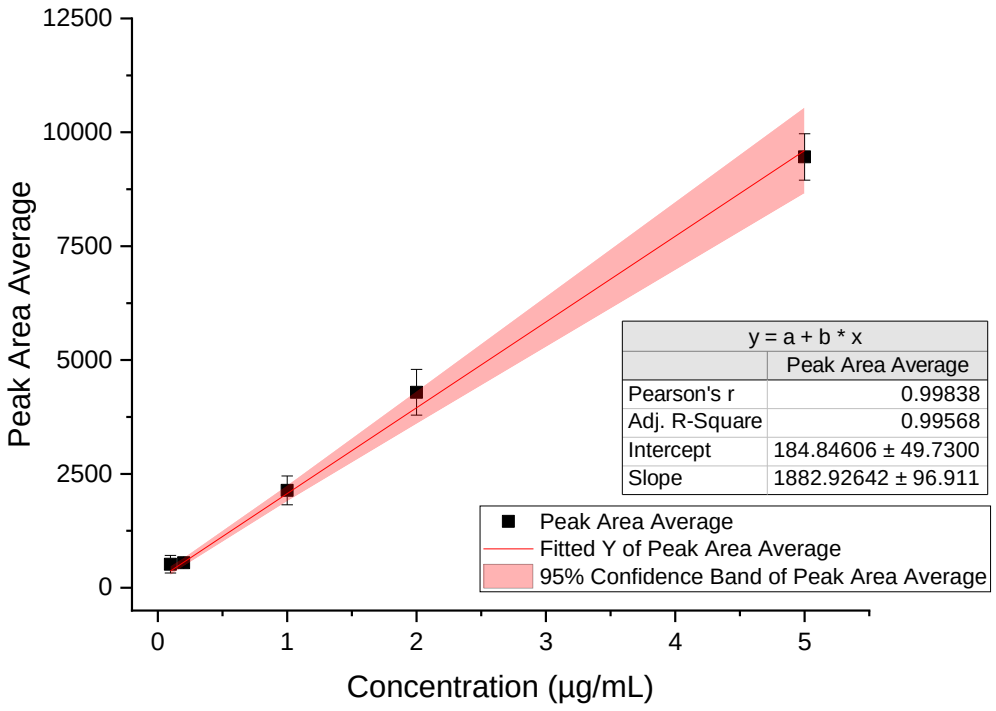

Figure 7.255 – Synapt positive mode loop injection calibration plot for phenylephrine using an extracted mass of *m/z* 150.14 (+/- 0.2 Da). Phenylephrine standards are in water and acetonitrile (50:50 v/v) with formic acid (0.1% v/v). Each plotted point is the average of three runs and the standard deviation is shown with error bars. The line of best fit has been plotted in red, with the shaded area representing the 95% confidence band.

QDa:

A range of concentrations were analysed by the QDa using a SIM method of *m/z* 150. The observed relationship between signal and concentration for this instrument is plotted in Figure 7.256 and a line of best fit has been plotted. The correlation is very good (greater than 0.99) and the error is consistent across the range of concentrations analysed. Only the lowest point does not fit the linear relationship suggesting that the

lowest limit of quantification for the QDa is 0.2 µg/mL, although phenylephrine could be detected at the lower concentration of 0.098 µg/mL.

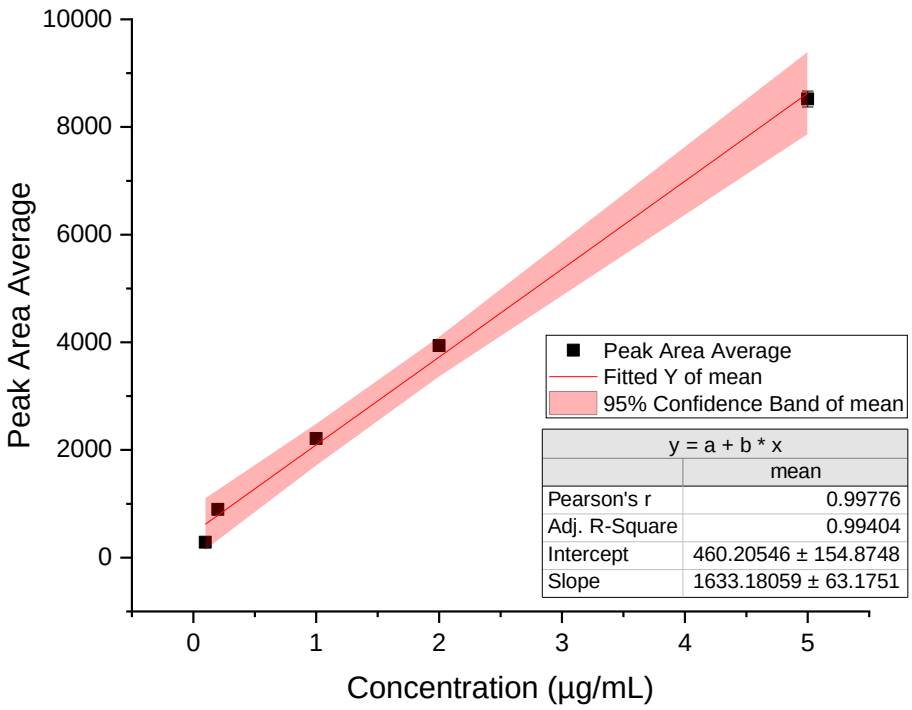

Figure 7.256 – QDa positive ESI-MS calibration plot for phenylephrine using the SIM channel of *m/z* 150. Each plotted point is the average of three runs and the standard deviation is shown with error bars. The line of best fit has been plotted in red, with the shaded area representing the 95% confidence band.

Finally, it should be noted that the phenylephrine ion (*m/z* 150) is detected at a mass close to the primary paracetamol ion (*m/z* 152) so care must be taken in subsequent work to distinguish between them if both APIs are being analysed concurrently.

7.3.8 Lactose

Lactose is a commonly used excipient with several pharmaceutical functions and is available in a variety of forms or grades.[110] It is a disaccharide sugar with a monoisotopic mass of 342.116212 Da, see Figure 7.257. It exists as two interchangeable stereoisomers, which differ in the configuration of one hydroxyl group and are described as alpha (axial) or beta (equatorial).[110] In its crystalline form, each alpha lactose molecule also has one water molecule integrated into the crystal lattice, which, in addition to the hydroxyl configuration gives rise to different solid state

properties, with α-lactose monohydrate exhibiting better flow, and β-lactose superior at binding formulations.[325] The Flowlac brand of alpha lactose monohydrate, produced for direct compression by Meggle Pharma, was used for this work.

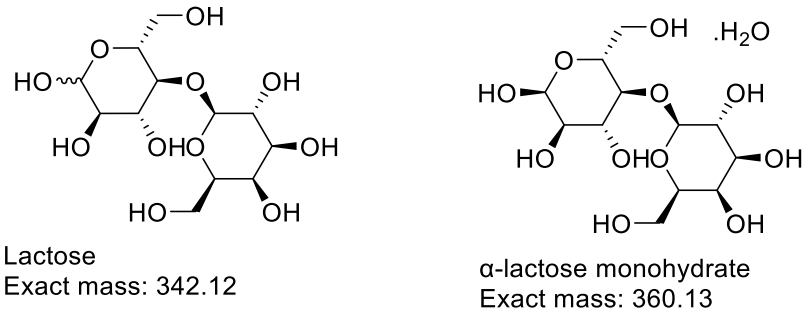

Figure 7.257 – Lactose chemical structures highlighting the hydroxyl group that defines it is as alpha or beta on the left, and the alpha-lactose monohydrate structure complete with water molecule outlined on the right.

Lactose was confirmed to ionise by positive ESI-MS and produce $[M+Na]^+$ at *m*/*z* 365, in keeping with the earlier work by Lewis *et al.*[15] A series of concentrations of lactose in water and acetonitrile 50:50 v/v with formic acid 0.1% v/v were analysed to explore the relationship between concentration and signal for the Synapt and QDa, see Figure 7.258 and Figure 7.259, respectively. The Synapt data suggests a linear relationship starting from the lower limit of detection, which in this case is 0.005 µg/mL, and up to a suggested upper limit for quantification of 80 µg/mL. The R-squared value for this linear regression is greater than 0.98, confirming that the correlation is good, although there are clear outliers and an increase in error above 20 µg/mL as highlighted by the widened confidence band. The signal also starts to plateau at 80 µg/mL suggesting detector saturation occurs at and above this concentration.

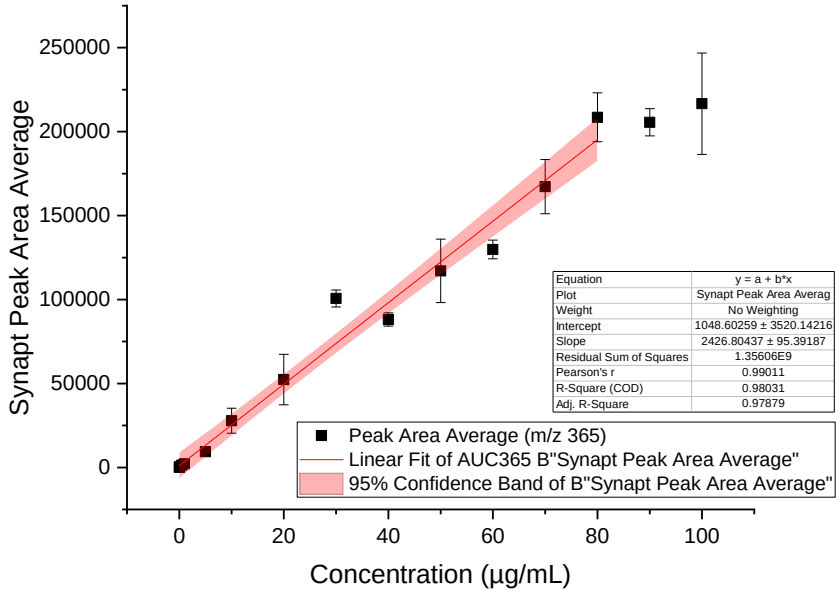

Figure 7.258 – Synapt calibration plot for lactose in water and acetonitrile (50:50 v/v) with formic acid (0.1% v/v) using *m/z* 365 peak area data. Each plotted point is the average of three runs with the standard deviation shown using error bars. Regression analysis has been applied to the first fifteen points (0.005 to 80 µg/mL inclusive), with additional data inset.

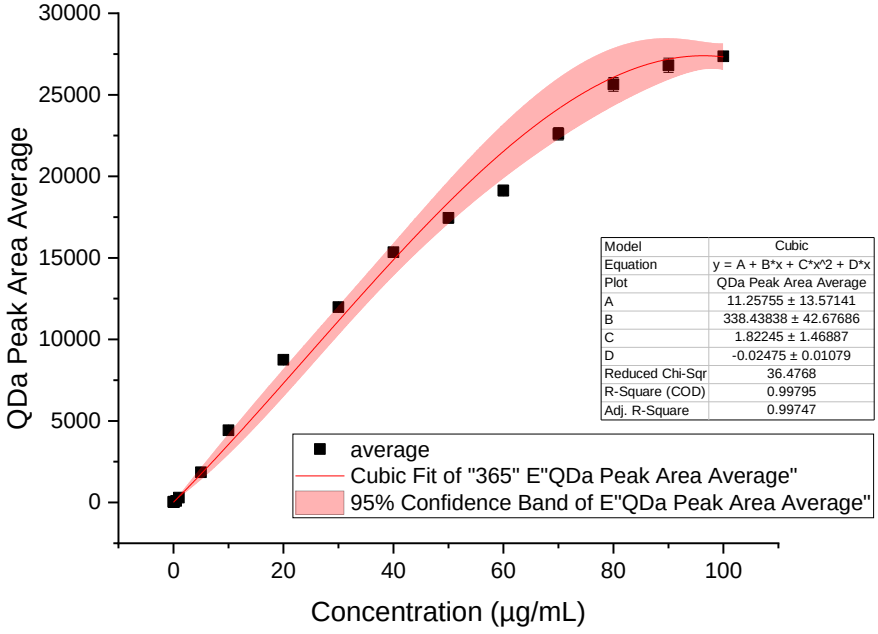

Figure 7.259 - QDa calibration plot for lactose in water and acetonitrile (50:50 v/v) with formic acid (0.1% v/v) using *m/z* 365 peak area data. Each plotted point is the average of three runs with the standard deviation shown using error bars. Regression analysis has been applied with additional data inset.

The regression analysis in Figure 7.259, suggests a cubic relationship between concentration and signal for the samples analysed on the QDa. The adjusted R-squared value for the fit is greater than 0.99 suggesting very good correlation, although there is an increase in the width of the confidence band above 50 µg/mL and it is unclear whether a plateau begins here or it is simply a result of outlying data points. In general however, the error bars on the QDa data are much narrower than on the Synapt data, confirming less variation in signal with the QDa.

The sodium adduct $[M+Na]^+$ can be observed across the full concentration range, from 0.005 to 100 µg/mL for both instruments and enables its relationship with signal to be quantified, however, an additional ion was also noted corresponding to $[2M+Na]^+$, the lactose dimer, at *m*/*z* 707. For the QDa this appears at concentrations above 10 µg/mL and increases with the concentration of lactose undergoing analysis but not consistently and is not present in sufficient quantities to alter overall analysis of the calibration plot, see Figure 7.260 - note the small peak area as compared with Figure 7.259.

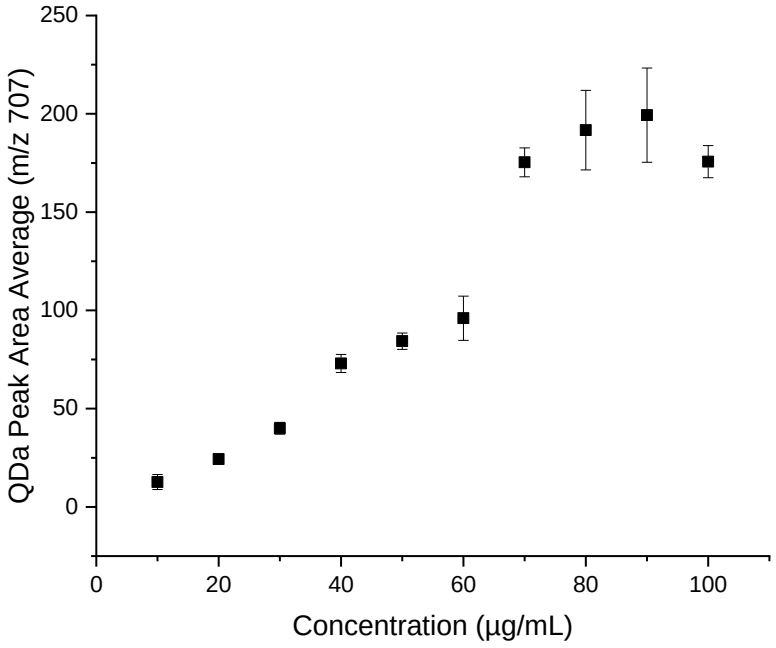

Figure 7.260 – QDa calibration plot for lactose in water and acetonitrile (50:50 v/v) with formic acid (0.1% v/v) using *m*/*z* 707 peak area data. Each plotted point is the average of three runs with the standard deviation shown using error bars.

However, on the Synapt, the presence of the additional ion (*m/z* 707) appears at concentrations of lactose as low as 0.005 µg/mL and in greater quantities relative to the QDa. An additional calibration plot has been produced using solely the lactose dimer for interest, see Figure 7.261. The outlier at 30 µg/mL is consistent with the earlier Synapt plot in Figure 7.258, but is not present in either of the QDa data sets, despite the same samples being used for both. Regression analysis has been applied with an adjusted R-squared of greater than 0.97, although the confidence band increases rapidly in width above 40 µg/mL suggesting uncertainty increases. The error bars are more variable above this concentration too and a plateau looks to be appearing after 80 µg/mL, in line with analysis of the sodium adduct.

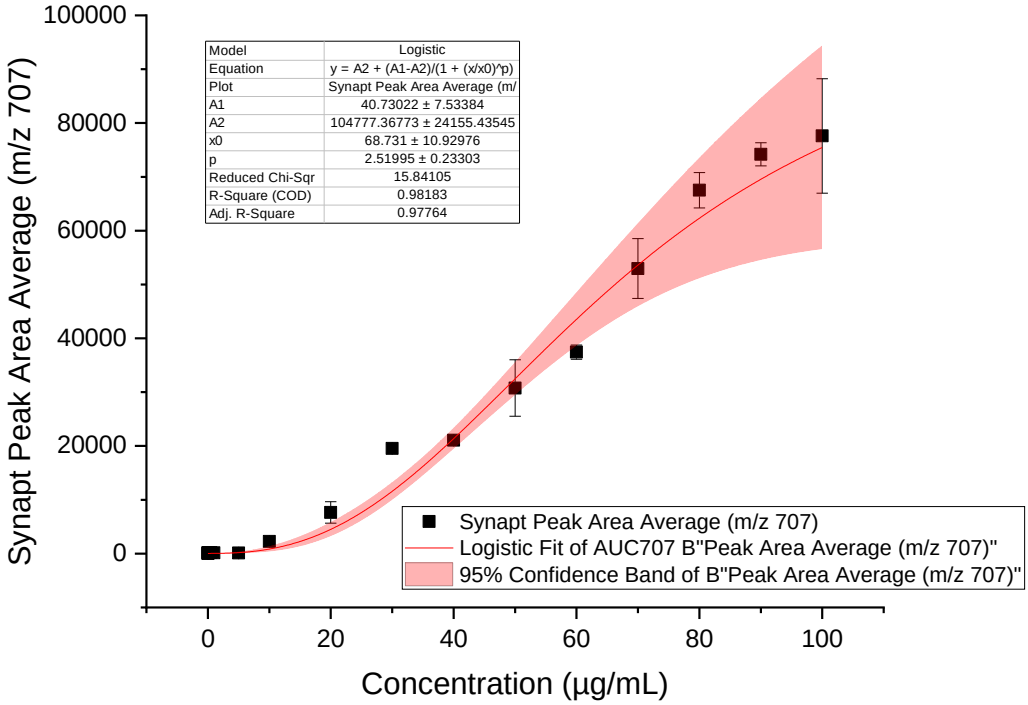

Figure 7.261 – Synapt calibration plot using lactose in water and acetonitrile (50:50 v/v) with formic acid (0.1% v/v) using *m/z* 707 peak area data. Each plotted point is the average of three runs with the standard deviation shown using error bars. Regression analysis has been applied with additional data inset.

Three additional concentrations of sample were run in triplicate on both instruments and the data analysed to determine whether concentration could be calculated using the previously described *m/z* 365 calibration plots (Figure 7.258 and Figure 7.259). In

addition the dimer calibration plot from the Synapt data (Figure 7.261) has also been included in the calculations with all results presented in Table 7.29.

Table 7.29 – Synapt and QDa determined concentrations using peak area for three additional samples. The extracted mass used to calculate the concentrations is stated for each instrument. The lower and upper 95% confidence limits are given in brackets.

Prepared concentration (µg/mL)	**Synapt – peak area experimentally determined concentration**		**QDa – peak area experimentally determined concentration (*m/z* 365)**
	***m/z* 365**	***m/z* 707**	
2.2	3.8 (-5.8 to 13.3)	6.5 (5.0 to 9.6)	2.6 (2.2 to 3.3)
9.3	15.5 (6.1 to 24.9)	17.1 (14.9 to 19.7)	13.2 (11.4 to 15.3)
13.5	27.8 (18.5 to 37.2)	22.7 (20.5 to 24.9)	17.9 (15.8 to 20.1)

The experimentally determined concentrations are consistently higher than expected for all three columns, although the QDa data is more closely aligned than the Synapt. The dimer data confirms that quantification using the primary ion at *m/z* 365 is more appropriate for this range of concentrations, and insufficient dimer ions in the QDa signal thwarted any attempts to utilise this data for further exploration. The dimer will however be monitored in future work to determine whether its appearance is influenced by the presence of additional components during ionisation and to ensure it does not affect quantification.

7.3.9 Mannitol

Mannitol is a hexahydric alcohol with a monoisotopic mass of 182.079041 Da, see Figure 7.262. It is a versatile and commonly used excipient present in varying formulations and is also used as a bulking agent within the food industry.[110] The grade used in this work is Roquette's Pearlitol 160 C, which refers to its large mean particle diameter of 160 µm and its crystalline state. It is inert and non-hygroscopic so often used to combat moisture sensitive APIs within oral formulations.[326]

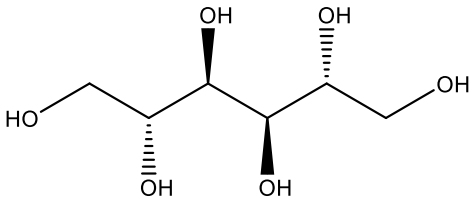

Figure 7.262 – Mannitol chemical structure and stereochemistry.

It was analysed by both positive and negative ESI-MS and a number of ions found in each. Additional QToF analysis confirmed that in positive mode an ion at *m*/*z* 205 corresponds to $[M+Na]^+$ and in negative mode, $[M-H]^-$ can be found at *m*/*z* 181. The conclusion that mannitol can be ionised in both modes with distinguishable ions in each highlights it as an interesting excipient for further work exploring ion suppression and enhancement. A series of concentrations of mannitol in water and acetonitrile 50:50 v/v with formic acid 0.1% v/v were therefore analysed to understand the relationship between signal and concentration.

Synapt negative mode:

Figure 7.263 shows the linear section of the calibration plot for mannitol analysed by negative ESI-MS using the Synapt. The line of best fit has been calculated with an R-squared greater than 0.99; the lowest concentration analysed was 0.005 µg/mL but the lower limit for detection is higher at 0.5 µg/mL. The upper limit for quantification with a line of best fit is 40 µg/mL, however, the plot can be extended further and shows an unusual pattern at the higher concentrations, see Figure 7.264. This shows two linear sections and two plateaus, the first plateau is between 40 and 60 µg/mL and the second after 90 µg/mL. It is unclear why this might occur; the first plateau cannot be explained by detector saturation, nor are there clear differences between the chromatograms to explain the changes although additional ions were present.

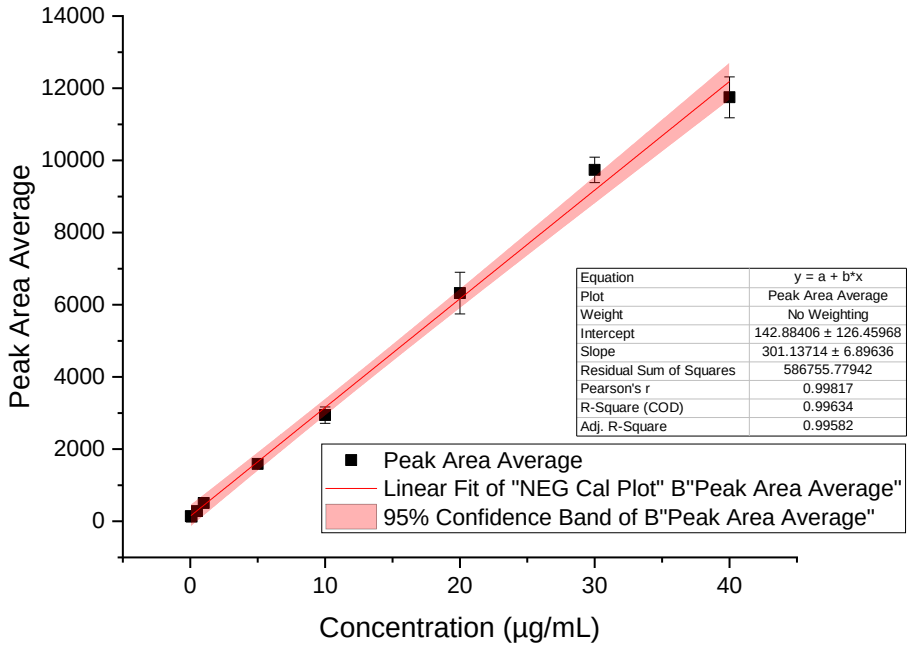

Figure 7.263 – Synapt negative ESI-MS calibration plot for mannitol in water and acetonitrile (50:50 v/v) with formic acid (0.1% v/v) using *m/z* 181.1 (± 0.1 Da) peak area data. Each plotted point is the average of three runs with the standard deviation shown using error bars. Linear regression has been applied with additional data inset.

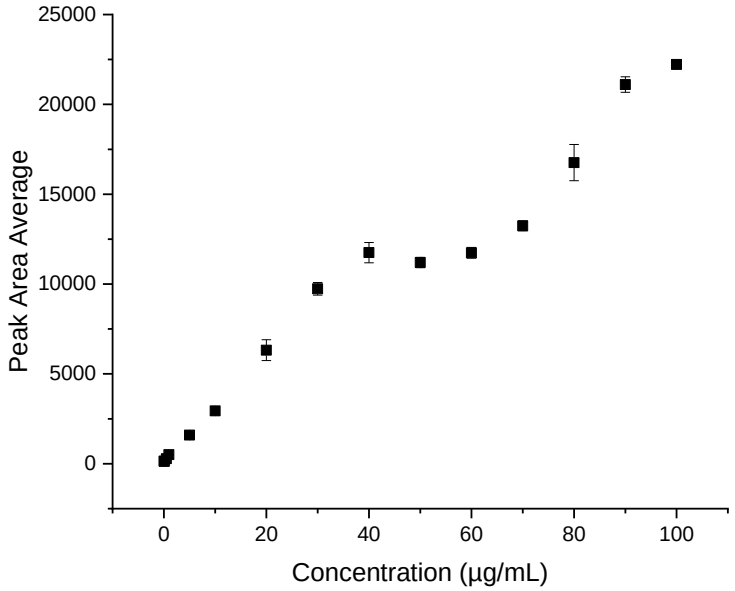

Figure 7.264 – Extended Synapt negative ESI-MS calibration plot for mannitol in water and acetonitrile (50:50 v/v) with formic acid (0.1% v/v) using *m/z* 181.1 (± 0.1 Da) peak area data. Each plotted point is the average of three runs with the standard deviation shown using error bars.

Synapt positive mode:

The samples run in negative mode ESI-MS on the Synapt were also run using its positive mode and the calibration plot can be found in Figure 7.265. The overall shape is comparable with the negative ESI-MS plot, with two linear sections interrupted by a plateau, see also Figure 7.264. However, the lower limit for detection now extends to 0.05 µg/mL (from 0.5 µg/mL) and the signal appears to continue increasing at 100 µg/mL instead of showing signs of another plateau. The variability of data also increases after 30 µg/mL, as shown by the error bars widening, which is not consistent with the previous plot using negative ESI-MS, although the peak areas obtained are ten times greater than in the positive mode (the runs were carried out on the same instrument on the same day). Exploration of the chromatograms confirm again that there are no clear differences between the chromatograms to explain the changes, although again, additional ions were present.

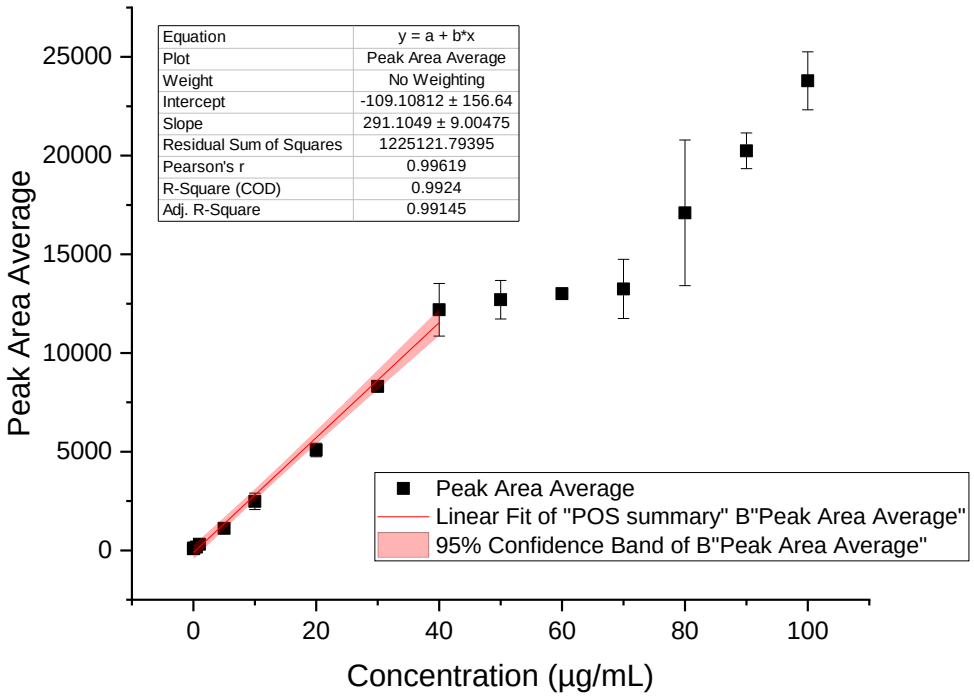

Figure 7.265 – Synapt positive ESI-MS calibration plot for mannitol in water and acetonitrile (50:50 v/v) with formic acid (0.1% v/v) using *m/z* 205.1 (± 0.1 Da) peak area data. Each plotted point is the average of three runs with the standard deviation shown using error bars. Linear regression has been applied to the initial section of the plot (from 0.05 to 40 µg/mL) with additional data inset.

The linear sections of data from Figure 7.263 (negative ESI-MS) and Figure 7.265 (positive ESI-MS) were used to calculate concentration from signal for three additional samples run at the same time, and the results can be found in Table 7.30. The experimentally-determined concentrations are comparably close to the prepared concentrations for both positive and negative data, although the confidence limits of the positive data are wider suggesting more variability.

Table 7.30 – Synapt determined concentrations using peak area for three additional samples. The negative mode ESI-MS used an extracted mass of *m*/z 181.1 (± 0.1 Da) and the positive mode ESI-MS used an extracted mass of *m*/z 205.1 (± 0.1 Da). The lower and upper 95% confidence limits are provided in brackets.

Prepared concentration (µg/mL)	Negative - experimentally determined concentration (µg/mL)	Positive - experimentally determined concentration (µg/mL)
2.2	4.0 (1.6 to 6.5)	3.0 (-0.3 to 6.2)
9.3	11.9 (9.5 to 14.3)	8.1 (4.8 to 11.3)
13.5	14.9 (12.5 to 17.3)	9.5 (6.2 to 12.7)

QDa:

A reduced number of samples of mannitol dissolved in water and acetonitrile 50:50 v/v with formic acid 0.1% v/v were run in negative mode ESI-MS on the QDa with the SIM method again following *m/z* 181 to determine whether the same unusual relationship between signal and concentration occurred. Figure 7.266 shows a linear calibration plot between 10 and 80 µg/mL for the QDa, with signs of a plateau between 80 and 100 µg/mL, but no loss of linearity between 40 and 80 µg/mL as seen with the Synapt data. The precision of data points is good, but the signal is quite low relative to that observed with other components.

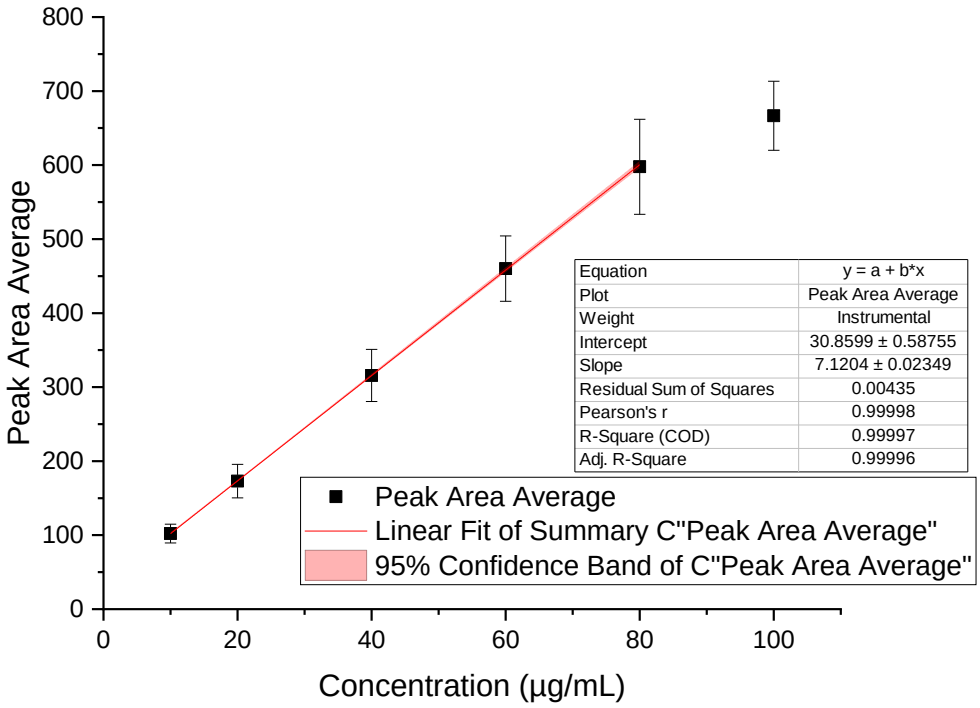

Figure 7.266 – QDa calibration plot for mannitol dissolved in water and acetonitrile (50:50 v/v) with formic acid (0.1% v/v) analysed in negative mode using the SIM channel of *m/z* 181. Each point is the average of three runs and the standard deviation is shown with error bars. The line of best fit has been plotted in red, with the shaded area representing the 95% confidence band.

The samples were also run in the positive mode on the QDa, however, mannitol could only be detected at *m/z* 205 at a concentration of 1 mg/mL using this method. Further exploration of the samples was therefore carried out to determine whether any additional ions might be able to explain the unusual calibration plots for the Synapt or the lack of ionisation for the QDa. An MS/MS method on the QToF was used to explore both *m/z* 389 and 387 ions in the positive and negative modes, respectively; this confirmed the likely presence of a contaminant rather than a mannitol-related ion. Each appeared in greater quantities at higher concentrations of mannitol. Exploration of other grades of mannitol were not feasible within the timescale of this work but would help clarify whether these challenges are specific to the brand selected.

7.3.10 Povidone

Povidone is also referred to as PVP, polyvinylpyrrolidone or polyvidone, and is a versatile excipient that is manufactured in multiple grades for a variety of formulations

ranging from tablets to transdermal patches.[110] It is a polymer and therefore behaves differently from the excipients and APIs previously described. The repeating unit, *N*-vinylpyrrolidone, is shown in Figure 7.267.

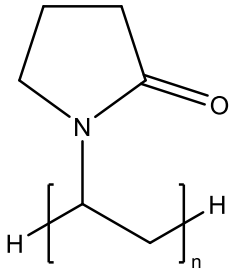

Figure 7.267 – Povidone chemical structure of repeating unit, *N*-vinylpyrrolidone.

Two versions of povidone were explored in this work, povidone 30 and povidone CL. Povidone "30" refers to the *K*-value, which is characterised by viscosity in aqueous solutions and relates to molecular weight. Povidone 30 has an approximate molecular weight of 50, 000 Da and is soluble allowing it to be utilised as a wet binder. Povidone CL, however, is a crosslinked homopolymer of *N*-polyvinylpyrollidone with a molecular weight greater than 1,000,000 Da. It is water-insoluble, instead swelling and wicking, which results in it working as a disintegrant. This insoluble nature of povidone CL inhibits easy analysis by ESI-MS, but an attempt was made to dissolve it in a water and acetonitrile mixture (50:50 v/v), and the resultant product filtered and analysed by ESI-MS on the Synapt. The initial scoping runs for both versions of povidone at a potential maximum concentration of 1 mg/mL are shown in Figure 7.268.

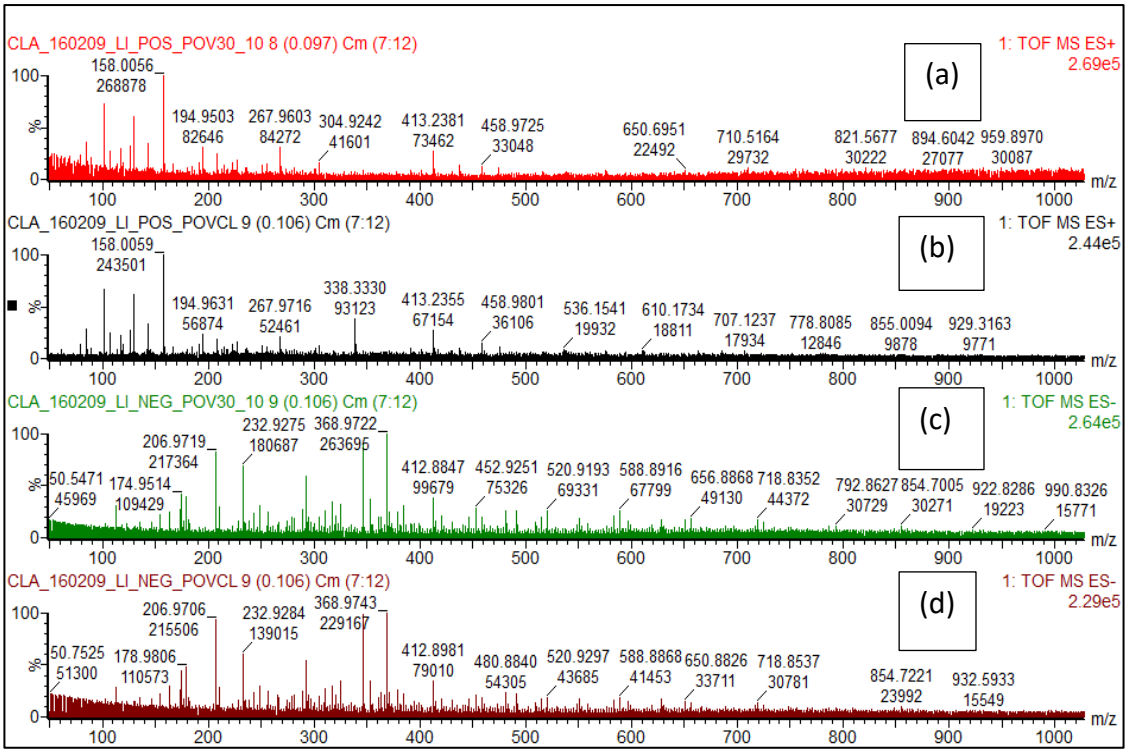

Figure 7.268 - Povidone in water and acetonitrile (50:50 v/v) with formic acid (0.1% v/v) analysed by Synapt: (a) positive mode povidone 30 (b) positive mode povidone CL (c) negative mode povidone 30 and (d) negative mode povidone CL.

There are a number of consistent ions between both the povidone 30 and CL in both the positive and negative modes, but no identifiable ions can be observed for either polymer suggesting that they are not easily ionised by ESI-MS on the Synapt using the standard settings. This is to be expected of a polymer with an average molecular weight of 44,000 to 54,000 and a repeating monomer unit of 110.14, and provides evidence that povidone is not appropriate for simple analysis using the QDa.

7.3.11 Additional insoluble excipients

The following excipients were found to be insufficiently soluble to analyse simply using ESI-MS: croscarmellose sodium (CCS), magnesium stearate, microcrystalline cellulose (MCC), sodium stearyl fumarate (SSF), sodium starch glycollate (SSG) and starch. An excess of each was placed in a solution of water and acetonitrile (50:50), the resulting samples were sonicated and a vortex mixer used to dissolve as much as possible before they were placed in a centrifuge and a filtered sample taken for analysis with the Synapt in both positive and negative mode. The plan was to observe whether any

identifiable ions could be found, even if they do not lend themselves to quantification, their presence may be possible to detect.

CCS and SSG are cross-linked polymers that swell and wick rapidly when in contact with water. The brand of CCS used was Primellose® and the brand of SSG was Primojel®, both made by DFE Pharma and marketed as superdisintegrants. As expected no obvious ions of interest were observed in either mode for either excipient, see Figure 7.269.

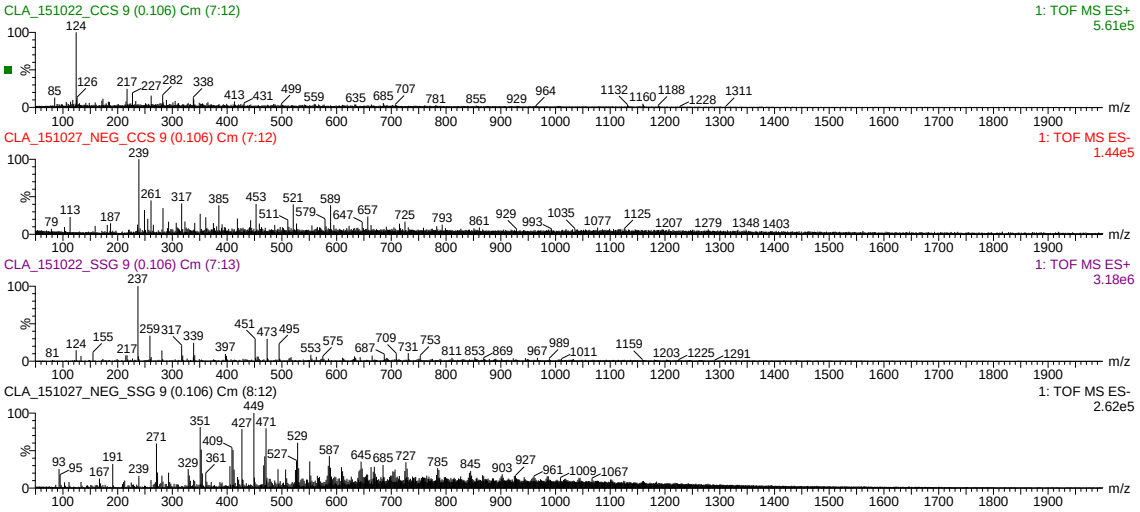

Figure 7.269 – Synapt analysis of CCS in positive and negative mode, and SSG in positive and negative mode (from top to bottom).

MCC and starch are versatile excipients, used as binders, diluents, disintegrants and fillers.[110] Both are composed of the same glucose unit structure, with differing degrees of polymerisation and glycosidic links; MCC is termed a partially depolymerized cellulose, whereas starch is composed of a linear chain amylose and a highly branched amylopectin.[327] The Starch 1500® used in this work is a partially pregelatinised version whereby a bond between sections of the amylose and amylopectin is broken, which results in partial solubility. Nevertheless, neither excipient produced obvious ions of interest in either positive or negative mode, see Figure 7.270.

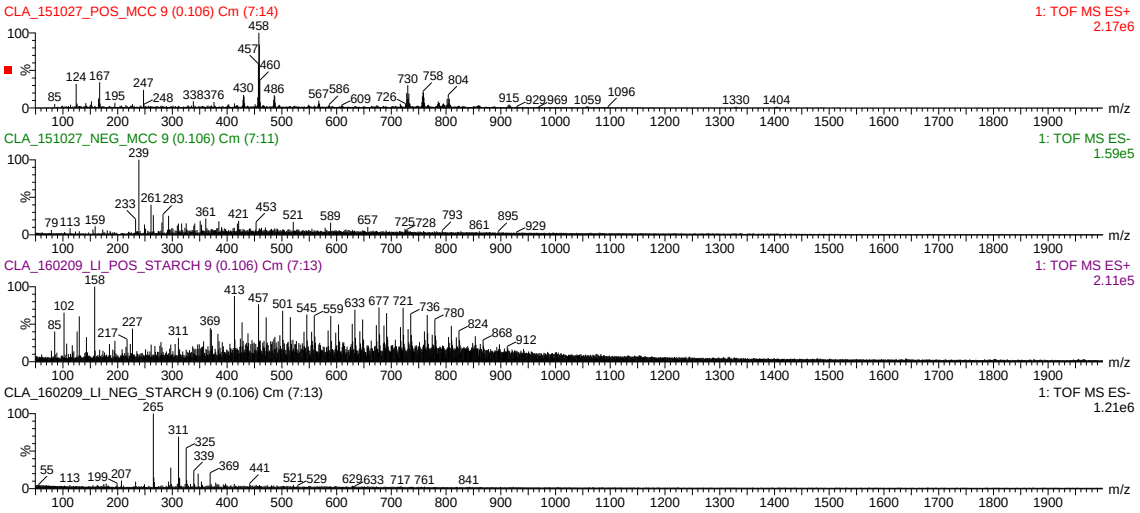

Figure 7.270 – Synapt analysis of MCC in positive and negative mode, and starch in positive and negative mode (from top to bottom).

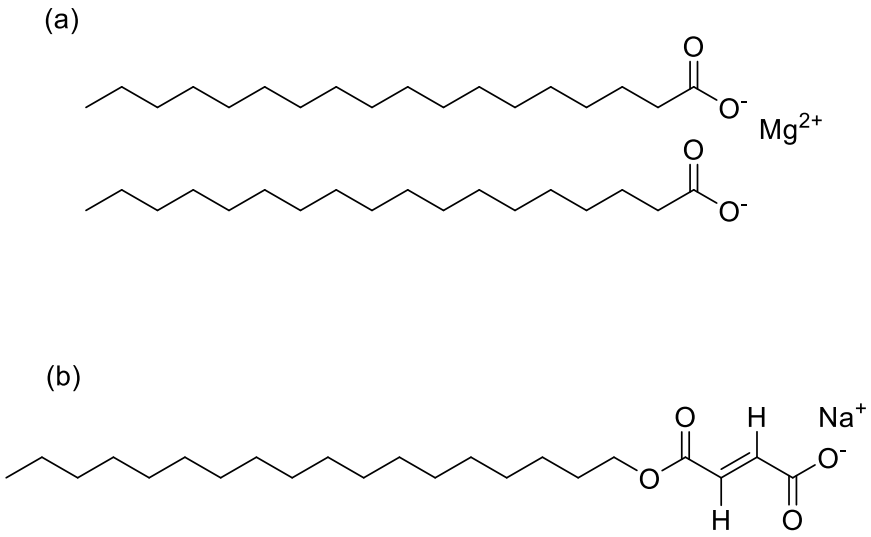

Figure 7.271 – Chemical structures of (a) magnesium stearate and (b) sodium stearyl fumarate (SSF).

Magnesium stearate and SSF are lubricants designed to reduce friction for example during ejection of tablets. Lubripharm (SSF manufactured by Forum SPI Pharma) is marketed as a less hydrophobic alternative to magnesium stearate, and both are small molecules by MS standards at 390.5 g/mol and 591.2 g/mol, respectively, see Figure 7.271. The sample containing magnesium stearate was unable to be analysed due to the suspension of particles throughout. The sample containing SSF produced the spectra in Figure 7.272, with distinct polymeric repeating patterns of + 68 in both the positive and negative modes.

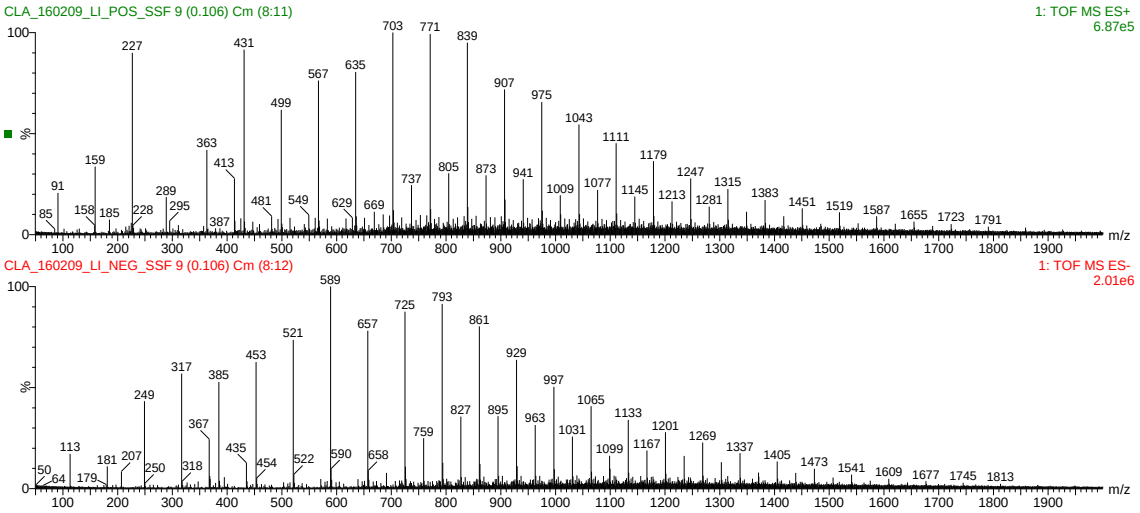

Figure 7.272 – Synapt analysis of SSF in positive and negative mode (from top to bottom).

The poor solubility of all these excipients could potentially be improved by altering the dissolving solvents or utilising additional MS analysis, however, the purpose of this initial work was to explore the ease by which individual formulation components could be analysed and quantified using ESI-MS so that they may be explored further in the next chapter. Hence these insoluble excipients have been excluded from further analysis, and a conclusion drawn that insoluble excipients present in formulations are likely to be filtered out prior to MS analysis preventing them from impacting upon ionisation, although this may require further confirmation including consideration of each excipient's particle size distribution.

7.4 Conclusions

The choice of solvent(s) and the addition of ionisation modifiers are important decisions when first embarking upon quantification studies as highlighted by the APIs and excipients studied in this chapter. First and foremost sufficient solubility is required in the solvent(s) being used in order that they may be introduced in solution to the ESI-MS. Understanding the component in solution is important in assessing their ability to ionise efficiently, for example, paracetamol was found to ionise most efficiently from a solution containing water, acetonitrile and formic acid, compared with only water. Additionally, research suggests that in addition to analyte concentration, properties such as the polarity of molecules, which will vary with the

solvent(s) and any ionisation modifier(s) used, may be a risk factor for susceptibility to ionisation suppression and enhancement.[236,243,328–330]

Ionisation modifiers, such as formic acid, are commonly used in positive ESI-MS to alter the pH of a solution thereby improving formation of $[M+H]^+$ during ionisation. However, their use in negative ion electrospray to encourage $[M-H]^-$ formation is clearly more complex than simple pH adjustment.[298] Furosemide is shown in this work to be ionised from a solution containing formic acid in negative mode ESI-MS enabling its quantification. Ionisation of ibuprofen sodium proved to be problematic and could not be analysed using the QDa in either mode, either with or without formic acid. Literature suggested the use of trimethylamine (TEA) as a more appropriate modifier for obtaining the deprotonated molecular ion for standard ibuprofen (in negative mode).[320] However, it was not possible to explore within the time constraints of this research, hence ibuprofen sodium quantification utilised a BPI method for the Synapt that would not be appropriate for studies involving multiple components ionised concurrently.

The next and arguably most important step in exploring concentration and signal is defining the most appropriate ion to follow for each component in the solvent(s) and modifier(s) of choice. The use of a high resolution mass spectrometer (Synapt and QToF) aided this understanding, and was supported by the use of MS-MS in cases where it was unclear whether ions were related to the component being analysed. A disadvantage of using a detailed analytical technique such as mass spectrometry for monitoring dissolution is that a wide variety of ions can be observed, hence this clarification is extremely important as highlighted by the majority of the APIs studied (furosemide, paracetamol and phenylephrine) and particularly the excipients, lactose and mannitol. Additionally, the precision of the *m*/*z* value for extracting and quantifying components should be borne in mind. The high resolution ESI-MS will easily differentiate between ions close in mass, such as phenylephrine and paracetamol, but the QDa will require close monitoring to ensure that ions from each API are being selected appropriately by the SIM method.

The next step involves consistency with equipment set up and aliquot injection volumes, to ensure that analysis is undertaken in the same way for a set of analyses.

Ion signal is considered to be largely independent of flow rate and injection volume, however, injection volume was shown to impact upon chloramphenicol signal, so consistency is recommended.[236] The same MS should be used and samples should be analysed at the same time as the calibration plot run.[303] Scan time should be considered to ensure that the full extent of the peak can be seen and aliasing is avoided, whilst also balancing this with the ion statistics and data burden. Scan time can additionally be affected by the ionisation efficiency of the component being analysed, hence it should be considered early on when working through the quantification method.

Quantification can, as shown explicitly with chloramphenicol, be carried out using either peak area or peak height of injected aliquots, however, this should be consistent for each set of analyses. Peak area was selected for the majority of initial work as a result of the consistent rather than optimised scan times, which were observed to alter the peak height more than peak area (see Figure 7.217). Peak shape should also be paid attention to, with smoothing avoided and instead data extracted to a software such as Origin to enable detailed integration of peak area or measurement of peak height. Once peak shape is confirmed to be appropriate then the MassLynx software (and QuanLynx) may be useful for this step, but in the initial stages of developing a method they can result in important details being overlooked.

The calibration plots obtained for each of the components explored highlight that the relationship between concentration and signal is infrequently linear across the concentration ranges studied, even prior to detector saturation and response plateaus. Research into ionisation mechanisms has offered an explanation that distinct ionisation mechanisms may be occurring at each concentration.[331,332] Differing regression analyses may therefore be applied to distinct sections of the concentration range, with some research defining a low concentration mechanism and a high concentration mechanism for ion release from droplets based upon surface activities.[333] The mechanism by which ionisation is occurring is outside the scope of this research, but understanding that this may vary with concentration highlights the importance of designing calibration plots appropriately.

Regression analysis was used successfully to describe and quantify the relationships

between signal and concentration for each of the components, with the exception of ibuprofen and the insoluble excipients. This information was also successfully utilised to calculate concentration from signal for a number of additional samples. The concentrations used were selected to include small and precise concentrations to explore the level of detail that one might expect to obtain. The results confirm that mass spectrometry can be used to calculate concentration from signal for almost all of the APIs and soluble excipients analysed in this chapter. The level of precision is good, and the level of accuracy may be improved if needed by narrowing the range of concentrations included in the calibration plot. Finally, a summary of the limits for quantification using the peak area method for each API and excipient has been summarised in Table 7.31.

Table 7.31 – QDa summary table for the current limits of detection found so far using simple solvents only (water and acetonitrile 50:50 with 0.1% formic acid v/v). Those highlighted with (*) did not contain formic acid.

	***m/z (s)* of interest**	**Lower limit for quantification (µg/mL)**	**Upper limit for quantification (µg/mL)**
Chloramphenicol*	$[M-H]^-$	1	70
Furosemide	$[M-H]^-$ & $[M-COOH]^-$	0.5	80
Guaifenesin	$[M+Na]^+$	0.2	10
Haloperidol	$[M+H]^+$	0.05	20
Paracetamol	$[M+H]^+$	0.1	100
Phenylephrine	$[M+H-H_2O]^+$	0.2	5
Lactose	$[M+Na]^+$ $[2M+Na]^+$	0.05 10	50 60
Mannitol	$[M-H]^-$ $[M+Na]^+$	10 1000	80 1000

This chapter provides the basis for expanding our current understanding of dissolution monitoring by ESI-MS. Exploring the relationship between concentration and signal for a range of different APIs and excipients provides detailed insights into the ability to detect and quantify components accurately, as well as the extent of variation observed, which will support studies of ion enhancement and suppression when

monitoring multiple components. The work has included a range of APIs and excipients with differing solubility, some of which can be monitored routinely through the presence of chromophores via UV-Vis and some of which cannot. Routine MS solvents have been used, both with and without the addition of ionisation modifiers, and confirm the impact of solvents upon signal. Finally, although single components were used in this chapter, attention to the impact of separation prior to ionisation highlighted that the presence of impurities, particularly in excipients, can still impact upon the chromatogram produced and has the potential to affect quantification. In summary, this section of work provides a good grounding for the next chapter determining the variation in signal for continuous flow analysis and exploring the relationship between multiple APIs and excipients.

8. Exploring multiple components in simple solvent systems with ESI-MS

8.1 Introduction

Routine dissolution techniques allow for quantification of the API(s) present in a formulation, most commonly through UV techniques. The primary reason for using mass spectrometry in place of UV analysis is the additional ability to monitor components without a chromophore.[15] This has the potential to elucidate dissolution mechanisms further than simply following the API release and therefore aid research and development for formulations. Chapter 7. Exploring single components in simple solvent systems with ESI-MS, explored the ease by which individual components could be detected, analysed and quantified using ESI-MS; the work confirmed that it was possible for a number of APIs and excipients, both with and without chromophores. It discovered that the relationship between signal and concentration was not consistently linear, but that differing regression analyses could be utilised to calculate concentration from signal for multiple APIs and excipients when analysed individually.

This chapter aims to develop the technique further and explore whether multiple API(s) and excipients may be monitored concurrently using ESI-MS without prior separation or extensive sample preparation. The impact of ion suppression and ion enhancement as a result of co-analysing API(s) and excipient(s) will be explored, and the impact of solvent(s) will be observed and considered for each step, as with the previous chapter. Additionally the use of alternative dissolution media will be trialled. While ionisation phenomena are frequently encountered in MS, the effects of ion suppression and enhancement are poorly understood and cannot currently be predicted.[334] This chapter therefore seeks to explore whether such phenomena are sufficiently reproducible that signal may be adjusted to enable quantification even when analysing multiple components.

Furthermore, the ability to detect and quantify components on-line and in real-time will be tested. The previous chapter introduced sample to the ESI-MS equipment through aliquot injections. This is similar to conventional dissolution techniques, which take samples at set time points throughout and analyse them. An alternative, however, would be to sample continuously thereby extracting more extensive

information about the dissolution process, enabling very rapid dissolution to be monitored and allowing a more complete dissolution profile to be obtained for better modelling. In conjunction with continuous flow MS analysis, this alternative method of sampling has the potential to visualise changes in concentration of both API(s) and excipients(s) more easily through monitoring each SIM signal. It also has the advantage of both on-line and real-time monitoring, although the challenge lies in understanding the stability of the signal and any ion enhancement or suppression that may be occurring. An additional advantage comes from the presence of the mass rate attenuator (MRA), which will enable the dilution of the dissolution bath sample to be adjusted manually according to the signal strength throughout the process. This means that samples at the start and end of the process can be analysed by diluting them a little or a lot, respectively, without reaching limits of quantification or saturation of the detector. The challenge will be to understand how changes in concentration and dilution translate to signal strength, and how this is changed when multiple components are ionised concurrently.

8.2 Method

The APIs and excipients successfully analysed in the previous chapter have been utilised again and include: chloramphenicol, furosemide, guaifenesin, haloperidol, paracetamol, phenylephrine, lactose and mannitol. The simple solvents used previously have also been used again: water and acetonitrile, both with and without formic acid, with the addition of simple dissolution media such as deionised water, blank FaSSIF and blank SGF. The earlier work determined the ions that were most appropriate to follow for quantifying the components. However, care has been taken in this chapter to explore whether additional or alternative ions form when multiple components are ionised concurrently or when different solvents (including dissolution media) are present.

Multiple methods and experimental designs are utilised for this chapter so a short description will be included with each set of results for clarity. Detailed explanations of each equipment set up are provided in Chapter 6. ESI-MS Equipment Set Up. In summary, aliquot analyses have been specified as either LC (includes chromatography) or LI (loop injection – no chromatography) and samples were analysed using the

Synapt and / or the QDa. Continuous flow analyses were undertaken using only the QDa due to the logistics of setting up continuous flow analysis with ESI-MS and therefore did not include LC prior to ionisation.

8.3 Results and Discussion

The results and discussion have been collated into two sections for clarity: i) aliquot injections of sample containing multiple components, and ii) continuous flow injection of sample from a single solution, which may contain multiple components, to mimic on-line analysis from a dissolution bath.

8.3.1 Aliquot MS analysis

Aliquot MS is useful for exploring the relationships between components ionised concurrently and sets the scene for on-line analyses. It involves extensive and time-consuming pre-work to enable quantification of the samples, however, and does not enable continuous or on-line monitoring. The following aliquot work has been broken down into subsections describing what was carried out, what can be understood from it and how it informs the next steps.

8.3.1.1 Confirmation of ionisation complexity

A Beechams® All-In-One cold and flu tablet was analysed using positive ESI-MS (ES+) on the Synapt to provide an overview of the extent of ion suppression and enhancement that can occur. The tablet was weighed, crushed and a sample of known mass dissolved in a known volume of solvents. The filtered samples were analysed both with and without chromatography (LC and LI, respectively) for comparison purposes. The tablet contains three APIs (paracetamol, guaifenesin and phenylephrine) as well as twelve excipients, which include lactose, see Table 2.5. The five minute reverse phase LCMS method was used and the following retention times were found, see Table 8.32. This provided confirmation that all four major components were present in the sample and able to be identified using ESI-MS. The additional peaks at retention times of 2.85 and 3.44 minutes contained multiple ions, likely a combination of the additional excipients present in the formulation.

Table 8.32 – Synapt five minute reverse phase LCMS method details for Beechams® All-In-One tablet dissolved in water and acetonitrile (50:50 v/v) with formic acid (0.1% v/v).

Retention Time (min)	Component and ion present
0.64	Lactose $[M+Na]^+$
0.78	Phenylephrine $[M+H-H2O]^+$
1.76	Paracetamol $[M+H]^+$
2.35	Guaifenesin $[M+Na]^+$
2.85	Unidentifiable
3.44	Unidentifiable

The samples were also analysed using the loop injection (LI) method to force all components to be ionised concurrently using the Synapt and each of the four major components were identified, see Figure 8.273. The extracted ion chromatograms highlight that each component produces signals which differ in strength, as would be expected due to their differing ionisation efficiencies and also their concurrent ionisation giving rise to the possibility that there is both suppression and enhancement occurring. The total ion current includes all soluble ionised components, with lactose and paracetamol showing greater relative signal strengths (observed simply as peak area or height) compared with guaifenesin and phenylephrine, which loosely follows their relative amounts within the tablet. A single tablet weighing 714 mg contains 35.0 % paracetamol, 14.0 % guaifenesin, 0.7% phenylephrine and the remaining mass contains each of the excipients listed, twelve in total, hence lactose could comprise an absolute maximum of 50.3 % of the tablet.

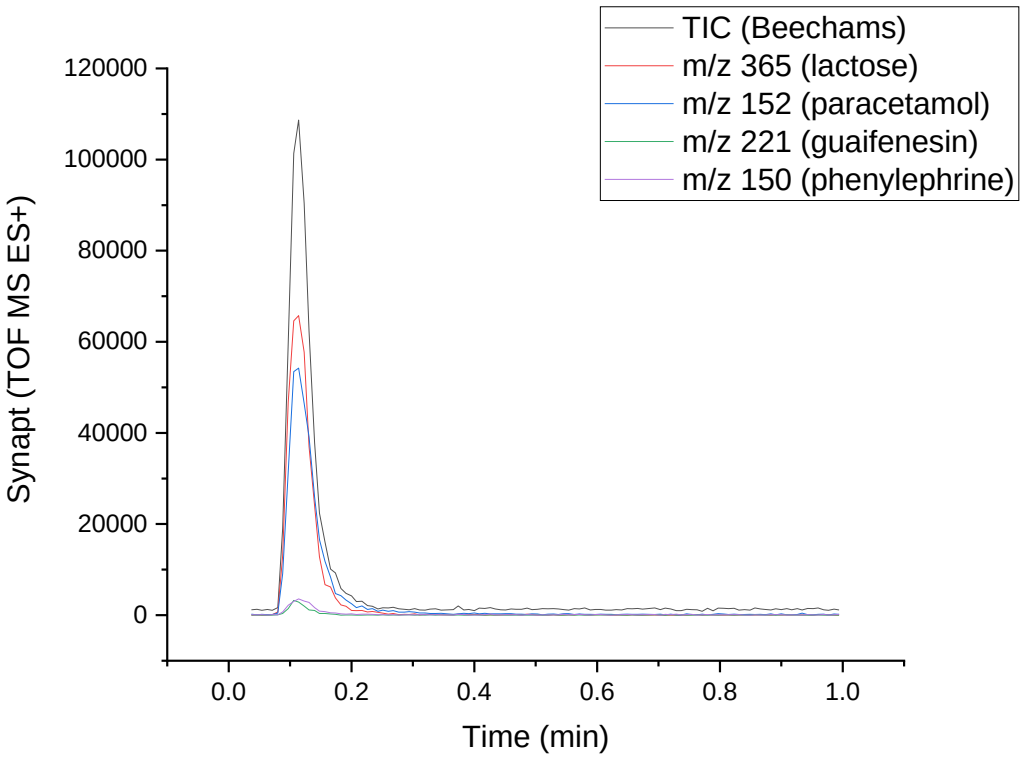

Figure 8.273 – Synapt positive ESI-MS loop injection chromatogram for Beechams® All-In-One tablet dissolved in water and acetonitrile (50:50 v/v) with formic acid (0.1% v/v). The total ion chromatogram (TIC) is shown along with four extracted chromatograms for each of the main components.

In line with the previous work, three standards for each API bracketing the expected concentration present in the tablet solution were also analysed using LI to produce calibration plots for each of the APIs and attempt to calculate concentration from signal. The concurrent ionisation of each tablet component and the presence of additional excipients aside from lactose contribute to the inaccuracy of these calculations, see Table 8.33.

Table 8.33 – Synapt LI MS estimation of concentration from signal for Beechams® All-In-One tablet. Note that the quantity of lactose in the tablet is not subject to the same controls as the APIs, hence it is not known and instead the maximum possible concentration that could be present is stated instead (*).

	Estimated concentration (μg/mL)	Actual concentration (μg/mL)
Paracetamol	3.8	3.6
Guaifenesin	2.7	1.5
Phenylephrine	0.1	0.073
Lactose	4.0	5.2 (max possible*)

The estimated and actual concentrations are different for each component, although we cannot be certain of the lactose content of the tablet. This highlights the impact that ionisation phenomena can have upon signal and therefore upon quantification using simple calibration plots. It confirms the importance of working through ionisation of multiple components in a step-wise manner so that these phenomena can be disentangled and potentially accounted for.

8.3.1.2 Dissolution media impact upon paracetamol compact dissolution

An experiment was designed to compare dissolution profiles obtained through off-line analysis methods. Simple paracetamol compacts consisting of paracetamol and lactose were made using the Gamlen benchtop press. This enables dissolution to be monitored for binary compacts containing only one API and one excipient (unlike commercial tablets). Three grades of lactose were available for compaction and were compared to determine the most appropriate, these included GranuLac®, PrismaLac® and SorboLac®. PrismaLac® proved to be the most successful of the three allowing compacts to be produced without lubricant, although there were ejection challenges with the press, which resulted in very few compacts being made.

Dissolution of the paracetamol compact was carried out in deionised water using the Sotax apparatus and samples taken regularly over 30 minutes. The samples were filtered and analysed by three methods: i) conventional UV analysis, ii) LI-MS by QDa and Synapt, and iii) LCMS by Synapt. The samples analysed by the Synapt were injected into a solvent mixture of water and acetonitrile 50:50 v/v with 0.1% v/v formic

acid by a method described earlier as loop injection (LI) because it bypasses the LC and directs the sample straight into the source so that all components are ionised concurrently. The full chromatogram was obtained and the paracetamol ions (*m*/*z* 152) extracted so that peak area could be quantified accordingly for each sample. Calibration plots were produced for each method using known concentrations of paracetamol dissolved in water. The resulting dissolution profile showing the cumulative amount of paracetamol dissolved in water can be found in Figure 8.274.

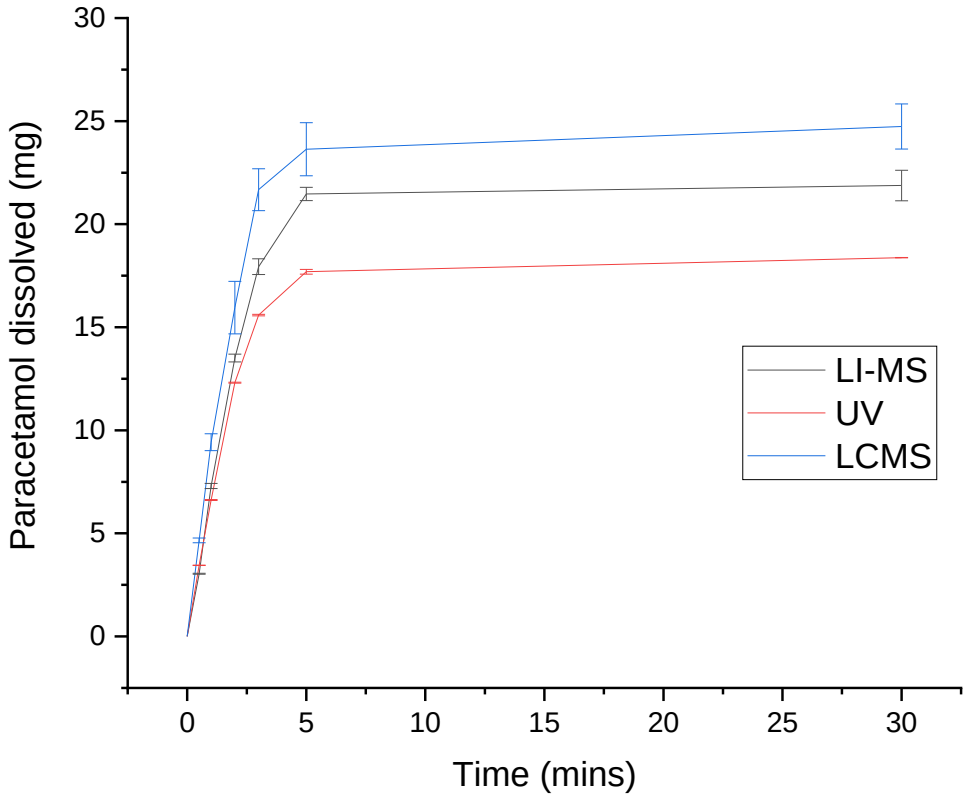

Figure 8.274 – Comparison of dissolution profiles obtained through three methods: i) loop injection MS, ii) UV analysis (243 nm) and iii) LCMS using the Synapt. Each point is the average of three runs with the standard deviation shown using error bars.

The profiles suggest that analysis by LI-MS is closer in value to conventional UV dissolution analysis, than the LCMS method, however, both MS methods show a greater level of variability than UV analysis. The mass of paracetamol within each tablet was 20 mg, hence both the LI and LC methods are subject to an unknown error which leads them to calculate the amount of paracetamol incorrectly high. In the case of the LI method, this could be a result of ionisation enhancement of the paracetamol signal by the lactose, which is additionally present in the sample. However, it is not

clear why this would occur with the LCMS analysis - paracetamol and lactose have different retention times (see Table 8.32) and therefore undergo ionisation separately. These findings suggest that there are significant limitations associated with using aliquot injections for monitoring dissolution. Logistical challenges meant that the UV samples were analysed on the same day as the dissolution was carried out, however, both the LI and LC analyses were run the following day at a different site. This may have contributed to the errors observed, hence on-line analysis development will reduce this delay between sampling and analysing. It also confirms that during development of this dissolution monitoring method, starting with defined concentrations of sample rather than analysing unknown samples, will enable a greater confidence in the interpretation of complex results.

Paracetamol compacts dissolved in blank FaSSIF and blank SGF were subjected to the same procedures and samples obtained in the same way. Synapt loop injection analysis of the FaSSIF and SGF samples for the calibration plots produced insufficient paracetamol ions for quantification, hence the dissolution samples were not run on this instrument. The blank dissolution media appears to cause ion suppression of paracetamol on this instrument, which will be explored further using the more robust QDa; dissolution media contains components which may result in equipment challenges, hence it is a safer place to begin than with the Synapt.

All the QDa analyses were run by injecting 1 µL aliquots of each sample into a continuous stream of water and acetonitrile 50:50 v/v with 0.1% v/v formic acid, which was continuously analysed by the QDa. Directly after each injection of sample, an aliquot of methanol was directed into the stream to clean the lines and the ionisation source; this was a precautionary measure taken to avoid build-up of the dissolution media, and methanol was selected due to its superior ability to efficiently ionise compounds.[335] A method including a full scan and two SIM channels, paracetamol (*m/z* 152) and lactose (*m/z 365)*, was used to observe the influence that the dissolution media exerted upon the ion signal. The chromatograms showing lactose and paracetamol signal as a result of the injection of sample (and methanol), for each dissolution media are provided in Figure 8.275, Figure 8.276 and Figure 8.277. The samples are (a) methanol for cleaning, (b) to (g) time points relating to 0.5, 1, 2, 3, 5

and 30 minutes, and (h) relating to blank dissolution media for FaSSIF and SGF only. Visual observations confirmed that the compact was fully dissolved by 4.5 mins in water, by 5 mins in FaSSIF and by 10 mins in SGF.

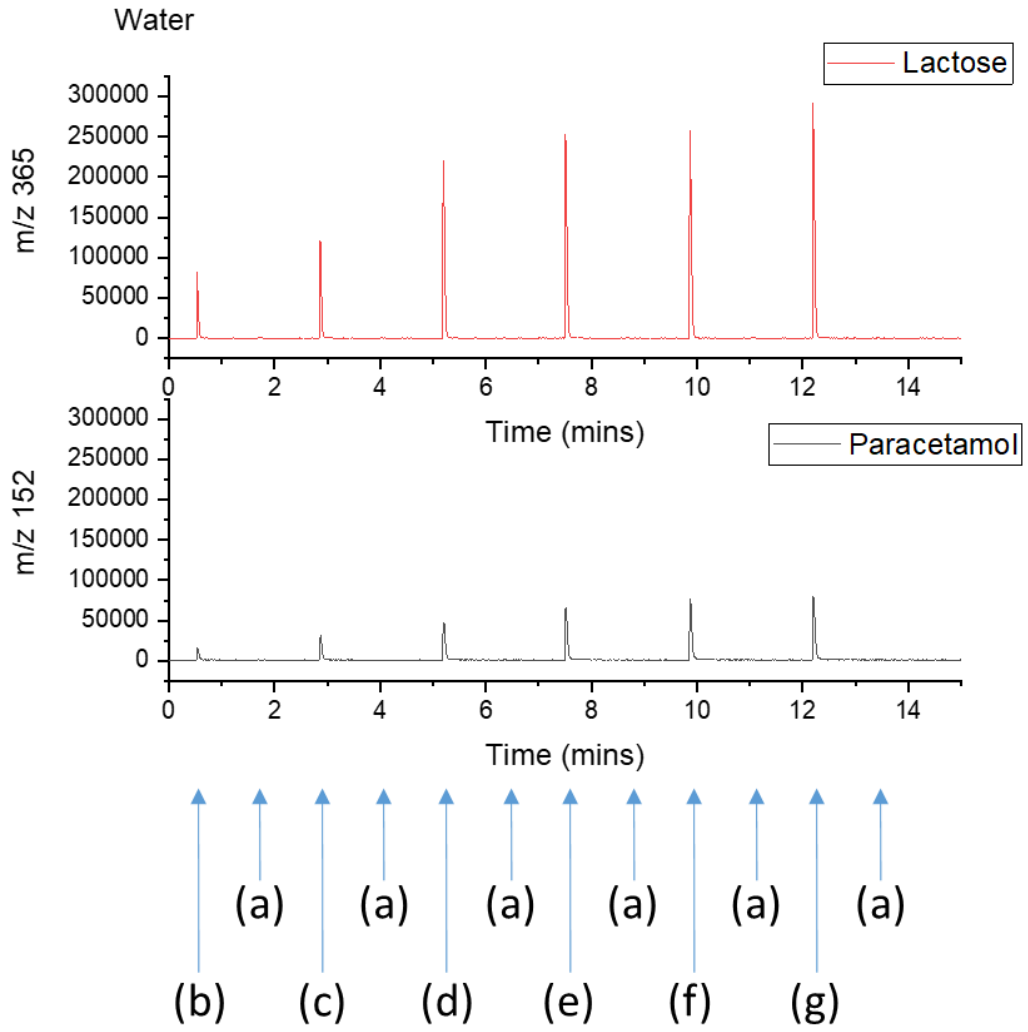

Figure 8.275 – QDa injection of paracetamol compact water dissolution samples into a continuous stream of water and acetonitrile (50:50 v/v) with formic acid (0.1% v/v). The top red chromatogram shows the lactose channel and the bottom black chromatogram shows the paracetamol channel. The points highlighted by the blue arrows labelled with (a) are features resulting from the injection of methanol for cleaning, and the peaks highlighted (b) to (g) are the result of the injection of samples taken from varying stages of the dissolution process (0.5, 1, 2, 3, 5 and 30 minutes).

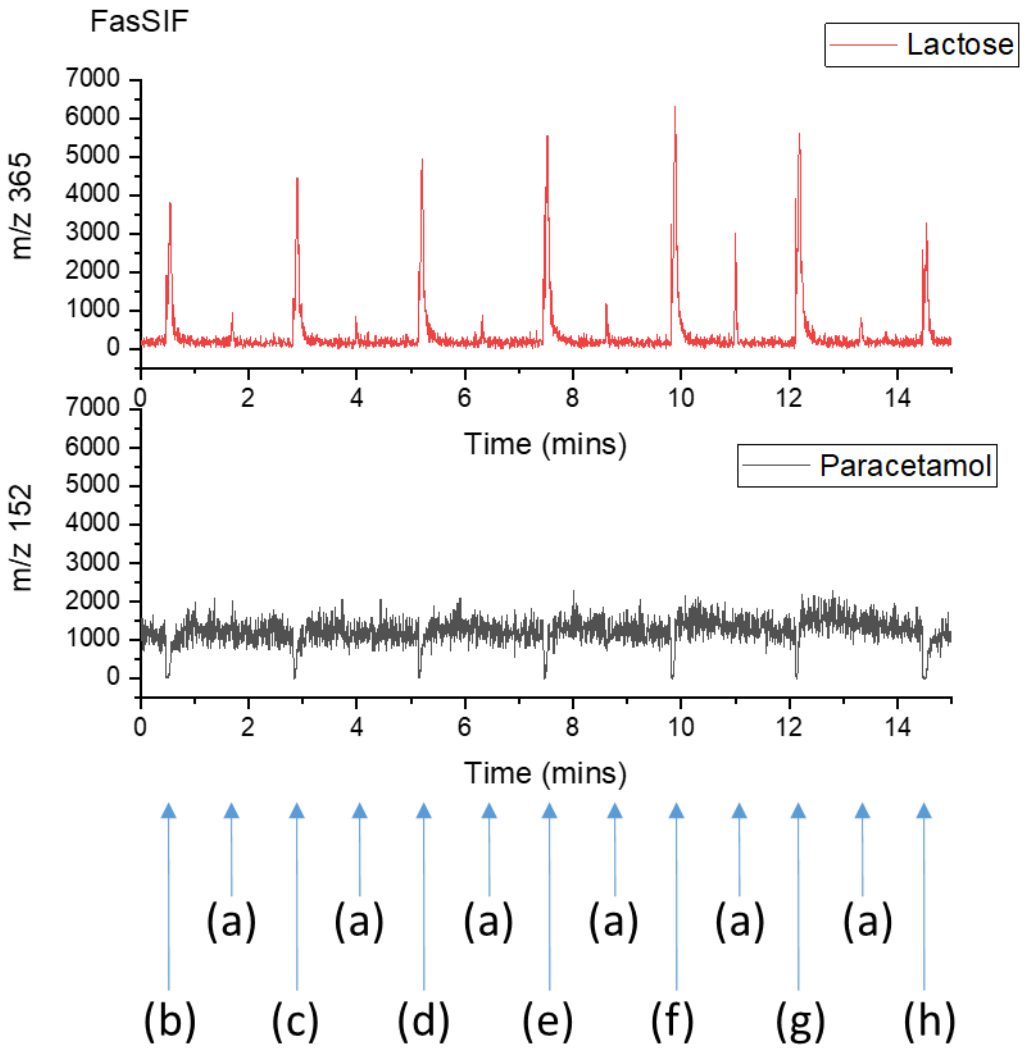

Figure 8.276 – QDa injection of paracetamol compact FaSSIF dissolution samples into a continuous stream of water and acetonitrile (50:50 v/v) with formic acid (0.1% v/v). The top red chromatogram shows the lactose channel and the bottom black chromatogram shows the paracetamol channel. The peaks highlighted by the blue arrows labelled with (a) are a result of the injection of methanol for cleaning, and peaks highlighted (b) to (g) are the result of the injection of samples taken from varying stages of the dissolution process (0.5, 1, 2, 3, 5 and 30 minutes) and (h) is blank FaSSIF.

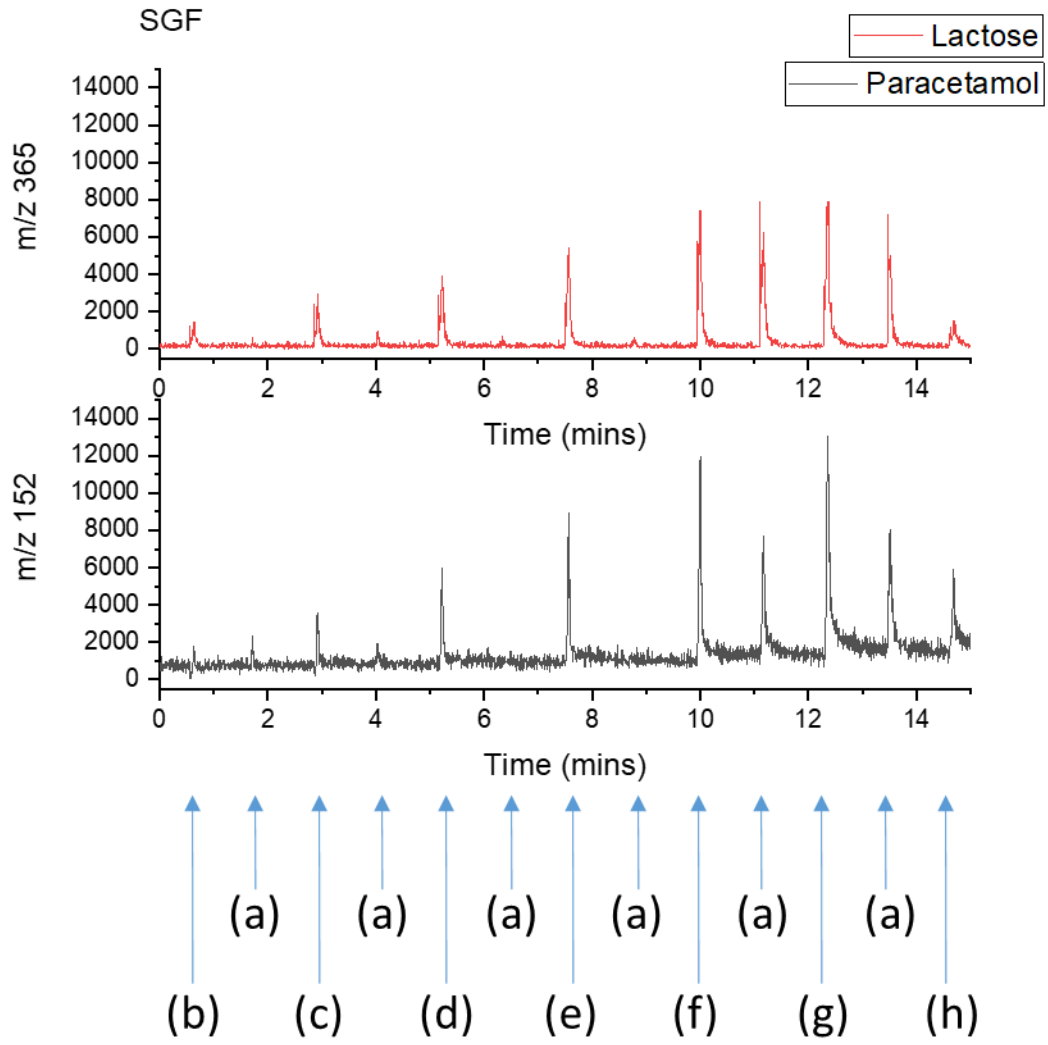

Figure 8.277 – QDa injection of paracetamol compact SGF dissolution samples into a continuous stream of water and acetonitrile (50:50 v/v) with formic acid (0.1% v/v). The top red chromatogram shows the lactose channel and the bottom black chromatogram shows the paracetamol channel. The peaks highlighted by the blue arrows labelled with (a) are a result of the injection of methanol for cleaning, and peaks highlighted (b) to (g) are the result of the injection of samples taken from varying stages of the dissolution process (0.5, 1, 2, 3, 5 and 30 minutes) and (h) is blank SGF.

Figure 8.275, for a compact dissolving in water, shows clear peaks in signal for both the paracetamol and lactose channels at each injection point, with no significant signal in-between samples when methanol is injected into the continuous solvent stream. The trend in each signal is in line with what would be expected, with the concentrations of both paracetamol and lactose increasing throughout their dissolution in water.

Figure 8.276, for a compact dissolving in FaSSIF, shows a peak in signal for the lactose channel at each injection of sample, in addition to peaks when methanol is injected.

The paracetamol channel shows no peaks relating to the injection of sample and instead appears to decrease in signal suggesting that the presence of FaSSIF dissolution media and / or the lactose, suppresses the ionisation of ions detected at *m*/*z* 152. A check of the full scan data confirms that alternative ions relating to paracetamol are not present either.

Figure 8.277, for a compact dissolving in SGF, shows a peak in signal for both the paracetamol and lactose channels for each sample injection, including methanol. The signal seen in response to methanol injection for both the FaSSIF and SGF runs confirms that dissolution sample containing lactose and paracetamol remains either in the tubing or more likely within the ionisation source.

The dissolution media differ in terms of pH and ingredients, with blank FaSSIF at pH 6.8 containing sodium dihydrogen phosphate (NaH_2PO_3) and sodium hydroxide (NaOH), and blank SGF at pH 4.5 containing sodium acetate trihydrate ($C_2H_9NaO_5$) and glacial acetic acid ($C_2H_4O_2$). The presence of FaSSIF may therefore be expected to result in sodium adducts and phosphate ions, however, the latter appear more commonly as negative mode (ES-) background ions, which may explain its ability to suppress *m*/*z* 152 ions.[234,336] The presence of acetic acid in SGF may also be expected to encourage sodium adducts, and being a weak acid, may act as a modifier thus supporting protonation of the analytes.[247,298] Chromatograms showing a comparison of the full scan total ion current (TIC) for each dissolution media are provided in Figure 8.278.

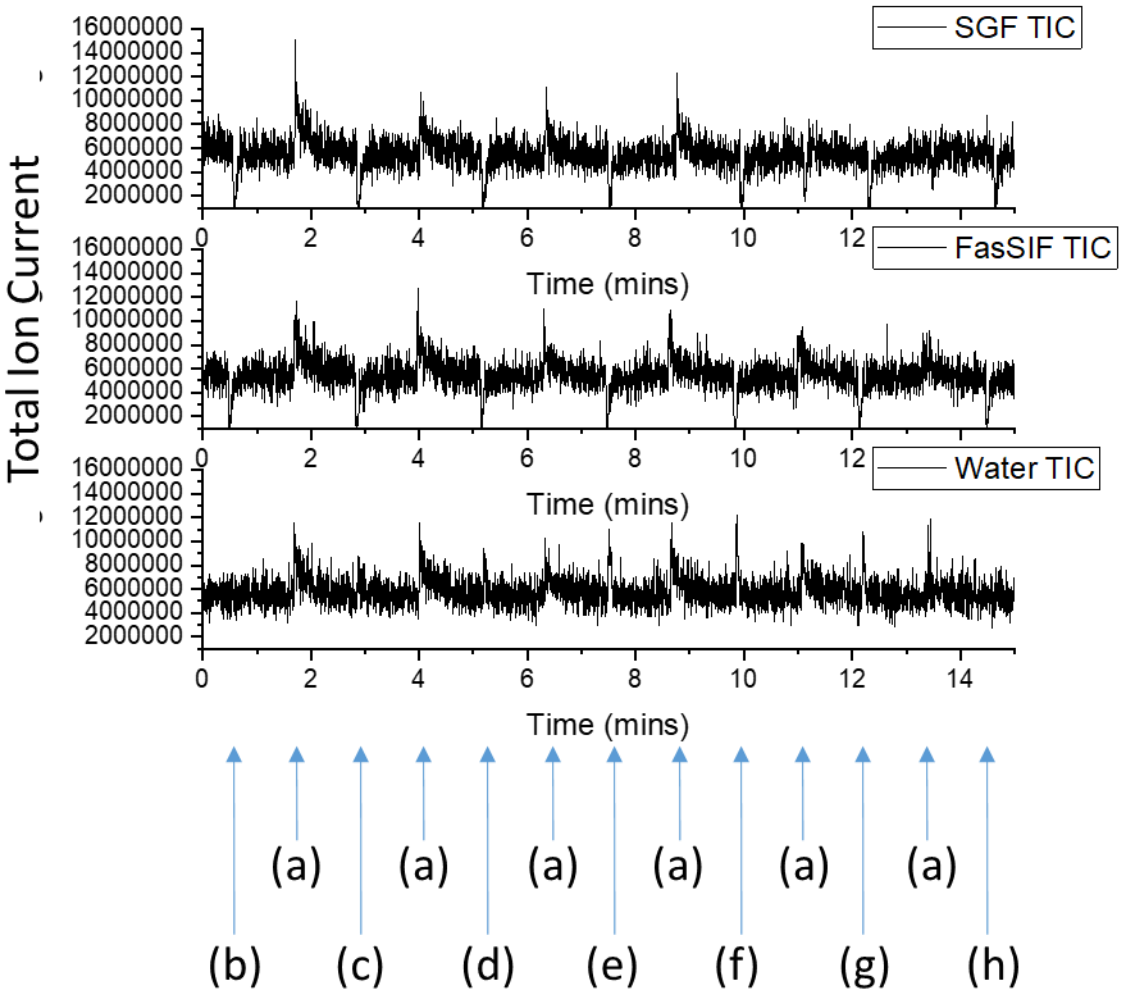

Figure 8.278 – QDa injection of paracetamol compact dissolution samples into a continuous stream of water and acetonitrile (50:50 v/v) with formic acid (0.1% v/v). Each chromatogram shows the total ion current from a scan of the full *m/z* range for the different dissolution media with SGF at the top, FaSSIF in the middle and water at the bottom. The blue arrows labelled (a) show signal resulting from the injection of methanol for cleaning, and those labelled (b) to (g) are the signal resulting from the injection of samples taken from varying stages of the dissolution process (0.5, 1, 2, 3, 5 and 30 minutes) and (h) shows injection of blank FaSSIF and blank SGF.

Figure 8.278 highlights that the injection of both FaSSIF and SGF reduces the full scan TIC, thereby confirming that their presence within the sample reduces ionisation efficiency and causes suppression in positive mode (ES+). The presence of water in the ionising sample, however, does not result in suppression of the overall signal, nor is there sample remaining in the tubing or ionisation source (shown by the stability of the lactose and paracetamol signal when methanol is injected between dissolution samples). It does, however, show that an injection of methanol results in an increase

in TIC for all three dissolution media, including water, in line with its superior ionisation efficiency, which is likely a result of its reduced surface tension.[337]

This work highlights a significant difference between the dissolution media, specifically between water and each simulated media (blank FaSSIF and blank SGF) and confirms that the matrix from which the samples are ionised can have a large impact on ionisation and quantification.[338] The benefit of using samples where the concentration of each component is known is once again shown to be relevant to reaping maximal understanding from the data; signal for each component in the different dissolution media cannot be compared due to the differing amount of paracetamol dissolved in each sample - logistical challenges meant that UV analysis was unable to be carried out on the FaSSIF and SGF samples.

8.3.1.3 Dissolution media impact upon furosemide compact dissolution

Furosemide compacts comprising of API and lactose were produced using the Gamlen benchtop press. A direct compression grade of lactose (FlowLac®) was selected to aid the compaction process as furosemide proved to be more challenging to formulate than paracetamol due to its cohesive nature. Simple 100 mg compacts containing 20 mg furosemide were produced for dissolution monitoring using off-line UV and MS analysis. Dissolution in deionised water, blank FaSSIF and blank SGF was carried out using the Sotax apparatus and samples were taken manually throughout. When compared with paracetamol, the furosemide compacts took longer to dissolve and there were still remains at the bottom of the vessel after 24 hours for both the water and the SGF runs, which can be explained by the pH-dependent solubility of furosemide.[311,312]

The samples were filtered and analysed by three methods: i) conventional UV analysis, ii) LI-MS on both the Synapt and the QDa and iii) LCMS using the Synapt. The MS samples were analysed using a solvent mixture of water and acetonitrile 50:50 v/v with 0.1% v/v formic acid. The samples run on the Synapt were analysed in positive mode and then in negative mode to enable both lactose (ES+ *m*/*z* 365) and furosemide (ES- *m*/*z* 285 and *m*/*z* 329) to be monitored, respectively, whereas the QDa SIM method was designed to include both ES+ and ES- at once, as well as both furosemide ions in

one channel. Calibration plots were attempted for each method, mode and dissolution media using known concentrations of furosemide dissolved in each media. At this stage it was deemed sufficient to quantify only furosemide using the MS techniques, particularly as UV analysis would allow a comparison of concentrations to be drawn. Lactose signal would not be quantified but would be observed to ensure that it ionised as expected and its signal could be extracted.

Figure 8.279 shows the dissolution profiles of a furosemide compact dissolving in water obtained through the LC and LI methods with the Synapt. Each is compared with the UV technique and the data has been extracted separately for each ion, *m/z* 285 and 329. A calibration plot was produced for each and the lines of best fit used to calculate concentration from signal. The profiles are shown between the start of dissolution and 90 mins in, and show a greater degree of variation within the LC data than the LI or UV. The final two time points are shown in Figure 8.280 to highlight the differences between methods. The UV data states a final amount of furosemide in solution of 20.0 mg after more than 24 hours, compared with calculated values of 17.9 mg for LI (both ions), 18.7 mg for LC using m/z 285 and 18.6 mg using m/z 329. The LC values remain lower than the UV data, and the LI values are lower still. The difference between LC and LI values suggests that the presence of lactose is suppressing ionisation of furosemide. The UV data suggests that the visual observation of white solid remaining after 24 hours dissolution in the water bath is likely a result of the lactose and not the furosemide.

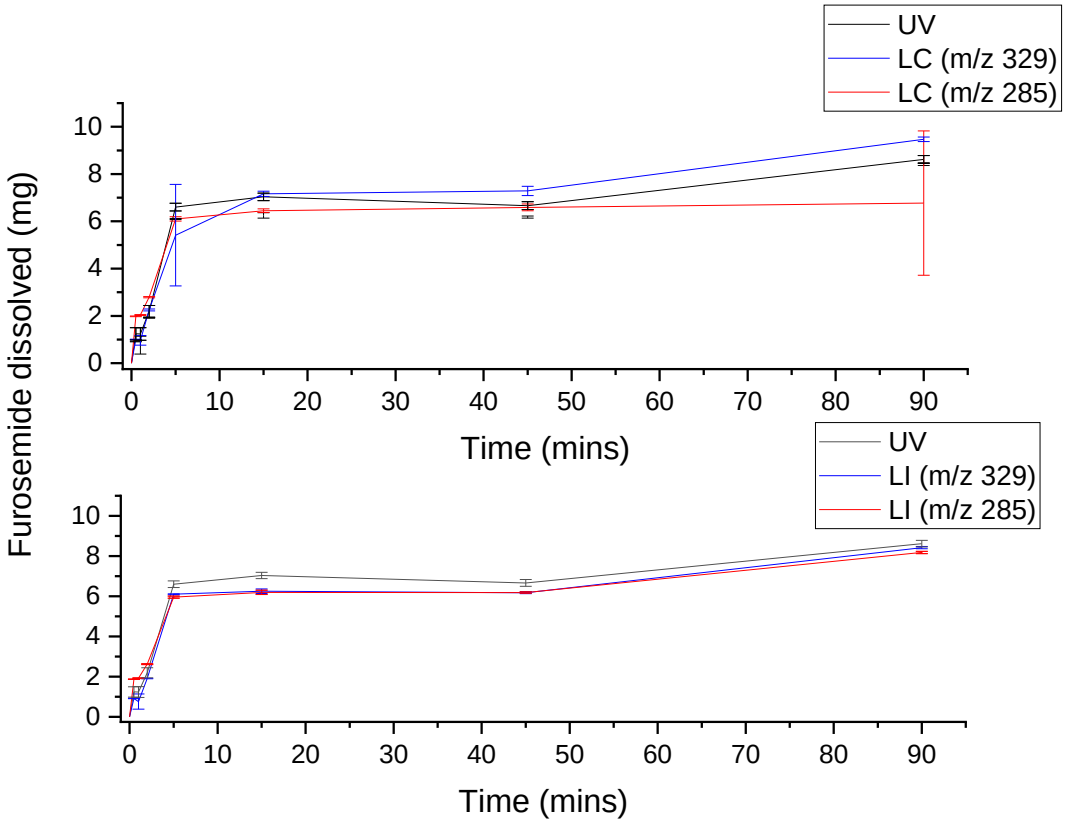

Figure 8.279 – Comparison of dissolution profiles for a furosemide compact dissolving in water. The profiles were obtained using three methods: UV, LCMS (Synapt) and LI-MS (Synapt). The top plot shows UV and LC-MS, and the bottom plot shows UV and LI MS. Each point is the average of three runs with the standard deviation shown using error bars. The data has been split across two graphs to show the difference between methods. Note also that each MS method is further split into each of the two ions found for furosemide, *m/z* 285 and *m/z* 329.

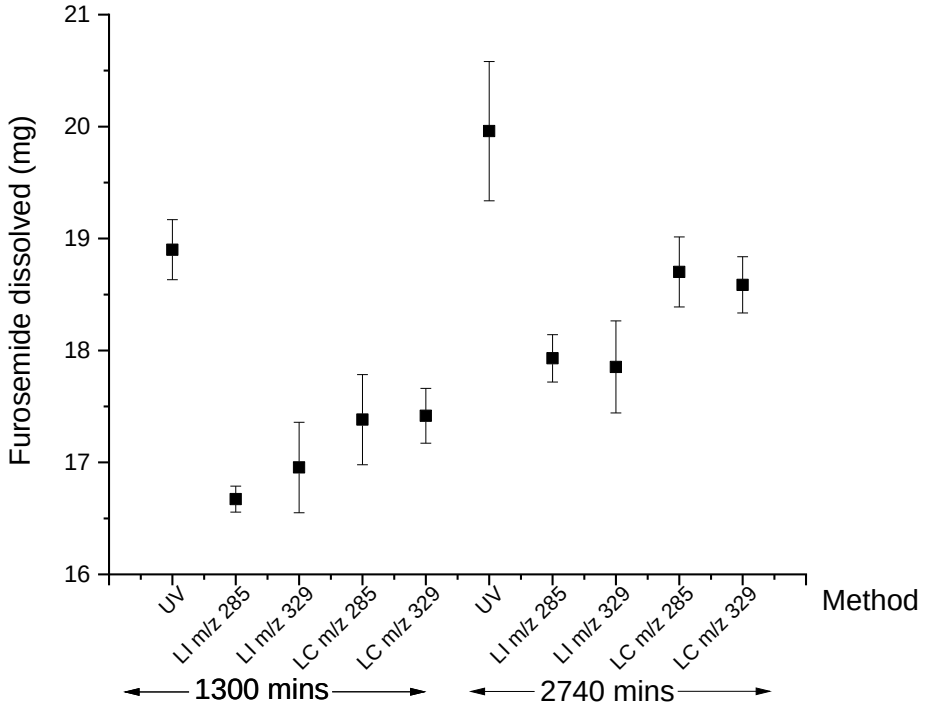

Figure 8.280 – Furosemide compact in water dissolution comparing the three methods for calculating the quantity of furosemide dissolved at the final time points. The time points are 1300 minutes and 2740 minutes. The methods are UV, LI-MS and LCMS, noting again that both MS methods calculate furosemide concentration using two ions, *m/z* 285 and *m/z* 329.

Further exploration of the Synapt data to observe the lactose ionisation, determined that both LC and LI analysis of the dissolution data failed to find these ions in ES+ at the previously determined *m/z* 365. The analyses were carried out in both positive and negative modes, however, only the LCMS chromatogram obtained in the negative mode showed any clear analytes aside from furosemide. An analyte of *m/z* 377 was found at a retention time (RT) of 0.64 mins, which correlates with the elution time for lactose when analysing the Beechams® tablet (see Table 8.32). It can be found at this RT throughout the negative LCMS analyses and is also detectable in the negative LI-MS data. This may relate to the lactose brand (FlowLac®) that was used as it can also be found in the LC data, suggestive of it not being a result of the concurrent ionisation of lactose and furosemide.

Analysis of the samples using the QDa proved to be more of a challenge due to the reduced sensitivity of this instrument. The early time points contained concentrations of furosemide that were too low for quantification purposes, so the calculation of concentration begins five minutes into the compact's dissolution. In contrast, the later

time points also contained concentrations that coincided with a calibration plot plateau. These should be diluted and re-analysed but due to the delay between running samples and analysing the data, this was not possible, instead it highlights the potential benefit of being able to adjust dilution through use of an MRA, which will be explored in the 8.3.2 Continuous flow MS analysis section.

The calibration plot has been provided first, see Figure 8.281, with the line of best fit included, although it can be seen to extend above the second to last point despite masking the final point due to the plateau of the signal. There is potential for a polynomial equation to be fitted to incorporate the plateau but this makes little difference to the calculated concentrations. It should also be noted that the calibration plot for furosemide in the previous chapter (Figure 7.229) was linear to 100 µg/mL when dissolved in water and acetonitrile 50:50 v/v with formic acid 0.1% v/v. This highlights again the impact of changing solvents from those that are easily ionised to those that are less so. In this plot furosemide is dissolved in water and injected into a stream of the same solvents so while there may be some mixing, the solution being ionised clearly has a different ionisation efficiency.

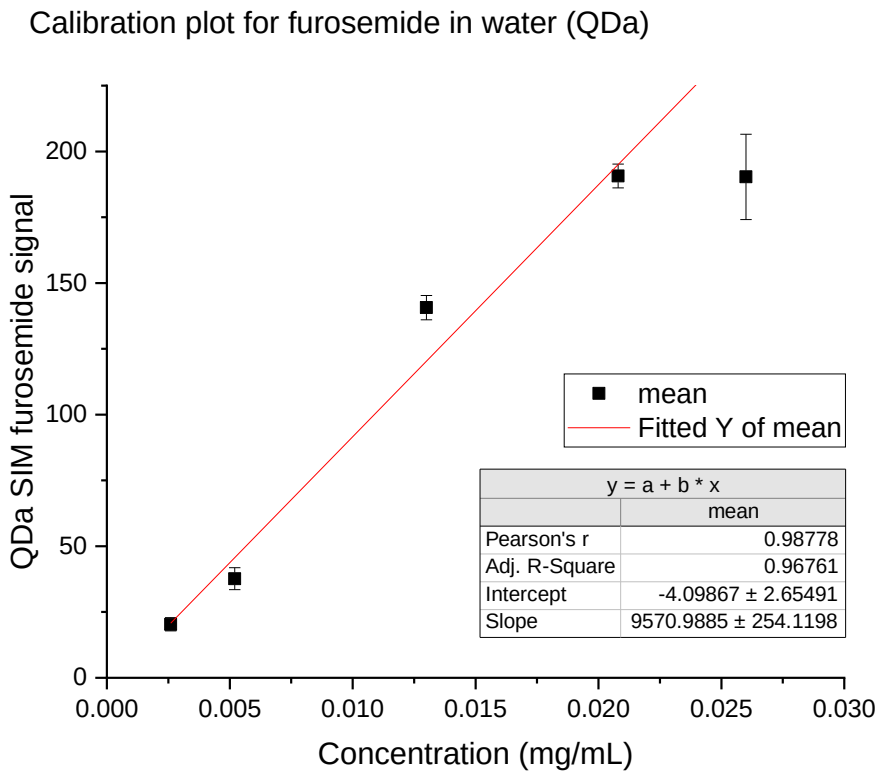

Figure 8.281 - QDa calibration plot for furosemide dissolved in water, with a red line of best fit. Each point is the average of three runs and standard deviation has been plotted using error bars.

Figure 8.282 provides the dissolution profiles of a furosemide compact dissolving in water using the UV technique, and using LI MS (with the QDa); the MS data has been extracted for each ion, m/z 285 and 329, using one SIM channel. The dissolution profile obtained using the QDa data suggests a higher dissolved concentration than the UV data, which may suggest ionisation enhancement. The same samples were analysed first using the Synapt (Figure 8.280) and then the QDa, hence there was an additional time delay from obtaining the UV data, which may explain why the QDa data suggests a greater amount of dissolved furosemide than the Synapt data. These findings confirm once more that development of on-line analysis will reduce this delay between sampling and analysing, and that starting with defined concentrations of sample rather than analysing unknown samples, will enable a greater confidence in the interpretation of complex results.

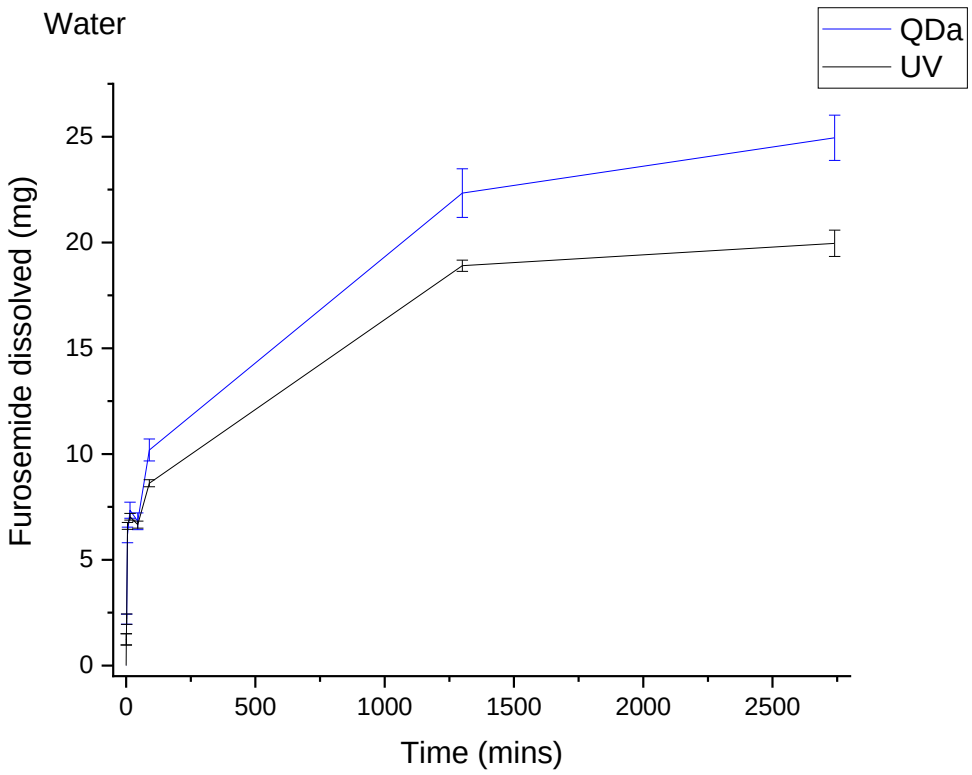

Figure 8.282 – Comparison of dissolution profiles for a furosemide compact dissolving in water. The profiles were obtained using UV analysis and LI-MS (QDa). Each point is the average of three runs with the standard deviation shown using error bars.

Analysis of the QDa dissolution samples also found lactose to be present at *m*/*z* 365 as expected throughout dissolution, with the signal increasing as dissolution progressed up to 90 minutes, when it starts to slowly reduce, see Figure 8.283. The additional ion at *m*/*z* 377 was also found but only after 1300 mins of dissolution. The reduction in signal at *m*/*z* 365 correlates with the appearance of the additional ion at *m*/*z* 377, which could suggest they are related. It was not explored further at this stage but will be considered for future experiments including lactose to determine whether it could be due to lactose brand used and whether it suggests degradation of the lactose is occurring with the degraded product forming an alternative adduct.

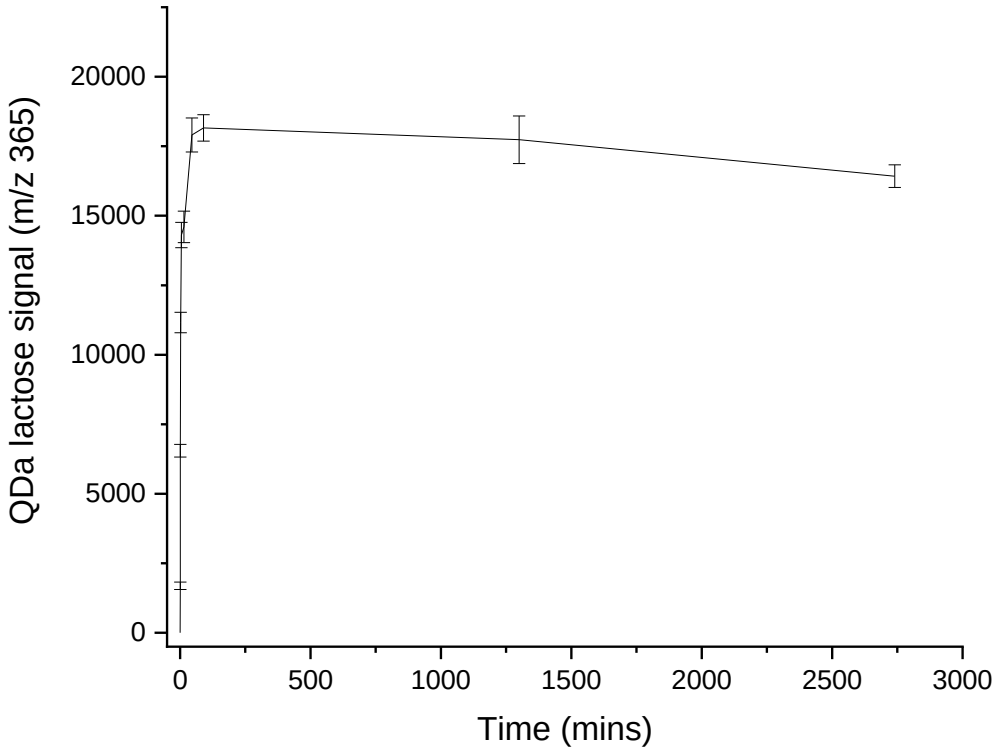

Figure 8.283 - QDa lactose signal throughout dissolution of a furosemide compact in water. The lactose signal was obtained through SIM channel *m/z* 365. Each point is the average of three runs with the standard deviation shown as error bars.

The samples of furosemide at known concentrations in blank FaSSIF and blank SGF were assessed using the Synapt in both ES+ and ES- LI-MS. The expected furosemide ions of *m/z* 285 and *m/z* 329 were not found and no clear alternative ions were found in place of them, for either mode. To confirm the presence of furosemide in solution for each of these dissolution media, UV and LCMS analysis was carried out. The UV data can be found in Figure 8.284 and confirms the presence of furosemide in solution for both media. It also correlates with the pH-dependent solubility of furosemide. Rapid and complete dissolution of furosemide can be seen to occur in FaSSIF media (pH 6.8) but it shows poor solubility in the SGF media (pH 1.2), which confirms the visual observations of compact remaining after more than 24 hours in the SGF dissolution bath. The LCMS data also confirmed that separating furosemide from the dissolution media prior to ionisation (with retention times of 4.32 and 0.64 mins for furosemide and the dissolution media, respectively) was successful in enabling ionisation of furosemide. This confirms that for the Synapt, furosemide ionisation is suppressed by blank FaSSIF and blank SGF.

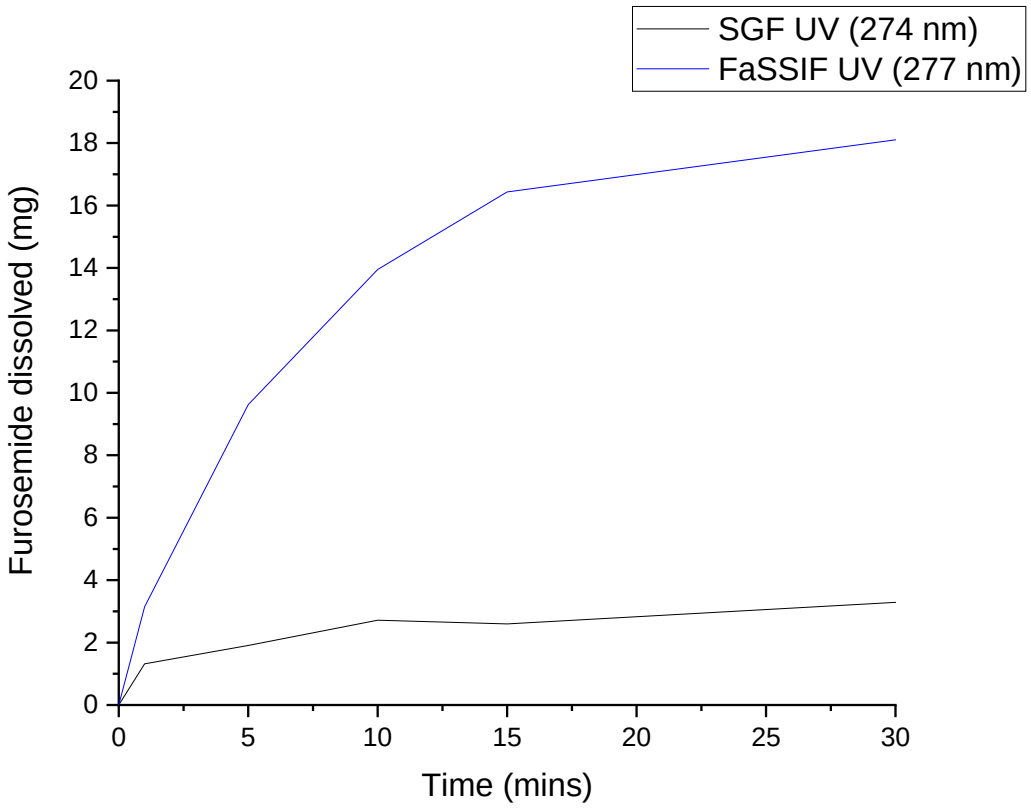

Figure 8.284 – Dissolution profiles of a furosemide compact dissolving in blank FaSSIF (black line) and blank SGF (blue line), obtained through UV analysis at wavelengths of 277 and 274 nm respectively.

The samples were additionally analysed with the QDa to understand whether different instruments resulted in different ionisation phenomena. A 1 µL aliquot of each was injected into a continuous stream of water and acetonitrile 50:50 v/v with 0.1% v/v formic acid, which was continuously analysed by the QDa at 0.5 mL/min. After each sample, an aliquot of methanol was injected into the stream to clean the lines and the ionisation source; as previously described this was a precautionary measure taken to avoid build-up of the dissolution media. The initial method followed a full scan TIC (ES+), furosemide (*m/z* 285 and 329 in ES-) and lactose (*m/z* 365 in ES+). The chromatograms showing furosemide and TIC (ES+) signal as a result of the injection of (a) methanol and (b) each known concentration sample, are provided in Figure 8.285 and Figure 8.286. The QDa SIM signal for each sample in each media is very poor and insufficient for quantitative purposes. In the case of the SGF samples there is a peak at 4.5 mins, which correlates with the injection of methanol and suggests that furosemide present either in the source or the fluidics was able to be ionised in this instance. There were no additional ions present in the TIC for either media that could

correlate to the presence of furosemide, although previous work had shown that furosemide in MS solvents ionised most effectively in the negative mode of ESI-MS.

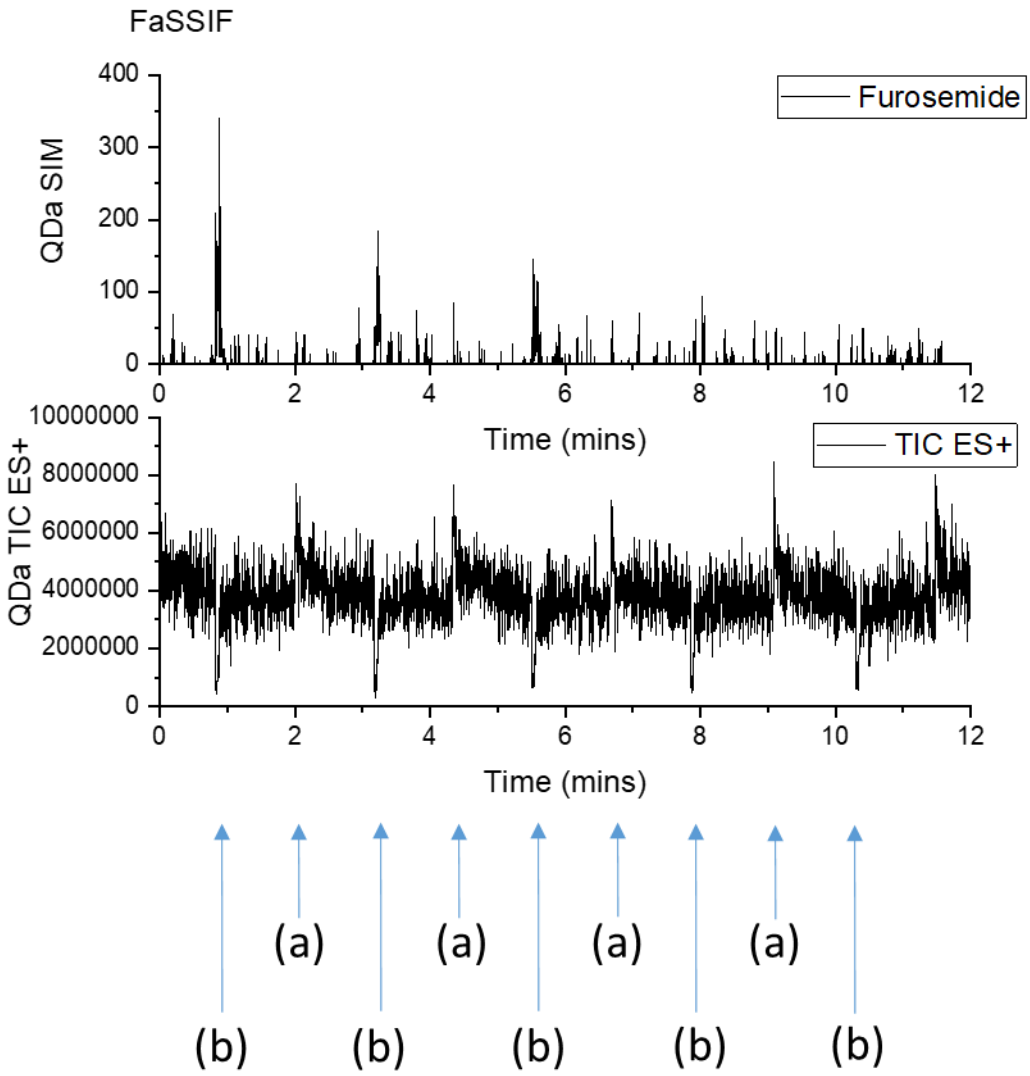

Figure 8.285 – QDa injection of furosemide FaSSIF samples into a continuous stream of water and acetonitrile (50:50 v/v) with formic acid (0.1% v/v). The top chromatogram shows negative (ES-) SIM for furosemide (channel includes both m/z 285 and 329) and the bottom chromatogram shows the positive (ES+) TIC. The peaks and troughs highlighted by the blue arrows labelled (a) are a result of the injection of methanol for cleaning, and those labelled (b) are the result of the injection of sample containing known concentrations of furosemide ranging from (0.026 mg/mL at the earliest time point to 0.0026 mg/mL at the latest).

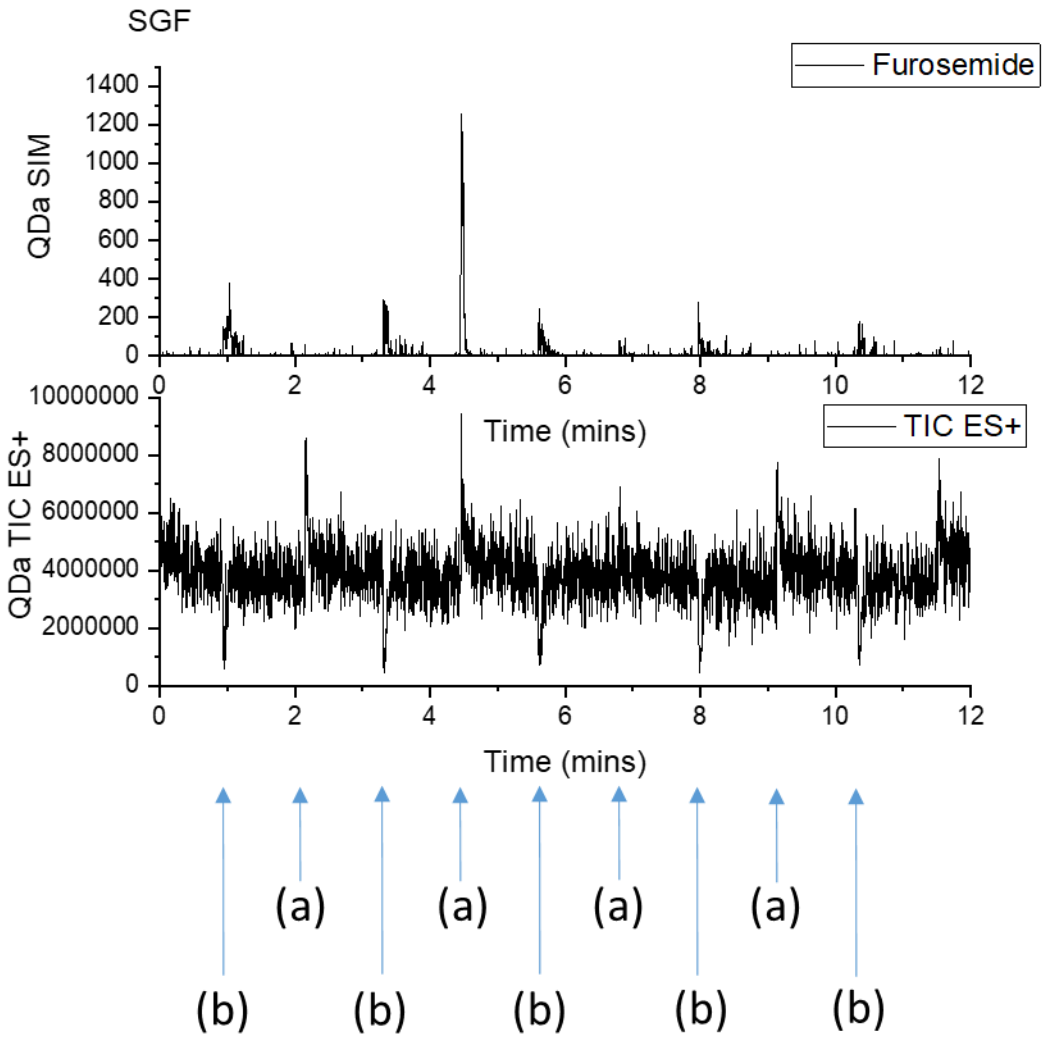

Figure 8.286 – QDa injection of furosemide SGF samples into a continuous stream of water and acetonitrile (50:50 v/v) with formic acid (0.1% v/v). The top chromatogram shows negative (ES-) SIM for furosemide (channel includes both m/z 285 and 329) and the bottom chromatogram shows the positive (ES+) TIC. The peaks and troughs highlighted by the blue arrows labelled with (a) are a result of the injection of methanol for cleaning, and those highlighted (b) are the result of the injection of sample containing known concentrations of furosemide ranging from (0.026 mg/mL at the earliest time point to 0.0026 mg/mL at the latest).

Analysis of the same samples was carried out using an altered SIM method following TIC ES- instead of ES+, in addition to the furosemide and lactose ions to allow further exploration of the signal. Figure 8.287 and Figure 8.288 show analysis of the same samples, though they were injected from low to high concentration in this experiment. The furosemide signal is still poor in both cases but they are comparable with Figure 8.285 and Figure 8.286, suggesting it is not linked to the method and confirms it is likely due to ion suppression. The additional TIC (ES-) chromatogram was explored for

each media in case a new dominant ion was presenting as a result of the FaSSIF or SGF instead of either *m*/*z* 285 or 329; this was not the case, confirming that the ionisation of furosemide has been suppressed in both instances, consistent with the Synapt findings.

The calibration plots could not be produced to enable quantification of furosemide, however, the dissolution samples were run on the QDa for completeness. Figure 8.289 and Figure 8.290 show each chromatogram highlighting with arrows the ionisation of methanol (a) and samples (b), running from the start of dissolution to the end. The furosemide signal in both cases is consistent with the previous analyses, although it does appear to increase slightly as dissolution progresses in the case of SGF, but not as clearly or significantly as the lactose signal.

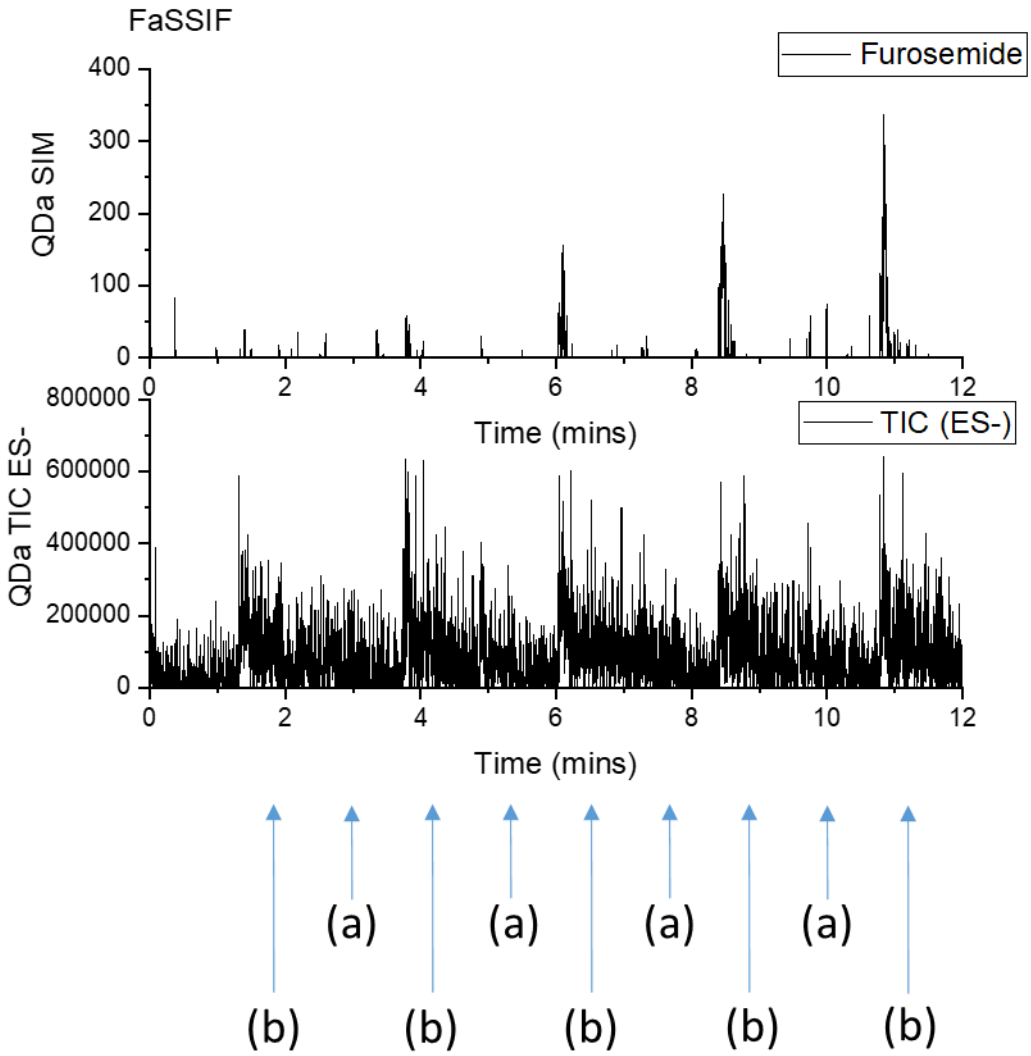

Figure 8.287 – QDa injection of furosemide FaSSIF samples into a continuous stream of water and acetonitrile (50:50 v/v) with formic acid (0.1% v/v). The top chromatogram shows negative (ES-) SIM for furosemide (channel includes both m/z 285 and 329) and the bottom chromatogram shows the negative (ES-) TIC. The peaks highlighted by the blue arrows labelled (a) are a result of the injection of methanol for cleaning, and those labelled (b) are the result of the injection of sample containing known concentrations of furosemide ranging from (0.0026 mg/mL at the earliest time point to 0.026 mg/mL at the latest).

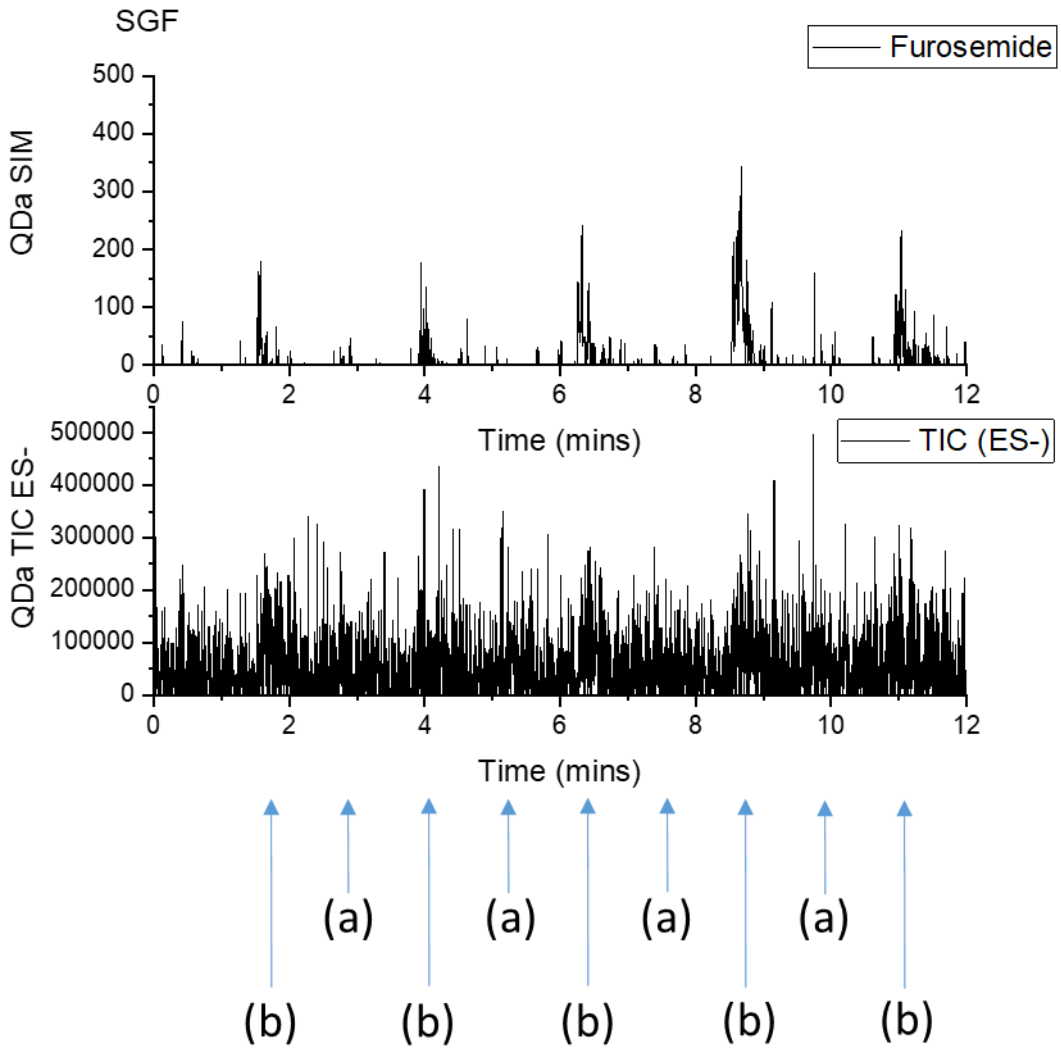

Figure 8.288 – QDa injection of furosemide SGF samples into a continuous stream of water and acetonitrile (50:50 v/v) with formic acid (0.1% v/v). The top chromatogram shows negative (ES-) SIM for furosemide (channel includes both m/z 285 and 329) and the bottom chromatogram shows the negative (ES-) TIC. The peaks highlighted by the blue arrows labelled with (a) are a result of the injection of methanol for cleaning, and those highlighted (b) are the result of the injection of sample containing known concentrations of furosemide ranging from (0.0026 mg/mL at the earliest time point to 0.026 mg/mL at the latest).

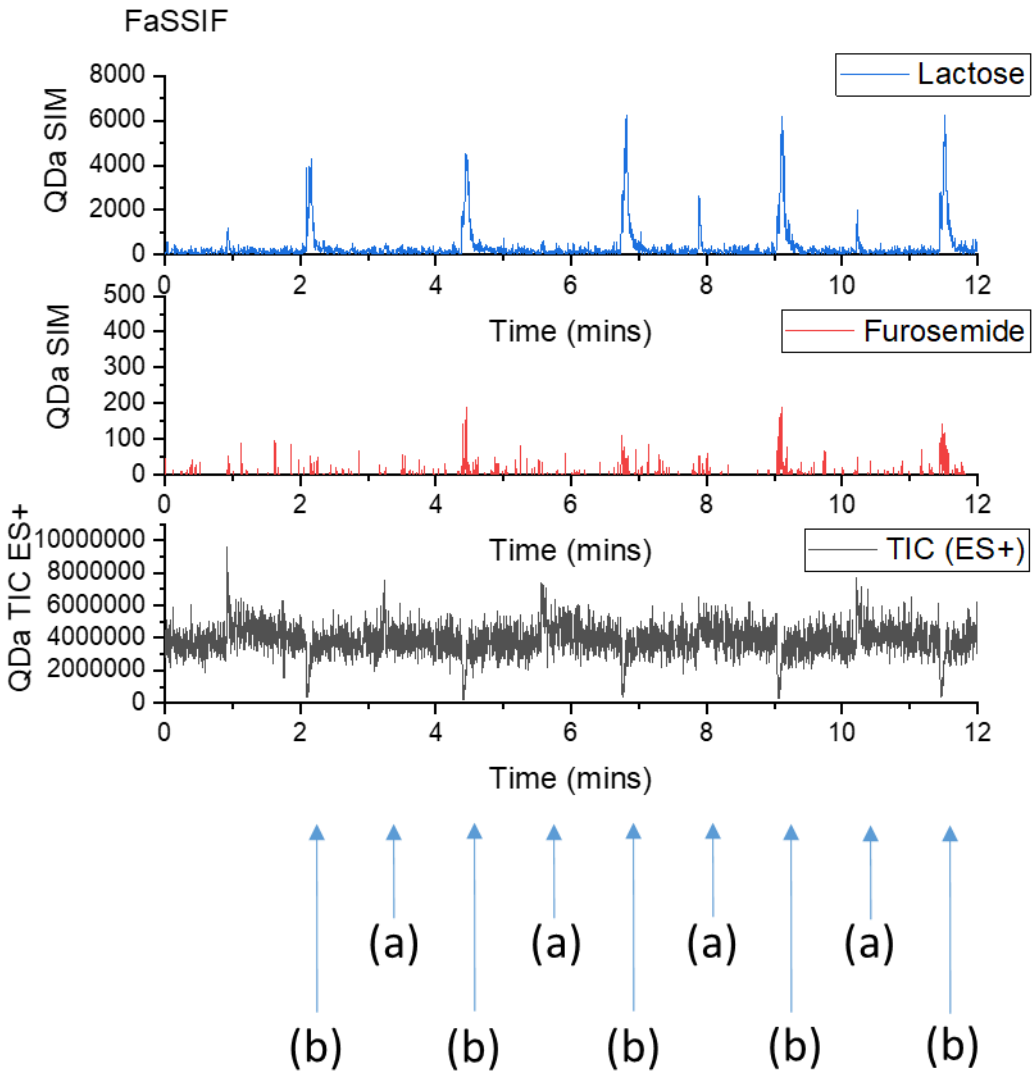

Figure 8.289 – QDa injection of furosemide compact FaSSIF dissolution samples into a continuous stream of water and acetonitrile (50:50 v/v) with formic acid (0.1% v/v). The top blue chromatogram shows the lactose channel (*m/z* 365 in ES+), the middle red chromatogram shows the furosemide channel (*m/z* of 285 and 329 in ES-) and the bottom black chromatogram shows the total ion current (ES+). The peaks and troughs highlighted by the blue arrows labelled with (a) are a result of the injection of methanol for cleaning, and peaks highlighted (b) are the result of the injection of samples taken from varying stages of the dissolution process.

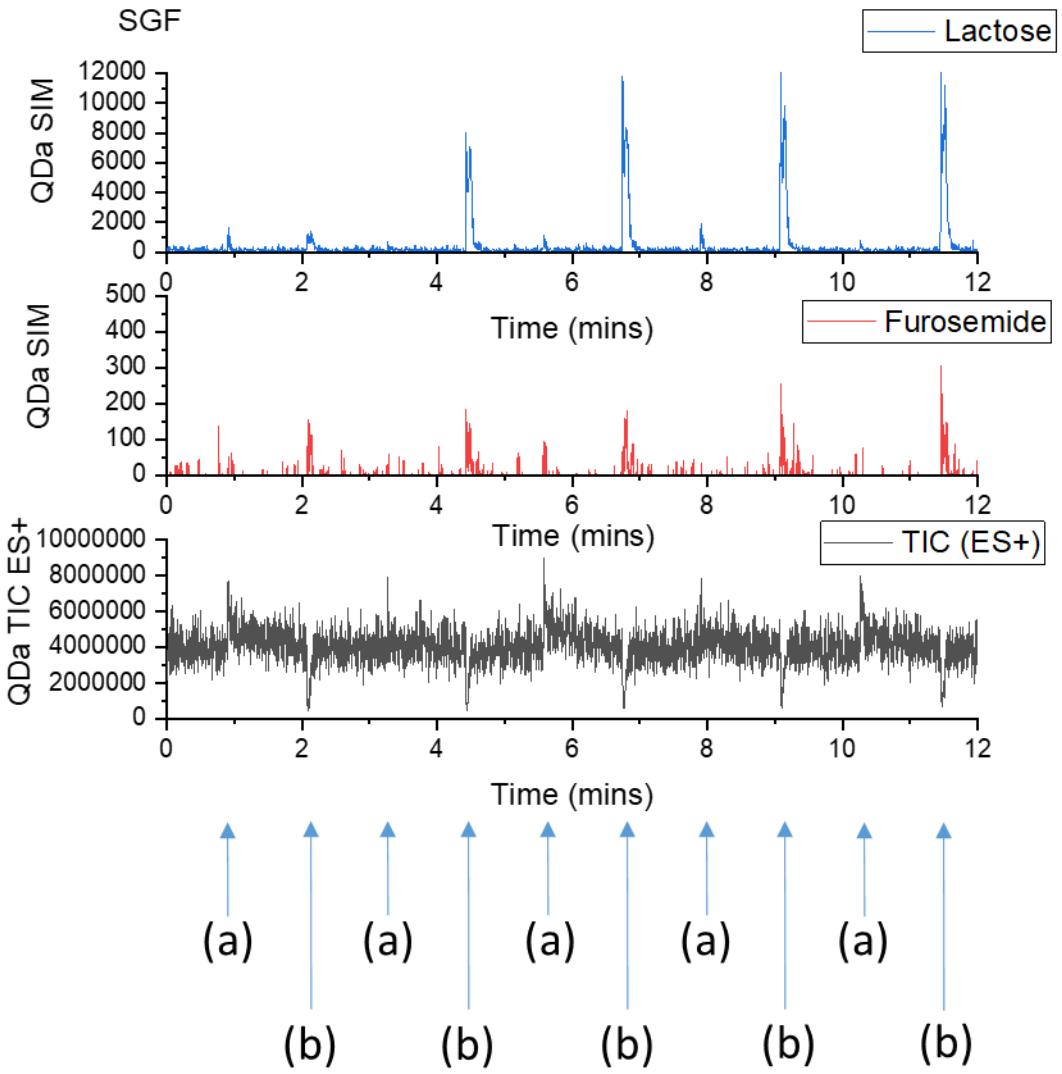

Figure 8.290 – QDa injection of furosemide compact SGF dissolution samples into a continuous stream of water and acetonitrile (50:50 v/v) with formic acid (0.1% v/v). The top blue chromatogram shows the lactose channel (*m/z* 365 in ES+), the middle red chromatogram shows the furosemide channel (*m/z* of 285 and 329 in ES-) and the bottom black chromatogram shows the total ion current (ES+). The peaks and troughs highlighted by the blue arrows labelled with (a) are a result of the injection of methanol for cleaning, and peaks highlighted (b) are the result of the injection of samples taken from varying stages of the dissolution process.

In addition to furosemide ionisation being suppressed by both FaSSIF and SGF, it may be affected by the presence of lactose, but further experimental work is required to confirm this. This section of work confirms the need to simplify experiments yet further and look at ionisation relationships for each component of a formulation prior to using more complex dissolution media. It highlights that dissolution media may affect different components to differing extents, ionisation relationships are different

on differing instruments, and it confirms that analysis using both ES+ and ES- may be necessary to gain full understanding.

8.3.1.4 API plus excipient ionisation relationships

This section looks at the impact upon ionisation phenomena of a changing but known amount of lactose or mannitol (excipient) upon a consistent concentration of either paracetamol, furosemide or haloperidol (API). Each component was dissolved in a solution of water and acetonitrile (50:50 v/v) with formic acid (0.1% v/v). Solutions containing either one API, one excipient, or one API plus one excipient, were then analysed by LI using the QDa and Synapt, and also by LC using the Synapt. Loop injection analyses will show the impact of ionisation phenomena upon both the API and the excipient, and the LC analyses have been carried out as confirmation that both components are present in solution and can be ionised individually after separation.

A 1 µL aliquot of each sample was injected into flowing solvent prior to analysis by each instrument and then injected directly into the instrument (loop injection) or through the HPLC column with a five minute reverse phase gradient method applied. Paracetamol, haloperidol and lactose are both monitored via ions present in positive mode ESI-MS (ES+), furosemide is monitored in negative mode ESI-MS (ES-), and mannitol was previously monitored in both modes. Mannitol was found to ionise in both modes on the Synapt but only at higher concentrations through ES+ on the QDa, hence it will be monitored primarily in ES- on the QDa, but the ES+ data will be explored for evidence of $[M+Na]^+$ at *m*/*z* 205. The QDa SIM methods are listed in Table 8.34 and highlight that in some circumstances both modes were used to enable both components to be monitored.

Table 8.34 – QDa SIM methods for each combination of components.

	API SIM		Excipient SIM	
Components	**Mode**	***m/z***	**Mode**	***m/z***
Paracetamol + lactose	ES+	152	ES+	365
Paracetamol + mannitol	ES+	152	ES-	181
Furosemide + lactose	ES-	285 & 329	ES+	365
Furosemide + mannitol	ES-	285 & 329	ES-	181
Haloperidol + lactose	ES+	376	ES+	365
Haloperidol + mannitol	ES+	376	ES-	181

The QDa data will be presented for each combination first, before the Synapt LI data is then discussed, and finally the LC data is outlined. It should be noted that only data plotted on the same graph will have been obtained during the same runs on the same day and may therefore be discussed quantitatively (peak areas are comparable). The peak area values between graphs are not comparable because they were obtained over a longer period of time and this delay can result in differences in the sensitivity of each instrument, in particular the Synapt due to the range of samples tested on this instrument for other projects.

QDa (Loop Injection)

The QDa peak area obtained for a paracetamol concentration of 20 µg/mL is plotted as the red circles in Figure 8.291 with a changing concentration of lactose present in the solution (and therefore ionised concurrently) which varied from 0 to 100 µg/mL. The expected paracetamol signal based upon the concentration present is shown by the dashed red line. Two additional black dashed lines have been plotted for comparison and highlight the signal observed when a paracetamol sample at half (10 µg/mL) and double (40 µg/mL) the concentration are ionised without lactose present in solution. These additional samples were run at the same time to provide consistent comparisons for the signal.

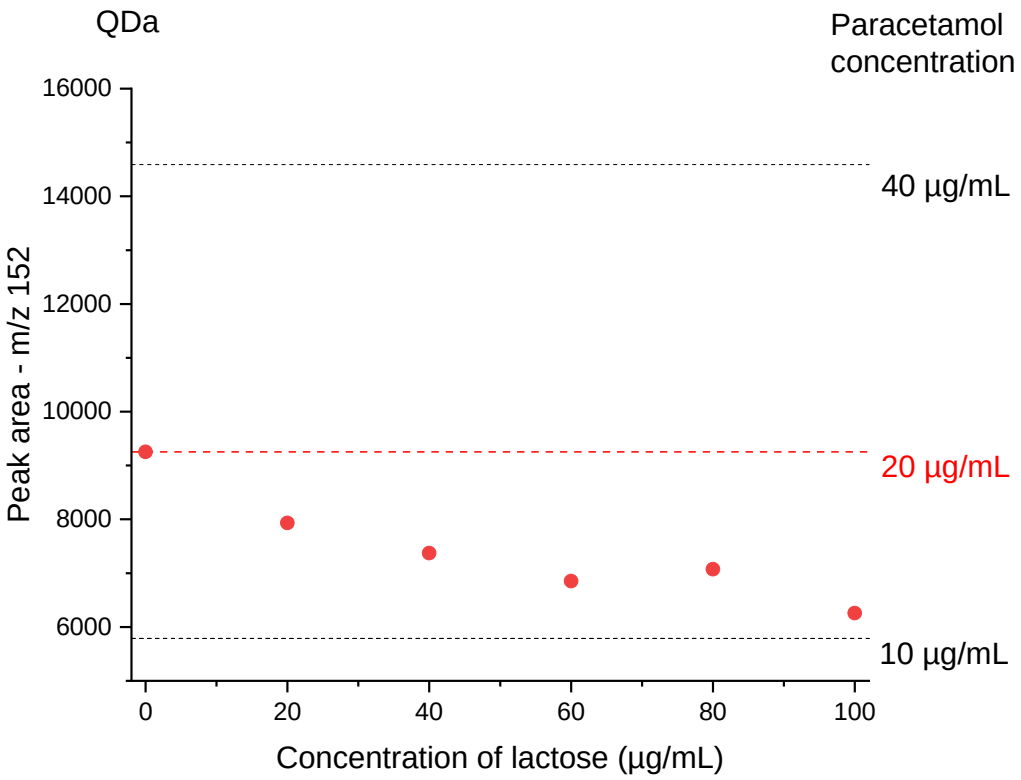

Figure 8.291 – QDa data showing the effect of increasing the concentration of lactose upon the peak area value (signal) obtained for paracetamol following a SIM channel of m/z 152. The concentration of paracetamol was kept constant at 20 µg/mL. Comparative signals obtained for paracetamol concentrations without lactose present are shown by the dashed lines, with a red line showing the concentration of 20 µg/mL, which is the same as that found in the solutions mixed with lactose, and two black lines showing 10 µg/mL and 40 µg/mL for comparison.

The presence of lactose in the solution can be seen to reduce the peak area observed for paracetamol, providing clear indication that it suppresses paracetamol ionisation, with an increasing amount of suppression at increased concentrations of lactose. The paracetamol signal is reduced to almost that of half the concentration when co-ionised with 100 µg/mL of lactose.

Figure 8.292 shows the data repeated but for a changing mannitol concentration. The presence of mannitol can be seen to reduce peak area, therefore suppressing ionisation of paracetamol, although the impact of 100 µg/mL of mannitol is less than 100 µg/mL of lactose; the suppressed peak area is still consistent with the peak area obtained for a concentration of 20 µg/mL of paracetamol.

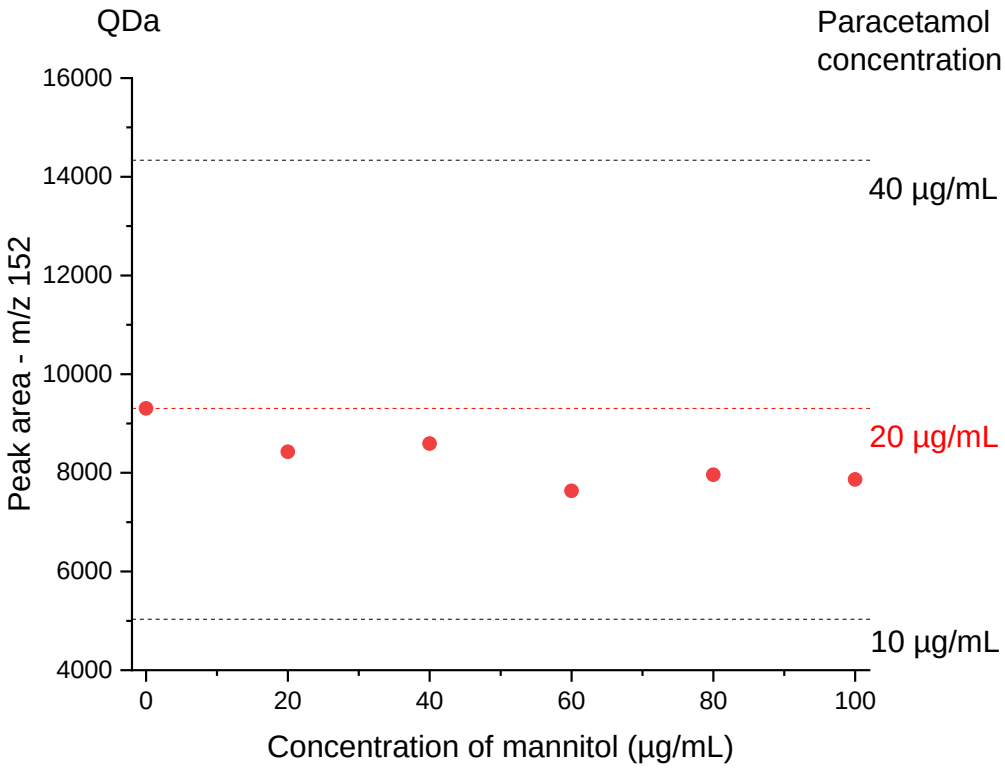

Figure 8.292 – QDa data showing the effect of increasing the concentration of mannitol upon the peak area value (signal) obtained for paracetamol following an ESI+ SIM channel of m/z 152. The concentration of paracetamol was kept constant at 20 µg/mL. Comparative signals obtained for paracetamol concentrations without mannitol present are shown by the dashed lines, with a red line showing the concentration of 20 µg/mL, which is the same as that found in the solutions mixed with mannitol, and two black lines showing 10 µg/mL and 40 µg/mL for comparison.

The impact of each excipient upon furosemide signal observed through the QDa peak areas can be seen in Figure 8.293 and Figure 8.294. The presence of lactose can be seen to increase the furosemide peak area, with an increasing amount of enhancement at increased concentrations of lactose. The furosemide peak area is more than doubled to more than the signal expected from double the concentration when co-ionised with 100 µg/mL of lactose. The furosemide signal also doubles in the presence of 100 µg/mL mannitol resulting in a signal consistent with that of a furosemide concentration containing double the amount actually present in the solution. Figure 8.294 suggests a linear relationship between mannitol concentration and furosemide enhancement. Both lactose and mannitol therefore enhance ionisation of furosemide. A quick comparison of these data sets confirms the prior warning that data obtained on different days should not be quantitatively compared, even for the same concentration of API ionised in isolation; the peak area observed for

20 µg/mL of furosemide is 165 in Figure 8.293 and 100 in Figure 8.294, and the peak area observed for 40 µg/mL of furosemide is 260 in Figure 8.293 and 200 in Figure 8.294. This highlights the importance of the red and black dashed lines obtained through analysing additional samples at the same time and therefore providing comparative values for peak area.

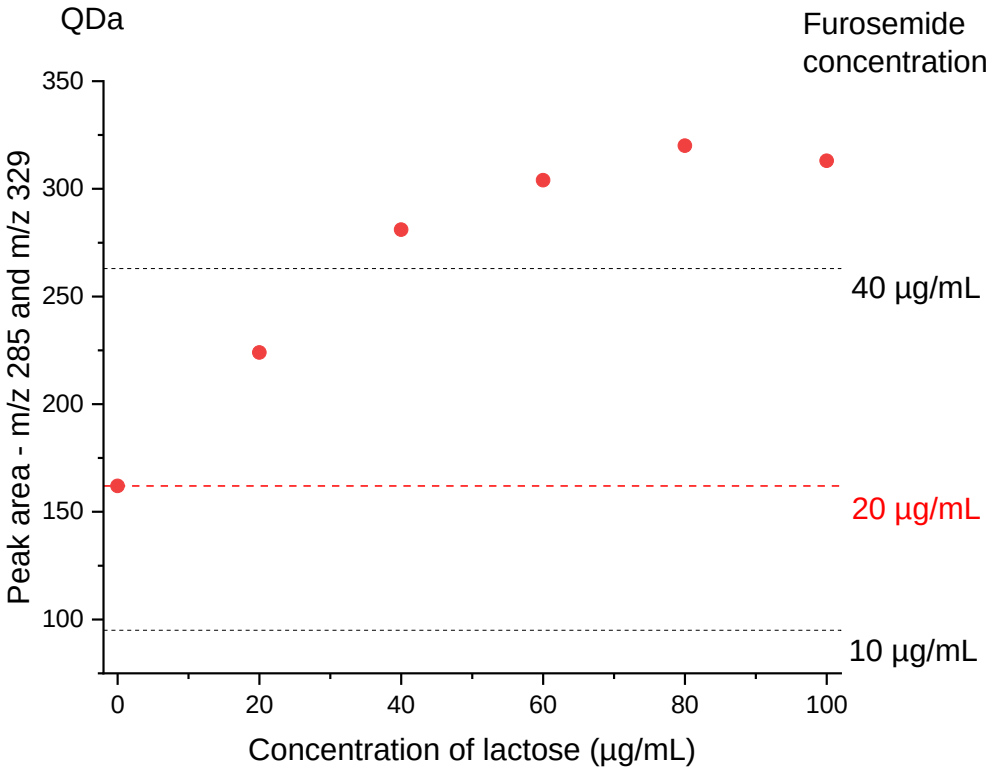

Figure 8.293 – QDa data showing the effect of increasing the concentration of lactose upon the peak area value (signal) obtained for furosemide following a SIM channel of m/z 285 and m/z 329. The concentration of furosemide was kept constant at 20 µg/mL. Comparative signals obtained for furosemide concentrations without lactose present are shown by the dashed lines, with a red line showing the concentration of 20 µg/mL, which is the same as that found in the solutions mixed with lactose, and two black lines showing 10 µg/mL and 40 µg/mL for comparison.

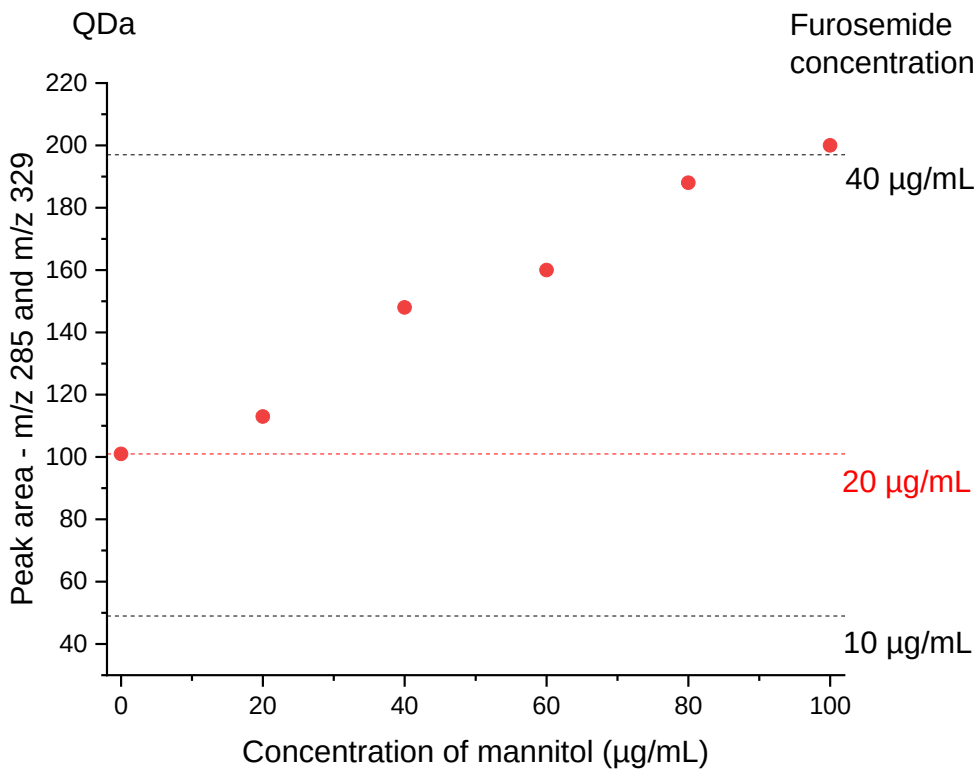

Figure 8.294 – QDa data showing the effect of increasing the concentration of mannitol upon the peak area value (signal) obtained for furosemide following an ES- SIM channel of m/z 285 and m/z 329. The concentration of furosemide was kept constant at 20 µg/mL. Comparative signals obtained for furosemide concentrations without mannitol present are shown by the dashed lines, with a red line showing the concentration of 20 µg/mL, which is the same as that found in the solutions mixed with mannitol, and two black lines showing 10 µg/mL and 40 µg/mL for comparison.

Haloperidol in combination with each excipient was analysed in triplicate to introduce an understanding of signal variation for samples run on the same day at the same time. Figure 8.295 shows haloperidol and lactose ionised concurrently using the QDa. The concentration of haloperidol has been maintained at 20 µg/mL as with the previous analyses of paracetamol and furosemide. Initial observations of the data suggest that lactose may enhance ionisation of haloperidol, however, the standard deviation error bar associated with the red dashed line shows that the difference in signal obtained for the samples containing both lactose and haloperidol is less than the variation observed when haloperidol was ionised in isolation. The error bars obtained for haloperidol ionised in isolation are far wider than those for haloperidol co-ionised with lactose, suggesting a possibility that there is a reduction in variability of haloperidol ionisation when ionised in combination with lactose.

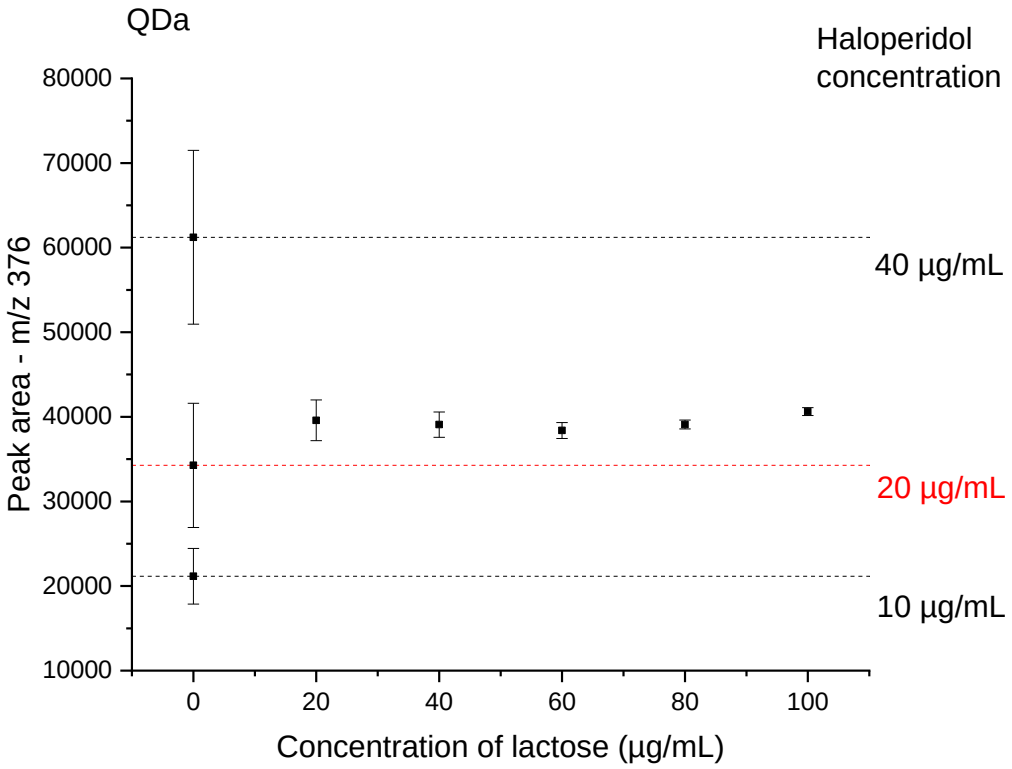

Figure 8.295 – QDa data showing the effect of increasing the concentration of lactose upon the peak area value (signal) obtained for haloperidol following an ES+ SIM channel of m/z 376. The concentration of haloperidol was kept constant at 20 µg/mL. Comparative signals obtained for haloperidol concentrations without lactose present are shown by the dashed lines, with a red line showing the concentration of 20 µg/mL, which is the same as that found in the solutions mixed with lactose, and two black lines showing 10 µg/mL and 40 µg/mL for comparison. Error bars showing standard deviation are included for each point, which are a result of each sample being run and analysed in triplicate.

Figure 8.296 shows haloperidol ionised in combination with differing amounts of mannitol. The variability of the isolated haloperidol signal is again greater than the variability observed when it is ionised in combination with mannitol. The presence of mannitol enhances the ionisation of haloperidol, with the greatest impact observed at a concentration of 40 µg/mL of mannitol. Concentrations greater than 40 µg/mL are also suggestive of ionisation enhancement, although the effect does not continue to increase with concentration as has been observed with the other molecules.

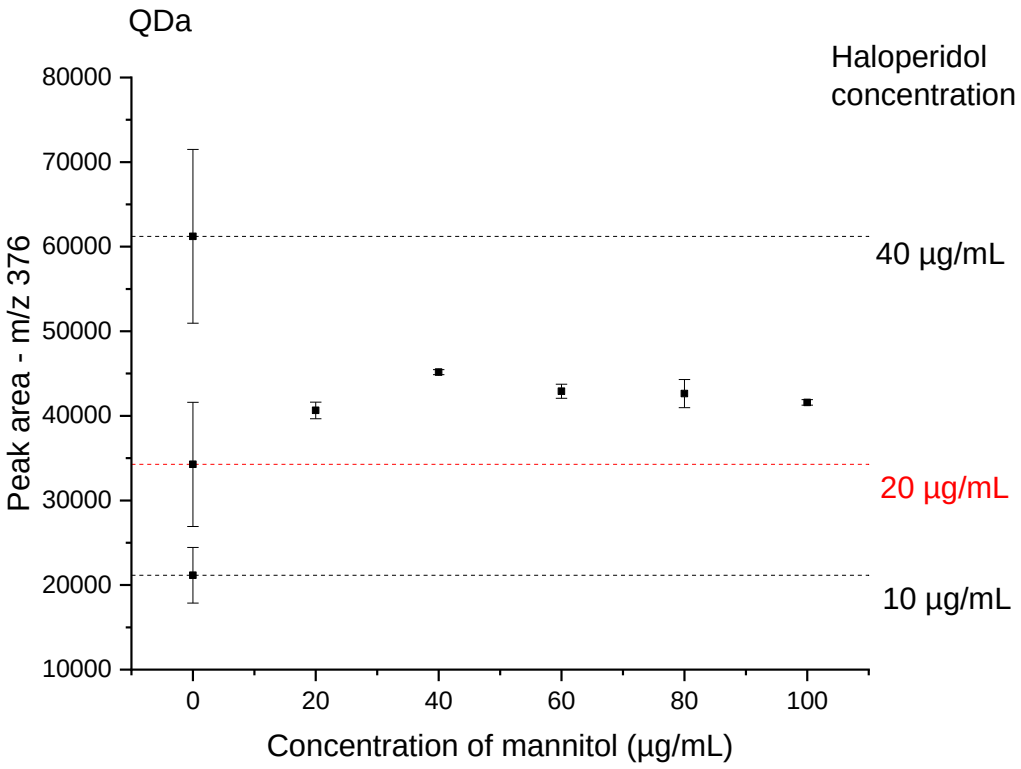

Figure 8.296 – QDa data showing the effect of increasing the concentration of mannitol upon the peak area value (signal) obtained for haloperidol following an ES+ SIM channel of m/z 376. The concentration of haloperidol was kept constant at 20 µg/mL. Comparative signals obtained for haloperidol concentrations without mannitol present are shown by the dashed lines, with a red line showing the concentration of 20 µg/mL, which is the same as that found in the solutions mixed with mannitol, and two black lines showing 10 µg/mL and 40 µg/mL for comparison. Error bars showing standard deviation are included for each point, which are a result of each sample being run and analysed in triplicate.

Conversely, the impact of paracetamol and furosemide upon the lactose signal is shown in Figure 8.297 and shows that furosemide may enhance the ionisation of lactose while paracetamol may suppress lactose ionisation. This suggests that as lactose may be enhancing furosemide ionisation, furosemide may be enhancing ionisation of the lactose, and a combination of lactose with paracetamol may result in the suppression of ionisation of both components. Lactose ionised alone (black squares) shows a reduction in signal between 80 and 100 µg/mL, which is consistent with the plateau observed during the single components work in the previous chapter, see Figure 7.259.

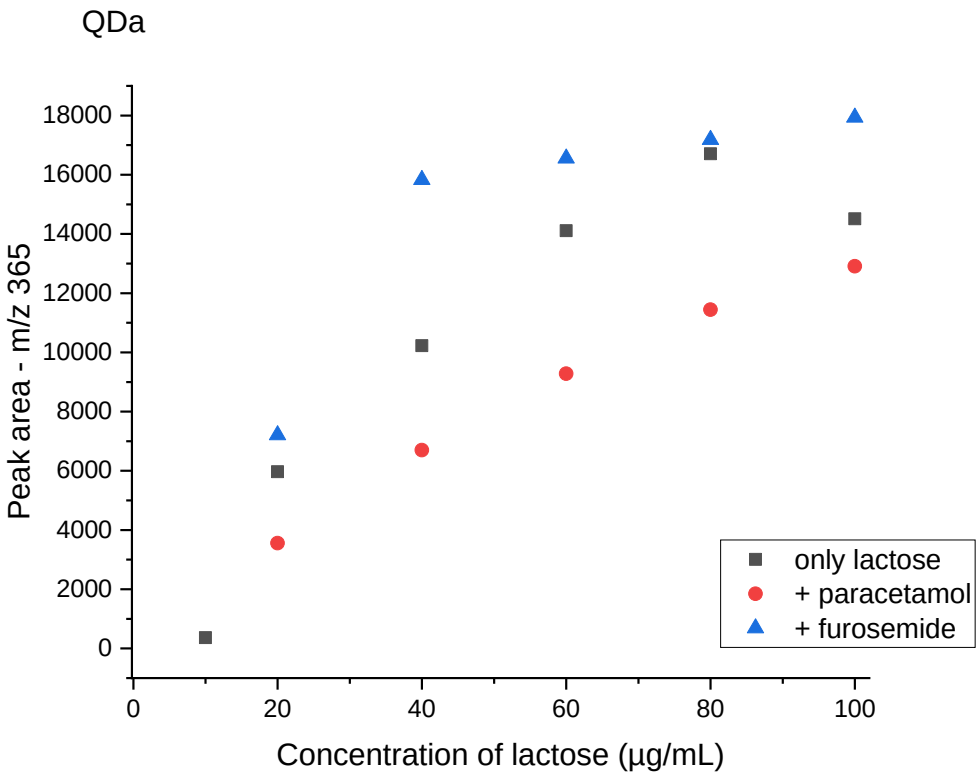

Figure 8.297 – QDa data showing the peak area of increasing concentrations of lactose in solution either alone (black squares), or with a concentration of 20 µg/mL of paracetamol (red circles) or furosemide (blue triangles). The SIM channel from which the signal was obtained followed m/z 365.

The impact of haloperidol upon lactose ionisation has been plotted separately because the samples were run at a different time and cannot be compared quantitatively. The samples were run in triplicate to allow error bars based upon standard deviation to be included, which give an idea of signal variability. The data in Figure 8.298 suggests that haloperidol suppresses lactose signal, and that lactose ionised in combination with haloperidol appears less variable. The suppression observed is more easily distinguishable from variation at higher concentrations of lactose, although there is consistently an overlap between error bars from lactose in isolation and in combination. Lactose has been monitored through the sodium ion adduct for both data sets, and although the presence of the dimer was observed it was found to be too small to quantify.

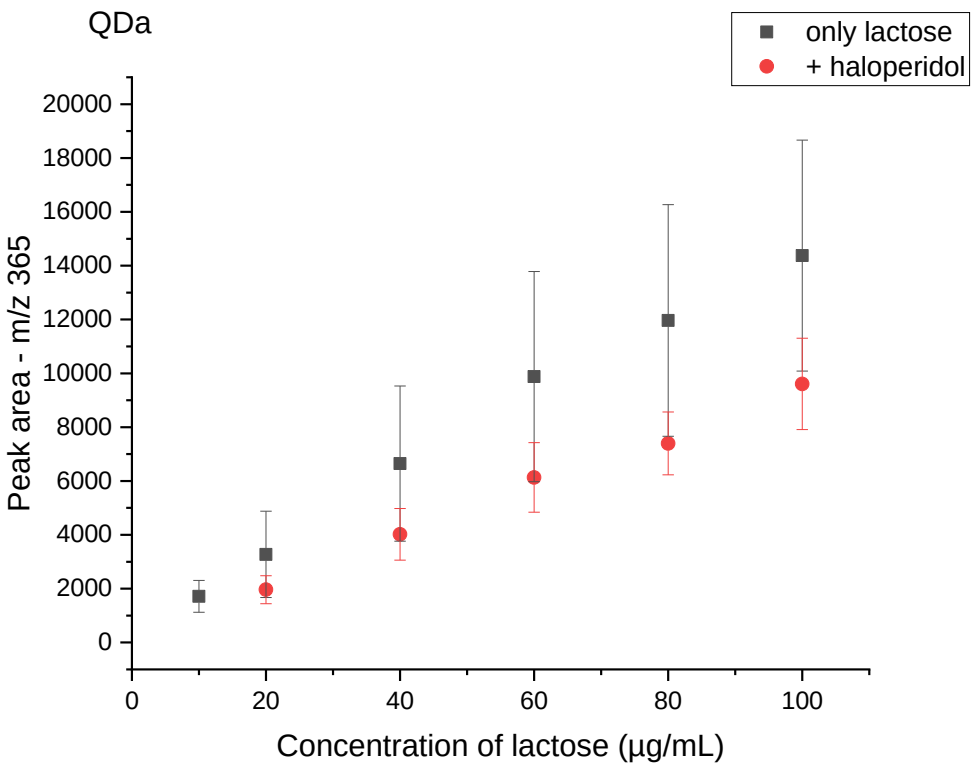

Figure 8.298 – QDa data showing the peak area of increasing concentrations of lactose in solution either alone (black squares), or with a concentration of 20 µg/mL of haloperidol (red circles). The SIM channel from which the signal was obtained followed m/z 365. Error bars showing standard deviation are included for each point, which are a result of each sample being run and analysed in triplicate.

Finally the impact of paracetamol and furosemide upon the peak area observed for mannitol is shown in Figure 8.299 and suggests that while the presence of paracetamol appears to have little impact upon mannitol ionisation, furosemide suppresses it. The relationship between peak area and concentration observed from mannitol alone is again consistent with the relationship observed previously, see Figure 7.266. The ES+ data was monitored closely for the presence of $[M+Na]^+$ at *m/z* 205 for all sets of data, but as with the original work observing mannitol using the QDa, it was not found.

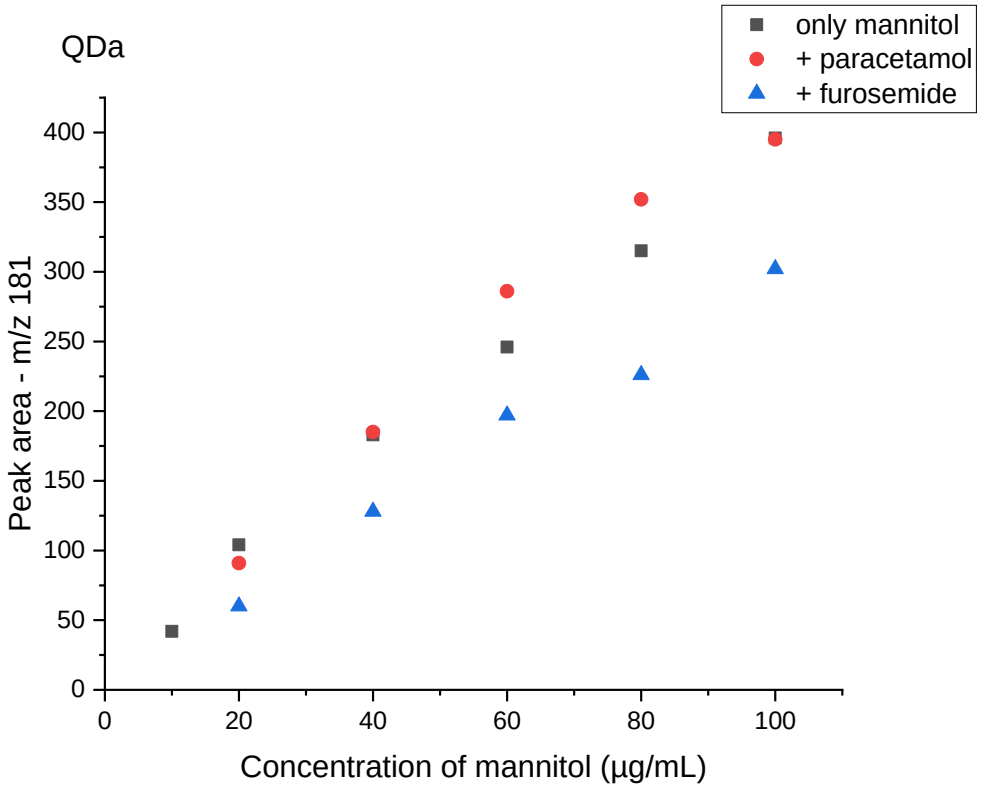

Figure 8.299 – QDa data showing the peak area value (signal) of increasing concentrations of mannitol in solution either alone (black squares), or with a concentration of 20 µg/mL of paracetamol (red circles) or furosemide (blue triangles). The ES- SIM channel from which the signal was obtained followed m/z 181.

The impact of haloperidol upon mannitol ionisation has again been plotted separately because these samples were run in triplicate to give an idea of signal variability, see Figure 8.300. The signal for mannitol obtained in the presence of haloperidol is consistently within the variation observed when mannitol is ionised alone, which suggests that haloperidol does not significantly enhance or suppress the ionisation of mannitol when analysed using the QDa.

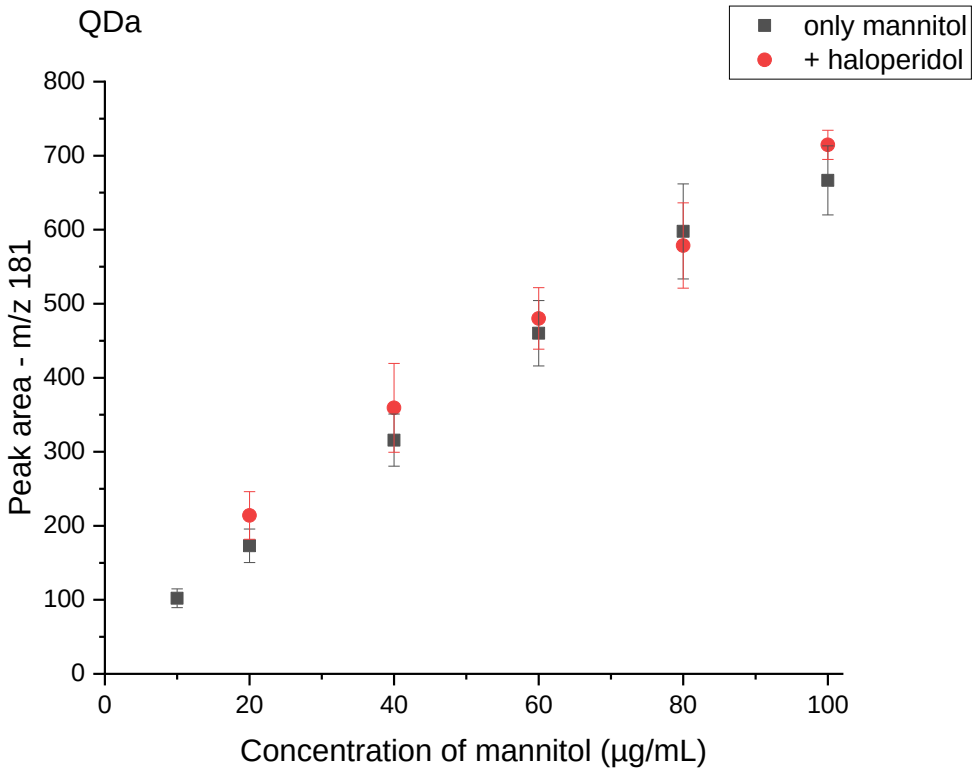

Figure 8.300 – QDa data showing the peak area value (signal) of increasing concentrations of mannitol in solution either alone (black squares), or with a concentration of 20 µg/mL of haloperidol (red circles). The ES- SIM channel from which the signal was obtained followed m/z 181. Error bars showing standard deviation are included for each point, which are a result of each sample being run and analysed in triplicate.

This work confirms that the data obtained for paracetamol and furosemide must be interpreted carefully because without replication to indicate variability, it may not provide a robust indication of suppression or enhancement, and may simply show the variability of the ESI-MS signal. Although it is important to note the limitations of the methods used, time and equipment constraints prevented repetition of the initial data (for paracetamol and furosemide), hence a summary of the conclusions that may still be drawn is provided. Table 8.35 provides a summary for the impact upon API ionisation of each excipient and Table 8.36 summarises the data showing the impact of each API upon ionisation of each of the excipients.

Table 8.35 – QDa ionisation phenomena summary: impact of each excipient upon paracetamol, furosemide or haloperidol.

	+ Lactose (ES+)	**+ Mannitol (ES-)**
Furosemide ionisation (ES-)	Enhanced	Enhanced
Haloperidol ionisation (ES+)	No impact	Enhanced when ≥ 40 µg/mL
Paracetamol ionisation (ES+)	Suppressed	Little impact

Table 8.36 – QDa ionisation phenomena summary: impact of each API upon lactose or mannitol.

	+ Furosemide (ES-)	**+ Haloperidol (ES+)**	**+ Paracetamol (ES+)**
Lactose ionisation (ES+)	No impact	Suppressed	Suppressed
Mannitol ionisation (ES-)	Suppressed	No impact	No impact

The theories underlying electrospray ionisation mechanisms are complex but there is discussion of competition between components in a solution for a finite charge dependent upon flow rates and applied voltages.[328,329,247,237,339] Additionally, ionisation efficiency (IE) scales have been discussed as a means to understand why some components convert to gas-phase ions easily and others are not detectable.[259,335] Such work highlights numerous properties as impacting upon IE, from ESI source and mobile phase, to pKa values, hydrophobicity and surface activity.[247,255,259] The mode of ionisation used and whether the charge is positive or negative, as well as the gas-phase ion formed, will therefore play an important role in ionisation phenomena, thus it may be used to help explain the relationships between API and excipients.

Paracetamol and lactose are analysed using ES+ methods, and their co-ionisation appears to result in mutual suppression suggesting that the competition for positive charge may be similar from both components. Paracetamol has been monitored through the protonated ion $[M+H]^+$ and lactose through its 1:1 sodium adduct $[M+Na]^+$ with the dimer $[2M+Na]^+$ not found in sufficient amounts to allow its quantification in this section of work. Haloperidol and lactose are also analysed using ES+ methods, but co-ionisation appears to result in suppression only of the lactose, suggestive of haloperidol competing more favourably although not sufficiently enough to result in

an enhanced haloperidol signal. Furosemide and mannitol, however, are both analysed using ES- methods, and their co-ionisation appears to result in both enhancement of furosemide and suppression of mannitol, suggestive of furosemide competing significantly more favourably. Furosemide is monitored through both its deprotonated ion $[M-H]^-$ and a fragmented ion $[M-COOH]^-$, but mannitol has again only been able to be monitored through $[M-H]^-$ in this instance.

The observation that mannitol enhances the ionisation of haloperidol, may be explained by a competition for charge, with mannitol preferring to gain negative charge, thus it may be acting similarly to an ionisation modifier (e.g. formic acid) in ES+ mode, although present at a much higher relative concentration. However, one would therefore expect mannitol to result in ionisation enhancement of the paracetamol signal too, but this was not the case. A possible explanation may be that mannitol ionisation can also produce the sodium adduct $[M+Na]^+$ in certain environments, although the exact requirements for this are not clear. The observation that lactose may also enhance the ionisation of furosemide in ES- could be explained by a similar argument comparing it with an ionisation modifier, although again at different relative concentrations, but lactose ionisation appears unaffected by the presence of furosemide, hence the relationships cannot be explained solely by ionisation method or charge competition. There is also evidence to suggest that the co-ionisation of either lactose or mannitol with haloperidol may reduce haloperidol signal variability, and haloperidol may in turn reduce variability of the lactose signal.

In summary, the complexities of ionisation suppression and enhancement relationships exceed our current mechanistic understanding of ESI-MS, although a summary of suggested enhancement or suppression can be stated for each pair of components analysed and an ionisation efficiency scale may be postulated for each mode. For ES+ an ionisation efficiency scale may look like: haloperidol > paracetamol = lactose, and for ES- the ionisation efficiency scale may look like: furosemide > mannitol.

Synapt (Loop Injection)

The Synapt LI data is presented first, noting that furosemide is monitored through two separate ions as a condition of the data analysis methods on this instrument. The Synapt LI analyses show little impact of lactose upon the ionisation of paracetamol, see Figure 8.301, and a slight impact of mannitol upon the ionisation of paracetamol suggestive of enhancement, see Figure 8.302. The enhancement by mannitol appears to be consistent regardless of the concentration of mannitol present, which again differs from the pattern observed in other examples. The paracetamol data strengthens the suggestion that differences exist between ESI-MS equipment when it comes to considering the impact of ionisation phenomena upon quantification.

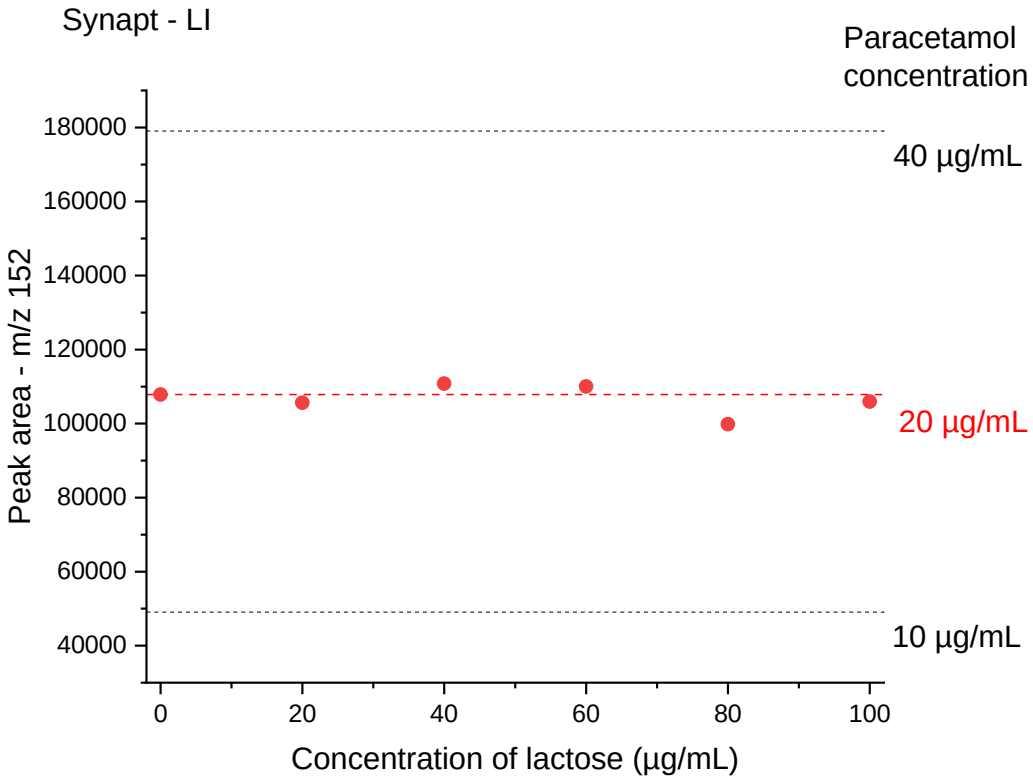

Figure 8.301 – Synapt LI data showing the effect of increasing the concentration of lactose upon the peak area value (signal) obtained for paracetamol following a SIM channel of m/z 152. The concentration of paracetamol was kept constant at 20 µg/mL. Comparative signals obtained for paracetamol concentrations without lactose present are shown by the dashed lines, with a red line showing the concentration of 20 µg/mL, which is the same as that found in the solutions mixed with lactose, and two black lines showing 10 µg/mL and 40 µg/mL for comparison.

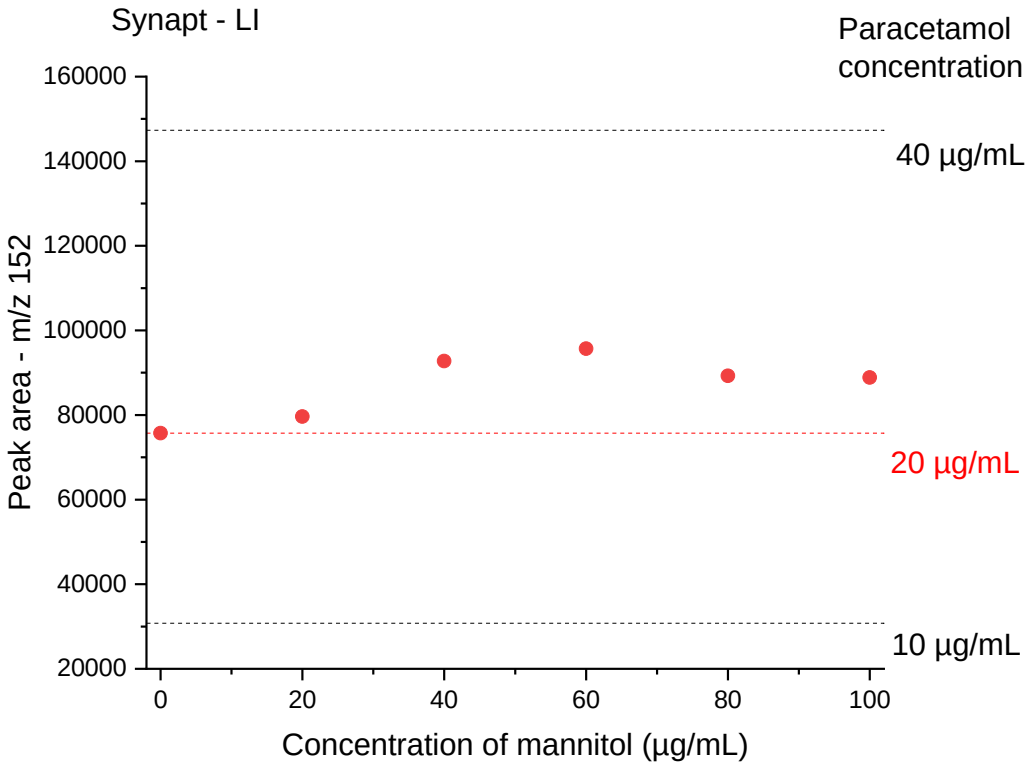

Figure 8.302 – Synapt LI data showing the effect of increasing the concentration of mannitol upon the peak area value (signal) obtained for paracetamol following an ES+ SIM channel of m/z 152. The concentration of paracetamol was kept constant at 20 µg/mL. Comparative signals obtained for paracetamol concentrations without mannitol present are shown by the dashed lines, with a red line showing the concentration of 20 µg/mL, which is the same as that found in the solutions mixed with mannitol, and two black lines showing 10 µg/mL and 40 µg/mL for comparison.

Lactose may slightly enhance ionisation of furosemide through LI on the Synapt, as shown in Figure 8.303 and Figure 8.304. These results are consistent with the QDa findings, which suggested that furosemide may be enhanced by the co-ionisation of lactose, and were observed for both *m/z* 285 and *m/z* 329. Figure 8.305 and Figure 8.306 show the co-ionisation of furosemide with mannitol through LI on the Synapt. The furosemide signal shows greater overall variability in the presence of mannitol, with no consistent effect upon *m/z* 285 but a slight enhancement of *m/z* 329 when 80 µg/mL and more of mannitol is present. The QDa findings showed significant enhancement of furosemide by mannitol (suggestive of a signal from double the concentration), which again differs from the Synapt findings.

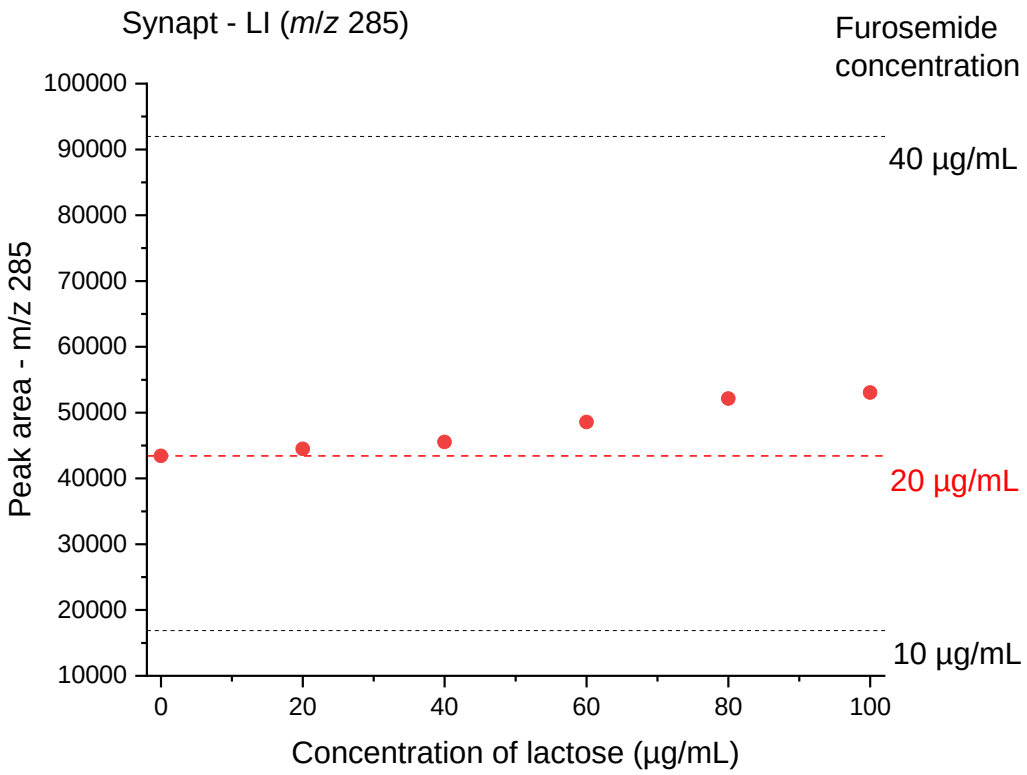

Figure 8.303 – Synapt LI data showing the effect of increasing the concentration of lactose upon the peak area value (signal) obtained for furosemide following a SIM channel of m/z 285. The concentration of furosemide was kept constant at 20 µg/mL. Comparative signals obtained for furosemide concentrations without lactose present are shown by the dashed lines, with a red line showing the concentration of 20 µg/mL, which is the same as that found in the solutions mixed with lactose, and two black lines showing 10 µg/mL and 40 µg/mL for comparison.

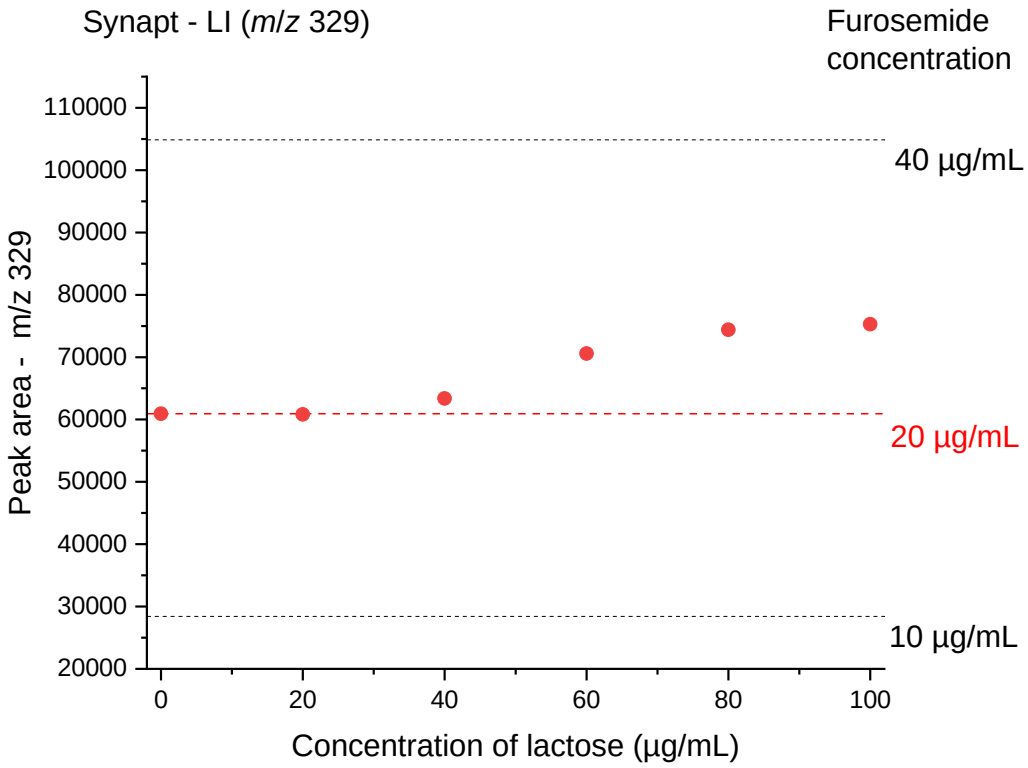

Figure 8.304 – Synapt LI data showing the effect of increasing the concentration of lactose upon the peak area value (signal) obtained for furosemide following a SIM channel of m/z 329. The concentration of furosemide was kept constant at 20 µg/mL. Comparative signals obtained for furosemide concentrations without lactose present are shown by the dashed lines, with a red line showing the concentration of 20 µg/mL, which is the same as that found in the solutions mixed with lactose, and two black lines showing 10 µg/mL and 40 µg/mL for comparison.

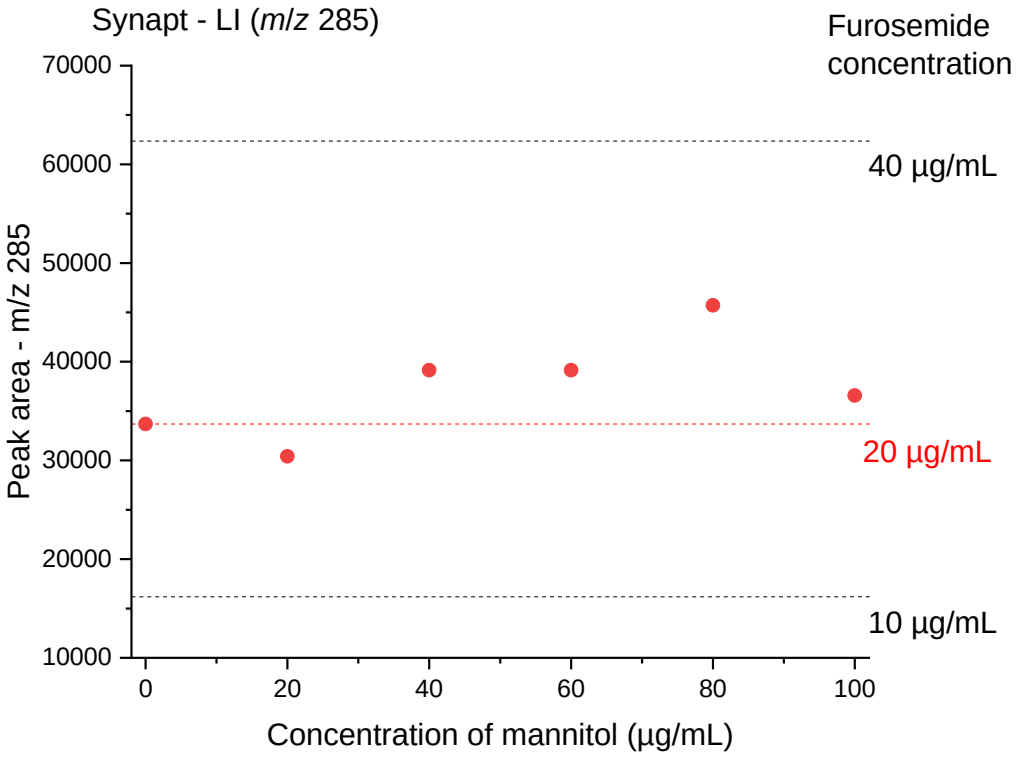

Figure 8.305 – Synapt LI data showing the effect of increasing the concentration of mannitol upon the peak area value (signal) obtained for furosemide following an ES- SIM channel of m/z 285. The concentration of furosemide was kept constant at 20 µg/mL. Comparative signals obtained for furosemide concentrations without mannitol present are shown by the dashed lines, with a red line showing the concentration of 20 µg/mL, which is the same as that found in the solutions mixed with mannitol, and two black lines showing 10 µg/mL and 40 µg/mL for comparison.

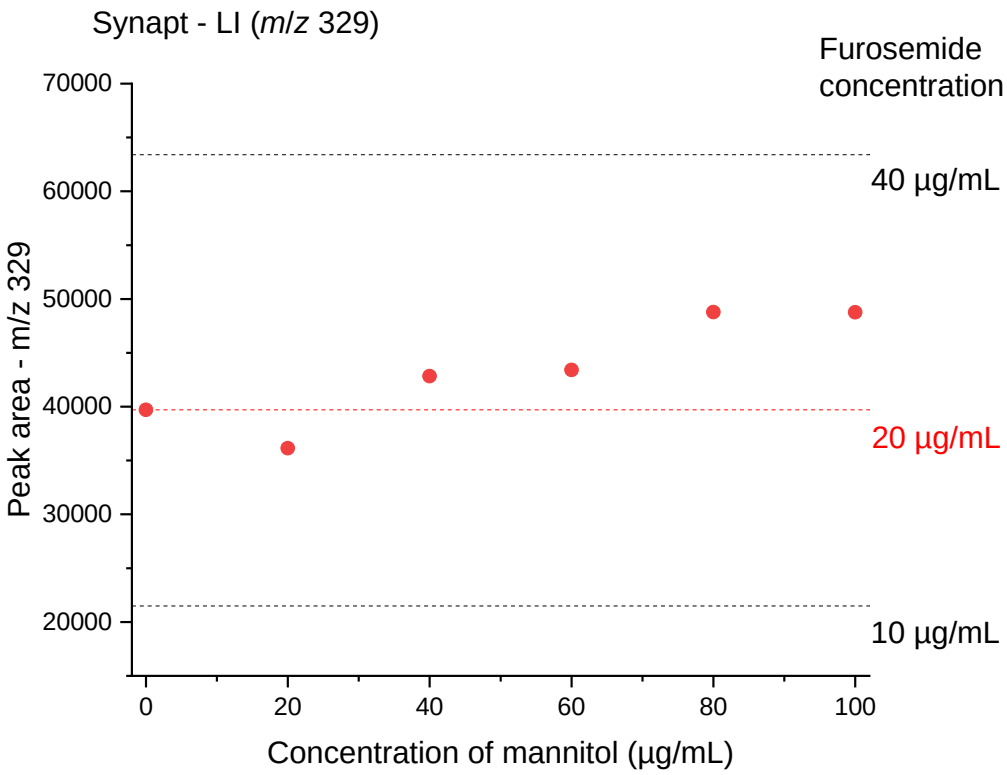

Figure 8.306 – Synapt LI data showing the effect of increasing the concentration of mannitol upon the peak area value (signal) obtained for furosemide following an ES- SIM channel of m/z 329. The concentration of furosemide was kept constant at 20 µg/mL. Comparative signals obtained for furosemide concentrations without mannitol present are shown by the dashed lines, with a red line showing the concentration of 20 µg/mL, which is the same as that found in the solutions mixed with mannitol, and two black lines showing 10 µg/mL and 40 µg/mL for comparison.

The Synapt LI haloperidol data has been analysed in triplicate, as previously explained, which provides confidence in the assertion from Figure 8.307 that lactose enhances haloperidol ionisation, and that the enhancement is unaffected by lactose concentration between 20 and 80 µg/mL. This QDa data found no significant impact of lactose upon haloperidol ionisation regardless of concentration due to the inherent haloperidol signal variability, although it did appear to be slightly enhanced. An enhancement of haloperidol ionisation can be seen with all concentrations of mannitol in Figure 8.308, although the extent appears consistent between 40 and 100 µg/mL. The Synapt LI data again shows reduced variability when compared with the QDa although both instruments show that ionisation enhancement is occurring.

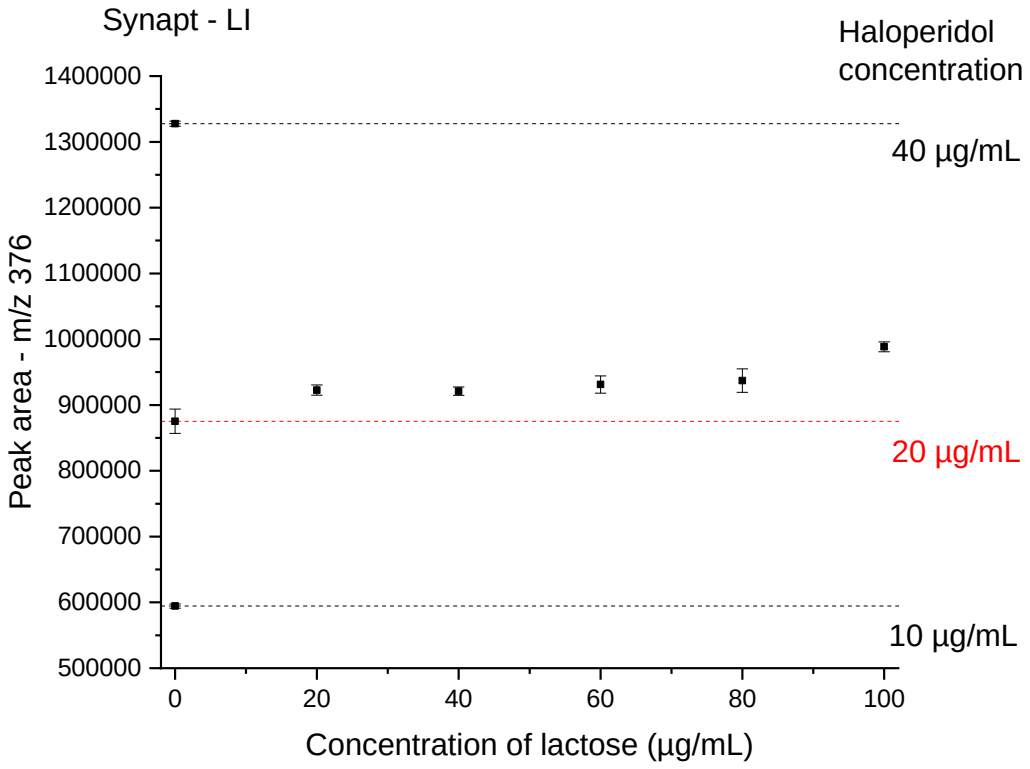

Figure 8.307 – Synapt LI data showing the effect of increasing the concentration of lactose upon the peak area value (signal) obtained for haloperidol following a SIM channel of m/z 376. The concentration of haloperidol was kept constant at 20 µg/mL. Comparative signals obtained for haloperidol concentrations without lactose present are shown by the dashed lines, with a red line showing the concentration of 20 µg/mL, which is the same as that found in the solutions mixed with lactose, and two black lines showing 10 µg/mL and 40 µg/mL for comparison. Error bars showing standard deviation are included for each point, which are a result of each sample being run and analysed in triplicate.

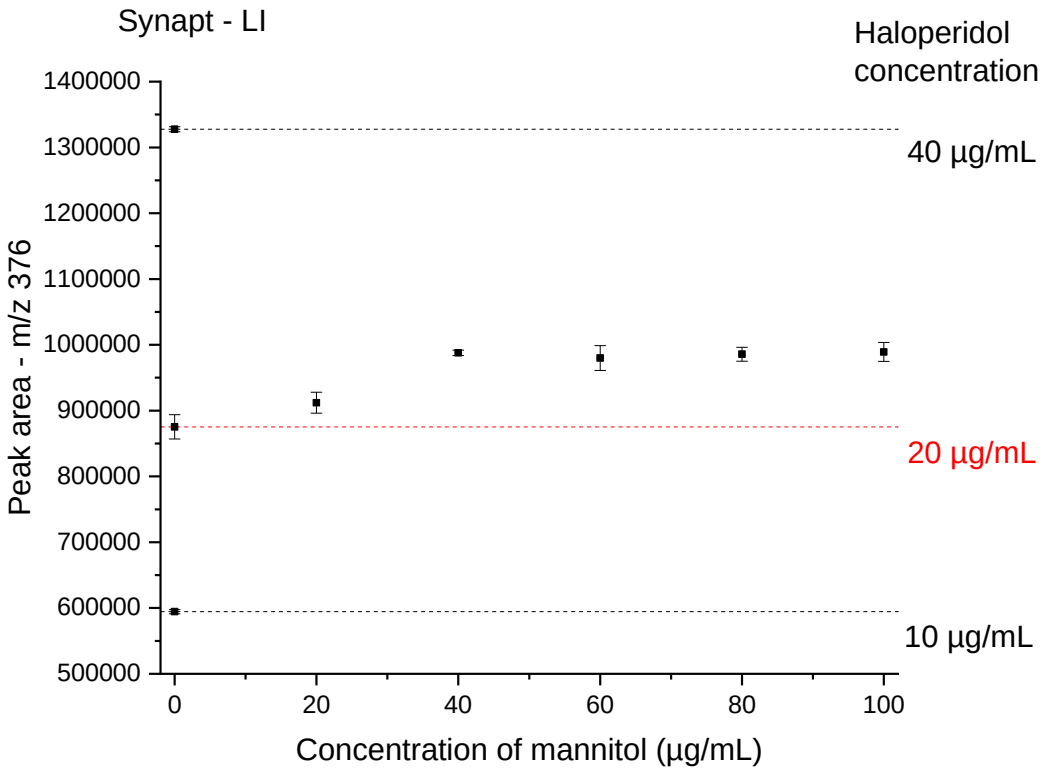

Figure 8.308 – Synapt LI data showing the effect of increasing the concentration of mannitol upon the peak area value (signal) obtained for haloperidol following a SIM channel of m/z 376. The concentration of haloperidol was kept constant at 20 µg/mL. Comparative signals obtained for haloperidol concentrations without mannitol present are shown by the dashed lines, with a red line showing the concentration of 20 µg/mL, which is the same as that found in the solutions mixed with mannitol, and two black lines showing 10 µg/mL and 40 µg/mL for comparison. Error bars showing standard deviation are included for each point, which are a result of each sample being run and analysed in triplicate.

Figure 8.309 suggests a less consistent impact of paracetamol and furosemide upon lactose, when compared with the QDa data described previously. There appears to be a significant cross-over between the signals observed when only lactose is ionised versus ionisation in the presence of either API, with the exception of haloperidol, shown in Figure 8.310. Lactose signal is clearly suppressed by the presence of haloperidol, which is consistent with the QDa data for this combination of components.

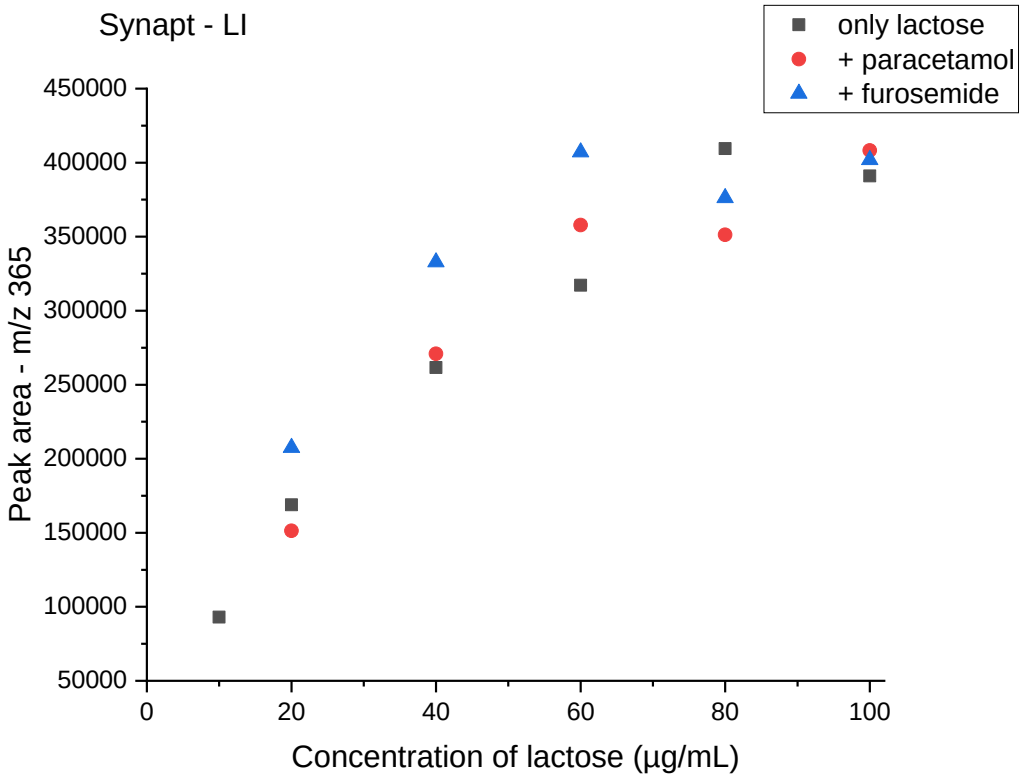

Figure 8.309 – Synapt data showing the peak area value (signal) of increasing concentrations of lactose in solution either alone (black squares), or with a concentration of 20 µg/mL of paracetamol (red circles) or furosemide (blue triangles). The SIM channel from which the signal was obtained followed m/z 365.

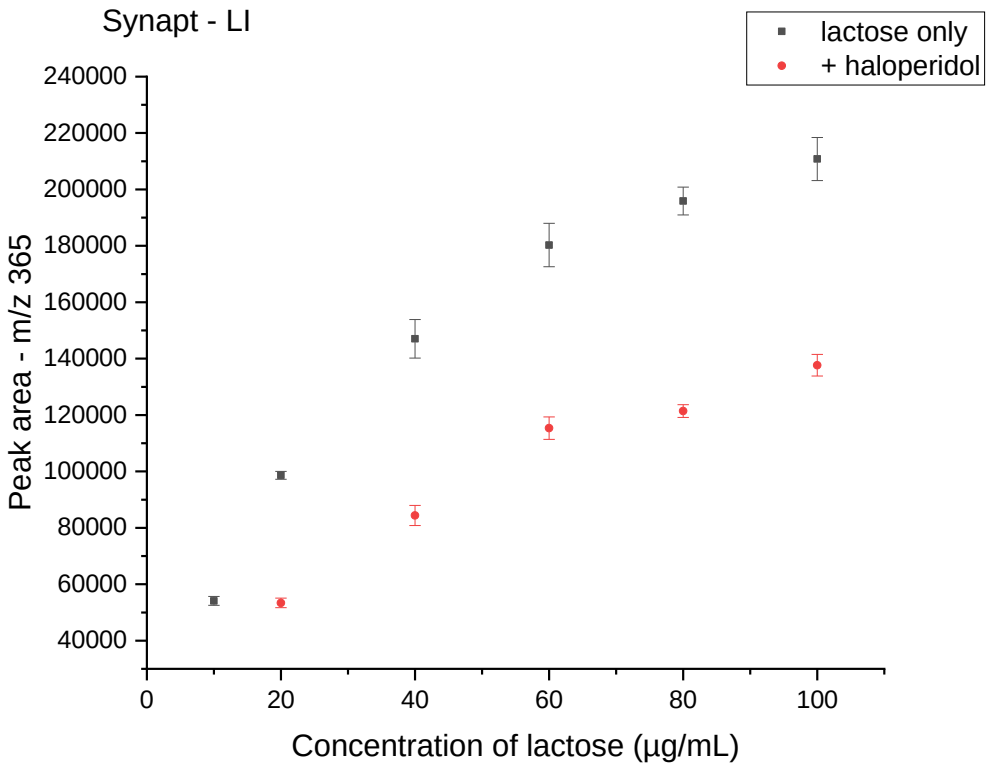

Figure 8.310 – Synapt LI data showing the peak area value (signal) of increasing concentrations of lactose in solution either alone (black squares), or with a concentration of 20 µg/mL of haloperidol (red circles). The ES+ SIM channel from which the signal was obtained followed m/z 365. Error bars showing standard deviation are included for each point, which are a result of each sample being run and analysed in triplicate.

The mannitol findings, shown in Figure 8.311, are consistent with the QDa work and suggest its ionisation is slightly suppressed by furosemide, but the presence of paracetamol has little impact. Figure 8.312, however, shows enhancement of the mannitol signal by haloperidol, which is not consistent with the QDa work. The mannitol signal was quantified in ES- for all analyses, and could only be observed in ES+ when in combination with paracetamol.

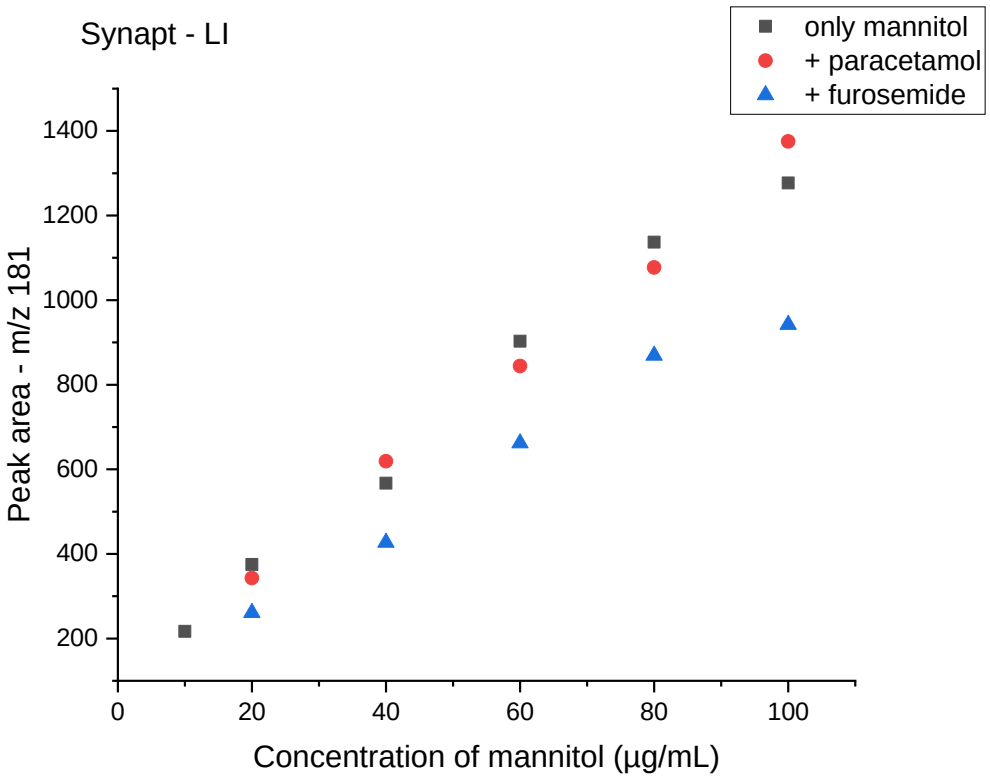

Figure 8.311 – Synapt data showing the peak area value (signal) of increasing concentrations of mannitol in solution either alone (black squares), or with a concentration of 20 µg/mL of paracetamol (red circles) or furosemide (blue triangles). The ES- SIM channel from which the signal was obtained followed m/z 181.

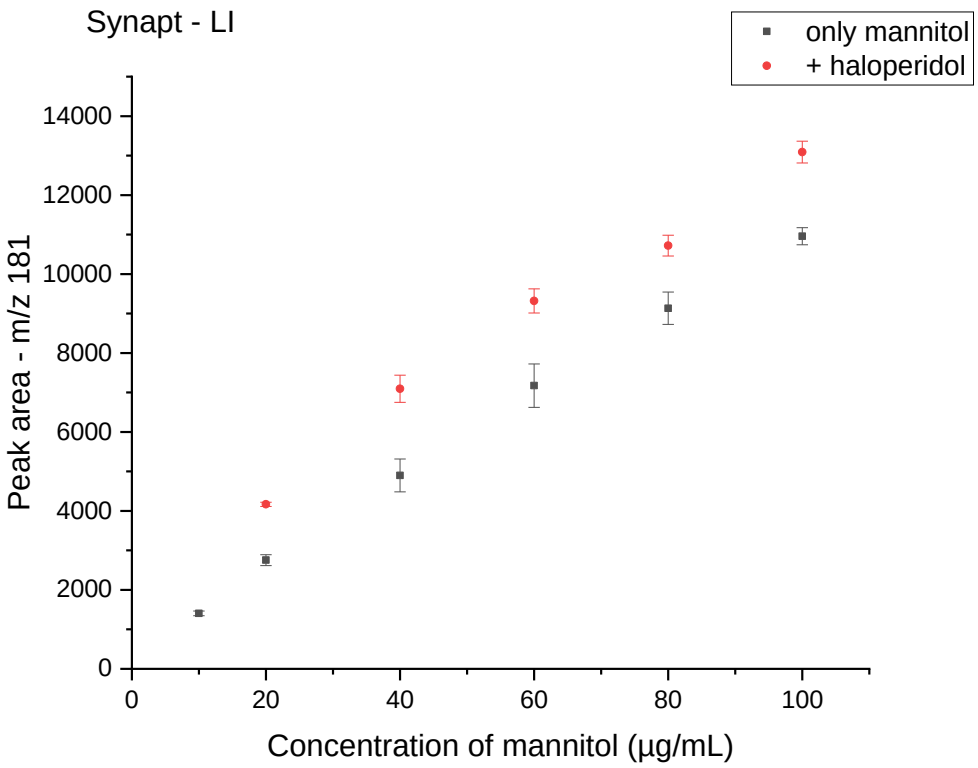

Figure 8.312 – Synapt LI data showing the peak area value (signal) of increasing concentrations of mannitol in solution either alone (black squares), or with a concentration of 20 µg/mL of haloperidol (red circles). The ES- SIM channel from which the signal was obtained followed m/z 181. Error bars showing standard deviation are included for each point, which are a result of each sample being run and analysed in triplicate.

Table 8.37 provides a summary of the impact of each excipient upon API ionisation and Table 8.38 summarises the impact of each API upon excipient ionisation. Consistent with the QDa (Loop Injection) work, the paracetamol and furosemide findings require careful interpretation, however, the haloperidol data allows more confident conclusions to be drawn as a result of the repetition, which provides an insight into signal variability.

Table 8.37 – Synapt LI ionisation phenomena summary: impact of each excipient upon paracetamol, furosemide or haloperidol.

	+ Lactose (ES+)	**+ Mannitol (ES-)**
Furosemide ionisation (ES-)	Some enhancement (both)	Variable m/z 285 signal but enhanced m/z 329 signal
Haloperidol ionisation (ES+)	Enhanced	Enhanced
Paracetamol ionisation (ES+)	No impact	Some enhancement

Table 8.38 – Synapt LI ionisation phenomena summary: impact of each API upon lactose or mannitol.

	+ Furosemide (ES-)	**+ Haloperidol (ES+)**	**+ Paracetamol (ES+)**
Lactose ionisation (ES+)	Little impact	Suppressed	Little impact
Mannitol ionisation (ES-)	Suppressed	Enhanced	Little impact

The furosemide findings are fairly consistent between the two instruments, suggesting that its ionisation may be enhanced by both lactose and mannitol. Haloperidol also appears to be enhanced by both excipients, although there is increased signal variability with the QDa that throws doubt upon this conclusion for the lactose experiments. This variability is likely influenced by the SIM channel method on the QDa versus the high resolution capacity of the Synapt allowing discrimination between ions with similar *m*/*z* values. Paracetamol findings from the QDa suggest suppression is possible with lactose although this is not seen clearly with the Synapt, and with mannitol there is likely some enhancement with the Synapt. The excipient findings are also consistent between the two instruments, with the exception of haloperidol and mannitol; the Synapt data shows the mannitol signal to be suppressed instead of showing no impact. Finally, the Synapt data is again much less variable than the QDa data, consistent with the instrument types.

In summary, although the findings are not conclusive for each instrument, there is no occurrence of one suggesting enhancement where the other suggests suppression, or vice versa, which is consistent with work that suggests that ionisation efficiency scales may be transferred between instruments.[340] Repetition of the paracetamol and furosemide data would have again proven useful in determining whether differences were a result of inherent signal variability or whether they were consistent with ionisation phenomena occurring. This requirement to run samples multiple times, and the need to set up runs for each mode on the Synapt (instead of being able to incorporate ES+ and ES- into one QDa method) adds significant time and complexity to the preparation of aliquot analyses and thereby limits its usefulness long-term. An advantage of observing relationships between APIs and excipients in this way, however, is that it highlights that enhancement and suppression of ionisation may

occur to different extents for different ratios of components, hence, an understanding of the relationship across the concentration range for each component will be required.

Synapt with LC

Finally, the Synapt analyses with LC prior to ionisation confirm that each component can be found in the mixtures. The peak area values from LC and LI methods cannot be directly compared due to the differences in methods, but the relationship between signal and concentration aids observations about the impact of ionisation phenomena. These plots would be expected to show consistent signal from each API regardless of the concentration of lactose because the LC method prevents co-ionisation and therefore avoids ion suppression or enhancement from occurring, see Table 8.39.

Table 8.39 – Retention times for lactose, paracetamol and furosemide using a five minute reverse phase gradient LC method coupled with the Synapt.

Component	Retention Time (mins)
Lactose	0.62
Paracetamol	1.80
Furosemide	3.00
Haloperidol	2.77
Mannitol	0.61

The paracetamol signal obtained through LCMS can be seen to vary slightly as shown in Figure 8.313 and Figure 8.314 but as expected there is no consistent increase or decrease in signal consistent with enhancement or suppression occurring. Both furosemide ions show signal variation with lactose, see Figure 8.315 and Figure 8.316, and also with mannitol, see Figure 8.317 and Figure 8.318. However, there may be a difference in the extent of fragmentation that is seen for each excipient. The haloperidol data shown in Figure 8.319 and Figure 8.320 again shows no consistent change with either excipient.

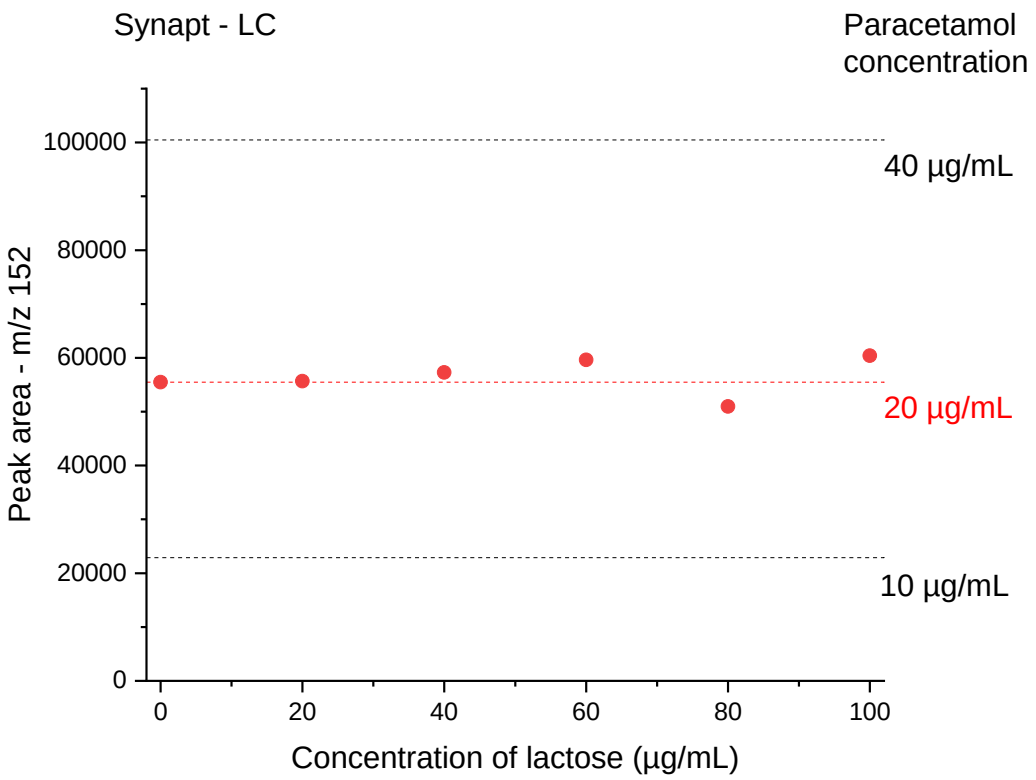

Figure 8.313 – Synapt LC data showing the effect of increasing the concentration of lactose upon the peak area value (signal) obtained for paracetamol following a SIM channel of m/z 152 with LC applied to separate the ions prior to ionisation. The concentration of paracetamol was kept constant at 20 µg/mL. Comparative signals obtained for paracetamol concentrations without lactose present are shown by the dashed lines, with a red line showing the concentration of 20 µg/mL, which is the same as that found in the solutions mixed with lactose, and two black lines showing 10 µg/mL and 40 µg/mL for comparison.

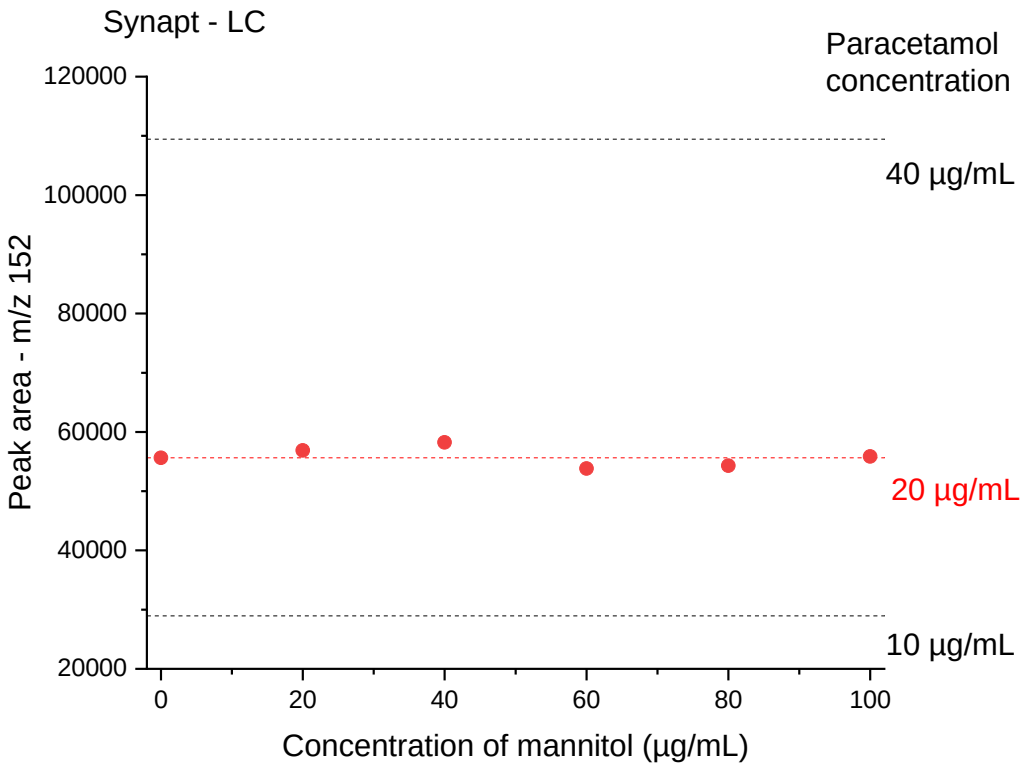

Figure 8.314 – Synapt LC data showing the effect of increasing the concentration of mannitol upon the peak area value (signal) obtained for paracetamol following an ES+ SIM channel of m/z 152 with LC applied to separate the ions prior to ionisation. The concentration of paracetamol was kept constant at 20 µg/mL. Comparative signals obtained for paracetamol concentrations without mannitol present are shown by the dashed lines, with a red line showing the concentration of 20 µg/mL, which is the same as that found in the solutions mixed with mannitol, and two black lines showing 10 µg/mL and 40 µg/mL for comparison.

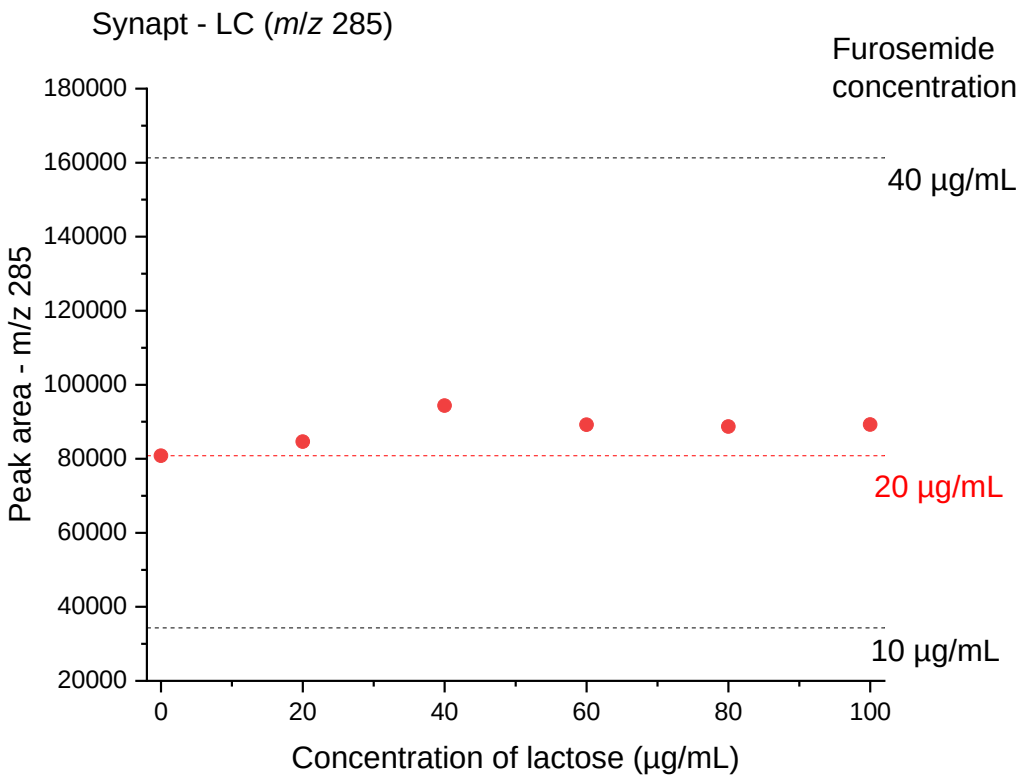

Figure 8.315 – Synapt LC data showing the effect of increasing the concentration of lactose upon the peak area value (signal) obtained for furosemide following a SIM channel of m/z 285 with LC applied to separate the ions prior to ionisation. The concentration of furosemide was kept constant at 20 µg/mL. Comparative signals obtained for furosemide concentrations without lactose present are shown by the dashed lines, with a red line showing the concentration of 20 µg/mL, which is the same as that found in the solutions mixed with lactose, and two black lines showing 10 µg/mL and 40 µg/mL for comparison.

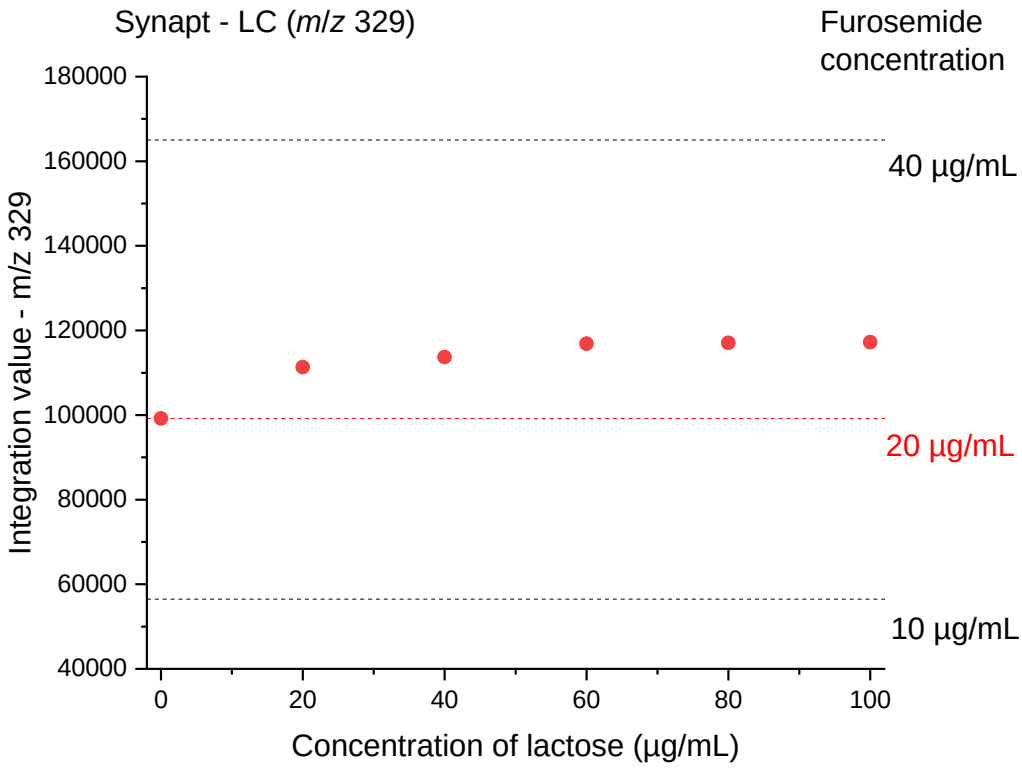

Figure 8.316 – Synapt LC data showing the effect of increasing the concentration of lactose upon the peak area value (signal) obtained for furosemide following a SIM channel of m/z 329 with LC applied to separate the ions prior to ionisation. The concentration of furosemide was kept constant at 20 µg/mL. Comparative signals obtained for furosemide concentrations without lactose present are shown by the dashed lines, with a red line showing the concentration of 20 µg/mL, which is the same as that found in the solutions mixed with lactose, and two black lines showing 10 µg/mL and 40 µg/mL for comparison.

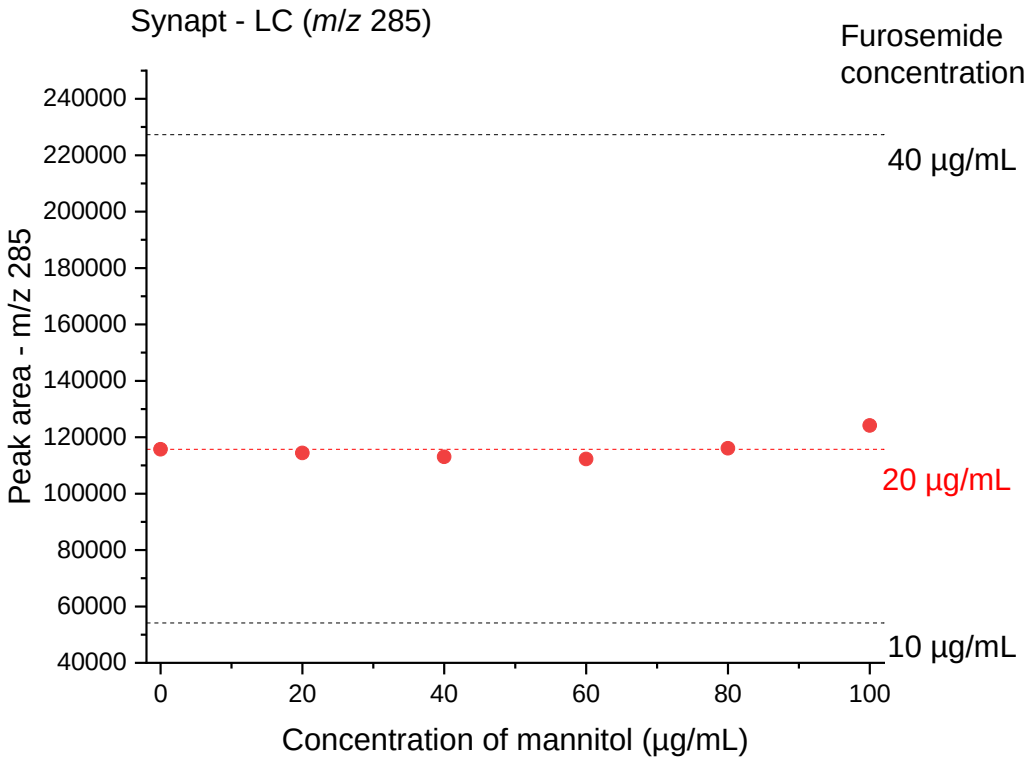

Figure 8.317 – Synapt LC data showing the effect of increasing the concentration of mannitol upon the peak area value (signal) obtained for furosemide following an ES- SIM channel of m/z 285 with LC applied to separate the ions prior to ionisation. The concentration of furosemide was kept constant at 20 µg/mL. Comparative signals obtained for furosemide concentrations without mannitol present are shown by the dashed lines, with a red line showing the concentration of 20 µg/mL, which is the same as that found in the solutions mixed with mannitol, and two black lines showing 10 µg/mL and 40 µg/mL for comparison.

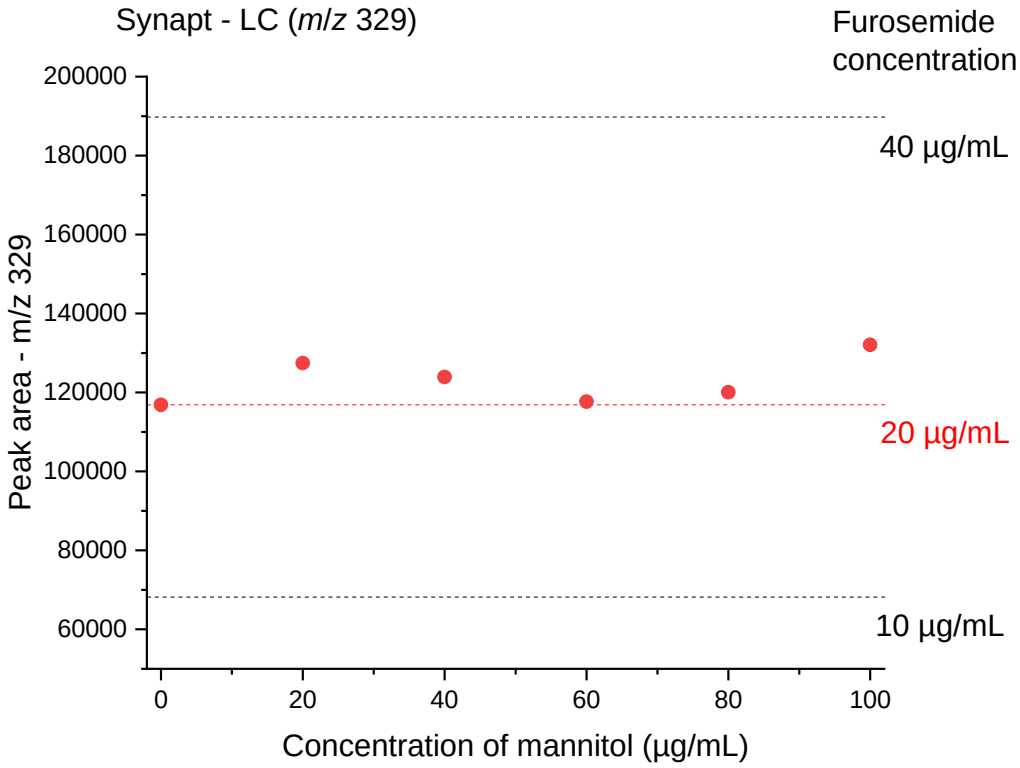

Figure 8.318 – Synapt LC data showing the effect of increasing the concentration of mannitol upon the peak area value (signal) obtained for furosemide following an ES- SIM channel of m/z 329 with LC applied to separate the ions prior to ionisation. The concentration of furosemide was kept constant at 20 µg/mL. Comparative signals obtained for furosemide concentrations without mannitol present are shown by the dashed lines, with a red line showing the concentration of 20 µg/mL, which is the same as that found in the solutions mixed with mannitol, and two black lines showing 10 µg/mL and 40 µg/mL for comparison.

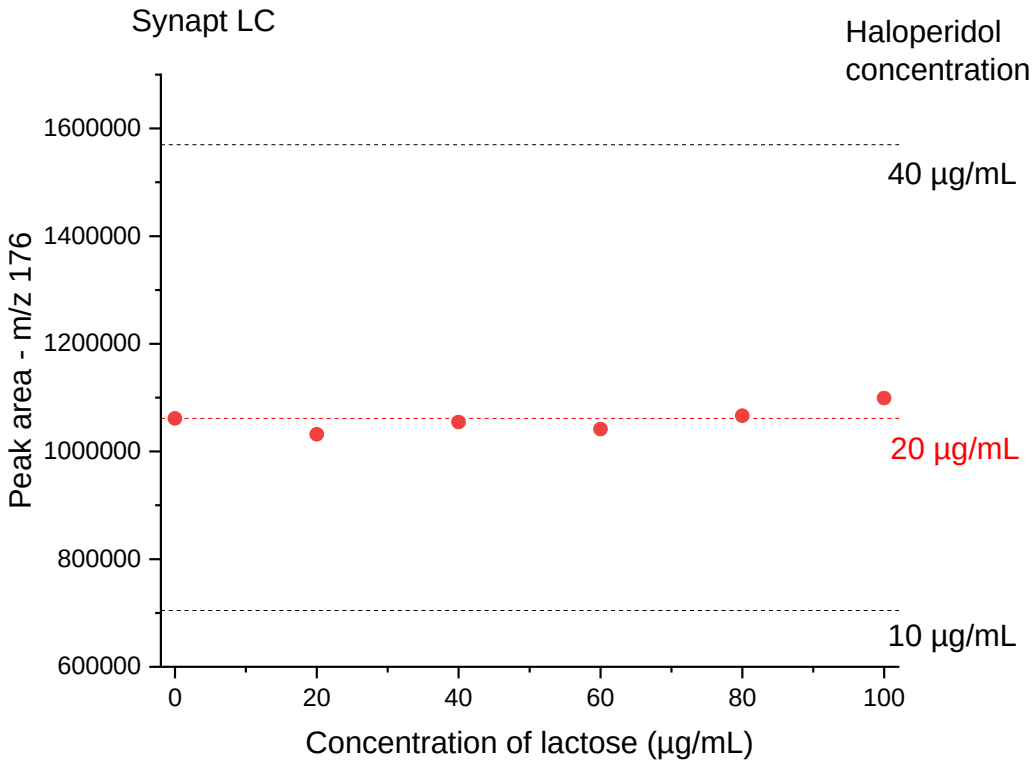

Figure 8.319 – Synapt LC data showing the effect of increasing the concentration of lactose upon the peak area (signal) obtained for haloperidol following an ES+ SIM channel of m/z 379 with LC applied to separate the components prior to ionisation. The concentration of haloperidol was kept constant at 20 µg/mL. Comparative signals obtained for haloperidol concentrations without lactose present are shown by the dashed lines, with a red line showing the concentration of 20 µg/mL, which is the same as that found in the solutions mixed with lactose, and two black lines showing 10 µg/mL and 40 µg/mL for comparison.

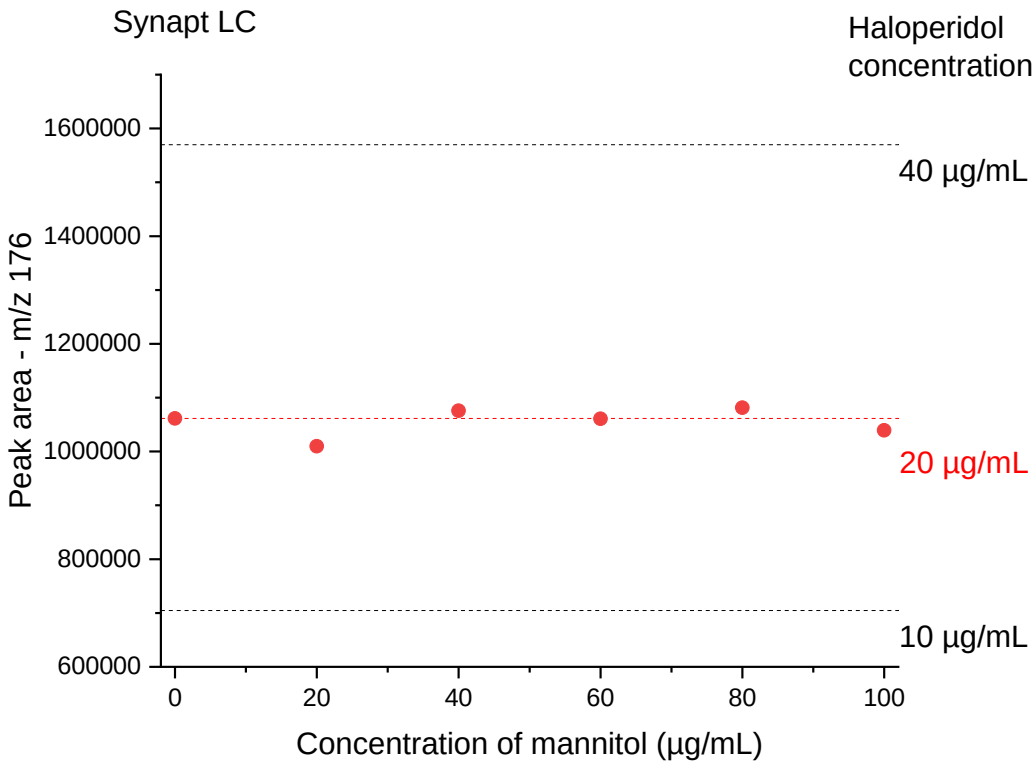

Figure 8.320 - Synapt LC data showing the effect of increasing the concentration of mannitol upon the peak area (signal) obtained for haloperidol following an ES+ SIM channel of m/z 379 with LC applied to separate the components prior to ionisation. The concentration of haloperidol was kept constant at 20 µg/mL. Comparative signals obtained for haloperidol concentrations without mannitol present are shown by the dashed lines, with a red line showing the concentration of 20 µg/mL, which is the same as that found in the solutions mixed with mannitol, and two black lines showing 10 µg/mL and 40 µg/mL for comparison.

The data has also been analysed for each excipient in combination with each API, with the haloperidol data obtained at a different time, hence it is plotted separately. Figure 8.321 and Figure 8.322 show the impact of each API upon lactose, and Figure 8.323 and Figure 8.324 show the impact of each API upon mannitol. There is clear variability in both the lactose and the mannitol data in combination with paracetamol and furosemide, with no consistent difference, as would be expected. The haloperidol data is less conclusive, with the data spreading above 40 µg/mL of excipient in both plots, although this is unlikely to be ionisation phenomena due to the very different retention times, see Table 8.39.

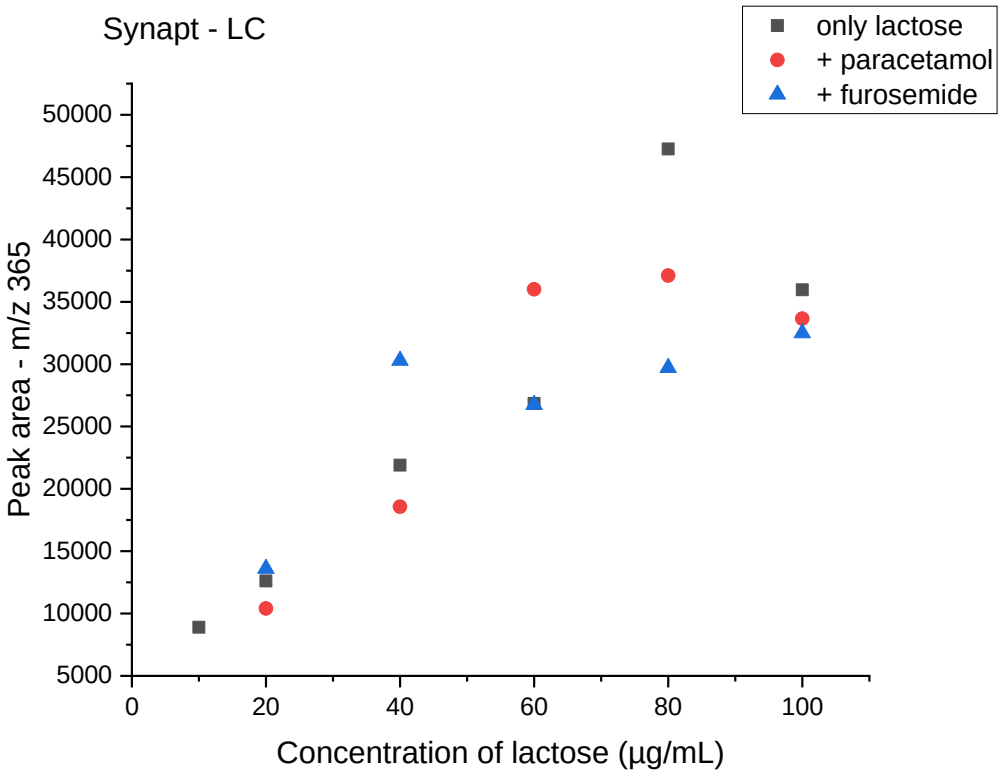

Figure 8.321 – Synapt data showing the peak area (signal) of increasing concentrations of lactose in solution with LC applied prior to ionisation, either alone (black squares), or with a concentration of 20 µg/mL of paracetamol (red circles) or furosemide (blue triangles). The SIM channel from which the signal was obtained followed m/z 365.

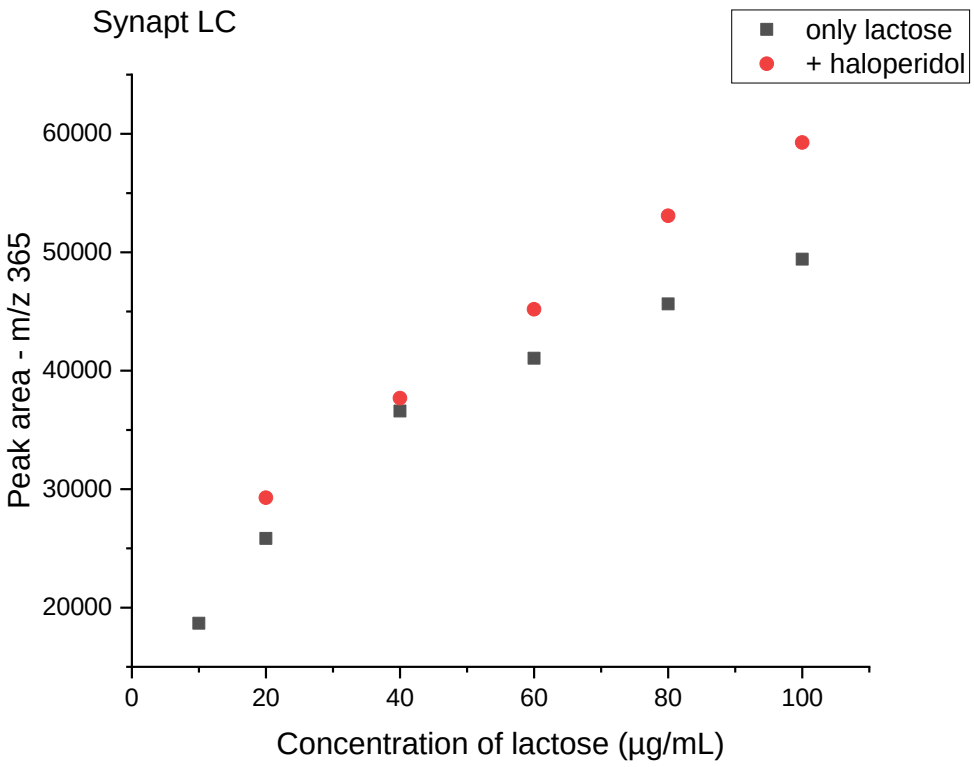

Figure 8.322 – Synapt LC data showing the peak area value (signal) of increasing concentrations of lactose in solution with LC applied prior to ionisation, either alone (black squares), or with a concentration of 20 µg/mL of haloperidol (red circles). The ES+ SIM channel from which the signal was obtained followed m/z 365.

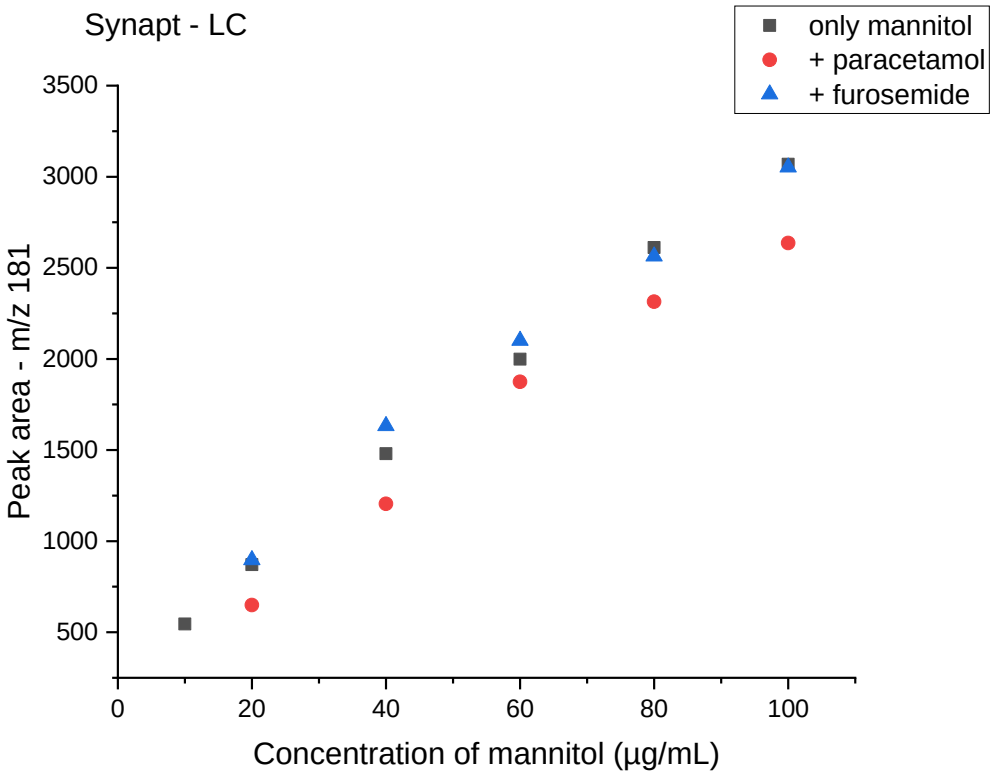

Figure 8.323 – Synapt data showing the peak area value (signal) of increasing concentrations of mannitol in solution with LC applied prior to ionisation, either alone (black squares), or with a concentration of 20 µg/mL of paracetamol (red circles) or furosemide (blue triangles). The ES- SIM channel from which the signal was obtained followed m/z 181.

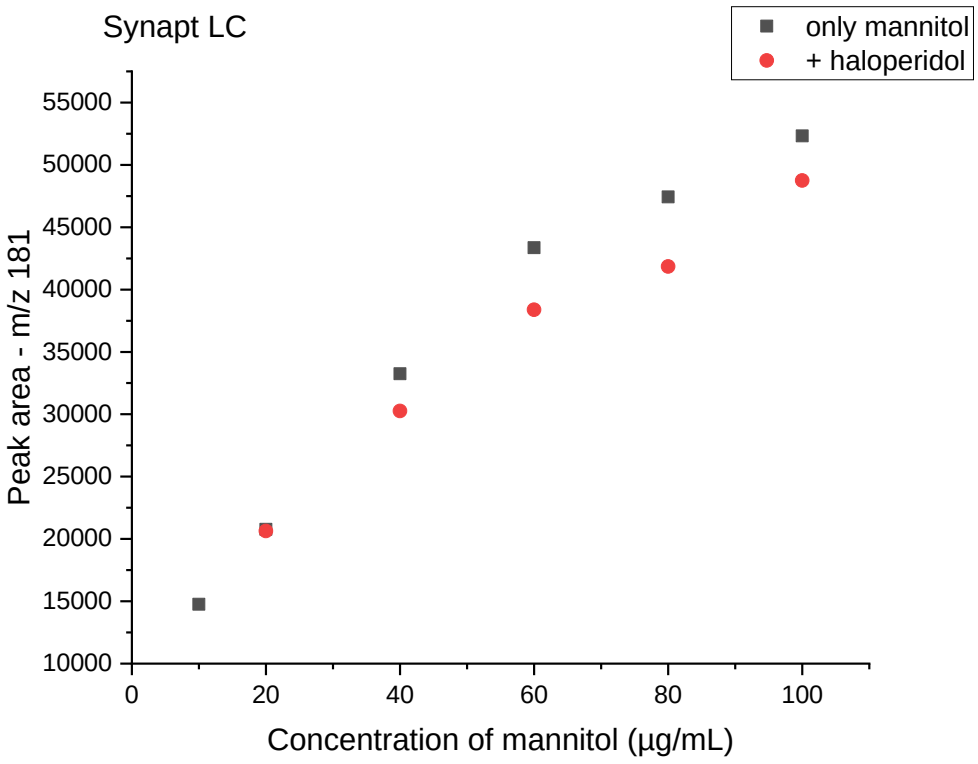

Figure 8.324 – Synapt data showing the peak area (signal) of increasing concentrations of mannitol in solution with LC applied prior to ionisation, either alone (black squares), or with a concentration of 20 µg/mL of paracetamol (red circles) or furosemide (blue triangles). The ES- SIM channel from which the signal was obtained followed m/z 181.

In summary, the LC data shows that each component is present in the mixtures of the solutions that have been made and can be isolated, ionised and monitored using LCMS analysis. It also confirms that there is inherent variation in signal, even in the absence of ionisation phenomena occurring, although the extent of this is not comparable between LC and LI analyses due to the differences in equipment set-up for each method.

8.3.1.5 Summary of aliquot MS analysis

This section of work uses a method that allows simple ionisation relationships to be observed and explored. The knowledge of each component's concentration in the solution allows for a greater understanding of the impact of co-ionisation. Maintaining a consistent concentration of API and varying the excipient concentration was useful for considering dissolution monitoring in terms of current dissolution requirements (API measurements), however, this work could be repeated varying the API concentrations with a consistent amount of excipient to expand understanding further

still, and ultimately the monitoring of true dissolution may result in varying concentrations of both API and excipient at the same time. There are significant differences in the quantity of signal obtained through LC and LI analyses, which confirm that these cannot be compared or used in combination for quantification purposes. There are also differences in the sensitivity of each instrument that likely result in different signal variation and therefore different conclusions as to whether they are sufficient to indicate ion suppression or enhancement. The aliquot MS data highlights the importance of understanding each relationship in isolation, as well as each relationship and how it changes across a range of concentrations for each component.

If unlimited resources, including time and access to equipment were available, running all the experiments in triplicate on the same day would offer a more detailed and conclusive insight into the variation differences between components as well as between LI and LC runs. However, the data obtained is sufficient to conclude that each component is present in solution (LC data) and that ionisation phenomena are occurring when multiple components are ionised together (both sets of LI data). Overall, repetition of the data is required to improve confidence in the details of the conclusions drawn from this data. However, one can conclude that ionisation phenomena will certainly occur during dissolution monitoring if multiple APIs and excipients are ionised at the same time, and that the relationship between each set of components is likely to be different. Additionally, the data suggests that ionisation phenomena can impact upon more than one ion at the same time; these conclusions will be explored further using continuous flow analysis.

8.3.2 Continuous flow MS analysis

Aliquot analyses have proven useful in extracting understanding from simple relationships, however, they require extensive sample analysis and repetition to fully understand signal variability. This limits the ability to conclude that changes in signal are a result of ionisation phenomena rather than inherent to the ESI-MS process. This has been observed repeatedly in each section of work, with changing MS solvents, using different dissolution media and the addition of new formulation components.

Altering the equipment set-up to enable continuous flow monitoring may provide a better opportunity to visualise and quantify this variation in signal.

The equipment challenges associated with continuous flow MS analysis were outlined in Chapter 1. Introduction, and described in detail in Chapter 6. ESI-MS Equipment Set Up. The use of an MRA allows adjustment of the amount of sample reaching the QDa and thereby enables the upper limit of quantification and detector saturation to be avoided. The MRA settings are complex hence the dilution will be provided as a ratio, although the method works by repeatedly injecting an aliquot of sample (either 0.022, 0.100 or 0.300 µL) into a flow of make-up solvent. The Synapt is a high resolution and highly sensitive instrument, hence this exploratory work will be carried out using the QDa, which is more robust and less likely to sustain significant damage if high concentrations of sample were to accidentally reach the detector.

The work has been divided into sub-headings according to the components analysed, with a brief description of each method used as well as a summary of what can be concluded in relation to both equipment set ups and ionisation phenomena. The APIs associated with the Beechams® tablet dissolution have been discussed first, both alone and in combination, before the two excipients and two additional APIs (chloramphenicol and haloperidol) are discussed.

8.3.2.1 API: paracetamol

A solution of 0.03 mg/mL paracetamol in MS solvent (water and acetonitrile 50:50 v/v without modifier) was run continuously into the QDa while altering a range of settings to further explore signal stability. The flow into the QDa was set to an optimal 0.5 mL/min with the MRA dilution at 1:31 (sample injection of 0.300 µL at 0.833 Hz) using MS solvent (without modifier). Figure 8.325 shows only the first four minutes, which highlight a fluctuating paracetamol signal. The start of QDa recording was staggered to coincide with flow through the MRA and tubing, so that there was no time lag, however, the signal looks to be increasing gradually and does not appear to have reached maximum ionisation efficiency by the end of the four minutes of recording.

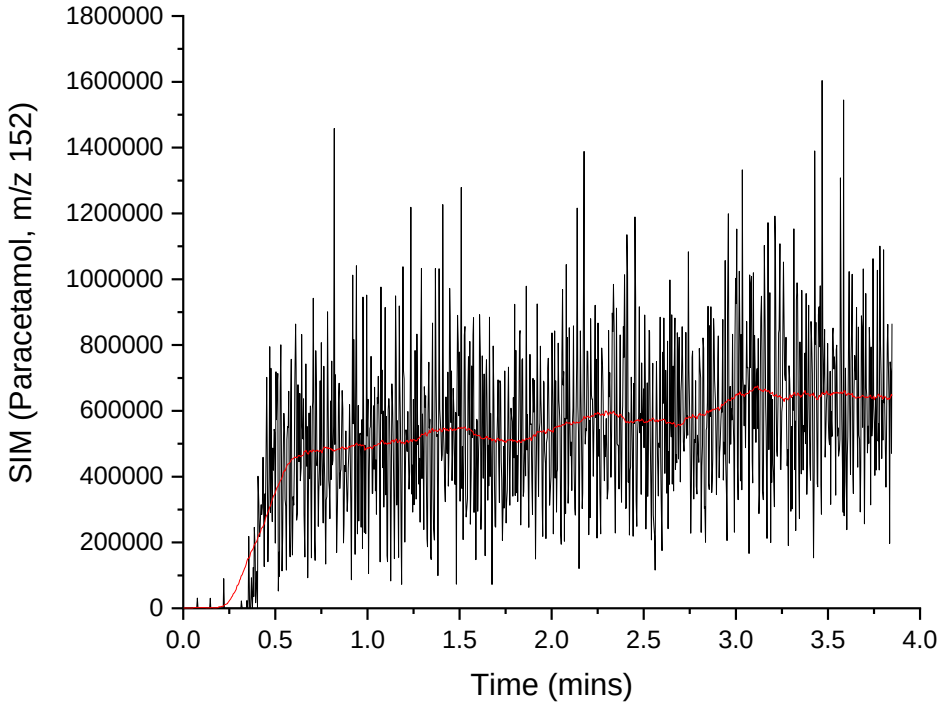

Figure 8.325 - QDa SIM at *m/z* 152 following paracetamol dissolved in water and acetonitrile by continuous flow analysis with a 100 point moving average represented by the red line.

The method was continued so that the signal might stabilise, and this appeared to occur after ten minutes of continuous flow. A five minute snapshot of the stabilised signal can be found in Figure 8.326 and in addition to the moving average, this time plotted as a green line, the mean signal has been plotted in orange, the maximum in blue and minimum in red. This confirms that the paracetamol signal continues to fluctuate and that the initial Figure 8.325 shows a much reduced signal, highlighting the importance of monitoring the signal for a period of time to avoid misinterpretation.

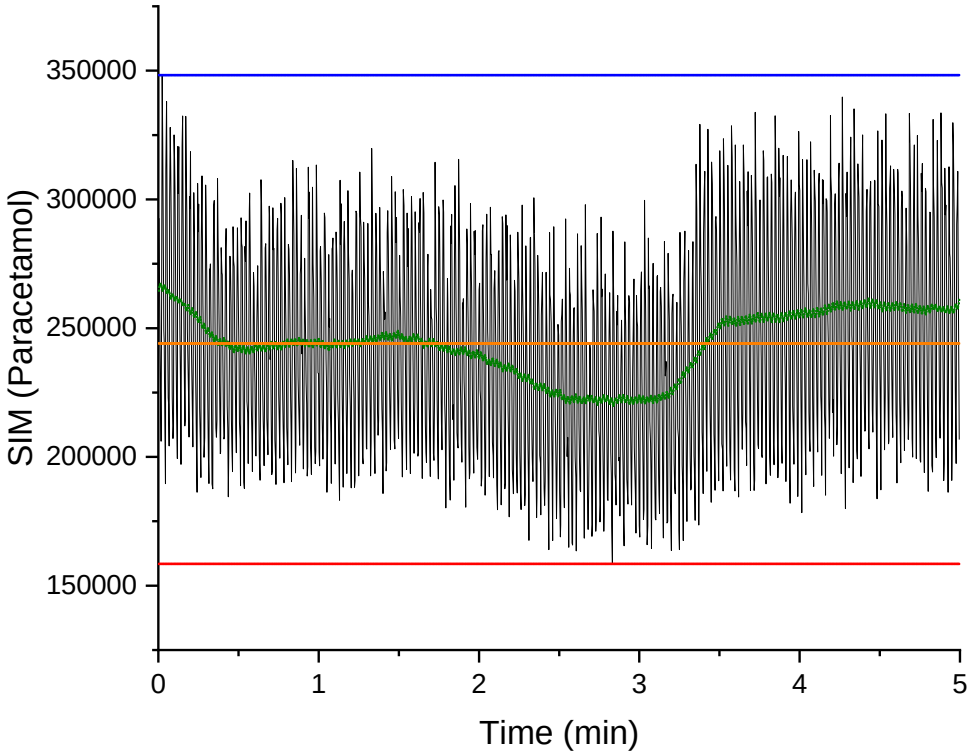

Figure 8.326 – QDa SIM at *m/z* 152 following paracetamol dissolved in water and acetonitrile by continuous flow analysis with a 100 point moving average represented by the green line.

The impact of changing capillary voltage, cone voltage and probe temperature upon paracetamol signal, inclduing their effect on fragmentation, was assessed as a means to expore how easily changes could be visualised using continuous flow monitoring. The following are snapshots from changing each variable and allowing the signal to stabilise for the new settings. Figure 8.327 highlights the impact of changing capillary voltage upon paracetamol signal. Detailed analysis of the spectra showed that paracetamol fragmentation (producing the known product found at *m/z* 110) was absent using a capillary voltage of 0.5 kV, however, ionisation efficiency was poor as seen by the scale of the signal observed. An increase in capillary voltage clearly increases ionisation efficiency as seen by the signal observed for both 1.0 kV and 1.5 kV, and the difference in fragmentation was consistent between these two, suggesting that 1.5 kV is an appropriate capillary voltage to maximise efficiency of the paracetamol signal without compromising fragmentation.

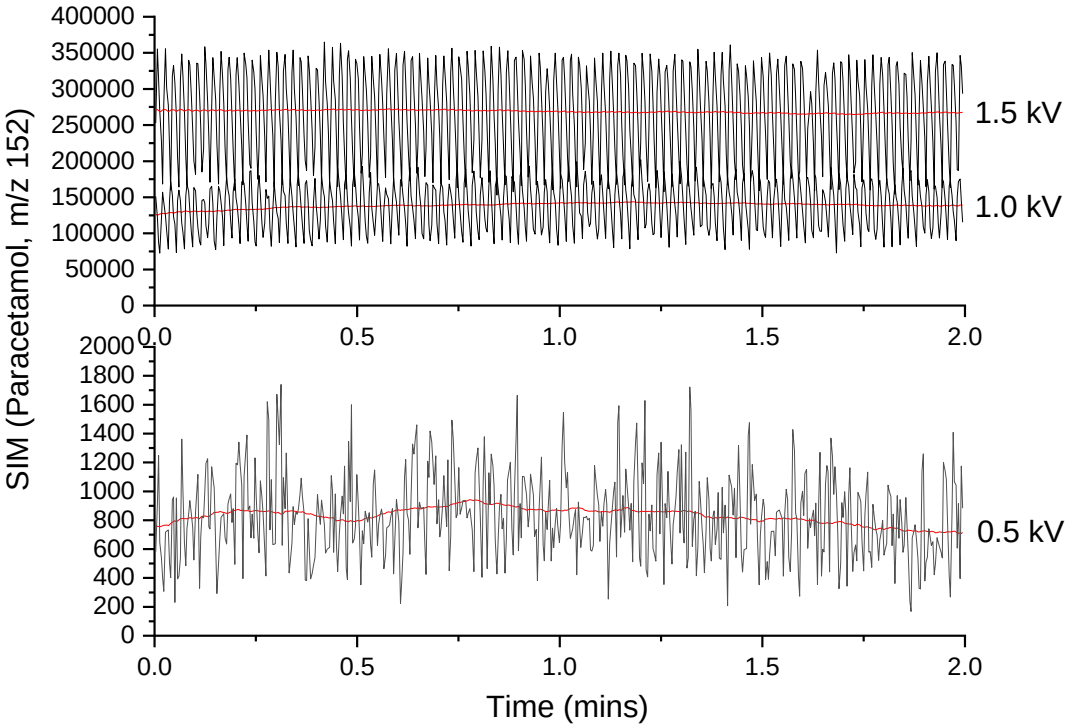

Figure 8.327 – QDa SIM at *m/z* 152 following paracetamol dissolved in water and acetonitrile by continuous flow analysis with a 100 point moving average represented by the red line. The top plot shows a capillary voltage of 1.0 and 1.5 kV, with the bottom plot set to a different scale y-axis in order to show a capillary voltage of 0.5 kV.

Figure 8.328 shows how altering cone voltage can impact upon paracetamol ionisation and confirms that such a change can be observed through the continuous monitoring of signal. A cone voltage of 20 V was selected as a compromise, providing a less variable signal in comparison with 10 V and an improved signal to noise ratio when compared with 50 V as a result of reducing fragmentation of paracetamol. Note that a cone voltage of 75 was also explored and paracetamol signal at *m/z* 152 found to be completely absent suggesting that it had all undergone fragmentation at such a high setting.

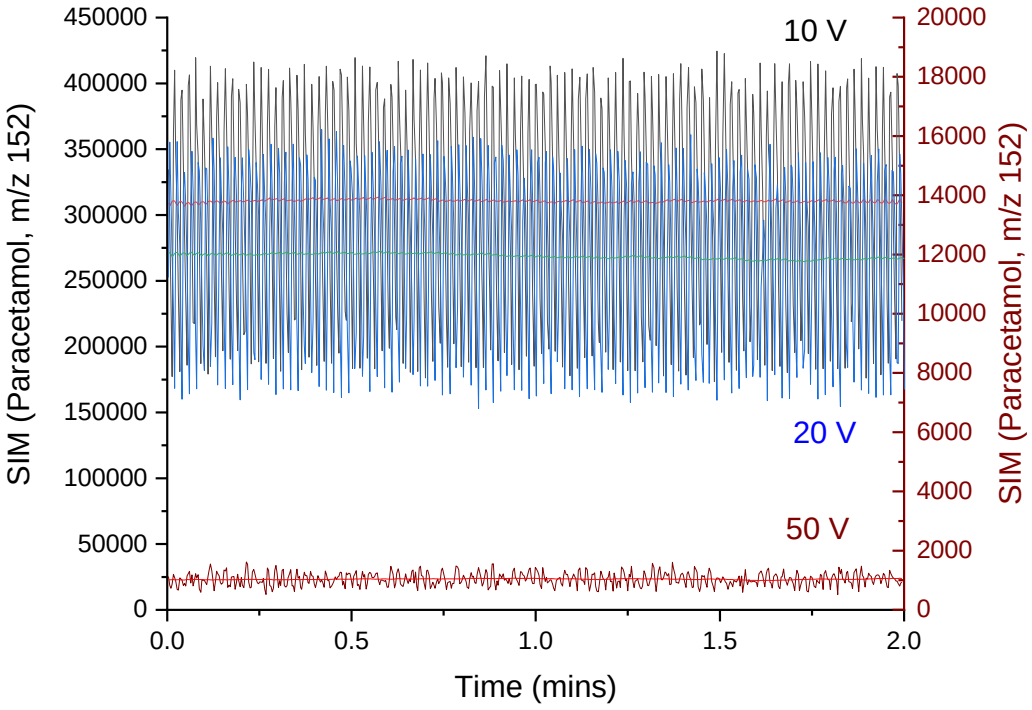

Figure 8.328 – QDa SIM at *m/z* 152 for continuous flow analysis of paracetamol dissolved in water and acetonitrile comparing the ion current intensity observed for three cone voltage values. Cone voltages of 10 and 20 are shown using the left black axis, with 50 V shown using the right red axis. Each set of data includes its own 100 point moving average represented by the top red line for 10 V, green line for 20 V and bottom red line for 50 V.

The probe temperature was also observed to impact upon signal and could be monitored easily through continuous flow analysis; Figure 8.329 shows the range of temperatures that were explored and the subsequent effect on signal as measured by SIM (*m/z* 152). The challenge associated with applying a high temperature are that desolvation may occur too quickly, which can result in a pulsing signal.[235] This risk would theoretically be reduced with less volatile solvents such as water and so a higher probe temperature may in that case prove to be useful. At lower temperatures, reduced (and less rapid) desolvation occurs, which leads to clusters of solvent molecules increasing the background noise and therefore lowering sensitivity, particularly for low molecular weight compounds. The lower temperatures therefore show a reduction in signal and when the mass spectra are explored in further detail, a significant improvement in signal to noise can be seen above 400°C confirming that a temperature above this is preferable.

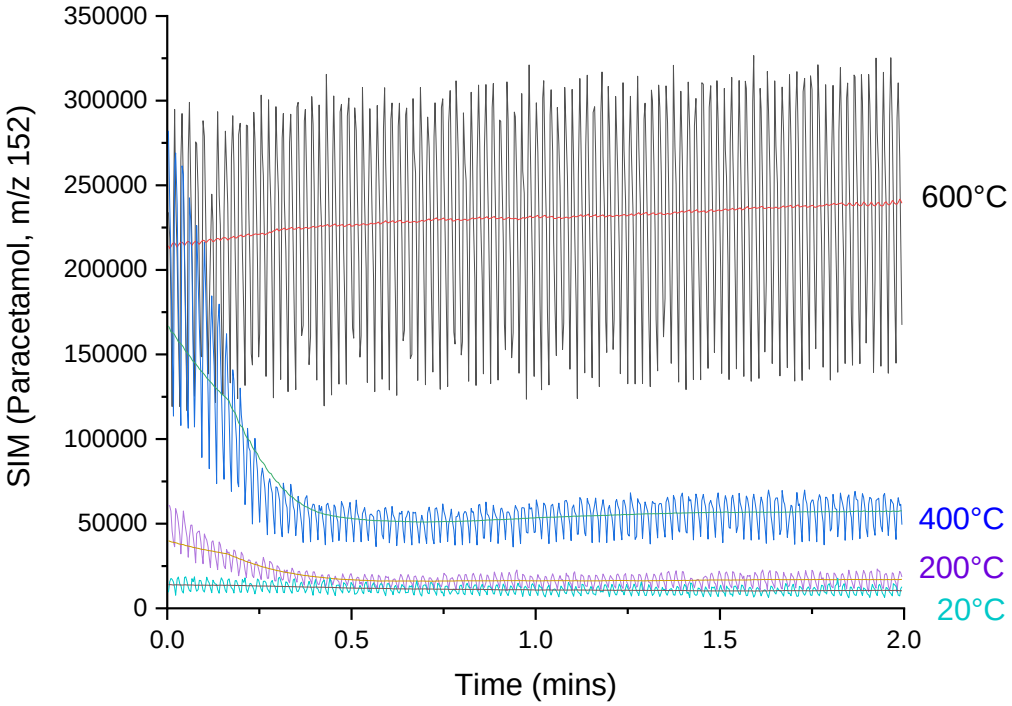

Figure 8.329 – QDa SIM at *m/z* 152 for continuous flow analysis of paracetamol dissolved in water and acetonitrile comparing the ion current intensity observed for four probe temperature settings: 20, 200, 400 and 600°C. Each set of data includes its own 100 point moving average, which can be seen running through the centres.

The QDa method used to monitor paracetamol signal was also explored to highlight the obvious impact it may have upon ion current. Paracetamol dissolved in water was analysed by the QDa through one of three methods: a) one SIM method only following *m/z* 152, b) full scan (ES+) only with paracetamol extracted using *m/z* 152, and c) one SIM method (*m/z* 152) alternating with a full scan (ES+). The data has been plotted in Figure 8.330 and shows that the ion intensity changes dependent upon the method as would be expected. This has implications for monitoring ions and requires the number of SIM methods used to be consistent between initial runs to monitor only one ion and subsequent methods following multiple ions if comparisons are to be drawn and these are to be used for quantification.

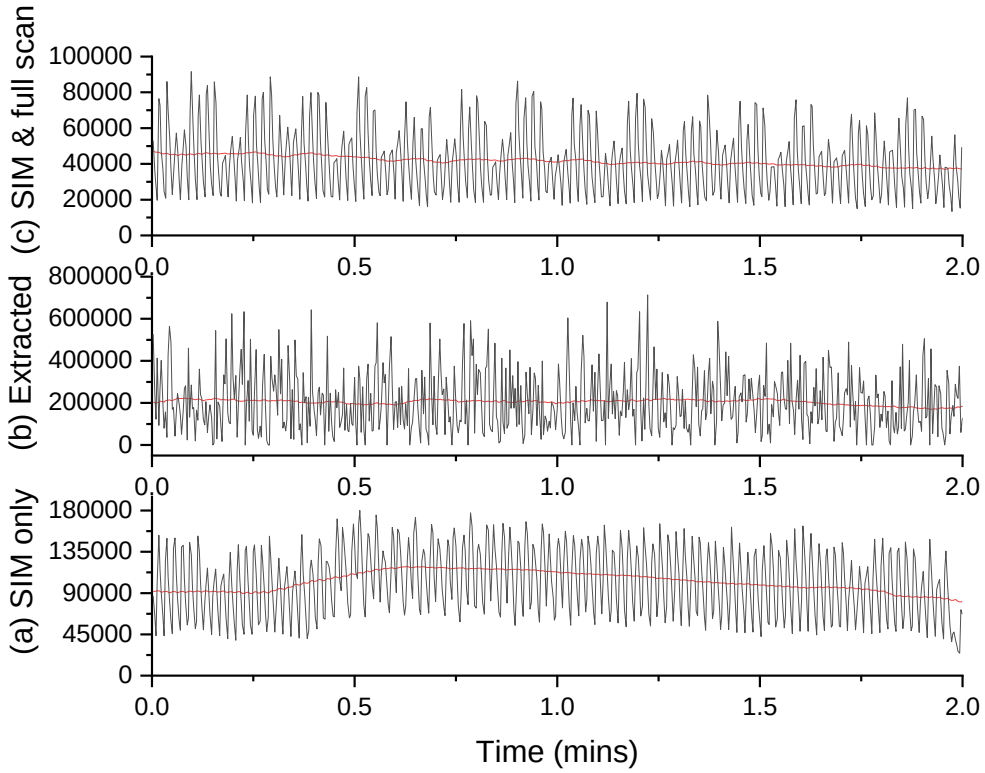

Figure 8.330 – QDa SIM and full scan data comparing ion current intensity with varying methods of following paracetamol signal: (a) SIM only, (b) extracted mass from a full ES+ scan and (c) SIM with full ES+ scan run in addition. Each set of data includes its own 100 point moving average, which can be seen running through the centres.

Finally, Figure 8.331 shows clearly the impact of changing solvents upon paracetamol signal monitored by continuous analysis. A sample of 0.03 mg/mL paracetamol dissolved in water only was pumped into the QDa through the MRA to dilute it 1:31 (0.300 µL at 0.833 Hz) with MS solvent (water and acetonitrile 50:50 v/v without modifier). This time the QDa was started at the same time to show once again the delay in efficient ionisation when sample first arrives at the instrument. The signal then fluctuates for the next twenty minutes. At twenty minutes, the sample solution was stopped from flowing and blank MS solvent was run through the lines to clean them. This provided an opportunity to observe how long the paracetamol signal would take to reduce and eventually disappear. An initial increase in paracetamol signal was first seen after the twenty minute mark – this is most likely the result of increasing the amount of acetonitrile reaching the ionisation source, thereby increasing volatility and ionisation efficiency of any remaining paracetamol either in the source or in the tubing. The signal then rapidly reduces as any remaining paracetamol is cleaned

through, although it remains present even after almost ten minutes of blank solvent flowing. The solvent and method was allowed to continue for a further thirty minutes to fully clean the lines and source and prevent any cross-contamination for future experiments.

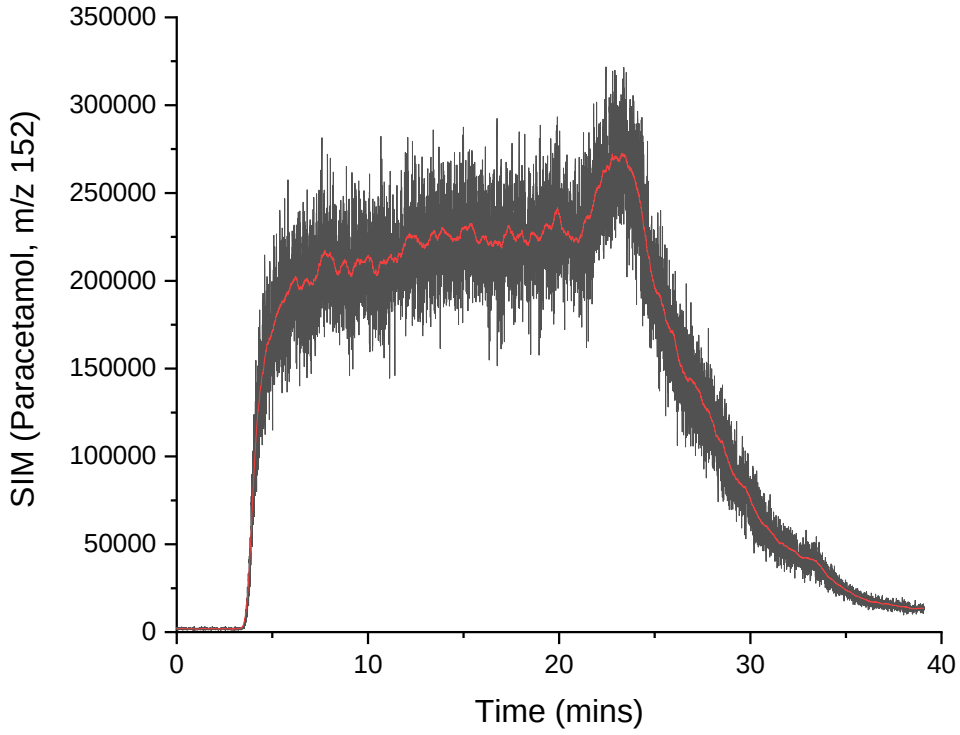

Figure 8.331 - QDa SIM at *m/z* 152 for continuous flow analysis of paracetamol dissolved in water diluted with MS solvent (water and acetonitrile 50:50 v/v). Flow of the sample was stopped at 20 minutes and a mixture of only MS solvent allowed to continue to pass through to the QDa for the remaining period of time.

The importance of consistency in equipment settings and methods, in addition to the solvents used is highlighted with this section of work. It also suggests that the solvent in which the sample is dissolved can impact upon the ability to remove it from the fluidics and / or the source. A thirty minute run of solvent mix, containing both water and acetonitrile, to improve volatility and ensure removal of sufficiently soluble components, was used to clean the lines and ensure there was no cross-contamination between runs for paracetamol, but this will require consideration for less soluble and less easily ionisable components.

8.3.2.2 API: guaifenesin

Guaifenesin was studied using continuous flow MS to determine the stability of the signal on the QDa. Guaifenesin at a concentration of 12 µg/mL dissolved in water only was diluted 125:1 by the MRA (0.100 µL at 0.667 Hz) using MS solvent with modifier (water and acetonitrile 50:50 v/v with formic acid 0.1% v/v) and injected continuously at a flow rate of 0.5 mL/min for 30 minutes. Figure 8.332 shows the SIM chromatogram for guaifenesin with a 100 point moving average plotted in green. Guaifenesin injection was started at the same time that the QDa started scanning (at t = 0). The plot shows a gradual increase between zero and seven minutes; this is a result of the lag time from injection to reaching the QDa, which was experimentally-determined as approximately four minutes for this flow rate, and also highlights that time is taken for guaifenesin to be ionised efficiently once it reaches the MS. The signal overall is variable and shows an initial increase between five and ten minutes, and then an overall decrease between ten and thirty minutes. One explanation for this variability in signal could be a solvent mixing effect within the fluidics; the guaifenesin dissolved in only water will show reduced volatility compared with the diluting MS solvent containing acetonitrile and formic acid (in addition to water). The sample aliquot (0.100 µL) is injected roughly every 1.5 secs (0.667 Hz) into the flowing MS solvent, providing an opportunity for some mixing or spreading of the injected plug of sample to occur, but it is unlikely to mix completely prior to ionisation. This may result in guaifenesin ionisation efficiency varying within the run dependent upon the concentration and solvent mixture it reaches the source in. Subsequently there may be an accumulation of guaifenesin that is not able to be ionised remaining in the source, which will present as an additional reduction in signal.

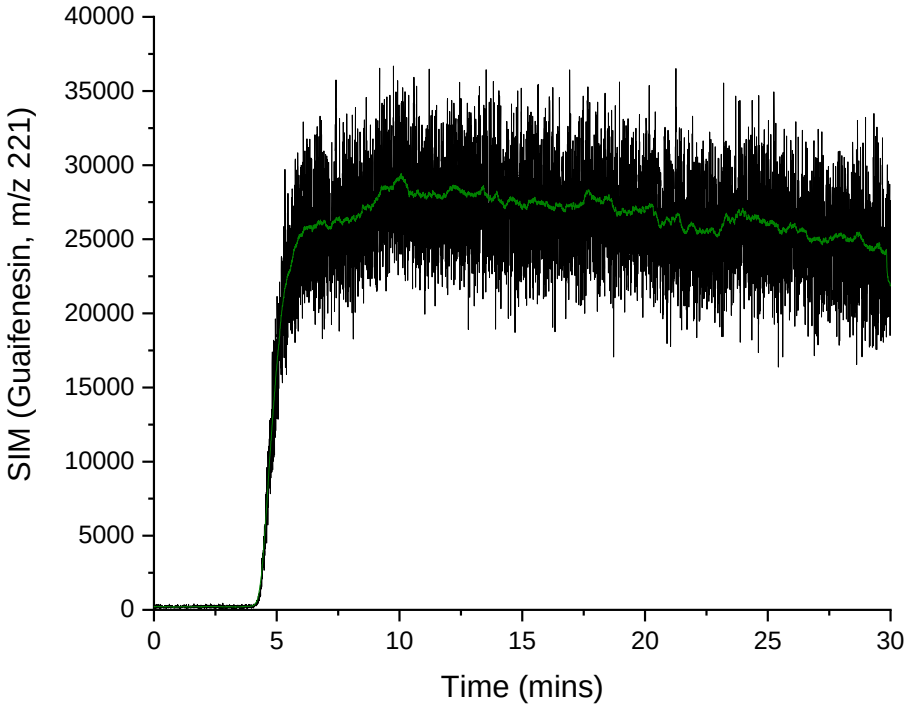

Figure 8.332 – QDa SIM at *m/z* 221 following guaifenesin dissolved in water by continuous flow analysis with a 100 point moving average represented by the green line.

The work was repeated with guaifenesin dissolved in water and acetonitrile 50:50 v/v and subjected to the same dilution with MS solvent as previously. Figure 8.333 shows the SIM chromatogram for guaifenesin with a 100 point moving average plotted in green. Injection of the sample started at the same time as the QDa began scanning, as before, at t = 0. A delay can be seen initially and the signal clearly fluctuates as shown by the moving average. In comparison with the previous signal, the initial increase takes only seven minutes instead of ten, the intensity of the signal is more than doubled and the moving average follows a repeating pattern of increasing and decreasing over approximately ten minute periods. The additional presence of acetonitrile in the original guaifenesin solution can therefore be concluded to improve overall ionisation efficiency likely through its increased volatility relative to water.[243] There is still signal variation suggesting that formic acid additionally improves upon the ionisation efficiency of guaifenesin, as this is unlikely to have the opportunity to spread evenly from the diluting MS solvent throughout the injection of sample prior to reaching the QDa.

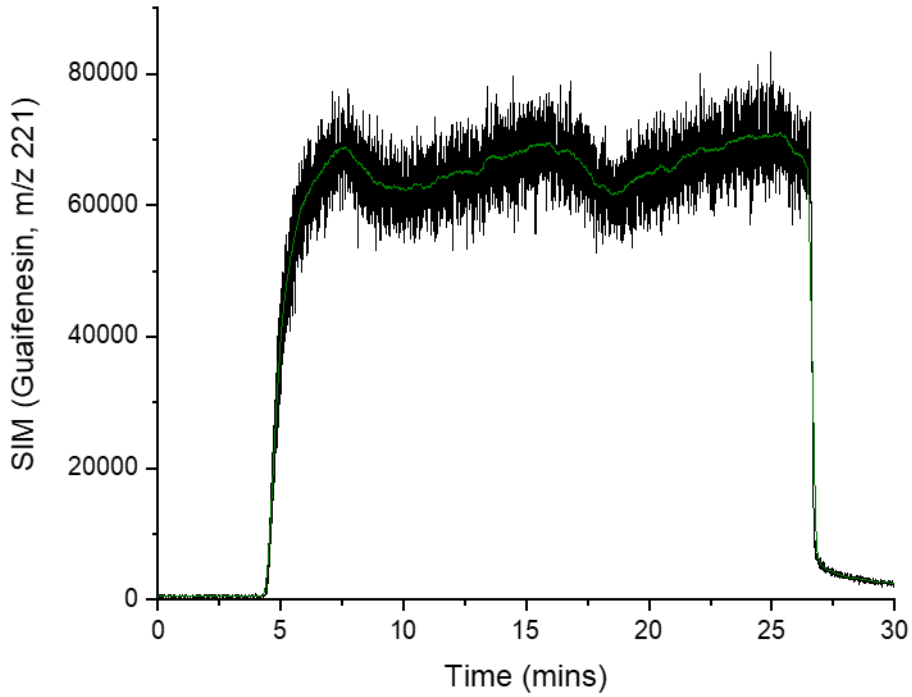

Figure 8.333 – QDa SIM at *m/z* 221 following guaifenesin dissolved in water and acetonitrile by continuous flow analysis with a 100 point moving average represented by the green line.

The flow of guaifenesin was stopped at t = 26.5 mins but the diluting MS solvent was allowed to continue flowing into the QDa at the same rate (0.5 mL/min). The signal can be seen to decrease almost instantly, but it does not return to the baseline seen between zero and four minutes. MS solvent was continuously flowed through the MRA into the QDa, and further analysis showed that it took an additional ten minutes of MS solvent running continuously to return to the baseline suggesting that guaifenesin must accumulate in the ionisation source and / or in the tubing between the MRA and QDa. This accumulation could also account for the variation in signal and the overall reduction seen in Figure 8.332. An additional consideration is that insufficient desolvation conditions (low temperature and / or insufficiently volatile solvents) may result in guaifenesin accumulation within the ionisation source that may then undergo degradation; the degraded sample may additionally compete for charge or alter surface activity of the droplets and therefore inhibit its own ionisation resulting in suppression of the signal.[329] This is one explanation for the variation in signal, however, the most likely is the variation in solvent volatility due to insufficient mixing time prior to ionisation; this results in varied solvent compositions and

therefore varied ionisation efficiencies of guaifenesin, which was shown in the previous chapter to be sensitive to ion suppression.

8.3.2.3 API: phenylephrine

A solution of phenylephrine in only water was analysed continuously by the QDa to understand its variability over time, see Figure 8.334. The MRA was again used to dilute the phenylephrine sample by 125:1 (0.100 µL at 0.667 Hz), this time with MS solvent without a modifier (water and acetonitrile 50:50 v/v). Flow of the sample started as the QDa began scanning, hence the characteristic delay can be observed between zero and five minutes. The delay is comparable with that seen for guaifenesin and suggests that time is again taken for efficient ionisation.

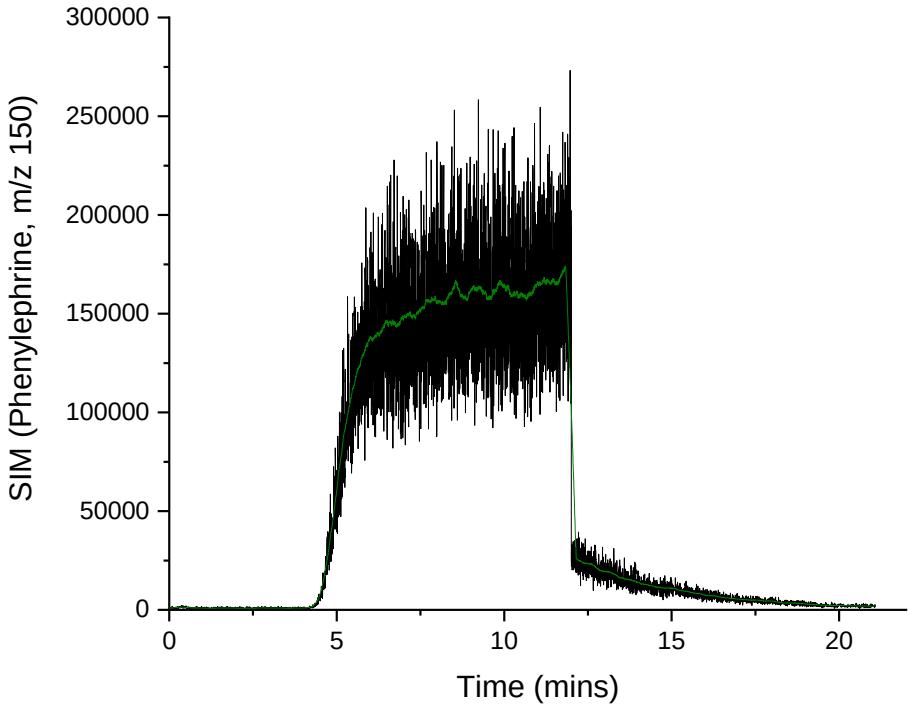

Figure 8.334 – QDa SIM at *m/z* 150 following phenylephrine dissolved in water by continuous flow analysis with a 100 point moving average represented by the green line.

The signal increases gradually and continuously fluctuates until the flow of the solution is stopped at 12 minutes. The diluting MS solvent continues to flow and the signal can be seen to reduce suddenly but it takes an additional 15 minutes for the signal to return to the baseline of zero, suggesting that phenylephrine may also accumulate in the tubing and / or in the ionisation source. The moving average shown in green also suggests that the signal may still have been increasing when flow of the sample was

stopped at 12 minutes. The phenylephrine sample was dissolved only in water, which was seen with the guaifenesin examples (Figure 8.332 and Figure 8.333) to impact upon ionisation efficiency and may result in greater signal variability overall. It is therefore important to allow sufficient time for the signal to stabilise, although this may vary depending upon the component being monitored, the solvents used and the presence of any modifier (e.g. formic acid).

8.3.2.4 API plus API: paracetamol and guaifenesin

A sample of water was run continuously into the QDa at 0.5 mL/min using the MRA to dilute it 1:125 (0.100 µL at 0.667 Hz) with MS solvent (water and acetonitrile 50:50 v/v without modifier). The QDa was set to a full scan ES+ method with two SIM channels, and after ten minutes a small volume sample of guaifenesin dissolved in water was mixed into the original water sample to make a solution 0.122 mg/mL. Ten minutes later a small volume sample of paracetamol (dissolved in water) was also added to the sample and mixed thoroughly to make a solution of 0.5 mg/mL. The concentrations were intended to mimic those that might be found at completion of the dissolution of a Beechams® tablet. Figure 8.335 shows the TIC, a SIM for guaifenesin (*m*/*z* 221) and a SIM for paracetamol (*m*/*z* 152).

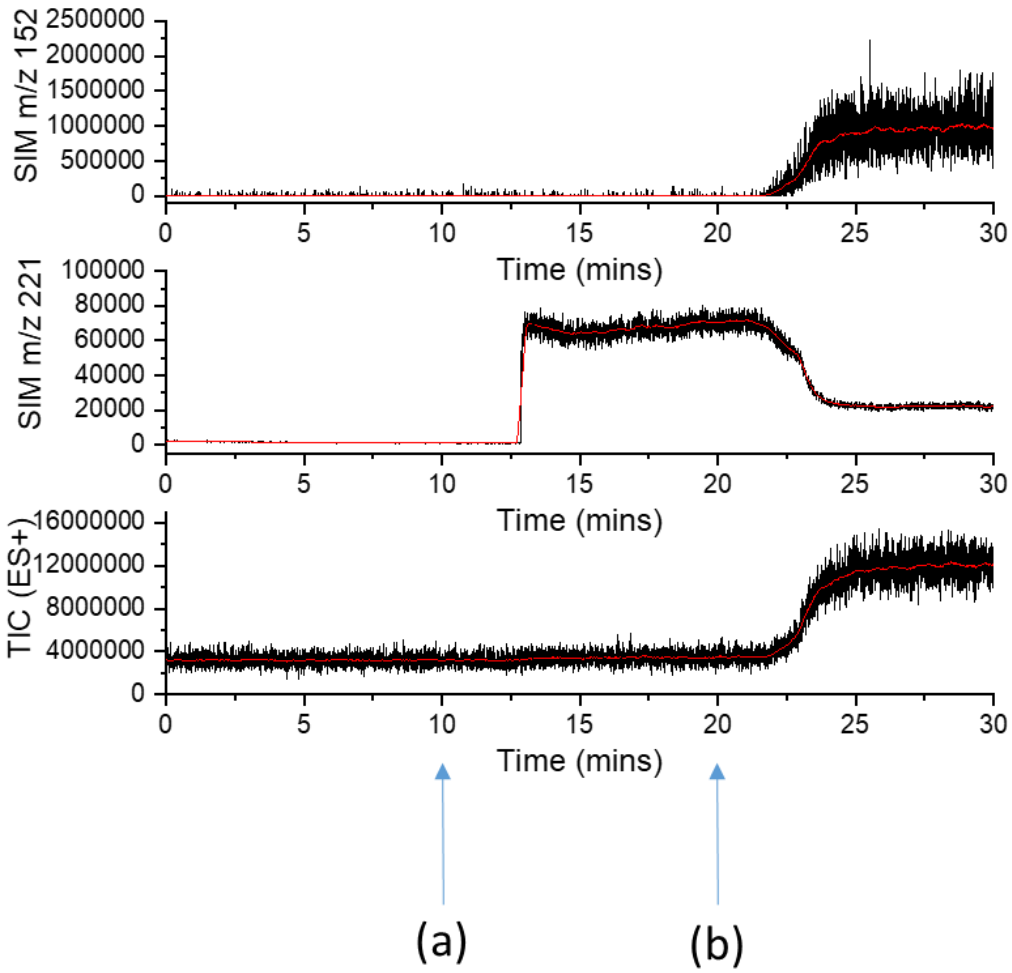

Figure 8.335 – QDa continuous flow monitoring following the TIC (ES+) and two SIM channels: guaifenesin (*m/z* 221) and paracetamol (*m/z* 152). The arrows highlight each component being added to the flowing water (a) guaifenesin and (b) paracetamol. Each set of data includes its own 100 point moving average, which is represented by the red line running through the centre of each plot.

Figure 8.335 shows the signal from ionisation of only water remains fairly stable with very little change upon the addition of guaifenesin, although the signal observed through the SIM channel for guaifenesin clearly increases as the sample moves through the fluidics, is ionised and reaches the detector. The addition of paracetamol, however, more than doubles the TIC signal observed and reduces the guaifenesin signal by two thirds. The delay between adding each component to solution and being detectable is in line with the previous work (approximately seven minutes). This experiment clearly shows that guaifenesin ionisation is suppressed by the co-ionisation of paracetamol.

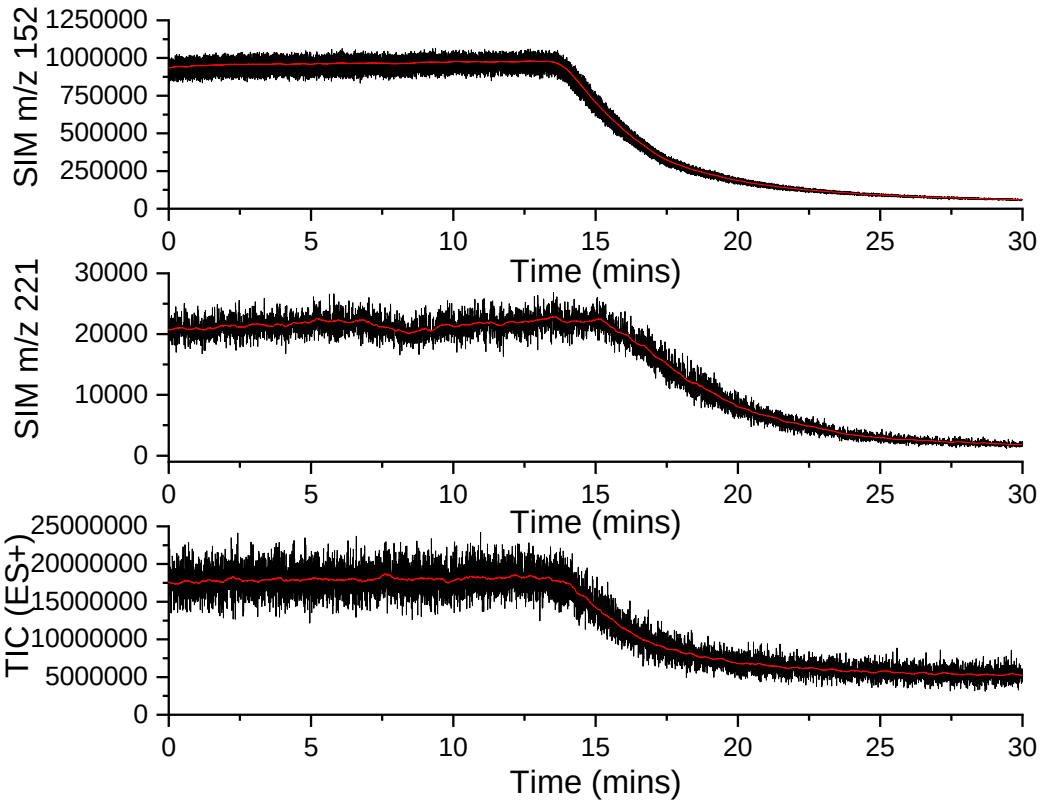

Figure 8.336 – QDa continuous flow monitoring following the TIC (ES+) and two SIM channels: guaifenesin (*m/z* 221) and paracetamol (*m/z* 152). Each set of data includes its own 100 point moving average, which is represented by the red line running through the centre of each plot.

The sample flow was maintained and another QDa method run straight after the first. After ten minutes the sample flow was stopped and only make-up solvent allowed to pass through the lines, see Figure 8.336. The SIM signals and TIC remain consistent until fourteen minutes in the case of paracetamol and TIC, and just over fifteen minutes in the case of guaifenesin. The paracetamol SIM signal, and therefore the TIC signal, reduce more quickly than the guaifenesin SIM signal suggesting that there is less accumulation in the lines and / or ionisation source. Twenty minutes after the flow of sample is stopped, however, all three signals appear to have levelled out suggesting that there is negligible sample left either in the fluidics or the source and confirming that continuing the flow of make-up solvent for at least twenty minutes in the case of guaifenesin and paracetamol is effective in ensuring that there is little to no cross-contamination or carry-over between runs.

There is a subtle difference in the reduction of the paracetamol signal between the earlier work observed in Figure 8.331 and this work in Figure 8.336. In the case of the former, the paracetamol signal can be seen to increase initially as the QDa receives only the make-up solvent (water and acetonitrile 50:50 v/v) instead of paracetamol dissolved in water. This change from paracetamol dissolved in water to blank make-up solvent happens in both cases, however, there is no initial peak in the latter figure. The peak and the difference can explained by the relative increase in volatile acetonitrile reaching the QDa source, which is different in each example. In the former experiment with the initial spike the dilution was 1:31 with an aliquot of 0.300 µL injecting into the solvent flow at 0.833 Hz, however, in the later experiment without the spike the dilution was 1:125 with an aliquot of 0.100 µL injecting into the solvent flow at 0.667 Hz; the relative change to a make-up solvent containing 50% v/v acetonitrile will therefore be different in each case.

8.3.2.5 Multiple APIs: paracetamol, guaifenesin and phenylephrine

A sample of guaifenesin dissolved in water was run continuously into the QDa and monitored with a SIM method consisting of four channels: guaifenesin (*m*/*z* 221), lactose (*m*/*z* 365), paracetamol (*m*/*z* 152) and phenylephrine (*m*/*z* 150). Additional components were added at specific time points with Figure 8.337 showing the QDa continuous monitoring of three of these four SIM channels.

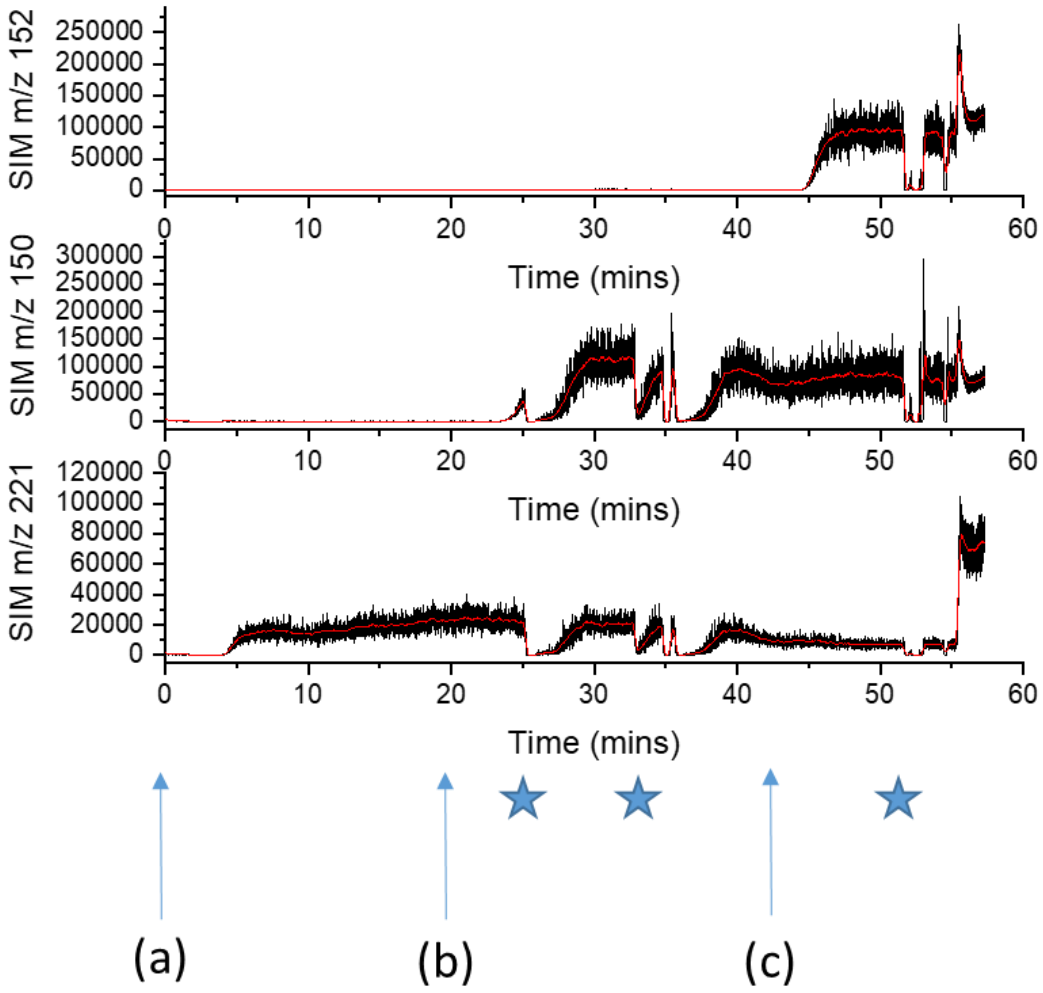

Figure 8.337 – QDa continuous flow monitoring following the SIM channels: guaifenesin (*m/z* 221), phenylephrine (*m/z* 150) and paracetamol (*m/z* 152). The arrows highlight each component being added to the flowing solution (a) guaifenesin, (b) phenylephrine, and (c) paracetamol. The blue stars highlight areas where air bubbles were visible in the flow of solution entering the QDa.

Twenty minutes after the guaifenesin solution was first injected a small volume sample of phenylephrine dissolved in water was added to the guaifenesin solution and mixed thoroughly. Twenty two more minutes later (forty two minutes after the start) a small volume sample of paracetamol dissolved in water was added to the same solution, and again mixed thoroughly. Each SIM channel clearly shows the point at which the relevant component is first detected - approximately five minutes after first being added to the solution. Guaifenesin signal appears to reduce as phenylephrine appears and reduces again when paracetamol appears, but there is a spike at the very end of the run, after 55 minutes. Phenylephrine signal also appears to reduce slightly as paracetamol appears but there are dips and spikes after 50 minutes. Unfortunately,

multiple air bubbles presented within the flow of solution entering the QDa, which led to very unstable signals at points (highlighted by the blue stars in Figure 8.337). The initial solution of guaifenesin in water was sonicated prior to using to remove as many air bubbles as possible, but the later mixing in of the additional components re-introduced air bubbles into the system. These could be seen passing through the fluidics but once present could not easily be removed and simply took time to pass, clearly disrupting the signal for each component and causing both spikes and dips. This limits the conclusions about ionisation phenomena, which can be drawn from this experiment, hence lactose was not added too, but highlights yet another important aspect of the experimental set up - careful exclusion of air bubbles.

8.3.2.6 API plus excipient: lactose and paracetamol

A sample of lactose dissolved in water was run continuously into the QDa via the MRA and set to a dilution factor of 1:1000 (0.022 µL at 0.385 Hz) with MS solvent (without modifier). A large dilution factor was used initially to explore the risk of lactose accumulation within the ionisation source. Three concentrations were studied initially: 0.01 mg/mL, 0.05 mg/mL and 0.1 mg/mL and each sample was run for twenty minutes in total. The lactose SIM channel included *m*/*z* 365 in addition to *m*/*z* 707, although at these concentrations and dilutions, no dimer was found, and only the sample at 0.1 mg/mL showed sufficient lactose signal for ease of monitoring (0.05 mg/mL was detectable but not consistent). The delay at the start of monitoring was removed by starting flow prior to acquiring the QDa data, see Figure 8.338. A moving average has been plotted, which shows the signal increase rapidly over a minute to then produce a more consistent signal, which can be seen to fluctuate slightly over the next two minutes of continuous data acquisition. It should be noted that the consistent peaks observed are due to the fluctuation from the MRA switching, hence the moving average has been included.

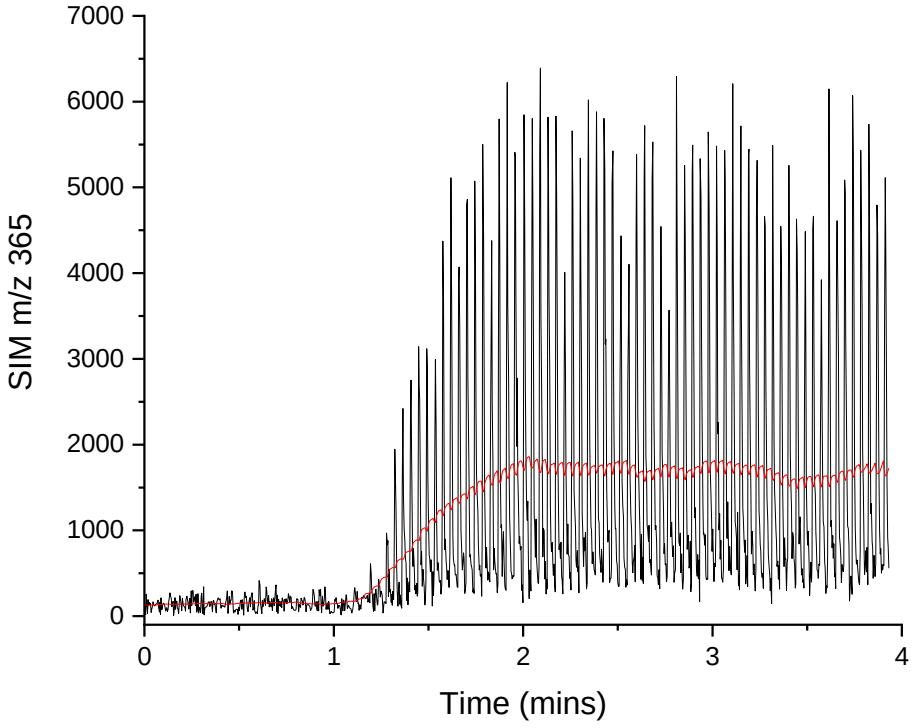

Figure 8.338 - QDa SIM at *m/z* 365 following lactose dissolved in water by continuous flow analysis with a 100 point moving average represented by the red line.

The moving average allows the signal to be monitored more easily, but the SIM signal can be seen to fluctuate significantly between counts of approximately 250 and more than 6000. A close up of the data points show that this is likely a combination of aliasing, the MRA switching and the differing ionisation efficiencies of lactose in the presence of either water or water with acetonitrile, see Figure 8.339.

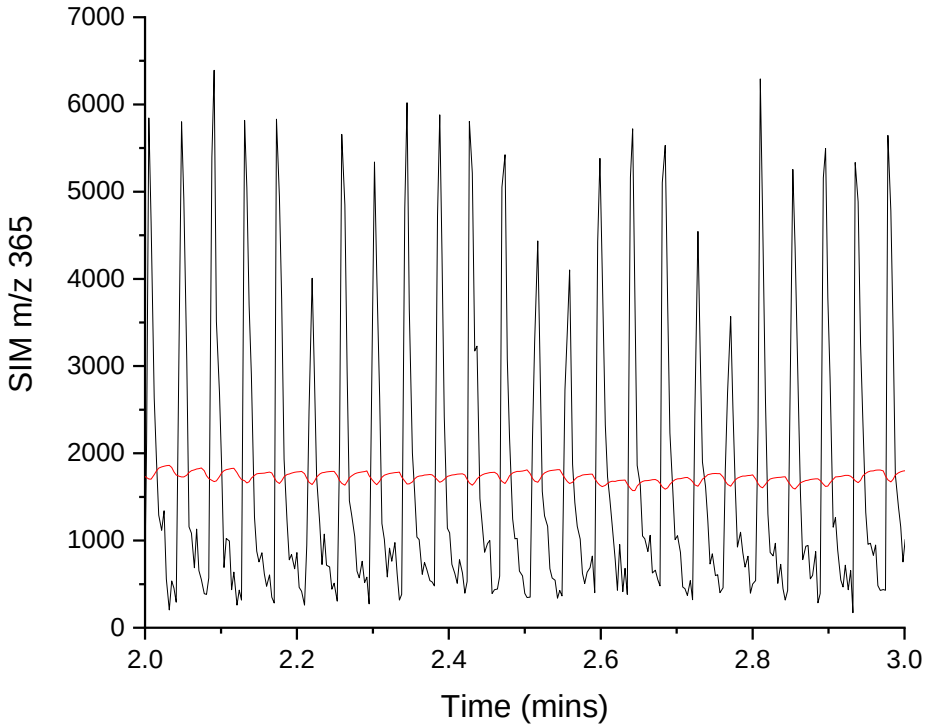

Figure 8.339 – QDa SIM at *m/z* 365 following lactose dissolved in water by continuous flow analysis with a 100 point moving average represented by the red line. This is a small section of the data from the previous plot, Figure 8.338.

There was found to be little to no accumulation of lactose within the source and the signal cleared quickly within five minutes of flowing only make-up solvent into the QDa. This provided reassurance for work at higher concentrations and lower dilution factors. A range of concentrations of lactose dissolved in water were again studied using continuous flow monitoring with the MRA set to a dilution factor of 1:31 (0.300 µL at 0.833 Hz) with MS solvent (without modifier). Figure 8.340 shows the SIM signal for lactose monitored over a period of two minutes with the moving average plotted for each data set.

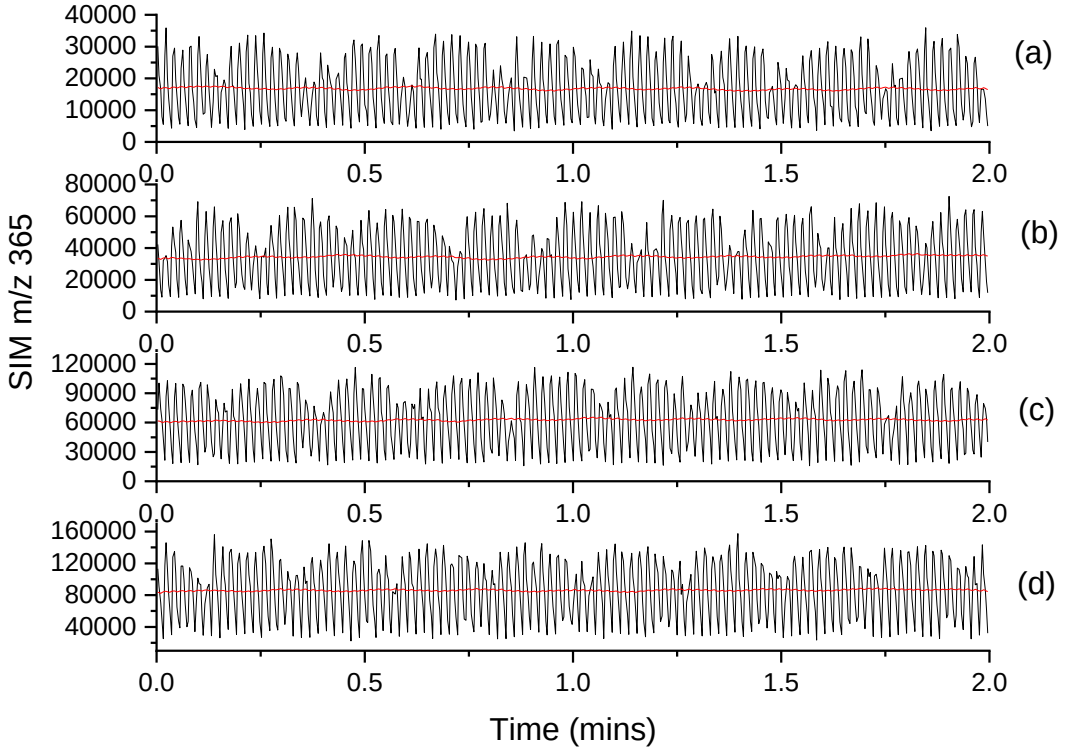

Figure 8.340 – QDa SIM at *m/z* 365 following lactose dissolved in water at four different concentrations monitored by continuous flow analysis with a 100 point moving average represented by each red line. The lactose concentrations are (a) 2.9 µg/mL, (b) 5.7 µg/mL, (c) 11.5 µg/mL and (d) 17.2 µg/mL and each is diluted 1:31 with make-up solvent.

The moving average is consistent for each concentration despite the fluctuation of the SIM signal. The extent of the fluctuation can be seen to increase as the concentration of lactose increases, however, and the minimum, maximum and mean values can be plotted as if to produce a calibration graph, see Figure 8.341. In summary therefore, although this set of data appears markedly different from the previous continuous flow monitoring analyses, sufficient information can be extracted to allow it to be utilised for quantification purposes.

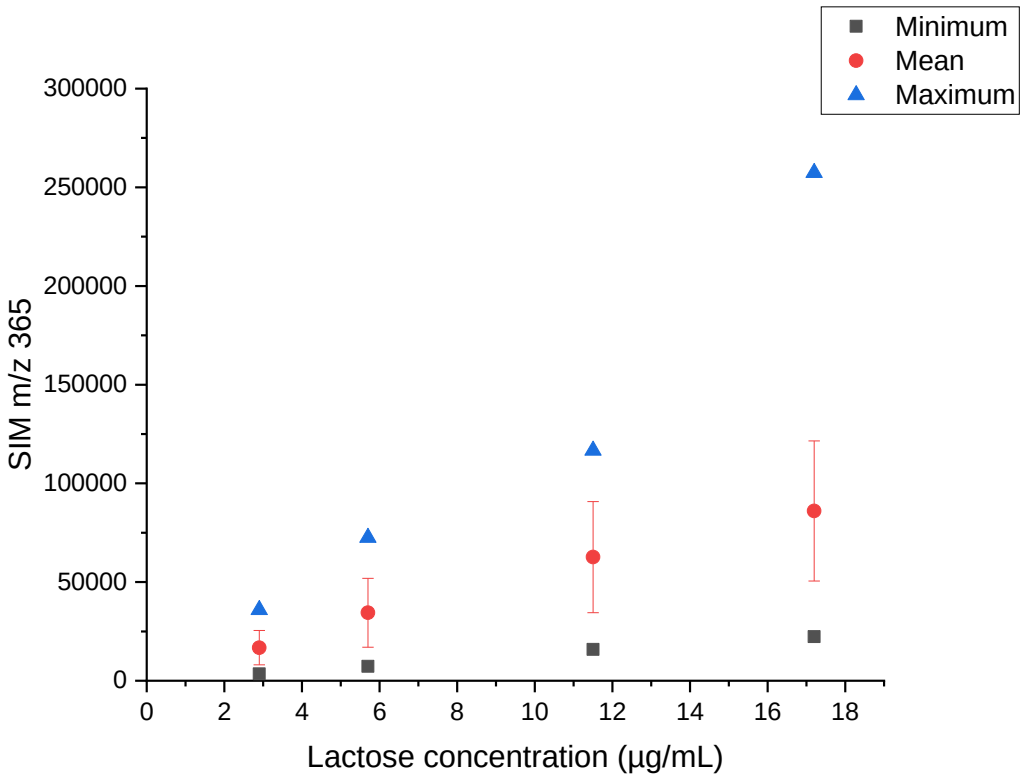

Figure 8.341 – QDa SIM at *m/z* 365 following lactose dissolved in water at four different concentrations monitored by continuous flow analysis. Each value has been calculated from the previous plot, Figure 8.340. The error bars associated with each mean point are the standard deviation from two minutes of continuous flow data.

It should be noted that this data cannot be directly compared with previous lactose calibration plots as the values have been extracted differently due to the continuous flow analysis. Additionally, the concentration of lactose plotted on the graph is the concentration present in the sample solution and does not account for the dilution factor of the MRA prior to QDa analysis. Nevertheless, this data was obtained at the same time as a series of samples of paracetamol mixed with lactose were analysed so as to observe whether the concentration of paracetamol and lactose could be calculated from the mixture using continuous flow analysis methods. The MRA settings were kept constant at a dilution factor of 1:31 (0.300 µL at 0.833 Hz) with a make-up solvent of water and acetonitrile (50:50 v/v) and flow into the QDa of 0.5 mL/min. A constant concentration of paracetamol dissolved in water (0.0292 mg/mL) was analysed in combination with a range of concentrations of lactose, and a summary of the results is presented in Figure 8.342.

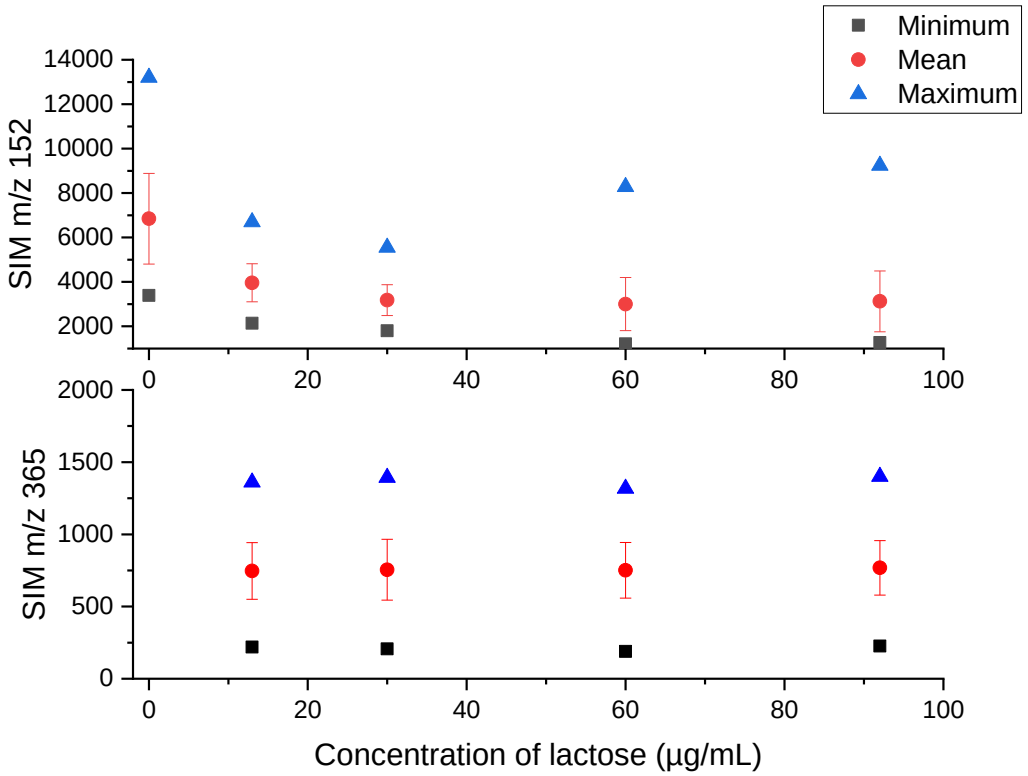

Figure 8.342 - QDa continuous flow monitoring of paracetamol (*m/z* 152) in combination with lactose (*m/z* 365) at a variety of concentrations (0, 0.013, 0.030, 0.060 and 0.092 mg/mL). Paracetamol was dissolved in water at a fixed concentration of 0.0292 mg/mL. Each data set was obtained from more than two minutes of continuous data acquisition. The top plot shows the paracetamol signal from each combination including an absence of lactose, and the bottom plot shows the lactose signal from the same combinations.

The paracetamol signal can clearly be seen to reduce in the presence of lactose – the paracetamol concentration in the sample did not change. This confirms that co-ionisation of lactose with paracetamol from a solution of water suppresses paracetamol ionisation. The extent of paracetamol suppression increases as lactose concentration increases, with signal reducing by more than half in combination with 0.092 mg/mL of lactose. The variability of the paracetamol signal also increases with increasing lactose, with the difference between the minimum and maximum observed signal widening and standard deviation for the mean increasing at increased concentrations of lactose. The signal observed for lactose, however, remains consistently low in the presence of paracetamol despite the concentration of lactose in the solution increasing and no dimer could be found at *m/z* 707. In comparison with the SIM *m/z* 365 values obtained for lactose ionised in isolation, see Figure 8.341, the values are significantly lower suggesting that it is not ionising effectively and may be

subject to ion suppression by paracetamol. The suggestion that co-ionisation of lactose and paracetamol results in suppression of both components is consistent with findings from the aliquot work with the QDa providing confirmation that both methods are able to provide useful data.

8.3.2.7 Excipient: mannitol

Blank water and acetonitrile 50:50 v/v was set to flow directly into the QDa at 0.5 mL/min and mannitol was added. The mannitol had previously been dissolved at a concentration of 1 mg/mL in water and acetonitrile 50:50 v/v so that aliquots of this "stock" solution could be added to the blank solvent mix to produce a sample of known concentration. The sample was mixed thoroughly after each addition so the process was felt to mimic dissolution but with known quantities and without the risk of undissolved solid entering the fluidics. Figure 8.343 shows the SIM method following *m*/*z* 205 in ES+ and highlights the time points at which two 5 µL aliquots of stock mannitol solution were added to the solvent mix. The plot confirms that it takes mannitol seven minutes from addition and mixing, to be ionised and detected by the QDa, but ten minutes for the signal to plateau suggesting it has reached maximum ionisation efficiency.

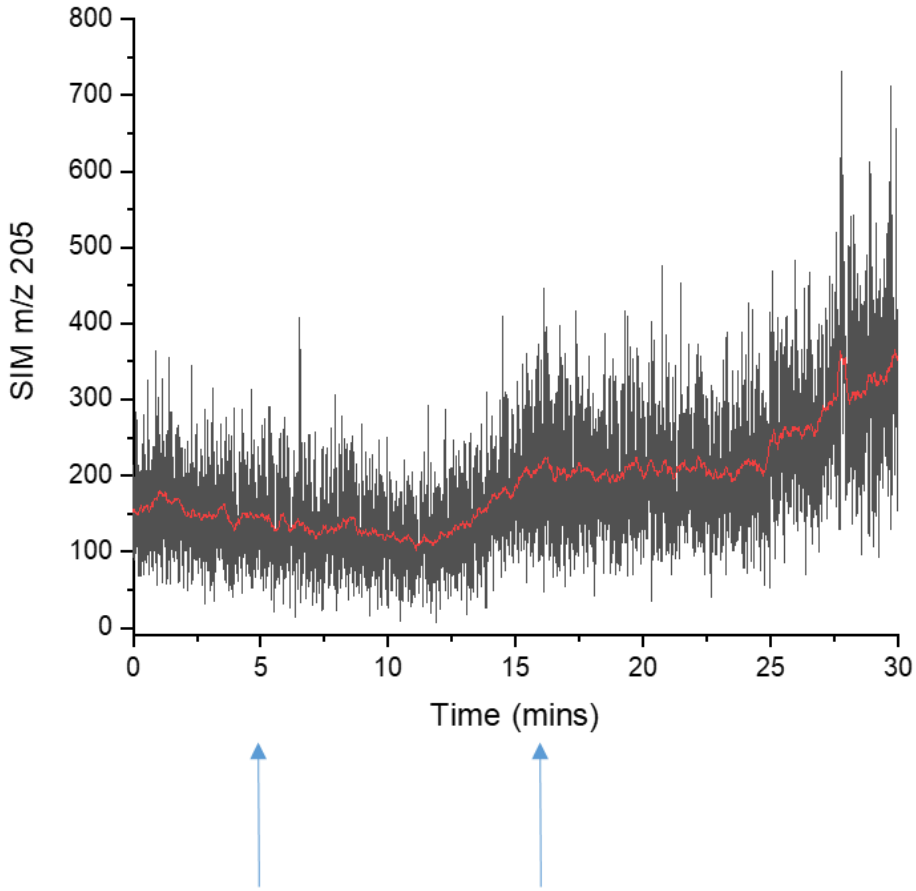

Figure 8.343 – QDa continuous flow monitoring of mannitol dissolved in water and acetonitrile 50:50 v/v using an ES+ SIM method following *m/z* 205. A 100 point moving average is represented by the red line and the blue arrows show the time of addition of the mannitol aliquots.

The concentration after 25 minutes was 0.25 µg/mL, but after a period of adding aliquots of mannitol and continuously monitoring the effect on mannitol signal, the concentration reached 20 µg/mL (0.02 mg/mL). The SIM signal increased gradually with each addition and reached a plateau at more than seventy times the signal seen for 0.25 µg/mL, for a concentration of eighty times this at 20 µg/mL, see Figure 8.344.

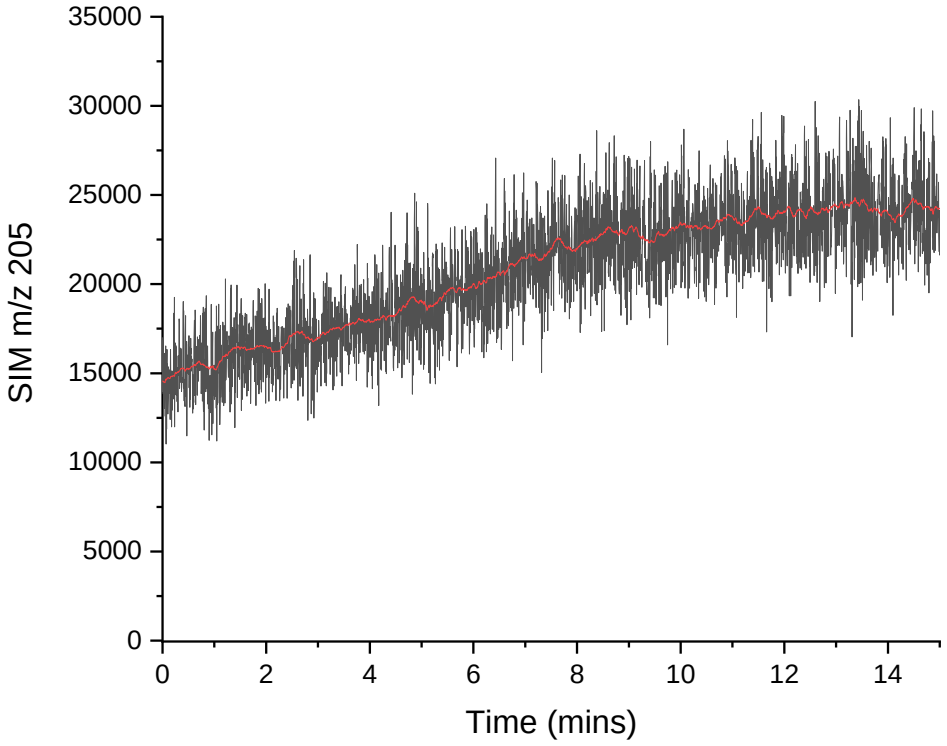

Figure 8.344 - QDa continuous flow monitoring of mannitol dissolved in water and acetonitrile 50:50 v/v using an ES+ SIM method following *m/z* 205. A 100 point moving average is represented by the red line. The concentration is increasing and therefore signal increasing; after twelve minutes the concentration is 0.02 mg/mL.

This confirmed that an increase in the concentration of mannitol in the sample, resulted in an increase in the SIM signal, which could be viewed on-line and in real-time without sample preparation. The delay between concentration changing in the sample and the SIM signal increasing on the QDa with this particular set up and for mannitol in these solvents, was seven minutes. An additional delay between first detection and reaching a maximum observable signal for each concentration also occurred and can be attributed to ionisation efficiency within the source. This meant that increasing the concentration resulted in an increasing signal but instead of this occurring in a step-wise fashion allowing signal to be easily correlated with concentration, it was visualised as a gradient increase. This more closely mimics what would likely be seen with true dissolution mointoring and highlights an important challenge associated with the technique: correlating signal with concentration at specific time points throughout the process.

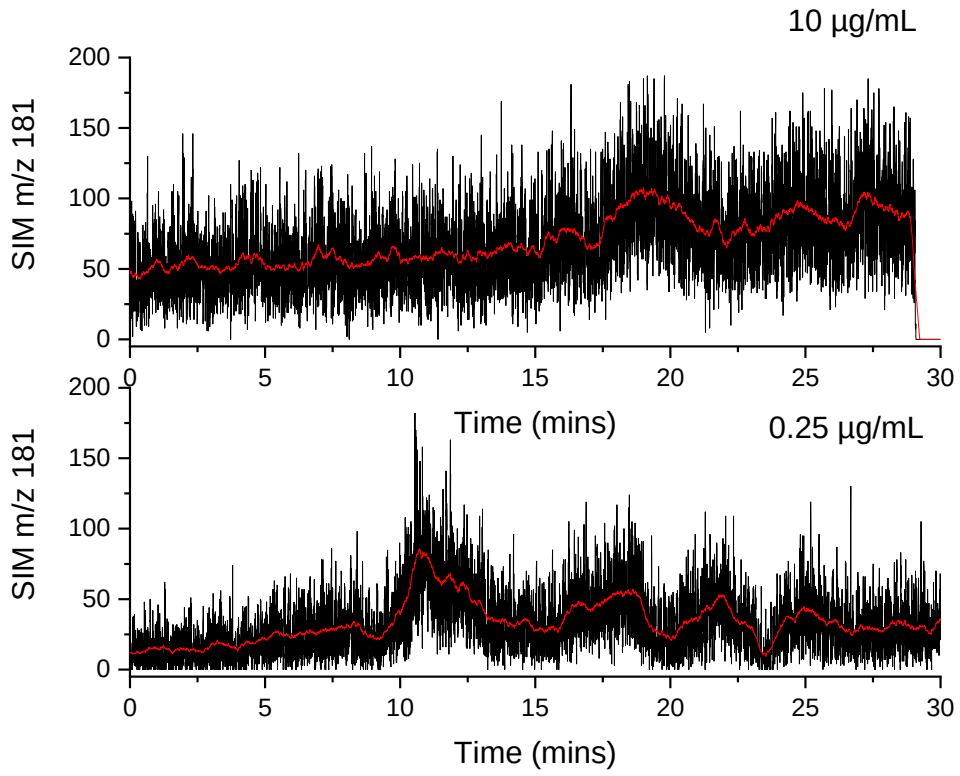

Figure 8.345 – QDa continuous flow monitoring of mannitol dissolved in water and acetonitrile 50:50 v/v using an ES- SIM method following *m/z* 181 comparing two concentrations: 0.25 µg/mL and 10 µg/mL. Each plot includes a 100 point moving average represented by the red lines.

A key point of interest from the initial work with mannitol was that it could be ionised and monitored in both positive and negative modes of ESI-MS, hence the work was repeated using an ES- method following *m/z* 181. The attempt to monitor the same initial concentration of mannitol through an ES- method proved to be more challenging, with much poorer ionisation efficiency in this mode. An increase in concentration to 10 µg/mL increased the signal very slightly, but it still remained unexpectedly low, see Figure 8.345. Increasing the concentration significantly higher risked overloading the source with a component that was not ionising efficiently and may be accumulating either in the source or in the fluidics under these conditions. Instead, an alternative component that could be monitored with ES- was analysed to explore whether the limitation may be a cause of experimental set up, method, a peculiarity of this component, the concentration or a combination of multiple factors.

8.3.2.8 API plus API: chloramphenicol and paracetamol

Chloramphenicol was found to be quantifiable using aliquot analyses in the ES- mode following *m/z* 321. A solution of 1 µg/mL in water and acetonitrile 50:50 v/v was continuously analysed by ES- using the QDa without the MRA in place, see Figure 8.346. The signal increases gradually after six minutes, suggesting that signifies the length of time taken to move from the dissolution bath to the QDa in this set up. The signal continues to increase over a period of four minutes, before reaching a plateau just ten minutes after the start of the experiment. The signal continues to fluctuate but remains stable for a period of at least ten further minutes. The experiment was allowed to continue and the signal remained steady for an additional ten minutes (thirty in total).

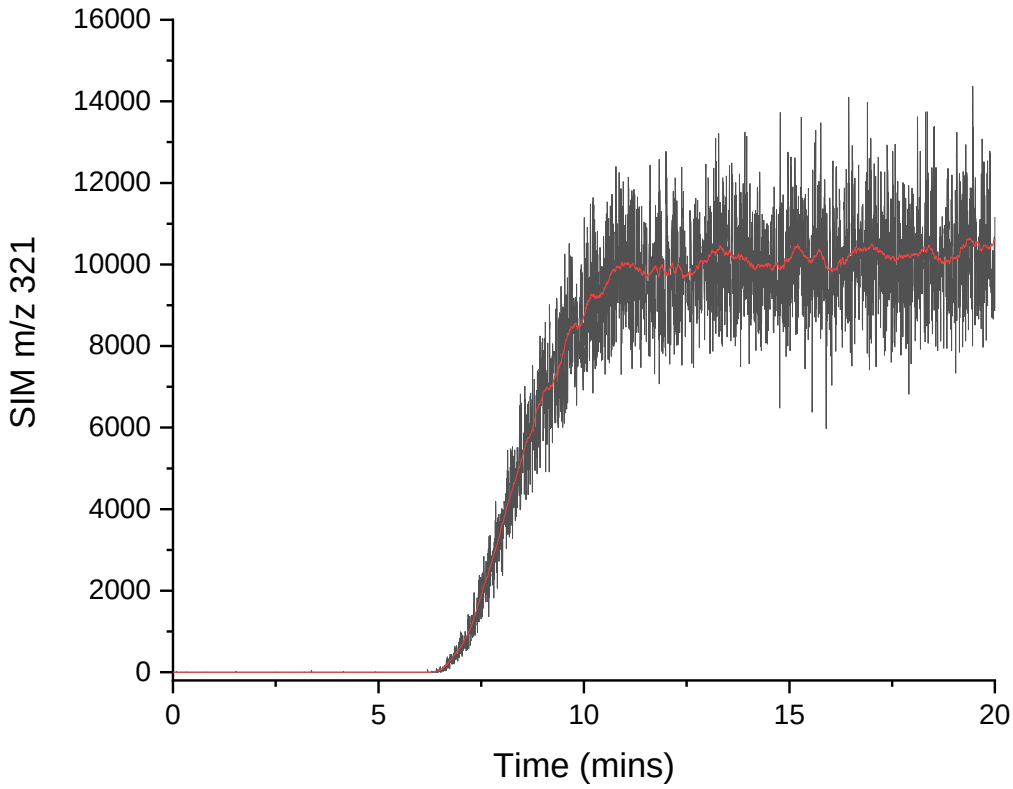

Figure 8.346 – QDa continuous flow monitoring of chloramphenicol dissolved in water and acetonitrile 50:50 v/v using an ES- SIM method following *m/z* 321. A 100 point moving average is represented by the red line.

An aliquot of paracetamol dissolved in water and acetonitrile 50:50 v/v was added to the chloramphenicol solution to produce a solution containing 1 µg/mL of both components. The signal relating to each API was then followed noting that

paracetamol is monitored in ES+ with *m/z* 152 and chloramphenicol was again monitored in ES- with *m/z* 321; the results can be found in Figure 8.347.

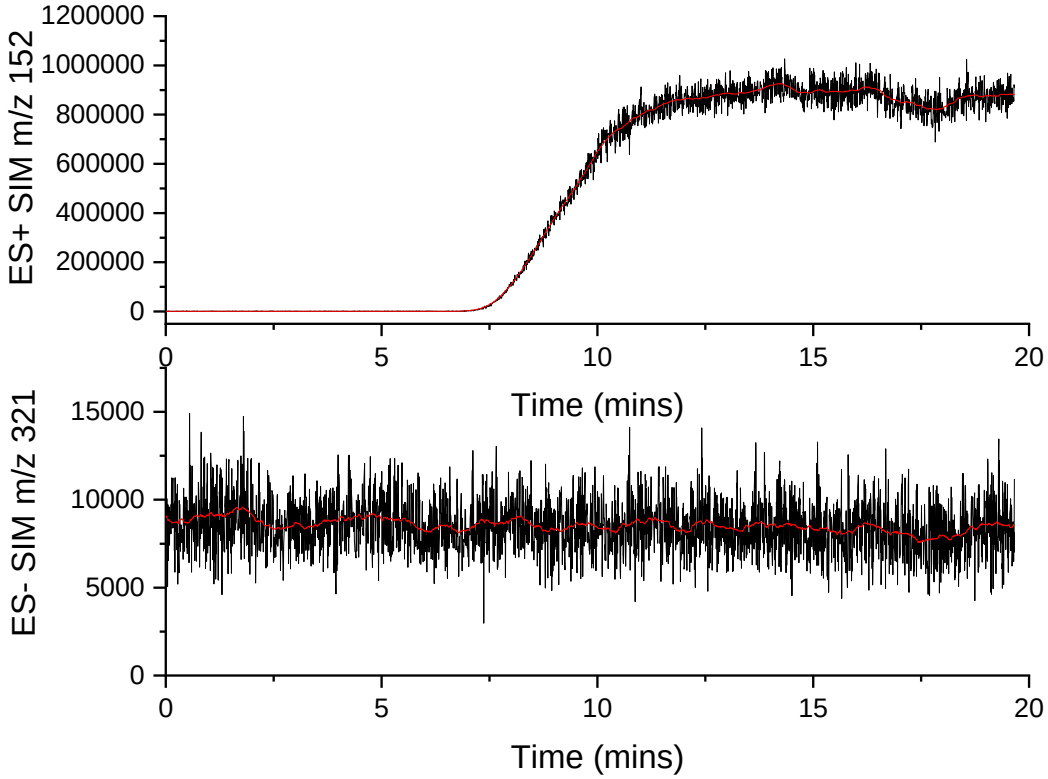

Figure 8.347 – QDa continuous flow monitoring of chloramphenicol and paracetamol dissolved in water and acetonitrile 50:50 v/v using an ES- SIM method following *m/z* 321 and an ES+ SIM method following *m/z* 152. A 100 point moving average has been calculated for each set of data and is highlighted by the red line on each plot.

The paracetamol solution was added at the start of the experiment and its signal starts to increase approximately seven minutes later, with a plateau being reached a little over ten minutes after its addition to the solution. This is consistent with the previous plot for chloramphenicol being monitored alone, see Figure 8.346. The chloramphenicol signal appears unaffected by the addition of paracetamol confirming that it is not subjected to ion suppression or ion enhancement by paracetamol in these solvents. An additional observation is that chloramphenicol reduced in signal quickly when blank water and acetonitrile was passed through thereby concluding that it does not accumulate in the lines or source. The signal observed with chloramphenicol provides reassurance that ES- can also be used to monitor components by continuous flow analysis with the QDa.

8.3.2.9 API plus API: haloperidol and paracetamol

A 1 µg/mL solution of haloperidol dissolved in water and acetonitrile 50:50 v/v was produced and analysed directly using an ES+ SIM method on the QDa following *m/z* 376. Figure 8.348 shows that it takes approximately seven minutes for haloperidol to be ionised and detected, consistent with previous analyses. However, the haloperidol signal then continues to fluctuate across a large range of signal values, with a mean signal between 10 and 30 minutes of 19681 (standard deviation of 8527); the minimum over this time is 1998 and the maximum is more than thirty times this at 72849.

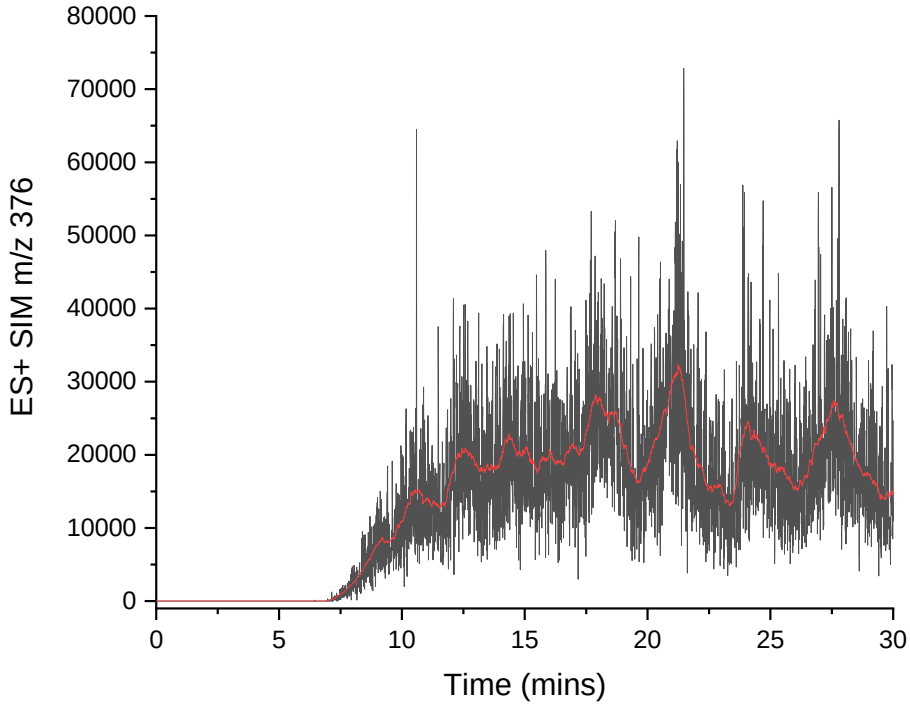

Figure 8.348 – QDa continuous flow monitoring of haloperidol dissolved in water and acetonitrile 50:50 v/v using an ES+ SIM method following *m/z* 376. A 100 point moving average is represented by the red line.

The variability observed in Figure 8.348 is unlikely to be explained by its poor solubility, as minimal signal variation was observed in Figure 7.241. The previous calibration plots did however include formic acid, which may have ensured a more consistent ionisation efficiency. Paracetamol solution (water and acetonitrile only) was added to the haloperidol solution five minutes after the start of the experiment and both

components were monitored, see Figure 8.349. The characteristic delay between paracetamol being added and being detected is seen yet again, and the paracetamol signal appears to fluctuate more widely than previously. The haloperidol signal reduces initially when paracetamol is first detected at around 12.5 minutes, but then appears to fluctuate less than it did previously when analysed in isolation, see Figure 8.348. The earlier findings for haloperidol in combination with lactose and mannitol, using aliquot analyses on the QDa, found that the variability of haloperidol signal was reduced in the presence of co-ionising components and this work with paracetamol and haloperidol suggests a consistent theme.

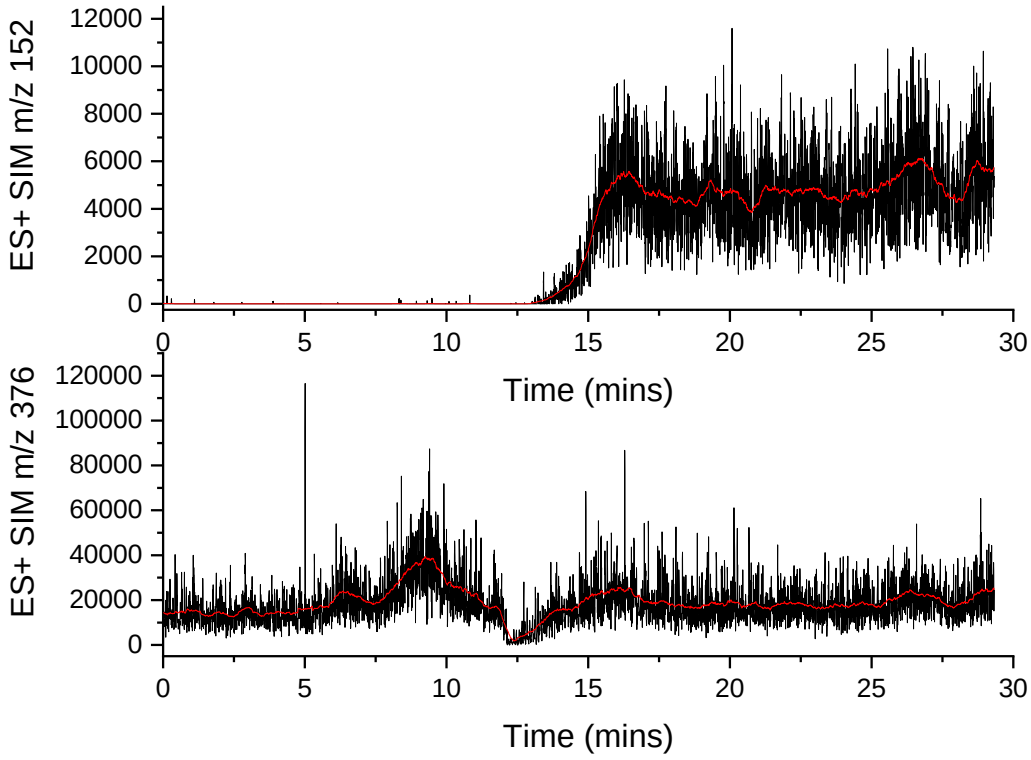

Figure 8.349 – QDa continuous flow monitoring of haloperidol and paracetamol dissolved in water and acetonitrile 50:50 v/v using an ES+ SIM method following *m/z* 376 and *m/z* 152. A 100 point moving average has been calculated for each set of data and is highlighted by the red line on each plot. Paracetamol solution was added to the haloperidol solution at the five minute mark.

The work was repeated for the same concentrations of each component but the paracetamol solution was analysed first, and haloperidol added to it, see Figure 8.350. The paracetamol signal had been given time to stabilise prior to adding the haloperidol, so the signal observed at the very start of this experiment is

representative of that observed when this concentration of paracetamol dissolved in water and acetonitrile 50:50 v/v is analysed using continuous flow analysis with the QDa. There is a sudden reduction in paracetamol signal prior to the haloperidol signal appearing, which is related to the presence of an air bubble in the fluidics. The paracetamol appears to start to recover from the air bubble but then reduces again more gradually this time as the haloperidol signal becomes detectable and starts to increase between five and ten minutes. The signal values are consistent with those found previously, see Figure 8.349, and suggest that paracetamol ionisation is suppressed by the co-ionisation of haloperidol under these conditions. This time however the haloperidol signal becomes more variable after twenty minutes of co-ionisation with paracetamol, and the paracetamol signal also appears slightly more variable at this time point, although no changes have occurred within the experimental set-up.

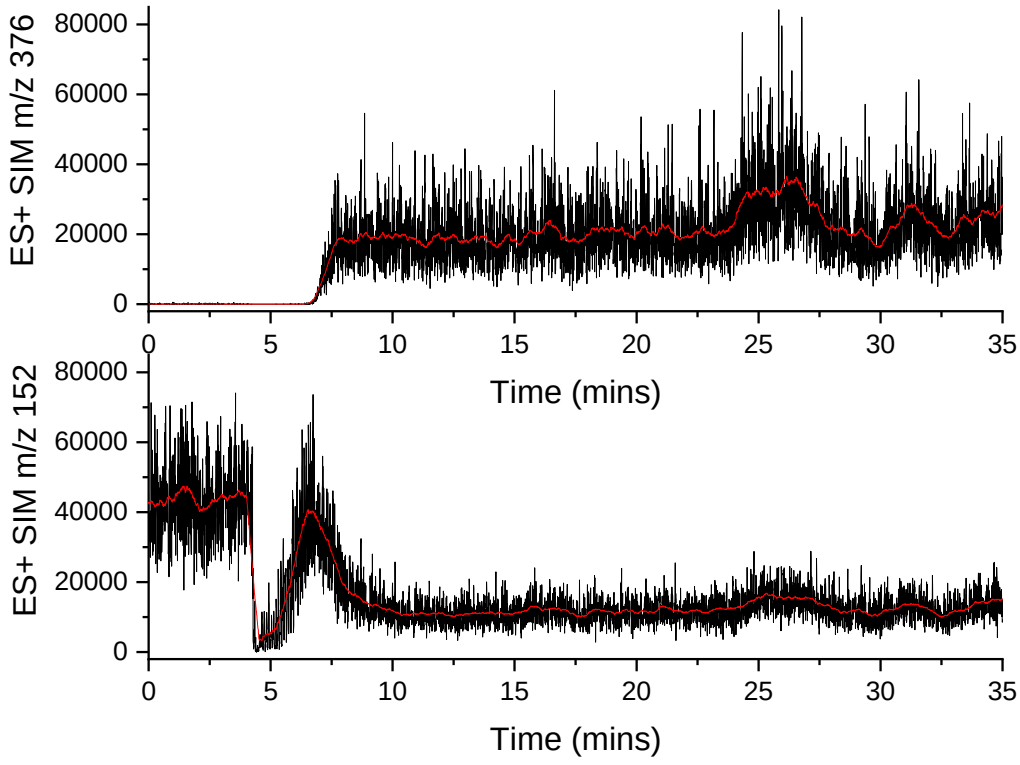

Figure 8.350 – QDa continuous flow monitoring of haloperidol and paracetamol dissolved in water and acetonitrile 50:50 v/v using an ES+ SIM method following *m/z* 376 and *m/z* 152. A 100 point moving average has been calculated for each set of data and is highlighted by the red line on each plot. Haloperidol was added to the paracetamol solution at the start of the experiment.

A significant learning point is that these experiments should ideally be run in combination so the effect on each component can be observed, as it was not clear from the initial experiment that paracetamol ionisation was suppressed by the co-ionisation of haloperidol. In both experiments, haloperidol reduced in signal as blank water and acetonitrile 50:50 v/v were passed through the lines and source, although not as quickly as chloramphenicol, suggesting that haloperidol may accumulate under these experimental conditions. Paracetamol reduced more slowly again but both were removed after thirty minutes of flushing the lines and source with the blank solvent mix. This highlights the importance of exploring how quickly a reduction in signal can be observed with line flushing, for each component being analysed.

8.3.2.10 Summary of continuous flow MS analysis

The QDa source was physically examined at various points throughout this work, particularly after using the less volatile solvents and the excipients. Residue was present on the source in most cases, which was cleaned easily but highlighted that accumulation and degradation were occurring and may therefore impact upon ionisation, particularly over longer periods of time. The set-up of the equipment for continuous monitoring can also result in air bubbles being introduced into the fluidics, which can impact significantly upon the chromatograms and mass spectra observed. This is less of a challenge with off-line analysis due to the logistics of introducing the sample into the MS. The presence of air bubbles in dissolution baths can prove to be a challenge for different reasons in traditional techniques, hence it cannot easily be excluded and simply needs to be monitored.[9]

The continuous flow analysis of components using the QDa is feasible for components requiring monitoring in either mode of ES and allows for a more timely understanding of the relationship between two components in solution than aliquot analyses. The use of QDa SIM methods to follow specific ions allows the signal relating to each component to be followed on-line and in real-time using the QDa MassLynx software, although this cannot yet be translated to concentrations. Off-line analysis to calculate and plot a moving average in addition to the SIM signal proved to be useful in observing how the signal changes and varies over time. The signal associated with each component was observed to fluctuate significantly over time and this could be

affected by many aspects of the work including dilution ratios, solvents, additional ionising components, equipment settings and also the SIM method being used. This therefore requires monitoring for sufficient time periods during preparation work to aid an understanding of when a change in signal is inherent and when it is a result of ionisation phenomena. Ionisation phenomena impacting upon ionisation efficiency appear to occur as a result of all combinations of components, including APIs, excipients, dissolution media and MS solvents (including the presence of modifiers).

This work highlights that some key considerations for continuous flow monitoring are i) to understand how quickly maximum ionisation efficiency occurs for each component, ii) to select the solvents used for MRA dilution as well as those present within the sample carefully after extensive preliminary work, and iii) to determine whether there is likely to be accumulation within the fluidics or ion source that could impact both upon ionisation over time and the time required to clean the instrument between experiments.

8.4 Conclusions and future work

This chapter has succeeded in building upon the work of the previous chapter in confirming that multiple API(s) and excipients may be monitored concurrently using ESI-MS without prior separation or extensive sample preparation. The variability of signal for each component has also been explored further and found to be dependent upon a number of factors: equipment settings such as probe temperature, the solvents from which they are being ionised (including the sample and the make-up solvent), the SIM method through which they are being monitored and the presence of any co-ionising components. The technique has been developed further still and enables quantification through both aliquot and continuous flow methods and analyses.

The on-line and real-time quantification of components, in addition to the ability to predict and adjust for the occurrence of ionisation phenomena has proven to be far more challenging than expected. The aliquot and continuous flow methods have clearly shown the requirement for extensive and repetitive sample analyses to be undertaken in order that quantification may even be attempted. An understanding of the extent of ion suppression and enhancement was able to be explored using both

methods and highlights the complexity of monitoring changing concentrations of each component when ionised concurrently. Each combination of API(s), excipients(s) and solvent(s) results in differing extents of ion enhancement, suppression and variation, which leads to a highly complex relationship. It can therefore be concluded that while dissolution monitoring with mass spectrometry may prove useful to simple binary or even tertiary mixtures of components, formulations containing multiple components will require such extensive work to enable quantitative conclusions as a result of the varying ionisation phenomena that may be occurring, that this may not prove to be a worthwhile endeavour. Monitoring without quantification could, however, prove to be beneficial simply by determining the likely presence or absence of a component from solution at points throughout dissolution, thereby elucidating some understanding of how formulations may deliver API.

Conclusions as to the relationships between components have been outlined in the summary of each section, however, these are not simply transferable to further work monitoring their dissolution due to the relationship between components, solvents and equipment set up. Therefore, instead of providing specific points of understanding for the components studied, a more useful conclusion from this work might be to provide an outline of considerations and methodology for exploring the monitoring of a formulation by mass spectrometry methods. The following is therefore a suggestion for developing such a method:

- Explore each formulation component for their ability to be ionised in ES+ and ES- using a range of concentrations in MS solvents (preferably water and acetonitrile without modifier) – check for multiple ions, dimers etc.
- Repeat the first step for each dissolution media to be used and check for additional ions.
- Set up a SIM method which incorporates each component to be monitored.
- Utilise design of experiment (DoE) software to find the most appropriate MS settings for each component and determine a compromise for each that will enable all components to be analysed successfully using consistent settings.
- Continuously monitor, using the aforementioned SIM method, each component at the maximum concentration possible according to the formulation and

volume of dissolution media to be used – this provides the maximum ion signal observable when each is ionised in isolation.

- Note whether any components require dilution to prevent detector saturation.
- Perform a series of experiments on each combination of components at these maximum concentrations to determine whether ion suppression or enhancement occurs (in either direction), thereby providing information about the maximum ion signal likely to be observed in combination (unless a component appears to be enhanced by more than one additional component).
- Note again whether any components may require dilution when in combination due to ion enhancement and note also whether any components may be undetectable due to ion suppression.
- Determine the time taken for the maximum concentration of each component to be cleared from the fluidics and ionisation source to prevent contamination between experiments.

The development of compact and user-friendly mass spectrometry equipment has led to the technique being applied to novel challenges, particularly on-line monitoring of reactions.[15,228,230] This has the potential to advance understanding in many areas but requires fundamental and detailed understanding of the ESI-MS technique being used to accurately distinguish between data that may allow conclusions to be drawn versus data which necessitates considerable further work. The monitoring of dissolution by mass spectrometry can be concluded to fall into both categories dependent upon the level of detail that is required of the data.

9. Concluding remarks

9.1 Surface dissolution imaging using UV-Vis technology

The novel dual wavelength SDi2 has been used to highlight the importance of visually monitoring dissolution using both UV and visible absorbance data. Unexpected physical processes, such as the movement of IDR samples from the holder seen with the I-TPI gels, as well as the more expected physical processes, such as sample erosion during dissolution, have been used to explain changes in reported concentration data. This work therefore offers evidence that the previously reported limitations of single wavelength imaging have been improved upon with the development of the SDi2.[13]

The development of a method to observe single crystal dissolution with the SDi2 has highlighted the instrument's versatility, particularly the opportunity to use both the 1.54 mL compact flow cell and the 60.3 mL whole dose cell for monitoring. The use of the two flow cells has clearly shown that each offers different hydrodynamic conditions for dissolution, including both laminar flow and turbulence, as well as altering diffusion, density gradients, advection and stagnation zones. The ability to probe this environment throughout dissolution and to explore the impact of this environment upon dissolution, provides further opportunities to enhance understanding of the many processes taking place.

The SDi2 is limited in its resolution when reporting absorbance data using the Pion software, however, this work confirms that the application of image analysis software allows absorbance values per pixel to be obtained from the SDi2 images. This also enables concentration and size changes to be quantified and correlated, providing the ability to report concentration values surrounding a changing sample throughout its dissolution. The ability to report both size changes and concentration changes allowed a series of solvates to be ranked according to their relative stabilities, thus confirming that the SDi2 may additionally be applied to solve non-pharmaceutical challenges.

A significant limitation of these methods, however, is that the image on screen and therefore UV-Vis absorbance data reported is a two-dimensional representation of a three-dimensional shape. This is a limitation of the equipment itself and cannot be overcome simply by changing analysis methods or even by using image analysis

software. The comparison of single crystals is also limited by the uniformity of crystals available, preventing experiments from being repeatable and thereby restricting data interpretation. The ability to fully index the single crystal by SCXRD using the newly developed sample holder will provide full crystal morphology and size data prior to dissolution, and will offer yet more information with which to explain both size and concentration changes during dissolution monitoring. Another idea for further development of the instrument may be to position a camera at the top of the compact flow cell using the hole originally created for a Raman probe – this may enable enhanced images of the sample to be obtained, although it will introduce yet more challenges with respect to light interference. Alternatively, recent research by Pallipurath et al. offers alternative technologies and modelling that may be used alongside the SDi2 to further explore face-specific dissolution for single crystals.[215,341]

Finally, the fundamentals of the intrinsic dissolution rate calculations using the SDi2 software also requires significant consideration. Approval from regulatory bodies to report dissolution data requires a fundamental understanding of the analytical technique used, hence the ability to replicate the SDi2-calculated IDR values is a critical step towards enabling the instrument to be used more frequently within the pharmaceutical industry.

9.2 Bulk dissolution monitoring using mass spectrometry

The primary advantage of using mass spectrometry for dissolution monitoring, when compared with UV-Vis techniques, is the ability to analyse molecules that do not contain UV-absorbing chromophores.[15] This research confirms the ability of ESI-MS to successfully detect and monitor a range of APIs and soluble excipients, with and without chromophores, respectively. The sensitivity of ESI-MS has also allowed the detection of small quantities of soluble formulation components, however, this was subject to significant limitations when multiple components were ionised concurrently.

The practical challenges associated with combining dissolution and mass spectrometry equipment have been largely overcome through the use of a mass rate attenuator in this and the previous work.[15] This technology enables high concentrations of sample to be injected into flowing MS solvents and directed at appropriate flow rates into the

MS instrument avoiding detector saturation in most circumstances. This is aided by understanding the fundamental relationship between concentration and response for each sample being analysed and the solvent from which it is being ionised. The acquisition time and duty cycle of ESI-MS also allowed multiple data points to be obtained rapidly with real-time monitoring achievable for a number of components when ionised in isolation.

The significant challenges presented themselves when multiple components were ionised concurrently. Solvents, ionisation modifiers, simple dissolution media and co-ionising components were each found to impact significantly upon the MS signal observed for both APIs and excipients, altering both the relationship between signal and response as well as resulting in the formation of alternative and additional ions in some instances. The relationship between components was unable to be accounted for, or predicted sufficiently to enable quantification without chromatographic separation prior to ionisation. Research into ionisation efficiency scales, pH effects and the mechanism of modifiers will further explain these relationships improving our ability to predict and counter the effects of ionisation phenomena such as ion suppression and ion enhancement.[335,340,342]

In summary, although the monitoring of dissolution using mass spectrometry allows non-chromophore containing compounds to be detected, the complexity of the relationship between each formulation component and the dissolution media being used, in addition to the solvents required for ionisation, result in the technique requiring such extensive pre-work that monitoring online and in real-time is currently an unrealistic expectation. It remains, however, a useful method for analysing samples off-line, particularly when multiple APIs are present or when they are unable to be monitored through conventional techniques. Future work exploring the ionisation phenomena of suppression and enhancement may, however, offer the opportunity to combine the techniques more successfully.

9.3 Summary

Monitoring dissolution, both on the surface and in the bulk, is a topic of particular relevance to the pharmaceutical industry, but its fundamentals extend into

engineering, chemistry and physics amongst many others. The two approaches explored in this work have focussed on different aspects of the dissolution process. Surface dissolution imaging has primarily enabled solid wetting and boundary layers to be monitored, in addition to diffusion and advection within the bulk dissolution media. Mass spectrometry, however, has monitored changes only within the bulk dissolution media, allowing soluble formulation components to be detected and in some circumstances, quantified. Each technique therefore provides complementary information about dissolution to be used in addition to, rather than instead of, conventional dissolution monitoring methods.

10. References

1 A. D. McNaught and A. Wilkinson, Eds., *IUPAC. Compendium of Chemical Terminology: Gold Book*, Blackwell Scientific Publications, Oxford, 2nd edn., 2009.

2 J. Siepmann and F. Siepmann, Mathematical modeling of drug dissolution, *Int. J. Pharm.*, 2013, **453**, 12–24.

3 M. E. Aulton and K. M. G. Taylor, *Aulton's Pharmaceutics: The Design and Manufacture of Medicines*, Churchill Livingstone Elsevier, Edinburgh, 2013.

4 B. T. Smith, *Physical pharmacy*, Pharmaceutical Press, London, 1st edn., 2016.

5 M. C. Matthews, C. R. I. Clayton and J. Rigby-Jones, Locating dissolution features in the Chalk, *Q. J. Eng. Geol. Hydrogeol.*, 2000, **33**, 125–140.

6 O. S. Pokrovsky and J. Schott, Surface Chemistry and Dissolution Kinetics of Divalent Metal Carbonates, *Environ. Sci. Technol.*, 2002, **36**, 426–432.

7 Q. Tang, H. Zhang, Y. Meng, B. He and L. Yu, Dissolution Engineering of Platinum Alloy Counter Electrodes in Dye-Sensitized Solar Cells, *Angew. Chem. Int. Ed.*, 2015, **54**, 11448–11452.

8 A. T. Florence and D. Attwood, *Physicochemical principles of pharmacy*, Palgrave Macmillan, Basingstoke, 2002.

9 J. B. Dressman and J. Krämer, Eds., *Pharmaceutical dissolution testing*, Taylor & Francis, Boca Raton, 2005.

10 H. Grady, D. Elder, G. K. Webster, Y. Mao, Y. Lin, T. Flanagan, J. Mann, A. Blanchard, M. J. Cohen, J. Lin, F. Kesisoglou, A. Hermans, A. Abend, L. Zhang and D. Curran, Industry's View on Using Quality Control, Biorelevant, and Clinically Relevant Dissolution Tests for Pharmaceutical Development, Registration, and Commercialization, *J. Pharm. Sci.*, 2018, **107**, 34–41.

11 S. Klein, Advancements in Dissolution Testing of Oral and Non-oral Formulations, *AAPS PharmSciTech*, 2019, **20**, 266, s12249-019-1479–8.

12 M. Kuentz, Analytical technologies for real-time drug dissolution and precipitation testing on a small scale, *J. Pharm. Pharmacol.*, 2015, **67**, 143–159.

13 J. Østergaard, UV imaging in pharmaceutical analysis, *J. Pharm. Biomed. Anal.*, 2018, **147**, 140–148.

14 J. H. Gross, *Mass spectrometry: a textbook*, Springer International Publishing, Cham, Third edition., 2017.

15 C. Lewis, A. Ray, T. Bristow and S. Wren, Determining the suitability of mass spectrometry for understanding the dissolution processes involved with pharmaceutical tablets, *Rapid Commun. Mass Spectrom.*, 2015, **29**, 1107–1114.

16 J. W. Steed and J. L. Atwood, *Supramolecular Chemistry (pre-print)*, John Wiley & Sons, Ltd, Chichester, UK, 3rd edn., 2020.

17 B. M. Couillaud, P. Espeau, N. Mignet and Y. Corvis, State of the Art of Pharmaceutical Solid Forms: from Crystal Property Issues to Nanocrystals Formulation, *ChemMedChem*, 2019, **14**, 8–23.

18 R. Censi and P. Di Martino, Polymorph Impact on the Bioavailability and Stability of Poorly Soluble Drugs, *Molecules*, 2015, **20**, 18759–18776.

19 S. Price, The computational prediction of pharmaceutical crystal structures and polymorphism, *Adv. Drug Deliv. Rev.*, 2004, **56**, 301–319.

20 Ö. Almarsson, M. B. Hickey, M. L. Peterson, S. L. Morissette, S. Soukasene, C. McNulty, M. Tawa, J. M. MacPhee and J. F. Remenar, High-Throughput Surveys of Crystal Form Diversity of Highly Polymorphic Pharmaceutical Compounds, *Cryst. Growth Des.*, 2003, **3**, 927–933.
21 G. Zhang, Phase transformation considerations during process development and manufacture of solid oral dosage forms, *Adv. Drug Deliv. Rev.*, 2004, **56**, 371–390.
22 J. Bauer, S. Spanton, R. Henry, J. Quick, W. Dziki, W. Porter and J. Morris, Ritonavir: an extraordinary example of conformational polymorphism, *Pharm. Res.*, 2001, **18**, 859–866.
23 J. Bernstein, *Polymorphism in Molecular Crystals*, Oxford University Press, 2007.
24 D. Singhal, Drug polymorphism and dosage form design: a practical perspective, *Adv. Drug Deliv. Rev.*, 2004, **56**, 335–347.
25 R. A. Storey and I. Ymen, *Solid state characterization of pharmaceuticals*, John Wiley & Sons, Chichester, U.K., 2011.
26 G. A. Ilevbare, W. Xu, C. T. John, J. D. Ormes, J. L. Kuiper, A. C. Templeton and A. Bak, in *Pharmaceutical Sciences Encyclopedia*, ed. S. C. Gad, John Wiley & Sons, Inc., Hoboken, NJ, USA, 2015, pp. 1–41.
27 G. R. Desiraju, J. J. Vittal and A. Ramanan, *Crystal engineering: a textbook*, World Scientific ; IISc Press, New Jersey, N.J, 2011.
28 G. Coquerel, Crystallization of molecular systems from solution: phase diagrams, supersaturation and other basic concepts, *Chem Soc Rev*, 2014, **43**, 2286–2300.
29 S. Karthika, T. K. Radhakrishnan and P. Kalaichelvi, A Review of Classical and Nonclassical Nucleation Theories, *Cryst. Growth Des.*, 2016, **16**, 6663–6681.
30 R. J. Davey, S. L. M. Schroeder and J. H. ter Horst, Nucleation of Organic Crystals-A Molecular Perspective, *Angew. Chem. Int. Ed.*, 2013, **52**, 2166–2179.
31 D. Erdemir, A. Y. Lee and A. S. Myerson, Nucleation of Crystals from Solution: Classical and Two-Step Models, *Acc. Chem. Res.*, 2009, **42**, 621–629.
32 K. Tsukamoto, in *Handbook of Crystal Growth*, Elsevier, 2015, pp. 1031–1060.
33 I. Pritula and K. Sangwal, in *Handbook of Crystal Growth*, Elsevier, 2015, pp. 1185–1227.
34 I. V. Markov, *Crystal growth for beginners: fundamentals of nucleation, crystal growth and epitaxy*, World Scientific, Singapore; River Edge, N.J., 2003.
35 N. J. Babu and A. Nangia, Solubility Advantage of Amorphous Drugs and Pharmaceutical Cocrystals, *Cryst. Growth Des.*, 2011, **11**, 2662–2679.
36 W. Ostwald, Studien über die Bildung und Umwandlung fester Körper, *Z. Für Phys. Chem.*, , DOI:10.1515/zpch-1897-2233.
37 S. R. Byrn, R. R. Pfeiffer and J. G. Stowell, *Solid-state chemistry of drugs*, Ssci Inc., West Lafayette, Ind., 2003.
38 B. C. Hancock and M. Parks, What is the true solubility advantage for amorphous pharmaceuticals?, *Pharm. Res.*, 2000, **17**, 397–404.
39 S. B. Murdande, M. J. Pikal, R. M. Shanker and R. H. Bogner, Solubility advantage of amorphous pharmaceuticals: I. A thermodynamic analysis, *J. Pharm. Sci.*, 2010, **99**, 1254–1264.
40 *United States Pharmacopeia and National Formulary (USP 43-NF 38)*, United States Pharmacopeial Convention, Rockville, MD, 2020.

41 R. V. Mantri, R. Sanghvi and H. (J.) Zhu, in *Developing Solid Oral Dosage Forms*, Elsevier, 2017, pp. 3–22.
42 A. T. M. Serajuddin and C. I. Jarowski, Effect of Diffusion Layer pH and Solubility on the Dissolution Rate of Pharmaceutical Bases and their Hydrochloride Salts I: Phenazopyridine, *J. Pharm. Sci.*, 1985, **74**, 142–147.
43 A. T. M. Serajuddin and C. I. Jarowski, Effect of Diffusion Layer pH and Solubility on the Dissolution Rate of Pharmaceutical Acids and Their Sodium Salts II: Salicylic Acid, Theophylline, and Benzoic Acid, *J. Pharm. Sci.*, 1985, **74**, 148–154.
44 A. T. M. Serajuddin, Salt formation to improve drug solubility, *Adv. Drug Deliv. Rev.*, 2007, **59**, 603–616.
45 J. Aaltonen and T. Rades, Commentary: Towards Physico-Relevant Dissolution Testing: The Importance of Solid-State Analysis in Dissolution, *Dissolution Technol.*, 2009, **16**, 47–54.
46 K. Greco and R. Bogner, Solution-Mediated Phase Transformation: Significance During Dissolution and Implications for Bioavailability, *J. Pharm. Sci.*, 2012, **101**, 2996–3018.
47 A. M. Kaushal, P. Gupta and A. K. Bansal, Amorphous Drug Delivery Systems: Molecular Aspects, Design, and Performance, *Crit. Rev. Ther. Drug Carrier Syst.*, 2004, **21**, 133–193.
48 H. Al-Obaidi, M. Majumder and F. Bari, Amorphous and crystalline particulates: challenges and perspectives in drug delivery, *Curr. Pharm. Des.*, 2016, **22**, 1–1.
49 P. T. Cardew and R. J. Davey, The kinetics of solvent-mediated phase transformations, *Proc. R. Soc. Lond. Math. Phys. Sci.*, 1985, **398**, 415–428.
50 R. J. Davey, P. T. Cardew, D. McEwan and D. E. Sadler, Rate controlling processes in solvent-mediated phase transformations, *J. Cryst. Growth*, 1986, **79**, 648–653.
51 D. Novakovic, L. Peltonen, A. Isomäki, S. J. Fraser-Miller, L. H. Nielsen, T. Laaksonen and C. J. Strachan, Surface Stabilization and Dissolution Rate Improvement of Amorphous Compacts with Thin Polymer Coatings: Can We Have It All?, *Mol. Pharm.*, 2020, **17**, 1248–1260.
52 N. Hisada, R. Takano, N. Takata, K. Shiraki, T. Ueto, S. Tanida, M. Kataoka and S. Yamashita, Characterizing the dissolution profiles of supersaturable salts, cocrystals, and solvates to enhance in vivo oral absorption, *Eur. J. Pharm. Biopharm.*, 2016, **103**, 192–199.
53 N. Kanikkannan, Technologies to Improve the Solubility, Dissolution and Bioavailability of Poorly Soluble Drugs, *J. Anal. Pharm. Res.*, , DOI:10.15406/japlr.2018.07.00198.
54 D. J. Berry and J. W. Steed, Pharmaceutical cocrystals, salts and multicomponent systems; intermolecular interactions and property based design, *Adv. Drug Deliv. Rev.*, 2017, **117**, 3–24.
55 S. Morissette, High-throughput crystallization: polymorphs, salts, co-crystals and solvates of pharmaceutical solids, *Adv. Drug Deliv. Rev.*, 2004, **56**, 275–300.
56 K. Edkins and A. J. Cruz-Cabeza, The solid state of pharmaceuticals, *CrystEngComm*, 2019, **21**, 2031–2033.
57 J. W. Steed, 21st century developments in the understanding and control of molecular solids, *Chem. Commun.*, 2018, **54**, 13175–13182.
58 P. A. Corner, D. J. Berry, J. F. McCabe, R. Barbas, R. Prohens, H. Du, H. Zhou and A. Llinas, Property prediction and pharmacokinetic evaluation of mixed

stoichiometry cocrystals of zafirlukast, a drug delivery case study, *CrystEngComm*, 2018, **20**, 1346–1351.

59 D. Markl and J. A. Zeitler, A Review of Disintegration Mechanisms and Measurement Techniques, *Pharm. Res.*, 2017, **34**, 890–917.

60 E. Kaunisto, A. Rasmuson, J. Bergenholtz, J. Remmelgas, L. Lindfors and S. Folestad, Fundamental Mechanisms for Tablet Dissolution: Simulation of Particle Deaggregation Via Brownian Dynamics, *J. Pharm. Sci.*, 2013, **102**, 1569–1577.

61 A. Dokoumetzidis and P. Macheras, A century of dissolution research: From Noyes and Whitney to the Biopharmaceutics Classification System, *Int. J. Pharm.*, 2006, **321**, 1–11.

62 J. Al-Gousous and P. Langguth, Oral Solid Dosage Form Disintegration Testing — The Forgotten Test, *J. Pharm. Sci.*, 2015, **104**, 2664–2675.

63 D. Wilson, S. Wren and G. Reynolds, Linking Dissolution to Disintegration in Immediate Release Tablets Using Image Analysis and a Population Balance Modelling Approach, *Pharm. Res.*, 2012, **29**, 198–208.

64 P. M. Desai, C. V. Liew and P. W. S. Heng, Review of Disintegrants and the Disintegration Phenomena, *J. Pharm. Sci.*, 2016, **105**, 2545–2555.

65 N. Donauer and R. Lobenberg, A mini review of scientific and pharmacopeial requirements for the disintegration test, *Int. J. Pharm.*, 2007, **345**, 2–8.

66 D. A. Fick, V. On liquid diffusion, *Lond. Edinb. Dublin Philos. Mag. J. Sci.*, 1855, **10**, 30–39.

67 A. A. Noyes and W. R. Whitney, The rate of solution of solid substances in their own solutions, *J. Am. Chem. Soc.*, 1897, **19**, 930–934.

68 L. Bruner and St. Tolloczko, Über die Auflösungsgeschwindigkeit fester Körper, *Z. Für Anorg. Chem.*, 1901, **28**, 314–330.

69 L. Bruner and St. Tołłoczko, Über die Auflösungsgeschwindigkeit fester Körper (III Mitteilung.), *Z. Für Anorg. Chem.*, 1903, **35**, 23–40.

70 E. Brunner, Reaktionsgeschwindigkeit in heterogenen Systemen, *Z. Für Phys. Chem.*, 1904, **47U**, 56–102.

71 A. W. Hixson and J. H. Crowell, Dependence of Reaction Velocity upon surface and Agitation, *Ind. Eng. Chem.*, 1931, **23**, 923–931.

72 W. Nernst, Theorie der Reaktionsgeschwindigkeit in heterogenen Systemen, *Z. Für Phys. Chem.*, 1904, **47U**, 52–55.

73 L. J. Edwards, The dissolution and diffusion of aspirin in aqueous media, *Trans. Faraday Soc.*, 1951, **47**, 1191.

74 E. Nelson, Solution Rate of Theophylline Salts and Effects from Oral Administration, *J. Am. Pharm. Assoc. Sci. Ed*, 1957, **46**, 607–614.

75 E. J. Fraser, R. H. Leach and J. W. Poston, Bioavailability of digoxin, *The Lancet*, 1972, **300**, 541.

76 J. C. Cloyd, R. J. Gumnit and T. S. Lesar, Reduced seizure control due to spoiled phenytoin capsules, *Ann. Neurol.*, 1980, **7**, 191–193.

77 V. G. Levich, *Physiochemical hydrodynamics*, Prentice-Hall, Englewood Cliffs, N.J., 1962.

78 W. I. Higuchi, Diffusional Models Useful in Biopharmaceutics, *J. Pharm. Sci.*, 1967, **56**, 315–324.

79 P. V. Danckwerts, Significance of Liquid-Film Coefficients in Gas Absorption, *Ind. Eng. Chem.*, 1951, **43**, 1460–1467.

80 P. J. Missel, L. E. Stevens and J. W. Mauger, Reexamination of convective diffusion/drug dissolution in a laminar flow channel: accurate prediction of dissolution rate, *Pharm. Res.*, 2004, **21**, 2300–2306.

81 X. J. H. Pepin, N. J. Sanderson, A. Blanazs, S. Grover, T. G. Ingallinera and J. C. Mann, Bridging in vitro dissolution and in vivo exposure for acalabrutinib. Part I. Mechanistic modelling of drug product dissolution to derive a P-PSD for PBPK model input, *Eur. J. Pharm. Biopharm.*, 2019, **142**, 421–434.

82 Q. T. Zhou and T. Li, Formulation and Manufacturing of Solid Dosage Forms, *Pharm. Res.*, 2018, **36**, DOI:10.1007/s11095-018-2547-6.

83 J. B. Dressman and C. Reppas, In vitro-in vivo correlations for lipophilic, poorly water-soluble drugs, *Eur. J. Pharm. Sci.*, 2000, **11 Suppl 2**, S73-80.

84 L. A. Bauer, *Applied clinical pharmacokinetics*, McGraw-Hill Medical, New York, 2008.

85 L. Lin and H. Wong, Predicting Oral Drug Absorption: Mini Review on Physiologically-Based Pharmacokinetic Models, *Pharmaceutics*, 2017, **9**, DOI:10.3390/pharmaceutics9040041.

86 S.-C. Chow, Bioavailability and Bioequivalence in Drug Development, *Wiley Interdiscip. Rev. Comput. Stat.*, 2014, **6**, 304–312.

87 B. J. Boyd, C. A. S. Bergström, Z. Vinarov, M. Kuentz, J. Brouwers, P. Augustijns, M. Brandl, A. Bernkop-Schnürch, N. Shrestha, V. Préat, A. Müllertz, A. Bauer-Brandl and V. Jannin, Successful oral delivery of poorly water-soluble drugs both depends on the intraluminal behavior of drugs and of appropriate advanced drug delivery systems, *Eur. J. Pharm. Sci.*, 2019, **137**, 104967.

88 J. B. Dressman, G. L. Amidon, C. Reppas and V. P. Shah, Dissolution testing as a prognostic tool for oral drug absorption: immediate release dosage forms, *Pharm. Res.*, 1998, **15**, 11–22.

89 G. L. Amidon, H. Lennernäs, V. P. Shah and J. R. Crison, A theoretical basis for a biopharmaceutic drug classification: the correlation of in vitro drug product dissolution and in vivo bioavailability, *Pharm. Res.*, 1995, **12**, 413–420.

90 Centre for Drug Evaluation, *Guidance for Industry: Waiver of In Vivo Bioavailability and Bioequivalence Studies for Immediate-Release Solid Oral Dosage Forms Based on a Biopharmaceutics Classification System*, 2017.

91 European Medicines Agency, ICH M9 guideline on biopharmaceutics classification system based biowaivers (EMA/CHMP/ICH/493213/2018), 2020, 18.

92 A. Dahan, J. M. Miller and G. L. Amidon, Prediction of Solubility and Permeability Class Membership: Provisional BCS Classification of the World's Top Oral Drugs, *AAPS J.*, 2009, **11**, 740–746.

93 J. M. Butler and J. B. Dressman, The developability classification system: application of biopharmaceutics concepts to formulation development, *J. Pharm. Sci.*, 2010, **99**, 4940–4954.

94 M. S. Landis, S. Bhattachar, M. Yazdanian and J. Morrison, Commentary: Why Pharmaceutical Scientists in Early Drug Discovery Are Critical for Influencing the Design and Selection of Optimal Drug Candidates, *AAPS PharmSciTech*, 2018, **19**, 1–10.

95 J. Rosenberger, J. Butler and J. Dressman, A Refined Developability Classification System, *J. Pharm. Sci.*, 2018, **107**, 2020–2032.

96 M. Baumann and I. R. Baxendale, The synthesis of active pharmaceutical ingredients (APIs) using continuous flow chemistry, *Beilstein J. Org. Chem.*, 2015, **11**, 1194–1219.
97 E. Hadjittofis, M. A. Isbell, V. Karde, S. Varghese, C. Ghoroi and J. Y. Y. Heng, Influences of Crystal Anisotropy in Pharmaceutical Process Development, *Pharm. Res.*, 2018, **35**, DOI:10.1007/s11095-018-2374-9.
98 R. Tinmanee, S. D. Stamatis, E. Ueyama, K. R. Morris and L. E. Kirsch, Polymorphic and Covalent Transformations of Gabapentin in Binary Excipient Mixtures after Milling-Induced Stress, *Pharm. Res.*, 2018, **35**, DOI:10.1007/s11095-017-2285-1.
99 J. Wang, M. Davidovich, D. Desai, D. Bu, M. Hussain and K. Morris, Solid-State Interactions of a Drug Substance and Excipients and Their Impact on Tablet Dissolution: A Thermal-Mechanical Facilitated Process-Induced Transformation or PIT, *J. Pharm. Sci.*, 2010, **99**, 3849–3862.
100 L. X. Yu, G. Amidon, M. A. Khan, S. W. Hoag, J. Polli, G. K. Raju and J. Woodcock, Understanding Pharmaceutical Quality by Design, *AAPS J.*, 2014, **16**, 771–783.
101 L. X. Yu, Pharmaceutical Quality by Design: Product and Process Development, Understanding, and Control, *Pharm. Res.*, 2008, **25**, 781–791.
102 A. Hermans, A. M. Abend, F. Kesisoglou, T. Flanagan, M. J. Cohen, D. A. Diaz, Y. Mao, L. Zhang, G. K. Webster, Y. Lin, D. A. Hahn, C. A. Coutant and H. Grady, Approaches for Establishing Clinically Relevant Dissolution Specifications for Immediate Release Solid Oral Dosage Forms, *AAPS J.*, 2017, **19**, 1537–1549.
103 G. Pifferi and P. Restani, The safety of pharmaceutical excipients, *Il Farm.*, 2003, **58**, 541–550.
104 P. Furrer, The central role of excipients in drug formulation, https://www.europeanpharmaceuticalreview.com/article/18434/the-central-role-of-excipients-in-drug-formulation-2/, (accessed 9 August 2019).
105 P. J. Crowley, Excipients as stabilizers, *Pharm. Sci. Technol. Today*, 1999, **2**, 237–243.
106 A. García-Arieta, Interactions between active pharmaceutical ingredients and excipients affecting bioavailability: Impact on bioequivalence, *Eur. J. Pharm. Sci.*, 2014, **65**, 89–97.
107 T. Flanagan, Potential for pharmaceutical excipients to impact absorption: A mechanistic review for BCS Class 1 and 3 drugs, *Eur. J. Pharm. Biopharm.*, 2019, **141**, 130–138.
108 D. C. Monkhouse and A. Maderich, Whither Compatibility Testing?, *Drug Dev. Ind. Pharm.*, 1989, **15**, 2115–2130.
109 V. S. Dave, in *Pharmaceutical Quality by Design*, eds. S. Beg and M. S. Hasnain, Academic Press, 2019, pp. 65–76.
110 R. C. Rowe, Ed., *Handbook of pharmaceutical excipients*, APhA, (PhP) Pharmaceutical Press, London, 6. ed., 2009.
111 G. Pifferi, P. Santoro and M. Pedrani, Quality and functionality of excipients, *Il Farm.*, 1999, **54**, 1–14.
112 H. Kalasz and I. Antal, Drug Excipients, *Curr. Med. Chem.*, 2006, **13**, 2535–2563.
113 J. van der Merwe, J. Steenekamp, D. Steyn and J. Hamman, The Role of Functional Excipients in Solid Oral Dosage Forms to Overcome Poor Drug Dissolution and Bioavailability, *Pharmaceutics*, 2020, **12**, 393.

114 S. Azarmi, W. Roa and R. Löbenberg, Current perspectives in dissolution testing of conventional and novel dosage forms, *Int. J. Pharm.*, 2007, **328**, 12–21.
115 P. Costa and J. M. Sousa Lobo, Modeling and comparison of dissolution profiles, *Eur. J. Pharm. Sci. Off. J. Eur. Fed. Pharm. Sci.*, 2001, **13**, 123–133.
116 V. Pillay and R. Fassihi, Unconventional dissolution methodologies, *J. Pharm. Sci.*, 1999, **88**, 843–851.
117 M. Siewert, J. Dressman, C. K. Brown, V. P. Shah, J.-M. Aiache, N. Aoyagi, D. Bashaw, C. Brown, W. Brown, D. Burgess, J. Crison, P. DeLuca, R. Djerki, J. Dressman, T. Foster, K. Gjellan, V. Gray, A. Hussain, T. Ingallinera, J. Klancke, J. Kraemer, H. Kristensen, K. Kumi, C. Leuner, J. Limberg, P. Loos, L. Margulis, P. Marroum, H. Moeller, B. Mueller, M. Mueller-Zsigmondy, N. Okafo, L. Ouderkirk, S. Parsi, S. Qureshi, J. Robinson, V. Shah, M. Siewert, R. Uppoor and R. Williams, FIP/AAPS guidelines to dissolution/in vitro release testing of novel/special dosage forms, *AAPS PharmSciTech*, 2003, **4**, 43–52.
118 N. Fotaki, Flow-Through Cell Apparatus (USP Apparatus 4): Operation and Features, *Dissolution Technol.*, 2011, **18**, 46–49.
119 Z. Gao, In Vitro Dissolution Testing with Flow-Through Method: A Technical Note, *AAPS PharmSciTech*, , DOI:10.1208/s12249-009-9339-6.
120 B. R. Rohrs, D. L. Burch-Clark, M. J. Witt and D. J. Stelzer, USP dissolution apparatus 3 (reciprocating cylinder): instrument parameter effects on drug release from sustained release formulations, *J. Pharm. Sci.*, 1995, **84**, 922–926.
121 Council of Europe, *European Pharmacopoeia*, EDQM, Strasbourg, France, 5th edn., 2004.
122 R. Havenaar, B. Anneveld, L. M. Hanff, S. N. de Wildt, B. A. E. de Koning, M. G. Mooij, J. P. A. Lelieveld and M. Minekus, In vitro gastrointestinal model (TIM) with predictive power, even for infants and children?, *Int. J. Pharm.*, 2013, **457**, 327–332.
123 J. Mann, J. Dressman, K. Rosenblatt, L. Ashworth, U. Muenster, K. Frank, P. Hutchins, J. Williams, L. Klumpp, K. Wielockx, P. Berben, P. Augustijns, R. Holm, M. Hofmann, S. Patel, S. Beato, K. Ojala, I. Tomaszewska, J.-L. Bruel and J. Butler, Validation of Dissolution Testing with Biorelevant Media: An OrBiTo Study, *Mol. Pharm.*, 2017, **14**, 4192–4201.
124 M. Gibaldi and S. Feldman, Establishment of sink conditions in dissolution rate determinations. Theoretical considerations and application to nondisintegrating dosage forms, *J. Pharm. Sci.*, 1967, **56**, 1238–1242.
125 D. J. Phillips, S. R. Pygall, V. B. Cooper and J. C. Mann, Overcoming sink limitations in dissolution testing: a review of traditional methods and the potential utility of biphasic systems: Dissolution testing: biphasic systems, *J. Pharm. Pharmacol.*, 2012, **64**, 1549–1559.
126 J. Posti and P. P. Speiser, Sink conditions in the flow-through cell during dissolution, *Int. J. Pharm.*, 1980, **5**, 101–107.
127 D. Hörter and J. B. Dressman, Influence of physicochemical properties on dissolution of drugs in the gastrointestinal tract, *Adv. Drug Deliv. Rev.*, 2001, **46**, 75–87.
128 S. Cammarn, Predicting dissolution via hydrodynamics: salicylic acid tablets in flow through cell dissolution, *Int. J. Pharm.*, 2000, **201**, 199–209.

129 D. M. D'Arcy, B. Liu, G. Bradley, A. M. Healy and O. I. Corrigan, Hydrodynamic and species transfer simulations in the USP 4 dissolution apparatus: considerations for dissolution in a low velocity pulsing flow, *Pharm. Res.*, 2010, **27**, 246–258.

130 D. C. Cox and W. B. Furman, Systematic Error Associated with Apparatus 2 of the USP Dissolution Test I: Effects of Physical Alignment of the Dissolution Apparatus, *J. Pharm. Sci.*, 1982, **71**, 451–452.

131 D. C. Cox, C. E. Wells, W. B. Furman, T. S. Savage and A. C. King, Systematic Error Associated with Apparatus 2 of the USP Dissolution Test II: Effects of Deviations in Vessel Curvature from That of a Sphere, *J. Pharm. Sci.*, 1982, **71**, 395–399.

132 S. A. Qureshi and I. J. McGilveray, Typical variability in drug dissolution testing: study with USP and FDA calibrator tablets and a marketed drug (glibenclamide) product, *Eur. J. Pharm. Sci. Off. J. Eur. Fed. Pharm. Sci.*, 1999, **7**, 249–258.

133 S. A. Qureshi and J. Shabnam, Cause of high variability in drug dissolution testing and its impact on setting tolerances, *Eur. J. Pharm. Sci. Off. J. Eur. Fed. Pharm. Sci.*, 2001, **12**, 271–276.

134 Z. Gao, T. W. Moore, L. F. Buhse and W. H. Doub, The Random Vibration Effects on Dissolution Testing with USP Apparatus 2, *J. Pharm. Sci.*, 2009, **98**, 297–306.

135 L. Zhang, K. Ha, B. Kleintop and S. Phillips, Differences in In Vitro Dissolution Rates Using Single-Point and Multi-Point Sampling, *Dissolution Technol.*, 2007, **14**, 27–31.

136 M. G. Issa and H. G. Ferraz, Intrinsic Dissolution as a Tool for Evaluating Drug Solubility in Accordance with the Biopharmaceutics Classification System, *Dissolution Technol.*, 2011, **18**, 6–13.

137 P. Zakeri-Milani, M. Barzegar-Jalali, M. Azimi and H. Valizadeh, Biopharmaceutical classification of drugs using intrinsic dissolution rate (IDR) and rat intestinal permeability, *Eur. J. Pharm. Biopharm.*, 2009, **73**, 102–106.

138 C. A. S. Bergström, K. Box, R. Holm, W. Matthews, M. McAllister, A. Müllertz, T. Rades, K. J. Schäfer and A. Teleki, Biorelevant intrinsic dissolution profiling in early drug development: Fundamental, methodological, and industrial aspects, *Eur. J. Pharm. Biopharm.*, 2019, **139**, 101–114.

139 A. Khan, Z. Iqbal, I. Khan, A. Khan, L. Ahmad, M. A. Mughal, A. Ullah and M. Kakar, Intrinsic dissolution testing: A tool for determining the effect of processing on dissolution behavior of the drug, *Dissolution Technol.*, 2017, **24**, 14–22.

140 L. X. Yu, A. S. Carlin, G. L. Amidon and A. S. Hussain, Feasibility studies of utilizing disk intrinsic dissolution rate to classify drugs, *Int. J. Pharm.*, 2004, **270**, 221–227.

141 J. H. Wood, J. E. Syarto and H. Letterman, Improved Holder for Intrinsic Dissolution Rate Studies, *J. Pharm. Sci.*, 1965, **54**, 1068.

142 A. Avdeef and O. Tsinman, Miniaturized Rotating Disk Intrinsic Dissolution Rate Measurement: Effects of Buffer Capacity in Comparisons to Traditional Wood's Apparatus, *Pharm. Res.*, 2008, **25**, 2613–2627.

143 K. Tsinman, A. Avdeef, O. Tsinman and D. Voloboy, Powder Dissolution Method for Estimating Rotating Disk Intrinsic Dissolution Rates of Low Solubility Drugs, *Pharm. Res.*, 2009, **26**, 2093–2100.

144 Y.-C. Tseng, M. Patel and Y. Zhao, Determination of Intrinsic Dissolution Rate Using Miniaturized Rotating and Stationary Disk Systems, *Dissolution Technol.*, 2014, **21**, 24–29.

145 W. L. Hulse, J. Gray and R. T. Forbes, A discriminatory intrinsic dissolution study using UV area imaging analysis to gain additional insights into the dissolution behaviour of active pharmaceutical ingredients, *Int. J. Pharm.*, 2012, **434**, 133–139.
146 B. Shekunov and E. R. Montgomery, Theoretical Analysis of Drug Dissolution: I. Solubility and Intrinsic Dissolution Rate, *J. Pharm. Sci.*, 2016, **105**, 2685–2697.
147 K. Etherson, C. Dunn, W. Matthews, H. Pamelund, C. Barragat, N. Sanderson, T. Izumi, C. da C. Mathews, G. Halbert, C. Wilson, M. McAllister, J. Mann, J. Østergaard, J. Butler and I. Khadra, An interlaboratory investigation of intrinsic dissolution rate determination using surface dissolution, *Eur. J. Pharm. Biopharm.*, 2020, **150**, 24–32.
148 L. Z. Benet, The Role of BCS (Biopharmaceutics Classification System) and BDDCS (Biopharmaceutics Drug Disposition Classification System) in Drug Development, *J. Pharm. Sci.*, 2013, **102**, 34–42.
149 J. Alsenz, E. Haenel, A. Anedda, P. Du Castel and G. Cirelli, Miniaturized INtrinsic DISsolution Screening (MINDISS) assay for preformulation, *Eur. J. Pharm. Sci.*, 2016, **87**, 3–13.
150 A. Ward, K. Walton, K. Box, J. Østergaard, L. J. Gillie, B. R. Conway and K. Asare-Addo, Variable-focus microscopy and UV surface dissolution imaging as complementary techniques in intrinsic dissolution rate determination, *Int. J. Pharm.*, 2017, **530**, 139–144.
151 A. Ward, K. Walton, N. Mawla, W. Kaialy, L. Liu, P. Timmins, B. R. Conway and K. Asare-Addo, Development of a novel method utilising dissolution imaging for the measurement of swelling behaviour in hydrophilic matrices, *Int. J. Pharm. X*, 2019, **1**, 100013.
152 K. Asare-Addo, M. Alshafiee, K. Walton, A. Ward, A.-M. Totea, S. Taheri, N. Mawla, A. O. Adebisi, S. Elawad, C. Diza, P. Timmins and B. R. Conway, Effect of preparation method on the surface properties and UV imaging of indomethacin solid dispersions, *Eur. J. Pharm. Biopharm.*, 2019, **137**, 148–163.
153 H.-H. Perkampus, *UV-VIS Spectroscopy and Its Applications*, Springer Berlin Heidelberg, Berlin, Heidelberg, 1992.
154 L. M. Harwood and T. D. W. Claridge, *Introduction to organic spectroscopy*, Oxford Univ. Press, Oxford, Repr., 2003.
155 T. Soderberg, in *Organic Chemistry with a Biological Emphasis*, University of Minnesota, Morris, vol. [Internet].
156 P. W. Atkins, in *Physical chemistry*, Oxford Univ. Press, Oxford, 2001.
157 S. F. Dyke, Ed., *Organic spectroscopy: an introduction*, Penguin, Harmondsworth, 1971.
158 A. F. Marais, M. Song and M. M. De Villiers, Effect of compression force, humidity and disintegrant concentration on the disintegration and dissolution of directly compressed furosemide tablets using croscarmellose sodium as disintegrant, *Trop. J. Pharm. Res.*, , DOI:10.4314/tjpr.v2i1.14577.
159 W. L. Bell, I. L. Crawford and G. K. Shiu, Reduced Bioavailability of Moisture-Exposed Carbamazepine Resulting in Status Epilepticus, *Epilepsia*, 1993, **34**, 1102–1104.
160 A. J. S. Chapman and D. M. Goodall, A novel approach to measurement of hydrodynamic radius for a standard protein using UV area imaging detection,

http://www.chromatographytoday.com/article/autosamplers/36/paraytec-ltd/a-novel-approach-to-measurement-of-hydrodynamic-radius-for-a-standard-protein-using-uv-area-imaging-detection/522, (accessed 1 April 2020).
161 S. Wren and J. Lenke, Pharmaceutical Dissolution and UV Imaging, https://americanlaboratory.com/914-Application-Notes/1108-Pharmaceutical-Dissolution-and-UV-Imaging/, (accessed 8 July 2019).
162 X. Lu and C. A. Zordan, From Detection to Imaging: UV Spectroscopy for Dissolution in Pharmaceutical Development, https://www.americanpharmaceuticalreview.com/Featured-Articles/177714-From-Detection-to-Imaging-UV-Spectroscopy-for-Dissolution-in-Pharmaceutical-Development/, (accessed 7 August 2019).
163 J. Østergaard, J. Lenke, Y. Sun and F. Ye, UV Imaging for In Vitro Dissolution and Release Studies: Initial Experiences, *Dissolution Technol.*, 2014, **21**, 27–38.
164 J. P. Boetker, J. Rantanen, T. Rades, A. Müllertz, J. Østergaard and H. Jensen, A New Approach to Dissolution Testing by UV Imaging and Finite Element Simulations, *Pharm. Res.*, 2013, **30**, 1328–1337.
165 J. Østergaard, J. X. Wu, K. Naelapää, J. P. Boetker, H. Jensen and J. Rantanen, Simultaneous UV Imaging and Raman Spectroscopy for the Measurement of Solvent-Mediated Phase Transformations During Dissolution Testing, *J. Pharm. Sci.*, 2014, **103**, 1149–1156.
166 J. Østergaard, H. Jensen, S. W. Larsen, C. Larsen and J. Lenke, Microenvironmental pH measurement during sodium naproxenate dissolution in acidic medium by UV/vis imaging, *J. Pharm. Biomed. Anal.*, 2014, **100**, 290–293.
167 Y. Sun and J. Østergaard, Application of UV Imaging in Formulation Development, *Pharm. Res.*, 2017, **34**, 929–940.
168 Pion UK Ltd, *SDi2 Instruction Manual Rev 4*, 2019.
169 S. S. Jensen, H. Jensen, D. M. Goodall and J. Østergaard, Performance characteristics of UV imaging instrumentation for diffusion, dissolution and release testing studies, *J. Pharm. Biomed. Anal.*, 2016, **131**, 113–123.
170 Y. Sun, A. Chapman, S. W. Larsen, H. Jensen, N. J. Petersen, D. M. Goodall and J. Østergaard, UV–vis Imaging of Piroxicam Supersaturation, Precipitation, and Dissolution in a Flow-Through Setup, *Anal. Chem.*, 2018, **90**, 6413–6418.
171 A. Müllertz, Y. Perrie and T. Rades, Eds., *Analytical techniques in the pharmaceutical sciences*, Springer, New York, 2016.
172 T. Felicijan, A. Krese, A. Mrhar and M. Bogataj, Applicability of Bottom-View Cameras for Evaluation of Tablet Performance During Dissolution Testing, *Dissolution Technol.*, 2016, **23**, 24–32.
173 K. G. Nelson and A. C. Shah, Convective diffusion model for a transport-controlled dissolution rate process, *J. Pharm. Sci.*, 1975, **64**, 610–614.
174 K. G. Nelson and A. C. Shah, Evaluation of a Convective Diffusion Drug Dissolution Rate Model, *J. Pharm. Sci.*, 1975, **64**, 1518–1520.
175 J. Lenke, in *Two Dimensional Orthogonal Imaging of Laminar Fluid Flow across API Surface: Insight into Dosage Concentration inside GI Lumen and Permeability*, MDPI, Sciforum, 2011, p. 523.
176 H.-K. Chan and D. J. W. Grant, Influence of compaction on the intrinsic dissolution rate of modified acetaminophen and adipic acid crystals, *Int. J. Pharm.*, 1989, **57**, 117–124.

177 K. Löbmann, K. Flouda, D. Qiu, T. Tsolakou, W. Wang and T. Rades, The Influence of Pressure on the Intrinsic Dissolution Rate of Amorphous Indomethacin, *Pharmaceutics*, 2014, **6**, 481–493.
178 M. Kakhi, Classification of the flow regimes in the flow-through cell, *Eur. J. Pharm. Sci.*, 2009, **37**, 531–544.
179 J. Kukura, P. E. Arratia, E. S. Szalai and F. J. Muzzio, Engineering Tools for Understanding the Hydrodynamics of Dissolution Tests, *Drug Dev. Ind. Pharm.*, 2003, **29**, 231–239.
180 J. L. Baxter, J. Kukura and F. J. Muzzio, Hydrodynamics-induced variability in the USP apparatus II dissolution test, *Int. J. Pharm.*, 2005, **292**, 17–28.
181 G. Shiko, L. F. Gladden, A. J. Sederman, P. C. Connolly and J. M. Butler, MRI Studies of the Hydrodynamics in a USP 4 Dissolution Testing Cell, *J. Pharm. Sci.*, 2011, **100**, 976–991.
182 V. Todaro, T. Persoons, G. Grove, A. M. Healy and D. M. D'Arcy, Characterization and Simulation of Hydrodynamics in the Paddle, Basket and Flow-Through Dissolution Testing Apparatuses - A Review, *Dissolution Technol.*, 2017, **24**, 24–36.
183 K. Kaufmann, CMOS Technology for Scientific Imaging, http://www.spectroscopyonline.com/cmos-technology-scientific-imaging?date=&id=&pageID=3&sk=, (accessed 1 April 2020).
184 Sirius Analytical Application Notes, https://pion-inc.com/resources/resource-library, (accessed 1 June 2020).
185 T. N. Hiew, M. I. B. Alaudin, S. M. Chua and P. W. S. Heng, A study of the impact of excipient shielding on initial drug release using UV imaging, *Int. J. Pharm.*, 2018, **553**, 229–237.
186 Y. Lu and M. Li, Simultaneous Rapid Determination of the Solubility and Diffusion Coefficients of a Poorly Water-Soluble Drug Based on a Novel UV Imaging System, *J. Pharm. Sci.*, 2016, **105**, 131–138.
187 A. Niederquell and M. Kuentz, Biorelevant dissolution of poorly soluble weak acids studied by UV imaging reveals ranges of fractal-like kinetics, *Int. J. Pharm.*, 2014, **463**, 38–49.
188 K. Asare-Addo, K. Walton, A. Ward, A.-M. Totea, S. Taheri, M. Alshafiee, N. Mawla, A. Bondi, W. Evans, A. Adebisi, B. R. Conway and P. Timmins, Direct imaging of the dissolution of salt forms of a carboxylic acid drug, *Int. J. Pharm.*, 2018, **551**, 290–299.
189 S. Gordon, K. Naelapää, J. Rantanen, A. Selen, A. Müllertz and J. Østergaard, Real-time dissolution behavior of furosemide in biorelevant media as determined by UV imaging, *Pharm. Dev. Technol.*, 2013, **18**, 1407–1416.
190 L. H. Nielsen, S. Gordon, J. P. Pajander, J. Østergaard, T. Rades and A. Müllertz, Biorelevant characterisation of amorphous furosemide salt exhibits conversion to a furosemide hydrate during dissolution, *Int. J. Pharm.*, 2013, **457**, 14–24.
191 N. Qiao, K. Wang, W. Schlindwein, A. Davies and M. Li, In situ monitoring of carbamazepine–nicotinamide cocrystal intrinsic dissolution behaviour, *Eur. J. Pharm. Biopharm.*, 2013, **83**, 415–426.
192 P. Madelung, P. Bertelsen, J. Jacobsen, A. Müllertz and J. Østergaard, Dissolution enhancement of griseofulvin from griseofulvin-sodium dodecyl sulfate discs investigated by UV imaging, *J. Drug Deliv. Sci. Technol.*, 2017, **39**, 516–522.

193 J. Østergaard, E. Meng-Lund, S. W. Larsen, C. Larsen, K. Petersson, J. Lenke and H. Jensen, Real-Time UV Imaging of Nicotine Release from Transdermal Patch, *Pharm. Res.*, 2010, **27**, 2614–2623.
194 J.-X. Chen, Z. Guo, H.-Y. Li, L. Wu, Z.-G. He, R.-F. Hu and J.-W. Zhang, [Real-time UV imaging of chloramphenicol intrinsic dissolution characteristics from ophthalmic in situ gel], *Yao Xue Xue Bao*, 2013, **48**, 1156–1163.
195 S. S. Jensen, H. Jensen, E. H. Møller, C. Cornett, F. Siepmann, J. Siepmann and J. Østergaard, In vitro release studies of insulin from lipid implants in solution and in a hydrogel matrix mimicking the subcutis, *Eur. J. Pharm. Sci.*, 2016, **81**, 103–112.
196 Y. Sun, H. Jensen, N. J. Petersen, S. W. Larsen and J. Østergaard, Phase separation of in situ forming poly (lactide-co-glycolide acid) implants investigated using a hydrogel-based subcutaneous tissue surrogate and UV–vis imaging, *J. Pharm. Biomed. Anal.*, 2017, **145**, 682–691.
197 F. Ye, S. W. Larsen, A. Yaghmur, H. Jensen, C. Larsen and J. Østergaard, Real-time UV imaging of piroxicam diffusion and distribution from oil solutions into gels mimicking the subcutaneous matrix, *Eur. J. Pharm. Sci.*, 2012, **46**, 72–78.
198 S. S. Jensen, H. Jensen, C. Cornett, E. H. Møller and J. Østergaard, Insulin diffusion and self-association characterized by real-time UV imaging and Taylor dispersion analysis, *J. Pharm. Biomed. Anal.*, 2014, **92**, 203–210.
199 S. S. Jensen, H. Jensen, C. Cornett, E. H. Møller and J. Østergaard, Real-time UV imaging identifies the role of pH in insulin dissolution behavior in hydrogel-based subcutaneous tissue surrogate, *Eur. J. Pharm. Sci.*, 2015, **69**, 26–36.
200 C. M. Long, K. Tang, H. Chokshi and N. Fotaki, Surface Dissolution UV Imaging for Investigation of Dissolution of Poorly Soluble Drugs and Their Amorphous Formulation, *AAPS PharmSciTech*, , DOI:10.1208/s12249-019-1317-z.
201 P. Zarmpi, T. Flanagan, E. Meehan, J. Mann and N. Fotaki, Surface dissolution UV imaging for characterization of superdisintegrants and their impact on drug dissolution, *Int. J. Pharm.*, 2020, **577**, 119080.
202 A. Sarnes, J. Østergaard, S. S. Jensen, J. Aaltonen, J. Rantanen, J. Hirvonen and L. Peltonen, Dissolution study of nanocrystal powders of a poorly soluble drug by UV imaging and channel flow methods, *Eur. J. Pharm. Sci.*, 2013, **50**, 511–519.
203 P. R. Unwin and J. V. Macpherson, New strategies for probing crystal dissolution kinetics at the microscopic level, *Chem. Soc. Rev.*, 1995, **24**, 109–119.
204 K. V. R. Prasad, R. I. Ristic, D. B. Sheen and J. N. Sherwood, Dissolution kinetics of paracetamol single crystals, *Int. J. Pharm.*, 2002, **238**, 29–41.
205 J. N. Clark, J. Ihli, A. S. Schenk, Y.-Y. Kim, A. N. Kulak, J. M. Campbell, G. Nisbet, F. C. Meldrum and I. K. Robinson, Three-dimensional imaging of dislocation propagation during crystal growth and dissolution, *Nat. Mater.*, 2015, **14**, 780–784.
206 T. H. Muster and C. A. Prestidge, Face specific surface properties of pharmaceutical crystals, *J. Pharm. Sci.*, 2002, **91**, 1432–1444.
207 Y. Kim, M. Matsumoto and K. Machida, Specific surface energies and dissolution behavior of aspirin crystal., *Chem. Pharm. Bull. (Tokyo)*, 1985, **33**, 4125–4131.
208 J. Y. Y. Heng, A. Bismarck, A. F. Lee, K. Wilson and D. R. Williams, Anisotropic Surface Energetics and Wettability of Macroscopic Form I Paracetamol Crystals, *Langmuir*, 2006, **22**, 2760–2769.

209 A. Danesh, S. D. Connell, M. C. Davies, C. J. Roberts, S. J. Tendler, P. M. Williams and M. J. Wilkins, An in situ dissolution study of aspirin crystal planes (100) and (001) by atomic force microscopy, *Pharm. Res.*, 2001, **18**, 299–303.
210 S. Svanbäck, H. Ehlers and J. Yliruusi, Optical microscopy as a comparative analytical technique for single-particle dissolution studies, *Int. J. Pharm.*, 2014, **469**, 10–16.
211 S. Svanbäck, H. Ehlers, O. Antikainen and J. Yliruusi, High-Speed Intrinsic Dissolution Rate in One Minute Using the Single-Particle Intrinsic Dissolution Rate Method, *Anal. Chem.*, 2015, **87**, 11058–11064.
212 M. Adobes-Vidal, F. M. Maddar, D. Momotenko, L. P. Hughes, S. A. C. Wren, L. N. Poloni, M. D. Ward and P. R. Unwin, Face-Discriminating Dissolution Kinetics of Furosemide Single Crystals: In Situ Three-Dimensional Multi-Microscopy and Modeling, *Cryst. Growth Des.*, 2016, **16**, 4421–4429.
213 F. M. Maddar, M. Adobes-Vidal, L. P. Hughes, S. A. C. Wren and P. R. Unwin, Dissolution of Bicalutamide Single Crystals in Aqueous Solution: Significance of Evolving Topography in Accelerating Face-Specific Kinetics, *Cryst. Growth Des.*, 2017, **17**, 5108–5116.
214 M. Guo, K. Wang, N. Qiao, V. Yardley and M. Li, Investigating Permeation Behavior of Flufenamic Acid Cocrystals Using a Dissolution and Permeation System, *Mol. Pharm.*, 2018, **15**, 4257–4272.
215 A. R. Pallipurath, J. M. Skelton, A. Erxleben and P. McArdle, Shining Light on Growth-Dependent Surface Chemistry of Organic Crystals: A Polarized Raman Spectroscopic and Computational Study of Aspirin, *Cryst. Growth Des.*, 2019, **19**, 1288–1298.
216 J. Østergaard, F. Ye, J. Rantanen, A. Yaghmur, S. W. Larsen, C. Larsen and H. Jensen, Monitoring lidocaine single-crystal dissolution by ultraviolet imaging, *J. Pharm. Sci.*, 2011, **100**, 3405–3410.
217 Q. Wang, D. Ma and J. P. Higgins, Analytical Method Selection for Drug Product Dissolution Testing, *Dissolution Technol.*, 2006, **13**, 6–13.
218 Q. Wang, J.-G. Zhao, J. M. Ballard, S. M. Shambor, E. W. Tsai and D. Ip, Purdue University, 1999.
219 X.-Z. Qin, E. W. Tsai, T. Sakuma and D. P. Ip, Pharmaceutical application of liquid chromatography-mass spectrometry, *J. Chromatogr. A*, 1994, **686**, 205–212.
220 E. Hoti, R. Censi, M. Ricciutelli, L. Malaj, L. Barboni, S. Martelli, M. Valleri and P. Di Martino, Validation of an HPLC–MS method for rociverine tablet dissolution analysis, *J. Pharm. Biomed. Anal.*, 2008, **47**, 422–428.
221 M. Kovačevič, A. Gartner and M. Novič, Determination of bisphosphonates by ion chromatography–inductively coupled plasma mass spectrometry, *J. Chromatogr. A*, 2004, **1039**, 77–82.
222 G. Lamprecht, In vitro Determination of the Release of Alendronic Acid from Alendronate Tablets of Different Brands During Deglutition, *J. Pharm. Sci.*, 2009, **98**, 3575–3581.
223 C. K. Zacharis and P. D. Tzanavaras, Determination of bisphosphonate active pharmaceutical ingredients in pharmaceuticals and biological material: A review of analytical methods, *J. Pharm. Biomed. Anal.*, 2008, **48**, 483–496.
224 Z. Ouyang and R. G. Cooks, Miniature Mass Spectrometers, *Annu. Rev. Anal. Chem.*, 2009, **2**, 187–214.

225 W. Xu, N. E. Manicke, G. R. Cooks and Z. Ouyang, Miniaturization of Mass Spectrometry Analysis Systems, *J. Assoc. Lab. Autom.*, 2010, **15**, 433–439.
226 X. Bu, E. L. Regalado, S. E. Hamilton and C. J. Welch, The emergence of low-cost compact mass spectrometry detectors for chromatographic analysis, *TrAC Trends Anal. Chem.*, 2016, **82**, 22–34.
227 D. T. Snyder, C. J. Pulliam, Z. Ouyang and R. G. Cooks, Miniature and Fieldable Mass Spectrometers: Recent Advances, *Anal. Chem.*, 2016, **88**, 2–29.
228 A. Ray, T. Bristow, C. Whitmore and J. Mosely, On-line reaction monitoring by mass spectrometry, modern approaches for the analysis of chemical reactions, *Mass Spectrom. Rev.*, 2018, **37**, 565–579.
229 D. L. Browne, S. Wright, B. J. Deadman, S. Dunnage, I. R. Baxendale, R. M. Turner and S. V. Ley, Continuous flow reaction monitoring using an on-line miniature mass spectrometer: Continuous flow mass spectrometry, *Rapid Commun. Mass Spectrom.*, 2012, **26**, 1999–2010.
230 T. W. T. Bristow, A. D. Ray, A. O'Kearney-McMullan, L. Lim, B. McCullough and A. Zammataro, On-line Monitoring of Continuous Flow Chemical Synthesis Using a Portable, Small Footprint Mass Spectrometer, *J. Am. Soc. Mass Spectrom.*, 2014, **25**, 1794–1802.
231 M. Sargent, *Guide to achieving reliable quantitative LC-MS measurements*, RSC Analytical Methods Committee, 1st Ed., 2013.
232 I. Nir and X. Lu, In Situ UV Fiber Optics for Dissolution Testing – What, Why, and Where We Are After 30 Years, *Dissolution Technol.*, 2018, **25**, 70–77.
233 E. de Hoffmann and V. Stroobant, *Mass spectrometry: principles and applications*, J. Wiley, Chichester, West Sussex, England ; Hoboken, NJ, 3rd edn., 2007.
234 Great Britain and Department of Trade and Industry, *Best practice guide for generating mass spectra*, LGC, Teddington, 2006.
235 L. Konermann, E. Ahadi, A. D. Rodriguez and S. Vahidi, Unraveling the Mechanism of Electrospray Ionization, *Anal. Chem.*, 2013, **85**, 2–9.
236 A. P. Bruins, Mechanistic aspects of electrospray ionization, *J. Chromatogr. A*, 1998, **794**, 345–357.
237 M. Wilm, Principles of Electrospray Ionization, *Mol. Cell. Proteomics*, 2011, **10**, M111.009407.
238 M. Dole, L. L. Mack, R. L. Hines, R. C. Mobley, L. D. Ferguson and M. B. Alice, Molecular Beams of Macroions, *J. Chem. Phys.*, 1968, **49**, 2240–2249.
239 M. Yamashita and J. B. Fenn, Electrospray ion source. Another variation on the free-jet theme, *J. Phys. Chem.*, 1984, **88**, 4451–4459.
240 C. M. Whitehouse, R. N. Dreyer, Masamichi. Yamashita and J. B. Fenn, Electrospray interface for liquid chromatographs and mass spectrometers, *Anal. Chem.*, 1985, **57**, 675–679.
241 S. J. Gaskell, SPECIAL FEATURE: TUTORIAL Electrospray: Principles and Practice, *J. Mass Spectrom.*, 1997, **32**, 677–688.
242 P. Kebarle and U. H. Verkerk, Electrospray: From ions in solution to ions in the gas phase, what we know now, *Mass Spectrom. Rev.*, 2009, **28**, 898–917.
243 T. M. Annesley, Ion suppression in mass spectrometry, *Clin. Chem.*, 2003, **49**, 1041–1044.

244 T. R. Covey, B. A. Thomson and B. B. Schneider, Atmospheric pressure ion sources, *Mass Spectrom. Rev.*, 2009, **28**, 870–897.
245 P. Kebarle and L. Tang, From ions in solution to ions in the gas phase - the mechanism of electrospray mass spectrometry, *Anal. Chem.*, 1993, **65**, 972A-986A.
246 P. Kebarle and M. Peschke, On the mechanisms by which the charged droplets produced by electrospray lead to gas phase ions, *Anal. Chim. Acta*, 2000, **406**, 11–35.
247 N. B. Cech and C. G. Enke, Practical implications of some recent studies in electrospray ionization fundamentals, *Mass Spectrom. Rev.*, 2001, **20**, 362–387.
248 A. T. Blades, M. G. Ikonomou and Paul. Kebarle, Mechanism of electrospray mass spectrometry. Electrospray as an electrolysis cell, *Anal. Chem.*, 1991, **63**, 2109–2114.
249 E. D. B. Foley, M. A. Zenaidee, R. F. Tabor, J. Ho, J. E. Beves and W. A. Donald, On the mechanism of protein supercharging in electrospray ionisation mass spectrometry: Effects on charging of additives with short- and long-chain alkyl constituents with carbonate and sulphite terminal groups, *Anal. Chim. Acta X*, 2019, **1**, 100004.
250 L. Konermann, H. Metwally, Q. Duez and I. Peters, Charging and supercharging of proteins for mass spectrometry: recent insights into the mechanisms of electrospray ionization, *The Analyst*, 2019, **144**, 6157–6171.
251 I. Peters, H. Metwally and L. Konermann, Mechanism of Electrospray Supercharging for Unfolded Proteins: Solvent-Mediated Stabilization of Protonated Sites During Chain Ejection, *Anal. Chem.*, 2019, acs.analchem.9b01470.
252 D. W. Koppenaal, C. J. Barinaga, M. B. Denton, R. P. Sperline, G. M. Hieftje, G. D. Schilling, F. J. Andrade, J. H. Barnes and I. Iv, MS Detectors, *Anal. Chem.*, 2005, **77**, 418 A-427 A.
253 A. G. Marshall, G. T. Blakney, T. Chen, N. K. Kaiser, A. M. McKenna, R. P. Rodgers, B. M. Ruddy and F. Xian, Mass Resolution and Mass Accuracy: How Much Is Enough?, *Mass Spectrom.*, 2013, **2**, S0009–S0009.
254 H. Stahnke, S. Kittlaus, G. Kempe, C. Hemmerling and L. Alder, The influence of electrospray ion source design on matrix effects: Influence of ESI source design on matrix effects, *J. Mass Spectrom.*, 2012, **47**, 875–884.
255 J. Liigand, A. Kruve, I. Leito, M. Girod and R. Antoine, Effect of Mobile Phase on Electrospray Ionization Efficiency, *J. Am. Soc. Mass Spectrom.*, 2014, **25**, 1853–1861.
256 J. B. Fenn, Ion formation from charged droplets: roles of geometry, energy, and time, *J. Am. Soc. Mass Spectrom.*, 1993, **4**, 524–535.
257 C. R. Mallet, Z. Lu and J. R. Mazzeo, A study of ion suppression effects in electrospray ionization from mobile phase additives and solid-phase extracts, *Rapid Commun. Mass Spectrom.*, 2004, **18**, 49–58.
258 H. Mei, Y. Hsieh, C. Nardo, X. Xu, S. Wang, K. Ng and W. A. Korfmacher, Investigation of matrix effects in bioanalytical high-performance liquid chromatography/tandem mass spectrometric assays: application to drug discovery, *Rapid Commun. Mass Spectrom.*, 2003, **17**, 97–103.

259 M. Oss, A. Kruve, K. Herodes and I. Leito, Electrospray Ionization Efficiency Scale of Organic Compounds, *Anal. Chem.*, 2010, **82**, 2865–2872.
260 S. B. E. Andersson, C. Alvebratt, J. Bevernage, D. Bonneau, C. da Costa Mathews, R. Dattani, K. Edueng, Y. He, R. Holm, C. Madsen, T. Müller, U. Muenster, A. Müllertz, K. Ojala, T. Rades, P. Sieger and C. A. S. Bergström, Interlaboratory Validation of Small-Scale Solubility and Dissolution Measurements of Poorly Water-Soluble Drugs, *J. Pharm. Sci.*, 2016, **105**, 2864–2872.
261 X. Zheng and Z. Silber-Li, Measurement of velocity profiles in a rectangular microchannel with aspect ratio α = 0.35, *Exp. Fluids*, 2008, **44**, 951–959.
262 P. Bukovec, A. Meden, M. Smrkolj and F. Vrečer, Influence of Crystal Habit on the Dissolution of Simvastatin Single Crystals, *Acta Chim. Slov.*, 2015, 958–966.
263 R. B. Hammond, K. Pencheva, K. J. Roberts and T. Auffret, Quantifying solubility enhancement due to particle size reduction and crystal habit modification: Case study of acetyl salicylic acid, *J. Pharm. Sci.*, 2007, **96**, 1967–1973.
264 P. Espeau, R. Céolin, J. Tamarit, M. Perrin, J. Gauchi and F. Leveiller, Polymorphism of paracetamol: Relative stabilities of the monoclinic and orthorhombic phases inferred from topological pressure-temperature and temperature-volume phase diagrams, *J. Pharm. Sci.*, 2005, **94**, 524–539.
265 M.-A. Perrin, M. A. Neumann, H. Elmaleh and L. Zaske, Crystal structure determination of the elusive paracetamol Form III, *Chem. Commun.*, 2009, 3181.
266 L. R. Agnew, T. McGlone, H. P. Wheatcroft, A. Robertson, A. R. Parsons and C. C. Wilson, Continuous Crystallization of Paracetamol (Acetaminophen) Form II: Selective Access to a Metastable Solid Form, *Cryst. Growth Des.*, 2017, **17**, 2418–2427.
267 K. Greco, T. L. Bergman and R. Bogner, Design and characterization of a laminar flow-through dissolution apparatus: Comparison of hydrodynamic conditions to those of common dissolution techniques, *Pharm. Dev. Technol.*, 2011, **16**, 75–87.
268 Massachusetts Institute of Technology, *Illustrated Experiments in Fluid Mechanics: The National Committee of Fluid Mechanics Films and the Book of Film Notes*, 2008.
269 Pion UK Ltd, SDi2 Brochure, https://pion-inc.com/resources/resource-library/sdi2-brochure, (accessed 23 September 2020).
270 S. H. Yalkowsky, Y. He and P. Jain, *Handbook of aqueous solubility data*, CRC Press, Boca Raton (Fla.); London; New York (N.Y.), 2010.
271 J. L. Andrews, Durham Theses, Durham University, 2020.
272 J. L. Andrews, E. Pearson, D. S. Yufit, J. W. Steed and K. Edkins, Supramolecular Gelation as the First Stage in Ostwald's Rule, *Cryst. Growth Des.*, 2018, **18**, 7690–7700.
273 C. Gu and D. J. W. Grant, Estimating the relative stability of polymorphs and hydrates from heats of solution and solubility data, *J. Pharm. Sci.*, 2001, **90**, 1277–1287.
274 S. E. Wolkenberg, D. D. Wisnoski, W. H. Leister, Y. Wang, Z. Zhao and C. W. Lindsley, Efficient Synthesis of Imidazoles from Aldehydes and 1,2-Diketones Using Microwave Irradiation, *Org. Lett.*, 2004, **6**, 1453–1456.
275 P. J. Taylor, Matrix effects: the Achilles heel of quantitative high-performance liquid chromatography–electrospray–tandem mass spectrometry, *Clin. Biochem.*, 2005, **38**, 328–334.

276 J. N. Miller and J. C. Miller, *Statistics and chemometrics for analytical chemistry*, Prentice Hall, Harlow, 6. ed., 2010.
277 K. Kiehm and J. B. Dressman, Evaluation of Drug Adsorption to Membrane Filters under Biowaiver Test Conditions, *Dissolution Technol.*, 2008, **15**, 13–17.
278 M. Lindenberg, C. Wiegand and J. B. Dressman, Comparison of the Adsorption of Several Drugs to Typical Filter Materials, *Dissolution Technol.*, 2005, **1**, 22–25.
279 V. Joshi, J. Blodgett, J. George and J. Brinker, Impact of Sample Preparation on Dissolution Testing: Drug Binding and Extractable Impurities and Their Effect on Dissolution Data, *Dissolution Technol.*, 2008, **15**, 20–27.
280 J. C. Tran and A. A. Doucette, Cyclic polyamide oligomers extracted from nylon 66 membrane filter disks as a source of contamination in liquid chromatography/mass spectrometry, *J. Am. Soc. Mass Spectrom.*, 2006, **17**, 652–656.
281 V. P. Sica, K. L. Krivos, D. E. Kiehl, C. J. Pulliam, I. D. Henry and T. R. Baker, The role of mass spectrometry and related techniques in the analysis of extractable and leachable chemicals, *Mass Spectrom. Rev.*, 2020, **39**, 212–226.
282 R. A. Meyers, Ed., *Encyclopedia of Analytical Chemistry: Applications, Theory and Instrumentation*, Wiley, 1st edn., 2006, vol. 6.
283 D. D. Sun, H. Wen and L. S. Taylor, Non-Sink Dissolution Conditions for Predicting Product Quality and In Vivo Performance of Supersaturating Drug Delivery Systems, *J. Pharm. Sci.*, 2016, **105**, 2477–2488.
284 C. A. Whitmore, Durham Theses, Durham University, 2020.
285 A. G. Marshall and F. R. Verdun, *Fourier transforms in NMR, optical, and mass spectrometry: a user's handbook*, Elsevier, Amsterdam, 1990.
286 D. Kurtz, To 'Quantify' or 'Quantitate', *Anal. Chem.*, 1982, **54**, 1456A-1458A.
287 J. R. Enders, J. P. Smith, S. Feng, E. C. Strickland and G. L. McIntire, Analytical Considerations When Developing an LC-MS/MS Method for More than 30 Analytes, *J. Appl. Lab. Med. AACC Publ.*, 2018, **2**, 543–554.
288 D. A. Armbruster and T. Pry, Limit of blank, limit of detection and limit of quantitation, *Clin. Biochem. Rev.*, 2008, **29 Suppl 1**, S49-52.
289 A. Shrivastava and V. Gupta, Methods for the determination of limit of detection and limit of quantitation of the analytical methods, *Chron. Young Sci.*, 2011, **2**, 21.
290 P. L. Urban, Quantitative mass spectrometry: an overview, *Philos. Trans. R. Soc. Math. Phys. Eng. Sci.*, 2016, **374**, 20150382.
291 N. A. Kasim, M. Whitehouse, C. Ramachandran, M. Bermejo, H. Lennernäs, A. S. Hussain, H. E. Junginger, S. A. Stavchansky, K. K. Midha, V. P. Shah and G. L. Amidon, Molecular Properties of WHO Essential Drugs and Provisional Biopharmaceutical Classification, *Mol. Pharm.*, 2004, **1**, 85–96.
292 M. Lindenberg, S. Kopp and J. B. Dressman, Classification of orally administered drugs on the World Health Organization Model list of Essential Medicines according to the biopharmaceutics classification system, *Eur. J. Pharm. Biopharm.*, 2004, **58**, 265–278.
293 BMJ Publishing Group, Royal Pharmaceutical Society of Great Britain, and British Medical Association, *British National Formulary March 2018 - September 2018. 75 75*, BMJ Group : Pharmaceutical Society of Great Britain, London, 2017.

294 T. D. Vijlder, D. Valkenborg, F. Lemière, E. P. Romijn, K. Laukens and F. Cuyckens, A tutorial in small molecule identification via electrospray ionization-mass spectrometry: The practical art of structural elucidation, *Mass Spectrom. Rev.*, 2018, **37**, 607–629.
295 I. Erngren, J. Haglöf, M. K. R. Engskog, M. Nestor, M. Hedeland, T. Arvidsson and C. Pettersson, Adduct formation in electrospray ionisation-mass spectrometry with hydrophilic interaction liquid chromatography is strongly affected by the inorganic ion concentration of the samples, *J. Chromatogr. A*, 2019, **1600**, 174–182.
296 N. Fotaki, W. Brown, J. Kochling, H. Chokshi, H. Miao, K. Tang and V. Gray, Rationale for Selection of Dissolution Media: Three Case Studies, *Dissolution Technol.*, 2013, **20**, 6–13.
297 R. Kostiainen and T. J. Kauppila, Effect of eluent on the ionization process in liquid chromatography–mass spectrometry, *J. Chromatogr. A*, 2009, **1216**, 685–699.
298 Z. Wu, W. Gao, M. A. Phelps, D. Wu, D. D. Miller and J. T. Dalton, Favorable Effects of Weak Acids on Negative-Ion Electrospray Ionization Mass Spectrometry, *Anal. Chem.*, 2004, **76**, 839–847.
299 P. Liigand, K. Kaupmees, K. Haav, J. Liigand, I. Leito, M. Girod, R. Antoine and A. Kruve, Think Negative: Finding the Best Electrospray Ionization/MS Mode for Your Analyte, *Anal. Chem.*, 2017, **89**, 5665–5668.
300 A. Kiontke, A. Oliveira-Birkmeier, A. Opitz and C. Birkemeyer, Electrospray Ionization Efficiency Is Dependent on Different Molecular Descriptors with Respect to Solvent pH and Instrumental Configuration, *PLOS ONE*, 2016, **11**, e0167502.
301 M. H. Amad, N. B. Cech, G. S. Jackson and C. G. Enke, Importance of gas-phase proton affinities in determining the electrospray ionization response for analytes and solvents, *J. Mass Spectrom. JMS*, 2000, **35**, 784–789.
302 M. A. Raji and K. A. Schug, Chemometric study of the influence of instrumental parameters on ESI-MS analyte response using full factorial design, *Int. J. Mass Spectrom.*, 2009, **279**, 100–106.
303 V. Barwick, *LGC Preparation of Calibration Curves A Guide to Best Practice*, 2003.
304 F. Raposo, Evaluation of analytical calibration based on least-squares linear regression for instrumental techniques: A tutorial review, *TrAC Trends Anal. Chem.*, 2016, **77**, 167–185.
305 L. M. Schwartz, Nonlinear calibration curves, *Anal. Chem.*, 1976, **48**, 2287–2288.
306 ICH Harmonised Tripartite Guideline: Q2 (R1) Validation of Analytical Procedures: Text and Methodology.
307 L. Bluck and D. A. Volmer, The Role of Naturally Occurring Stable Isotopes in Mass Spectrometry, Part I: The Theory, *Spectrosc. Springf. Or*, 2009, **23**, 36.
308 S.-C. Shin and J. Kim, Physicochemical characterization of solid dispersion of furosemide with TPGS, *Int. J. Pharm.*, 2003, **251**, 79–84.
309 G. E. Granero, M. R. Longhi, M. J. Mora, H. E. Junginger, K. K. Midha, V. P. Shah, S. Stavchansky, J. B. Dressman and D. M. Barends, Biowaiver Monographs for Immediate Release Solid Oral Dosage Forms: Furosemide, *J. Pharm. Sci.*, 2010, **99**, 2544–2556.

310 P. C. Rowbotham, J. B. Stanford and J. K. Sugden, Some aspects of the photochemical degradation of frusemide, *Pharm. Acta Helv.*, 1976, **51**, 304–307.
311 M. A. Gadalla and A. A. Ismail, Comparative dissolution rate studies of commercial furosemide tablets, *Pharm.*, 1981, **36**, 553–556.
312 V. K. Prasad, R. S. Rapaka, P. W. Knight and B. E. Cabana, Dissolution medium—a critical parameter to identify bioavailability problems of furosemide tablets, *Int. J. Pharm.*, 1982, **11**, 81–90.
313 M. Banik, S. P. Gopi, S. Ganguly and G. R. Desiraju, Cocrystal and Salt Forms of Furosemide: Solubility and Diffusion Variations, *Cryst. Growth Des.*, 2016, **16**, 5418–5428.
314 G. Loos, A. Van Schepdael and D. Cabooter, Quantitative mass spectrometry methods for pharmaceutical analysis, *Philos. Trans. R. Soc. Math. Phys. Eng. Sci.*, 2016, **374**, 20150366.
315 M. J. O'Neil, Ed., *The Merck index: an encyclopedia of chemicals, drugs, and biologicals*, Merck, Whitehouse Station, N.J, 13th ed., 2001.
316 K. Greco, D. P. McNamara and R. Bogner, Solution-Mediated Phase Transformation of Salts During Dissolution: Investigation Using Haloperidol as a Model Drug, *J. Pharm. Sci.*, 2011, **100**, 2755–2768.
317 S. Singh, T. Parikh, H. K. Sandhu, N. H. Shah, A. W. Malick, D. Singhal and A. T. M. Serajuddin, Supersolubilization and Amorphization of a Model Basic Drug, Haloperidol, by Interaction with Weak Acids, *Pharm. Res.*, 2013, **30**, 1561–1573.
318 J. K. Guillory, Handbook of Aqueous Solubility Data By Samuel H. Yalkowsky and Yan He. CRC Press, Boca Raton, FL. 2003. xii + 1496 pp. 18 × 26 cm. ISBN 0-89493-1532-8. $299.95., *J. Med. Chem.*, 2003, **46**, 4213–4213.
319 L. Miles, J. Hall, B. Jenner, R. Addis and S. Hutchings, Predicting rapid analgesic onset of ibuprofen salts compared with ibuprofen acid: T_{lag} , T_{low} , T_{med} , and a novel parameter, $T_{C\ maxRef}$, *Curr. Med. Res. Opin.*, 2018, **34**, 1483–1490.
320 K. Schug and H. M. McNair, Adduct formation in electrospray ionization. Part 1: Common acidic pharmaceuticals, *J. Sep. Sci.*, 2002, **25**, 759–766.
321 L. Kalantzi, C. Reppas, J. B. Dressman, G. L. Amidon, H. E. Junginger, K. K. Midha, V. P. Shah, S. A. Stavchansky and D. M. Barends, Biowaiver monographs for immediate release solid oral dosage forms: Acetaminophen (paracetamol), *J. Pharm. Sci.*, 2006, **95**, 4–14.
322 R. K. Gilpin and W. Zhou, Studies of the thermal degradation of acetaminophen using a conventional HPLC approach and electrospray ionization-mass spectrometry, *J. Chromatogr. Sci.*, 2004, **42**, 15–20.
323 C. K. Gelotte, An open-label, randomized, four-treatment crossover study evaluating the effects of salt form, acetaminophen, and food on the pharmacokinetics of phenylephrine, *Regul. Toxicol. Pharmacol.*, 2018, **95**, 333–338.
324 A. E. O'Leary, H. Oberacher, S. E. Hall and C. C. Mulligan, Combining a portable, tandem mass spectrometer with automated library searching – an important step towards streamlined, on-site identification of forensic evidence, *Anal. Methods*, 2015, **7**, 3331–3339.
325 C. F. Lerk, A. C. Andreae, A. H. Boer, G. K. Bolhuis, K. Zuurman, P. Hoog, K. Kussendrager and J. Leverink, Increased binding capacity and flowability of α-

lactose monohydrate after dehydration, *J. Pharm. Pharmacol.*, 1983, **35**, 747–748.

326 H. L. Ohrem, E. Schornick, A. Kalivoda and R. Ognibene, Why is mannitol becoming more and more popular as a pharmaceutical excipient in solid dosage forms?, *Pharm. Dev. Technol.*, 2014, **19**, 257–262.

327 X. Tan, X. Li, L. Chen and F. Xie, Solubility of starch and microcrystalline cellulose in 1-ethyl-3-methylimidazolium acetate ionic liquid and solution rheological properties, *Phys. Chem. Chem. Phys.*, 2016, **18**, 27584–27593.

328 R. Bonfiglio, R. C. King, T. V. Olah and K. Merkle, The effects of sample preparation methods on the variability of the electrospray ionization response for model drug compounds, *Rapid Commun. Mass Spectrom. RCM*, 1999, **13**, 1175–1185.

329 R. King, R. Bonfiglio, C. Fernandez-Metzler, C. Miller-Stein and T. Olah, Mechanistic investigation of ionization suppression in electrospray ionization, *J. Am. Soc. Mass Spectrom.*, 2000, **11**, 942–950.

330 J.-P. Antignac, K. de Wasch, F. Monteau, H. De Brabander, F. Andre and B. Le Bizec, The ion suppression phenomenon in liquid chromatography–mass spectrometry and its consequences in the field of residue analysis, *Anal. Chim. Acta*, 2005, **529**, 129–136.

331 S. Banerjee and S. Mazumdar, Electrospray Ionization Mass Spectrometry: A Technique to Access the Information beyond the Molecular Weight of the Analyte, *Int. J. Anal. Chem.*, 2012, **2012**, 1–40.

332 G. Wang and R. B. Cole, Mechanistic Interpretation of the Dependence of Charge State Distributions on Analyte Concentrations in Electrospray Ionization Mass Spectrometry, *Anal. Chem.*, 1995, **67**, 2892–2900.

333 L. Tang and P. Kebarle, Dependence of ion intensity in electrospray mass spectrometry on the concentration of the analytes in the electrosprayed solution, *Anal. Chem.*, 1993, **65**, 3654–3668.

334 A. Furey, M. Moriarty, V. Bane, B. Kinsella and M. Lehane, Ion suppression; A critical review on causes, evaluation, prevention and applications, *Talanta*, 2013, **115**, 104–122.

335 R. Rebane, A. Kruve, J. Liigand, P. Liigand, A. Gornischeff and I. Leito, Ionization efficiency ladders as tools for choosing ionization mode and solvent in liquid chromatography/mass spectrometry, *Rapid Commun. Mass Spectrom.*, 2019, **33**, 1834–1843.

336 H. Tong, D. Bell, K. Tabei and M. M. Siegel, Automated data massaging, interpretation, and e-mailing modules for high throughput open access mass spectrometry, *J. Am. Soc. Mass Spectrom.*, 1999, **10**, 1174–1187.

337 M. G. Ikonomou, A. T. Blades and P. Kebarle, Electrospray mass spectrometry of methanol and water solutions suppression of electric discharge with SF6 gas, *J. Am. Soc. Mass Spectrom.*, 1991, **2**, 497–505.

338 C. S. Ho, C. W. K. Lam, M. H. M. Chan, R. C. K. Cheung, L. K. Law, L. C. W. Lit, K. F. Ng, M. W. M. Suen and H. L. Tai, Electrospray ionisation mass spectrometry: principles and clinical applications, *Clin. Biochem. Rev.*, 2003, **24**, 3–12.

339 R. George, A. Haywood, S. Khan, M. Radovanovic, J. Simmonds and R. Norris, Enhancement and Suppression of Ionization in Drug Analysis Using HPLC-MS/MS

in Support of Therapeutic Drug Monitoring: A Review of Current Knowledge of Its Minimization and Assessment, *Ther. Drug Monit.*, 2018, **40**, 1–8.

340 J. Liigand, A. Kruve, P. Liigand, A. Laaniste, M. Girod, R. Antoine and I. Leito, Transferability of the Electrospray Ionization Efficiency Scale between Different Instruments, *J. Am. Soc. Mass Spectrom.*, 2015, **26**, 1923–1930.

341 L. E. Hatcher, M. R. Warren, A. R. Pallipurath, L. K. Saunders and J. M. Skelton, in *21st Century Challenges in Chemical Crystallography I*, eds. D. M. P. Mingos and P. R. Raithby, Springer International Publishing, Cham, 2020, vol. 185, pp. 199–238.

342 J. Liigand, A. Laaniste and A. Kruve, pH Effects on Electrospray Ionization Efficiency, *J. Am. Soc. Mass Spectrom.*, 2017, **28**, 461–469.